Integrative modeling of function-associated molecular recognition in protein-ligand, protein-peptide, and protein-protein complexes

Inaugural-Dissertation

zur Erlangung des Doktorgrades
der Mathematisch-Naturwissenschaftlichen Fakultät
der Heinrich-Heine-Universität Düsseldorf

vorgelegt von

Benedikt Frieg

aus Bocholt

Düsseldorf, Juni 2019

Aus dem Institut für Pharmazeutische und Medizinische Chemie
der Heinrich-Heine-Universität Düsseldorf

Gedruckt mit der Genehmigung der
Mathematisch-Naturwissenschaftlichen Fakultät der
Heinrich-Heine-Universität Düsseldorf

Berichterstatter:

1. Prof. Dr. Holger Gohlke
2. Prof. Dr. Birgit Strodel

Tag der mündlichen Prüfung: 21.11.2019

Eidesstattliche Erklärung

Ich versichere an Eides Statt, dass die vorliegende Dissertation von mir selbständig und ohne unzulässige fremde Hilfe unter Beachtung der „Grundsätze zur Sicherung guter wissenschaftlicher Praxis an der Heinrich-Heine-Universität Düsseldorf“ erstellt worden ist.

Diese Dissertation wurde in der vorgelegten oder einer ähnlichen Form noch bei keiner anderen Institution eingereicht, und es wurden bisher keine erfolglosen Promotionsversuche von mir unternommen.

Düsseldorf, im Juni 2019

„Alle sagten: Es geht nicht.
Da kam einer, der das nicht wusste und tat es einfach.“
- Goran Kikic -

TABLE OF CONTENTS

LIST OF PUBLICATIONS

This thesis is based on the following peer-reviewed publications (in chronological order):

Frieg, B., Görg, B., Homeyer, N., Keitel, V., Häussinger, D., Gohlke, H.

Molecular mechanisms of glutamine synthetase mutations that lead to clinically relevant pathologies. **PLoS Comput. Biol.** (2016), 12, e1004693.

Impact factor reported in 2016: 4.542

(B.F. performed the molecular simulations and free-energy computations, analyzed the associated data, displayed the data, and contributed to writing the manuscript)

Khosa, S.[§], **Frieg, B.**[§], Mulnaes, D., Kleinschrodt, D., Hoeppner, A., Gohlke, H., Smits, S.H.J.

Structural basis of lantibiotic recognition by the nisin resistance protein from Streptococcus agalactiae. **Sci. Rep.** (2016), 6, 18679.

Impact factor reported in 2016: 4.259

(B.F. performed the molecular simulations and free-energy computations, analyzed the associated data, displayed the data, and contributed to writing the manuscript)

Bhatia, S., Diedrich, D., **Frieg, B.**, Ahlert, H., Stein, S., Bopp, B., Lang, F., Zang, T., Kröger, T., Ernst, T., Kögler, G., Krieg, A., Lüdeke, S., Kunkel, H., Rodrigues Moita, A. J., Kassack, M. U., Marquardt, V., Opitz, F. V., Oldenburg, M., Remke, M., Babor, F., Grez, M., Hochhaus, A., Borkhardt, A., Groth, G., Nagel-Steger, L., Jose, J., Kurz, T., Gohlke, H., Hansen, F. K., Hauer, J.

Targeting HSP90's C-terminus is effective in Imatinib resistant CML and lacks heat shock response (HSR) induction. **Blood** (2018), 132, 307 – 320.

Impact factor reported in 2017: 15.132

(B.F. performed the molecular simulations and free-energy computations, analyzed the associated data, displayed the data, and contributed to writing the manuscript)

Frieg, B., Görg, B., Qvartskhava,.N, Jeitner, T., Homeyer, N., Häussinger, D., Gohlke, H. *Mechanism of fully-reversible, pH-sensitive inhibition of human glutamine synthetase by tyrosine nitration.* **submitted**.

(B.F. performed the molecular simulations and free-energy computations, analyzed the associated data, displayed the data, and contributed to writing the manuscript)

[§] Both authors contributed equally to this work.

During the time of the thesis, also the following publications resulted (in chronological order):

Peer-reviewed

Diedrich, D., Rodrigues Moita, A.J., Rüther, A., **Frieg, B.**, Reiss, G.J., Hoeppner, A., Kurz, T., Gohlke, H., Lüdeke, S., Kassack, M.U., Hansen, F. K.
α-Aminoxy oligopeptides: synthesis, secondary structure and cytotoxicity of a novel class of anticancer foldamers. **Chem. Eur. J.** (2016), 22, 17600–17611.
Impact factor reported in 2017: 5.160

Krieger, V., Ciglia, E, Thoma, R., Vasylyeva, V., **Frieg, B.**, de Sousa Amadeu, N., Kurz, T., Janiak, C., Gohlke, H., Hansen, F. K.
α-Aminoxy peptoids: A unique peptoid backbone with a preference for cis-amide bonds. **Chem. Eur. J.** (2017), 23, 3699-3707.[1]
Impact factor reported in 2017: 5.160

Kröger, T., **Frieg, B.**, Zhang, T., Hansen, F. K., Marmann, A., Proksch, P., Nagel-Steger, L., Groth, G., Smits, S. H. J., Gohlke, H.
EDTA aggregates induce SYPRO orange-based fluorescence in thermal shift assay. **PLoS ONE** (2017), 12, e0177024.
Impact factor reported in 2017: 2.766

[1] Highlighted in Angew. Chemie

Proceedings and conference contributions

Frieg, B., Homeyer, N., Gohlke, H.

Glutamine synthetase mutations that cause glutamine deficiency: mechanistic insights from molecular dynamics simulations. **Eur. J. Med. Res.** (2014), 19 (Suppl. 1), S. 15.

Frieg, B., Häussinger, D., Gohlke, H.

Towards restoring catalytic activity of glutamine synthetase with a clinically relevant mutation.

in: "**Proceedings of the NIC Symposium 2016**", Binder, K., Müller, M., Kremer, M., Schnurpfeil, A. (eds.), Jülich, 2016, 97-104.

ABBREVIATIONS

ABU	Aminobutyric acid
ADP	Adenosine diphosphate
ATP	Adenosine triphosphate
CML	Chronic myeloid leukemia
CNA	Constraint network analysis
CTD	C-terminal domain or carboxy terminal domain
FEP	Free energy perturbation
GGP	γ-glutamyl phosphate
GPCR	G protein-coupled receptor
GPU	Graphics processor unit
GS	Glutamine synthetase
HSP	Heat shock protein
HSP90	Heat shock protein of 90 kDa
HSR	Heat shock response
L. lactis	*Lactococcus lactis*
MD	Molecular dynamics
MM	Molecular mechanics
MM-GBSA	Molecular mechanics generalized Born surface area
MM-PBSA	Molecular mechanics Poisson-Boltzman surface area
NBD	Nucleotide binding domain
NMR	Nuclear magnetic resonance
NSR	Nisin resistance protein
NTD	N-terminal domain or amino terminal domain
MSO	Methionine sulfoximine
PDB	Protein data bank
PMF	Potential of mean force
PTN	Protein tyrosine nitration
S. agalactiae	*Streptococcus agalactiae*
*Sa*NSR	Nisin resistance protein NSR in *S. agalactiae*
SEM	Standard error of the mean

TI	Thermodynamic integration
TKI	Tyrosine kinase inhibitors
TM(1– 7)	Transmembrane helices 1 – 7 in GPCRs
US	Umbrella sampling
WHAM	Weighted histogram analysis method

Table 1: Overview of amino acids in alphabetical order.

Amino acid	Three letter code	One letter code
Alanine	Ala	A
Arginine	Arg	R
Asparagine	Asn	N
Aspartic acid	Asp	D
Cysteine	Cys	C
Dehydroalanine	Dha	
Dehydrobutyrine	Dhb	
Glutamic acid	Glu	E
Glutamine	Gln	Q
Glycine	Gly	G
Histidine	His	H
Isoleucine	Ile	I
Leucine	Leu	L
Lysine	Lys	K
Methionine	Met	M
Phenylalanine	Phe	F
Proline	Pro	P
Serine	Ser	S
Threonine	Thr	T
Tryptophan	Trp	W
3’-nitro tyrosinate	TYD	
3’-nitro tyrosine	TYN	
Tyrosine	Tyr	Y
Valine	Val	V

ZUSAMMENFASSUNG

Molekulare Erkennungsprozesse beschreiben wie biologische Makromoleküle miteinander oder mit kleineren Molekülen interagieren und so einen Komplex mit biologischer Funktion bilden. Der resultierende Komplex ist ein Produkt aus hoher Spezifität und Affinität zwischen den Interaktionspartnern. Eine detaillierte Erkundung dieser Erkennungsprozesse kann dazu beitragen, bisher noch ungeklärte biologische und medizinische Fragestellungen zu erläutern, denn häufig sind jene ungeklärten Ursachen auf Änderungen der Affinität oder Spezifität zwischen den Interaktionspartnern zurückzuführen.

Um diese fundamentalen Erkennungsprozesse und die damit einhergehenden funktionellen Konsequenzen von Struktur, Dynamik und Interaktionen biologischer Moleküle zu verstehen, habe ich ein breites Spektrum computergestützter Methoden angewendet. Ein Charakteristikum dieser Arbeit ist jedoch, dass die Ergebnisse der Simulationen stets im Sinne des integrativen Modellierens mit experimentellen Daten verknüpft wurden. So wurden die Experimente zur Verfeinerung und Validierung von meinen berechneten Ergebnissen herangezogen. Alternativ konnte ich durch meine computergestützten Methoden dazu beitragen experimentelle Beobachtungen auf funktionaler Ebene in atomarer Auflösung zu erklären.

So habe ich in PUBLICATION I und PUBLICATION II die molekularen Regulations- und Inhibierungsmechanismen der humanen Glutamin-Synthetase untersucht. Verlust der enzymatischen Glutamin-Synthetase-Aktivität steht im Zusammenhang mit schwersten klinischen Symptomen. In der vorliegenden Arbeit habe ich herausgefunden, dass sowohl angeborene Enzymvariationen als auch Tyrosinnitrierung die Affinität der Glutamin-Synthetase zum Substrat reduzieren, was wiederum zum Verlust der enzymatischen Aktivität führt. Diese Erkenntnisse können dazu beitragen, neue Strategien zu entwickeln, um die ursprüngliche Affinität des Enzyms zu seinem Substrat wiederherzustellen.

Hochspezifische Interaktionen zwischen einem Enzym und Substrat spielen in der Entwicklung von Resistenzmechanismen gegenüber antibakteriell wirkenden Substanzen eine bedeutende Rolle. So produziert *Streptococcus agalactiae*, im Zuge der Resistenzentwicklung, das Resistenzprotein NSR, welches hochspezifisch antibakteriell wirksames Nisin bindet, spaltet und somit ineffektiv macht. In der vorliegenden Arbeit, habe ich herausgefunden, wie und warum NSR spezifisch Nisin bindet (PUBLICATION III). Diese Einsichten bilden die Grundlage für die Identifizierung potentieller NSR Inhibitoren, um so die Bildung von Resitenzen zu verhindert.

Der eigentliche Prozess wie, zwei Moleküle aneinander binden, kann näherungsweise in zwei Reaktionsschritte geteilt werden; zuerst bewegen sich beide Moleküle frei und erst wenn sich beide Moleküle räumlich nähern, bildet sich als Resultat von hoher Spezifität und Affinität ein Komplex. In PUBLICATION IV ist es mir gelungen, den Bindungsprozess des neuen, potentiellen Arzneistoffes Aminoxyrone an sein Rezeptor zu rekonstruieren. Die Ergebnisse liefern Hinweise bezüglich eines neuen und zuvor unbekannten Wirkmechanismus. Diese Arbeit bildet somit das Fundament für die Entwicklung neuer Arzneistoffe in der Krebstherapie, die dem gleichen Wirkmechanismus wie Aminoxyrone folgen.

ABSTRACT

Molecular recognition describes the process of how biological macromolecules interact with each other or with smaller molecules to form a complex with a biological function. The complex is thus a product of high specificity and affinity. In many cases, enzymatic malfunction is often induced by a change in the affinity or specificity between the interaction partners. An in-depth understanding of the fundamental recognition processes can help to answer so far unresolved biological and medical questions. To study these fundamental recognition processes, I employed computer-aided methods, which are summarized under the term "*computational microscopy*". A fundamental aspect of this work, however, is that the results of the simulations were always linked to experimental data in the sense of integrative modeling. Hence, experiments were used to refine and validate my computational results. Alternatively, I was able to use my computer-aided methods to explain experimental observations at the functional level in atomic resolution.

In particular, I investigated the molecular regulation and inhibition mechanisms of the human glutamine synthetase, an enzyme essential for the human nitrogen metabolism. Loss of enzymatic activity is associated with severe clinical conditions. In the present work, I found that both innate enzyme variations and tyrosine nitration adversely affect the affinity the glutamine synthetase to its substrates. The reduced affinity provides a plausible explanation for the associated loss of enzymatic activity (PUBLICATION I and PUBLICATION II). The results may also help to develop new strategies to restore the initial affinity of the glutamine synthetase towards its substrates.

Highly specific interactions between an enzyme and a substrate play an important role in the development of resistance mechanisms to antibacterial substances. For example, in the course of resistance development *Streptococcus agalactiae* produces the resistance protein NSR, which binds and cleaves antibacterial nisin. The cleaved nisin, however, is antibacterial ineffective. In the present work, I found how and why NSR specifically recognizes nisin (PUBLICATION III). These insights form the basis for the identification of potential NSR inhibitors to prevent nisin inactivation.

The actual process of binding of two molecules can be described by two individual steps; first, both molecules move freely and only when both molecules approach each other does a complex form as a result of high specificity and affinity. In PUBLICATION IV, I succeeded

in reconstructing the binding process of the novel, first-in-class anticancer compound Aminoxyrone to its receptor. The insights suggest a new and previously unknown mode of action. This work thus forms the basis for the development of new compounds in cancer therapy, which follow the same mode of action as Aminoxyrone.

1. INTRODUCTION

How does an enzyme catalyze its reactants? How does the antibody specifically recognize its antigen, but does not associate with miscellaneous peptides or proteins? How is DNA replication controlled although a series of complex enzyme-catalyzed reactions participating in this procedure? How do ion channels distinguish between cations and anions? How does a G protein-coupled receptor (GPCR) recognize the correct G protein? And how does a drug bind to its target? These are only a few questions that address and share the same desire, namely, to understand how two or more molecules recognize and bind to each other.

In that sense, molecular recognition describes the process in which two or more molecules interact with or bind to each other to form a specific complex[1]. Until now, three different models, the lock-and-key[2], the induced fit[3], and the model of conformational selection[4-6] enjoy a profound level of popularity to explain protein-ligand interactions[1]. In his pioneering work, Emil Fischer described this process via a lock-and-key mechanism, such that only the correctly shaped ligand molecule (key) can bind or insert into its complementarily shaped binding pocket (lock) of a receptor molecule[2]. However, the lock-and-key model neglects any ligand or receptor flexibility. This major drawback was addressed in two additional models, namely the induced fit[3] and the conformational selection[4-6] models[1]. As to the induced fit model, the association of a rigid ligand and a flexible receptor molecule induces a conformational change in the receptor molecule, when the initial shapes of ligand and binding pocket do not match well[3,7]. As to the conformational selection model, the receptor structure is not a single rigid structure at all, but instead exists as a dynamic ensemble of multiple states, and the ligand binds to the receptor conformations that is complementary with its shape and shifts the ensemble towards this specific state[4-7]. Interestingly, there is also evidence that suggests that conformational selection can be followed by subsequent binding interface conformational adjustment via an induced fit mechanism[8,9]. Thus, whether the mechanisms of ligand binding can be narrowed down to one of the models or whether it is always a combined mechanism cannot be correctly answered and still needs further research. However, all models share the common key aspects that ligand binding is driven by high specificity and affinity between the ligand and the receptor molecules[1].

The change in Gibbs free energy upon ligand binding is a measure for the binding affinity and logarithmically related to the equilibrium binding- and unbinding constants[1,10] (details in section 2.1). A negative Gibbs free energy characterizes ligand binding processes that

occur spontaneously and without any external guiding force[10] and methods that provide access to the binding free energy are essential for the understanding of protein-ligand recognition and binding processes. Concerning the experimental methods, isothermal titration calorimetry (ITC) is the gold standard for obtaining estimates of the binding free energy related to the ligand binding process[11,12]. ITC experiments provide access to the complete thermodynamic profile, including the total change in Gibbs free energy and its enthalpic and entropic contributions[10]. However, ITC experiments lack structural information. X-ray crystallography, nuclear magnetic resonance (NMR) or cryo-electron microscopy provide structural information about protein-ligand complexes in full atomic or near-atomic resolution[1], but also denote laborious and time-consuming procedures and lack any energetic evaluation[1]. Here, theoretical or computational approaches denote a good compromise, as these methods are often less laborious, more economical, and faster than the experimental procedures[1] and provide access to both structural and energetic features of ligand binding (details in section 2.2). In that sense, binding free energy calculation methods (section 2.2.2) provide direct access to the thermodynamic properties of ligand binding and, complementarily, molecular dynamics (MD) simulations (section 2.2.1) denote a prominent approach that provides the structural information in full atomic detail[13]. In sum, an in-depth understanding of the structural and thermodynamic determinants of protein-ligand binding is essential for understanding any biological processes in which two or more molecules form complexes to fulfill its biological function.

One primary goal of modern biomedical research is to understand the function-associated consequences of the structure, dynamics, and interactions of biological molecules. In recent years, this was achieved by the close integration of experiments and simulations, such that experiments are used to refine and corroborated simulations and simulations are used to provide a molecular interpretation of experimentally derived observations[14]. The fact that computational methods provide a full energetic description and also provide structural insights into the binding mechanism makes these tools highly valuable to investigate ligand binding pro-cesses. Thus, it is not surprising that in recent years, MD simulations and free energy calcu-lations gained more and more attention in order to address sophisticated questions in the field of biomedical research[15] (section 2.2).

A prominent example is to explain the molecular consequences of enzyme variations or post-translational modifications that were related to reduced enzymatic activities. Often, these effects have been well described biochemically, but any molecular explanation has remained

elusive. Here, the integration of computational methods to the existing biochemical observations can provide structural and energetic insights into the functional consequences of enzyme variations and posttranslational modifications and may allow deriving strategies to counteract the functional consequences.

In this regard, I used MD simulations and free energy calculations in PUBLICATION I, to elucidate the molecular mechanisms of three enzyme variations that were linked to the reduced enzymatic activity of the human glutamine synthetase (GS), a pivotal enzyme in human nitrogen metabolism[16-19] (**Figure 1A**). Interestingly, human GS is also sensitive to posttranslational tyrosine nitration that was also linked to a reduced catalytic activity[20-22]. In PUBLICATION II, I provide the first molecular explanation by what means tyrosine nitration causes GS catalytic inhibition (**Figure 1A**). In both publications, my predictions were, subsequently, corroborated experimentally. Integration of simulation and experimental results provide the basis for the development of potential strategies to compensate for the inhibitory effects of point mutations and tyrosine nitration in human GS.

Additionally, computational methods can provide an in-depth understanding of the highly specific recognition mechanisms between ligand and receptor, which is of particular interest in the field of drug resistance mechanisms. Here, theoretical methods can provide valuable insights to support the understanding of drug resistance mechanisms and, furthermore, guide the development of novel drugs. Hence, in PUBLICATION III, combining results from computational simulations and results from biochemical experiments led to the first structural model of the antibiotic peptide nisin bound to a protease that specifically cleaves nisin, thereby inducing nisin resistance[23,24] (**Figure 1B**). Therefore, based on my results from computational simulations, I suggested amino acid substitution sites that were then experimentally characterized towards their effects on nisin resistance. The structural and functional insides build the basis for the subsequent search for molecules that inhibit the protease, thereby overcoming nisin resistance.

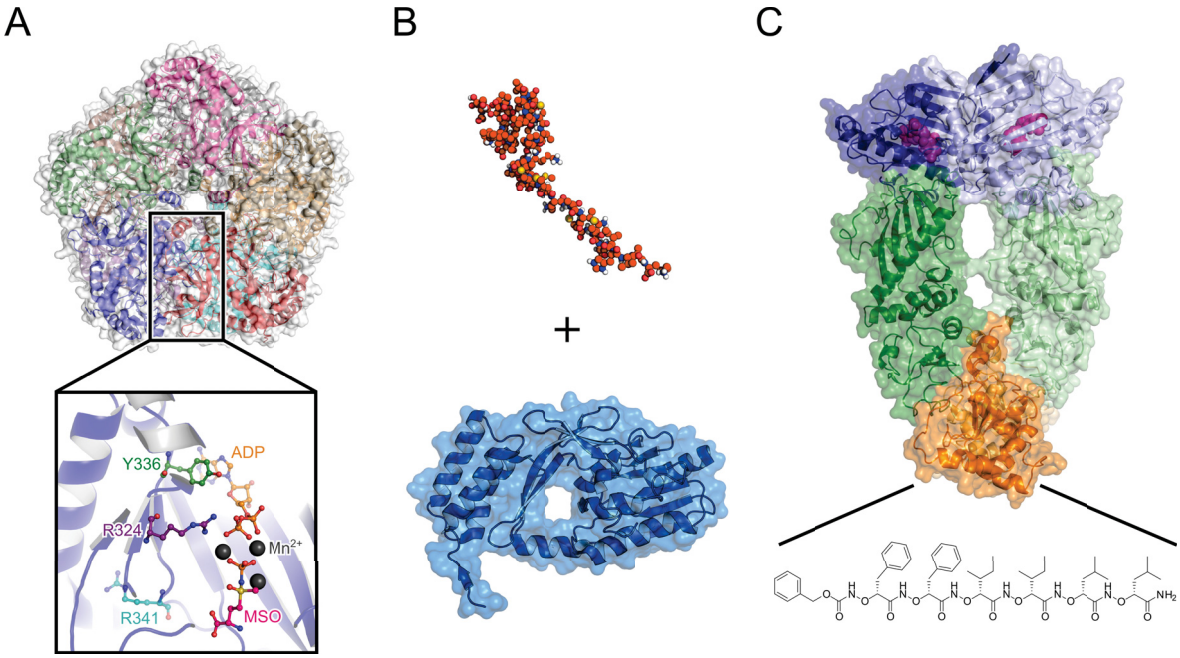

Figure 1: Overview of biological systems that were investigated throughout this thesis.
A: Top panel: 3D structure of the human glutamine synthetase (GS; PDB-ID: 2QC8[25]; subunits are colored differently). Lower panel: Close up view of the catalytic site of human (PDB-ID: 2QC8[25]) with R324 (purple), R341 (cyan), ADP (orange), and phosphorylated MSO (methionine sulfoximine; magenta) depicted as a ball-and-stick model. The structurally bound manganese ions (Mn^{2+}), which are essential for GS function[26], are depicted as gray spheres. In PUBLICATION I, the molecular consequences of three GS variants (R324C, R324S, and R341C) were investigated. PUBLICATION II addresses the question by what means Y336 nitration causes GS catalytic inhibition. **B:** Top panel: 3D structure of nisin resolved by solution NMR spectroscopy (PDB-ID: 1WCO[27]). Lower panel: 3D structure of the nisin resistance protein (NSR; PDB-ID: 4Y68[28]) that specifically binds and cleaves nisin. In PUBLICATION III, the first structural model of nisin bound to NSR is reported, which provides atomic-level insights into the recognition mechanisms of nisin by NSR. **C:** Top panel: 3D structure of the dimeric heat shock protein of 90 kDa (HSP90; PDB-ID 2CG9[29]; the N-terminal domains are colored blue, the middle domains green, and the C-terminal domains orange). Two ATP molecules (magenta spheres) are bound to the NTDs. Lower panel: 2D structure of Aminoxyrone. PUBLICATION IV provides a binding-mode model of Aminoxyrone bound the C-terminal domain of HSP90.

Recent advances of hardware and software enabled to investigate the complete protein-ligand association process. In PUBLICATION IV, I elucidate the binding process of Aminoxyrone, a novel and first-in-class anticancer compound, to its molecular target, namely the heat shock protein of 90 kDa (HSP90; **Figure 1C**). Initially, the C-terminal domain of HSP90 was identified as the target of Aminoxyrone. However, a molecular picture of how Aminoxyrone binds to the C-terminal domain has remained elusive. Here, I used unbiased MD simulations of Aminoxyrone binding to provide the first structural model of Aminoxyrone bound the HSP90. Interestingly, the findings suggest a novel and mode of action that opens a new avenue to target HSP90 for cancer therapy.

2. BACKGROUND

Throughout this thesis, I will, first, review the principles of molecular recognition that describe the process by which biomacromolecules, such as proteins, recognize or specifically bind to other molecules, such as proteins, peptides, nucleic acids, or small organic ligands, and thereby realize their functions. Second, I will provide an overview of computational methods to investigate molecular recognition, as I used these methods intensively to study molecular recognition processes for biological systems. I will also describe how the integration of results from biomolecular simulations and biophysical/-chemical experiments guide the understanding of sophisticated biological questions. After this, I will introduce the model systems, for which I determined the structural and energetic features of function-as-sociated protein-ligand, protein-peptide, and protein-protein interactions.

2.1 Kinetic and thermodynamic concepts of molecular recognition

Molecular recognition describes the process by which two or more molecules interact with each other through non-covalent interactions to form a specific complex[1]. In that sense, proteins likely constitute the most important class of all biomacromolecules as proteins are relevant in nearly all aspects of living[30] and proteins can form complexes with different types of ligand molecules, including proteins, peptides, nucleic acids, small organic ligands, and many more[1]. Thus, for clarity purposes, the term *protein* will always refer to a receptor molecule throughout the following sections. Similarly, the term *ligand* will denote to any molecule that can bind to the protein structure.

Consider the simple and straight-forward binding process of a protein (**P**) and any ligand (**L**) to form a non-covalently bound complex (**PL**). The association and dissociation reactions can then be described by the reaction, which is described by eq. (1)

$$P + L \rightleftarrows PL. \quad (1)$$

If the rate of the forward reaction (complex formation or ligand binding), described by the kinetic constant k_{on}, equals the rate of the reverse reaction (complex dissociation or ligand unbinding), described by k_{off}, the overall reaction reached its reaction equilibrium. At equilibrium, the binding constant K_b or dissociation constant K_d can be expressed by eq. (2)

$$K_b = \frac{k_{on}}{k_{off}} = \frac{[PL]}{[P][L]} = \frac{1}{K_d} \quad (2)$$

where [P], [L], and [PL] denote the equilibrium concentration of the respective species in molar units[15,31]. $K_{d,}$ in turn, is logarithmically related to the change in free energy upon ligand binding[31] ($\Delta G_{binding}$) by eq. (3)

$$\Delta G^0_{binding} = -RT \ln \frac{K_d}{c^0} \quad (3)$$

where R is the gas constant, T the absolute temperature, and c^0 the standard concentration in units consistent with the units of the concentrations in K_d[15,32]. The introduction of c^0 ensures that the logarithm in eq. (3) becomes dimensionless and allows the meaningful comparison of experimentally determined results with computational results[32,33]. A specialized case denotes to the change of standard free energy upon ligand binding, $\Delta G_b{}^0{}_{inding}$, which corresponds to the free energy change under standard conditions of 1 atm pressure, T = 298 K, and protein and ligand concentrations of 1 M[1,33].

In general, ΔG denotes the change in Gibbs free energy for a given system and is a measure for the potential of a system to do maximum work[1,34]. Processes that occur spontaneously and without external influence are characterized by a negative change in free energy[10]. If the free energy of a system is zero, the system is in equilibrium[10]. In terms of protein-ligand binding, this means that a ligand only binds to the protein, if $\Delta G_{binding}$ is negative, which makes this parameter a fundamental quantity for the characterization of protein-ligand interactions[15,33].

Alternatively, ΔG can be expressed by its individual enthalpic and entropic contributions following eq. (4)

$$\Delta G = \Delta H - T\Delta S \quad (4)$$

where ΔH denotes the change in enthalpy, ΔS the change in entropy, and T the absolute temperature[1]. ΔH describes energetic changes related to changes in interactions and (de)solvation upon ligand binding[10]. ΔS denotes the entropic contribution to ΔG and can be considered as an order parameter to describe how the energy is distributed over the thermodynamic system before and after ligand binding[10]. Importantly, even small entropic changes will result in large free energy changes, as, according to eq. (4), ΔS is weighted by the temperature in Kelvin. In sum, ΔH and ΔS can also be considered as the key determinants in protein-

ligand binding, as these quantities determine the magnitude and direction of the binding free energy ΔG[1]. The process of ligand binding and the free energy change associated with complex formation can be accessed via computational methods.

2.2 Biomolecular simulations to investigate protein-ligand interactions.

Although experimental procedures can provide the complete thermodynamic profile for a protein-ligand complex, these techniques are also often considered laborious, time-consuming, and expensive[1]. Computational procedures, by contrast, denote a valuable alternative to derive atomic-level insights into the key determinants of ligand binding[1]. A very detailed level of information can be obtained via quantum mechanical calculations, which considers the electronic properties of the relevant molecules[35]. However, quantum mechanical calculations are yet limited to very small systems and short time scales[35]. By contrast, coarse-grained simulations group many atoms into larger, single particles, which then allows studying complex biological systems on a much longer time scale[36]. By grouping multiple atoms into a larger particle, however, coarse grain methods allow to study huge systems[36], but one also loses the atomistic level of information. In this regard, MD simulations denote an excellent compromise to investigate the structure and dynamics of biological systems at the millisecond time scale[37] and, simultaneously, offer atomistic insights into the fundamental mechanisms of biomolecular systems, such that also the term "*computational microscopy*" was introduced for this method[13]. MD simulations cover a broad scope of application systems from rather small, for example, the effect of amino acid substitutions on the catalytic activity of enzymes[38,39], to highly complex and sophisticated, for example, an atomistic model of a bacterial cytoplasm[40,41]. Throughout this thesis, I applied MD simulations and related methods to study the function-associated principles of protein-ligand, protein-peptide, and protein-protein interactions (PPIs).

2.2.1 Unbiased molecular dynamics simulations to investigate ligand binding.

MD simulations denote a physical method for studying the time-dependent interaction and motion of atoms and molecules[15,42]. Starting from a static structure, MD simulations record the change of an atom's position over time, resulting in a trajectory[15,42]. The trajectory is obtained by integrating the second-order differential equation of Newton's second law of

motion[15,42]. Therefore, Newton's equation is integrated at distinct time steps, typically between 1 fs – 4 fs[43]. At each time step, forces on atoms are calculated by differentiating the potential energy at the positions of every atom in the system[44]. For MD simulations, a potential energy function V (eq. (5))

$$V = \sum_{\text{bonds}} K_r(r - r_{\text{eq}})^2 + \sum_{\text{angles}} K_\theta(\theta - \theta_{\text{eq}})^2 + \sum_{\text{dihedrals}} \frac{V_n}{2}[1 + \cos(n\varphi - y)] + \sum_{\substack{\text{nonbonded} \\ i<j}} \left[\frac{A_{ij}}{R_{ij}^{12}} - \frac{B_{ij}}{R_{ij}^{6}} + \frac{q_i q_j}{\epsilon R_{ij}}\right] \quad (5)$$

is introduced to describe the physical interactions between atoms, which is also referred to as the molecular mechanics (MM) force field[15,42]. Eq. (5) depicts the Amber force field[45-48] to describe protein systems, which was also applied throughout this thesis. Nowadays, almost all relevant biological systems can be described via force fields, including amino acids[45-48], nucleic acids[49,50], lipids[51,52], carbohydrates[53], and also small organic compounds[54]. Thus, MD simulations allow investigating a broad range of biologically relevant processes, such as function-related structural changes[55,56], protein folding and unfolding[57-59], and ligand binding[60,61].

In a very simplified representation of the protein-ligand binding process, the whole association process can be decomposed into two major events. First, protein and ligand molecules diffuse freely within the solvent environment until, second, a collision of both molecules introduces contacts, thereby promoting complex formation (**Figure 2**)[1,15]. Thus, the simplest way to investigate how a ligand binds to its target, one could imagine, is to track the diffusion process over time until the desired complex is formed. In recent years, MD simulations have been extensively used to investigate the principles of protein-ligand binding, as this procedure indeed allows to record the diffusion processes of protein and ligand molecules (**Figure 2**). As to slow binding events, very long MD simulations are required that were, until recently, beyond the range of MD simulations[15]. The design of a specialized supercomputer[62,63] and the increasing usage of graphics processor units (GPUs), however, opened new opportunities and shifted the boundaries in terms of timescales covered by MD simulations, for example, the first millisecond length MD simulation[64].

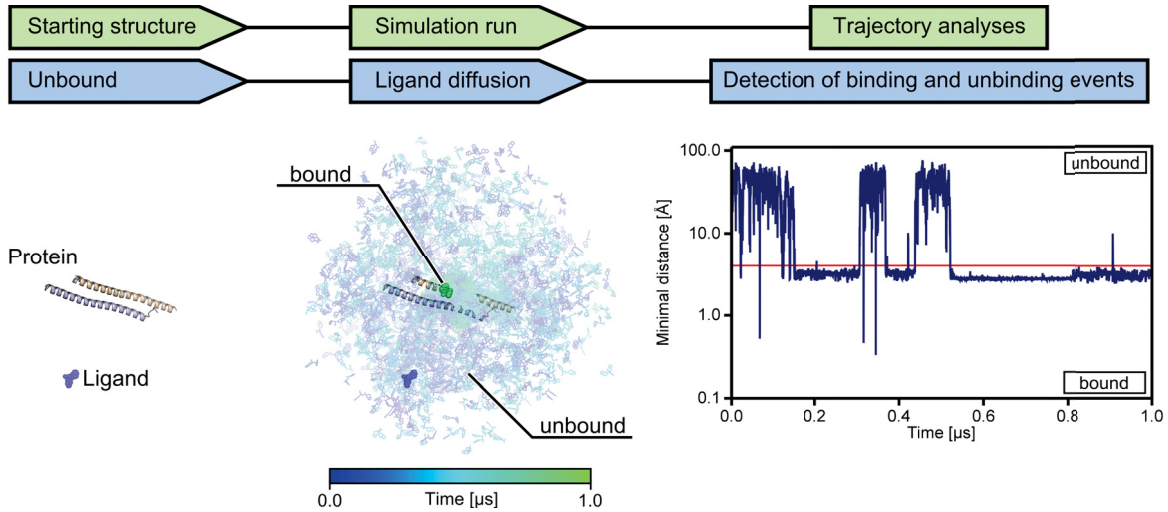

Figure 2: Schematic workflow of a ligand binding simulation.
From left to right: The starting structure denotes to a conformation in which the protein (cartoon representation) and ligand (sphere model) molecules are completely unbound. During molecular dynamics simulations of ligand binding, the protein and ligand structures diffuse freely and without guiding force (only the diffusion of the ligand is shown for clarity purposes; starting and final ligand poses are shown as sphere model). The ligand diffusion process (during diffusion the ligand is shown as stick models) is colored according to the progressing simulations time (see the color range). This procedure enables to analyze the resulting trajectory towards ligand binding to or unbinding from the protein structure. In this example, the minimal distance between the protein and ligand structure was used to characterize the (un-)binding events. The ligand is bound, if the minimal distance < 4 Å, which is indicated by the red line.

Shan *et al.* performed unbiased MD simulations of 35 µs and 115 µs length in which the anticancer drug Dasatinib and the kinase inhibitor PP1 bind, spontaneously and without any guiding force, to their target, namely the Src kinase[60]. Remarkably, the binding poses adopted by Dasatinib and PP1 agree almost perfectly with the crystallographic poses[60]. In a similar study, Shan *et al.* performed unbiased MD simulations in which Lapatinib, another anticancer drug, binds to the epidermal growth factor receptor adopting a binding pose virtually identical to that observed crystallographically[65]. Dror *et al.* performed unbiased MD simulations in which three β-adrenergic receptor antagonists and one agonist bind to either the β_1- or β_2-adrenergic receptor, again, with binding poses in agreement with the crystallographic ones[66]. Further, the authors reconstructed the complete binding path for these ligands and observed that initial protein-ligand association is followed by ligand dehydration before the ligand finally reaches its destination[66]. The dehydration process is accompanied by local receptor deformation, such that the ligand squeezes through a narrow passage towards the crystallographic binding site[66]. While the above examples provide structural insights originating from very long MD simulations, which are currently accessible only for a limited amount of people, new analysis techniques were developed to provide the same accuracy of insight, but for simulation data on a smaller time scale.

Markov state models denote such an analysis technique that allows extracting long-time kinetic information from multiple but much shorter simulations, based on the stochastic description of the kinetics[67-69]. In this regard, De Fabritis and co-workers constructed a Markov state model based on 495 independent MD trajectories, each of 100 ns length, to characterize the binding process of Benzamidine to *β*-trypsin[61]. Based on the simulation data, they built a full three-dimensional projection of the binding process, from which they computed kinetic and energetic information[61]. They found that Benzamidine rather binds to metastable binding sites before binding to the crystallographic binding site instead of directly binding from the bulk[61]. While the authors focused on the ligand binding process exclusively, Plattner and Noé later extended their analyses to the *apo* form of *β*-trypsin[70]. Employing a Markov state model for 150 μs of MD simulation data, they identified metastable *β*-trypsin conformations in the *apo* form that all differ in their substrate binding affinities and binding/dissociation constants[70]. Moreover, they observed that the presence of Benzamidine significantly shifts the conformational population of the protein structure, such that Benzamidine binding to *β*-trypsin can be explained by the principles of the conformational selection and induced fit models[70]. Just recently, Plattner *et al*. reported the first microscopic model of a complete protein-protein association process obtained by cumulative 2 ms MD simulation data and Markov state modeling[71]. An alternative approach to Markov state modeling was reported by Decherchi *et al*.[72], who integrated microsecond MD simulations into machine learning algorithms to study structural and dynamic features of ligand binding to the human purine nucleoside phosphorolysis[72].

While the studies above addressed the central question to reconstruct the ligand binding process towards an experimentally resolved ligand binding pose, ligand binding simulations can also be applied to identify novel binding sites for ligands[61,73]. In this regard, the first binding mode models of allosteric modulators of the M2 muscarinic acetylcholine receptor were determined[73] before any experimental evidence was available. The authors observed that the allosteric ligand reproducibly binds to a novel allosteric binding site within the receptor's extracellular vestibule, a region almost 15 Å from the orthosteric site for the native ligand[73]. Later, a crystallographic binding pose of a structurally similar ligand was available and confirmed the spatial location of the allosteric binding site[73,74]. Remarkably, the crystallographically resolved ligand pose is very similar to the ligand pose observed during the simulations[73,74]. Similarly, Bowman *et al.* built a Markov state model that revealed hidden allosteric

sites that were experimentally corroborated subsequently[75]. Finally, the use of MD simulations and flexible docking approaches led to the discovery of an at that time unknown binding trench in human immunodeficiency virus (HIV) integrase[76], which in turn led to the development of Raltegravir to treat HIV infections[77].

Besides providing an atomistic insight into the association process of ligand and receptor, MD simulations also provide valuable insights into ligand-induced structural adaptation mechanisms, which are connected to biological function. In this regard, MD simulations supported the understanding of the structural dynamics of GPCRs, particularly, how extracellular ligand binding induces structural changes that allow G proteins and other signaling molecules to bind to a GPCRs' intracellular surface[78]. Crystallographic studies of the active and inactive configurations of the β_2-adrenergic receptor revealed distinct rearrangements of transmembrane helices 5 – 7 (TM5 – 7)[79-83], however, the underlying mechanism of receptor activation/deactivation remained elusive. During unbiased MD simulations of the β_2-adrenergic receptor, Dror *et al.* observed that the receptor transitions from the crystallographic active state to the crystallographic inactive state via a metastable transition state, which is stable for several hundreds of nanoseconds to microseconds[84]. As long as the receptor resides in the transition state, TM7 adopts the crystallographically inactive conformation while TM6 is still in its active conformation[78,84]. Subsequently, NMR spectroscopy experiments of an agonist bound to the β_2-adrenergic receptor corroborated the findings, as the authors observed that strong agonists destabilize the inactive conformation, but do not fully stabilize the active conformation of the receptor[56]. Further, the authors suggest that the described agonist instead stabilizes an intermediate state that might correspond to the state observed during MD simulations[56,84]. Employing MD simulations, Neale *et al.* provided an explanation why negatively charged lipids favor GPCR activation[85], as they observed that anionic lipids bind to the G protein binding site, intercalating between the intracellular parts of TM6 and TM7, thereby stabilizing the active state of the receptor[86]. As to G protein regulation, MD simulations of, first, G proteins in the GDP bound and unbound state and, second, a crystal structure of a GPCR-G protein complex[80] provided atomistic insights into the nucleotide exchange mechanisms in heterotrimeric G proteins[87].

In a more generalized context, MD simulations provide molecular insights into the search of treatment for diseases. Toy *et al.* reported the consequences of mutations of the *ESR1* gene, which encodes for the estrogen receptor[39], a popular target for cancer therapy. The mutations are of clinical importance as they induce resistance towards the primary treatment[39].

However, the underlying mechanisms remained unclear[39]. Using MD simulations of the wild type estrogen receptor and the Y537S and D538G variants, the authors observed hydrogen bond interactions of the substituted amino acids that are not present in the wild type[39]. They suggest that these hydrogen bonds stabilize an agonist-like conformation of the receptor and, in turn, trigger downstream signaling in the absence of the native activator[39]. Fanning *et al.* observed that the D538G variant relaxes the H11-H12 loop of the estrogen receptor, thereby improving the packing of side chain residues, which, finally, stabilizes the receptor's agonist-like state in the absence of any ligand[38]. This agonist-like state also restricts ligand access to the estrogen binding pocket, which might explain the decreased affinity for estrogen[38]. Ihle *et al.* provided a structural explanation for the progression-free survival of cancer patients carrying the KRas-G12C or KRas-G12V variant compared to patients with wild type KRas or other KRas variants[88]. KRas interacts with different downstream effectors and the investigated amino acid substitutions in KRas result in different downstream behavior[88]. The simulation data suggests that conformational changes in the switch I and II regions caused by the KRas mutant control the interaction with downstream effectors, thereby resulting in different major signaling pathways[88]. By long-timescale MD simulations, Shan *et al.* provided a plausible explanation of why the widespread L834R variant in the EGFR kinase leads to high kinase activity, promoting EGFR dimerization. The activation of the kinase domain in EGFR depends on the formation of active dimers, in which the kinase C lobe of the activator interacts with the kinase N-lobe of the receiver[65]. The authors found that the N-lobe dimerization interface of wild type EGFR is intrinsically disordered, whereas the widespread L834R variant facilitates dimerization by suppressing the disorder[65].

In sum, MD simulations offer atomistic insight into the fundamental mechanisms of biomolecular systems[13]. In particular, MD simulations provide direct access to characterize how a ligand molecule binds to its target[15]. Moreover, the successful applications of ligand binding simulations to investigate how a ligand binds to its target demonstrate their potential to predict, and not just reproduce, plausible binding poses[15]. Nevertheless, to thoroughly understand the mechanisms of protein-ligand interactions, it remains indispensable to link the structural insights to the fundamental thermodynamics of protein-ligand association. As mentioned previously in section 2.1, the thermodynamic key determinant of protein-ligand association is the change in free energy ΔG upon ligand binding. Thus, deriving energetic features directly from the MD trajectories would complement the method. According to eq.

(3), the free energy difference ΔG can be linked to the equilibrium constant K_d, which quantifies the probability of the unbound relative to the bound state (eq. (2)). Just recently, Pan *et al.* performed MD simulations of several microsecond lengths to observe drug fragments spontaneously and repeatedly bind to and unbind from its target protein, which allowed to estimate binding affinities and kinetics directly from the simulation data[89]. However, to de-rive statistically meaningful probabilities of these states from an MD trajectory requires very long simulations, in which many binding and unbinding events must be recorded[15]. Alterna-tively, there are several free energy calculation methods to estimate (relative) binding affin-ities that require less computing time.

2.2.2 Binding free energy calculations

Binding free energy calculations of protein-ligand binding yield the free energy difference between the two states of the system (ligand-bound or unbound). As the free energy difference ΔG can be linked to the equilibrium constant K_d (eq. (3)), these methods provide an estimate about the binding affinities for complex formation. The free energy calculations can be classified into three main types of calculations: the alchemical free energy calculations, the path sampling methods, and the endpoint methods[1].

2.2.2.1 Alchemical free energy calculations

Alchemical free energy calculations employ a non-physical, alchemical pathway to determine the free energy difference between two states[90-92]. In many cases, these types of computations are also referred to as *alchemical transformation calculation* as these methods determine the free energy difference that is associated with the transformation of one chemical species into another one, which is slightly different[93]. Hence, to determine the free energy difference of two ligands **A** and **B** binding to the same protein structure, one would simulate the transformation of ligand **A** into ligand **B** in the unbound and bound state. The perturbations along this alchemical pathway are much smaller and converge much faster compared to the direct association path[94] in which also slow desolvation processes[95] and substantial conformational changes must be considered. Employing a thermodynamic cycle[93,94] (**Figure 3**) the relative binding free energy $\Delta\Delta G_{binding}$ of ligands **A** and **B** can be calculated[94,96]. Alternatively, by transforming amino acids of the protein structure, these methods also allow investigating the effects of amino acid substitutions on ligand binding[97].

In detail, instead of computing the change in free energy associated with the ligand binding to its protein ($\Delta G^{A}_{binding}$ and $\Delta G^{B}_{binding}$; horizontal arrows in **Figure 3**) alchemical transformation methods determine the changes in free energy associated with the vertical arrows, namely the transformation of ligand **A** into ligand **B** ($\Delta G^{unbound}_{A\rightarrow B}$ and $\Delta G^{bound}_{A\rightarrow B}$; **Figure 3**)[97,98]. Taking into consideration that the free energy is a state function, that changes in free energy are independent of the path connecting the end states, and that all free energy changes within a thermodynamic cycle add up to zero[97], the thermodynamic cycle enables to estimate the relative change in binding free energy $\Delta\Delta G_{binding}$ according to eq. (6)

$$\Delta\Delta G_{binding} = \Delta G^{B}_{binding} - \Delta G^{A}_{binding} = \Delta G^{bound}_{A\rightarrow B} - \Delta G^{unbound}_{A\rightarrow B}. \quad (6)$$

The transformation of **A** into **B** technically means that the potential energy function (force field; see eq. (5) in section 2.2.1) of **A** is transformed into the potential energy function of **B**[93]. Therefore, a coupling parameter is introduced that connects both potential energy functions[99]. This coupling parameter is frequently referred to as λ and ranges from $\lambda = 0$ for ligand **A** to $\lambda = 1$ for ligand **B**[99]. In practice, the simulations are broken down into a series of individual simulations for multiple values of λ[99]. With an increasing number of individual λ-steps, the accuracy of the calculations increases, however, so does the computational costs[99].

The free energy perturbation[99,100] (FEP) and thermodynamic integration[101] (TI) approaches are two widely applied methods in the class of alchemical free energy calculations[98]. To determine the free energy difference between the states **A** and **B**, FEP calculations use the principles of the Zwanzig relationship[100]. FEP calculations usually result in accurate estimates only, if the changes from **A** to **B** are small, which comes along with small differences in the potential energy functions[98]. TI calculations treat the free energy as a derivative of the coupling parameter λ[98]. To derive the free energy difference via TI, one simulates the transformation of ligand **A** into ligand **B** at discrete λ-steps and, subsequently, integrates over the averaged λ-dependent potentials[98]. In contrast to FEP calculations, the accuracy of TI calculations can always be increased by subsequently performing simulations at additional λ-steps[102], which, however, requires more computational resources[103].

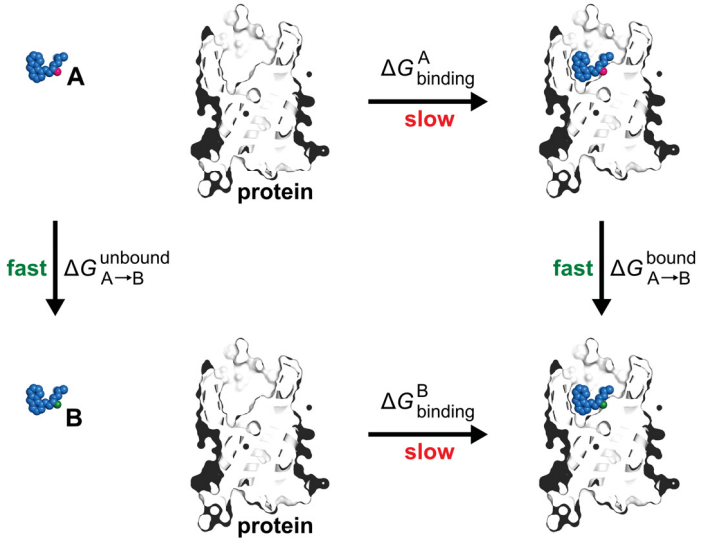

Figure 3: Thermodynamic cycle to calculate relative binding free energies.
The horizontal arrows depicted the binding process of ligand **A** and ligand **B** to the receptor structure that, in this example, is a protein structure. The vertical arrows depict the transformation reaction of ligand **A** (magenta) into ligand **B** (green) performed in unbound (left) and bound (right) states. During the transformation in the unbound state, no protein structure is present during the computations. FEP and TI calculations calculate the changes in free energy associated with the vertical lines ($\Delta G^{unbound}_{A\rightarrow B}$ and $\Delta G^{bound}_{A\rightarrow B}$) and calculate the relative difference according to eq. (6). (Figure is adapted from ref.[94].)

Jorgensen *et al.* performed the first alchemical free energy calculation to study relative solvation free energies for methanol and ethan[104], but alchemical free energy calculations gain more importance to study protein-ligand free energies of binding, which makes these techniques also relevant in rational drug discovery and drug design[92,96]. An explanation might be the development of new simulation techniques to increase the level of accuracy and to accelerate the computations[105]. Wong and McCammon reported the first study that investigated ligand binding to a protein structure[106]. First, they computed relative binding free energies of Benzamidine (would denote ligand **A**) and *p*-Fluorobenzamidine (would denote ligand **B**) binding to trypsin. Second, they compared changes of binding free energy when Benzamidine binds to trypsin (would denote receptor **A**) or binds the G216A variant (would denote receptor **B**)[106]. Their results were in agreement with experimental binding affinities, such that the authors concluded that alchemical free energy calculations enable the analysis and prediction of affinities in large biomolecular systems[95]. T4 lysozyme has become a prominent system to study ligand binding for both theoreticians and experimentalist[96]. Mobley *et al.* studied the binding of small organic fragment-like ligands to the binding site of the L99A variant of T4 lysozyme[107], obtaining a good agreement with experimentally determined energies[107]. Later, Boyce *et al.* calculated binding free energies of thirteen compounds, which were not tested experimentally before, to a polar cavity in the L99A/M102Q variant of T4 lysozyme. This study also addressed the question of whether the calculations

could prospectively distinguish binding compounds from non-binding compounds[108]. Based on the binding free energies, they predicted that eight of these ligands would most likely bind to the T4 lysozyme whereas the remaining five ligands will likely not bind and, finally, ten of 13 predictions were correct[108].

In recent years, alchemical free energy calculations performed well in retrospective and prospective studies in active drug discovery projects[92,96,109,110]. Rombouts *et al.* applied alchemical free energy calculations to predict the structure-activity relationship of drug candidates binding to a lipophilic roof pocket of phosphodiesterase 2 and identified novel phosphodiesterase 2 inhibitors[111]. Prospective alchemical free energy calculations were also successfully applied to optimize *β*-secretase 1 inhibitors[112,113]. Interestingly, the authors suggest strategies to characterize the convergence of computational sampling[112], such that the correlation to experiments was improved by repeating simulations with different initial velocities and longer simulation times[113]. Kuhn *et al.* reported the first study that applied alchemical free energy calculations to covalent inhibitors of the cysteine protease cathepsin L[114]. Therefore, the authors designed a thermodynamic cycle that, first, describes non-covalent ligand binding and, second, the chemical reaction to form a covalent bond[114]. The recent successes are likely connected to the significant improvements concerning the accuracy and computing time for such sophisticated calculations[115]. In this context, Wang *et al.* developed a fully automated calculation protocol, which was retrospectively and prospectively validated across a broad range of ligands and targets (over 200 ligands and ten targets)[115]. One might speculate that future advances in specialized hardware and highly accurate software will promote alchemical free energy calculations to study protein-ligand binding. In this regard, the workflow tool for free energy calculations of ligand binding was designed to prepare, conduct, and analyze various kinds of free energy calculations efficiently[116,117].

2.2.2.2 Path sampling methods

While alchemical transformation methods calculate the change in free energy along a non-physical path, path sampling methods describe the change in free energy along a physically meaningful path, termed reaction coordinate hereafter[1]. In this regard, path sampling methods also allow observing relevant conformational rearrangements of the molecules during the actual binding process[15]. Path sampling methods are based on the assumption that the dynamics of biomolecules can be described in terms of a free energy landscape where free

energy is expressed as a function of distinct configurations[56,118]. However, to study protein-ligand binding the reaction coordinate or ligand binding path must be defined *a priori*[15], such that some knowledge about a likely binding path must be guaranteed.

Path sampling methods provide access to the free energy profile or landscape of a complete protein-ligand association process, including energetic barriers along the binding path[34] (**Figure 4**). The projection of the free energy profile along a reaction coordinate is also referred to as a potential of mean force (PMF)[101]. In the context of ligand binding processes, the PMF is a measure for the work spent to move the ligand from the unbound to the bound state[34]. PMF calculations also allow estimating absolute protein-ligand binding free energies[119,120] or the kinetic determinants, k_{on} and k_{off} (eq. (2) in section 2.1), of protein-ligand binding[15].

Figure 4 depicts a simplified and schematic free energy profile for the association/dissociation of a ligand with/from its target structure, which can be approximated by a PMF. The reaction coordinate can be considered as the shortest pathway connecting the unbound (ligand fully solvated in bulk solvent) and bound state (ligand non-covalently bound to the protein structure). In **Figure 4**, the bound conformation is energetically more favorable compared to the unbound state. The bound and unbound conformations are separated by a transition state of relatively high free energy, which points to a practical issue one has to address for pathway sampling methods. In conventional MD simulations, the probability of visiting any microstate is proportional to the Boltzmann factor, with the consequence that high-energy configurations, such as the transition state in **Figure 4**, are less frequently visited than low energy configurations[15]. Even small energetic barriers can hamper sufficient sampling of the configurational space, which is, however, required to estimate binding thermodynamics accurately[1]. Therefore, various techniques were introduced to overcome the limitations of insufficient sampling, which are also summarized under the term of enhanced sampling methods[1]. They can be divided into equilibrium-based methods and non-equilibrium methods[1].

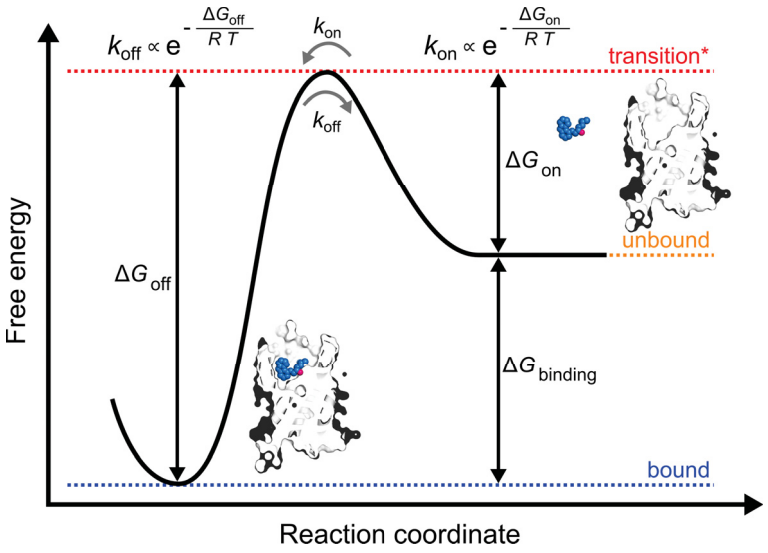

Figure 4: A schematic free energy profile of protein-ligand binding.
A simplified free energy profile that describes the protein-ligand (un)binding process. The reaction coordinate describes the physical association/dissociation pathway between protein and ligand. The bound state corresponds to the free energy minimum and the unbound state to a higher free energy state. The free energy difference between the bound and unbound states ($\Delta G_{binding}$) quantifies the binding affinity. The kinetics of (un)binding are described by k_{on} or k_{off}, and are related to ΔG_{on} or ΔG_{off} via eq. (3) (see section 2.1), respectively, where R is the gas constant and T the absolute temperature in Kelvin. ΔG_{on} or ΔG_{off} quantify the free energy difference of the unbound or bound state relative to the transition state. (Figure adapted from refs.[15,31].)

The Umbrella sampling (US) method[121] denotes a prominent example for an equilibrium-based method, while steered MD simulations in combination with Jarzynski's equality[122] is a popular non-equilibrium approach to compute the PMF[123]. The idea of the US method is to break the reaction coordinate down into a series of windows (umbrellas). For each window, a simulation is run where the system is restraint close the center of the window using harmonic potentials[124]. This procedure allows the rather efficient sampling even at high-energy states[124]. To compute the PMF, the unbiased distribution of sampled states must be extracted from the simulation data[124]. The weighted histogram analysis method (WHAM)[125] is a popular postprocessing method, but the umbrella integration method can be used alternatively[126]. The principal idea of steered MD simulations is to pull or push the system along the reaction coordinate with a constant velocity, thereby forcing the system away from its equilibrium or low energy condition[127]. From the steered simulations, one can derive the applied force, and the work spent to steer the system into the desired state[127]. Repeating the simulations for slightly different reaction coordinates enables to compute the PMF on principles of Jarzynski's equality[122], which connects the equilibrium free energy difference to work done through non-equilibrium processes[128], over the average work spent for many pathways[123,128]. There is, however, some evidence that suggests that the more complex the investigated systems are, the more the US method outperforms steered MD-based methods in terms of the

needed computing time to generate reliable PMFs[129]. Nevertheless, both methods are valuable tools to study protein-ligand interactions as they provide, first, an estimate about protein-ligand affinities, and, second, insights into the structural adaptation mechanisms associated with the ligand binding process.

Historically, PMF calculations were routinely used to study the mechanisms of ion permeation through a wide variety of different channels[130-135], but in recent years these methods were applied to study the thermodynamics of ligand binding. Sun *et al.* applied US to study the (un)binding process of type II kinase inhibitors through different pathways and found evidence that suggests that inhibitors might bind or dissociate through an allosteric channel[136]. In 2010 Colizzi *et al.* reported a steered MD-based computational protocol that could be applied to discriminate between binders and non-binders or active and inactive compounds[137]. Therefore, the authors computed the forces needed to steer structurally related inhibitors of *β*-hydroxyacyl-ACP dehydratase from the binding pocket and found that rupture forces are higher for active compounds than those observed for inactive compounds[137]. Patel *et al.* investigated the unbinding mechanisms of cyclin-dependent kinase 5 inhibitors and could also qualitatively discriminate binders from non-binders[138]. Li and co-workers performed unbinding experiments of neuraminidase inhibitors from their binding pocket and compared the rupture force profiles to commercially available compounds[139]. From the rupture force profiles, they suggest that some of the new ligands are supposed to bind stronger to the protein structure than the marketed drugs[139]. Recently, Palermo *et al.* determined the unbinding mechanism of topoisomerase II inhibitor F14512 and found that the polyamine moiety contributes to a hydrogen bond network, which provides a plausible explanation for its increased potency with respect to other drugs[140]. To corroborate their MD results, the authors designed and synthesized five new compounds bearing a polyamine chain[140]. All of these compounds showed anti-topoisomerase II activity, and four of five were more potent than Etoposide, a known topoisomerase II inhibitor, which denotes an excellent example for the prospective potencies of steered MD-based methods[140]. While the above studies provided a mechanistic insight in protein-ligand (un)binding processes, Woo and Roux applied an US-based approach to accurately compute the absolute binding free energy for a peptide binding to the human Lck kinase[120]. This method was subsequently applied to study antibiotics binding to the bacterial ribosome, and the ranking according to computed binding affinities of all ligands was in agreement with the experimentally observed ranking[141]. Later, Doudou *et al.*[119] and Lee and Olson[142] introduced similar strategies to estimate protein-ligand affinities

based on PMF calculations. Again, the computational results were in reasonable agreement with experiment[119,142].

In sum, the US method is likely one of the most accurate methods to computed changes in binding free energy[15], although it might be considered laborious, as many overlapping windows have to be carefully prepared, equilibrated, and sampled. The same applies to steered MD-based methods that require many individual (un)binding simulations to construct the PMF[15]. Wojtas-Niziurski *et al.* addressed this point and developed an automatized US strategy for calculating multidimensional PMF-based on a significantly smaller number of umbrella windows without any loss in accuracy[143]. For larger ligand data sets, however, binding free energy estimation based on PMF calculations is not yet feasible.

2.2.2.3 Endpoint methods

One reason for the relatively high computational costs of the non-physical and physical pathway methods is that these methods derive the binding free energy from a series of individual simulations along the reaction pathway[144]. Contrarily, endpoint methods compute the binding free energy only considering the free and unbound states of the system and thereby reduce computational costs[1]. One such method is the linear interaction energy approach[145] that uses only data from two simulations, one with the ligand-free in solution and one with the ligand bound to the protein structure[103]. The binding free energy is derived from averaged changes in van der Waals and electrostatic interactions when the ligand changes from the unbound to the bound state[103].

In the class of endpoint methods, the molecular mechanics Poisson-Boltzmann surface area (MM-PBSA) and molecular mechanics generalized Born surface area (MM-GBSA) approaches are well-known proceduers[144]. In contrast to all other methods described so far, MM-PBSA and MM-GBSA use a continuum or implicit solvent model to treat solvent effects[144,146], such that computational costs can be further reduced. In MM-PBSA and MM-GBSA the binding free energy $\Delta G_{\text{binding}}$ is calculated as the sum of gas phase energies and entropic contribution plus solvation free energies according to eq. (7)

$$\Delta G_{\text{binding}} = \Delta E_{\text{MM}} + \left(\Delta G_{\text{solv}}^{\text{complex}} - \Delta G_{\text{solv}}^{\text{protein}} - \Delta G_{\text{solv}}^{\text{ligand}} \right) - T\Delta S_{\text{conf.}} \qquad (7)$$

where ΔE_{MM} and $\Delta S_{\text{conf.}}$ are the changes of the gas phase MM energy and configurational entropy upon ligand binding, respectively, ΔG_{solv} is the change in solvation free energy for

complex, protein, and ligand, respectively, and T is the temperature in Kelvin[144,147]. In practice, whether to use the MM-PBSA or MM-GBSA approach to estimate binding free energies is a question of interest; while MM-PBSA is considered the more rigorous method to calculate absolute binding free energies, MM-GBSA is considered faster and better in ranking structurally similar ligands[146,148,149].

The quality of computed binding free energies, in general, is strongly dependent on the parameters that were chosen for the calculations, in particular, the selected implicit solvent model, the dielectric constant, the method that was applied to derive atomic partial charges, and the simulation protocol to generate the configurational ensemble[146,148-151]. If the relative binding free energies of similar ligands shall be computed, the entropic contribution upon binding is often neglected without decreasing the accuracy of the calculations[148], yielding effective binding free energies[152]. In MM-PBSA and MM-GBSA calculations, binding free energies are computed over a configurational ensemble generated from a single MD simulation of the protein-ligand complex (single-trajectory approach) or three independent simulations for complex, free protein, and free ligand (three-trajectory approach)[144]. The precision of computed binding free energies is also dependent on the simulation protocol. Thus, instead of computing binding free energies over a long trajectory, the accuracy could be increased by computing binding free energies over many but short and independent simulations[153,154]. Interestingly, Hou *et al.* observed that the accuracy of MM-GBSA results varied with the simulation length, but that simulations longer than four nanoseconds do not increase the accuracy of the results when the single-trajectory approach is used[148]. The MM-PBSA and MM-GBSA calculations also allow decomposing the binding free energy into its individual contributions according to eq. (7). There are also strategies established to decompose the binding free energy into the per-residue contributions upon ligand binding[152,155], allowing to study the molecular mechanism of protein-ligand binding in even higher detail.

Comprehensive studies on large data sets were performed by Hou and co-workers or Yang *et al.* to investigate the performance of both methods under changing conditions. They successively resolved the influence of the solute dielectric constant, simulation time, force fields, or charge models[148-151,156]. These studies suggest that the level of accuracy of the binding energy predictions and the correlation with experiment are strongly dependent on structural features of the protein-ligand systems and computation-specific properties. Thus, best correlations were found for data sets of similar ligand that bind to a predominant hydrophobic binding site[148,156]. Homeyer *et al.* studied the performance of MM-PBSA, MM-GBSA, and

TI calculations for three “real life” data sets of compounds from industrial lead optimization and also found that the predictions of binding free energies are of valuable accuracy when considering set-specific features[157]. However, the authors also stressed that care must be taken during all steps of computations, from the preparation of the protein-ligand structures to the interpretation of results[157]. Alternatively, MM-PBSA and MM-GBSA calculations were frequently applied to study the influence of amino acid substitutions in proteins on ligand binding, in particular concerning drug resistance mechanisms. In this respect, recent successes contributed to a better understanding of drug resistance mechanisms of the HIV protease[158-160]. MD simulations, MM-PBSA calculations, and TI calculations revealed that amino acid substitutions induce a pronounced decrease of binding energy towards the tested HIV protease inhibitors[158-160]. Interestingly, some of these substitutions are neither directly involved in drug nor substrate binding, but cause a loss in binding energy[160]. This observation highlights the fact that these methods can also be considered to study long-range influences[160]. Leonis *et al.* also included a novel compound in their calculations and found that the loss in binding free energy is comparable to the marketed ones, but the novel compound shows a favorable change in the polar contribution to the solvation energy upon binding to certain variants[158]. In sum, the good performance and the moderate computational costs make endpoint methods highly valuable to study protein-ligand binding.

2.3 The integration of biophysical experiments and biomolecular simulations

Modern biomedical research intends to understand the function-associated consequences of the structure, dynamics, and interactions of biological molecules on an atomic-level description[14]. In recent years, these challenges were accomplished by the close integration of experiments and simulations[14]. Experimentalists collect lots of data to characterize biological molecules in highly complex environments, and this data must be transformed into a compatible model[14]. Computational scientists often reversely address these question so that they first build a model, which then can be compared with the experimental data, to guide the interpretation of experimental data and to design and predict the outcome of future experiments[14,37]. On the other hand, experiments are indispensable for the corroboration of computational predictions and the further refinement of the model[14].

The term *integrative modeling*, sometimes also referred to as *hybrid modeling*[161], originates from the field of structure determination in classical structural biology[162,163]. In this regard,

experimental data is combined with theoretical information to build a model to increase the accuracy, precision, and efficiency of structure determination[162]. Integrative modeling is of particular relevance for biological molecules that cannot be characterized by a classical structural biology method, such as, for example, X-ray crystallography, NMR spectroscopy, or 3D electron microscopy, as the molecules might be hard to crystallize, are insoluble, or do not retain their spatial configuration over the course of the experimental procedures[162]. As an example, integrative modeling guided the determination of the molecular architecture of the nuclear pore complex, for which the authors combined diverse experimental and theoretical information in an iterative series: (i) data generation by experiment and (ii) translation into spatial restraints, (iii) generation of a structural ensemble by satisfaction of these restraints, and (iv) the analysis of the ensemble to extract the final structure[164,165]. As another example, the molecular assembly of the pore-forming toxin Aerolysin was determined by integrating data from X-ray crystallography, cryo-EM, MD simulations, and computational modeling[166,167]. Furthermore, MD trajectories were screened for agreement with Förster resonance energy transfer data, to describe the molecular architecture of the productive HIV-1 reverse transcriptase:DNA primer-template complex[168]. Alternatively, molecular simulations can also be directly restrained with experimental data[14], such that the physical force field is combined with an experimentally derived biasing potential[169], yielding accurate protein structures when using data from chemical shifts experiments[170,171]. MD simulations with NMR restraints also led to the first structural model of the complex between single-stranded DNA and the single-stranded DNA-binding protein of the filamentous phage M13[172]. Loquet *et al.* considered experimental restraints from solid-state NMR and electron microscopy in Rosetta modeling to derive a model of the bacterial type III secretion needle[173]. To investigate the molecular architecture of the 26S proteasome, Lasker *et al.* derived restraints from electron microscopy, X-ray crystallography, chemical cross-linking, and proteomics and used the Integrative Modeling Platform package[174] to resolve a 3D structural model[175].

Besides structure determination, integrative modeling also provides insight into the function-associated consequences of the structure, dynamics, and interactions of biological molecules[14,37]. By combining data from X-ray crystallography, long and unbiased MD simulations, and *in vitro* mutagenesis experiments, Latorraca *et al.* elucidated an alternating access mechanism in a sugar transporter, providing an atomic-level description how the substrate is carried across the membrane[176]. Similarly, integrating *in vitro* structural and functional

data and computational analyses provided evidence suggesting that the nitrate/nitrite porter NarK functions as an antiporter and that substrate recognition induces structural changes enabling the transport across the membrane[177]. By combining MD simulations and NMR spectroscopy, the allosteric inhibition mechanism of a small molecule binding to a regulator of a G protein signaling molecule was clarified[178]. The integration of homology modeling, docking, and molecular simulations alongside functional *in vitro* experiments provided insights into how substrates and inhibitors bind to a dopamine transporter[179]. Pogoryelov *et al.* provided detailed insights into the rotation mechanism of the ATP-synthase rotor by combining data from free energy MD simulations with data from mass spectroscopy, biochemical experiments, and X-ray crystallography[180]. Microsecond timescale coarse-grained simulations of a model of the influenza A virion, which was derived by combining results from X-ray crystallography, NMR spectroscopy, cryo-EM, and lipidomics, revealed that specific glycoproteins alter the lipid mobility of the virion membrane, which provides a plausible explanation why the influenza virus is robust to changing environmental conditions[181].

Taking together, complementary tools of experimental and theoretical origin often provide insights into different structural aspects of a biological system, and tight integration of these data might provide a deeper level of understanding, which is out of reach for any standalone method[14,37]. In this regard, insights from molecular simulations complement the structural and functional data from experiments. Thus, it is not surprising that in recent years, computational methods gained more and more attention to address sophisticated questions in the field of biomedical research[13,15,37].

2.4 Function-associated molecular recognition in biological processes

So far, I reviewed the principles of protein-ligand recognition and binding. The thermodynamic driving force of the binding reaction is the free energy of binding. I introduced three different classes of computational approaches to compute the binding free energy, from which the alchemical transformation reactions are the most accurate but less efficient approaches, while the endpoint approaches are much faster but less accurate[1]. Besides, I showed how computational alongside experimental methods provide an in-depth understanding of molecular structure and function, which is not possible by any of these methods alone. In the following chapters, I will introduce the reader to three model systems, for which

I in collaboration with experimentalist, in the sense of integrative modeling, investigated the structural, energetic, and functional consequences of molecular recognition processes. In particular, we provide (i) insights into the molecular and functional consequences of amino acid substitutions and posttranslational modifications on enzyme activity (section 2.4.1), (ii) how an antibiotic peptide is recognized by a highly specific protease (section 2.4.2), and (iii) how a novel PPI inhibitor binds to a shallow protein-protein interface.

2.4.1 Protein-ligand recognition in human glutamine synthetase

The GS (glutamine synthetase, glutamate-ammonia ligase, EC 6.3.1.2) catalyzes the ATP-dependent ligation of glutamate and ammonia to glutamine[182]. Based on sequences, structural, and functional aspects, and currently, three classes of GS have been described (**Figure 5**). GS class I enzymes have been found in prokaryotes, in both bacteria and archaea[183], and constitute oligomers of twelve identical subunits[184,185] (**Figure 5**). GS class II enzymes are composed of ten identical subunits and can be found in eukaryotes and in bacteria in families of *Rhizobiaceae*[186], *Frankiaceae*[187], and *Streptomycetaceae*[188] (**Figure 5**). GS class III enzymes, the most different class with less than 10 % sequence identity relative to GS class I and II enzymes[189], was first found in *Bacteroides fragilis*[190] and, later, also in protozoans[191]. GS class III enzymes are organized as homododecamers, such as GS class I (**Figure 5**), but with a much larger amino acid chain (about 730 in GS class III vs. about 450 in GS class III vs. about 360 GS class I)[189]. In sum, all of the known GS structures show a similar organization with some specialized features found in the individual classes (**Figure 5**).

The human GS is encoded by a single gene, *GLUL*[192], and belongs to class II of GS enzymes[193]. Thus, ten identical subunits form a homodecamer in which two pentameric rings stack against each other[25] (**Figure 5**). The *β*-barrel active sites are formed by the association of two adjacent subunits resulting in ten catalytic sites in total. For the glutamine synthesis of GS, a two-step mechanism has been suggested[193-196] and, recently, this two-step mechanism was corroborated by two computational studies for the reaction mechanism on human GS[197,198] and one complementary study on *Mycobacterium tuberculosis* GS[199]. In the first step of glutamine synthesis, adenosine triphosphate (ATP) binds to GS and induces conformational changes to enable the binding of glutamate[194]. After glutamate has bound, the terminal phosphate group of ATP is transferred to the γ-carboxylate group of glutamate yield-

ing adenosine diphosphate (ADP) and γ-glutamyl phosphate (GGP), the reactive intermediate. In the second step of glutamine synthesis, an ammonium ion binds to a negatively charged site pocket formed by D63, E96, and E305[198] (according to the residue numbering of human GS in ref.[25]). Subsequently, ammonia attacks GGP via an S_N2 reaction, which results in inorganic phosphate and glutamine[198]. To yield ammonia as the nucleophile, Krajewski *et al.* proposed that E305 and D63 are involved in ammonium deprotonation[200], later corroborated by computational studies[198,199]. On the other hand, Issoglio *et al*. calculated a $pK_a \sim 7.8$[197] for E305, such that E305 could be protonated (E305-H) at the beginning of the catalytic reaction. They also observed that glutamate binding promotes the interaction of E305-H with D63 by hydrogen bond interactions[197] and concluded that it seems unlikely that any of these residues would be responsible for the deprotonation of ammonium even though they are directly interacting with ammonium[197]. Instead, they propose that the phosphate moiety could be a good candidate for deprotonation of ammonium (in the case of not being already protonated), besides making it an excellent leaving group[197]. While both study results disagree in the point of ammonium generation, such that further research is needed to clarify the open question, both groups agree that the second step is likely the limiting step of the reaction kinetics[197-199]. Both groups calculated an activation free energy for ammonium deprotonation of ~19 kcal mol^{-1} [197,198].

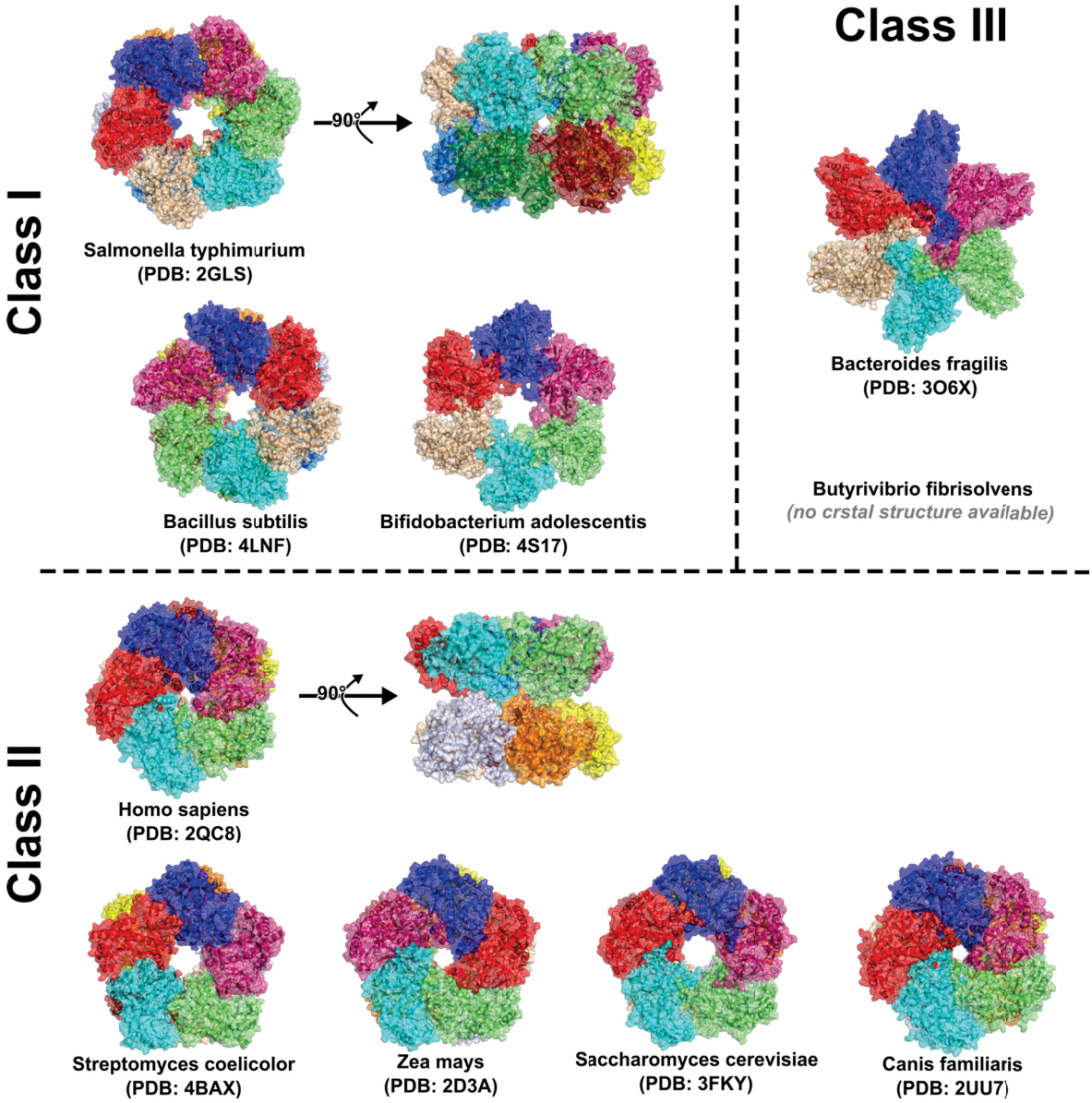

Figure 5: 3D structures and classes of glutamine synthetases.
3D structures of class I[184,185,201], II[25,202-204], and III GS[189]. Corresponding organisms and PDB entries[205,206] are depicted below the GS structures. The individual subunits are colored differently and depicted in surface representation. The structures of class I *S. typhimurium* GS[184] and class II *H. sapiens* GS[25] are rotated by 90° around the x-axis.

Although GS is ubiquitously expressed in human tissues, high concentrations of GS can be found in two different compartments. First, high expression levels of GS are found in brain tissue (**Figure 6**). In particular, GS can be found in astrocytes[207,208], but also in oligodendrocytes, ependymal cells, and some neurons of human brain[209]. In astrocytes, GS is the major route for the removal of ammonia[210-213], which enters the brain mainly by diffusion[214], and to date, there is no other enzyme known that sufficiently replaces GS in cases of GS dysfunction[210,213,215]. The GS-catalyzed reaction is also the predominant route for the removal of glutamate, the major excitatory neurotransmitter in the brain[216]. Benjamin and Quastel

suggested a glutamate-glutamine cycle in the brain[217] (**Figure 6**): (i) astrocytes take up glutamate, which was released from neurons during signal transmission, as a precursor for glutamine and (ii) neurons accumulate glutamine, which was released from astrocytes, as a precursor for the neurotransmitter glutamate[217]. Hence, astrocyte GS is crucial for the cerebral detoxification of ammonia and maintenance of glutamate concentrations between neurons and astrocytes[218].

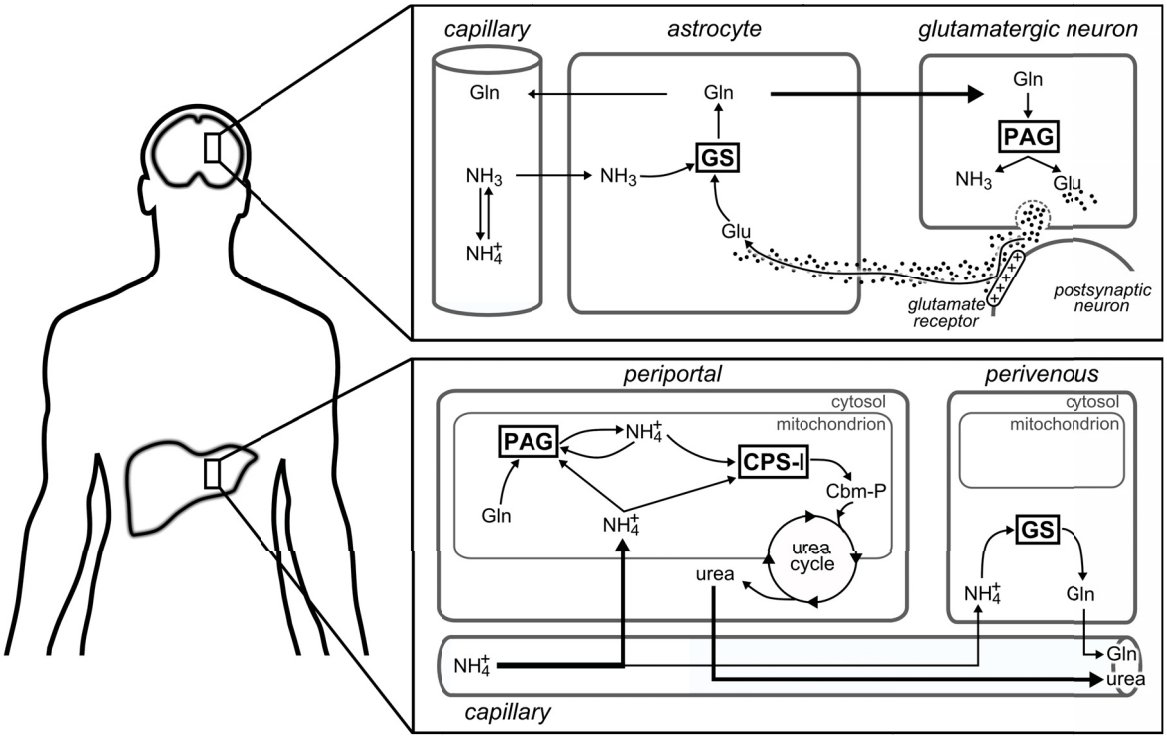

Figure 6: The role of cerebral and hepatic glutamine synthetase in glutamine metabolism.
Abbreviations: GS = glutamine synthetase, PAG = phosphate-activated glutaminase, CPS-I = carbamoylphosphate synthetase I, Cbm-P = carbamoylphosphate, Gln = glutamine, Glu = glutamate, NH_3 = ammonia, NH_4^+ = ammonium ion. The arrow width schematically depicts a likelihood-gradient with wider arrows defining the main route of metabolites. (Figure adapted from refs.[218-220].)

High concentrations of GS can also be found in perivenous hepatocytes[221,222], where GS is one component of the intercellular glutamine cycle and essential for ammonia detoxification by the liver[221,223,224] (**Figure 6**). Under physiological conditions, ammonia-rich blood enters the liver via the portal vein and initially passes periportal hepatocytes capable of urea synthesis[221]. Subsequently, hepatic GS, exclusively found in perivenous hepatocytes, catalyzes glutamine synthesis from ammonia that escaped periportal removal during urea synthesis[221]. This functional hepatocyte heterogeneity represents a periportal low-affinity but high capacity system (urea synthesis) and a perivenous high-affinity system for ammonia detoxication (glutamine synthesis)[220,221,223,225] such that perivenous hepatocytes function as scavenger

cells for ammonia escaping periportal ureogenesis[226] (**Figure 6**). Inhibition of GS with methionine sulfoximine (MSO)[221] or elimination of perivenous hepatocytes with CCl_4[225] hampers efficient ammonia detoxification resulting in increased concentrations of blood ammonia after leaving the liver. Taken together, cerebral and hepatic glutamate clearance, ammonia detoxification, and glutamine formation make GS essential for the human nitrogen metabolism[220,221,227] and neurological functionality.

Accordingly, changes in GS activity or changes in GS expression levels have been linked to several neurological disorders, including Alzheimer's disease[228-230], hepatic encephalopathy [213,224,231,232] and epilepsy[219,233-235] but also general aging[236] and learning processes[237,238]. In particular, inherent GS deficiency, an ultra-rare disease, results in systemic glutamine deficiency and chronic hyperammonemia[16,17,19,239]. Currently, inherent GS deficiency was confirmed in only three patients[16,17,19,239], although there is some evidence that suggests a fourth patient[19]. Patient 1 carried the R324C and patient 2 the R341C variation of GS[16,17,19]. In both patients, GS deficiency resulted in severe brain malformations, multiorgan failure, and, finally, in neonatal death[16,17,19]. The biochemical explanation was a reduced GS catalytic activity for both of the variants[16]. Remarkably, patient 3 who carried the R324S variant survived the neonatal age[239]. The authors' plausible, but not proven explanation for the longer survival of patient 3, compared to patients 1 and 2, was a higher level of GS residual activity compared to the other two GS variants[18]. Nevertheless, due to low glutamine and high ammonia levels, the patient was neurologically compromised and suffered severe episodes of epileptic seizures[18,239]. Enteral and parenteral glutamine supplementation partially improved the clinical status[18], but at the age of six, the patient died from an acute respiratory decompensation[19]. Just recently, another GS variant, which carries the A165D and R319H variants, in a five-year-old boy was reported although the authors state that they cannot confirm the diagnosis of a GS deficiency in this patient[19]. In all cases, however, the molecular mechanisms of how these mutations lead to glutamine deficiency have remained elusive.

In the crystal structure of human GS, residue R324 is directly interacting with ADP[25]. However, it is not clear why the R324C GS is presumably less catalytically active compared to the R324S GS[16]. Residue R341 is neither part of the catalytic site nor interacting with any of the substrates[25]. How the R341C variant causes the deactivation of GS is also not clear. In PUBLICATION I, we, in collaboration with the Clinic for Gastroenterology, Hepatology, and Infectious Diseases at the Heinrich Heine University Düsseldorf, director Prof. Dr. D. Häussinger, provide the first molecular explanation of how the R324C and R341C mutations

cause GS deactivation leading to neonatal death[16,17,19]. Further, we explain why the R324S variant likely conserves a higher level of GS residual activity[18], concerning the R324C variant[16]. In a subsequent study, we found that betaine (trimethylglycine), first, binds to S324 in the R324S GS variant, and, second, stabilizes ATP within the binding site[240]. These find-ings might stimulate the search for new strategies to counteract the effect of an inborn GS deficiency, as, currently, no appropriate medication is available.

Another essential feature of human GS is its sensitivity to protein tyrosine nitration (PTN). Tyrosine nitration in GS was observed for both perivenous GS after treatment with lipopolysaccharide[20] and astrocyte GS after treatment with benzodiazepines[21] and inflammatory cytokines[22]. In all studies, GS tyrosine nitration is always related to GS catalytic inhibition[20-22]. Loss of the catalytic function of GS is also of clinical importance, as lack of GS activity in perivenous hepatocytes leads to hyperammonemia and cerebral ammonia intoxication[224]. However, how this modification causes inhibition of GS catalytic activity is, so far, not understood. In PUBLICATION II, we, in collaboration Clinic for Gastroenterology, Hepatology, and Infectious Diseases at the Heinrich Heine University Düsseldorf, director Prof. Dr. D. Häussinger, provide the first explanation about the inhibitory mechanisms of tyrosine nitration in human GS. These findings indicate a novel, fully-reversible, pH-sensitive mechanism for the regulation of GS function by tyrosine nitration. We also provide a strategy on how to counteract the inhibitory effect of tyrosine nitration in human GS.

2.4.2 Highly specific protein-peptide recognition in the nisin resistance protein

In 1928, Alexander Fleming discovered penicillin[241], the first widespread antibiotic that changed medicine and provided cures for many infections[242]. However, due to the extensive consumption of antibiotics, also the number of antibiotic-resistant bacterial strains increases[243,244]. Today, antibiotic resistance is rising to threatening high levels all over the world, such that the World Health Organization publishes reports to guide resistance prevention[245] and the development of new antibiotic drugs[246].

In recent years, bacteriocins have become of particular interest for various applications, such as antibiotic alternatives or for the application as food preservatives[247-249]. Bacteriocins are ribosomally synthesized and bacterially produced peptides or proteins that exhibit antibacterial activity against other bacteria[250,251]. Lanthipeptides or lantibiotics[252] (from hereafter the term lantibiotic is used for both) represent a large sub-group of bacteriocins[253-256].

Lantibiotics exhibit antimicrobial activities in the nanomolar range[254,255,257], and currently, some lantibiotics are in the preclinical and clinical stages for medical application[258].

In general, these peptides are mostly produced by gram-positive bacteria and contain cyclic structures, the lanthionine rings. Therefore, the ribosomally synthesized peptides undergo posttranslational modifications in terms of dehydration of threonine to dehydrobutyrine (Dhb) and serine to dehydroalanine (Dha)[259]. Both Dhb and Dha residues can react with a cysteine side chain via a Michael addition, yielding the lanthionine rings[259]. However, the number and exact location of the lanthionine rings vary within lantibiotics[259].

Nisin (**Figure 7A, B**) was the first reported lantibiotic[260], which was officially approved in 1969 as a safe food preservative by the joint Food and Agriculture Organization/World Health Organization. Today, nisin and its variants become more important also for biomedical applications including infections associated with drug-resistant pathogens, such as the methicillin-resistant *Staphylococcus aureus*[261-265]. Antibacterial active nisin consists of 34 amino acids and contains five lanthionine-based rings (rings A – E)[27]; rings A, B, and C are separated from rings D and E by a flexible hinge region[266,267]. (**Figure 7A, B**). The antibacterial effect is based on a dual mode of action; first, nisin inhibits cell wall biosynthesis and, second, it disrupts membrane integrity and induces pore formation[268-270]. The nisin N-terminus, carrying rings A, B, and C, binds to lipid II, a precursor molecule for the synthesis of the bacterial cellular membrane, such that the rings A and B form a cage that binds to the pyrophosphate moiety of lipid II[27,268,269] thereby inhibiting cell wall biosynthesis[269]. Alternatively, nisin also induces the formation of pores in the cytoplasmic membrane[268,271], also by binding to lipid II[272]. Here, the highly flexible hinge region allows the C-terminal rings D and E to flip into the membrane[268]. The resulting cytoplasmatic pores are composed of four lipid II and eight nisin molecules[273] with an average pore diameter of ~2.5 nm[268], such that the barrier function is disabled and small molecules can escape from the cell[270]. Remarkably, hardly any resistance against lantibiotics has developed although some bacterial strains have been reported to be congenitally resistant against nisin[274] via different mechanisms, such as cell wall modifications, biofilm formation or the expression of resistance proteins[28,275].

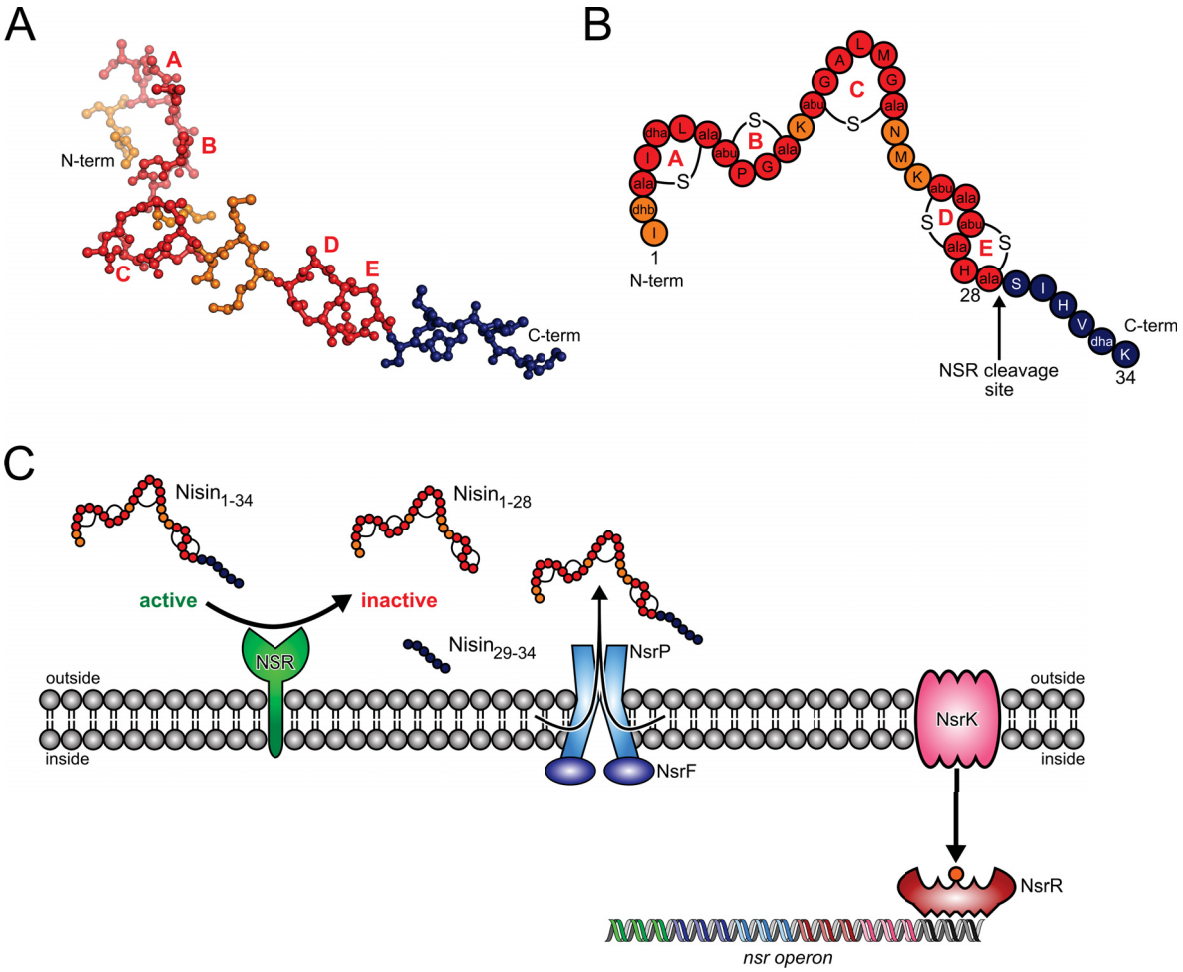

Figure 7: Schematic structure of nisin and its deactivation.
A, B: 3D structure of nisin resolved by solution NMR spectroscopy (**A**; PDB-ID: 1WCO[27]) and schematic representation of nisin (**B**). Residues 1-28 are depicted as orange spheres and residues 29-34 as blue spheres, respectively, with one/three letter amino acid code (ala-S-X = lanthionine rings). Lanthionine rings A-E are labeled with red letters. Numbers below spheres (I1, ala28, and K34) are residue numbers. **C:** Schematic representation of nisin resistance. Nisin resistance can be induced by peptide-bond cleavage between residues 28 and 29 by the membrane-associated (gray bilayer) nisin resistance protein NSR (green) or by the export of nisin from the membrane by NsrFP[276] (blue). NsrRK (red) denotes a two components system that controls the expression of the *nsr* operon (encodes for NSR, NsrFP, and NsrRK) in the presence of nisin upon phosphorylation of NsrR. (Figure adapted from refs.[24,270].)

As to nisin, in particular, the *nsr* operon in *Streptococcus agalactiae* (*S. agalactiae*) was identified to be important for nisin resistance[23]. The *nsr* operon carries the genes *nsr*, *nsrF*, *nsrP*, *nsrR*, and *nsrK*[23]. These genes encode the proteins involved in nisin resistance, namely NSR (the nisin resistance protein), NsrFP (an ATP binding cassette (ABC) transporter), NsrR (a response regulator), and NsrK (a histidine kinase)[23,24]. As to the two latter proteins, NsrR and NsrK built the two-component system NsrRK that is responsible for the controlled expression of the *nsr*, *nsrF*, and *nsrP* genes[23] (**Figure 7C**). Therefore, the kinase domain (NsrK) phosphorylates supposedly D55 of NsrR, which in turn enables NsrR to bind to promotor molecules, initiating the transcription of the target gene[23,277] (**Figure 7C**). As to NsrF

and NsrP, both proteins together set up a functional ABC transporter, in which NsrF represents the nucleotide binding domain and NsrP the transmembrane domain[23] (**Figure 7C**). It is suggested that NsrFP functions as an exporter, such that it exports nisin from the cellular membrane[23,276]. The NSR protein has been described as a membrane-associated protease that cleaves nisin between methyllanthionine 28 (MeLan28) and S29[28,274,278] (**Figure 7B, C**). The cleaved and truncated $nisin_{1-28}$ has a reduced affinity towards the cellular membrane and revealed a 100-fold less antimicrobial activity, although all five lanthionine rings are still present[278]. Remarkably, when the NSR from *S. agalactiae* ATCC 13813 (*Sa*NSR) is expressed in *Lactococcus lactis* (*L. lactis*), the bacterium gains a nisin resistance, which is 20-fold higher compared to non-expressing *L. lactis*[23].

Taking into consideration that the lanthionine rings, in particular, the intertwined rings D and E, usually cause a steric hindrance for protease cleavage, nisin cleavage by NSR is impressive[269]. How NSR specifically recognizes nisin is, so far, unknown. In PUBLICATION III, we, in collaborations with the research group of Dr. S. Smits, report the first 3D structure of *Sa*NSR. Further, we provide a binding mode model of nisin bound to *Sa*NSR that explains why nisin is specifically recognized and cleaved by *Sa*NSR. To overcome the resistance mechanism by *Sa*NSR, we used the reported binding model as a template for the search of the first *Sa*NSR inhibitor.

2.4.3 Targeting protein-protein interactions in human HSP90 for cancer therapy

It has been estimated that in human, more than 80 % of proteins operate in multi-protein complexes[279,280], highlighting the importance of PPIs in biological processes. In particular, PPIs play an essential role in the cellular organization and regulation processes such as cellular growth or apoptosis, which makes PPIs an attractive drug target for cancer therapeutics[281,282]. Proteostasis, also referred to as the protein homeostasis, describes the maintenance of the integrity of the cellular protein network[283] and includes the controlling of protein concentration, conformation, interactions, and localizations[284]. Unbalanced proteostasis due to cellular stress events leads to protein misfolding and aggregation and, thus, constitutes the basis for numerous pathological conditions[284,285]. Chaperones denote a group of proteins that assist in protein folding of newly synthesized proteins, refolding of misfolded proteins, and break up of protein aggregates[285]. Thus, these chaperones are essential for cellular quality control.

Many chaperones are heat shock proteins (HSPs)[286]. The expression of HSPs is sensitive to increased temperature and other stress conditions, such that HSPs are also known as stress proteins[286]. The HSP of 90 kDa (HSP90) is found in nearly all cellular compartments in eukaryotes, but in particular in the cytoplasm where it constitutes 1-2 % of the total protein concentration[285]. HSP90 belongs to the gyrase, HSP90, His kinase, and MutL (GHKL) family of "split ATPases"[283,287], and hence uses the energy released from ATP hydrolysis to fulfill its biological function, namely binding, stabilization, and maturation of numerous proteins[286].

HSP90 is a large and highly flexible protein that operates as homodimer[288,289]. Dimerization is mandatory for it's *in vivo* activity[288,289], but higher oligomeric complexes have been reported, too[290,291]. Each monomer in the HSP90 dimer is composed of three subunits; a highly conserved N-terminal domain (NTD), a middle domain, and a C-terminal domain (CTD) (**Figure 8**). The NTD harbors the ATP binding site and mediates ATP hydrolysis in conjunction with the middle domain[292]. The NTD is connected with the middle domain via a charged and flexible linker, which is also relevant for the client and co-chaperone recognition and binding[285,292-294]. Recently, Verda *et al*. were successful in obtaining a 3.9 Å cryo-electron microscopy structure of a full-length human HSP90–Cdc37–Cdk4 (chaperone–co-chaperone–client) structure, which revealed that both, Cdc37 and Cdk4, predominantly bind to the middle domain with HSP90 clamping around the client protein[293]. The CTD mediates dimerization of HSP90 monomers[295,296], via inter-subunit PPIs and is essential for the *in vivo* activity of HSP90[288]. There is evidence that suggests a second nucleotide binding site within the CTD[297,298], for which, however, currently no structural evidence is available. Finally, the CTD ends in a flexible linker that contains the MEEVD motif that plays a crucial role in co-chaperon recognition[299].

To recognize co-chaperones and client proteins, the HSP90 dimer has to undergo large and highly dynamic conformational shifts, which are also known as the HSP90 chaperone cycle[283,286,300,301] (the complete cycle is summarized in **Figure 8**). In general, during the chaperone cycle, the structural rearrangements are similar to the opening and closing motion of a clamp[301]. Initially, HSP90 adopts a wide-open, V-shaped conformation in the *apo* state, in a way that both NTDs are separated and both CTDs are dimerized[302]. Although HSP90 dimerization can be considered very stable, with a K_D in the nanomolar range[295,303], Ratzke *et al.* reported C-terminal opening and closing dynamics on the time scale of seconds[304]. ATP

binds fast[305,306], but weakly (apparent $K_D \approx 400$ µm[307]) to the highly conserved NTD nucleotide binding site that consists of an α- and β-sandwich motif[286,308]. ATP binding induces the lid region to close over the ATP binding site, leading to an intermediate state[283,301]. The lid closing, in turn, induces NTD dimerization and formation of the closed state[29,283], thereby promoting ATP hydrolysis yielding ADP and inorganic phosphate[309]. These large conformational rearrangements result in a closed state and are considered the rate-limiting step of the whole chaperone cycle[306,310]. After ATP hydrolysis, the chaperone adopts a highly compact state in which the NTDs have rotated downwards, making inter-monomeric contacts[311]. Finally, the lid opens again, HSP90 returns to the open V-shaped conformation, and ADP and inorganic phosphate are released from the nucleotide binding site[283,301,312].

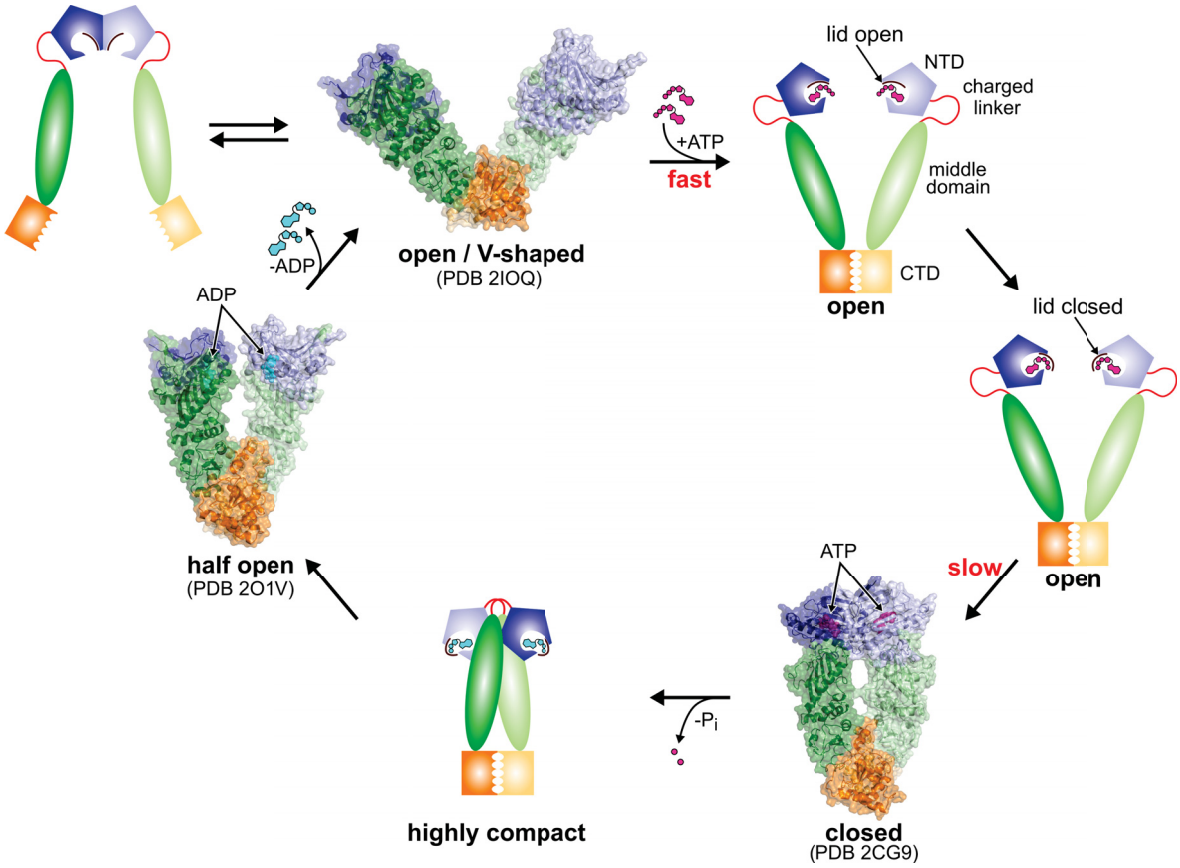

Figure 8: The chaperone cycle of HSP90.
Schematic representation of the proposed HSP90 conformational cycle. In the absence of ATP, HSP90 is in its open, V-shaped conformation (PDB-ID: 2IOQ[302]) and dimerized via the CTD, but in equilibrium with at CTD-open and NTD-closed conformation. ATP binding induces closure of the "lid" followed by the dimerization of the NTD (PDB-ID: 2CG9[29]). ATP hydrolysis leads to a highly compact state before the chaperone partially opens (PDB-ID: 2O1V[313]) and ADP gets released from the binding site. The N-terminal domain (NTD), is colored blue, the middle domain green, and the C-terminal domain (CTD) orange. (Figure was adapted from refs.[283,285,300].)

HSP90 holds a central role in cell regulation and interacts with a myriad of client proteins[b], such as steroid hormone receptors, kinases, or transcription factors[283,314-316]. HSP90 has been reported to be involved in many human diseases in particular neurodegenerative diseases, infectious diseases, and cancer[283]. As to the latter one, many of the chaperone's client proteins have been linked to cellular processes that are associated with the hallmarks of cancer, namely proliferation, evasion of apoptosis, immortalization, invasion, angiogenesis, and metastasis[317] and are, thus, key players in tumor cell growth, proliferation, and survival[318]. There is also some evidence that suggests that cancer cells contain HSP90 complexes in an activated, high-affinity conformation that facilitate malignant progression[319]. In line, increased levels of HSP90 expression were associated with decreased survival rates in breast cancer[320], explaining why HSP90 has been recognized as promising anticancer target[321,322].

Inhibition of HSP90 will interfere with the chaperone cycle, which, in turn, leads to inhibition of client protein activity, promotes proteasomal degradation of oncogenic client proteins, and, thus may counteract the uncontrolled proliferation of cancer cells[323]. Many clinical trials on HSP90 inhibitors that targeted a wide range of different tumor types have been performed, but no inhibitor has been approved for cancer treatment yet[283,324]. Most of the HSP90 inhibitors address the N-terminal nucleotide binding site, as the kinked binding pose of ATP[325] (**Figure 9A, B**) allows specific inhibition of HSP90 by chemical compounds[283]. The natural product Geldanamycin, extracted from *Streptomyces* bacteria, was the first HSP90 inhibitor and blocked the N-terminal ATP binding site[326,327] (**Figure 9B**). Although Geldanamycin showed promising antitumor activity in more than 50 cell lines, poor solubility and stability, and marked liver toxicity in animal models hampered its clinical success[328]. However, many other compounds have been developed that also target the NTD of HSP90[324,329], such as NVP-AUY 922[330] (also known as Luminespib) (**Figure 9B**).

Although a blockade of the ATP binding pocket seems the simplest way to interfere with HSP90's chaperone function, HSP90 inhibitors that bind to the N-terminal ATP binding pocket induce a resistance mechanism called heat shock response (HSR). The HSR is a cellular response that initiates the synthesis of further HSPs, in particular, HSP70 and HSP27, which in turn limit the activity of HSP90 inhibitors as they coordinate malignant protein folding, support tumor growth, hamper apoptosis, and, thereby, induce cancer cell growth[323,331]. Alternatively, molecules that target the CTD of HSP90, such as Novobiocin

[b] A comprehensive list of HSP90 clients is provided by the Picard research group (see https://www.picard.ch/downloads).

(**Figure 9C**) and its coumarin derivatives, do not trigger HSR[331,332]. Interestingly, these molecules are suggested to bind to a second, C-terminal nucleotide binding site of unknown location, thereby interfering with the chaperone function of HSP90[298,333]. Remarkably, the proteasomal degradation of the BCR-ABL, an oncogenic fusion protein with tyrosine kinase activity, sufficient to propagate and sustain cancergrowth[334], was promoted in Novobiocin treated leukemia cells[329]. Alternatively, targeting the interaction between HSP90 and its co-chaperones also shows promising effects[335].

Recently, it was shown that peptides mimicking key interactions in the CTD helix bundle[296] (**Figure 9C**) inhibit HSP90 dimerization[336]. As CTD dimerization is essential for HSP90's chaperone function[289], inhibitors of CTD dimerization may constitute a promising alternative to modulate HSP90 function. Although peptides are frequently used as therapeutics[337], they also bear disadvantages, such as a high degree of conformational flexibility and poor bioavailability due to proteolytic degradation[338]. The use of peptidomimetics may help to circumvent these issues.

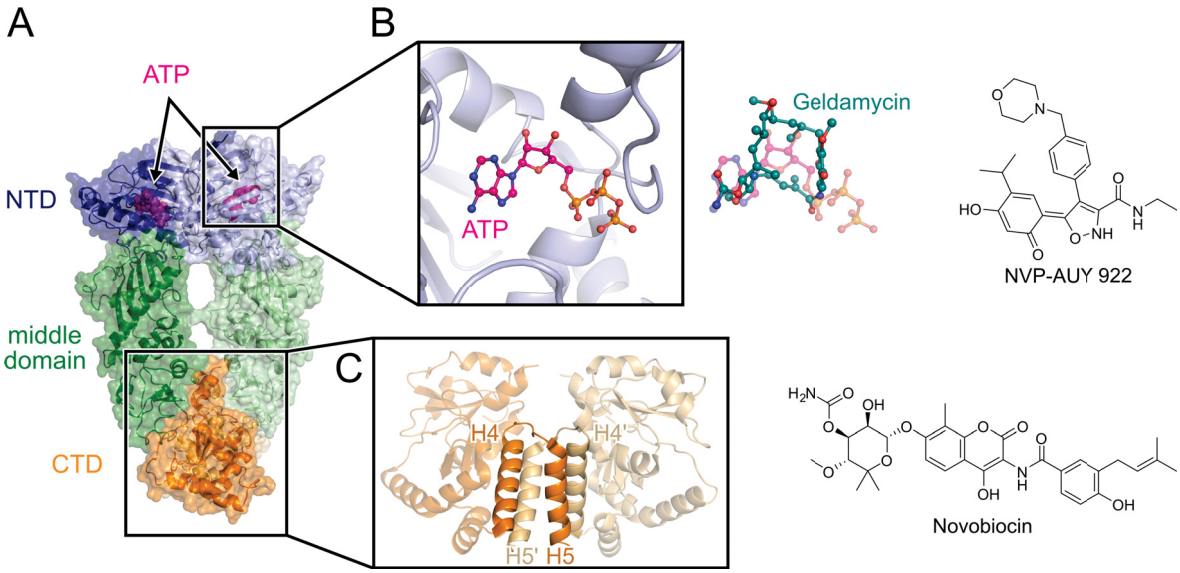

Figure 9: HSP90 inhibitors.
A: 3D structure of ATP bound to the N-terminal domain of HSP90 from *S. cerevisiae* (PDB-ID 2CG9[29]). **B:** Close up view of ATP in its NTD binding site of human HSP90 (PDB-ID 5FWK[293]), overlay of the NTD inhibitor Geldanamycin (after superimposing the protein structure from PDB-ID 1YET[326]), and the 2D structural formula of the NTD inhibitor NVP-AUY 922. **C:** Close up view of the C-terminal domain (CTD) of human HSP90 (extracted from PDB-ID 3Q6M7[290]) and the 2D structural formula of the CTD inhibitor Novobiocin. The helices H4, H4', H5, and H5' form the CTD dimerization interface.

Following the definition of Vagner, Qu, and Hruby[339], peptidomimetics are molecules that mimic a natural peptide in 3D space, interact with the biological target, produce the same effect as the native peptide, but show improved stability and bioavailability. In a previous study, we found that oligomeric α-aminoxy peptides fold into a 2_8-helical conformation,

thereby mimicking the spatial arrangement of peptide side chains in α-helices[340]. Now, we target HSP90 dimerization via the CTD by α-aminoxy peptides as a new class of HSP90 inhibitors. In PUBLICATION IV, we have developed a novel, first-in-class, PPI inhibitor of HSP90 function interfering with HSP90 CTD dimerization.

3. SCOPE OF THE THESIS

In biological systems, molecular recognition describes the process in which macromolecular structures, such as proteins, interact with ligand molecules to form a specific complex (section 2.1). One key determinant of the recognition process between protein and ligand is the affinity between the interacting molecules, and changes in binding affinity might have a marked influence on protein-ligand complex formation.

Enzymes usually show a high affinity towards their substrates, which is a prerequisite for a specific enzymatic activity. However, disturbed recognition mechanisms between an enzyme and its substrate will result in enzymatic malfunction and, in turn, might also result in severe clinical conditions. One example is the human GS that is a pivotal enzyme in the human nitrogen metabolism, and loss of hepatic GS function triggers systemic hyperammonemia (section 2.4.1). In particular, congenital GS variants (R324C, R324S, and R341C) lead to reduced catalytic activity and result in early death (sections 2.4.1 and 4.1). In addition, nitration of residue Y336 in human GS has also been linked to reduced catalytic activity (sections 2.4.1 and 5.1). However, why and how the GS variants and Y336 nitration decrease GS activity has been remained elusive.

Another key determinant of the recognition process between protein and ligand is the high specificity between the interacting molecules, and even ligands that contain an unusual 3D structure can be recognized by specialized enzymes (section 2.1). The recognition of the antibiotic nisin by the resistance protein NSR from *S. agalactiae* denotes an interesting case of enzymatic specificity (section 2.4.2 and 6.1). Nisin shows antimicrobial activity and gains more and more relevance for medicinal applications, including infections associated with multi drug-resistant pathogens. However, NSR specifically cleaves nisin between MeLan28 and S29 and, unfortunately, cleaved nisin is antimicrobial inactive such that NSR expression denotes a known resistance mechanism. Nisin cleavage is simply impressive if one considers, in particular, the intertwined rings in nisin that usually prevent protease cleavage. This raises questions about the determining factors for nisin recognition by NSR.

From a very simplified point of view, the protein-ligand recognition process can be described as the diffusion of ligand and receptor molecules until both molecules come close to each other to form non-covalent or covalent contacts. Recent technical advances enabled to study the complete recognition and binding process in full atomic detail by unbiased MD simulations (section 2.2.1). This is of particular interest in the field of drug development, as MD

simulations can provide a picture of how a novel drug could bind to its target, which might then stimulate further research. In this regard, MD simulations of drug binding can help to guide the understanding of the underlying mode of action. This is of particular interest if the drug binding site is unknown and/or experimentally only difficult to access, as it was the case for a novel HSP90 inhibitor (sections 2.4.3 and 7.1). Most of the HSP90 inhibitors address the N-terminal ATP binding site, but blockade of the ATP binding site induces a resistance mechanism that counteracts HSP90 inhibition. Alternatively, molecules that target the CTD do not trigger these resistance mechanisms. Thus, a drug that targets the CTD is clinically desirable and a promising alternative in cancer therapy.

In the present work, I used MD simulations (section 2.2.1) and binding free energy calculations (section 2.2.2) to investigate the function-associated consequences of protein-ligand, protein-peptide, and PPIs in atomic resolution. In particular, I determined the functional consequences of amino acid substitutions and posttranslational modifications on substrate binding, I predicted a binding mode of an antibiotic peptide bound a binding pocket, and I derived a binding mode model of a novel PPI inhibitor bound to a shallow protein surface. All questions were addressed in an integrative manner (section 2.3), such that results from *in vitro* and *in vivo* experiments[c] were combined with my computational results. In this regard, my computations played a crucial role in the structural interpretation of experimental data, and/or were applied prospectively, such that experiments were subsequently used to corroborate my models. In particular, by combining the results from computations and *in vitro* and/or *in vivo* experiments, we answered the following questions:

I. What are the molecular consequences of the human GS variations that lead to clinically relevant pathologies?
II. How does tyrosine 336 nitration reduce the catalytic activity of human GS?
III. What are the key determinants for nisin recognition and cleavage by NSR from *S. agalactiae*?
IV. How does the novel HSP90 inhibitor Aminoxyrone bind to its target?

which led to the following publications.

[c] The *in vitro* and/or *in vivo* experiments were performed in collaboration with research groups that are explicitly mentioned in the following chapters.

4. PUBLICATION I

Molecular mechanisms of glutamine synthetase mutations that lead to clinically relevant pathologies.

Frieg, B., Görg, B., Homeyer, N., Keitel, V., Häussinger, D., Gohlke, H.
PLoS Comput. Biol. (2016), 12, e1004693.

Original publication, see PUBLICATION I in section 11.1; contribution: 30 % (details provided below).

(The following text was adapted from the above publication.)

4.1 Inborn glutamine synthetase deficiency

The GS catalyzes the ATP-dependent ligation of toxic ammonia and glutamate to glutamine, the most substantial free amino acid[182,194]. Changes in GS activity have been linked to neurological disorders, such as Alzheimer's disease[229,230], hepatic encephalopathy[213,224,231,232], and epilepsy[233-235]. In particular, patients that suffer congenital GS deficiency, an ultra-rare inborn error of glutamine biosynthesis, suffer systemic glutamine deficiency, and chronic hyperammonemia[16,17,19,239]. Initially, the two GS variants R324C (patient 1) and R341C (patient 2) have been linked to congenital GS deficiency[16,17,19]. These variants led to a drop of GS catalytic activity that finally resulted in neonatal death of both patients after a few weeks of life[16,17,19]. Later, another GS variant (R324S) was identified in a three-year-old boy (Patient 3), who was neurologically compromised[19,239]. A plausible but not proven explanation for the longer survival of this patient would be that the R324S variant conserves a higher level of GS catalytic activity compared to the other two GS variants[18]. However, during the disease, glutamine concentrations in blood plasma and cerebrospinal fluid decreased[239] such that the patient received a trial of enteral and parenteral glutamine supplementation[18]. Although glutamine supplementation improved the clinical status and partially rescued the biochemical phenotype[18], the patient finally died from an acute respiratory decompensation after six years of life[19].

The clinical and biochemical phenotypes of the different variants are well described[16,17,19,239]. However, a molecular explanation of how these variants lead to glutamine deficiency has been remained elusive. The crystal structure of human GS[25] revealed that residue R324 is part of the catalytic site and binding to ADP (**Figure 10**). However, why the R324S variant

most likely retains a higher level of GS activity relative to the R324C is not clear. Remarkably, the amino acid R341 is pointing away from the catalytic site and is separated by more than 10 Å (**Figure 10**). Thus, any direct influence of the R341C variant on any substrate is rather unlikely. The mechanism of how the R341C variant causes GS deactivation is also not clear yet.

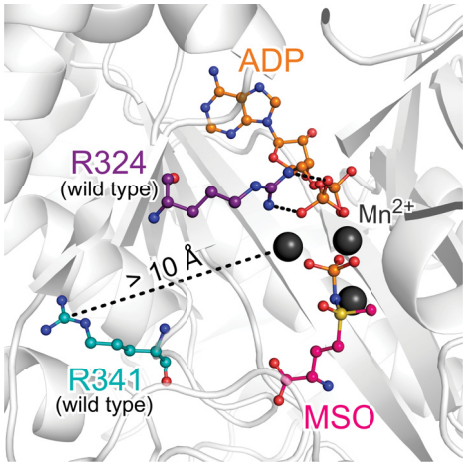

Figure 10: The catalytic site of the human GS.
Close up view of the crystallographic catalytic site of human GS (PDB-ID: 2QC8[25]) with R324 (purple), R341 (cyan), ADP (orange), and phosphorylated MSO (methionine sulfoximine; magenta) depicted as a ball-and-stick model. The structurally bound manganese ions (Mn^{2+}), which are essential for GS function[26], are depicted as gray spheres. The salt-bridge between R324 and ADP is depicted as a black dotted line. R341 is separated by from the catalytic site, schematically depicted by a black dotted line.

Here we set out to determine changes in the GS structure, dynamics, and energetics at the molecular level caused by the three GS variants R324C, R324S, and R341C. Additionally, we determined the differences between both R324C and R324S variants, to provide a plausible explanation of why the R324S likely retains some residual activity[18].

4.2 Molecular consequences of inborn glutamine synthetase mutations

To investigate the molecular consequences of the three GS variants R324C, R324S, and R341C, I performed a set of unbiased MD simulations, binding free energy calculations and rigidity analyses for wild type GS and all three variants. After my calculations, the results were corroborated by *in vitro* experiments performed at the Clinic for Gastroenterology, Hepatology, and Infectious Diseases at the Heinrich Heine University Düsseldorf, director Prof. Dr. D. Häussinger. Together we showed that all GS variants hamper the first steps of glutamine formation, namely ATP or glutamate binding[341].

In detail, I performed unbiased all-atom MD simulations of wild type GS and the three GS variants (GS variants R324C, R324S, and R341C) in explicit solvent. I investigated four different states that represent the individual steps of glutamine synthesis by GS[193-196]. In these states, GS is either bound to ATP (this state is further referred to as GS_{ATP}), to ATP and glutamate ($GS_{ATP+GLU}$), or ADP and GGP ($GS_{ADP+GGP}$). Additionally, I investigated the *apo* state of GS without any ligand bound (GS_{Apo}). For all systems, three replicates were performed each of 100 ns length, which resulted in 3 × 4 × 4 = 48 MD simulations and a total simulation time of 4.8 μs. All results are reported as the mean ± standard error of the mean (SEM) over $n = 3$.

As to the R324S and R324C variants, I found that the direct interactions between the wild type R324 and ATP and ADP (**Figure 10**) are lost in both of the GS variants that explain, why both of the GS variants lead to a reduced GS activity[16-19]. As a measure for the interactions between GS and ATP/ADP, I calculated the distance between the functional groups in the side chains of R324, R324C, and R324C in wild type GS and GS variants, respectively, and the β-phosphate group of ATP and ADP. While the mean distances for wild type GS are not larger than 3.5 Å (SEM < 0.1 Å), the mean distances for both variants are not smaller than 7 Å (SEM < 0.1 Å), which makes any direct contact in both variants impossible (**Figure 11A**). Thus, I hypothesized that the loss of the direct interactions with ATP must be partially replaced by indirect interaction with ATP in R324S GS that may explain the suggested higher residual activity of R324S GS relative to R324C GS[18].

I found indirect water-mediated interactions between R324S/R324C and ATP that are more frequent in the R324S variant. First, I computed the distribution of water molecules around the side chain oxygen (R324S) or sulfur (R324C) (**Figure 11B**). As to R324S GS, I found the first water shell at ~2.8 Å[342] and the second shell at ~4.5 Å (**Figure 11B**). Remarkably, as to R324S GS, the distance of the first water shell peaks at a range of a strong hydrogen bond (2.5 – 3.2 Å[343]), such that two water molecules likely connect the side chain of S324 and ATP (**Figure 11C**). As to R324C GS, the first shell peaks at ~3.2 Å and is ~30 % smaller compared to R324S (**Figure 11B**). Thus, the water shell is considerably more structured in the R324S GS, demonstrating stronger hydrogen bonding, as expected[344]. Next, I computed the occurrence of weak (distance cutoff between hydrogen bond donor and acceptor of d_{cut} = 3.2 Å[343]) and strong (d_{cut} = 2.8 Å[343]) water-mediated hydrogen bonds between R324S or R324C and the β-phosphate group of ATP (**Figure 11D**). The hydrogen bond interactions are more frequent in R324S compared to R324C (**Figure 11D**). Thus, as to R324S GS, the

loss of the direct interaction (**Figure 11A**) is replaced by water-mediated hydrogen bonds (**Figure 11C, D**), which likely explains the suggested higher catalytic activity of R324S GS[18,19].

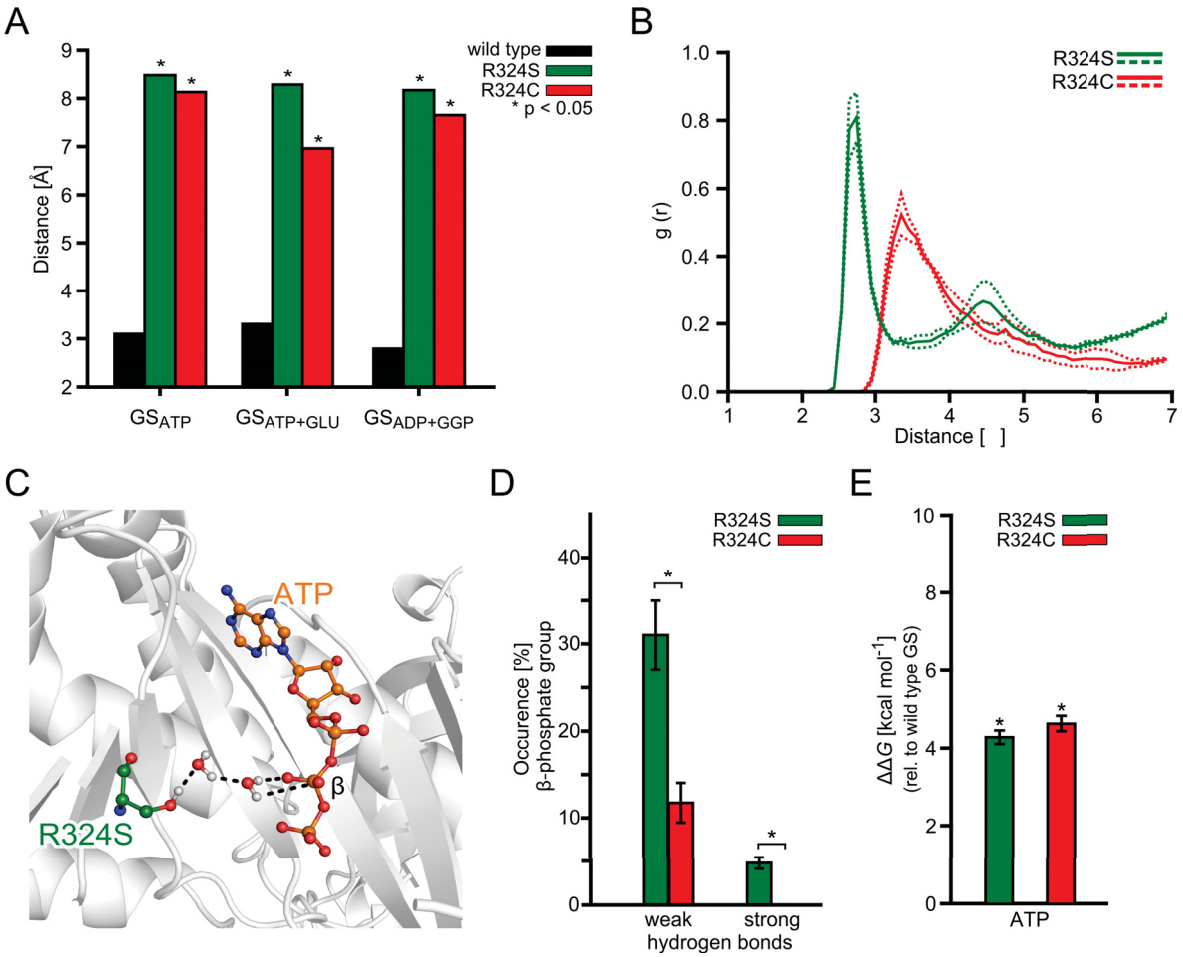

Figure 11: Indirect interactions for R324S and R324C with ATP.
A: Mean distances between R324 (wild type GS), or S324 and C324 in GS variants and the β-phosphate group of ATP/ADP in the GS_{ATP}, $GS_{ATP+GLU}$, and $GS_{ADP+GGP}$ state. Stars indicate significant differences ($p < 0.05$) relative to wild type GS. The SEM is < 0.1 Å and not shown. **B**: Radial distribution function (RDF) of water molecules around side chains of S324 and C324 in GS variants in the $GS_{ATP+GLU}$ state. The solid lines depict the mean RDF, and dashed lines indicate mean ± SEM. **C**: A representative structure extracted from the MD trajectory that depicts the water-mediated interaction between S324 (green ball-and-stick model) and ATP (orange ball-and-stick model), bound to the R324S GS (protein structure depicted as a white cartoon). Hydrogen bonds are shown as black dashed lines. For clarity reasons, only water molecules that are involved in the interactions are shown in this plot. **D**: Mean relative occurrence of water-mediated hydrogen bonds that connect the β-phosphate group of ATP and residues S324 or C324 in the GS variants. The distance cutoff for strong and weak hydrogen bonds was set to 2.8 Å and 3.2 Å[343], respectively. The error bars denote the SEM and the stars indicate a significant difference ($p < 0.05$) between both variants. **E**: Mean effective binding energies relative to wild type GS ($\Delta\Delta G$) calculated by the MM-PBSA approach for ATP binding to R324S and R324C GS. Error bars indicate SEM_{total} (eq. 3 in PUBLICATION I[341]); stars indicate a significant difference ($p < 0.05$) between wild type and variant. In **A**, **B**, and **D**, mean values and SEM were calculated over three trajectories each. Results for wild type, R324S, and R324C GS are always shown in black, green, and red, respectively. (Figures and caption are taken from PUBLICATION I[341].)

The favored water-mediated hydrogen bonds in R324S GS are also in agreement with results from MM-PBSA calculations that suggest that ATP binding is energetically more favored in R324S GS compared to R324C GS (**Figure 11E**). Nevertheless, ATP binding is significantly disfavored in both variants with respect to wild type GS (**Figure 11E**), which provides a plausible explanation for the impaired catalytic activity of both variants[16,17,19,239].

As to the R341C variant, I found a long-range effect between the catalytic site and the region around helix H8 (residues 266-288) on the outside on the protein surface. Therefore, I first investigated the influence of variant R341C on GS' mechanical stability and applied the constraint network analysis[345]. The loss of interactions of R341 leads to a significant destabilization of the C-terminus of the GS, in particular in the region around helix H8 (**Figure 12A**). I identified that R341 forms hydrogen bonds with H281, H284, and Y288 on H8 (**Figure 12B**) that could be relevant for structural integrity. Thus, I analyzed the structural stability of H8 during MD simulations of wild type and R341C GS. The secondary structure analysis of helix H8 revealed an increased loop probability for H8 residues in R341C compared to wild type GS (**Figure 12C**). To further corroborate this finding, I introduced another GS variant (H281A/H284A/Y288A variant; named HHY hereafter) that mimics the loss of interactions between R341 and helix H8. Again the loop probability of residues on H8 increases relative to wild type GS (**Figure 12C**), which further supports the conclusion that R341 stabilizes H8 in wild type GS; this stabilizing influence is lost in both the R341C and HHY variants. As ATP binding to GS induces a shift of H8[25] that is a prerequisite for glutamate binding[25], I hypothesized that glutamate binding might be hampered in the R341C var-iant. The hypothesis was corroborated by MM-PBSA calculations that revealed energetically disfavored glutamate binding for the R341C variant relative to wild type GS (**Figure 12D**).

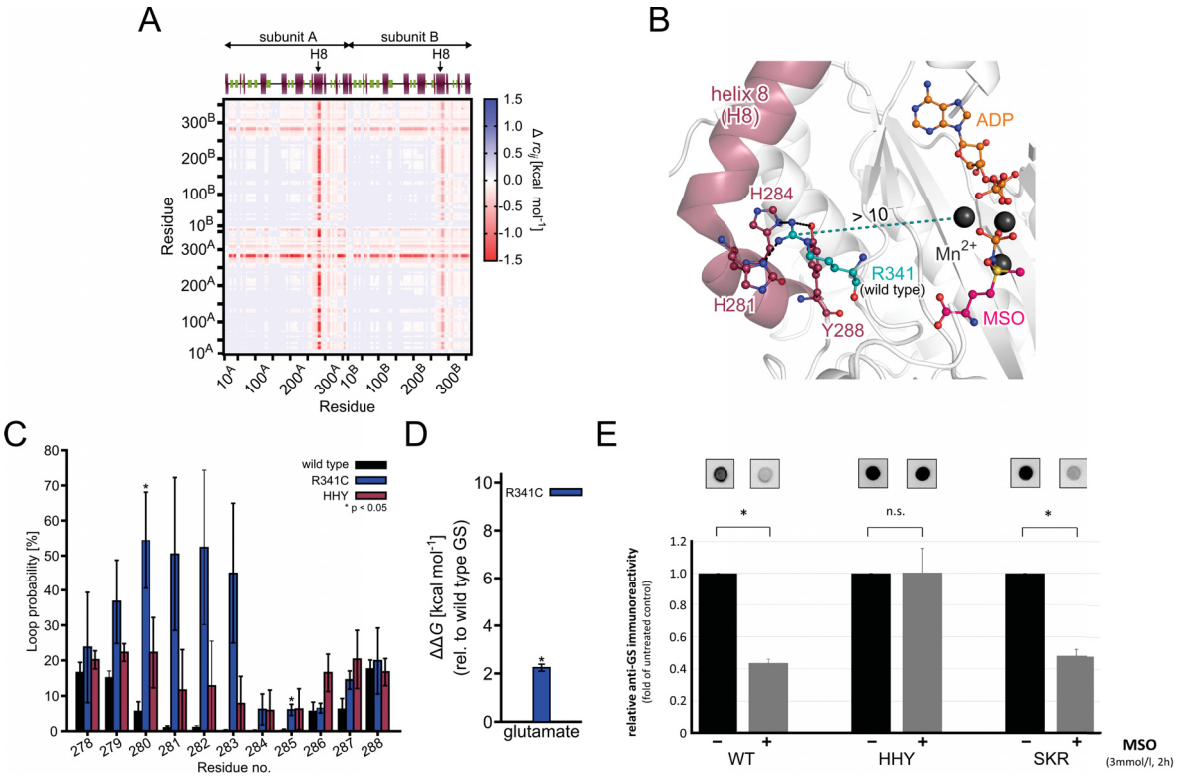

Figure 12: Structural changes in the R341C variant and experimental validation by dot-blot analysis. **A:** Stability map depicting significant differences ($p < 0.05$) in the structural stability as computed by constraint network analysis[345] between wild type GS and the R341A variant. Red colored areas in stability map[346] depict areas, where the variant is less stable compared to wild type GS. The GS secondary structure is depicted on the top, with green bars representing β-strands and raspberry bars representing α-helices. The horizontal arrows indicate subunits A and B. The vertical arrows point to H8. **B:** Close up view of the crystal structure of human GS (PDB-ID: 2QC8[25]) around R341 that shows the interactions between R341 (cyan) and H281, H284, and Y288 on helix 8 (H8; raspberry), depicted by black dashed lines. The structurally bound ADP (orange), MSO (magenta), and manganese ions (Mn^{2+}, gray spheres) depict the location of the catalytic site. **C:** Loop probability for residues 278 to 288 of H8 for 3 × 100 ns MD simulations of wild type GS, the R341C variant, and the HHY variant in the GS_{ATP} state. The error bars denote the SEM and the stars significant differences ($p < 0.05$) relative to the wild type. **D**: Mean effective binding energies relative to wild type GS ($\Delta\Delta G$) calculated by the MM-PBSA approach for glutamate binding to the R341C GS. Error bars indicate SEM_{total} (eq. 3 in PUBLICATION I[341]); stars indicate a significant difference ($p < 0.05$) between wild type and variant. **E:** GS-YFP-transfected human embryonic kidney cells (HEK293) were either left untreated (-) or treated (+) with the GS inhibitor MSO for two hours. Equal amounts of GS were spotted onto a nitrocellulose membrane and detected by dot-blot analysis, followed by densitometric quantification of anti-GS immunoreactivity. Anti-GS immunoreactivity in MSO-treated cells is given relative to the untreated control. Stars denote significant differences ($p < 0.05$) relative to untreated control. n.s.: not statistically significantly different. (Figures and caption are taken from PUBLICATION I[341].)

Next, we investigated the role of the R341C/HHY interactions *in vitro*[d]. Previous studies revealed that MSO binding to GS masks the epitope for a monoclonal antibody raised against GS[347]. As MSO binds to the glutamate binding site[25] and irreversibly inactivates the enzyme[348], MSO binding was used as a surrogate for glutamate binding. As residue R341 is essential for antibody binding, we used the HHY GS variant in our *in vitro* experiments. As

[d] The biochemical experiments were performed at the "Clinic for Gastroenterology, Hepatology, and Infectious Diseases, Heinrich Heine University Düsseldorf, Düsseldorf, Germany", director Prof. Dr. D. Häussinger.

a control, another GS variant (S278A, K279A, and R280A; named SKR hereafter) was introduced. In the SKR variant, the modified residues are also located on H8 but do not interact with R341. We hypothesized that MSO would mask the epitope for a monoclonal antibody in wild type GS and SKR GS, but not in HHY GS. **Figure 12E** shows that MSO-treatment significantly reduced anti-GS immunoreactivity in wild type GS and SKR GS. By contrast, anti-GS immunoreactivity was unchanged in MSO-treated HHY GS, indicating impaired substrate binding to the catalytic center, which is in perfect agreement with the computational results. In sum, impaired substrate binding provides a plausible explanation for the loss of enzymatic activity[16,17,19] (**Figure 12E**).

4.3 Conclusion and significance

In this study, I significantly contributed to a collaborative study, in which we investigated the molecular mechanisms, how the three clinically relevant GS variants R324C, R324S, and R341C cause GS catalytic deactivation[16-19]. To do so, we combined atomistic simulations with biochemical experiments and found strong evidence that suggests that all three variants hamper the first steps of GS' catalytic cycle, namely ATP or glutamate binding.

As principal results, we found that:

- the first steps of the GS catalytic reaction, namely ATP and glutamate binding, are hampered in all three variants, which explains GS deactivation,
- the direct interaction between the wild type R324 and ATP is lost in both R324S and R324C variants. As to the R324S variant this loss is partially compensated by an indirect water-mediated interaction via hydrogen bonds, which likely explains the residual R324S GS catalytic activity[18],
- loss of interactions between R341 and amino acids on helix H8 leads to a pronounced destabilization of H8, which negatively affects glutamate binding and *in vitro* experiments supported for my predictions.

This study provides the first molecular insights into the impaired catalytic mechanisms of clinically relevant GS variants. It also provides the structural basis for identifying potential strategies to counteract the effects of the GS variants, as currently, no therapy is available to

treat inborn GS deficiency. In the search for a treatment of this ultra-rare disease, our findings could stimulate the development of ATP binding enhancing molecules for the R324S variant by which the R324S GS variant can be "repaired" extrinsically[349].

5. PUBLICATION II

Mechanism of fully-reversible, pH-sensitive inhibition of human glutamine synthetase by tyrosine nitration.

Frieg, B., Görg, B., Qvartskhava, N. Jeitner, T., Homeyer, N., Häussinger, D., Gohlke, H. *submitted.*

Original manuscript, see original PUBLICATION II in section 11.2; contribution: 30 % (details provided below)

(The following text was adapted from the above publication.)

5.1 Protein tyrosine nitration in human glutamine synthetase

Hepatic and cerebral GS is highly sensitive to PTN that, in turn, causes GS catalytic inhibition[20-22]. PTN is a post-translation modification under "nitroxidative stress" conditions yielding 3'-nitro tyrosine[350,351] (in the following named TYN and referring to the nitrated amino acid in solution; **Figure 13A**) and causes a drop of the pK_a of the phenolic hydroxyl group by three log units[352]. Thus, also the deprotonated phenolate variant (in the following named TYD and referring to the nitrated amino acid in solution; **Figure 13A**) is also relevant under physiological condition. As to human GS, tyrosine 336 (Y336; according to the crystal structure numbering[25]) was identified to be the target of nitration[20,353] and linked to hepatic and cerebral GS inhibition[20-22]. In the crystallographically resolved structure of human GS[25], Y336 is part of a predominately hydrophobic pocket that harbors the purine ring of ADP, thereby interacting via face-to-face stacking with ADP (**Figure 13B**). It is reasonable to assume that Y336 most likely interacts similarly with ATP, the precursor for ADP. Although PTN modifies key properties of the amino acid, such as phenol group pK_a, redox potential, hydrophobicity, and volume[351,354], any molecular explanation has been remained elusive how Y336 nitration causes GS catalytic inhibition.

In the present work, I performed unbiased MD simulations as well as binding and configurational free energy calculations to clarify the molecular mechanisms of GS catalytic inhibition by Y336 nitration. My results guided the design of subsequent biophysical and biochemical *in vitro* experiments. Together we revealed a novel regulatory mechanism of human GS function by Y336 nitration.

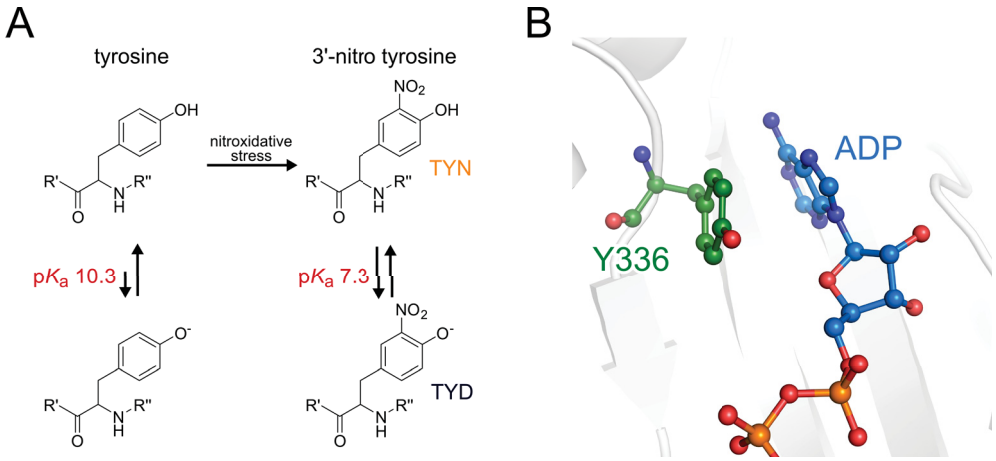

Figure 13: Protein tyrosine nitration in human glutamine synthetase.
A: Schematic mechanism of tyrosine nitration. Tyrosine nitration decreases the pK_a of the phenolic hydroxyl group by three log units[351], such that there is an equilibrium between the protonated (TYN) and deprotonated (TYD) state at physiological pH (figure adapted from ref.[351]). **B:** ADP (blue) and tyrosine 336 (Y336, green) depicted as a ball-stick model in crystallographic poses[25]. (Figures and caption are taken from PUBLICATION II.)

5.2 The pH sensitivity of glutamine synthetase inhibition by Y336 nitration

To address the unresolved question, how Y336 nitration causes GS inhibition, I performed unbiased all-atom MD simulations in explicit solvent of three different GS variants; i) wild type GS carrying Y336, ii) GS carrying TYN336 (the protein system is always referred to as GS_{TYN}), and iii) GS carrying TYD336 (the protein system is always referred to as GS_{TYD}) bound to ATP. All GS variants were subjected to 5 × 500 ns of unbiased MD simulations, such that total simulation time of unbiased MD simulations cumulate to 7.5 µs.

To characterize the stacking interactions between the phenyl ring of Y336/TYN336/TYD336 and the purine ring system of ATP, the MD trajectories were analyzed towards the distance between the centers of mass (**Figure 14A**) and the angle η between the planes of these ring systems (**Figure 14B**). The measurements indicate that the major populations are found at short distances ($d \approx 3.8$ Å, **Figure 14A**) and for an almost parallel orientation of the ring systems ($\eta \approx 8°$, **Figure 14B**) for all GS variants, although the relative frequencies of the changes decrease from wild type GS to GS_{TYN} to GS_{TYD}. The shapes of the histograms also reveal populations at higher distances or angles, in particular for GS_{TYD} (**Figure 14A, B**). *Ab initio* calculations found that interactions for face-to-face tyrosine/adenine arrangements are strongest for a coplanar arrangement between the ring systems (at distances < 4 Å and $\eta \approx 10°$, respectively[355]). Thus, these distance and angle measurements suggest that Y336 nitration weakens the tyrosine/adenine interaction, especially in GS_{TYD}. Configurations extracted from the MD ensemble revealed that the coplanar

orientation of the rings is partially lost and ATP is more mobile in both nitrated GS variants (**Figure 14C**). By computing the root mean square fluctuations (RMSF), a measure for mobility, for all non-hydrogen atoms in ATP, I corroborated this hypothesis as ATP bound to GS_{TYD} shows a significantly increased mobility relative to ATP bound to wild type GS (**Figure 14D**). These results again suggest that TYD336/ATP interactions are weakened in the GS_{TYD} variant compared to the Y336/ATP interactions in wild type GS.

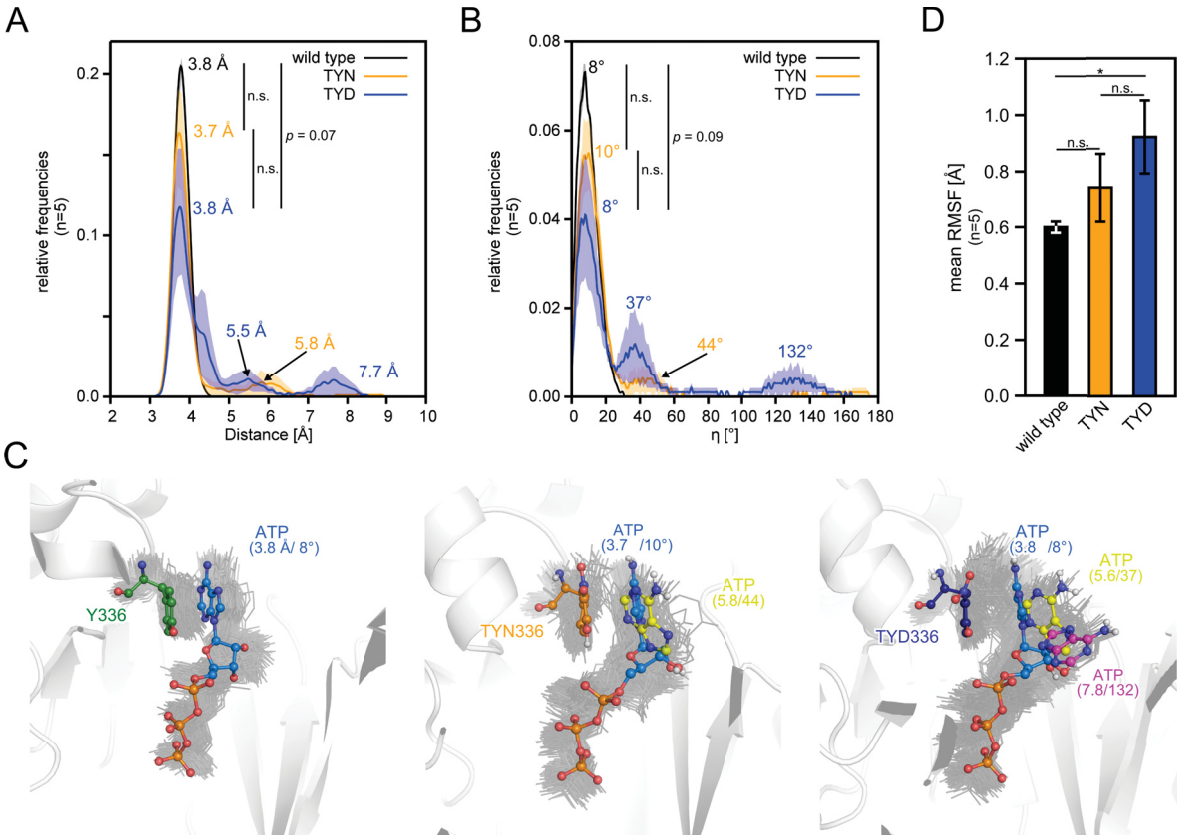

Figure 14: Structural consequences of Y336 nitration.
A, B: Mean relative frequencies (normalized by the sum of all bins) with standard error of the mean (SEM; depicted as filled curve) for (**A**) the distance between the centers of mass of the phenyl ring (residue Y336/YTN336/TYD336) and the purine ring system (ATP) (bin size 0.1 Å) and (**B**) the angle between the ring planes of the phenyl ring (residue Y336/YTN336/TYD336) and the purine ring system (ATP) (bin size 1°). **C:** Representative structures extracted from the MD trajectory for wild type GS (left), GS_{TYN} (middle), and GS_{TYD} (right). In the foreground, representative ATP configurations belonging to the main populations in **A** and **B** (see respective labels depicting "distance [Å]/η [°]" combinations) are depicted as an opaque ball-stick model. For representative purposes, for ATP molecules that do not belong to the major population, only the adenine system is shown. In the background, an overlay of ATP configurations extracted in 10 ns intervals is depicted as gray sticks that visualizes the motion of ATP throughout the MD simulations. **D:** Mean root mean square fluctuation (RMSF) with SEM (error bars) calculated for all non-hydrogen atoms in ATP. * Statistically significantly different compared to wild type GS ($p < 0.05$). n.s.: not significantly different. (Figures and caption are taken from PUBLICATION II.)

In agreement with the structural analyses, I computed, by means of subsequent MM-PBSA calculations, that ATP binding is energetically disfavored in GS_{TYD} ($\Delta\Delta G_{effective}$ = 4.57 kcal mol^{-1} ± 0.06 kcal mol^{-1}; $p < 0.01$) but, interestingly, favored in GS_{TYN} ($\Delta\Delta G_{effective}$ = -2.84 kcal mol^{-1} ± 0.04 kcal mol^{-1}; $p < 0.01$) relative to wild type GS (**Figure 15A**).

While MD simulations and MM-PBSA both suggest that ATP binding is significantly weakened in GS_{TYD}, both methods also suggest that GS_{TYN} does not affect or even slightly promote ATP binding. However, instead of influencing the thermodynamics of ATP binding, Y336 nitration might also influence the ATP binding process by introducing a barrier along the ATP binding path.

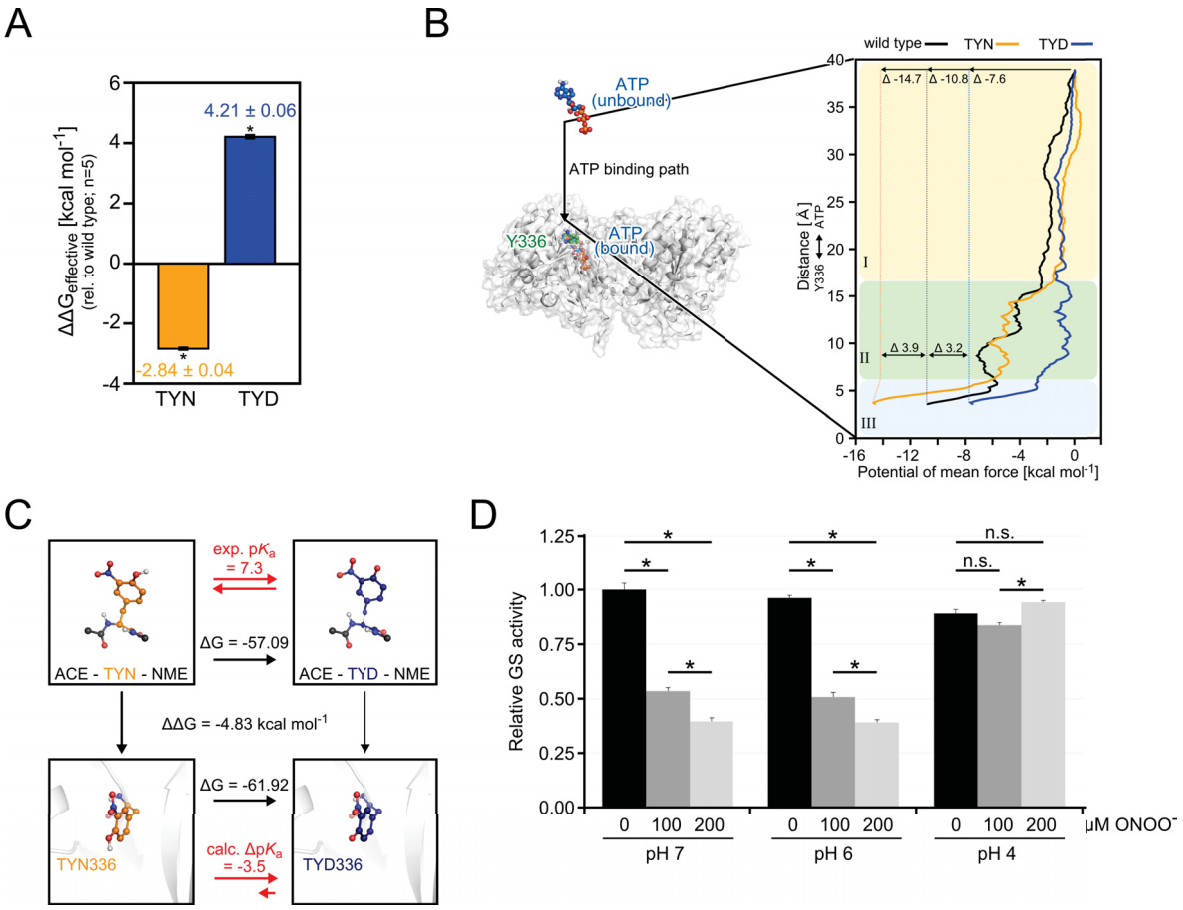

Figure 15: pH-sensitive inhibition of GS activity.
A: Mean relative effective binding energies relative to wild type GS ($\Delta\Delta G_{effective}$). $\Delta\Delta G$ values were calculated by using the MM-PBSA approach for ATP binding to both nitro variants GS_{TYN} (orange) and GS_{TYD} (blue). Error bars indicate SEM; stars indicate a significant difference ($p < 0.05$) between wild type GS and GS_{TYN} or GS_{TYD}, respectively and labels depict $\Delta\Delta G_{effective}$ ± SEM in kcal mol^{-1}. **B:** Schematic depiction of the ATP binding path and the corresponding potential of mean force (PMF), for ATP binding to wild type GS (black), GS_{TYN} (orange), and GS_{TYD} (blue). **I** (yellow background), **II** (green background), and **III** (cyan background) depict the phases of ATP binding. Configurational free energies are normalized relative to the unbound state (Distance = 38.9 Å). Labels depict relevant changes in the PMF (in kcal mol^{-1}). **C**: Thermodynamic cycle employed for studying the protonation state of nitrated Y336. The free energy differences ΔG were calculated by thermodynamic integration for transformations of TYN into TYD (top panel depicts the transformation for ACE-TYN/TYD-NME, the bottom panel for TYN336/TYD336 in the GS structure). The difference in free energy $\Delta\Delta G$ was calculated according to eq. (6) and the pK_a shift (calc. ΔpK_a) according to eq. (9). The experimentally determined pK_a (exp. pK_a) was measured for free 3-nitro tyrosine[352]. At physiological pH (~7.4), the TYD state in GS is preferred over the TYN state (schematically depicted by red arrows). **D:** pH dependence of $ONOO^-$-mediated inhibition of GS activity. Purified human GS was exposed to different concentrations of $ONOO^-$ (0, 100, or 200 μM), and aliquots were taken for measuring GS activity. GS activity in vehicle-treated control at pH 7.0 was set to 1, and activities measured under the other experimental conditions are given relative to it. *: statistically significantly different. n.s.: not statistically significantly different. (Figures and caption are taken from PUBLICATION II.)

Thus, I performed US simulations of ATP binding to wild type GS, GS_{TYN}, and GS_{TYD}. The complete ATP binding path covers a distance of ~37 Å, divided into 75 windows/umbrellas and each window/umbrella was sampled for 60 ns. Thus, US simulations cumulate to a total simulation time of 3 × 75 × 60 ns = 13.5 µs. Subsequently, the PMF was derived by using WHAM and revealed several interesting facts (summarized in **Figure 15B**). First, the ATP bound state is markedly favorable over the unbound state for all GS variants. Second, the ATP binding process can be separated into three phases (I, II, and III). During phase I, ATP diffuses freely around all GS variants (see original PUBLICATION II in section 11.2). During phase II, ATP gets weakly rejected in GS_{TYD}, which may hamper further ATP binding. By contrast, in GS_{TYN} and wild type GS, ATP becomes bound via hydrogen bonds involving the phenolic hydroxyl group (see original PUBLICATION II in section 11.2). During phase III, ATP reaches the bound state with a minimum in the PMF at $\approx$ 3.7 Å for all GS variants. In the bound state, relative changes between wild type GS, GS_{TYN}, and GS_{TYD} reveal that ATP binding is thermodynamically disfavored in GS_{TYD}, but, again, is favored in GS_{TYN}, mirroring the results from MM-PBSA calculations (**Figure 15A**). Taken together, results from MD simulations and free energy calculations suggest that ATP binding is thermodynamically disfavored in GS_{TYD}, but favored in GS_{TYN}.

Nitration of free tyrosine decreases the pK_a value of the phenolic hydroxyl group by three log units[351] (**Figure 13A**), but the protein environment may further influence the pK_a of amino acids[356]. To probe whether such influence also exists in the present case, I computed the pK_a shift of TYN336 (within the protein environment) relative to free TYN. Therefore, I used the relation of the equilibrium constant K_a and the standard free energy ΔG (adapted from eq. (3) in section 2.1) that can also be expressed as

$$\mathrm{p}K_a = -\log K_a = \frac{1}{2.303\,RT}\Delta G \tag{8}$$

or

$$\mathrm{p}K_{a,\mathrm{prot.}} = \mathrm{p}K_{a,\mathrm{model}} + \frac{1}{2.303\,RT}\Delta\Delta G \tag{9}$$

where R is the gas constant of 0.001987 kcal mol^{-1} K^{-1}, T = 300 K, and $\Delta\Delta G$ is the difference in free energy between the protein-embedded and the free amino acid[357]. $\Delta\Delta G$ in eq. (9) was computed by evaluation of the thermodynamic cycle derived using TI computations, yielding $\Delta\Delta G$ = -4.83 kcal mol^{-1} (**Figure 15C**), indicating a marked decrease of the pK_a (-3.5 log

units) of TYN336 embedded in GS to pK_a ≈ 4. Hence, at physiological pH (≈ 7.4), the TYN336:TYD336 ratio thus amounts to ~1:4,000, such that only TYD336 is relevant under these conditions. These findings are further supported by *in vitro* experiments[e] showing a reduced catalytic activity of nitrated GS at pH 7 and pH 6, but not at pH 4 (**Figure 15D**). Together with the above findings that ATP binding is weakened in GS_{TYD}, this result explains how tyrosine nitration leads to GS inhibition[20,358].

5.3 Conclusion and significance

In the present work, I significantly contributed to a collaborative study that set out to determine the molecular mechanisms of how Y336 nitration causes inhibition of human GS. For this, we combined atomistic simulations with biochemical experiments and found strong evidence that suggests that nitration of Y336 hampers binding of the substrate ATP in a pH-dependent manner.

As principal results, we found that:

- Y336 nitration weakens the interactions between Y336 and the substrate ATP, but only if nitrated Y336 exists in its deprotonated TYD336 state,
- nitrated Y336 predominantly exists in the deprotonated TYD form at physiological pH conditions,
- by decreasing the pH *in vitro,* we showed that the inhibitory effect of Y336 is fully-reversible.

So far, tyrosine nitration has been related to three effects on protein function: loss of function, a gain of function, and no change on protein function (for a comprehensive review, see ref.[359]). This study, however, indicates a novel regulatory mechanism of protein function mediated by PTN. As the pK_a value of 3‘-nitrotyrosine can vary within a protein, depending on the environment, the observed pH sensitivity on the impact of tyrosine nitration on protein function will have to be considered in evaluating existing and future studies on PTN.

The observed pH sensitivity of GS function due to Y336 nitration may be of clinical importance, as a reduced GS activity leads to hyperammonemic conditions[224], which, in turn,

[e] The biochemical experiments were performed at the “Clinic for Gastroenterology, Hepatology, and Infectious Diseases, Heinrich Heine University Düsseldorf, Düsseldorf, Germany”, director Prof. Dr. D. Häussinger.

may then completely abolish GS activity. A strategy to shift the TYN336:TYD336 equilibrium towards the TYN336 state in tissues with high GS expression denotes a plausible but also sophisticated route to counteract the inhibition of GS by Y336 nitration. Interestingly, the ionophore Nigericin lowers the intracellular pH from ~7 to ~5.5 in nonproliferating rat hepatocytes in primary monolayer culture, which might denote a promising starting point for further research in that direction[360].

6. PUBLICATION III

Structural basis of lantibiotic recognition by the nisin resistance protein from *Streptococcus agalactiae*.

Khosa, S.[§], **Frieg, B.**[§], Mulnaes, D., Kleinschrodt, D., Hoeppner, A., Gohlke, H., Smits, S.H.J.

Sci. Rep. (2016), 6, 18679

[§] Both authors contributed equally to this work.

Original publication, see original PUBLICATION III in section 11.3; contribution: 30 % (details provided below)

(The following text was adapted from the above publication.)

6.1 Lantibiotics, nisin, and nisin resistance

Lantibiotics are antimicrobial peptides, synthesized by bacteria[253,254,256,270], exhibit antimicrobial activities in the nanomolar range[254,255,257], and represent a promising class for future therapeutic application to overcome existing antibiotic resistances[253,254,256,270,361]. Nisin was the first described lantibiotic[260], shows high efficiency in the treatment of staphylococcal mastitis in human[270,362] and dairy cows[270,363], and is commercially used as food preservative[270,364-366] (E234, Nisaplin®). Although nisin exhibits its antimicrobial activity via multiple modes of actions[27,268,269,273,367], some bacterial strains have been reported to be naturally resistant towards nisin[274,275].

In particular, the nisin resistance protein NSR from *S. agalactiae* ATCC 13813 (*Sa*NSR), a protease that cleaves the peptide bond between MeLan28 in ring E and S29 in nisin (**Figure 7C**), induced a 20-fold increased resistance towards nisin when expressed in *L. lactis*[23]. Taking into consideration that the bulky lanthionine rings usually cause a steric hindrance that prevents peptide cleavage[24], the cleavage of nisin by *Sa*NSR is impressive. However, the underlying mechanisms of how NSR recognizes nisin has remained elusive. A thorough understanding of the underlying mechanisms by what means *Sa*NSR recognizes nisin may encourage the research and development of new therapeutic strategies and/or new antibiotic drugs. Here we set out to clarify by what means nisin is recognized, cleaved, and thereby inactivated by *Sa*NSR.

6.2 Structural determinants of nisin recognition

In the present work, the first three-dimensional structure of NSR from *Sa*NSR (PDB-ID: 4Y68)[28] was resolved[f] (**Figure 16A**). The *Sa*NSR monomer is composed by eleven helices and *β*-strands, which together form three individual domains: (i) an N-terminal helix bundle, (ii) a protease cap domain, and (iii) a protease core that contains the catalytically active serine at position 236[23], which is also part of the conserved "TASSAEM" region (**Figure 16A**). These domains form a hydrophobic tunnel (**Figure 16A**), which could very well bind a nisin molecule. Although we put extraordinary efforts, we were not successful in obtaining a crystal structure of a *Sa*NSR/nisin complex. One explanation might be that nisin gets cleaved as soon as it binds to *Sa*NSR. Thus, we derived a *Sa*NSR/nisin complex model, by site-directed mutagenesis guided by MD simulations and free energy calculations.

Initially, to determine nisin substructures essential for *Sa*NSR recognition, the two C-terminal cysteine(s) in nisin were mutated to alanine *in vitro*[g], which led to nisin substructures containing only rings A-D or A-C (see original PUBLICATION III in section 11.3). In addition, truncated nisin variants were prepared by removing residues from the C-terminus. All nisin variants were analyzed for the resistance mediated by the expression of the *Sa*NSR protein in the NZ9000 *Sa*NSR strain[368]. That way it was elucidated that in particular ring E is highly essential for nisin recognition by *Sa*NSR[368].

In the next step, I generated a set of nisin structures bound to *Sa*NSR and performed unbiased MD simulations and MM-PBSA calculations[144,147], employing the residue-wise decomposition scheme[152,155]. I found that, besides ring E, also ring D and I30 in nisin are essential for binding to *Sa*NSR[368] (see original PUBLICATION III in section 11.3). Thus, rings D and E as well as I30 form the binding motive (hereafter name $Nisin_{core}$), which is essential for nisin recognition by *Sa*NSR. Binding of the $Nisin_{core}$ ensures that residue Ser_{29} at the nisin cleavage site is correctly positioned close to the catalytic dyad of *Sa*NSR.

[f] The three-dimensional structure was obtained by X-ray crystallography by the research group of Dr. Sander Smits at the "Institute of Biochemistry, Heinrich Heine University Düsseldorf, Universitätsstr. 1, 40225 Düsseldorf, Germany".

[g] Site-directed mutagenesis and activity measurements were performed by the research group of Dr. Sander Smits at the "Institute of Biochemistry, Heinrich Heine University Düsseldorf, Universitätsstr. 1, 40225 Düsseldorf, Germany".

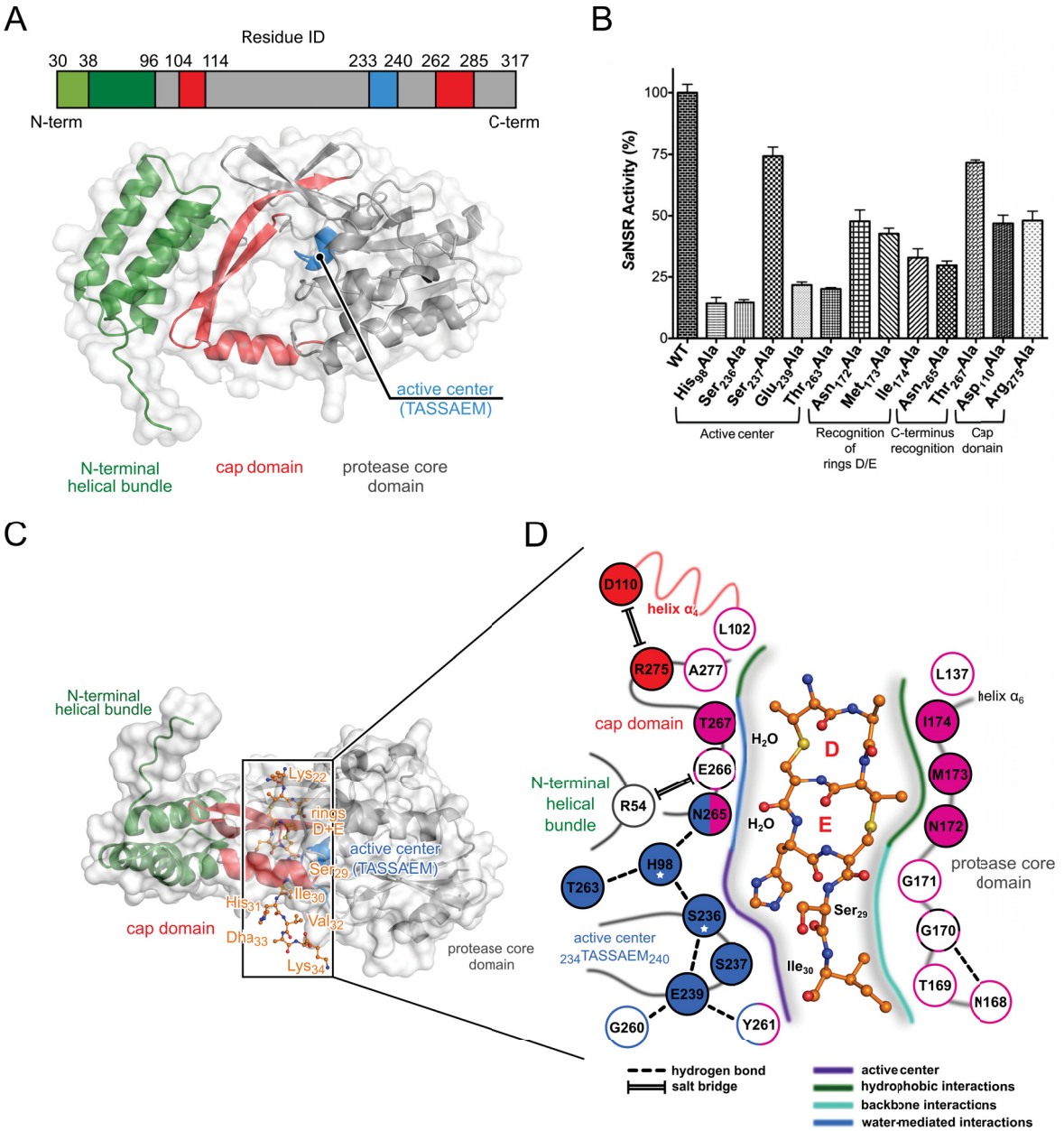

Figure 16: The crystal structure, activity data, and nisin bound model of *Sa*NSR.
A: Top panel: an illustration of the domain organization. Bottom panel: a monomeric structure of *Sa*NSR shown as a cartoon-surface representation that illustrates the hydrophobic tunnel in the center of the protein structure. The N-terminal helical bundle is colored green, protease cap domain in red, the protease core domain in gray, and the catalytic site containing the TASSAEM region in blue. Residue numbering in the top panel is in accordance with the crystal structure[28]. **B:** The activity of wild type (WT) *Sa*NSR and its variations (is determined using the *L. lactis* NZ9000 strain). Normalization of the IC50 values was done by setting the values exhibited by the empty vector (NZ9000Erm) and NZ9000*Sa*NSR to 0 % and 100 %, respectively. The error bars denote the standard error of at least three independent experiments[368]. **C:** Representative structure of nisin (residues 22-34; extracted from the MD trajectory) bound to the hydrophobic tunnel of *Sa*NSR. **D:** Schematic representation of the $Nisin_{core}$ (rings D+E (red labels), Ser_{29}, and Ile_{30}) bound to *Sa*NSR residues. Residues that compose the catalytic site are colored in blue, residues that contribute to nisin binding in magenta, residues that have an indirect effect on binding in black-magenta, and residues with a supposedly regulatory function in *Sa*NSR in red[368]. For residues with an opaquely colored background, *Sa*NSR activity information for alanine mutants is available (**B**). Residues marked with a star form the catalytic dyad. The nisin structure is depicted as an orange ball-and-stick model. (Figures and captions are taken from PUBLICATION III[28].)

Next, I performed a series of MD simulations and free energy calculations and predicted amino acids that are likely important for nisin recognition and *Sa*NSR specificity towards

nisin. Subsequently, the suggested amino acids were substituted to alanine, and the catalytic activity of the new *Sa*NSR variants was measured experimentally[h] (**Figure 16B**). By combining results from computations and *in vitro* experiments, we derived the first structural model of nisin bound to *Sa*NSR that revealed several exciting facts about nisin recognition by *Sa*NSR and its specificity.

First, *Sa*NSR acts via a catalytic dyad mechanism in which Ser326[23] and His98 form the catalytic dyad (**Figure 16C, D**) and alanine variants in these positions reduce *Sa*NSR catalytic activity (**Figure 16B**). Second, the highly conserved sequence motif "TASSAEM" (**Figure 16A**) is structurally stabilized via a hydrogen bond network (**Figure 16C, D**), and any disruption of this network results in a reduced *Sa*NSR catalytic activity (**Figure 16B**). Third, *Sa*NSR binds nisin via hydrophobic (Leu102, Leu137, Met173, Ile174, Ala277) and polar/charged amino acids (Asn172 and Glu266), but also via water-mediated interactions (Asn265 and Thr267) (**Figure 16B, C**). Finally, we found that Asp110 and Arg275, although not interacting with nisin, are essential for *Sa*NSR catalytic activity (**Figure 16B**), such that these amino acids stabilize the secondary structure of helix α_4 of the cap domain that is required for *Sa*NSR function (**Figure 16B, C**). The loss of Asp110 or Arg275 results in a reduced catalytic activity relative to wild type GS. By using these findings as experimental restraints, I screened the MD trajectory towards a representative structure of nisin bound to *Sa*NSR. In this structure, rings D and E bind to a hydrophobic pocket, which, in turn, ensures the correct spatial orientation of the nisin cleavage site towards the catalytic residues in *Sa*NSR (**Figure 16C, D**)

6.3 Conclusion and significance

In the present study, I significantly contributed to a collaborative study that shed light onto the question by what means *Sa*NSR recognizes and cleaves nisin. By the integration of biomolecular simulations with biochemical experiments, the first structural model in full atomic detail of how nisin is bound to *Sa*NSR is generated. Our *Sa*NSR/nisin binding model revealed that *Sa*NSR recognizes specifically the C-terminal lanthionine rings of nisin[28].

Taken together, as principal results, we found:

[h] Site-directed mutagenesis and activity measurements were performed by the research group of Dr. Sander Smits at the "Institute of Biochemistry, Heinrich Heine University Düsseldorf, Universitätsstr. 1, 40225 Düsseldorf, Germany".

- the first 3D structure of NSR from *S. agalactiae* at 2.2 Å resolution (PDB-ID: 4Y68[28]),
- that *Sa*NSR is composed of three structural domains that together form a hydrophobic tunnel that harbors the nisin molecule,
- that *Sa*NSR specifically binds to the C-terminal lanthionine rings (rings D and E) and residue I30 in nisin. This determines the nisin specificity of *Sa*NSR and ensures the precise coordination of the nisin cleavage site at the catalytic important TASSAEM region.

These findings and our model of the *Sa*NSR/nisin complex open up a new avenue in the understanding of lantibiotic resistance by human pathogens[28]. These findings might also encourage the development of therapeutics to overcome nisin resistance.

7. PUBLICATION IV

Targeting HSP90's C-terminus is effective in Imatinib resistant CML and lacks heat shock response induction.

Bhatia, S., Diedrich, D., **Frieg, B.**, Ahlert, H., Stein, S., Bopp, B., Lang, F., Zang, T., Kröger, T., Ernst, T., Kögler, G., Krieg, A., Lüdeke, S., Kunkel, H., Rodrigues Moita, A. J., Kassack, M. U., Marquardt, V., Opitz, F. V., Oldenburg, M., Remke, M., Babor, F., Grez, M., Hochhaus, A., Borkhardt, A., Groth, G., Nagel-Steger, L., Jose, J., Kurz, T., Gohlke, H., Hansen, F. K., Hauer, J.

Blood (2018), 132, 307 – 320.
Original publication, see original PUBLICATION IV in section 11.4; contribution: 15 % (details provided below)

(The following text was adapted from the above publication.)

7.1 Role of HSP90 in chronic myeloid leukemia, peptidomimetics, and α-aminoxy peptides

The presence of the "Philadelphia chromosome", a translocation of chromosomes 9 and 22, constitutes the hallmark of chronic myeloid leukemia (CML)[369]. The Philadelphia chromosome induces the synthesis of the oncogenic fusion protein BCR-ABL[334,370]. The BCR-ABL protein constitutes tyrosine kinase activity, and its activation was linked to cell survival by inhibition of apoptosis, inhibition of differentiation, and loss of tumor suppressor function[371]. Hence, the discovery of tyrosine kinase inhibitors (TKI) and their development to the next generations have revolutionized the treatment of CML[371]. However, long-term treatments on TKIs increase the risk of resistance and subsequent disease progression to blast crisis, a clinical state challenging to treat with current therapies[372]. Therefore, novel treatment approaches are needed for treating BCR-ABL induced leukemia resistant to TKIs.

In CML cells, HSP90 levels are elevated and HSP90 protects BCR-ABL by inhibition with its proteasomal degradation[373]. Thus, inhibiting the interaction between BCR-ABL and HSP90 with HSP90 inhibitors promotes BCR-ABL proteasomal degradation[373], as previously shown for Novobiocin and NVP-AUY 922[329,374]. In this regard, HSP90 denotes a promising target to treat distinct types of cancer, related to high BCR-ABL concentrations.

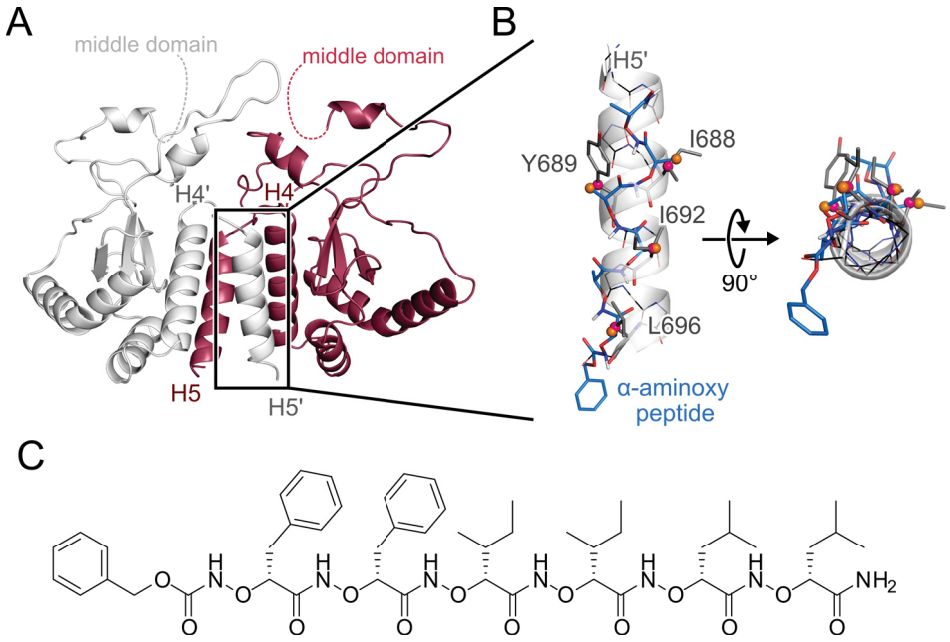

Figure 17: Crystal structures of human HSP90 CTD and structure of Aminoxyrone.
A: Crystal structure of the dimeric human HSP90 C-terminal domain (extracted from PDB-ID 3Q6M[290]). Helices H4 and H5 form the dimerization interface. **B:** Overlay of C_β atoms (orange spheres) of the α-aminoxy moiety (blue sticks) side chains (after quantum mechanical energy minimization) onto the C_β atoms of residues I688, Y689, I692, and L696 on helix H5. **C:** 2D structure of Aminoxyrone. (Figures A-C are taken from PUBLICATION IV.)

Most of the HSP90 inhibitors target the N-terminal ATP binding site and thereby induce HSR that weakens HSP90 inhibition[323,331]. Molecules targeting the CTD do not promote HSR. As CTD dimerization is essential for HSP90's chaperone function[289], molecules that inhibit the inter-subunit PPI constitute a promising alternative. When trying to interfere with a system, the most direct way is to mimic the protein's epitope in their biological environment[375]. As to HSP90, the CTD dimerization interface is formed by a helix bundle (**Figure 17A**), and recently it was shown that the amino acids I688, Y689, I692, and L696, which are part of the dimerization interface, are essential for CTD dimerization[296]. Furthermore, peptides mimicking these critical interactions in the CTD helix bundle interfere with HSP90 dimerization[336]. Although peptides are used as therapeutics[337], poor bioavailability due to proteolytic degradation[338] limit their clinical application. In this regard, the use of peptidomimetics, molecules that mimic a natural peptide in 3D space, interact with the biological target, produce the same effect as the native peptide, and show improved stability and bioavailability[339], denote a promising alternative for cancer therapy. α-Aminoxy peptides constitute a class of peptidomimetic foldamers that fold into a 2_8-helical conformation, thereby mimicking the spatial arrangement of the side chains in α-helices[340] (**Figure 17B**).

In the present study, we have developed the novel, first-in-class HSP90 inhibitor Aminoxyrone (**Figure 17C**). By combining results from biomolecular simulations with results from

in vitro and *in vivo* experiments, our data suggest a novel mode of action, in that Aminoxyrone inhibits the C-terminal dimerization of HSP90.

7.2 Conformational analysis and biological evaluation

Initially, the biological properties of Aminoxyrone were elucidated *in vitro*[i]. First, Aminoxyrone inhibits HSP90 dimer formation (see original PUBLICATION IV in section 11.4). Second, a $K_D = 27.4$ μM of Aminoxyrone binding to purified CTD of HSP90 was measured (see original PUBLICATION IV in section 11.4), and the *in vitro* efficacy in a cell-based luciferase refolding assay is comparable to the efficacy of the C-terminal inhibitor Novobiocin and the N-terminal inhibitor NVP-AUY 922 (see original PUBLICATION IV in section 11.4). In sum, the results revealed the specific binding of Aminoxyrone to the HSP90 CTD.

Next, we set out to clarify Aminoxyrone's mode of action. Although Aminoxyrone was found to be able to either dissociate oligomeric species or suppress HSP90 CTD oligomerization (see original PUBLICATION IV in section 11.4)[j], a picture of how Aminoxyrone binds to the CTD has remained elusive. Thus, to further elucidate the mode of action of Aminoxyrone in full atomic detail, I performed MD simulations of Aminoxyrone binding to HSP90 CTD. Beforehand, in order to focus the computational time available on sampling of Aminoxyrone configurations around the CTD, I established a simulation procedure that allows the usage of a monomeric CTD model (sequence Glu527 – Gly697; extracted from the crystal structure[290]; see original PUBLICATION IV in section 11.4) rather than the full-length HSP90 structure, which would had been computationally more demanding.

Although MD simulations have been successfully applied to study and reconstruct the binding process of smaller ligands in classical drug targets, such as GPCRs[60,61,65,73], the structural features of PPIs provide quite a challenge when applying MD simulations of ligand binding to protein-protein interfaces. First, in contrast to classical drug targets, the protein-protein interfaces are much larger, are often shallow, and lack deep, well-defined pockets[376,377]. In this regard, the contact surface in PPIs varies between 1500 – 3000 Å^2 [378,379], or even larger, while the contact area in classical target varies between 300 – 1000 Å^2 [378,380]. Second, the

[i] The experiments were performed by the research group of Prof. Dr. J. Jose at the "Institute for Pharmaceutical and Medicinal Chemistry, PharmaCampus, Westphalian Wilhelms University, Münster, Germany".

[j] The experiments were performed by the research group of Dr. L. Nagel-Steger at the "Institute for Physical Biology, Heinrich Heine University Düsseldorf, Düsseldorf, Germany" and the "Institute of Complex Systems, Structural Biochemistry (ICS-6), Forschungszentrum Jülich GmbH, Jülich, Germany".

binding epitopes between the protein binding partners are often described as discontinuous, in that amino acids from different, not necessarily connected, regions are crucial for the PPI, the so-called hot-regions[376,377]. Interestingly, within these hot-regions only some amino acids contribute largely to binding, the so call hot-spots[376,377]. One strategy to target PPIs is to mimic the spatial orientation and interactions of hot-spot residues by structural analogs, such as peptidomimetics.

I found that Aminoxyrone predominantly binds to the helices H4 and H5 in the dimerization interface, thereby mimicking key interactions of the previously defined hot-spot residues (summarized in **Figure 18**). Therefore, I performed a set of 60 unbiased all-atom MD simulations of Aminoxyrone binding to the HSP90 CTD. The MD simulations were initiated from conformations in which a single Aminoxyrone molecule was randomly placed around the HSP90 CTD (see original PUBLICATION IV in section 11.4), such that each simulation can be considered as independent from the rest of the simulations (see original PUBLICATION IV in section 11.4). In all starting conditions, the minimal distance between Aminoxyrone and the HSP90 CTD was at least 10 Å, such that Aminoxyrone was not influenced by the HSP90 CTD right from the start. During all simulations, Aminoxyrone was free to move and not biased by a guiding force. All systems were subjected to production simulations of at least 400 ns length, each, such that the total simulation time cumulates to 24 µs. With progressing simulation time, the number of simulations in which Aminoxyrone is bound to the dimerization interface of the CTD (referred to as ①) increases. After 400 ns, in the majority of my MD simulations (in 22 of the simulations), Aminoxyrone binds to the dimerization interface ① (**Figure 18A-C**). Using MM-GBSA calculations throughout the MD simulations, I also found the most favorable effective binding energies for Aminoxyrone binding at the site ① (see original PUBLICATION IV in section 11.4). In the remaining simulations, Aminoxyrone binds to a hydrophobic site (referred to as ②) occupied by the middle domain in full-length HSP90 or Aminoxyrone temporarily binds to locations scattered across the CTD surface (**Figure 18A-C**). When extending the simulation times to 1 µs, however, Aminoxyrone unbinds from HSP90 and, finally, binds to the dimerization interface (see original PUBLICATION IV in section 11.4). Interestingly, as soon as Aminoxyrone is bound at site ①, it does not unbind on the 1 µs timescale (see original PUBLICATION IV in section 11.4), which supports the view that site ① is likely the main binding site for Aminoxyrone.

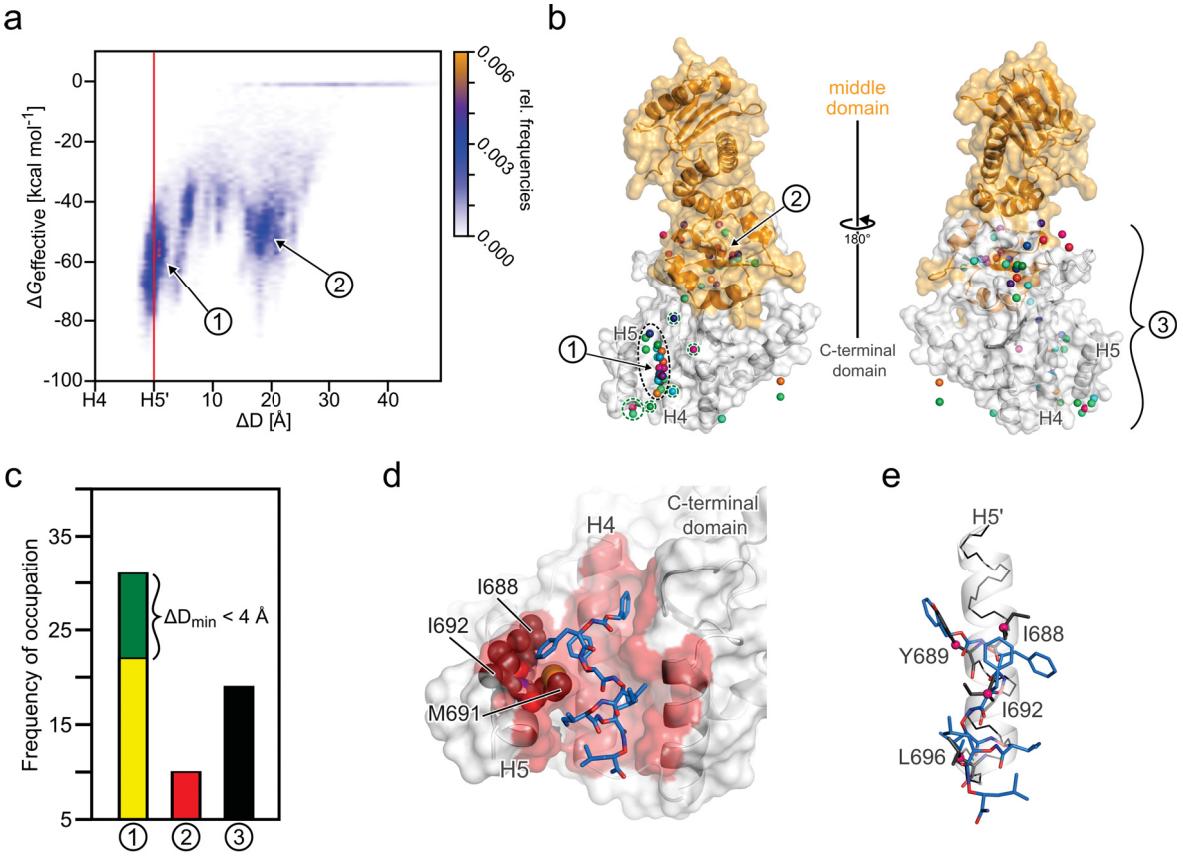

Figure 18: Results of MD simulations of Aminoxyrone binding to HSP90.
(a) Relative frequencies of ligand poses (see color scale) as a function of the relative distance between the center of mass of Aminoxyrone and helix H4 in the dimerization interface (ΔD; Aminoxyrone was designed to mimic hot-spot amino acids[290] on helix H5' of the adjacent CTD in the dimeric HSP90, such that the distances are expressed as relative distances (ΔD) with respect to the distance between the backbone COMs of helices H4 and H5' in the crystal structure[290]) and computed effective energies of binding ($\Delta G_{effective}$). (**b**) Locations of the center of mass of Aminoxyrone (spheres) after 400 ns for 60 MD simulations, with each simulation result colored differently. The black dashed line highlights all conformations that are bound to dimerization interface ① with $\Delta D_{min} \leq 0$ Å, the green dashed line those with $\Delta D_{min} < 4$ Å. The protein structure is shown as surface representation with the middle domain (not present during MD simulations) in orange and the CTD in white. In the left panel, the structure is rotated by 180° around the y-axis. **(c)** The frequency of occupation of binding sites ① (yellow), close to ① (green; with $\Delta D_{min} \leq 4$ Å), ② (red), or ③ (black) by Aminoxyrone across 60 MD simulations. **(d)** Binding mode model of Aminoxyrone. The left panel shows a representative conformation of Aminoxyrone bound to the CTD, extracted from the MD trajectory. Residues I688, I692, and M691 (gray spheres) bind to the side chain of Aminoxyrone. **(e)** The right panel shows an overlay of Aminoxyrone onto helix H5' extracted from the crystal structure (PDB-ID: 3Q6M[290]). Aminoxyrone is depicted as blue sticks, hot-spot amino acids I688, Y689, I692, and L696[296] as gray sticks with C_β atoms as magenta spheres, helix H5' as white cartoon with black backbone atoms, and the CTD in the left panel as surface representation, with all residue within 3 Å of Aminoxyrone colored in red. In **(a, b, c)** ①, ②, and ③ denote the binding sites of Aminoxyrone where ③ represents all binding sites besides ① and ②. (Figure and caption are taken from PUBLICATION IV.)

Finally, I calculated effective binding energies for configurations showing the minimal distance between Aminoxyrone and the CTD dimerization interface during 60 MD simulations of 400 ns length. Strong interactions energies were found for Aminoxyrone bound to site ①, while interactions energies for Aminoxyrone bound to sites ② and ③ are, in general, weaker (see original PUBLICATION IV in section 11.4), suggesting, again, that Aminoxyrone most likely binds to the site ①. Visual inspection of the Aminoxyrone binding poses at the site ①

revealed that Aminoxyrone binds to the dimerization interface, such that its side chains partially align with side chains of hot-spot residues[296] of helix H5 (**Figure 18D**, **E**). In sum, results from MD simulations and free energy calculations suggest that Aminoxyrone binds to the HSP90 CTD dimerization interface, thereby mimicking hot-spot residues, which are crucial for CTD dimerization[296]. That way, Aminoxyrone likely acts as a PPI modulator and suppresses HSP90 CTD dimerization, which denotes a novel mode of action to modulate HSP90 function.

One of the major challenges with HSP90 inhibitors in the preclinical and clinical testing phase is their non-selectivity and the induction of HSR[331], which decreases the HSP90 inhibitor efficacy. *In vitro* and *in vivo* experiments[k], however, revealed that Aminoxyrone shows a potent anti-BCR-ABL effect without inducing HSR. In this regard, Aminoxyrone inhibits cell proliferation, induces apoptosis, and also shows cytotoxic efficacy (see original PUBLICATION IV in section 11.4). Next, the *in vivo* efficacy of Aminoxyrone was investigated in primary CML^{CD34+} patient-derived cells. The findings revealed that Aminoxyrone, again, inhibits cell proliferation and induces apoptosis at reasonable concentrations without inducing any HSR. Next, $BCR\text{-}ABL^{+}$ cells were transplanted in an *in vivo* xenograft model. The growing tumor was treated locally with Aminoxyrone for 17 days. Aminoxyrone leads to a significant reduction in tumor weight, indicating that Aminoxyrone has anti-oncogenic potential *in vivo*. Finally, the efficacy of Aminoxyrone was tested in Imatinib-resistant clinically relevant BCR-ABL variants and found to be superior over Imatinib (see original PUBLICATION IV in section 11.4).

7.3 Conclusion and significance

The BCR-ABL oncoprotein constitutes tyrosine kinase activity and is the molecular hallmark of CML[371]. However, the increasing number of resistances towards TKIs highlights the importance of novel therapeutic strategies[372]. HSP90 levels are increased in CML cells and HSP90, in turn, stabilizes BCR-ABL and inhibits its proteasomal degradation[373]. Thus,

[k] The experiments were performed by the research group of Prof. Dr. J. Hauer at the "Department of Pediatric Oncology, Hematology and Clinical Immunology, Medical Faculty, Heinrich Heine University Düsseldorf, Düsseldorf, Germany".

HSP90 inhibitors lead to BCR-ABL destabilization and promote proteasomal degradation[329,374]. In this collaborative study, we developed Aminoxyrone as a novel PPI inhibitor of HSP90 that suppresses HSP90 dimerization via its CTD.

As principal results, we found that:

- Aminoxyrone inhibits HSP90 function via a novel mode of action. Results from MD simulations and free energy calculations suggest that Aminoxyrone acts as a PPI inhibitor, which interferes with the CTD dimerization by mimicking hot-spot residues, which are crucial for CTD dimerization,
- modulation of HSP90 function by CTD dimerization inhibitors denotes a novel therapeutic strategy, in order resistances towards established anti-cancer drugs,
- Aminoxyrone acts in a reasonable therapeutic window and does not induce HSR, neither *in vitro* nor *in vivo.*

Remarkably, Aminoxyrone is the first-in-class peptidomimetic that interferes with the CTD dimerization via a novel mode of action. One might anticipate that Aminoxyrone or its derivatives could be applied to other species of leukemia or diseases as HSP90 stabilizes many different proteins with critical functions in diseases (see section 2.4.3). This study may also facilitate the development of additional therapeutics, that follow the same mode of action as Aminoxyrone, namely as CTD dimerization inhibitors.

8. SUMMARY AND PERSPECTIVE

Throughout this thesis, I used computer-aided techniques to elucidate the molecular mechanisms of function-associated ligand binding processes in three different systems. In particular, I determined the functional consequences of point mutations and posttranslational modifications on substrate binding, I predicted a binding mode of a peptide to its target, and I derived a binding mode model of a novel PPI inhibitor bound to a shallow protein surface. In all studies, my results and predictions were corroborated with experimental results, which highlights the enormous potential of the strategy to combine theoretical modeling studies with experimental procedures.

Thus, in PUBLICATION I and PUBLICATION II, I determined the molecular mechanisms of human GS deactivation either by mutations R324C, R324S, and R341C (PUBLICATION I) or by Y336 nitration (PUBLICATION II). In both cases, substrate binding to GS is hampered via direct or indirect effects. Furthermore, PUBLICATION II demonstrates a novel mechanism of GS regulation mediated by Y336 nitration. So far, tyrosine nitration has been related to three effects on protein function: loss of function, a gain of function, or no change on protein function[359] and, so far, Y336 nitration in human GS has been associated with a loss of GS function[20,358,381,382]. However, PUBLICATION II provides the first evidence that indicates that the inhibitory effect of Y336 nitration in human GS is fully-reversible depending on the pH of the protein environment. While PUBLICATION II demonstrates that the catalytic activity of nitrated GS can be fully restored by changing to a more acidic environment, there is currently no therapeutic strategy available to counteract the inhibitory effects of inborn GS mutations. Based on PUBLICATION I that suggests that ATP binding is weakened in the R324S GS variant, our findings could stimulate the search of ATP binding enhancing molecules for the R324S variant, by which the R324S GS variant can be "repaired" extrinsically[349]. In an initial study[240], we focused on trimethylglycine (betaine) as one such molecule and found that betaine weakly stabilizes ATP within its binding site of the R324S GS[240]. Currently, betaine and structural analogs are investigated concerning their *in vitro* potency to restore the R324S GS activity[1].

PUBLICATION III provides the first binding mode model of the antibiotic peptide nisin bound to the resistance protease *Sa*NSR in full atomic detail. Based on it, I predicted amino

[1] The *in vitro* experiments are performed by the research group of Prof. Dr. D. Häussinger at the "Clinic for Gastroenterology, Hepatology, and Infectious Diseases, Heinrich Heine University Düsseldorf, Düsseldorf, Germany".

acids in *Sa*NSR that are crucial for recognition. Site-directed mutagenesis and *in vitro* activity measurements of *Sa*NSR in the research group of Dr. S. Smits confirmed their critical roles in the recognition and coordination of nisin by *Sa*NSR. That way, PUBLICATION III provides an enhanced understanding of lantibiotic resistance by human pathogens and may also promote the development of therapeutics to overcome nisin resistance. Thus, in search of a novel therapeutic, I identified a set of potential *Sa*NSR inhibitors. Currently, these compounds are in the stage of *in vitro* evaluation of their inhibitory potency[m].

Finally, in PUBLICATION IV, I provided the first picture in atomic detail of how the novel anticancer drug Aminoxyrone binds to its target, namely HSP90. Importantly to note, Aminoxyrone is the first-in-class peptidomimetic that acts as a PPI inhibitor. In detail, Aminoxyrone binds to the HSP90 CTD dimerization interface, thereby preventing HSP90 dimerization, which interferes with the HSP90 function. In particular, Aminoxyrone mimics the spatial side chain orientation of amino acids that are crucial for the CTD dimerization. Considering Aminoxyrone's high efficiency also in specific drug resistance cells, Aminoxyrone or analogs show a promising potential to be clinically relevant to other cancer types. Furthermore, small molecules that also mimic the spatial helical side chain orientation, such as trispyrimidonamide derivatives[383], denote promising alternatives to inhibit HSP90 function following the same mode of action as Aminoxyrone.

As demonstrated in the above examples, the combined use of multiple techniques of theoretical and experimental origin can guide the understanding of complex biological systems. In this context, MD simulations play a key role in the interpretation of existing data[14,37]. Alternatively, MD simulations should always be corroborated by experiments or, at least, be directly compared to experimental observables[14,37]. As to biomolecular simulations in general, substantial progress in software and hardware has been made that provided access to study even very complex systems. One might anticipate that future software and hardware developments will then allow addressing even more complex biological processes such as, for example, molecule transport via the nuclear pore complex, the principles of transcription and translation during protein biosynthesis, or the molecular aspects of ATP production.

[m] The *in vitro* experiments are performed by the research group of Dr. Sander Smits at the "Institute of Biochemistry, Heinrich Heine University Düsseldorf, Universitätsstr. 1, 40225 Düsseldorf, Germany".

9. ACKNOWLEDGEMENT

First, I would like to thank my supervisor Prof. Dr. H. Gohlke for providing me an opportunity to carry out my research as part of his research group, for his guidance throughout my work, and the encouraging discussions.

Special thanks to all of my colleagues and friends of the CPClab. In particular, I would like to thank Dr. N. Homeyer for her engagement and support through the initial learning processes. Thanks to Dr. C. Pfleger, M. Bonus, Dr. C. G. W. Gertzen, Dr. D. Schmidt, and B. Schmitz for their constant and valuable help and profound discussions throughout my research.

Thanks to Prof. Dr. D. Häussinger, Dr. B. Görg, Dr. N. Qvartskhava, and Prof. Dr. V. Keitel for the fruitful cooperation to resolve the molecular mechanisms of GS regulation and deactivation.

Thanks to Dr. S. H. J. Smits, Dr. S. Khosa, D. Mulnaes, Dr. D. Kleinschrodt, and Dr. A. Hoeppner for the successful collaboration to elucidate the structural determinants of nisin recognition by NSR.

Thanks also to Dr. S. Bhatia, Dr. D. Diedrich, Dr. B. Bopp, Prof. Dr. J. Jose, Prof. Dr. T. Kurz, Jun.-Prof. Dr. F. K. Hansen, Prof. Dr. J. Hauer and many more for the productive collaboration that brought success to our efforts to inhibit HSP90 dimerization.

My special appreciation goes to my parents, who were always there for me.

Last but not least, special thanks to Alina for your unconditional love and support throughout this chapter of my life.

10. REPRINT PERMISSIONS

PUBLICATION I (pages LXXII - CVI), **Figure 11** (page 43), and **Figure 12** (page 46)

Reprinted from ”*Molecular mechanisms of glutamine synthetase mutations that lead to clinically relevant pathologies”*, Frieg, B., Görg, B., Homeyer, N., Keitel, V., Häussinger, D., Gohlke, H., **PLoS Comput. Biol.** (2016), 12, e1004693.

PUBLICATION III (pages CLXII - CXCII), and **Figure 16** (page 58)

Reprinted from “*Structural basis of lantibiotic recognition by the nisin resistance protein from Streptococcus agalactiae”,* Khosa, S., Frieg, B., Mulnaes, D., Kleinschrodt, D., Hoeppner, A., Gohlke, H., Smits, S.H.J. **Sci. Rep.** (2016), 6, 18679, DOI: 10.1038/srep18679.

PUBLICATION IV (pages CXCIV - CCLXII), **Figure 17** (page 62), and **Figure 18** (page 65)

Reprinted from “*Targeting HSP90’s C-terminus is effective in Imatinib resistant CML and lacks heat shock response (HSR) induction*”, Bhatia, S., Diedrich, D., Frieg, B., Ahlert, H., Stein, S., Bopp, B., Lang, F., Zang, T., Kröger, T., Ernst, T., Kögler, G., Krieg, A., Lüdeke, S., Kunkel, H., Rodrigues Moita, A. J., Kassack, M.U., Marquardt, V., Opitz, F. V., Oldenburg, M., Remke, M., Babor, F., Grez, M., Hochhaus, A., Borkhardt, A., Groth, G., Nagel-Steger, L., Jose, J., Kurz, T., Gohlke, H., Hansen, F.K., Hauer, J. **Blood** (2018), 132, 307 – 320, DOI: 10.1182/blood-2017-10-810986.

11. PUBLICATIONS

11.1 PUBLICATION I

Molecular mechanisms of glutamine synthetase mutations that lead to clinically relevant pathologies.

Frieg, B., Görg, B., Homeyer, N., Keitel, V., Häussinger, D., Gohlke, H.

PLoS Comput. Biol. (2016), 12, e1004693.

PLOS | COMPUTATIONAL BIOLOGY

RESEARCH ARTICLE

Molecular Mechanisms of Glutamine Synthetase Mutations that Lead to Clinically Relevant Pathologies

Benedikt Frieg[1], Boris Görg[2], Nadine Homeyer[1], Verena Keitel[2], Dieter Häussinger[2]*, Holger Gohlke[1]*

1 Institute for Pharmaceutical and Medicinal Chemistry, Heinrich-Heine-University, Düsseldorf, Germany, **2** Clinic for Gastroenterology, Hepatology, and Infectious Diseases, Heinrich-Heine-University, Düsseldorf, Germany

* haeussin@uni-duesseldorf.de (DH); gohlke@uni-duesseldorf.de (HG)

OPEN ACCESS

Citation: Frieg B, Görg B, Homeyer N, Keitel V, Häussinger D, Gohlke H (2016) Molecular Mechanisms of Glutamine Synthetase Mutations that Lead to Clinically Relevant Pathologies. PLoS Comput Biol 12(2): e1004693. doi:10.1371/journal.pcbi.1004693

Editor: Alexander MacKerell, Baltimore, UNITED STATES

Received: May 25, 2015

Accepted: December 3, 2015

Published: February 2, 2016

Data Availability Statement: All relevant data are within the paper and its Supporting Information files.

Funding: This work was supported by the NRW Research School BioStruct, by grants from the Ministry of Innovation, Science, Research and Technology of the German Federal State North Rhine-Westphalia (NRW) and from the "Entrepreneur Foundation for the Advancement of Science and Young Researchers at HHU Düsseldorf", and by the Deutsche Forschungsgemeinschaft through the Collaborative Research Center SFB 974 ("Communication and Systems Relevance during

Abstract

Glutamine synthetase (GS) catalyzes ATP-dependent ligation of ammonia and glutamate to glutamine. Two mutations of human GS (R324C and R341C) were connected to congenital glutamine deficiency with severe brain malformations resulting in neonatal death. Another GS mutation (R324S) was identified in a neurologically compromised patient. However, the molecular mechanisms underlying the impairment of GS activity by these mutations have remained elusive. Molecular dynamics simulations, free energy calculations, and rigidity analyses suggest that all three mutations influence the first step of GS catalytic cycle. The R324S and R324C mutations deteriorate GS catalytic activity due to loss of direct interactions with ATP. As to R324S, indirect, water-mediated interactions reduce this effect, which may explain the suggested higher GS residual activity. The R341C mutation weakens ATP binding by destabilizing the interacting residue R340 in the *apo* state of GS. Additionally, the mutation is predicted to result in a significant destabilization of helix H8, which should negatively affect glutamate binding. This prediction was tested in HEK293 cells overexpressing GS by dot-blot analysis: Structural stability of H8 was impaired through mutation of amino acids interacting with R341, as indicated by a loss of masking of an epitope in the glutamate binding pocket for a monoclonal anti-GS antibody by L-methionine-*S*-sulfoximine; in contrast, cells transfected with wild type GS showed the masking. Our analyses reveal complex molecular effects underlying impaired GS catalytic activity in three clinically relevant mutants. Our findings could stimulate the development of ATP binding-enhancing molecules by which the R324S mutant can be repaired extrinsically.

Author Summary

Glutamine synthetase (GS) catalyzes the ATP-dependent ligation of ammonia and glutamate to glutamine, which makes the enzyme essential for human nitrogen metabolism. Three mutations in human GS, R324C, R324S, and R341C, had been identified previously

PLOS | COMPUTATIONAL BIOLOGY

Liver Damage and Regeneration", Düsseldorf). The funders had no role in study design, data collection and analysis, decision to publish, or preparation of the manuscript.

Competing Interests: The authors have declared that no competing interests exist.

that lead to a glutamine deficiency, resulting in neonatal death in the case of R324C and R341C. However, the molecular mechanisms underlying this impairment of GS activity have remained elusive. Our results from computational biophysics approaches suggest that all three mutants influence the first step of GS' catalytic cycle, namely ATP or glutamate binding. The analyses reveal a complex set of effects including the loss of direct interactions to substrates, the involvement of water-mediated interactions that alleviate part of the mutation effect, and long-range effects between the catalytic site and structural parts distant from it. As to the latter, experimental validation is in line with our prediction of a significant destabilization of helix H8 in the R341C mutant, which should negatively affect glutamate binding. Finally, our findings could stimulate the development of ATP-binding enhancing molecules for the R324S mutant, which has been suggested to have residual activity, that way extrinsically "repairing" the mutant.

Introduction

Glutamine synthetase (GS, glutamate ammonia ligase, EC 6.3.1.2) catalyzes the ATP-dependent ligation of glutamate and ammonia to glutamine [1]. GS is ubiquitously expressed in human tissues. High expression levels of GS are found in astrocytes in brain tissues [2], where it is part of glutamate-glutamine cycling [3], and in perivenous hepatocytes, where it is part of the intercellular glutamine cycle and essential for ammonia detoxification by the liver [4–6]. Glutamate clearance, ammonia detoxification, and glutamine formation make GS essential for the human nitrogen metabolism [7, 8] and for neurological functionality. Accordingly, several links between changes in GS activity and neurological disorders have been described, including Alzheimer's disease [9, 10], schizophrenia [11], hepatic encephalopathy [12–14] and epilepsy [15, 16]. In particular, two mutations in the GS gene (R324C in patient 1 and R341C in patient 2; throughout the manuscript, the sequence numbering of human GS is used) have been linked to congenital human GS deficiency with severe brain malformations resulting in multiorgan failure and neonatal death [17, 18]. In immortalized lymphocytes, R324C GS activity was reduced to about 12% of that found in wild type controls [17]. In fibroblasts from the father of patient 2, a 50% drop in specific GS activity was found, which may have been compensated for by a parallel increase in GS expression [17]. In a single case known to date, another GS mutation (R324S) was identified in a boy, now seven years old (patient 3), who is neurologically compromised due to the lack of ammonia detoxification and glutamine synthesis [19]. A plausible but not proven explanation for the survival of this patient would be the assumption of a higher level of GS residual activity compared to the other two GS mutants [20]. However, the molecular mechanisms for how these mutations lead to glutamine deficiency have not been understood.

Human GS belongs to class II of GS enzymes [21] and forms a homodecamer [22] in which two pentameric rings stack to each other; a bifunnel-shaped catalytic site is located in each interface formed by two adjacent subunits, resulting in ten catalytic sites in total (Fig 1A and 1B). For glutamine formation by GS, a two-step mechanism has been suggested [23, 24]: In the first step adenosine triphosphate (ATP) binds to GS, which induces conformational changes to enable binding of glutamate [24]. After glutamate bound to the complex, the terminal phosphate group of ATP is transferred to the γ-carboxylate function of glutamate yielding adenosine diphosphate (ADP) and γ-glutamyl phosphate (GGP), a reactive acyl-phosphate intermediate. In the second step, an ammonium ion binds to a negatively charged pocket formed by D63, S66, Y162, and E305. The ammonium ion transfers a proton to D63 to yield

PLOS | COMPUTATIONAL BIOLOGY

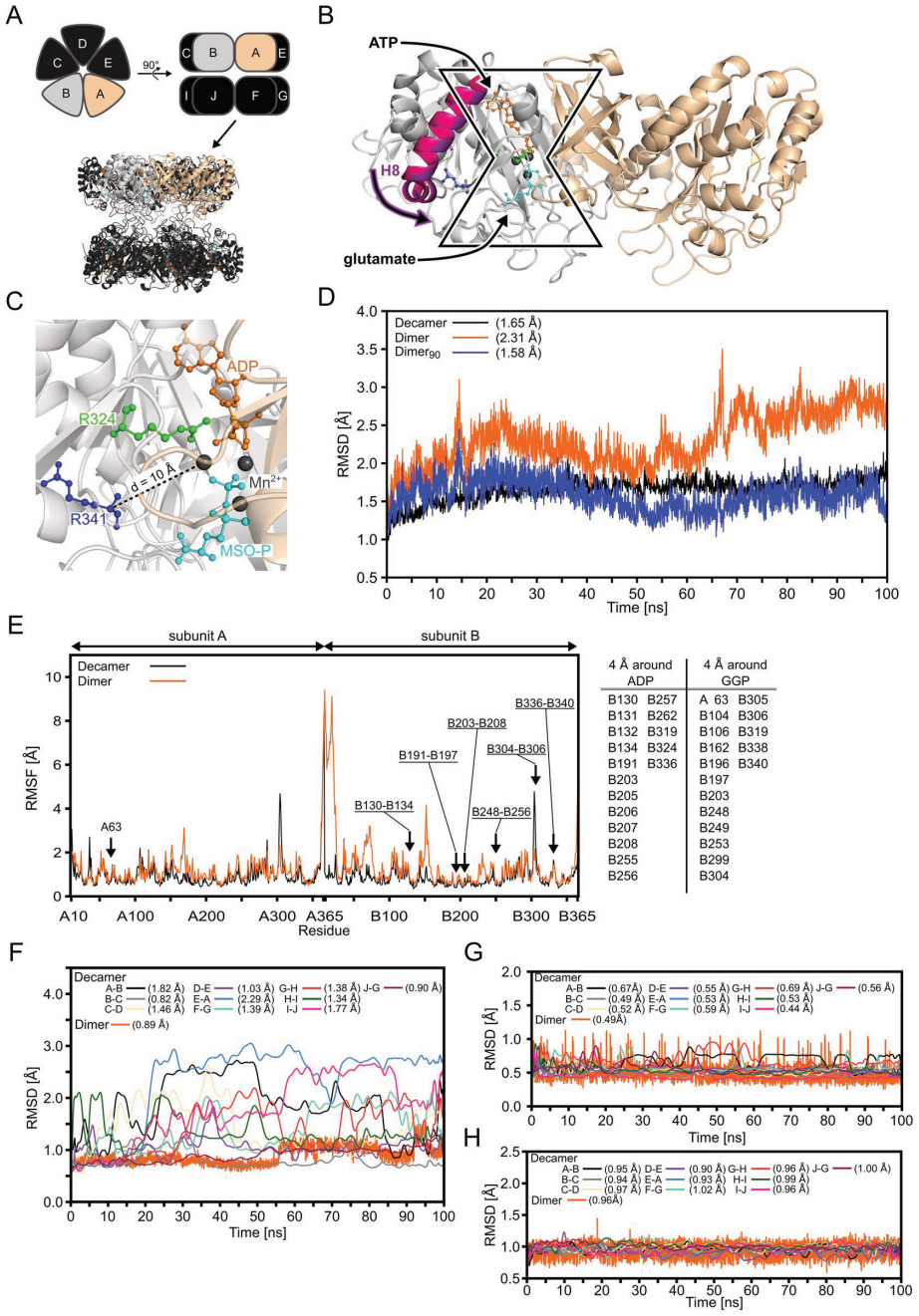

Fig 1. Structure of human GS, the dimeric model system, and the binding site in the crystal structure and during MD simulations. (A): Schematic representation of the GS decamer in top (top, left) and side (top, right) view. Subunits are labelled A to J. Below, the crystal structure of GS (PDB entry 2QC8 [22]) is shown in cartoon representation. Subunits A (beige) and B (grey) used for the dimeric model system are highlighted, as in the schematic representation. **(B):** Close-up view of the dimeric model system. Subunits A (beige) and B (grey) extracted from the GS decamer are shown in cartoon representation. ADP (orange) and the GS inhibitor L-methionine-*S*-sulfoximine phosphate (MSO-P, cyan) are depicted in ball-and-stick representation bound to the bifunnel-shaped catalytic site in the interface between two subunits; manganese ions (Mn^{2+}) ions are shown as black spheres. ATP binding promotes a

shift of helix 8 (H8; magenta from PDB entry 2UU7 of canine GS in the *apo* form [22]; violet from PDB entry 2QC8 of human GS bound to ATP and MSO-P [22]) that enables glutamate binding. **(C):** Close-up view of the binding site of GS in the crystal structure with ADP (orange), MSO-P (cyan), and both mutated residues [17, 18] R324 (green) and R341 (blue) in ball-and-stick representation. Mn^{2+} ions are shown as black spheres. Residue R341 is separated by ~ 10 Å from the center of the binding site (dashed line). **(D):** Backbone RMSD relative to the starting structure during 100 ns of MD simulations of the GS decamer (Decamer) and the dimeric model including all residues (Dimer) or only residues of the core region ($Dimer_{90}$); the $GS_{ADP+GGP}$ state was simulated. The core region comprises 90% of the residues with the lowest RMSF. Respective mean RMSD values are listed in brackets; SEM < 0.1 Å in all cases. **(E):** Residue wise RMSF for subunits A and B in the GS decamer and the dimeric model system during 100 ns of MD simulations of the $GS_{ADP+GGP}$ state. The table lists residues that are separated by $\leq$ 4 Å from ADP or GGP; regions encompassing such residues are highlighted with an arrow and labeled in the figure. **(F):** Backbone RMSD of residues listed in the table in panel E relative to the starting structure during 100 ns of MD simulations for ten dimeric pairs in the GS decamer and the dimeric model. For the decamer, the backbone RMSD was plotted as smoothed cubic spline. Respective mean RMSD values are listed in brackets; SEM < 0.1 Å in all cases. **(G):** RMSD of ADP relative to the starting structure after superimpositioning of the protein atoms during 100 ns of MD simulations for ten dimeric pairs in the GS decamer and the dimeric model. For the decamer the RMSD was plotted as smoothed cubic spline. Respective mean RMSD values are listed in brackets; SEM < 0.1 Å in all cases. **(H):** RMSD of GGP relative to the starting structure after superimpositioning of the protein atoms during 100 ns of MD simulations for ten dimeric pairs in the GS decamer and the dimeric model. For the decamer the RMSD was plotted as smoothed cubic spline. Respective mean RMSD values are listed in brackets; SEM < 0.1 Å in all cases.

doi:10.1371/journal.pcbi.1004693.g001

ammonia. Subsequently, ammonia attacks GGP, which results in inorganic phosphate and a tetrahedral, positively charged reaction intermediate that is stabilized by E305 via a salt bridge interaction. E305 then gets protonated, which destabilizes the salt bridge, leading to the opening of the glutamate binding site and glutamine release.

Residue R324, which is mutated to cysteine (R324C) or serine (R324S), is located in the catalytic site and forms an ionic salt bridge with the β-phosphate group of ADP in the crystal structure (Fig 1C) [22]. It is reasonable to assume that R324 interacts analogously with the GS substrate ATP, although no crystal structure of human GS with ATP or an ATP analog is available. Residue R341 is located 10 Å away from the catalytic site (Fig 1C). No explanation has been put forward how the R341C mutation influences GS' catalytic activity over that distance.

Here, we investigated changes in GS structure, dynamics, and energetics at the atomistic level due to the three GS mutations R324C, R324S, and R341C by molecular dynamics (MD) simulations, rigidity analysis [25, 26], and free energy calculations. Our data show direct effects of the R324C/S mutations on the ATP binding, which are attenuated in the case of R324S due to the emergence of water-mediated interactions to ATP. In contrast, for R341C, we demonstrate a long-range influence on both ATP and glutamate binding: First, R341 indirectly influences ATP binding as a stabilizing element in an amino acid triplet; second, R341 connects two topologically separated regions between which information transmission is essential for glutamate binding. *In vitro* studies on the GS mutant H281A-H284A-Y288A (HHY), predicted to mimic the loss of interactions in the R341C mutant, provide evidence for this influence. These results can semi-quantitatively explain the observed GS deficiencies linked to the three mutations [17–19] and provide a basis for investigations how to counteract the effect due to the R324S mutation.

Materials and Methods

Molecular dynamics simulations

We performed molecular dynamics (MD) simulations of the wild type GS and the three GS mutants, R324C, R342S, and R341C. Coordinates of human GS were obtained from a crystal structure available from the Protein Data Bank (PDB) [27] as PDB entry 2QC8 [22] solved at 2.6 Å resolution. Human GS is a homodecamer with ten identical subunits, each consisting of 373 amino acids. As MD simulations of the GS decamer are computationally highly expensive, we considered a dimeric model system containing only two adjacent subunits forming a single catalytic site. The dimeric model was generated by extracting two adjacent monomers from the GS crystal structure (chains A and B). The validity of the dimeric model was checked by

comparative MD simulations of the GS wild type decamer and the GS wild type dimer. Both systems were simulated in the presence of bound ADP, the intermediate GGP, and magnesium ions (Mg^{2+}).

Using the dimeric model we investigated the influence of the three mutations on four different states according to the suggested mechanism of glutamine formation [24]: GS without a ligand (GS_{APO}), with bound ATP (GS_{ATP}), with bound ATP and glutamate ($GS_{ATP+GLU}$), and with bound ADP and GGP ($GS_{ADP+GGP}$). All states were modelled for wild type GS and the three GS mutants R324C, R342S, and R341C. Models of GS mutants were obtained by amino acid exchanges in the wild type dimer using the SwissPDBViewer [28]. For all mutants the best ranked side chain rotamers were used as starting conformations.

The GS crystal structure contains non-covalently bound ADP, the inhibitor L-methionine-*S*-sulfoximine phosphate (MSO-P), manganese ions (Mn^{2+}), chloride ions, and crystal water [22]. For the GS_{ATP} and $GS_{ATP+GLU}$ states, ADP was changed to ATP by adding the missing atoms with the *LEaP* program [29] of AmberTools 1.4 [30] according to the library of Meagher *et al.* [31]. In the case of $GS_{ADP+GGP}$, ADP coordinates were taken directly from the crystal structure, and hydrogen atoms were added according to the library of Meagher *et al* [31]. To generate $GS_{ATP+GLU}$ and $GS_{ADP+GGP}$, glutamate and GGP were manually modelled based on the coordinates of the structurally similar inhibitor MSO-P present in the crystal structure. Structurally bound Mn^{2+} ions were changed into Mg^{2+} ions, for which well-validated simulation parameters [32] are available. Moreover, GS is catalytically active with Mg^{2+} ions [33]. Magnesium ions were present in all states GS_{APO}, GS_{ATP}, $GS_{ATP+GLU}$, and $GS_{ADP+GGP}$ because the absence of divalent cations leads to a "relaxed" and inactive variant of GS [34, 35]. Nonetheless, we had to remove one Mg^{2+} ion in the case of GS_{ATP} and $GS_{ATP+GLU}$ because the additional phosphate group of ATP causes clashes in the starting structure. Protonation states of histidines were assigned according to the protonation that was found to be most likely by visually inspecting the histidine environment.

The generated model systems were prepared for MD simulation with the *LEaP* program [29] of AmberTools 1.4 [30]. Sodium counter ions were added to the above described structures to neutralize each system. Model systems were placed in a truncated octahedral box of TIP3P water [36], leaving a distance of at least 11 Å between the solute and the border of the box. The finally obtained GS dimer systems comprised ~112,000 atoms. A system of the wild type GS decamer, prepared analogously, comprised ~354,000 atoms. For the polyphosphate chains of ADP and ATP, atomic partial charges and force field parameters were obtained from Meagher *et al.* [31]. Atomic partial charges for the substrate glutamate and the intermediate GGP were derived according to the restraint electrostatic potential fit (RESP) procedure [37]. Geometry optimizations and subsequent single point calculations were conducted with Gaussian03 [38] using the HF/6-31G* basis set. The resulting electrostatic potentials were fitted using *respgen* of AmberTools 1.4 [30]. Angle parameters for the phosphate group in GGP were taken from Homeyer *et al.* [39]. All other parameters were taken from the Amber ff99SB force field [40, 41].

The systems were relaxed by three steps of energy minimization, performed with the *sander* module of Amber11 [42]. First, harmonic restraints with a force constant of 5 $kcal \cdot mol^{-1} \cdot Å^{-2}$ were applied to all protein atoms, ligands, and structurally bound ions within the catalytic site while all other atoms were free to move (500 cycles steepest descent (SD) and 2000 cycles conjugate gradient (CG) minimization). Second, we reduced the harmonic restraints and applied a force constant of 1 $kcal \cdot mol^{-1} \cdot Å^{-2}$ (2000 cycles SD and 8000 cycles CG minimization). Finally, the positional restraints were removed completely, and all atoms were free to move (1000 cycles SD and 4000 cycles CG minimization).

The MD simulation procedure started by heating the respective system from 0 K to 100 K in a canonical (NVT) MD simulation of 50 ps length. During this heating step positional

restraints of 1 kcal·mol^{-1}·Å^{-2} were applied to all protein atoms, ligands, and structurally bound ions within the catalytic site. Afterwards, the temperature was raised from 100 K to ~300 K during 50 ps of isobaric-isothermal (NPT) MD. Subsequently, the density was adjusted to 1 g·cm^{-3} during 200 ps of NPT-MD. Finally, the harmonic positional restraints were removed by gradually decreasing the force constant from 1 to 0 kcal·mol^{-1}·Å^{-2} in six NVT-MD runs of 50 ps length each. In the MD simulations, the particle mesh Ewald (PME) method [43–45] was employed to treat long-range electrostatic interactions. The SHAKE algorithm [46] was applied to all bonds involving hydrogens. A time step of 2 fs was used for the integration of the equations of motion. The distance cutoff for short range non-bonded interactions was set to 9 Å. In order to setup three independent MD production simulations, the target temperature was set to 299.9 K, 300.0 K, and 300.1 K in the equilibration, so that we obtained three different starting structures for subsequent MD production runs. Production MD simulations were performed in the NVT ensemble at 300 K for 100 ns. Coordinates were saved in a trajectory file every 20 ps. Using this MD simulation protocol, we generated three independent MD simulations for four different states (see above), for wild type GS and the GS mutants R324C, R324S, and R341C, which resulted in $3 \times 4 \times 4 = 48$ MD simulations and an aggregate simulation time of 4.8 μs.

The 20–100 ns interval of each production run was considered for analysis. The analysis of the MD trajectories was carried out with *ptraj* [47] of AmberTools 1.4 [30]. The following measures were computed: the root mean-square fluctuation (RMSF) as a measure of mobility, the root mean-square deviation (RMSD) as a measure of structural similarity, the average secondary structure along the MD trajectory, water density grids, and distances. In addition, hydrogen bond interactions were determined using a distance of 2.8 Å between the two donor and acceptor atoms and an angle (donor atom, H, acceptor atom) of 120° as cutoff criteria for strong hydrogen bonds, and a distance of 3.2 Å and an angle of 120° as cutoff criteria for weak hydrogen bonds [48]. We analyzed whether a water-mediated chain of hydrogen bonds exists between ATP and C324 or S324, respectively. A water-mediated interaction was considered present when all hydrogen bonds in the water chain fulfilled the above distance and angle criteria. Results from three independent trajectories of the same system are expressed as means ± standard error of the mean (SEM). Results were analyzed with the R software [49] using the two-sided Student's *t*-test. P values < 0.05 were considered significant.

Constraint network analysis

The Constraint Network Analysis (CNA) approach allows linking biomacromolecular structure, flexibility, (thermo-)stability, and function [26]. To analyze the effect of R341 on the structural stability of GS, we extracted an ensemble of 4000 structures from the 20–100 ns interval of the MD simulation of wild type GS in the $GS_{ADP+GGP}$ state that was equilibrated at 300.1 K; in this interval, the RMSD of GS relative to the starting structure remained particularly stable on average (~ 2 Å). In addition, we extracted an ensemble of 400 equally distributed structures from the 20–100 ns interval of MD simulations of the decameric wild type GS in the $GS_{ADP+ADP}$ state. Coordinates (excluding water molecules, ions, and ligands) were extracted by *mm_pbsa.pl* [50] of Amber 11 [42]. Coordinates of an R341A GS mutant, used to mimic the loss of interactions of the R341 side chain with its environment, were generated employing the Ala-scan functionality of *mm_pbsa.pl*. This led to two sets of coordinates for dimeric and decameric GS, respectively, that differed only in residue 341. With CNA, thermal unfolding simulations of wild type GS and R341A GS were then performed to identify differences in the GSs' structural stability [51]. For this, a hydrogen bond energy cutoff in the range of 0 to 6 kcal·mol^{-1} with steps of 0.1 kcal·mol^{-1} was used [26]. Stability maps [51] were then generated, which report

when a rigid contact between two amino acids i and j (rc_{ij}) vanishes during the thermal unfolding simulation [25]. Finally, a difference stability map was calculated as rc_{ij}(wild type GS)–rc_{ij}(R341A GS); differences with $p < 0.05$ according to a Welch test [52] were considered significant.

Computation of effective binding energies

Effective binding energies, i.e., the sum of gas-phase energies plus solvation free energies [53, 54], for the substrates ATP and glutamate were computed by the molecular mechanics Poisson-Boltzmann surface area (MM-PBSA) approach [55, 56]. The computations were performed with the *mm_pbsa.pl* script [50] of Amber 12 [57], using the ff99SB force field [40, 41] as in the MD simulations. The polar part of the solvation free energy was computed with the PBSA solver implemented in Amber 12 using dielectric constants of 4 and 80 for the solute and the solvent, respectively, and Parse radii [58] for the solute atoms. A solute dielectric constant of 4 was recommended for highly charged binding sites of proteins [59, 60], as given in the case of GS [22], to adequately account for screening effects of the binding site region.

Effective binding energies were computed according to the 1-trajectory MM-PBSA approach, in which snapshots of complex, receptor, and ligand are obtained from MD simulation of the complex [55]. While this approach neglects energetic effects due to conformational changes upon binding, it generally results in lower statistical uncertainties [55]. Contributions due to changes in the configurational entropy of the ligand or the receptor upon complex formation were neglected, too, in order to avoid introducing additional uncertainty in the computations [53, 59, 61]. Conformational ensembles for the computations were generated by extracting 4000 snapshots from the 20–100 ns interval of the MD trajectories of the GS_{ATP} and $GS_{ATP+GLU}$ states of wild type GS and all three mutants R324C, R324S, and R341C. In the case of the $GS_{ATP+GLU}$ state, effective binding energy calculations were performed considering glutamate as the ligand, whereas ATP was considered part of the receptor. The effective binding energies were averaged over the respective ensembles.

Relative effective binding energies ($\Delta\Delta G$) were calculated by subtracting the effective binding energy of the wild type ($\Delta G_{\text{wild type}}$) from the effective binding energy of the mutant ΔG_{mutant} for trajectory {1, 2, 3} (eq 1).

$$\Delta\Delta G_{\{1,\,2,\,3\}} = \Delta G_{\text{mutant},\{1,\,2,\,3\}} - \Delta G_{\text{wild type},\{1\,,2,\,3\}} \tag{1}$$

Results from the three independent MD simulations for a system are expressed as mean over the $\Delta\Delta G_{\{1,\,2,\,3\}}$. The SEM over the three independent MD simulations for a system X (SEM_X) was calculated by error propagation according to eq 2.

$$SEM = \sqrt{SEM_1{}^2 + SEM_2{}^2 + SEM_3{}^2} \tag{2}$$

where $SEM_{\{1,2,3\}}$ is the SEM for trajectory {1, 2, 3}. The SEM of the relative effective binding energy (eq 2) was calculated according to eq 3.

$$SEM_{total} = \sqrt{SEM_{mutant}{}^2 + SEM_{wild\ type}{}^2} \tag{3}$$

A one-sample t-test with $\Delta\Delta G = 0$ as reference was performed using the R software [49]. P values < 0.05 were considered significant.

Materials

L-methionine-*S*-sulfoximine (MSO) and polyclonal antibodies raised against the C-terminus of glutamine synthetase were from Sigma (Deisenhofen, Germany). The monoclonal antibody

directed against GS (clone 6) was from Beckton-Dickinson (Heidelberg, Germany). The monoclonal antibody against GFP (green fluorescent protein), which cross-reacts with the YFP-variant (yellow fluorescent protein), was from Miltenyi-Biotech (Bergisch-Gladbach, Germany). Horseradish peroxidase-coupled goat anti-mouse IgG antibodies were from Bio-Rad International (Munich, Germany). Horseradish peroxidase-coupled goat anti-rabbit IgG antibodies were from Dako (Eching, Germany). The monoclonal antibody against glyceraldehyde-3-phosphate dehydrogenase (GAPDH) was from Biodesign International (Cologne, Germany). Lipofectamine 2000 was from Life Technologies (Darmstadt, Germany).

Culturing and experimental treatment of HEK293 cells

Human embryonic kidney 293 (HEK293) cells were cultured on Petrie dishes (diameter = 60 mm) in minimal essential medium (MEM) containing Earle´s salt, L-glutamine and 5% fetal bovine serum (PAA, Linz, Austria). HEK293 cells were grown to about 70% confluency before cDNA (2 μg/dish) was introduced by lipofection using Lipofectamin 2000 according to the manufacturer's instructions. 24 h after transfection, cells were either treated with L-methionine-*S*-sulfoximine (MSO, 3 mmol/l) or were left untreated for 2 h.

Cloning and site-directed mutagenesis of human GS

Human glutamine synthetase was cloned using human liver cDNA and the following primers GS-YFP-for: 5'-CGGAATTCATGACCACCTCAGCAAGTTC-3' and GS-YFP-rev: 5'-CGGGATCCGCGTAATTTTTGTACTGGAAGG-3'. The forward primer contained an EcoRI restriction site, and the stop codon in the reverse primer was replaced by a BamHI site. The PCR product was cloned into the pEYFP-N1 vector (Clontech, Palo Alto, CA). Mutations were introduced into WT-GS-YFP using the QuikChange Multi Site-Directed Mutagenesis Kit (Agilent Technologies, Santa Clara, USA) and the following mutagenesis primers GS-R341A: 5'-GGTTACTTTGAAGATCGTGCCCCCTCTGCCAACTGCG-3' and GS-SKR: 5'-GGCCATT GAGAAACTAGCCGCGGCGCACCAGTACCACATCC-3'. For the HHY variant the mutations were introduced sequentially using the following primers: GS-H281/84A-for: 5'-GAGAAAC TAAGCAAGCGGGCCCAGTACGCCATCCGTGCCTATGATCC-3' and GS-Y288A: 5'-CAG TACGCCATCCGTGCCGCTGATCCCAAGGGAGGCCTGG-3'. Successful cloning and mutagenesis was verified by sequencing (GenBank accession number: NM_002065).

Western- and dot-blot analysis

Western-blot analysis was performed as described recently [62]. In brief, at the end of the experimental procedure proteins were purified from HEK293 cells and protein content was determined by the BioRad protein assay (BioRad, Munich, Germany). After polyacrylamide gel electrophoresis (10%), proteins were transferred onto nitrocellulose membranes using a semi-dry blotting chamber (BioRad, Munich, Germany). Membranes were incubated in bovine serum albumin (BSA, 10%) for 30 min and incubated with antibodies against GS (mAb, 1:5,000; pAb, 1:5,000), green fluorescent protein (GFP mAb 1:5,000), or glyceraldehyde-3-phosphate dehydrogenase (GAPDH, mAb, 1:5,000). Primary antibodies were detected using horseradish peroxidase-coupled anti-mouse or anti-rabbit IgG antibodies (1:10,000, 2 h at room temperature), respectively.

Dot-blot analysis was performed as described recently [62, 63] by spotting 2 μg of protein in a volume of 2 μl protein lysis buffer on a nitrocellulose membrane. After spots were dried for 30 min. at room temperature, immunodetection was performed using the membrane as described above for Western-blot analysis.

Peroxidase activity on the membranes was detected using Western-Lightning chemiluminescence reagent plus (Perkin Elmer, Waltham, USA). Digital images were captured using the Kodak Image Station 4000MM. Signal intensities were measured by densitometric analysis using the Kodak Molecular Imaging Software.

Immunofluorescence analysis

Immunofluorescence analysis was performed by confocal laserscanning microscopy (LSM510-META (Carl Zeiss AG, Oberkochem, Germany). HEK293 cells were seeded on MaTek dishes (MatTek Corporation, Ashland, USA) and transfected with cDNA constructs as described above. At the end of the transfection procedure, cells were incubated with Hoechst34580 (1:10,000; Life Technologies, Darmstadt, Germany) for 10 min at 37°C in an incubator (5% CO_2). Cells were washed twice with phosphate-buffered saline before MatTek dishes were mounted on the LSM510-META and analyzed for YFP and Hoechst34580 immunofluorescence.

Analysis of results

For statistical analysis, experiments were carried out with three separate HEK293 seedings. Results are expressed as mean values ± SEM and compared using a two-sided Student's *t*-test (Excel for Windows; Microsoft, Redmond, USA). P values < 0.05 were considered significant.

Results

Validation of the dimeric model system

In order to perform MD simulations more efficiently and, thus, improve conformational sampling of wild type GS and GS mutants, we established a model system consisting of two adjacent subunits of the GS decamer forming a single catalytic site (Fig 1B and 1C). The dimeric model system and the decameric structure of wild type GS in the $GS_{ADP+GGP}$ state were subjected to MD simulations of 100 ns length at $T = 300$ K to probe the stability of the systems and to validate that the binding site structure does not deteriorate in the model system.

First, the RMSD, a measure of structural deviation along the MD trajectories, of all protein backbone atoms relative to the starting structure was analyzed (Fig 1D). The RMSD values for both systems increase until 20 ns. After this period, the RMSD of the GS decamer remains constant and below 2.0 Å (mean RMSD over 100 ns: 1.65 Å (SEM < 0.1 Å)). Thus, the structure of the GS decamer shows only minor changes during the MD simulation. The dimeric model system yields a mean RMSD of 2.31 Å (SEM < 0.1 Å), with a maximal value of ~3.5 Å after 70 ns (Fig 1D). The overall structural change of the dimeric model system is slightly larger than that of the GS decamer. Still, these values are in the range observed for other protein systems of that size during MD simulations of that length [64, 65]. Regions in the dimeric model that show particularly large conformational variations were identified by computing the RMSF per residue; the RMSF is a measure of the average atomic mobility. The largest differences in the conformational variability between the dimeric model and the GS decamer occur at the N- and C-termini of the subunits (Fig 1E). The lower RMSF values for the GS decamer result from all terminal protein chains interacting with adjacent subunits; such interactions are missing for the termini of the dimeric model. Hence, when considering only those 90% of the residues with the lowest RMSF ("core region") in the RMSD calculations, the mean RMSD of the dimeric model decreases to 1.58 Å (SEM < 0.1 Å) (Fig 1D, $Dimer_{90}$), which is comparable to the value for the GS decamer (see above).

Second, we focused our analysis on the binding site region, i.e., all residues that are within 4 Å of the bound ADP and GGP (Fig 1E). These residues show low mean RMSD values relative to the starting structure of 0.89 Å (SEM < 0.1 Å) in the MD simulations of the dimeric model system and for the GS decamer in the range of 0.82–2.29 (SEM < 0.1 Å) (Fig 1F). Regarding the bound ligands themselves, mean RMSD for ADP (GGP) (Fig 1G and 1H) of 0.44–0.69 Å (0.90–1.03 Å) in the case of the decamer and 0.49 Å (0.96 Å) in the case of the dimeric model were found (SEM < 0.1 Å in all cases).

In summary, small structural deviations of similar magnitude are found for the core regions, the binding sites, and the ligands of both the dimeric model system and the GS decamer with respect to the starting structures, demonstrating that both systems remain structurally stable over the simulation time. The dimeric model will thus be used to investigate the effects of the GS mutations.

Effects of mutations of R324 on interactions to ATP

Residue R324 is located in the catalytic site and forms a salt bridge with the β-phosphate group of ADP (Fig 1C) [22]. Although no crystal structure information for ATP-bound human GS is available, it is likely that R324 is interacting with the β-phosphate group of ATP, too. The substitution of R324 with cysteine reduces GS activity to about 12% of that of the wild type [17]. The substitution of R324 with serine likely partially conserves GS activity [20]. Initially, we investigated whether the R324S or R324C mutations induce structural changes within the catalytic site. For this, we computed the backbone RMSD of the residues of the catalytic site (Fig 1E) for both mutants in the GS_{APO} state (Fig 2A). In the case of the R324S mutant, the RMSD remains largely constant during three independent MD simulations (mean RMSD: 0.86 Å, 0.85 Å, and 1.26 Å (SEM < 0.1 Å)) (Fig 2A). In the case of the R324C mutant, the RMSD remains largely constant in two MD simulations (mean RMSD: 1.04 Å and 0.84 Å (SEM < 0.1 Å)) (Fig 2A). During one MD simulation, however, the RMSD fluctuates up to 3.5 Å, with a mean RMSD of 1.53 Å (SEM < 0.1 Å) (Fig 2A). Visual inspection of the respective trajectory revealed a highly mobile loop (termed "Glu flap" [21, 24]), formed by residues 304–306, as the cause for these fluctuations; excluding those three residues results in a mean RMSD of 0.95 Å (SEM < 0.1). All mean RMSD values are thus comparable with the mean RMSD obtained for the catalytic site of wild type GS (Fig1F). This demonstrates that neither the R324S nor the R324C mutation changes the catalytic site structure markedly.

Next, we hypothesized that differences in GS activity in the R324C and R324S mutants arise from differences in the interactions between arginine and the mutated residues, respectively, with ATP in the first step of glutamine formation. To investigate this, we subjected wild type GS and the R324C and R324S mutants in the GS_{ATP}, $GS_{ATP+GLU}$, and $GS_{ADP+GGP}$ states to MD simulations. Distances were measured over the respective structural ensembles between the terminal guanidine nitrogens of R324 and oxygens oriented towards R324 of the β-phosphate group of ADP in the $GS_{ADP+GGP}$ state, or ATP in the GS_{ATP} and $GS_{ATP+GLU}$ states. The distance measurements confirmed the existence of a salt bridge interaction in the wild type for ADP [22] and revealed such an interaction for ATP (mean distances < 3.5 Å (SEM < 0.1 Å)) (Fig 2B), which is lower than the threshold of 4 Å used to define a salt bridge interaction [66]. This interaction is permanently present in eight out of nine trajectories (Figure A in S1 file), and is formed after ~65 ns in one trajectory (Figure A in S1 file) and remains stable thereafter. In contrast, in both R324 mutants, the mean distances between the thiol group of cysteine and the hydroxyl group of serine, respectively, and the β-phosphate group of ADP or ATP are > 7 Å (SEM < 0.1 Å) (Fig 2B). The differences in the mean distances with respect to the wild type are significant ($p < 0.05$). In addition, time series of the distances over the course of the

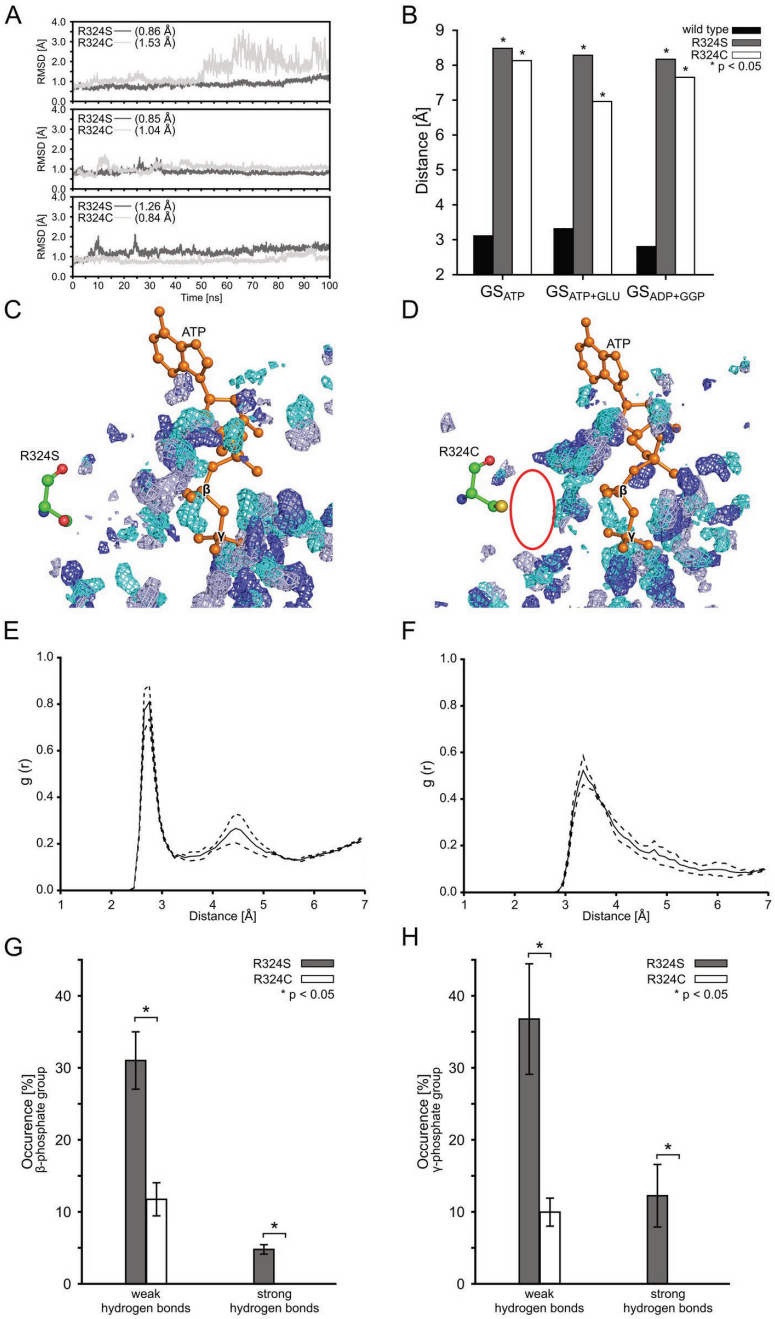

Fig 2. Structural changes and water structure in the binding sites of the R324S and R324C mutants. **(A):** Backbone RMSD of catalytic site residues (for definition see Fig 1E) of the R324S (dark grey) and R324C (light grey) mutants in the GS_{APO} state during 100 ns of MD simulations (each subpanel shows MD simulations initiated from a different starting structure (see section "Experimental procedures" above)). Respective mean RMSD values are listed in brackets; SEM < 0.1 Å in all cases. (**B):** Mean distances

between R324 (wild type GS), or S324 and C324 in GS mutants, and the β-phosphate group of ATP in states GS_{ATP} and $GS_{ATP+GLU}$ or ADP in state $GS_{ADP+GGP}$, respectively. Stars indicate significant differences ($p < 0.05$) with respect to the wild type. In all cases, SEM < 0.1 Å. **(C, D):** Density distribution of water around ATP in the binding site during MD simulations of R324S (C) and R324C (D) in the $GS_{ATP+GLU}$ state. Regions where water is most present are indicated by water density grids for three MD simulations (cyan, light blue, and dark blue; isopleths were plotted such that they encompass 80% of the maximum occupancy). ATP (orange) and the mutated amino acid 324 are shown in ball-and-stick representation. The red oval indicates an area of pronounced difference in the water density between the R324S and R342C mutants. **(E, F):** Radial distribution function (RDF) of water oxygens around the side chain oxygen or sulfur, respectively, of S324 (E) and C324 (F) in the $GS_{ATP+GLU}$ state. The solid line shows the mean RDF, and dashed lines indicate ± SEM. **(G, H):** Mean relative occurrence of water-mediated hydrogen bonds between the β-phosphate group (G) or the γ-phosphate group (H) of ATP and residues S324 (gray) or C324 (white), respectively, in the $GS_{ATP+GLU}$ state. The distance cutoff for the hydrogen bonds was set to 2.8 Å for strong hydrogen bonds and 3.2 Å for weak hydrogen bonds. Error bars denote the SEM; stars indicate a significant difference ($p < 0.05$) between both mutants. For panels B—H, data from the 20–100 ns intervals of the respective MD simulations was taken.

doi:10.1371/journal.pcbi.1004693.g002

MD simulations did not show the formation of hydrogen bonds between S324 or C324 and the β-phosphate group of ADP or ATP, respectively, in any conformation (Figure A in S1 file). Thus, neither residue at position 324 forms a direct hydrogen bond with the β-phosphate group of ADP or ATP in the R324C and R324S mutants. The lack of a direct interaction between the residue at position 324 and the β-phosphate group of ATP could lead to an increased mobility of ATP within the catalytic site. This could distort the proper mutual arrangement of the substrates prior to the reaction, leading to a loss in catalytic activity. However, the RMSF of ATP bound to wild type GS or one of the mutants do not differ significantly (Figure B in S1 file), which suggests that the mutation at position 324 may rather influence the affinity of the substrate ATP towards GS (see section "Relative effective binding energies of GS substrates" below).

Subsequently, we investigated why the R324S mutant likely leads to a higher residual GS activity than the R324C mutant [20]. We hypothesized that the direct interaction between the sidechain of R324 in the wild type could be replaced by water-mediated interactions in the R324S mutant but not the R324C mutant. Therefore, we determined the water density between residue 324 and ATP in MD trajectories by counting the presence of water molecules within a cubic grid of 0.33 Å spacing. Isopleth plots of the density distribution that encompass 80% of the maximum occupancy of water molecules in three independent MD simulations of the R324S and R324C mutants, respectively, in the $GS_{ATP+GLU}$ state are shown in Fig 2C and 2D. These results qualitatively reveal a much broader region of high water density between R324S and the β-and γ-phosphate groups of ATP than in the R324C case, resulting in regions of high water occupancy close to the R324S side chain. For a quantitative analysis, radial distribution functions (RDF) for oxygen atoms of water molecules around the side chain oxygen (R324S) or sulfur (R324C) were computed (Fig 2E and 2F). The RDF reveals two shells of water molecules around R324S, with the first shell peaking at ~2.8 Å, consistent with previous findings [67], and the second shell at ~4.5 Å (Fig 2E). The distance of the first shell peak is in line with that of a strong hydrogen bond (2.5–3.2 Å) [48]. In the case of R324C, the first shell peaks at ~3.2 Å (Fig 2F). This difference with respect to R324S reflects a similar difference of the van der Waals radii of oxygen and sulfur [68]. More notable, the water density at the position of the first shell is 30% higher in the case of R324S than for R324C, and the second shell is considerably more structured in the former case (Fig 2E), demonstrating stronger hydrogen bonding interactions between serine and water, as expected [69].

Finally, we determined the frequency of occurrence of water-mediated hydrogen bonds between R324S or R324C and the β- and γ-phosphate groups of ATP (Fig 2G and 2H). From the distance between the two side chains and the β-phosphate group of ~ 7.0–8.5 Å, respectively,

(Fig 2B) and a water diameter of 2.9 Å [70], one can deduce that between two to three water molecules can bridge this gap. In the analysis, we distinguished between weak (distance cutoff between hydrogen bond donor and acceptor of d_{cut} = 3.2 Å) and strong (d_{cut} = 2.8 Å) hydrogen bonds. Only hydrogen bonds with a distance $< d_{cut}$ were considered for analyses. The frequency of occurrence of water-mediated hydrogen bonds between R324S and the β- and γ-phosphate groups of ATP is significantly higher than for R324C for both weak (31.0 ± 4.0% *versus* 11.8 ± 2.3%; 36.8 ± 7.7% *versus* 9.9 ± 2.0%; Fig 2G and 2H) and strong (4.8 ± 0.7% *versus* 0%; 12.2 ± 4.4% *versus* 0%; Fig 2G and 2H) hydrogen bonds.

In summary, our analyses show the absence of a direct hydrogen bonding interaction between the side chains of R324S and R324C mutants and the β-phosphate group of ATP, in contrast to the wild type GS. In the case of the R324S mutant, the direct interaction is replaced by water-mediated hydrogen bonds; such hydrogen bonds are significantly less frequently observed in the R324C mutant.

Effect of the R341C mutation on the first step of the catalytic cycle

In fibroblasts from the father of a patient with an R341C mutation in GS, a 50% drop in specific GS activity was found [17]. As R341 is located at a distance of 10 Å from the catalytic site (Fig 1C) and its side chain points away from this site (Fig 3A), the influence of the R341C mutation on GS activity must arise from a long-range effect that percolates through the GS structure. Analysis of the GS crystal structure [22] revealed R341 as part of an amino acid triplet (Fig 3A; termed triad hereafter) consisting of R341, D339, and R340. While R341 is at the most distant end of the triad with respect to the catalytic site, R340 makes hydrogen bond and salt bridge interactions with the sulfoximine phosphate part of MSO-P (Fig 3A).

During our MD simulations of wild type GS in the $GS_{ADP+GGP}$ state, we also observe a hydrogen bond between R340 and GGP (mean distance between the terminal guanidine nitrogens of R340 and the carbonyl oxygen in GGP: 2.63 Å (SEM < 0.1 Å); Fig 3B), in agreement with the crystal structure. This interaction is stable over 100 ns MD simulations (Figure C in S1 file). R340 does not interact with glutamate in the $GS_{ATP+GLU}$ state, however (mean distance between the center of the terminal guanidine nitrogens of R340 and the center of the γ-carboxylic function in glutamate: 4.05 Å (SEM < 0.1 Å); Fig 3B, Figure C in S1 file). Rather, R340 interacts with the γ-phosphate group of ATP in the $GS_{ATP+GLU}$ state (mean distance between the center of the terminal arginine nitrogens and the center of the oxygens oriented towards R340 of the γ-phosphate group of ATP: 3.06 Å (SEM < 0.1 Å)) as it does in the GS_{ATP} state (mean distance between the center of the terminal arginine nitrogens and the center of the oxygens oriented towards R340 of the γ-phosphate group of ATP: 2.88 Å (SEM < 0.1 Å)) (Fig 3B). Again, the interactions with the γ-phosphate group are stable over the course of 100 ns MD simulations (Figure C in S1 file). The observed shift of the interaction of R340 with ATP in the GS_{ATP} and $GS_{ATP+GLU}$ states to one with GGP in the $GS_{ADP+GGP}$ state suggests a prominent involvement of R340 in the first step of the catalytic cycle of GS.

Within the triad, D339 and R341 form a salt bridge in the crystal structure (Fig 3A, [22]). The mean distances SB^1 and SB^2 (Fig 3A, black dashed lines) between side chains of D339 and R341 are < 3 Å (SEM < 0.1 Å) in all states for wild type GS (Fig 3C). This interaction is present ≥ 98% of the time during MD simulations of wild type GS of all states (Fig 3D, SB^1 and SB^2 occupancy determined for salt bridges with d_{cut} < 4.0 Å). These findings suggest that D339 and R341 stabilize R340 as flanking residues. This stabilization counteracts the inherent flexibility of the loop region all three residues are located in (Fig 3A). In the R341C mutant, the mean distances SB^1 and SB^2 between the carboxylate oxygens of D339 and the thiol function of C341 is > 4.5 Å (SEM < 0.1) in all states (Fig 3C). Employing d_{cut} < 3.2 Å and angle < 120°, a

PLOS | COMPUTATIONAL BIOLOGY

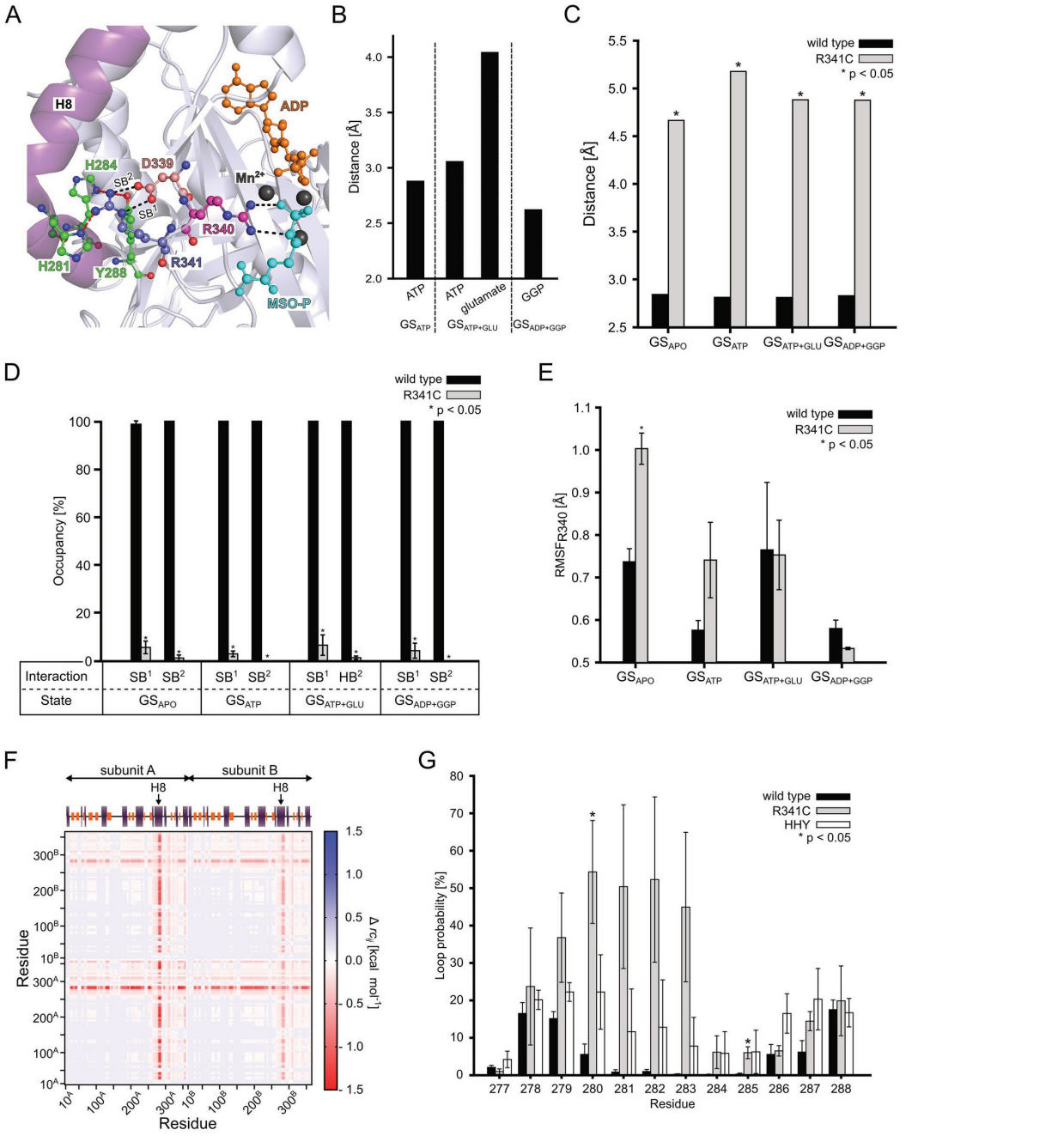

Fig 3. Structural and stability changes in the R341C mutant. (A): Close-up view of the crystal structure of human GS (PDB entry 2QC8 [22]) around R341. The triad composed of residues D339, R340, and R341, and residues H281, H284, and Y288 on helix 8 (H8; raspberry) are shown in ball-and-stick representation. The salt bridge between D339 and R341 (SB^1 and SB^2)) and the interaction between R340 and L-methionine-*S*-sulfoximine phosphate (MSO-P) are indicated by black dashed lines. Interactions between R341 and H281, H284, and Y288, respectively, are indicated by red dashed lines. ADP (orange) and MSO-P (cyan) are depicted in ball-and-stick representation, and Mn^{2+} ions are shown as black spheres. **(B):** Mean distances between terminal

guanidino nitrogens in R340 and the oxygens of the γ-phosphate group of ATP oriented towards R340, the center of oxygens of the γ-carboxylic group of glutamate, and the carbonylic oxygen in GGP. SEM < 0.1 Å in all cases. GS_{ATP}, $GS_{ATP+GLU}$, and $GS_{ADP+GGP}$ were considered. **(C):** Mean distances of interactions SB^1 and SB^2 (see panel A) for wild type GS and when considering the thiol group of C341 in the R341C mutant. SEM < 0.1 Å in all cases. Stars indicate a significant difference ($p < 0.05$) between wild type and mutant. **(D):** Mean occupancy of interactions SB^1 and SB^2 (see panel A) for wild type GS and when considering the thiol group of C341 in the R341C mutant. Error bars denote the SEM; stars indicate a significant difference ($p < 0.05$) between wild type and mutant. **(E):** All-atom RMSF of residue R340 in wild type GS and the R341C mutant. Error bars denote the SEM; stars indicate a significant difference ($p < 0.05$) between wild type and mutant. **(F):** Stability map depicting significant differences ($p < 0.05$) in the structural stability as computed by CNA between wild type GS and the R341A mutant. Protein structures were extracted from the $GS_{ADP+GGP}$ state: Blue colors indicate that two residues are less stably connected in wild type, red colors that two residues are less stably connected in the R341A mutant. The secondary structure of GS is depicted on the top, with orange bars representing β-strands and blue bars representing α-helices; H8 is labelled. Subunits are indicated by arrows. **(G):** Probability for residues 277 to 288 of H8 to be in a loop conformation during MD simulations of wild type GS, the R341C mutant, and the HHY mutant in the GS_{ATP} state. Error bars denote the SEM; stars indicate significant differences ($p < 0.05$) with respect to the wild type. Results in panels B-G are based on snapshots recorded during the 20–100 ns interval of the respective MD simulations.

doi:10.1371/journal.pcbi.1004693.g003

hydrogen bond between the carboxylate oxygens of D339 and the thiol function of C341 is present in $\leq$ 5% of the time during MD simulations of all states (Fig 3D). These results suggest that the stabilizing effect of residue 341 on R340 is largely lost in the R341C mutation. To substantiate this, we computed residue-wise RMSF of R340 for wild type GS and the R341C mutant in all states (Fig 3E). For GS_{APO}, the RMSF is significantly ($p < 0.05$) larger in the R341C mutant (1.00 ± 0.03 Å) than the wild type GS (0.74 ± 0.03 Å) (Fig 3E). In contrast, no significant changes were observed for states GS_{ATP}, $GS_{ATP+GLU}$, and $GS_{ADP+GGP}$ (Fig 3E), likely because R340 is then stabilized by interactions with the substrates (see above; Fig 3B). These results suggest that the R341C mutation indirectly affects the first step of the catalytic cycle, particularly ATP binding, by influencing the R340 mobility in the GS_{APO} state.

Effect of the R341C mutation on signal transmission between the catalytic site and helix 8

In order to investigate the influence of mutant R341C on GS' mechanical stability, we applied Constrained Network Analysis (CNA), where biomolecular structures are represented as molecular frameworks [26] and analyzed by means of rigidity theory [71]. That way, regions that are either structurally stable ("rigid") or flexible are identified. We compared results for wild type GS to those obtained for a perturbed structural ensemble in which interactions by the side chain of R341 are abolished (see "Experimental procedures" for how this ensemble was generated). The result is depicted as a difference stability map Δrc_{ij} [51], which shows if a rigid contact between two residues becomes less stable in the perturbed structural ensemble (red colors in Fig 3F; a rigid contact exists if two residues belong to the same rigid region). The loss of side chain interactions of R341 results in a significant ($p < 0.05$) destabilization of the C-terminus of the GS dimer model (residues 265–365; Fig 3F). Control calculations performed for the GS decamer corroborate this finding (Figure D in S1 file). In this region, helix 8 (H8, residues 266–288), located on the outside of the GS subunit (Fig 3A), shows the most pronounced loss in structural stability (with Δrc_{ij} values of -1.4 kcal·mol^{-1}; see ref. [25] for an explanation of the energy values). Visual inspection of the GS crystal structure [22] reveals that the guanidino group of R341 forms hydrogen bonds with three residues on H8 (H281, H284, and Y288) (Fig 3A).

To substantiate these results, we analyzed the structural stability of H8 during MD simulations of wild type GS and the R341C mutant in the GS_{ATP} state, as well as of an H281A/H284A/Y288A triple mutant in the same state (hereafter termed HHY mutant). The HHY mutant serves as a mimic of the R341C mutant because here, as in the R341C mutant, no hydrogen bonds between residue 341 and residues 281, 284, and 288, respectively, can be formed. We computed the probability that residues 266–288 form a loop in the course of the MD simulations (Fig 3G). For wild type GS, this loop probability is below 20% for residues

278, 279, and 288, below 10% for residues 280, 286, and 287, and below 5% for the remaining amino acids (Fig 3G). For the R341C mutant, in contrast, a markedly increased loop probability is found for residues 279 to 283 (up to 50%; Fig 3G). In this region, mutant HHY shows the most distinct increases in the loop probability compared to wild type GS, too (up to 22%; Fig 3G). For residues 266–276, there are no differences in loop probability between wild type GS and R341C or HHY mutant, respectively. These results demonstrate that R341 has a stabilizing influence on H8 in wild type GS; this influence is lost in both the R341C and HHY mutants. Considering the above results on R341's role in the triad, this suggests that R341 can relay information between the catalytic site and H8. Of note in this context, Krajewski *et al.* observed a shift of H8 in the first step of the catalytic cycle that closes GS' catalytic site when ATP is bound [22]; this ATP binding-induced shift has been recognized as a prerequisite for glutamate binding [22]. Hence, we hypothesized that the loss of the relaying function in the R341C mutant hampers glutamate binding to GS. For the same reason, glutamate binding should be hampered in the HHY mutant.

Overexpression of glutamine synthetase in human embryonic kidney cells

YFP-tagged wild type and mutated (R341A; HHY; S278A/K279A/R280A = SKR, the latter mutant was introduced as a negative control to HHY, as S278, K279, and R280 are located on H8 but do not interact with R341) human GS were transiently expressed in HEK293 cells. Expression of human GS-YFP in HEK293 cells was monitored by confocal laser scanning microscopy (Fig 4A) and verified by Western-blot analysis, which showed that YFP-tagged GS-constructs coding for human GS were strongly expressed in HEK293 cells (Fig 4B). Treating GS-YFP transfected HEK293 cells with MSO (3 mmol/l, 2 h) had no effect on GS-YFP expression levels in wild type-, R341A-, or HHY-treated cells compared to the respective control (Fig 4B and 4C). However, anti-YFP-immunoreactivity was slightly elevated in MSO-treated HEK293 cells transfected with SKR-mutated GS-YFP (Fig 4B and 4C).

GS was also detected in GS-YFP transfected cells by Western-blot using a monoclonal antibody formerly shown not to react with GS when arginine at position 341 was mutated to cysteine (R341C) (15). As shown in Fig 4D, the monoclonal anti-GS antibody strongly detected overexpressed wild type-GS as well as HHY- and SKR-mutated GS-YFP but failed to detect GS when arginine 341 is mutated to alanine (R341A). In contrast, when using a polyclonal antibody (Sigma, Deisenhofen, Germany) raised against the C-terminus of GS (amino acids 357–373), GS-YFP mutated on arginine 341 (R341A) was readily detected, as were wildtype- and HHY- or SKR-mutated GS-YFP (Fig 4E). MSO-treatment had no effect on detectability of GS-YFP by Western-blot using the monoclonal antibody raised against GS (Fig 4D).

HEK293 cells also expressed GS endogenously (Fig 4D and 4E). However, overexpression of GS-YFP (Fig 4D and 4E) as well as MSO-treatment in GS-YFP transfected HEK293 cells had no effect on endogeneous GS expression levels (Fig 4D).

The results show that wildtype-, as well as R341A-, HHY- and SKR-mutated GS-YFP is efficiently expressed in HEK293 cells by lipofection and that GS-YFP expression levels are not affected by MSO-treatment compared to the respective control. The results also show that wildtype-, HHY- and SKR-mutated but not R341A-mutated GS is recognized by a monoclonal antibody raised against GS (BD, clone 6) in Western-blot. This is explained by the specificity of a monoclonal antibody, which recognizes only a single epitope, and by the interaction of the paratope of an antibody with an epitope, which is mediated by only about 5 amino acids [72]. Therefore, mutations that are located far away from the presumed recognition site (R341) such as S278 are not expected to impair the binding of the anti-GS antibody.

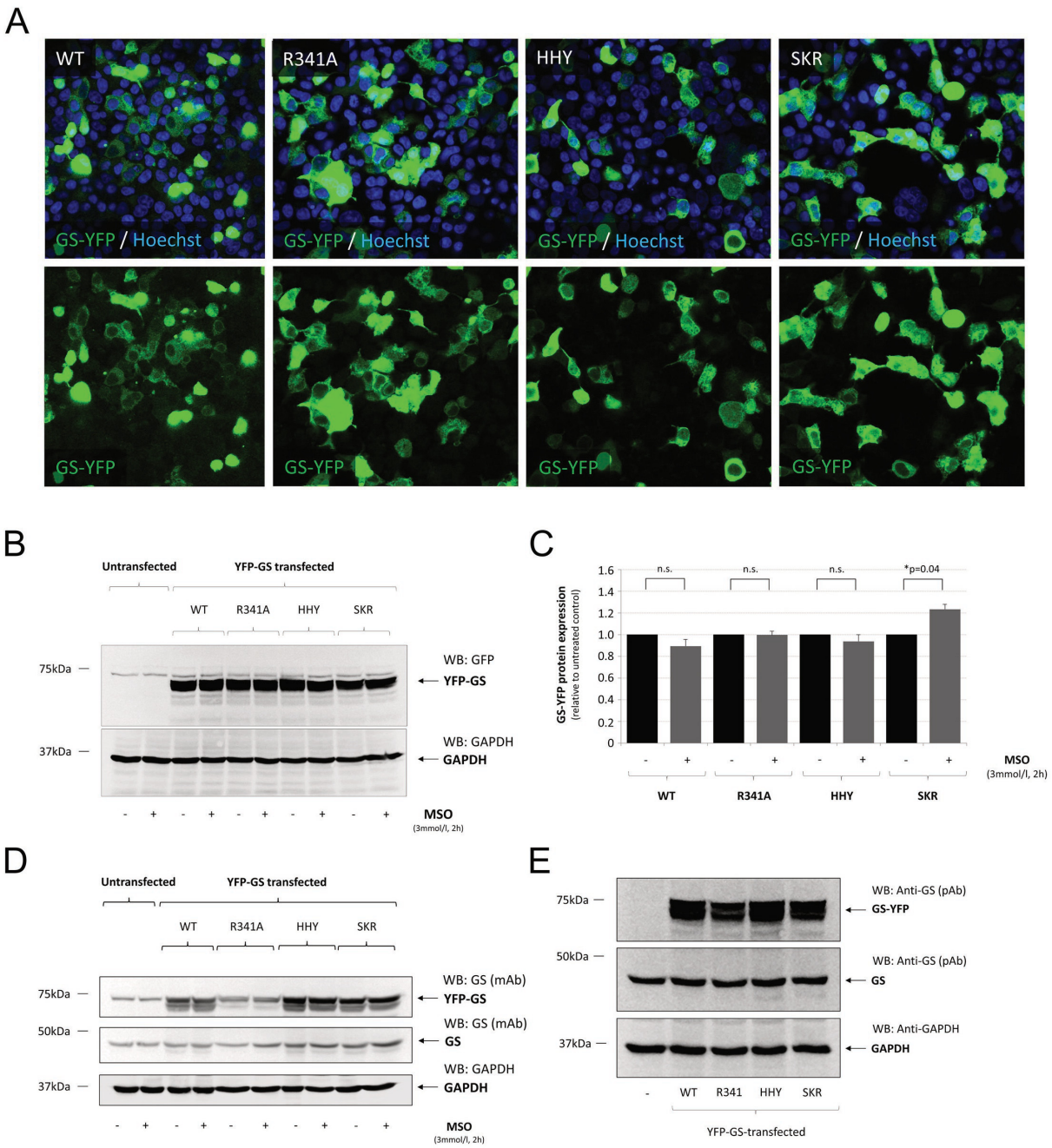

Fig 4. Verification of GS-YFP transfection and overexpression in human embryonic kidney cells. Human embryonic kidney cells (HEK293) were transfected with cDNA constructs coding for YFP-tagged human glutamine synthetase (GS-YFP) without (WT) or with mutations at the indicated positions within the GS amino acid sequence (H281A, H284A, Y288A = HHY; S278A, K279A, R280A = SKR). HEK293 cells were either left untreated or were treated with the GS-inhibitor L-methionine-*S*-sulfoximine (MSO, 3 mmol/l, 2 h). **(A):** Transfection efficiency was verified by confocal laserscanning microscopy in Hoechst34580 stained cells. (**B):** Detection of YFP-GS by Western-blot using anti-GFP antibodies. (**C):** Densitometric quantification of GS-YFP expression

levels as detected by anti-GFP antibodies. Anti-GFP immunoreactivity in MSO-treated cells is given relative to the respective untreated control. **(D):** Detection of GS by Western-blot after heat- and detergent-mediated release of MSO from the enzyme, which restores recognition of GS by the monoclonal anti-GS antibody (BD, clone6). GAPDH served as a loading control. **(E):** Detection of overexpressed human GS-YFP and endogenously expressed GS by Western-blot using polyclonal anti-GS antibodies (Sigma, Deisenhofen, Germany). GAPDH served as a loading control. * Statistically significantly different compared to untreated YFP-GS-transfected HEK293 cells ($p < 0.05$). n.s.: not statistically significantly different.

doi:10.1371/journal.pcbi.1004693.g004

Effect of mutating amino acids H281, H284 and Y288 or S278, K279 and R280 on binding of L-methionine-*S*-sulfoximine to glutamine synthetase

MSO binds non-covalently to the glutamate-binding pocket of GS [73] thereby masking an epitop which is recognized by a monoclonal antibody (BD, clone 6) [62]. Therefore, loss of anti-GS immunoreactivity after MSO treatment may serve as a surrogate marker for glutamate binding to the catalytic site of GS.

As shown by dot-blot analysis using native protein, anti-GS immunoreactivity was significantly diminished by about 50% after MSO-treatment in HEK293 cells transfected with wild type- or SKR-mutated GS but remained unchanged in HEK293 cells expressing HHY-mutated GS compared to untreated controls (Fig 5A). In contrast, upon heat- and detergent-mediated protein denaturation, anti-GS immunoreactivity was similar in untreated and MSO-treated, GS-transfected HEK293 cells (Fig 5B).

The results suggest that MSO binds to the glutamate-binding pocket of wildtype- and SKR-mutated-GS but not to the pocket of HHY-mutated GS.

Relative effective binding energies of GS substrates

In order to determine energetic consequences of the GS mutations on substrate binding, effective binding energies relative to wild type GS ($\Delta\Delta G$, eq 1) were computed by the MM-PBSA approach for ATP bound to the R342S, R342C, and R341C mutants in the GS_{ATP} state and for glutamate bound to R342S, R342C, and R341C in the $GS_{ATP+GLU}$ state. The average drift in the effective binding energy $\Delta G_{wildtype}$ of glutamate binding to the $GS_{ATP+GLU}$ state over the last 80 ns of the MD simulations used for analysis is 0.04 kcal·mol^{-1}·ns^{-1}, as determined by the slope of the least-squares line of best fit from a correlation analysis (Fig 6A). The magnitude of the average drifts in all other effective binding energies $\Delta G_{wildtype}$ or ΔG_{mutant} is < 0.15 kcal mol^{-1} ns^{-1} (Figure E and F in S1 file). The magnitude of these drifts is comparable to those found for ligands binding to other proteins [74] or ribosomal RNA [64] and indicates converged estimates of $\Delta G_{wild\ type}$ or ΔG_{mutant}.

The computed $\Delta\Delta G$ for ATP in the GS_{ATP} state is 4.29 ± 0.19 kcal·mol^{-1} for the R324S mutant and 4.64 ± 0.21 kcal·mol^{-1} for the R324C mutant (Fig 6B). While these results demonstrate that ATP binding to the mutants is disfavorable compared to binding to wild type GS, the difference between the two mutants is not significant. The latter finding is unexpected considering that both mutations lead to different clinical outcomes. Likely, the similar $\Delta\Delta G$ result from neglecting explicit water molecules in the MM-PBSA computations, which, consequently, results in missing favorable energetic contributions due to water-mediated hydrogen bonds between S324 and ATP, as observed in the MD simulations (Fig 2G and 2H). Including tightly bound structural water molecules in MM-PBSA calculations may provide a possibility to overcome this shortcoming [55, 75]. However, in the case of R324S GS, this approach does not appear applicable to us as we observed frequent exchanges of water molecules involved in the hydrogen bond formations.

For mutant R341C, $\Delta\Delta G$ is 5.93 ± 0.23 kcal·mol^{-1} for ATP and 2.24 ± 0.16 kcal·mol^{-1} for glutamate binding (Fig 6B). Thus, our results show that ATP binding is weakened in all GS mutants; at $T = 300$ K, the magnitudes of $\Delta\Delta G$ relate to decreases in the binding constants of ATP of 1.6 to

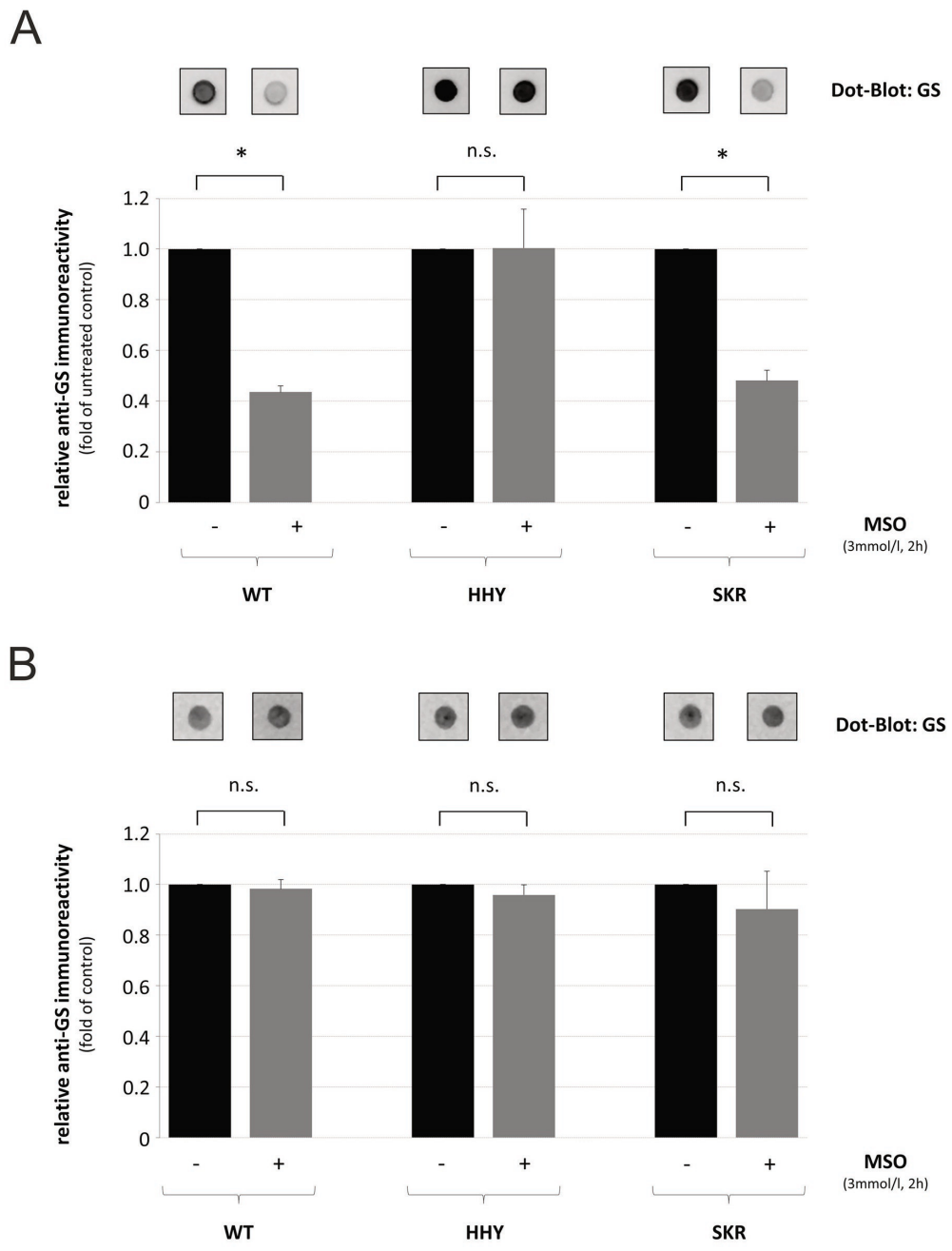

Fig 5. Detection of GS by dot-blot analysis in human embryonic kidney cells. Glutamine synthetase-YFP-transfected human embryonic kidney cells (HEK293) were either left untreated or treated with the GS-inhibitor L-methionine-*S*-sulfoximine (MSO) for 2 h. Equal amounts of **(A)** native or **(B)** heat- and detergent-denaturated protein were spotted onto a nitrocellulose membrane, and GS was detected by dot-blot analysis followed by densitometric quantification of anti-GS immunoreactivity. Anti-GS immunoreactivity in MSO-treated cells is given relative to the respective untreated control. * Statistically significantly different compared to untreated controls ($p < 0.05$). n.s.: not statistically significantly different.

doi:10.1371/journal.pcbi.1004693.g005

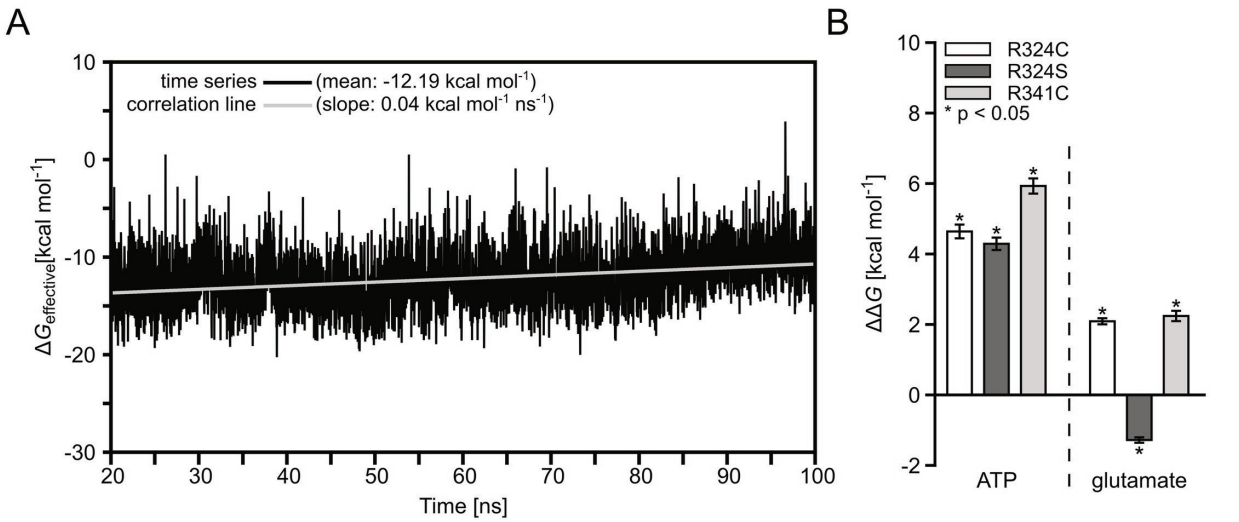

Fig 6. Mean relative effective binding energies of ATP or glutamate. (A): Time-series of effective binding energies calculated for 4000 snapshots extracted in 20 ps intervals from the last 80 ns of MD simulations of glutamate bound to wild type GS in the $GS_{ATP+GLU}$ state (black line) and least-squares line of best fit from a correlation analysis (grey line). The mean of the effective binding energies and the slope of the least-squares line of best fit are given in the legend. **(B):** Mean effective binding energies with respect to wild type GS ($\Delta\Delta G$, eq 1). $\Delta\Delta G$ values were calculated by the MM-PBSA approach for ATP in the GS_{ATP} state and for glutamate in the $GS_{ATP+GLU}$ state for GS mutants R324C, R324S, and R341C. Error bars indicate SEM_{total} (eq 3); stars indicate a significant difference ($p < 0.05$) between wild type and mutant.

doi:10.1371/journal.pcbi.1004693.g006

4.3 log units. From a qualitative point of view, the weakening in the R341C mutant is in line with the above findings that the mutation results in a destabilization of R340 (Fig 3E), which, in turn, interacts with ATP in the GS_{ATP} state (Fig 3B, Figure C in S1 file). From a quantitative point of view, it is surprising that of all mutants the R341C mutant shows the largest effect on ATP binding, although residue 341 does not directly interact with ATP. Part of this effect may be caused by neglecting energetic contributions due to conformational changes in the solutes upon binding in the 1-trajectory approach pursued here, or by neglecting changes in the configurational entropy of the solutes upon complex formation (see section Materials and Methods).

Glutamate binding is weakened in the R324C (R341C) GS mutant by $\Delta\Delta G = 2.09 \pm 0.10$ kcal mol^{-1} ($\Delta\Delta G = 2.29 \pm 0.16$ kcal mol^{-1}) but not in R324S GS ($\Delta\Delta G = -1.28 \pm 0.09$ kcal mol^{-1}) (Fig 6B). Considering that, according to Krajewski *et al.* [22], an ATP binding-induced conformational change in GS' catalytic site is a prerequisite for glutamate binding, our findings are in line with our above structural and energetic analyses according to which ATP binding is particularly weakened in the R324C and R341C mutants.

Discussion

The molecular mechanisms of how the three mutations R324C, R324S, and R341C in human GS [17, 19] lead to a glutamine deficiency, resulting in neonatal death in the case of R324C and R341C, have not been understood. Furthermore, it has remained elusive why the R324S mutation, but not the R324C mutation, likely partially conserves GS activity [20]. Here, we show by MD simulations and binding free energy calculations that both R324 mutations lead to a loss of direct interactions with the β-phosphate group of ADP or ATP compared to wild type GS, and weakened ATP binding. In the case of the R324S mutant, the direct interaction is replaced by water-mediated hydrogen bonds, which are significantly less frequently observed in the

R324C mutant. MD simulations and binding free energy calculations demonstrate that the R341C mutation indirectly weakens ATP binding. In addition, rigidity analysis reveals that the R341C mutation particularly destabilizes helix H8, which should hamper glutamate binding to GS; *in vitro* studies provide evidence for this influence.

Initially, we established a model system consisting of two adjacent subunits of the GS decamer forming a single catalytic site for performing MD simulations in a computationally efficient way. During 100 ns of MD simulations, small structural deviations (RMSD $<$ 1.7 Å; Fig 1D) from the starting structure were found for the core regions of both the dimeric model and the decamer reference. Likewise, structural deviations of the binding site region and the bound ligands computed for the dimeric model were at the lower end (RMSD = 0.89 Å (Fig 1F), 0.49 Å (Fig 1G), and 0.96 Å (Fig 1H), respectively) of the range of values found for the decamer (RMSD $<$ 2.3 Å (Fig 1F) and $<$ 0.7 Å (Fig 1G) or $<$ 0.7 Å (Fig 1H), respectively). Thus, no gross conformational changes were observed for the dimeric model despite the lack of interactions to neighboring subunits. These results are in agreement with a crystallographic study that shows no major allosteric changes within or between the pentamers of human GS upon MSO binding as well as only small (RMSD $<$ 0.35 Å) structural differences between canine GS in the *apo* state and human GS in ligand-bound states [22]. Similarly, only small structural alterations in catalytic site loops during catalysis have been reported for prokaryotic GS of class I-β [21, 24]. Regarding the divalent metal ions required by eukaryotic GS for activity [35], we considered Mg^{2+} ions in our dimeric model system rather than Mn^{2+} ions. We did so as only 20–30% of GS subunits from ovine brain tissue have been found trapped with Mn^{2+} under physiological Mg^{2+} and Mn^{2+} concentrations [76], and human GS from brain is 10-fold more active with Mg^{2+} bound than with Mn^{2+} [77]. For investigating the effects of the R324S, R324C, and R314C mutations, three independent MD simulations were performed for each of the four states of GS (GS_{APO}, GS_{ATP}, $GS_{ATP+GLU}$, $GS_{ADP+GGP}$) of wild type GS and the three mutants, respectively. The replicate MD simulations allow probing for the influence of the starting conditions and determining the statistical significance of the computed results [78].

Regarding the R324S and R324C mutations, we first tested if they distort the structure of the catalytic site in the GS_{APO} state. We excluded residues of the Glu flap loop (residues 304–306) from the analysis because this loop was identified to be highly mobile in a previous study [24], which is in line with our results (Fig 1E). For both mutants, the mean backbone RMSD of the residues of the catalytic site is $\leq$ 1.26 Å with respect to the starting structure (Fig 2A). These conformational changes are only slightly larger than those found in the MD simulations of the dimeric model of wild type GS (RMSD = 0.89 Å (Fig 1F)), which demonstrates that neither mutation changes the catalytic site markedly. In contrast, a significant difference between the wild type residue R324 and serine or cysteine at position 324 is found with respect to interactions with the β-phosphate group of bound ADP or ATP: R324 forms salt bridge interactions with the substrates, respectively (Fig 2B), as also observed in the crystal structure of human GS complexed with ADP [22]; however, neither do S324 nor C324 interact directly with ADP or ATP (Fig 2B). This interaction loss does not result in a significant change of the ATP mobility within the catalytic site of the R324S and R324C mutants compared to wild type GS, likely reflecting the structure-stabilizing influence of the Mg^{2+} ion at the metal binding site n2, which interacts with the nucleotide [24, 79]. Yet, the mutations result in effective energies for binding of ATP that are disfavorable by about 4 kcal mol^{-1} with respect to wild type GS (Fig 6B). Neglecting contributions due to changes in the configurational entropy of the solute molecules upon binding [53, 59, 61], this change in the effective binding energies is equivalent to an about 1000-fold lower association constant of ATP. Taken together, these results strongly suggest that the R324S and R324C mutations deteriorate GS catalytic activity by weakening ATP binding in the first step of the catalytic cycle.

The analysis of indirect, water-mediated interactions between R324S or R342C and the β- and γ-phosphate groups of ATP, respectively, suggested that the extent by which the R324S mutation weakens ATP binding is smaller than the effect of the R324C mutation. This suggestion was based on three independent but related analyses. First, the visual inspection of computed water density between residue 324 and the β- and γ-phosphate groups of ATP in MD trajectories of the $GS_{ATP+GLU}$ state revealed a much broader region of high water density between R324S and ATP than between R324C and ATP (Fig 2C and 2D). Second, RDFs for oxygen atoms of water molecules around the sidechain oxygen of R324S or sulfur of R324C, respectively, demonstrated a 30% higher water density at the first shell peak for R324S than for R324C, and a considerably more structured second shell in the case of R324S (Fig 2E and 2F). Third, the frequency of occurrence of water-mediated hydrogen bonds between residue 324 and the β- and γ-phosphate groups of ATP is significantly higher for R324S than for R324C for both weak and strong hydrogen bonds (Fig 2G and 2H). Water at the interface of biomolecular complexes can provide increased ligand or substrate affinity [76, 79, 80] due to it mediating the interaction between polar groups *via* hydrogen bonds and/or filling space providing van der Waals interactions [81]. The higher water density, more ordered water structure, and increased number of hydrogen bonds found for R324S compared to R324C is in line with findings that more hydrophilic groups generally lead to a higher number of water molecules at a binding interface [82] and that hydrogen bonds involving sulfur are more elusive and weaker than those involving oxygen [83–86], resulting in a larger hydrogen bonding potential of serine than of cysteine in proteins [83]. Our finding of significantly more frequent water-mediated hydrogen bonds between R324S and the β- and γ-phosphate groups of ATP can thus provide an explanation for the suggestion that GS residual activity is higher in the R324S mutant than in the R324C mutant [20]. This residual activity has been linked with the survival of the now seven-year old boy [20]. As this boy still suffers from hyperammonemia [19], the finding could also stimulate the development of better ATP binding-enhancing molecules by which the R324S mutant can be "repaired" extrinsically [87].

The wild type residue R341 is part of an amino acid triplet located on a loop region including also D339 and R340 [22]. While the sidechain of R341 points away from the catalytic site, R340 points to it (Fig 3A). In the course of our MD simulations, we observed a persistent hydrogen bond of the guanidino function of R340 to GGP in the $GS_{ADP+GGP}$ state (Fig 3B) as also found in the crystal structure [22]. In contrast, for the state $GS_{ATP+GLU}$, we observed a shift of the side chain position of R340 during the MD simulations, leading to a salt-bridge interaction with the γ-phosphate group of ATP (Fig 3B). The loss of salt bridge interactions due to the R341C mutation, observed between R341 and D339 in wild type GS (Fig 3C and 3D), results in a destabilization of R340 in the GS_{APO} state, as manifested by significantly smaller RMSF of that residue in wild type GS than the R341C mutant (Fig 3E). No such changes in R340 mobility were observed for the other three GS states. Hence, this strongly suggests that the R341C mutation indirectly weakens ATP binding in the first step of the catalytic cycle. This suggestion was corroborated by the computed relative effective energy of binding of ATP, which is about 6 $kcal \cdot mol^{-1}$ (equivalent to an approximately 10000-fold lower association constant) less favorable for the R341C mutant than for wild type GS (Fig 6B).

An even more indirect, long-range effect of the R341C mutation on the catalytic efficiency of GS was revealed starting from rigidity theory-based analyses [26, 71] of the structural stability of the GS_{ATP} state. These analyses demonstrated that the loss of side chain interactions in the R341C mutant, particularly to H281, H284, and Y288 on H8, result in a significant destabilization of the C-terminus of GS compared to wild type (Fig 3F). These results were confirmed by the analysis of secondary structure of H8 during MD simulations of wild type GS, the R341C mutant, and the triple alanine mutant of H281, H284, and Y288 (HHY) considered to

act as a mimic of the R341C mutant: For the latter two cases, a marked increase in loop probability was found for the central region of H8 (Fig 3G). Together with the above results on R341's role in the triad, this suggests that R341 can relay stability information between the catalytic site and H8. Remarkably, these results can provide an explanation at the atomistic level as to why addition of ATP to human GS increases the melting temperature of the enzyme by 11.5°C [22].

From comparative crystal structure analysis, a connection between ATP binding in the first step of the catalytic cycle of GS and a shift of H8 that closes GS' catalytic site was recognized; this shift is considered a prerequisite for glutamate binding and should be hampered in the R341C or HHY mutants [22], which should weaken glutamate binding as suggested by the computed relative effective energy of binding of about 2.2 kcal·mol^{-1} (equivalent to an approximately 40-fold lower association constant) (Fig 6B). We therefore tested the role of amino acids H281, H284, Y288 in human GS for substrate binding to the glutamate binding pocket in HEK293 cells overexpressing HHY-mutated YFP-tagged GS using MSO as a substrate (Fig 4C, 4D and 4E).

MSO binds non-covalently to the glutamate binding pocket of GS and irreversibly inactivates the enzyme [73] thereby masking an epitope which was recently shown to be recognized by a monoclonal antibody raised against GS [62]. In line with this, MSO-treatment strongly reduced anti-GS immunoreactivity in wildtype-YFP-GS transfected HEK293 cells compared to untreated controls (Fig 5A). In contrast, anti-GS immunoreactivity was unchanged in MSO-treated HEK293-cells transfected with HHY-mutated GS, indicating impaired substrate binding to the catalytic center and suggesting loss of enzymatic activity. Mutation of neighboring amino acids S278, K279, and R280, which do not interact with R341 and were suggested to not play a role for maintenance of the tertiary structure of the catalytic center, did not prevent MSO-binding to GS as indicated by reduced anti-GS immunoreactivity (Fig 5A). Reduced anti-GS immunoreactivity in MSO-treated HEK293 cells was not due to MSO-mediated down-regulation of YFP-GS in the respective transfected HEK293 cells (Fig 4C).

In order to validate that MSO masks an epitope recognized by the monoclonal anti-GS antibody, protein samples were denaturated, which was shown to release MSO from GS [73] and to recover recognition of GS by the anti-GS antibody [62]. Indeed, this treatment completely restored anti-GS immunoreactivity in MSO-treated HEK293 cells transfected with wild type- and SKR-mutated GS as shown by dot-blot analysis (Fig 5B). In line with this, anti-GS immunoreactivity was unchanged in MSO-treated GS-transfected HEK293 cells compared to untreated controls when analysed by Western-blot using heat- and detergent-treated protein samples (Fig 4D).

Binding of ATP to GS is a prerequisite for accessibility of the active center for glutamate [23, 24]. Thus, impaired glutamate binding as indicated by unchanged anti-GS immunoreactivity in MSO-treated HEK293 cells transfected with HHY-mutated GS (Fig 5A) may be a consequence of impaired binding of ATP. This hypothesis was verified by precipitating ATP-binding proteins from HEK293 cells transfected with wildtype- or HHY-mutated GS by N^6-(6-aminohexyl)-ATP-agarose and anti-GS Western-blot analysis. Both endogenous and overexpressed wildtype- or HHY-mutated YFP-GS were detected in precipitates of ATP-binding proteins from HEK293 cell lysates (Figure G in S1 file). Almost no anti-GS immunoreactivity was detected when ATP-binding proteins were precipitated in the presence of excess ATP (10 mmol/l; Figure G in S1 file). These data suggest that mutating amino acids H281, H284, and Y288 of GS does not affect the binding of ATP to GS but that of glutamate.

The present findings also confirm earlier results [17] showing that arginine 341 is critical for recognition by a monoclonal antibody (BD, clone6) raised against GS (Fig 4D). In line with this, mutating amino acids H281, H284 and Y288 or S278, K279 and R280 had no impact on GS-recognition by the monoclonal antibody (Fig 4D).

These results suggest that amino acids H281, H284 and Y288 on helix H8 in human GS may stabilize the tertiary structure of the glutamate-binding site through interaction with R341, that way enabling glutamate binding to the catalytic center.

In summary, we identified the molecular mechanisms of the GS mutations R324S, R324C, and R341C that lead to clinically relevant glutamine deficiency. All three mutants are suggested to influence the first step of GS' catalytic cycle, namely ATP or glutamate binding. Our analyses reveal a complex set of effects including the loss of direct interactions to substrates, the involvement of water-mediated interactions that alleviate part of the mutation effect, and long-range effects between the catalytic site and structural parts distant from it. As to the latter, dot-blot analysis of HEK293 cells overexpressing GS is in line with our prediction of a significant destabilization of helix H8 in the R341C mutant, which should negatively affect glutamate binding.

Supporting Information

S1 File. The file *S1_file.pdf* contains additional information to the manuscript: supplemental methods on purification of ATP-binding proteins, distances over the course of the 20–100 ns interval of MD simulations between the side chain of residue 324 and the β-phosphate group of the ATP and/or ADP (Figure A), the mobility of ATP bound to wild type GS and both R324C/S GS mutants (Figure B), time series of distances between the side chain of residue R340 and ATP, glutamate, and ADP (Figure C), results from rigidity analysis of decameric GS expressed as stability map (Figure D), correlation analyses of effective binding energies for ATP (Figure E) and glutamate (Figure F) binding to GS, effect of mutating amino acids H281, H284, and Y288 on binding of ATP to GS (Figure G).
(PDF)

Acknowledgments

We are grateful to the "Zentrum für Informations- und Medientechnologie" (ZIM) at the Heinrich-Heine-University Düsseldorf for providing computational support and to the Jülich Supercomputing Center for granting computing time on the supercomputer JUROPA (NIC project ID HDD13) to us. Expert technical assistance was provided by Torsten Janssen.

Author Contributions

Conceived and designed the experiments: BG DH HG. Performed the experiments: BF BG NH VK. Analyzed the data: BF BG NH VK DH HG. Wrote the paper: BF BG NH VK DH HG.

References

1. Meister A. 23. Glutamine synthetase of mammals. The enzymes. 1974; 10:699–754.
2. Martinez-Hernandez A, Bell KP, Norenberg MD. Glutamine synthetase: glial localization in brain. Science. 1977; 195(4284):1356–8. 14400. PMID: 14400
3. Petroff OAC, Errante LD, Rothman DL, Kim JH, Spencer DD. Glutamate-glutamine cycling in the epileptic human hippocampus. Epilepsia. 2002; 43(7):703–10. PMID: 12102672
4. Häussinger D. Hepatocyte heterogeneity in glutamine and ammonia metabolism and the role of an intercellular glutamine cycle during ureogenesis in perfused-rat-liver. Eur J Biochem. 1983; 133 (2):269–75. PMID: 6852039
5. Häussinger D, Sies H, Gerok W. Functional hepatocyte heterogeneity in ammonia metabolism—the intercellular glutamine cycle. J Hepatol. 1985; 1(1):3–14. PMID: 2865284
6. Qvartskhava N, Lang PA, Görg B, Pozdeev VI, Ortiz MP, Lang KS, et al. Hyperammonemia in gene-targeted mice lacking functional hepatic glutamine synthetase. Proc Natl Acad Sci U S A. 2015; 112 (17):5521–6. doi: 10.1073/pnas.1423968112 PMID: 25870278

7. Häussinger D. Nitrogen metabolism in liver: structural and functional organization and physiological relevance. Biochem J. 1990; 267(2):281–90. PMID: 2185740

8. Häussinger D. Hepatic glutamine transport and metabolism. Adv Enzymol Relat Areas Mol Biol. 1998; 72:43–86. PMID: 9559051

9. Gunnersen D, Haley B. Detection of glutamine synthetase in the cerebrospinal-fluid of Alzheimer diseased patients—a potential diagnostic biochemical marker. Proc Natl Acad Sci U S A. 1992; 89 (24):11949–53. PMID: 1361232

10. Tumani H, Shen G, Peter JB, Bruck W. Glutamine synthetase in cerebrospinal fluid, serum, and brain: a diagnostic marker for Alzheimer disease? Arch Neurol. 1999; 56(10):1241–6. PMID: 10520940

11. Bruneau EG, McCullumsmith RE, Haroutunian V, Davis KL, Meador-Woodruff JH. Increased expression of glutaminase and glutamine synthetase mRNA in the thalamus in schizophrenia. Schizophr Res. 2005; 75(1):27–34. PMID: 15820321

12. Brusilow SW, Koehler RC, Traystman RJ, Cooper AJL. Astrocyte glutamine synthetase: importance in hyperammonemic syndromes and potential target for therapy. Neurotherapeutics. 2010; 7(4):452–70. doi: 10.1016/j.nurt.2010.05.015 PMID: 20880508

13. Häussinger D, Laubenberger J, Dahl SV, Ernst T, Bayer S, Langer M, et al. Proton magnetic-resonance spectroscopy studies on human brain myo-linositol in hypo-osmolarity and hepatic-encephalopathy. Gastroenterology. 1994; 107(5):1475–80. PMID: 7926510

14. Häussinger D, Kircheis G, Fischer R, Schliess F, vom Dahl S. Hepatic encephalopathy in chronic liver disease: a clinical manifestation of astrocyte swelling and low-grade cerebral edema? J Hepatol. 2000; 32(6):1035–8. PMID: 10898326

15. Eid T, Behar K, Dhaher R, Bumanglag AV, Lee TSW. Roles of glutamine synthetase inhibition in epilepsy. Neurochem Res. 2012; 37(11):2339–50. doi: 10.1007/s11064-012-0766-5 PMID: 22488332

16. Eid T, Thomas MJ, Spencer DD, Runden-Pran E, Lai JCK, Malthankar GV, et al. Loss of glutamine synthetase in the human epileptogenic hippocampus: possible mechanism for raised extracellular glutamate in mesial temporal lobe epilepsy. Lancet. 2004; 363(9402):28–37. PMID: 14723991

17. Häberle J, Görg B, Rutsch F, Schmidt E, Toutain A, Benoist J, et al. Brief report—Congenital glutamine deficiency with glutamine synthetase mutations. N Engl J Med. 2005; 353(18):1926–33. PMID: 16267323

18. Häberle J, Görg B, Toutain A, Rutsch F, Benoist JF, Gelot A, et al. Inborn error of amino acid synthesis: human glutamine synthetase deficiency. J Inherit Metab Dis. 2006; 29(2–3):352–8. PMID: 16763901

19. Häberle J, Shahbeck N, Ibrahim K, Hoffmann GF, Ben-Omran T. Natural course of glutamine synthetase deficiency in a 3 year old patient. Mol Genet Metab. 2011; 103(1):89–91. doi: 10.1016/j.ymgme.2011.02.001 PMID: 21353613

20. Häberle J, Shahbeck N, Ibrahim K, Schmitt B, Scheer I, O'Gorman R, et al. Glutamine supplementation in a child with inherited GS deficiency improves the clinical status and partially corrects the peripheral and central amino acid imbalance. Orphanet J Rare Dis. 2012; 7(48):1–10.

21. Liaw SH, Eisenberg D. Structural model for the reaction-mechanism of glutamine-synthetase, based on 5 crystal-structures of enzyme-substrate complexes. Biochemistry. 1994; 33(3):675–81. PMID: 7904828

22. Krajewski WW, Collins R, Holmberg-Schiavone L, Jones TA, Karlberg T, Mowbray SL. Crystal structures of mammalian glutamine synthetases illustrate substrate-induced conformational changes and provide opportunities for drug and herbicide design. J Mol Biol. 2008; 375(1):217–28. PMID: 18005987

23. Berlicki L. Inhibitors of glutamine synthetase and their potential application in medicine. Mini Rev Med Chem. 2008; 8(9):869–78. PMID: 18691144

24. Eisenberg D, Gill HS, Pfluegl GM, Rotstein SH. Structure-function relationships of glutamine synthetases. Biochim Biophys Acta. 2000; 1477(1–2):122–45. PMID: 10708854

25. Pfleger C, Radestock S, Schmidt E, Gohlke H. Global and Local Indices for Characterizing Biomolecular Flexibility and Rigidity. J Comput Chem. 2013; 34(3):220–33. doi: 10.1002/jcc.23122 PMID: 23007873

26. Pfleger C, Rathi PC, Klein DL, Radestock S, Gohlke H. Constraint Network Analysis (CNA): a python software package for efficiently linking biomacromolecular structure, flexibility, (thermo-)stability, and function. J Chem Inf Model. 2013; 53(4):1007–15. doi: 10.1021/ci400044m PMID: 23517329

27. Bernstein FC, Koetzle TF, Williams GJ, Meyer EF Jr., Brice MD, Rodgers JR, et al. The Protein Data Bank. A computer-based archival file for macromolecular structures. Eur J Biochem. 1977; 80(2):319–24. PMID: 923582

28. Guex N, Peitsch MC. SWISS-MODEL and the Swiss-PdbViewer: an environment for comparative protein modeling. Electrophoresis. 1997; 18(15):2714–23. PMID: 9504803

29. Schafmeister CEAF, Ross WS, Romanovski V. LEaP. University of California, San Francisco. 1995.
30. Case DA, Cheatham TE III, Darden T, Gohlke H, Luo R, Merz KM, et al. The Amber biomolecular simulation programs. J Comput Chem. 2005; 26(16):1668–88. PMID: 16200636
31. Meagher KL, Redman LT, Carlson HA. Development of polyphosphate parameters for use with the AMBER force field. J Comput Chem. 2003; 24(9):1016–25. PMID: 12759902
32. Allner O, Nilsson L, Villa A. Magnesium ion-water coordination and exchange in biomolecular simulations. J Chem Theory Comput. 2012; 8(4):1493–502. doi: 10.1021/ct3000734 PMID: 26596759
33. Shapiro BM, Ginsburg A. Effects of specific divalent cations on some physical and chemical properties of glutamine synthetase from Escherichia coli. Taut and relaxed enzyme forms. Biochemistry. 1968; 7 (6):2153–67. PMID: 4873174
34. Segal A, Stadtman ER. Variation of the conformational states of Escherichia coli glutamine synthetase by interaction with different divalent cations. Arch Biochem Biophys. 1972; 152(1):367–77. PMID: 4403693
35. Pinkofsky HB, Maurizi MR, Ginsburg A. Binding Mn^{2+} or Mg^{2+} to active-sites of glutamine-synthetase from bovine brain. Fed Proc. 1985; 44(5):1807-.
36. Jorgensen WL, Chandrasekhar J, Madura JD, Impey RW, Klein ML. Comparison of Simple Potential Functions for Simulating Liquid Water. J Chem Phys. 1983; 79(2):926–35.
37. Bayly CI, Cieplak P, Cornell WD, Kollman PA. A Well-Behaved Electrostatic Potential Based Method Using Charge Restraints for Deriving Atomic Charges—the Resp Model. J Phys Chem. 1993; 97 (40):10269–80.
38. Frisch MJT, G. W.; Schlegel, H. B.; Scuseria, G. E.; Robb, M. A.; Cheeseman, J. R.; Montgomery, Jr., J. A.; Vreven, T.; Kudin, K. N.; Burant, J. C.; Millam, J. M.; Iyengar, S. S.; Tomasi, J.; Barone, V.; Mennucci, B.; Cossi, M.; Scalmani, G.; Rega, N.; Petersson, G. A.; Nakatsuji, H.; Hada, M.; Ehara, M.; Toyota, K.; Fukuda, R.; Hasegawa, J.; Ishida, M.; Nakajima, T.; Honda, Y.; Kitao, O.; Nakai, H.; Klene, M.; Li, X.; Knox, J. E.; Hratchian, H. P.; Cross, J. B.; Bakken, V.; Adamo, C.; Jaramillo, J.; Gomperts, R.; Stratmann, R. E.; Yazyev, O.; Austin, A. J.; Cammi, R.; Pomelli, C.; Ochterski, J. W.; Ayala, P. Y.; Morokuma, K.; Voth, G. A.; Salvador, P.; Dannenberg, J. J.; Zakrzewski, V. G.; Dapprich, S.; Daniels, A. D.; Strain, M. C.; Farkas, O.; Malick, D. K.; Rabuck, A. D.; Raghavachari, K.; Foresman, J. B.; Ortiz, J. V.; Cui, Q.; Baboul, A. G.; Clifford, S.; Cioslowski, J.; Stefanov, B. B.; Liu, G.; Liashenko, A.; Piskorz, P.; Komaromi, I.; Martin, R. L.; Fox, D. J.; Keith, T.; Al-Laham, M. A.; Peng, C. Y.; Nanayakkara, A.; Challacombe, M.; Gill, P. M. W.; Johnson, B.; Chen, W.; Wong, M. W.; Gonzalez, C.; and Pople, J. A. Gaussian03. Gaussian, Inc, Wallingford CT. 2004.
39. Homeyer N, Horn AH, Lanig H, Sticht H. AMBER force-field parameters for phosphorylated amino acids in different protonation states: phosphoserine, phosphothreonine, phosphotyrosine, and phosphohistidine. J Mol Model. 2006; 12(3):281–9. PMID: 16240095
40. Cornell WD, Cieplak P, Bayly CI, Gould IR, Merz KM, Ferguson DM, et al. A second generation force field for the simulation of proteins, nucleic acids, and organic molecules. J Am Chem Soc. 1995; 117 (19):5179–5197.
41. Hornak V, Abel R, Okur A, Strockbine B, Roitberg A, Simmerling C. Comparison of multiple Amber force fields and development of improved protein backbone parameters. Proteins: Struct, Funct, Bioinf. 2006; 65(3):712–25.
42. Case DA, Darden TAD, Cheatham TE III, Simmerling CL, Wang J, Duke RE, et al. AMBER 11. University of California, San Francisco. 2010.
43. Darden T, York D, Pedersen L. Particle mesh Ewald: An N· log (N) method for Ewald sums in large systems. J Chem Phys. 1993; 98(12):10089–92.
44. Salomon-Ferrer R, Gotz AW, Poole D, Le Grand S, Walker RC. Routine microsecond molecular dynamics simulations with Amber on GPUs. 2. Explicit solvent particle mesh ewald. J Chem Theory Comput. 2013; 9(9):3878–88. doi: 10.1021/ct400314y PMID: 26592383
45. York DM, Darden TA, Pedersen LG. The effect of long-range electrostatic interactions in simulations of macromolecular crystals—a comparison of the ewald and truncated list methods. J Chem Phys. 1993; 99(10):8345–8.
46. Ryckaert JP, Ciccotti G, Berendsen HJC. Numerical integration of cartesian equations of motion of a system with constraints molecular dynamics of n-alkanes. J Comput Phys. 1977; 23(3):327–41.
47. Roe DR, Cheatham TE. PTRAJ and CPPTRAJ: Software for Processing and Analysis of Molecular Dynamics Trajectory Data. Journal of Chemical Theory and Computation. 2013; 9(7):3084–95. doi: 10.1021/ct400341p PMID: 26583988
48. Desiraju GR, Steiner T. Weak hydrogen Bond: Oxford University Press New York; 2001.
49. Team RC. TEAM: R: a language and environment for statistical computing. R Foundation for Statistical Computing, Vienna, Austria. 2008.

50. Miller BR, McGee TD, Swails JM, Homeyer N, Gohlke H, Roitberg AE. MMPBSA.py: an efficient program for end-state free energy calculations. J Chem Theory Comput. 2012; 8(9):3314–21. doi: 10.1021/ct300418h PMID: 26605738

51. Radestock S, Gohlke H. Protein rigidity and thermophilic adaptation. Proteins: Struct, Funct, Bioinf. 2011; 79(4):1089–108.

52. Welch BL. The generalization of student's' problem when several different population variances are involved. Biometrika. 1947:28–35. PMID: 20287819

53. Gohlke H, Case DA. Converging free energy estimates: MM-PB(GB)SA studies on the protein-protein complex Ras-Raf. J Comput Chem. 2004; 25(2):238–50. PMID: 14648622

54. Homeyer N, Stoll F, Hillisch A, Gohlke H. Binding free energy calculations for lead optimization: Assessment of their accuracy in an industrial drug design context. J Chem Theory Comput. 2014; 10:3331–44. doi: 10.1021/ct5000296 PMID: 26588302

55. Homeyer N, Gohlke H. Free energy calculations by the molecular mechanics Poisson-Boltzmann surface area method. Mol Inf. 2012; 31(2):114–22.

56. Srinivasan J, Cheatham I, T. E., Cieplak P, Kollman PA, Case DA. Continuum solvent studies of the stability of DNA, RNA, and phosphoramidate—DNA helices. J Am Chem Soc. 1998; 120(37):9401–9.

57. Case DA, Darden TA, Cheatham III TE, Simmerling CL, Wang J, Duke RE, et al. AMBER 12. University of California, San Francisco. 2012.

58. Sitkoff D, Sharp KA, Honig B. Accurate Calculation of Hydration Free-Energies Using Macroscopic Solvent Models. J Phys Chem. 1994; 98(7):1978–88.

59. Hou T, Wang J, Li Y, Wang W. Assessing the performance of the MM/PBSA and MM/GBSA methods. 1. The accuracy of binding free energy calculations based on molecular dynamics simulations. J Chem Inf Model. 2011; 51(1):69–82. doi: 10.1021/ci100275a PMID: 21117705

60. Yang TY, Wu JC, Yan CL, Wang YF, Luo R, Gonzales MB, et al. Virtual screening using molecular simulations. Proteins-Structure Function and Bioinformatics. 2011; 79(6):1940–51.

61. Weis A, Katebzadeh K, Soderhjelm P, Nilsson I, Ryde U. Ligand affinities predicted with the MM/PBSA method: dependence on the simulation method and the force field. J Med Chem. 2006; 49(22):6596–606. PMID: 17064078

62. Bidmon HJ, Görg B, Palomero-Gallagher N, Schleicher A, Häussinger D, Speckmann EJ, et al. Glutamine synthetase becomes nitrated and its activity is reduced during repetitive seizure activity in the pentylentetrazole model of epilepsy. Epilepsia. 2008; 49(10):1733–48. doi: 10.1111/j.1528-1167.2008.01642.x PMID: 18479397

63. Görg B, Foster N, Reinehr R, Bidmon HJ, Hongen A, Häussinger D, et al. Benzodiazepine-induced protein tyrosine nitration in rat astrocytes. Hepatology. 2003; 37(2):334–42. PMID: 12540783

64. Saini JS, Homeyer N, Fulle S, Gohlke H. Determinants of the species selectivity of oxazolidinone antibiotics targeting the large ribosomal subunit. Biol Chem. 2013; 394(11):1529–41. Epub 2013/09/06. doi: 10.1515/hsz-2013-0188 PMID: 24006327

65. Widderich N, Pittelkow M, Hoppner A, Mulnaes D, Buckel W, Gohlke H, et al. Molecular Dynamics Simulations and Structure-Guided Mutagenesis Provide Insight into the Architecture of the Catalytic Core of the Ectoine Hydroxylase. J Mol Biol. 2014; 426(3):586–600. doi: 10.1016/j.jmb.2013.10.028 PMID: 24184278

66. Barlow DJ, Thornton JM. Ion-pairs in proteins. J Mol Biol. 1983; 168(4):867–85. PMID: 6887253

67. Matsuoka D, Nakasako M. Probability distributions of hydration water molecules around polar protein atoms obtained by a database analysis. J Phys Chem B. 2009; 113(32):11274–92. doi: 10.1021/jp902459n PMID: 19621908

68. Bondi A. Van der Waals volumes + radii. J Phys Chem. 1964; 68(3):441–51.

69. Rajagopal S, Vishveshwara S. Short hydrogen bonds in proteins. FEBS J. 2005; 272(8):1819–32. PMID: 15819878

70. Cotton FA. Chemical applications of group theory, 3rd ed.: Wiley India; 2008.

71. Jacobs DJ, Thorpe MF. Generic rigidity percolation—the pebble game. Phys Rev Lett. 1995; 75 (22):4051–4. PMID: 10059802

72. Frank SA. Specificity and Cross-Reactivity. Immunology and Evolution of Infectious Disease: Princeton University Press, Princeton (NJ); 2002.

73. Ronzio RA, Meister A. Phosphorylation of methionine sulfoximine by glutamine synthetase. Proc Natl Acad Sci U S A. 1968; 59(1):164–70. PMID: 5242120

74. Metz A, Pfleger C, Kopitz H, Pfeiffer-Marek S, Baringhaus KH, Gohlke H. Hot spots and transient pockets: predicting the determinants of small-molecule binding to a protein-protein interface. J Chem Inf Model. 2012; 52(1):120–33. doi: 10.1021/ci200322s PMID: 22087639

75. Zhu YL, Beroza P, Artis DR. Including explicit water molecules as part of the protein structure in MM/PBSA calculations. J Chem Inf Model. 2014; 54(2):462–9. doi: 10.1021/ci4001794 PMID: 24432790

76. Wedler FC, Ley BW. Kinetic, ESR, and trapping tvidence for in-vivo binding of Mn(II) to glutamine-synthetase in brain-cells. Neurochem Res. 1994; 19(2):139–44. PMID: 7910378

77. Yamamoto H, Konno H, Yamamoto T, Ito K, Mizugaki M, Iwasaki Y. Glutamine-synthetase of the human-brain—purification and characterization. J Neurochem. 1987; 49(2):603–9. PMID: 2885398

78. Galindo-Murillo R, Roe DR, Cheatham TE 3rd. Convergence and reproducibility in molecular dynamics simulations of the DNA duplex d(GCACGAACGAACGAACGC). Biochim Biophys Acta. 2015; 1850 (5):1041–58. doi: 10.1016/j.bbagen.2014.09.007 PMID: 25219455

79. Barelier S, Boyce SE, Fish I, Fischer M, Goodin DB, Shoichet BK. Roles for ordered and bulk solvent in ligand recognition and docking in two related cavities. PLoS One. 2013; 8(7):e69153. doi: 10.1371/journal.pone.0069153 PMID: 23874896

80. Gohlke H, Klebe G. Approaches to the description and prediction of the binding affinity of small-molecule ligands to macromolecular receptors. Angew Chem. 2002; 41(15):2645–76.

81. Li Z, Lazaridis T. Water at biomolecular binding interfaces. Phys Chem Chem Phys. 2007; 9(5):573–81. PMID: 17242738

82. Poornima CS, Dean PM. Hydration in drug design .1. Multiple hydrogen-bonding features of water molecules in mediating protein-ligand interactions. J Comput-Aided Mol Des. 1995; 9(6):500–12. PMID: 8789192

83. Gregoret LM, Rader SD, Fletterick RJ, Cohen FE. Hydrogen bonds involving sulfur atoms in proteins. Proteins: Struct, Funct, Bioinf. 1991; 9(2):99–107.

84. Pal D, Chakrabarti P. Different types of interactions involving cysteine sulfhydryl group in proteins. J Biomol Struct Dyn. 1998; 15(6):1059–72. PMID: 9669552

85. Pimentel GC, McClellan AL. The hydrogen bond. San Francisco: W. H. Freeman And Company; 1960.

86. Zhou P, Tian F, Lv F, Shang Z. Geometric characteristics of hydrogen bonds involving sulfur atoms in proteins. Proteins: Struct, Funct, Bioinf. 2009; 76(1):151–63.

87. Chondrogianni N, Petropoulos I, Grimm S, Georgila K, Catalgol B, Friguet B, et al. Protein damage, repair and proteolysis. Mol Aspects Med. 2014; 35:1–71. doi: 10.1016/j.mam.2012.09.001 PMID: 23107776

Supporting Information

Molecular Mechanisms of Glutamine Synthetase Mutations that Lead to Clinically Relevant Pathologies

Benedikt Frieg[1], Boris Görg[2], Nadine Homeyer[1], Verena Keitel[2], Dieter Häussinger[2$] and Holger Gohlke[1$]

[1]Institute for Pharmaceutical and Medicinal Chemistry, Heinrich-Heine-University, Düsseldorf, Germany

[2]Clinic for Gastroenterology, Hepatology, and Infectious Diseases, Heinrich-Heine-University, Düsseldorf, Germany

[$] Corresponding authors: (H.G.) Universitätsstr. 1, 40225 Düsseldorf, Germany, Phone: (+49) 211 81 13662, Fax: (+49) 211 81 13847, E-mail: gohlke@uni-duesseldorf.de; (D.H.) Moorenstr. 5, 40225 Düsseldorf, Phone : (+49) 211 81 16330, Fax : (+49) 211 81 18752, E-mail : haeussin@uni-duesseldorf.de

Supplemental Methods

Purification of ATP-binding proteins

Prior to purification of ATP-binding proteins, endogenous ATP was removed from HEK293 protein samples using Amicon ® Ultra-4 centrifugal filter devices (Merck/Millipore, Darmstadt, Germany) with a molecular weight cutoff of 10,000 Dalton. ATP-binding proteins were purified from 300 µg of ATP-depleted HEK293 protein samples by precipitation with N^6-(6-Aminohexyl)-ATP-agarose using a commercial kit (ATP AffiPur Kit III, Jena Bioscience, Jena, Germany) according to the instructions of the manufacturer. Precipitates were washed 3 times with washing buffer, and ATP-binding proteins were eluted by incubation of the agarose with elution buffer for 20 min at 4°C. Where indicated, precipitation and washing of ATP-binding proteins with N^6-(6-Aminohexyl)-ATP-agarose was performed in the presence of excess ATP (10 mmol/l).

Supplemental Figures

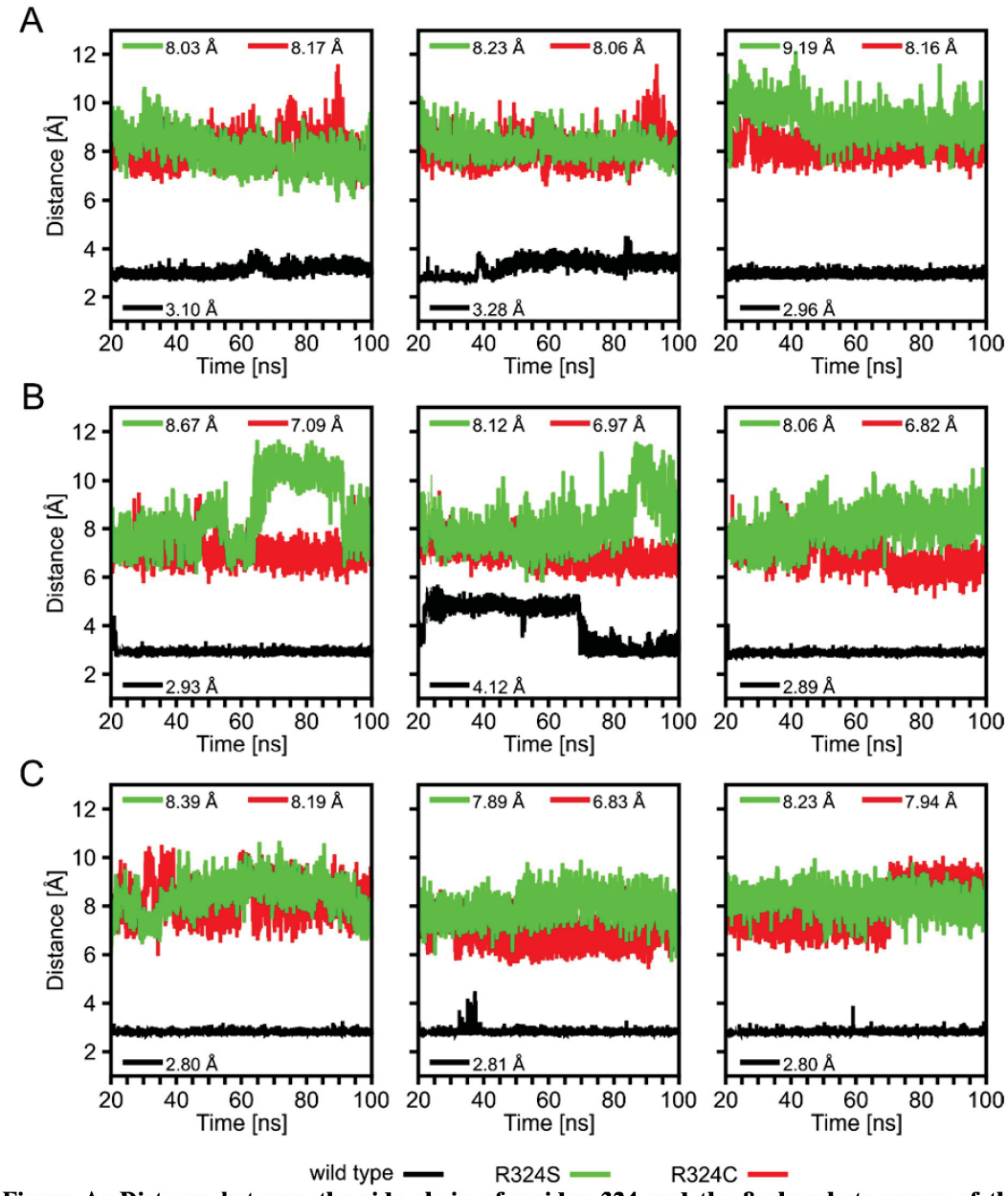

Figure A: Distance between the side chain of residue 324 and the β-phosphate group of the nucleotide.

Distances between R324 (wild type GS; depicted as black lines), or S324 (depicted as green lines) and C324 (depicted as red lines) in GS mutants, and the β-phosphate group of ATP in states GS_{ATP} (**A**) and $GS_{ATP+GLU}$ (**B**) or ADP in state $GS_{ADP+GGP}$ (**C**), respectively, during the 20 – 100 ns interval. The left/middle/right columns show trajectories that were equilibrated at 299.9/300.0/300.1 K, respectively. Mean distances of the respective trajectory are provided in the legend (mean standard error < 0.1 Å).

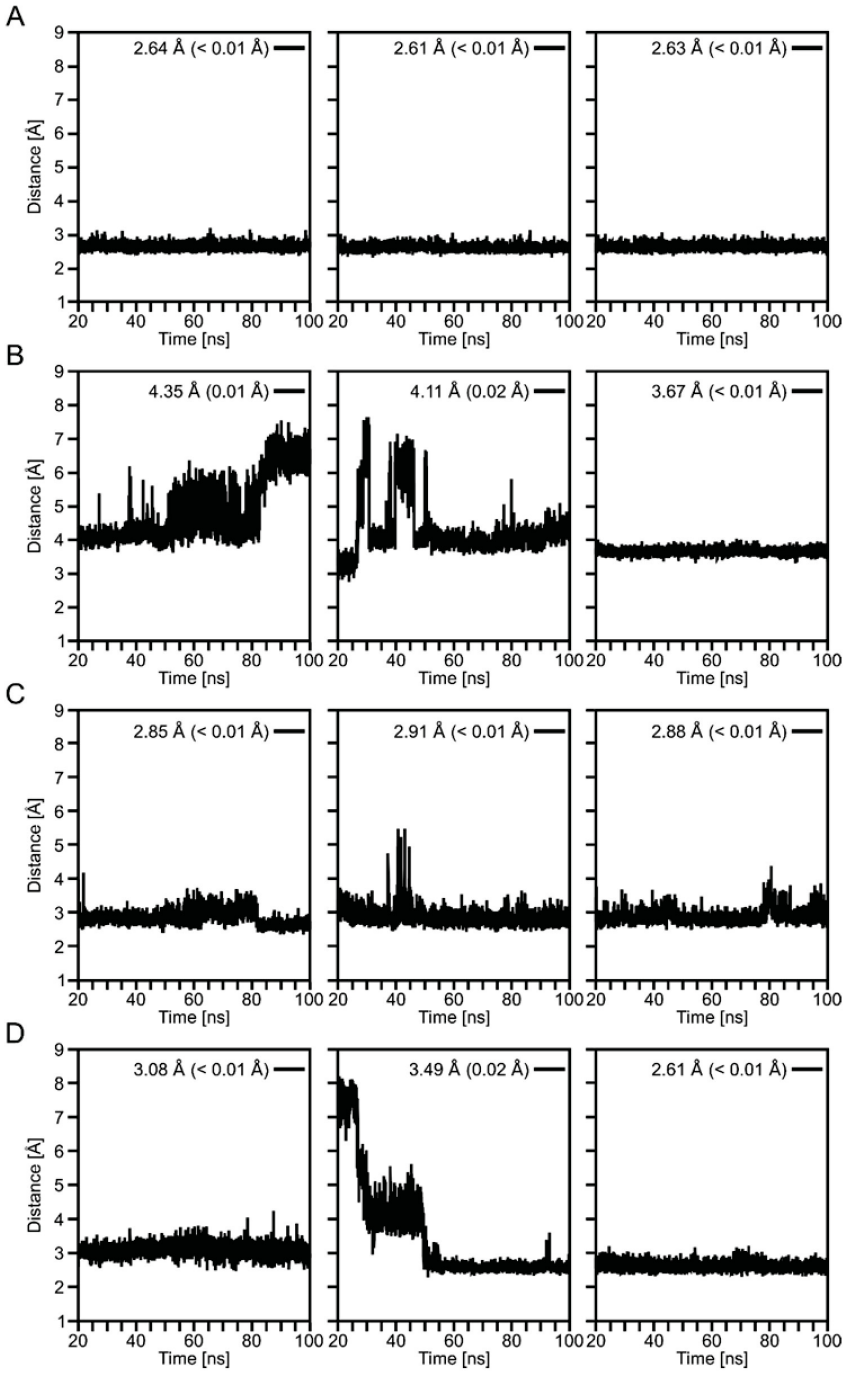

Figure B: Salt bridge interactions between R340 and the substrates.
Distances between R340 and (**A**) the carbonyl oxygen of GGP in state $GS_{ADP+GGP}$, (**B**) the γ-carboxylic function of glutamate in state $GS_{ATP+GLU}$, (**C**) the γ-phosphate group of ATP in state GS_{ATP}, and (**D**) the γ-phosphate group of ATP in state $GS_{ATP+GLU}$. The left/middle/right columns show trajectories that were equilibrated at 299.9/300.0/300.1 K, respectively. Mean distances of the respective trajectory are provided in the legend with mean standard error in parentheses.

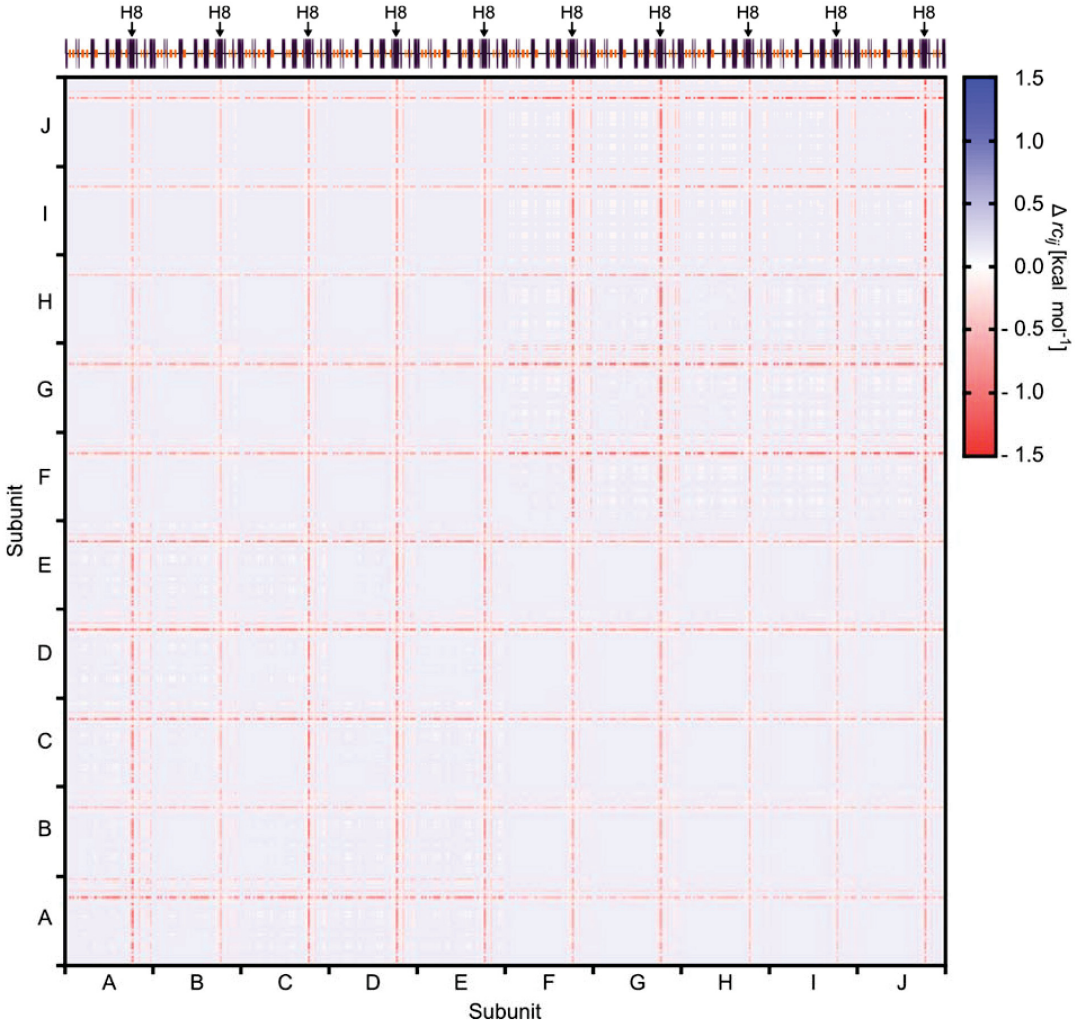

Figure C: Stability changes in decameric GS.
Stability map depicting significant differences ($p < 0.05$) in the structural stability for the GS decamer as computed by CNA between wild type GS and the R341A mutant. Protein structures were extracted from the $GS_{ADP+GGP}$ state. Blue colors indicate that two residues are less stably connected in the wild type, red colors that two residues are less stably connected in the R341A mutant. The secondary structure of GS is depicted on the top, with orange bars representing β-strands and black bars representing α-helices; H8 is labelled.

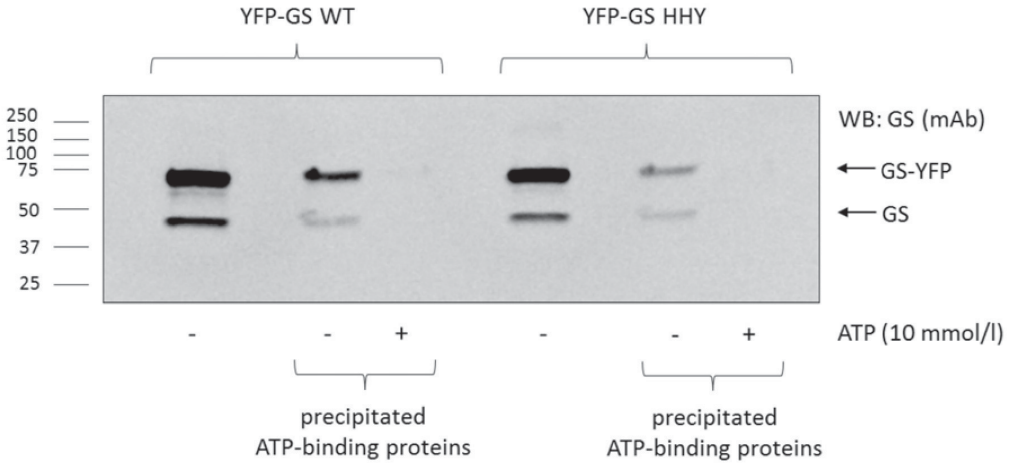

Figure D: Effect of mutating amino acids H281, H284, and Y288 on binding of ATP to glutamine synthetase.
Human embryonic kidney cells (HEK293) were transfected with cDNA constructs coding for YFP-tagged human GS without (WT) or with mutations at positions H281A, H284A, Y288A (HHY). ATP-binding proteins were purified from HEK293 cell protein lysates using N^6AH-ATP-agarose as described in Supplemental Methods, and GS was detected using the monoclonal anti-GS antibody (BD, clone6) by Western-blot analysis. Where indicated, precipitation of ATP-binding proteins was performed in the presence of excess ATP (10 mmol/l). One representative Western-blot out of five is shown.

11.2 PUBLICATION II

Mechanism of fully-reversible, pH-sensitive inhibition of human glutamine synthetase by tyrosine nitration.

Frieg, B., Görg, B., Qvartskhava, N. Jeitner, T., Homeyer, N., Häussinger, D., Gohlke, H.

submitted.

Mechanism of fully-reversible, pH-sensitive inhibition of human glutamine synthetase by tyrosine nitration

Benedikt Frieg[1,2], Boris Görg[3], Natalia Qvartskhava[3], Thomas Jeitner[4], Nadine Homeyer[1], Dieter Häussinger[3*] and Holger Gohlke[1,2*]

[1] Institute for Pharmaceutical and Medicinal Chemistry, Heinrich Heine University Düsseldorf, Düsseldorf, Germany

[2] John von Neumann Institute for Computing (NIC), Jülich Supercomputing Centre (JSC), and Institute for Complex Systems - Structural Biochemistry (ICS-6), Forschungszentrum Jülich GmbH, Jülich, Germany

[3] Clinic for Gastroenterology, Hepatology, and Infectious Diseases, Heinrich Heine University Düsseldorf, Düsseldorf, Germany

[4] Department of Biochemistry and Molecular Biology, New York Medical College, Valhalla, NY, USA

Author ORCID
Benedikt Frieg: 0000-0002-7877-0262
Holger Gohlke: 0000-0001-8613-1447

Running title: *Glutamine synthetase inhibition by tyrosine nitration.*

Keywords: protein tyrosine nitration, molecular dynamics simulations, binding energy, MM-PBSA, umbrella sampling, thermodynamic integration, pK_a prediction, pH sensitivity, enzyme regulation

[*]Corresponding authors: (H.G.) Universitätsstr. 1, 40225 Düsseldorf, Germany, Phone: (+49) 211 81 13662, Fax: (+49) 211 81 13847, E-mail: gohlke@uni-duesseldorf.de or h.gohlke@fz-juelich.de; (D.H.) Moorenstr. 5, 40225 Düsseldorf, Phone : (+49) 211 81 16330, Fax : (+49) 211 81 18752, E-mail : haeussin@uni-duesseldorf.de

Abstract

Glutamine synthetase (GS) catalyzes an ATP-dependent condensation of glutamate and ammonia to form glutamine. This reaction – and therefore GS – are indispensable for the hepatic nitrogen metabolism. Nitration of tyrosine 336 (Y336) inhibits human GS activity. GS nitration and the consequent loss of GS function are associated with a broad range of neurological diseases. The mechanism by which Y336 nitration inhibits GS, however, is not understood. Here, we show by means of unbiased MD simulations, binding and configurational free energy computations that Y336 nitration hampers ATP binding, but only in the deprotonated and negatively-charged state of residue 336. By contrast, for the protonated and neutral state, our computations indicate an increased binding affinity for ATP. pK_a computations of nitrated Y336 within GS predict a pK_a of ~4. Thus, at physiological pH nitrated Y336 exists almost exclusively in the deprotonated and negatively-charged state. *In vitro* experiments confirm these predictions, in that, the catalytic activity of nitrated GS is decreased at pH 7 and pH 6, but not at pH 4. These results indicate a novel, fully reversible, pH-sensitive mechanism for the regulation of GS activity by tyrosine nitration.

Introduction

Glutamine synthetase (GS, glutamate ammonia ligase, EC 6.3.1.2) catalyzes the condensation of glutamate and ammonia to form glutamine in a reaction that requires the ATP-dependent phosphorylation of glutamate[1]. Human GS is composed of ten identical subunits[2] (**Figure 1A**), with catalytic sites residing in the interfaces of two adjacent subunits. High levels of GS are found in astrocytes[3], where it is part of glutamate-glutamine cycling[4], and in perivenous hepatocytes, where it is part of the intercellular glutamine cycle and essential for hepatic ammonia detoxification[5-7]. Ammonia detoxification and glutamine synthesis make GS essential for the human nitrogen metabolism[8-9]. Significant changes in GS activity occur in neurological disorders such as Alzheimer's disease[10-11], hepatic encephalopathy[12-14], and epilepsy[15-16]. Thus, elucidating the mechanisms by which GS acts or is regulated will add in the development of new treatment strategies for the aforementioned disorders. Recently, we showed that mutations that cause human GS inhibition and lead to clinically relevant pathologies act to hamper ATP and glutamate binding: the first steps[17] of glutamine formation[18].

-- Figure 1 --

Nitration of tyrosine 336 (Y336; native amino acids are reported according to crystal structure numbering[2] hereafter)[20-24] inhibits human GS activity. This protein tyrosine nitration (PTN) yields 3'-nitro tyrosine[19, 25] (in the following named TYN and referring to the nitrated amino acid in solution; **Figure 1B**) and decreases the pK_a of the phenolic hydroxyl group by three log units[26]. Thus, at physiological pH, nitrated tyrosine exist partially in the deprotonated phenolate form (in the following named TYD and referring to the nitrated, deprotonated amino acid in solution; **Figure 1B**). PTN is an established biomarker of cellular "nitroxidative stress"[19].

The structure of human GS complexed with ADP[2] indicates that Y336 forms face-to-face stacking interactions with this nucleotide (**Figure 1A**). ADP is formed within the enzyme following phosphorylation of glutamate by ATP. Although no crystal structure of GS with bound ATP is yet available, Y336 most likely forms similar face-to-face stacking interactions with ATP. The GS catalytic site is typically depicted as two opposing funnels, conjoined at their apices, with ATP binding the upper funnel and glutamate binding the lower funnel[17]. Y336 is situated in the upper funnel close to the bound ATP. Substrates other than ATP are ~10 Å away from Y336[2]. An

influence of Y336 nitration on other substrates is therefore unlikely. Even so, the mechanism by which Y336 nitration inhibits GS activity at an atomistic level remained elusive.

Here, we investigated the molecular mechanism of how Y336 nitration inhibits human GS activity by a combined computational and experimental study. These investigations included unbiased molecular dynamics (MD) simulations, binding free energy calculations, and potential of mean force (PMF; configurational free energy) computations of the interactions of nitrated Y336 with GS-bound ATP and ATP binding process. *In vitro* activity measurements of GS confirmed the pH sensitivity of nitrated GS, in that, the catalytic activity of nitrated GS is decreased at neutral, but not at pH 4. The pH sensitivity of tyrosine-nitrated GS indicates a novel regulation of protein function due to PTN.

Results

Y336 nitration weakens interactions with ATP in the GS_{TYD} variant

In order to address, at an atomistic level, how Y336 nitration inhibits GS activity, we performed unbiased MD simulations of three GS variants: wild type GS, GS bearing the protonated TYN336 (*i.e.,* GS_{TYN}), and GS bearing the deprotonated TYD336 (*i.e.,* GS_{TYD}), each bound to ATP. For each system, five replicates of MD simulations of 500 ns length each were performed. To characterize the stacking interactions between the phenyl ring of Y336/TYN336/TYD336 and the purine ring system of ATP, we analyzed the MD trajectories with respect to the distance between the centers of mass (COM) and the angle between the planes of these ring systems. The distance measurements indicate that the major populations are found at short distances ($d \approx 3.8$ Å) for all GS variants, although the rank order of these changes decreases from wild type GS to GS_{TYN} to GS_{TYD} (**Figure 2A**). For both tyrosine-nitrated variants, we found additional populations at longer distances ($d \approx 5.5$ Å) and, exclusively for GS_{TYD}, another one at $d \approx 7.7$ Å (**Figure 2A**). The shapes of the histograms for the plane angle are similar, with the major population found for an almost parallel orientation of the ring systems ($\eta \approx 8°$) for all GS variants (**Figure 2B**). Additional populations are found at increased η for GS_{TYN} and GS_{TYD} ($\eta \approx 40°$) and for GS_{TYD} exclusively ($\eta \approx 132°$) (**Figure 2B**). These results suggest that Y336 nitration weakens the tyrosine/adenine interaction, especially in the GS_{TYD} variant.

-- Figure 2 --

Representative sets of configurations of Y336/TYN336/TYD336 and ATP extracted from the MD trajectories (grayish structures in **Figure 2C**) indicate that ATP is more mobile after Y336 nitration, in particular in the region of the adenine moiety. This finding is confirmed by computing root mean square fluctuations (RMSF), a measure for mobility, for all non-hydrogen atoms in ATP after superimposing all GS_{core} (see **Supporting Information** for details) backbone atoms to the crystal structure: ATP bound to GS_{TYD} shows a significantly increased mobility (RMSF = 0.92 Å ± 0.13 Å; $p < 0.05$) with respect to ATP bound to wild type GS (**Figure 2D**). By contrast, the mean RMSF between ATP bound to GS_{TYN} or wild type GS ($p = 0.31$), or between ATP bound to GS_{TYN} or GS_{TYD} ($p = 0.34$), do not differ significantly (**Figure 2D**). These results further support the conclusion that TYD336/ATP interactions are weakened in the GS_{TYD} variant compared to wild type GS.

Y336 nitration decreases the effective binding energy of ATP in the GS_{TYD} variant

In order to determine energetic consequences of the Y336 nitration on ATP binding, the effective energies of ATP binding relative to wild type GS ($\Delta\Delta G_{effective}$, eq. 1) were computed using the MM-PBSA approach. The computed $\Delta\Delta G_{effective}$ indicate that ATP binding is disfavored in GS_{TYD} ($\Delta\Delta G_{effective}$ = 4.57 kcal mol^{-1} ± 0.06 kcal mol^{-1}; $p < 0.01$) but favored in GS_{TYN} ($\Delta\Delta G_{effective}$ = -2.84 kcal mol^{-1} ± 0.04 kcal mol^{-1}; $p < 0.01$) (**Figure 3A**). The MM-PBSA results for GS_{TYD} are thus consistent with the results of the structural analyses (**Figure 2**). Analysis of the frequencies of the normalized $\Delta G_{effective}$ computed for configurations along the MD trajectories reveals two main populations for the GS_{TYD} system: one with a maximum at $\Delta G_{effective} \approx 0$ kcal mol^{-1}, which relates to configurations of the major population in **Figure 2A, B** (distance/η combination: 3.8 Å / 8°), and another with a maximum at $\Delta G_{effective} \approx 14$ kcal mol^{-1} (**Figure 3B**), which relates to configurations that are part of the minor populations in **Figure 2A, B** (distance/η combinations: 5.5 Å /37° and 7.7/132°). As to GS_{TYN}, the frequencies of normalized $\Delta G_{effective}$ computed for configurations along the MD trajectories also reveal two main populations: one with a maximum at $\Delta G_{effective} \approx$ -6 kcal mol^{-1} (**Figure 2B**), which relates to configurations of the major population in **Figure 2A, B** (distance/η combination: 3.7 Å / 10°) and another that forms a shoulder at $\Delta G_{effective} \approx 10$ kcal mol^{-1}, which relates to configurations with of the minor populations in **Figure 2A, B** (distance/η combination: 5.8 Å / 44°). Hence, in both cases, a coplanar arrangement between TYN336 or TYD336 and ATP's purine ring system is energetically neutral or favorable as

compared to non-nitrated Y336. Deviations from a coplanar arrangement, as they occur for TYN336 or TYD336 (**Figure 2**), are energetically disfavorable, mirroring results from *ab initio* calculations[27]. In order to independently validate the energetic analysis and to further elucidate the effect of Y336 nitration on ATP binding, we performed PMF computations of ATP binding to the GS variants.

-- Figure 3 --

Y336 nitration weakly influences ATP binding kinetics

In addition to influencing the thermodynamics of ATP binding, nitration of Y336 might also introduce a steric and/or electrostatic barrier that hampers access of ATP to the binding site and thereby influence the binding kinetics. The PMF of ATP binding was computed along a binding path (**Figure S1A**) determined by random acceleration (expulsion) MD[28]. In agreement with the suggested mechanism of glutamine synthesis by GS, ATP enters and exits the active site via the upper funnel[17]. The triphosphate moiety of ATP is thought to first enter the site and to pass by Y336, along with the ribose unit, to finally position the adenine group close to this residue. Umbrella sampling[29] simulations of this path were performed for wild type GS, GS_{TYN}, and GS_{TYD}, using as a reaction coordinate the distance r between the centers of mass of the phenyl ring of Y336/TYN336/TYD336 and ATP's purine ring system (**Figure S1A, B**). As the binding path is almost straight, r increases monotonously if ATP unbinds. The PMF was then derived by the Weighted Histogram Analysis Method (WHAM)[30].

The PMFs for all GS variants are consistent with the ATP bound state being markedly favored over the unbound state ($\Delta G_{\text{wild type}}$ = -10.8 kcal mol^{-1}, $\Delta G_{\text{total, TYN}}$ = -14.7 kcal mol^{-1}, $\Delta G_{\text{total, TYD}}$ = -7.6 kcal mol^{-1}; SEM always < 0.06 kcal mol^{-1}) (**Figure 4A**). Relative changes between wild type GS and the 3'-nitro variants ($\Delta\Delta G_{\text{TYD - wild type}}$ = 3.34 kcal mol^{-1} and $\Delta\Delta G_{\text{TYN - wild type}}$ = -3.9 kcal mol^{-1}) are in good agreement with $\Delta\Delta G$ values from MM-PBSA calculations (**Figure 3A**). Hence, two independent methods indicate that ATP binding is thermodynamically disfavored in GS_{TYD} but favored in GS_{TYN}.

By contrast, the PMFs suggest that Y336 nitration only weakly influences the kinetics of ATP binding. Going from the unbound state ($r \approx 38$ Å) to the bound state ($r \approx 4$ Å), ATP binding to GS can be separated into three phases (I, II, and III) (**Figure 4A**). Phase I contains all ATP states with

$r > 17$ Å. In this phase, ATP diffuses almost freely on the outside of the protein (**Figure 4B**), which is reflected in rather flat PMF parts that differ by < 2.5 kcal mol^{-1} with respect to the reference point at r = 38.9 Å. The region explored by ATP during the umbrella sampling simulations is qualitatively the same for all GS variants, such that one can assume that the rotational and translational volume sampled by unbound ATP is also similar in all three cases; hence, from a thermodynamic point of view, the unbound state is equally favorable (or disfavorable) for all GS variants. During phase II of ATP binding (6 Å < $r \leq$ 17 Å), the PMFs reveal similar, small energetic barriers for GS_{TYD} ($\Delta G_{16.7\,Å \rightarrow 14.9\,Å}$ = 1.2 kcal mol^{-1}), GS_{TYN} ($\Delta G_{10\,Å \rightarrow 8\,Å}$ = 1.2 kcal mol^{-1}), and wild type GS ($\Delta G_{8.7\,Å \rightarrow 6\,Å}$ = 1.4 kcal mol^{-1}) (**Figure 4A**). In the case of GS_{TYD}, the PMF increases ($\Delta G_{16.7\,Å \rightarrow 14.9\,Å}$ = 1.2 kcal mol^{-1}) as the ATP's negatively-charged phosphate chain passes by the negatively-charged TYD leading to a repulsion between these moieties (**Figure 4C**). By contrast, ATP hydrogen bonds with the phenolic groups of Y336 or TYN336 (**Figure S2**). As exemplified for wild type GS (**Figure 4D**), the binding of ATP to Y336 or TYN336 is further stabilized at this stage by hydrogen bonding with R45, W60, N61 and I206, as well as hydrophobic (with P208), cation-π (with R45), and chelating interactions (with Mg^{2+}). Together, these bonds lead to the overall drop in the PMFs of wild type GS and GS_{TYN} and the small local minima in phase II, from which ATP escapes to reach phase III. Finally, in phase III of ATP binding ($r \leq$ 6 Å), ATP attains a bound state with a global minimum at $r \approx$ 3.7 Å for all three GS variants (**Figure 4A**). The location of this minimum is in very good agreement with the location of the peak of the most frequently sampled distance in unbiased MD simulations (**Figure 2A**). To conclude, the PMF computations indicate that Y336 nitration influences the thermodynamics of ATP binding to GS, but not the kinetics of this binding.

Nitrated Y336 predominantly exists in the deprotonated TYD form

The pK_a value of the phenolic hydroxyl group belonging to free 3'-nitrotyrosine is three log units lower than that of tyrosine[19] (**Figure 1B**). Local protein environment can further influence the pK_a of ionizable residues[31]. To probe such an influence, we computed the pK_a shift of TYN336 relative to free 3'-nitrotyrosine according to eq. 6 (see **Supporting Information** for details). The relevant $\Delta\Delta G$ values were computed by evaluating the thermodynamic cycle depicted in **Figure 5A** by means of thermodynamic integration[32-33] (eq. 7). These calculations were done by the use of acetyl- and *N*-methyl capped TYN and TYD as model systems for (free) 3'-nitro tyrosine. The transformations from (free) TYN into TYD, and TYN336 into TYD336, yields

$\Delta\Delta G$ = -4.83 ± 0.03 kcal mol^{-1}, a marked decrease of the pK_a of TYN336 of ~3.5 log units to a pK_a ~4 (**Figure 5A**). Hence, at a physiological pH of 7.4, the TYN336:TYD336 ratio amounts to ~1:4,000, such that only the negatively-charged TYD variant is relevant under these conditions. The observations that nitration of Y336 decreases the pK_a of its' phenolic hydroxyl group and that binding of ATP to GS_{TYD} is weakened (see above) are consistent with the finding that GS activity is inhibited under physiological conditions[20-21]. One implication of these observations is that the inhibition of GS activity by Y336 nitration should be relieved by lowering the pH below the pK_a of the nitrated Y336.

-- Figure 4 --

Peroxynitrite-induced tyrosine nitration of human GS

In order to test the hypothesis that lowering pH would relieve inhibition of GS activity due to Y336 nitration, we first established that peroxynitrite ($ONOO^-$) causes the nitration of human GS. Thus, purified human GS was exposed to 0, 5, 50, 100, or 200 µM $ONOO^-$ and then analyzed for the content of nitrated and total GS by Western Blot. As shown in **Figure 5B**, $ONOO^-$ induces a concentration-dependent increase of GS NO_2-Tyr immunoreactivity that is particularly evident at higher $ONOO^-$ concentrations. $ONOO^-$, however, has no effect on anti-GS immunoreactivity at concentrations as high as 200 µM (**Figure 5B**). Thus, under our experimental conditions, exposure of human GS to $ONOO^-$ results in the nitration of this enzyme but not its degradation.

Effects of peroxynitrite on the catalytic activity of human GS

Next, purified human GS was exposed to different concentrations of $ONOO^-$ (0, 100, and 200 µM), and catalytic activity of GS was measured in reaction mixtures adjusted to pH 7.0, 6.0, or 4.0 (see **Supporting Information** for details). As shown in **Figure 5C**, GS activity was significantly reduced in samples treated with 100 or 200 µM $ONOO^-$ as compared to vehicle-exposed controls (0 µM) at pH 7 and to similar extent at pH 6. Lowering the pH of the reaction mixture to 4, however, restored GS activity in $ONOO^-$-exposed samples to control values. At pH 4, GS activity was significantly higher in samples exposed to 200 µM rather than 100 µM $ONOO^-$, presumably reflecting the greater extent of nitration depicted in **Figure 5B**. The activity of nitrated GS is restored by incubation at pH 4 and not pH 6 or 7.

-- Figure 5 --

Discussion

The molecular mechanism of how Y336 nitration leads to inhibition of GS catalytic activity was unknown. Here, we show by means of unbiased MD simulations, as well as binding and configurational free energy computations that Y336 nitration hampers substrate (ATP) binding, but only in the deprotonated and negatively-charged TYD336 state. By contrast, our computations indicate an increased binding affinity of the protonated and neutral TYN336 state for ATP. pK_a computations of nitrated Y336 within GS predict a pK_a of ~4 such that under physiological pH conditions (pH ≈ 7.4) nitrated Y336 almost exclusively exists in the TYD336 state. *In vitro* experiments confirm these predictions, in that catalytic activity of tyrosine-nitrated GS is decreased at pH 7 and pH 6, but not at pH 4. Furthermore, at pH 4, GS activity was significantly higher in samples exposed to 200 µM compared to 100 µM $ONOO^-$. Together, these data reveal a unique pH-sensitive mechanism of GS inhibition due to nitration of Y336.

Our computational results suggest that stacking interactions between Y336/TYN33/TYD336 and ATP (**Figure 1A**) are weakened in the TYD336 state and this weakening is the most likely cause for the decreased affinity of nitrated GS for ATP. These results are based on five independent MD simulations performed for wild type GS, as well as GS_{TYN} and GS_{TYD} variants (for a detailed assessment of the computational procedures used, see **Supporting Information**.) Using the distance d and angle η between the phenyl ring of Y336/TYN33/TYD336 and the purine ring system of ATP to characterize respective stacking geometries, a predominately coplanar arrangement of both rings for wild type GS was revealed ($d \approx 3.8$ Å and $\eta \approx 8°$; **Figure 2A-C**). This coplanar arrangement is temporarily absent for GS_{TYN} and GS_{TYD} ($d \approx 5.5$ Å and $\eta \approx 40°$; $d \approx 7.7$ Å and $\eta \approx 132°$ **Figure 2A-C**). As *ab initio* calculations indicate strong interactions between tyrosine and adenine for distances < 4 Å and plane angles ≈ 10°[27], these structural assessments suggest that Y336 nitration weakens interactions with ATP, in particular between TYD336 and ATP. These results mirror the analysis of atomic mobility of bound ATP (**Figure 2D**).

In line with the structural analyses, effective energy calculations for ATP binding to nitrated GS variants reveal disfavored ATP binding for GS_{TYD} relative to wild type GS (**Figure 3**). Interestingly, these calculations suggest that ATP binding is favored for GS_{TYN}, relative to wild type GS. This is corroborated by PMF computations describing the ATP binding process; for the completely bound state, the PMFs suggest that ATP binding is disfavored for GS_{TYD}, but favored for GS_{TYN} (**Figure 4A**). Both methods, thus, independently suggest that only the TYD336 variant

causes inhibition of GS activity. We note that the difference in the PMF between the unbound and completely bound state does not equate to an absolute binding free energy[34]. Yet, considering that the specified reaction coordinate is the same in all three investigated cases and that the sampled unbound state is very similar (**Figure 4B**), the differences in the PMFs relative to the unbound state can be interpreted as differences in the binding energetics among the three systems.

For TYN336, a pK_a shift of ~3.5 log units was computed relative to (free) TYN in solution. Such a magnitude of a pK_a shift is within the range of pK_a shifts reported before for titratable amino acids by experiments and computations[35-37]. The uncertainty in our free energy computation is in fair agreement with those reported in related studies[38]. Together with the above structural and energetic analyses of ATP binding to GS_{TYD} or GS_{TYN} *versus* wild type GS, the pK_a computations led to the prediction that nitrated GS is less active at physiological pH, where GS_{TYD} prevails, whereas increased activity is expected at acidic pH, where GS_{TYN} is favored.

These findings are supported by our *in vitro* experiments showing a reduced catalytic activity of nitrated GS at pH 7 and pH 6, but not at pH 4 (**Figure 5C**). Importantly, within this pH-range, 3'-nitrotyrosine was reported to be chemically stable[39], thereby ruling out that a chemical denitration accounts for the recovery of the catalytic activity. The data of the present study also corroborate previous findings showing that nitration of rat, sheep, or human GS inhibits their catalytic activity at physiological pH[20-21, 40-41]. Notably, in line with the computational predictions that ATP binding to GS_{TYN} is more favorable (**Figure 3A, 4A**), GS activity is significantly higher in samples exposed to 200 µM as compared to 100 µM $ONOO^-$ at pH 4.0. A plausible explanation for the increased stacking interactions between TYN336 and ATP is that the electron withdrawing effect of the nitro group may reduce repulsive forces between the phenyl ring and the electron-rich purine ring system of ATP[42]. A similar effect has been reported for aldose reductase inhibitors bearing an *m*-nitrophenyl group[43]. By contrast, the additional negative charge on TYD336 increases the electron density in the phenolate ring, which may increase repulsive forces with the electron-rich purine ring system of ATP and, hence, lead to weakened stacking interactions.

Modifications other than Y336 nitration[20, 22] may account for the loss of activity of human GS subjected to nitrative stress. One such modification is the formation of a di-tyrosine linkage between Y185 and Y269 leading to the generation of high molecular GS aggregates [44]. However, we did not detect high molecular aggregates even after treatment of native GS with 200 µM $ONOO^-$

(**Figure 6B**). Mapping of Y185 and Y269 onto the crystal structure of human GS[2] reveals that neither residue makes a direct interaction with a GS substrate; rather, they are located on the protein surface (**Figure S8**). Hence, a direct influence of Y185 or Y269 nitration on the catalytic mechanism appears unlikely.

Recently, the molecular consequences of PTN on human manganese superoxide dismutase (MnSOD) were investigated by steered MD simulations[45]. Y34 nitration inhibits MnSOD[46] by hampering the passage of the superoxide radical anion in the channel leading to the active center[45]. The authors found a high energetic barrier on the way to the active site for both 3'-nitrotyrosine variants[45] that they attributed to steric effects[47]. By contrast, our computations indicate that Y336 nitration in GS impacts the *affinity* of the modified enzyme for ATP, rather than the binding *kinetics*, and it does so with opposite effects depending on the TYD336 or TYN336 state of the tyrosyl residue. This comparison thus suggests that the underlying effect of tyrosine nitration on enzyme activity depends on the type of substrate and/or topology of the binding site. As to the latter, while MnSOD's binding site resembles a binding channel that can be blocked by insertion of a single nitro group[19, 45], the GS binding site is bifunnel-shaped[17] with Y336 located at the top of the funnel (**Figure S8**). Thus, ATP, in particular the negatively-charged phosphate groups, might have enough room to escape the direct influence of nitrated Y336 during the binding process.

So far, tyrosine nitration is thought to have one of three effects on protein function: loss of function, gain of function, or no change on protein function (for a comprehensive review, see ref.[48]). As to the latter, only two proteins have been reported to date (antichymotrypsin and transferrin)[48-49]. Cytochrome c is a well-studied example for a gain of function, in which nitration triggers structural rearrangements yielding a protein conformation with increased catalytic activity[48, 50-51]. Proteins that show a loss of function after tyrosine nitration form the largest group[48] and, so far, human GS is considered part of this group as well[20-21, 40-41]. However, here we provide the first evidence that indicates that the inhibitory effect of Y336 nitration is fully reversible depending on the pH of the protein environment (**Figure 3A, 4A, 5C**). To our knowledge, these results indicate a novel mechanism for the regulation of protein function by PTN.

Pathological ammonia concentrations trigger oxidation processes, including the nitration of tyrosine, in the rat and human brain, respectively[7, 20-21]. GS nitration and the related deficiency in GS function are associated with a broad range of neurological diseases[16, 52-53], including

Alzheimer's disease[54-55]. It has been hypothesized that human GS is sensitive to age-related oxidation[55]. The lack of GS activity due to nitration progressively leads to incomplete ammonia detoxification, which in turn promotes a vicious circle, where increases in ammonia[7, 20-21] foster further oxidation and/or nitration of GS. Furthermore, the hyperammonemic conditions may lead to pH increases that may further reduce GS activity.

Taken together, we found that Y336 nitration weakens interactions between human GS and the substrate ATP, but only in the in its negatively-charged TYD336 state. Furthermore, our computations suggest that only TYD336 is relevant under physiological conditions. By contrast, for the protonated and neutral TYN336 state, an increased binding affinity for ATP is predicted and supported by a significantly higher GS activity in samples exposed to 200 µM $ONOO^-$. These results indicate a novel, fully reversible, pH-sensitive mechanism for the regulation of protein function by tyrosine nitration. We speculate that such a mechanism may keep enzymes in an inactive state in the cytosol, but trigger their activation after translocation into an acidic compartment, such as lysosomes. Since the pK_a values of 3'-nitrotyrosine vary markedly, depending on their location within proteins, the effect of pH on the impact of tyrosine nitration on protein function will have to be considered in evaluating existing and future studies of this modification[48].

Methods

Please see the **Supporting Information** for a detailed description.

Unbiased molecular dynamics simulations

We performed unbiased MD simulations of wild type GS, GS_{TYN}, and GS_{TYD} bound to ATP with water represented explicitly. The general simulation protocol was adapted from ref.[18]. After energy minimization, thermalization, and density adaptation, the systems were subjected to 5 × 500 ns of unbiased MD simulations. The MD trajectories were analyzed towards structural features that characterize stacking interactions between ATP and residue Y336/YTN226/TYD336. All simulations were performed using GPU acceleration with the *pmemd.cuda* module implemented in Amber[56].

Computation of effective binding energies

Subsequent to the MD simulations, we computed effective binding energies. The effective binding energies ($\Delta G_{effective}$) were averaged over five trajectories ($\overline{\Delta G}_{effective}$). Relative effective binding energies ($\Delta\Delta G_{effective}$) were calculated by subtracting the mean $\Delta G_{effective}$ of the wild type ($\overline{\Delta G}_{wild\ type}$) from the effective binding energy of the nitro variant ($\overline{\Delta G}_{nitro}$) (eq. 1 in **Supporting Information**). The results are expressed as $\Delta\Delta G_{effective} \pm SEM_{total}$ (eq. 2, 3 in **Supporting Information**).

Potential of mean force calculations

We performed PMF (configurational free energy) calculations of ATP unbinding from its binding site within wild type GS, GS_{TYN}, and GS_{TYD}. We computed the PMF of ATP unbinding employing umbrella sampling[29] and the Weighted Histogram Analysis Method (WHAM)[30]. As a reaction coordinate r, we used the distance between the centers of mass of Y336/TYN336/TYD336's benzene ring and ATP's purine ring. The resulting PMFs were normalized relative to the completely unbound state.

Calculating pK_a shifts from free energies

To calculate the pK_a shift of TYN336 due to the protein environment, we applied the method reported by Simonson *et al.*[57]. We used TI to calculate ΔG for the transformation of TYN into TYD in our model and TYN336 into TYD336 in the protein structure. The transformation simulations were performed at λ = 0.1, 0.3, …, 0.9 for 60 ns per λ-step.

Expression and purification of human GS

A plasmid expressing human GS was donated to us by Dr. Norma Allewell and used to transform *E. coli* and to express the enzyme in these cells, as described by Listrom *et al.*[58]. The subsequent of human GS was adapted from the methods published by Listrom *et al.*[58].

In brief, clarified sonicates of *E. coli* suspensions expressing human GS underwent successive purification on HA Ultrogel®, DEAE–Sepharose, and MonoQ resins, using linear: 100 to 500 mM potassium phosphate buffer (pH 7.2), step: imidazole-NaOH at pH 7.99, and linear: 0 to 250 mM NaCl in 20 mM Tris-HCl, respectively. The potassium phosphate buffer also contained 5 mM 2-mercaptoethanol. Similarly, the imidazole-NaOH buffers also contained 1 mM EDTA and 5 mM 2-mercaptoethanol. The first two separations were performed at room temperature, while the final chromatography was carried out at 4°C and yielded a protein that was > 99% pure as judged by SDS-PAGE. The purified human GS was combined with glycerol at a final concentration of 10% and stored at 4°C. GS activity during the purification was assessed using hydroxamate assay, as described by Jeitner and Cooper[59].

Peroxynitrite treatment of human GS

Purified human GS was incubated in 0.1 M KH_2PO_4 (pH 7.0) and nitrated by addition of peroxynitrite ($ONOO^-$, in 0.1 M KOH) under constant stirring as described before[21].

Western blot analysis

Western blot analysis was performed as described before[21]. Briefly, equal amounts of isolated human GS were subjected to sodium dodecyl sulfate polyacrylamid gel electrophoresis (SDS-PAGE) using 10% gels. Blots were probed for 2 h at room temperature with antibodies against 3´-nitrotyrosine (mAb, Upstate) or GS (mAb, Becton Dickinson, 1:5,000).

GS activity assay

Human GS activity was measured according to ref.[60] by using a commercial kit (SPGLUT11, Sigma, Deisenhofen, Germany). In this assay, the conversion of ATP to ADP by GS is coupled to the oxidation of NADH to NAD^+ by L-lactic dehydrogenase. GS activity in $ONOO^-$-exposed samples is expressed relative to vehicle-treated control at pH 7.0.

Acknowledgment

B.F. and H.G. are grateful to the Jülich Supercomputing Centre at the Forschungszentrum Jülich for computing time on the supercomputer JURECA and JUWELS (NIC project IDs: HDD13, HKF7) and to the "Zentrum für Informations- und Medientechnologie" (ZIM) at the Heinrich Heine University Düsseldorf for providing computational support. Financial support by Deutsche Forschungsgemeinschaft (DFG) for funds (INST 208/704-1 FUGG) to purchase the hybrid computer cluster used in this study is gratefully acknowledged by H.G. This work was supported by the Deutsche Forschungsgemeinschaft through the Collaborative Research Center SFB 974 ("Communication and Systems Relevance during Liver Damage and Regeneration", Düsseldorf).

Competing interests

The authors declare no competing interests.

Author contributions

Conceived and designed the experiments: BG DH HG. Performed the experiments: BF BG NQ NH TJ. Analyzed the data: BF BG NH DH HG. Wrote the paper: BF BG TJ NH DH HG.

References

1. Meister, A., Glutamine synthetase from mammalian tissues. *Methods Enzymol* **1985,** *113*, 185-199.
2. Krajewski, W. W.; Collins, R.; Holmberg-Schiavone, L.; Jones, T. A.; Karlberg, T.; Mowbray, S. L., Crystal structures of mammalian glutamine synthetases illustrate substrate-induced conformational changes and provide opportunities for drug and herbicide design. *J. Mol. Biol.* **2008,** *375* (1), 217-28.
3. Martinez-Hernandez, A.; Bell, K. P.; Norenberg, M. D., Glutamine synthetase: glial localization in brain. *Science* **1977,** *195* (4284), 1356-8.
4. Petroff, O. A. C.; Errante, L. D.; Rothman, D. L.; Kim, J. H.; Spencer, D. D., Glutamate-glutamine cycling in the epileptic human hippocampus. *Epilepsia* **2002,** *43* (7), 703-710.
5. Häussinger, D., Hepatocyte heterogeneity in glutamine and ammonia metabolism and the role of an intercellular glutamine cycle during ureogenesis in perfused-rat-liver. *Eur. J. Biochem.* **1983,** *133* (2), 269-275.
6. Häussinger, D.; Sies, H.; Gerok, W., Functional hepatocyte heterogeneity in ammonia metabolism - the intercellular glutamine cycle. *J. Hepatol.* **1985,** *1* (1), 3-14.
7. Qvartskhava, N.; Lang, P. A.; Görg, B.; Pozdeev, V. I.; Ortiz, M. P.; Lang, K. S.; Bidmon, H. J.; Lang, E.; Leibrock, C. B.; Herebian, D.; Bode, J. G.; Lang, F.; Häussinger, D., Hyperammonemia in gene-targeted mice lacking functional hepatic glutamine synthetase. *Proc. Natl. Acad. Sci. U. S. A.* **2015,** *112* (17), 5521-5526.
8. Häussinger, D., Nitrogen metabolism in liver: structural and functional organization and physiological relevance. *Biochem. J.* **1990,** *267* (2), 281-90.
9. Häussinger, D., Hepatic glutamine transport and metabolism. *Adv. Enzymol. Relat. Areas. Mol. Biol.* **1998,** *72*, 43-86.
10. Gunnersen, D.; Haley, B., Detection of glutamine synthetase in the cerebrospinal-fluid of Alzheimer diseased patients - a potential diagnostic biochemical marker. *Proc. Natl. Acad. Sci. U. S. A.* **1992,** *89* (24), 11949-11953.
11. Tumani, H.; Shen, G.; Peter, J. B.; Bruck, W., Glutamine synthetase in cerebrospinal fluid, serum, and brain: a diagnostic marker for Alzheimer disease? *Arch. Neurol.* **1999,** *56* (10), 1241-6.
12. Brusilow, S. W.; Koehler, R. C.; Traystman, R. J.; Cooper, A. J. L., Astrocyte glutamine synthetase: importance in hyperammonemic syndromes and potential target for therapy. *Neurotherapeutics* **2010,** *7* (4), 452-470.
13. Häussinger, D.; Laubenberger, J.; Dahl, S. V.; Ernst, T.; Bayer, S.; Langer, M.; Gerok, W.; Hennig, J., Proton magnetic-resonance spectroscopy studies on human brain myo-Iinositol in hypo-osmolarity and hepatic-encephalopathy. *Gastroenterology* **1994,** *107* (5), 1475-1480.
14. Häussinger, D.; Kircheis, G.; Fischer, R.; Schliess, F.; vom Dahl, S., Hepatic encephalopathy in chronic liver disease: a clinical manifestation of astrocyte swelling and low-grade cerebral edema? *J. Hepatol.* **2000,** *32* (6), 1035-1038.
15. Eid, T.; Behar, K.; Dhaher, R.; Bumanglag, A. V.; Lee, T. S. W., Roles of glutamine synthetase inhibition in epilepsy. *Neurochem. Res.* **2012,** *37* (11), 2339-2350.
16. Eid, T.; Thomas, M. J.; Spencer, D. D.; Runden-Pran, E.; Lai, J. C. K.; Malthankar, G. V.; Kim, J. H.; Danbolt, N. C.; Ottersen, O. P.; de Lanerolle, N. C., Loss of glutamine synthetase in the human epileptogenic hippocampus: possible mechanism for raised extracellular glutamate in mesial temporal lobe epilepsy. *Lancet* **2004,** *363* (9402), 28-37.
17. Eisenberg, D.; Gill, H. S.; Pfluegl, G. M.; Rotstein, S. H., Structure-function relationships of glutamine synthetases. *Biochim. Biophys. Acta.* **2000,** *1477* (1-2), 122-45.
18. Frieg, B.; Görg, B.; Homeyer, N.; Keitel, V.; Häussinger, D.; Gohlke, H., Molecular mechanisms of glutamine synthetase mutations that lead to clinically relevant pathologies. *PLoS Comput. Biol.* **2016,** *12* (2), e1004693.
19. Radi, R., Protein tyrosine nitration: biochemical mechanisms and structural basis of functional effects. *Acc. Chem. Res.* **2013,** *46* (2), 550-559.
20. Görg, B.; Wettstein, M.; Metzger, S.; Schliess, F.; Häussinger, D., Lipopolysaccharide-induced tyrosine nitration and inactivation of hepatic glutamine synthetase in the rat. *Hepatology* **2005,** *41* (5), 1065-1073.
21. Görg, B.; Qvartskhava, N.; Voss, P.; Grune, T.; Häussinger, D.; Schliess, F., Reversible inhibition of mammalian glutamine synthetase by tyrosine nitration. *FEBS Lett.* **2007,** *581* (1), 84-90.
22. Görg, B.; Wettstein, M.; Metzger, S.; Schliess, F.; Häussinger, D., LPS-induced tyrosine nitration of hepatic glutamine synthetase. *Hepatology* **2005,** *42* (2), 499-499.
23. Görg, B.; Bidmon, H. J.; Keitel, V.; Foster, N.; Goerlich, R.; Schliess, F.; Häussinger, D., Inflammatory cytokines induce protein tyrosine nitration in rat astrocytes. *Arch. Biochem. Biophys.* **2006,** *449* (1-2), 104-114.
24. Görg, B.; Foster, N.; Reinehr, R.; Bidmon, H. J.; Hongen, A.; Häussinger, D.; Schliess, F., Benzodiazepine-induced protein tyrosine nitration in rat astrocytes. *Hepatology* **2003,** *37* (2), 334-342.
25. Radi, R., Nitric oxide, oxidants, and protein tyrosine nitration. *Proc. Natl. Acad. Sci. U. S. A.* **2004,** *101* (12), 4003-8.

26. Souza, J. M.; Peluffo, G.; Radi, R., Protein tyrosine nitration - functional alteration or just a biomarker? *Free Radic. Biol. Med.* **2008,** *45* (4), 357-366.
27. Copeland, K. L.; Pellock, S. J.; Cox, J. R.; Cafiero, M. L.; Tschumper, G. S., Examination of Tyrosine/Adenine Stacking Interactions in Protein Complexes. *J. Phys. Chem. B* **2013,** *117* (45), 14001-14008.
28. Ludemann, S. K.; Lounnas, V.; Wade, R. C., How do substrates enter and products exit the buried active site of cytochrome P450cam? 1. Random expulsion molecular dynamics investigation of ligand access channels and mechanisms. *J. Mol. Biol.* **2000,** *303* (5), 797-811.
29. Kottalam, J.; Case, D. A., Dynamics of ligand escape from the heme pocket of myoglobin. *J. Am. Chem. Soc.* **1988,** *110* (23), 7690-7697.
30. Kumar, S.; Bouzida, D.; Swendsen, R. H.; Kollman, P. A.; Rosenberg, J. M., The weighted histogram analysis method for free-energy calculations on biomolecules. 1. The method. *J. Comput. Chem.* **1992,** *13* (8), 1011-1021.
31. Li, H.; Robertson, A. D.; Jensen, J. H., Very fast empirical prediction and rationalization of protein pKa values. *Proteins: Struct., Funct., Bioinf.* **2005,** *61* (4), 704-21.
32. Homeyer, N.; Stoll, F.; Hillisch, A.; Gohlke, H., Binding free energy calculations for lead optimization: Assessment of their accuracy in an industrial drug design context. *J. Chem. Theory Comput.* **2014,** *10*, 3331–3344.
33. Steinbrecher, T.; Case, D. A.; Labahn, A., A multistep approach to structure-based drug design: studying ligand binding at the human neutrophil elastase. *J. Med. Chem.* **2006,** *49* (6), 1837-1844.
34. Doudou, S.; Burton, N. A.; Henchman, R. H., Standard free energy of binding from a one-dimensional potential of mean force. *J. Chem. Theory Comput.* **2009,** *5* (4), 909-918.
35. Onufriev, A. V.; Alexov, E., Protonation and pK changes in protein-ligand binding. *Q. Rev. Biophys.* **2013,** *46* (2), 181-209.
36. Ranganathan, A.; Dror, R. O.; Carlsson, J., Insights into the role of Asp79(2.50) in beta(2) adrenergic receptor activation from molecular dynamics simulations. *Biochemistry* **2014,** *53* (46), 7283-7296.
37. Stanton, C. L.; Houk, K. N., Benchmarking pKa prediction methods for residues in proteins. *J. Chem. Theory Comput.* **2008,** *4* (6), 951-66.
38. Giese, T. J.; York, D. M., A GPU-accelerated parameter interpolation thermodynamic integration free energy method. *J. Chem. Theory Comput.* **2018,** *14* (3), 1564-1582.
39. Liu, M. C.; Yasuda, S.; Idell, S., Sulfation of nitrotyrosine: Biochemistry and functional implications. *IUBMB Life* **2007,** *59* (10), 622-627.
40. Görg, B.; Qvartskhava, N.; Bidmon, H. J.; Palomero-Gallagher, N.; Kircheis, G.; Zilles, K.; Häussinger, D., Oxidative stress markers in the brain of patients with cirrhosis and hepatic encephalopathy. *Hepatology* **2010,** *52* (1), 256-265.
41. Schliess, F.; Görg, B.; Fischer, R.; Desjardins, P.; Bidmon, H. J.; Herrmann, A.; Butterworth, R. F.; Zilles, K.; Häussinger, D., Ammonia induces MK-801-sensitive nitration and phosphorylation of protein tyrosine residues in rat astrocytes. *FASEB J.* **2002,** *16* (3), 739-741.
42. Martinez, C. R.; Iverson, B. L., Rethinking the term "pi-stacking". *Chem. Sci.* **2012,** *3* (7), 2191-2201.
43. Steuber, H.; Heine, A.; Klebe, G., Structural and thermodynamic study on aldose reductase: Nitro-substituted inhibitors with strong enthalpic binding contribution. *J. Mol. Biol.* **2007,** *368* (3), 618-638.
44. Bartesaghi, S.; Campolo, N.; Issoglio, F.; Zeida, A.; Grune, T.; Estrín, D.; Radi, R., Oxidative inactivation of human glutamine synthetase: biochemical and computational studies. *Free Radic. Biol. Med.* **2016,** *100*, S19.
45. Moreno, D. M.; Marti, M. A.; De Biase, P. M.; Estrin, D. A.; Demicheli, V.; Radi, R.; Boechi, L., Exploring the molecular basis of human manganese superoxide dismutase inactivation mediated by tyrosine 34 nitration. *Arch. Biochem. Biophys.* **2011,** *507* (2), 304-9.
46. Yamakura, F.; Taka, H.; Fujimura, T.; Murayama, K., Inactivation of human manganese-superoxide dismutase by peroxynitrite is caused by exclusive nitration of tyrosine 34 to 3-nitrotyrosine. *J. Biol. Chem.* **1998,** *273* (23), 14085-14089.
47. Quint, P.; Reutzel, R.; Mikulski, R.; McKenna, R.; Silverman, D. N., Crystal structure of nitrated human manganese superoxide dismutase: Mechanism of inactivation. *Free Radic. Biol. Med.* **2006,** *40* (3), 453-458.
48. Ferrer-Sueta, G.; Campolo, N.; Trujillo, M.; Bartesaghi, S.; Carballa, S.; Romero, N.; Alvarez, B.; Radi, R., Biochemistry of peroxynitrite and protein tyrosine nitration. *Chem. Rev.* **2018,** *118* (3), 462-1408.
49. Gole, M. D.; Souza, J. M.; Choi, I.; Hertkorn, C.; Malcolm, S.; Foust, R. F.; Finkel, B.; Lanken, P. N.; Ischiropoulos, H., Plasma proteins modified by tyrosine nitration in acute respiratory distress syndrome. *Am. J. Physiol. Lung Cell. Mol. Physiol.* **2000,** *278* (5), L961-L967.
50. Batthyany, C.; Souza, J. M.; Duran, R.; Cassina, A.; Cervenansky, C.; Radi, R., Time course and site(s) of cytochrome c tyrosine nitration by peroxynitrite. *Biochemistry* **2005,** *44* (22), 8038-8046.

51. Cassina, A. M.; Hodara, R.; Souza, J. M.; Thomson, L.; Castro, L.; Ischiropoulos, H.; Freeman, B. A.; Radi, R., Cytochrome c nitration by peroxynitrite. *J. Biol. Chem.* **2000,** *275* (28), 21409-21415.
52. Spodenkiewicz, M.; Diez-Fernandez, C.; Rufenacht, V.; Gemperle-Britschgi, C.; Häberle, J., Minireview on glutamine synthetase deficiency, an ultra-rare inborn error of amino acid biosynthesis. *Biology (Basel)* **2016,** *5* (4).
53. Leprince, G.; Delaere, P.; Fages, C.; Lefrancois, T.; Touret, M.; Salanon, M.; Tardy, M., Glutamine synthetase (GS) expression is reduced in senile dementia of the Alzheimer-type. *Neurochem. Res.* **1995,** *20* (7), 859-862.
54. Robinson, S. R., Neuronal expression of glutamine synthetase in Alzheimer's disease indicates a profound impairment of metabolic interactions with astrocytes. *Neurochem. Int.* **2000,** *36* (4-5), 471-482.
55. Smith, C. D.; Carney, J. M.; Starkereed, P. E.; Oliver, C. N.; Stadtman, E. R.; Floyd, R. A.; Markesbery, W. R., Excess brain protein oxidation and enzyme dysfunction in normal aging and in Alzheimer disease. *Proc. Natl. Acad. Sci. U. S. A.* **1991,** *88* (23), 10540-10543.
56. Salomon-Ferrer, R.; Götz, A. W.; Poole, D.; Le Grand, S.; Walker, R. C., Routine microsecond molecular dynamics simulations with Amber on GPUs. 2. Explicit solvent particle mesh Ewald. *J. Chem. Theory Comput.* **2013,** *9* (9), 3878-3888.
57. Simonson, T.; Carlsson, J.; Case, D. A., Proton binding to proteins: pK(a) calculations with explicit and implicit solvent models. *J. Am. Chem. Soc.* **2004,** *126* (13), 4167-4180.
58. Listrom, C. D.; Morizono, H.; Rajagopal, B. S.; McCann, M. T.; Tuchman, M.; Allewell, N. M., Expression, purification, and characterization of recombinant human glutamine synthetase. *Biochem. J.* **1997,** *328*, 159-163.
59. Jeitner, T. M.; Cooper, A. J. L., Inhibition of human glutamine synthetase by L-methionine-S, R-sulfoximine-relevance to the treatment of neurological diseases. *Metab. Brain Dis.* **2014,** *29* (4), 983-989.
60. Kingdon, H. S.; Hubbard, J. S.; Stadtman, E. R., Regulation of glutamine synthetase. XI. The nature and implications of a lag phase in the Escherichia coli glutamine synthetase reaction. *Biochemistry* **1968,** *7* (6), 2136-2142.

Figures

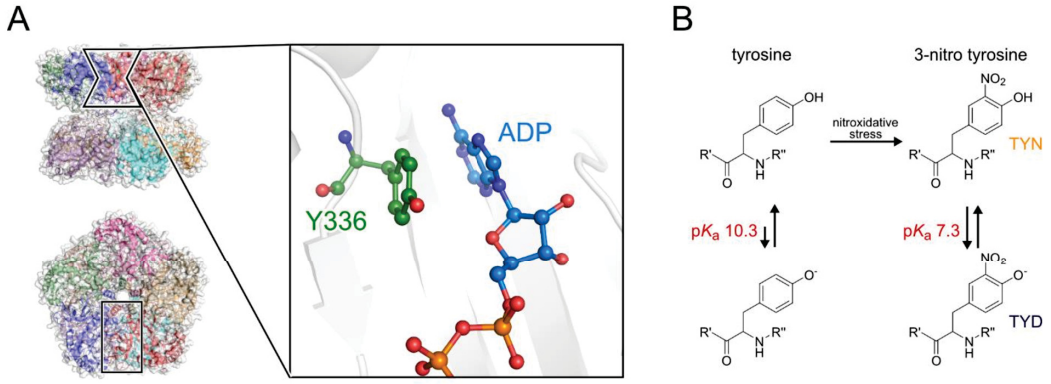

Figure 1: Nitration of Y336 in human GS.
A: Crystal structure of human GS (PDB entry: 2QC8[2]) in side (top) and top view (bottom), and close-up view of the ATP/ADP binding site (right). Each subunit is colored differently and depicted in cartoon-surface representation. Bifunnel[17] and box depict the location of the catalytic site in the GS decamer. ADP (blue) and Y336 (green) are depicted as ball-stick models. **B:** Scheme of tyrosine nitration. Nitration causes a decrease of the pK_a of the phenolic hydroxyl group by three log units[19]. At physiological pH (~7.4), both 3'-nitrotyrosine variants TYN and TYD are almost equally populated (panel B is adapted from ref.[19]). TYN and TYD refers to the nitrated amino acids in solution.

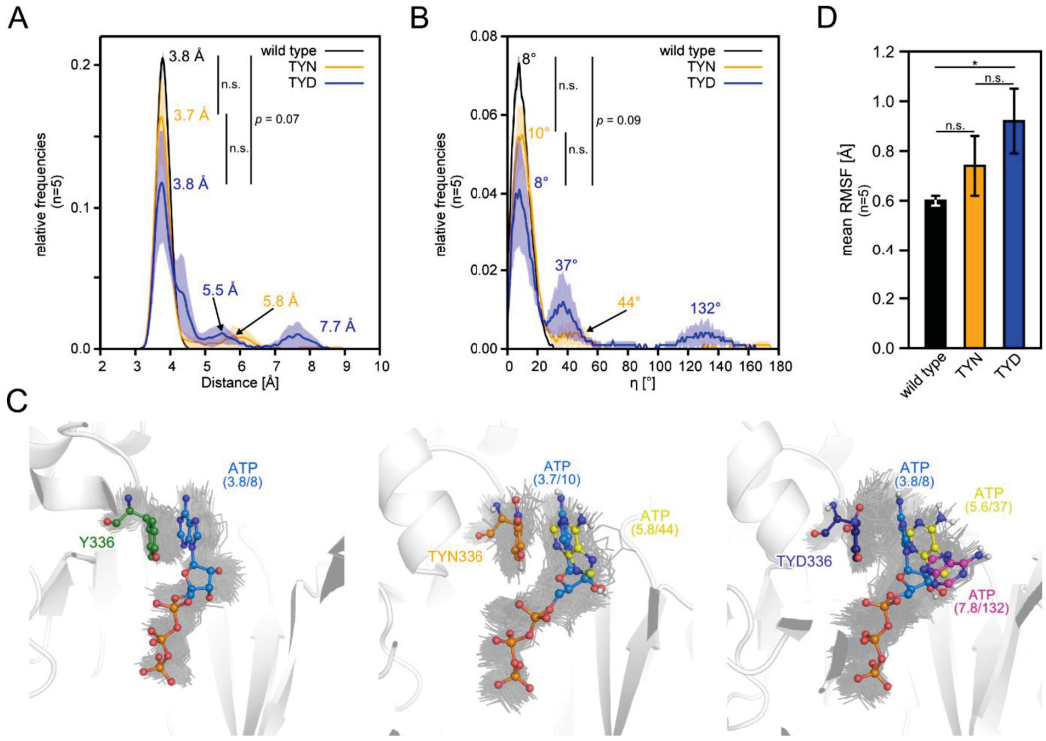

Figure 2: Results from unbiased MD simulations.
A, B: Mean fractional populations (normalized by the sum of all bins) with standard error of the mean (SEM; depicted as filled curve) for (**A**) the distance between the centers of mass of the phenyl ring (residue Y336 and nitro variants) and the purine ring system (ATP) (bin size 0.1 Å) and (**B**) the angle between the ring planes of the phenyl ring (residue Y3367YTN336/TYD336) and the purine ring system (ATP) (bin size 1°). **C:** Representative structures extracted from the MD trajectory for wild type GS (left), GS_{TYN} (middle), and GS_{TYD} (right). In the foreground, representative ATP configurations belonging to the main populations in **A** and **B** (see respective labels depicting "distance [Å]/η [°]" combinations) are depicted as opaque ball-stick model. For representative purposes, for ATP molecules that do not belong to the major population, only the adenine system is shown. In the background, an overlay of ATP configurations extracted in 10 ns intervals is depicted as gray sticks that visualizes the motion of ATP over the course of the MD simulations. **D:** Mean root mean square fluctuation (RMSF) with SEM (error bars) calculated for all non-hydrogen atoms in ATP. * Statistically significantly different compared to wild type GS ($p < 0.05$). n.s.: not significantly different.

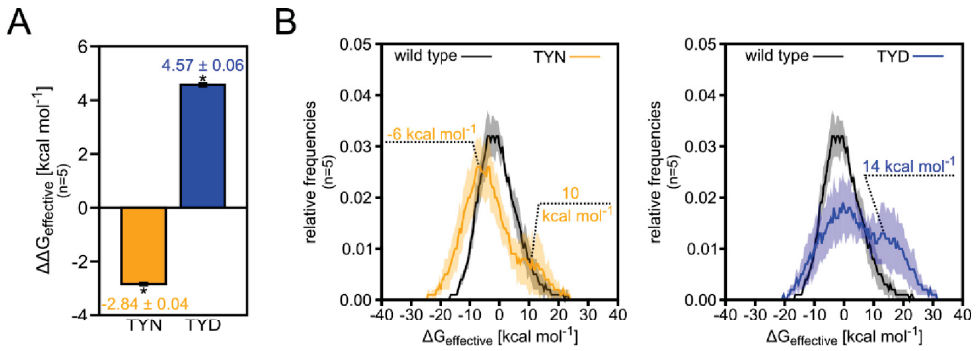

Figure 3: Results from MM-PBSA calculations.
A: Mean relative effective binding energies with respect to wild type GS ($\Delta\Delta G_{effective}$). $\Delta\Delta G$ values were calculated by the MM-PBSA approach for ATP binding to both nitro variants GS_{TYN} (orange) and GS_{TYD} (blue). Error bars indicate SEM_{total} (eq. 3); stars indicate a significant difference ($p < 0.05$) between wild type GS and GS_{TYN} or GS_{TYD}, respectively. Labels depict $\Delta\Delta G_{effective} \pm SEM_{total}$ in kcal mol^{-1}. **B:** Mean relative frequencies (normalized by the sum of all bins; bin size 0.5 kcal·mol^{-1}) of relative effective binding energies and standard error of the mean (filled curve). Effective binding energies of ATP binding to GS_{TYN} (left) or GS_{TYD} (right) were normalized to the mean effective binding energy of ATP binding to wild type GS, such that the histogram for wild type GS was shifted to zero and the GS_{TYN} and GS_{TYD} ones were shifted accordingly.

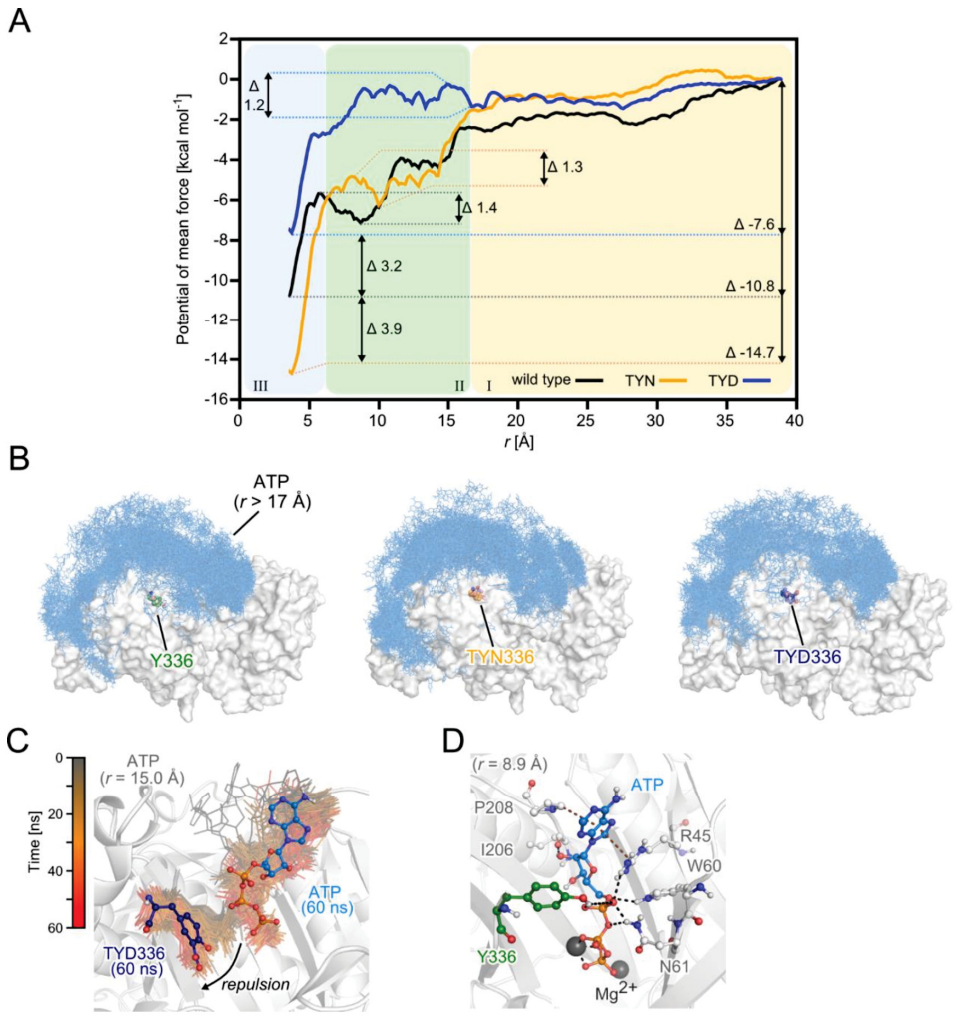

Figure 4: Energetic and structural description of the ATP binding process.
A: Potential of mean force (PMF), derived by umbrella sampling and WHAM, for ATP binding to wild type GS (black), GS_{TYN} (orange), and GS_{TYD} (blue). **I** (yellow background), **II** (green background), and **III** (cyan background) depict the phases of ATP binding. Configurational free energies are normalized relative to the unbound state (r = 38.9 Å). Labels depict relevant changes in the PMF (in kcal mol^{-1}). **B:** ATP diffusion for simulations restrained to 17 Å < r < 38.7 Å. ATP poses were extracted in 0.5 ns intervals for wild type GS (left), GS_{TYN} (middle), and GS_{TYD} (right). **C:** Time traces of ATP and TYD336 during umbrella sampling simulations (colored according the color ranges on the left) that were restrained to r = 15.0 Å. The major motion of TYD336 is depicted by an arrow. **D**: ATP temporarily bound (at r = 8.9 Å) to wild type GS. The interacting residues of wild type GS are shown as white ball-stick models. Hydrogen bonds are show as black lines, contacts with purine in ATP as brown lines. In the interest of clarity, in **B** only the protein starting structures for all variants (white surface) and purine fragments of ATP are shown. All configurations shown were extracted after superimposing the protein structure to the initial structure.

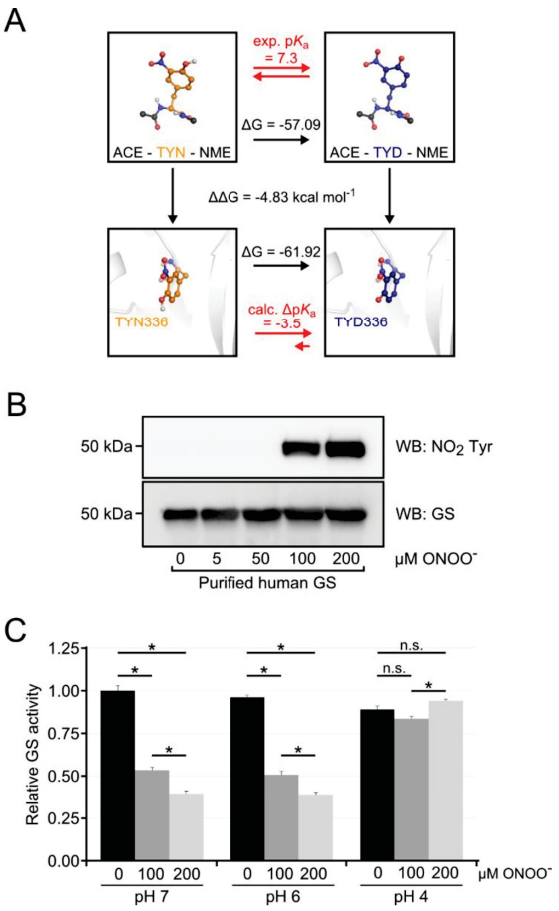

Figure 5: pH-sensitive inhibition of GS activity
A: Thermodynamic cycle employed for studying the protonation state of nitrated Y336. The free energy differences ΔG were calculated by thermodynamic integration for transformations of TYN into TYD (top panel depicts the transformation for ACE-TYN/TYD-NME, the bottom panel for TYN336/TYD336 in the GS structure). The difference in free energy $\Delta\Delta G$ was calculated according to eq. 6 and the pK_a shift (calc. ΔpK_a) according to eq. 5 (see **Supporting Information & Material** for details). The experimentally determined pK_a (exp. pK_a) was measured for free 3-nitro tyrosine[19]. At physiological pH (~7.4), the TYD state in GS is preferred over the TYN state (schematically depicted by red arrows). **B:** *In vitro* nitration of purified human GS. Purified human GS was exposed to vehicle (0 µM ONOO-, control) or different concentrations of $ONOO^-$ (5, 50, 100, or 200 µM), and 3´-nitrotyrosine (top) and non-nitrated GS (bottom) were detected by Western Blot analysis. **C:** pH dependence of $ONOO^-$-mediated inhibition of GS activity. Purified human GS was exposed to different concentrations of $ONOO^-$ (0, 100, or 200 µM), and aliquots were taken for measuring GS activity as described in (see **Supporting Information & Material** for details). GS activity in vehicle-treated control at pH 7.0 was set to 1, and activities measured under the other experimental conditions are given relative to it. *: statistically significantly different. n.s.: not statistically significantly different.

Supporting Information

Mechanism of fully-reversible, pH-sensitive inhibition of human glutamine synthetase by tyrosine nitration

Benedikt Frieg[1,2], Boris Görg[3], Natalia Qvartskhava[3], Thomas Jeitner[4], Nadine Homeyer[1], Dieter Häussinger[3*] and Holger Gohlke[1,2*]

[1] Institute for Pharmaceutical and Medicinal Chemistry, Heinrich Heine University Düsseldorf, Düsseldorf, Germany

[2] John von Neumann Institute for Computing (NIC), Jülich Supercomputing Centre (JSC), and Institute for Complex Systems - Structural Biochemistry (ICS-6), Forschungszentrum Jülich GmbH, Jülich, Germany

[3] Clinic for Gastroenterology, Hepatology, and Infectious Diseases, Heinrich Heine University Düsseldorf, Düsseldorf, Germany

[4] Department of Biochemistry and Molecular Biology, New York Medical College, Valhalla, NY, USA

[*]Corresponding authors: (H.G.) Universitätsstr. 1, 40225 Düsseldorf, Germany, Phone: (+49) 211 81 13662, Fax: (+49) 211 81 13847, E-mail: gohlke@uni-duesseldorf.de or h.gohlke@fz-juelich.de; (D.H.) Moorenstr. 5, 40225 Düsseldorf, Phone : (+49) 211 81 16330, Fax : (+49) 211 81 18752, E-mail : haeussin@uni-duesseldorf.de

Table of contents

Supporting Figures

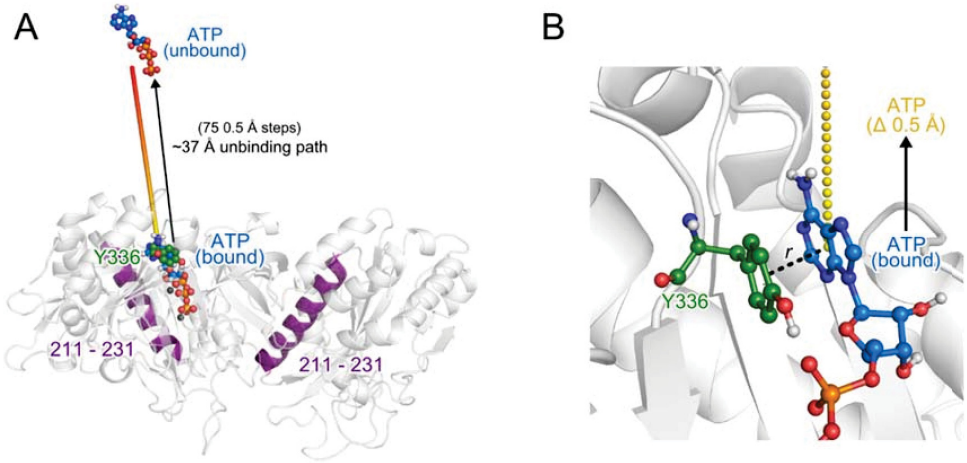

Figure S1: Setup of potential of mean force calculations.
A: GS_{ATP} dimer (white cartoon) as used for umbrella sampling. ATP (blue) was placed along a ~37 Å unbinding path determined by random acceleration molecular dynamics[1]. Each center of mass (COM) of the purine ring is depicted as spheres colored yellow-orange-red. Residues 211 – 231 (purple) of both subunits are fixed with positional restraints of 0.5 kcal mol^{-1} $Å^{-2}$ during simulations to ensure the correct relative orientation of the protein. **B**: Close-up view of the ATP binding site. ATP (blue) and Y336 (green) form stacking interactions in the bound state. For umbrella sampling, the ATP molecule was initially placed in 0.5 Å intervals (ATP, red) along the unbinding path (schematically depicted by COM spheres of the purine ring system and an arrow). The reaction coordinate *r* for umbrella sampling simulations is defined as the distance between the centers of mass of Y336's benzene ring and ATP's purine ring system.

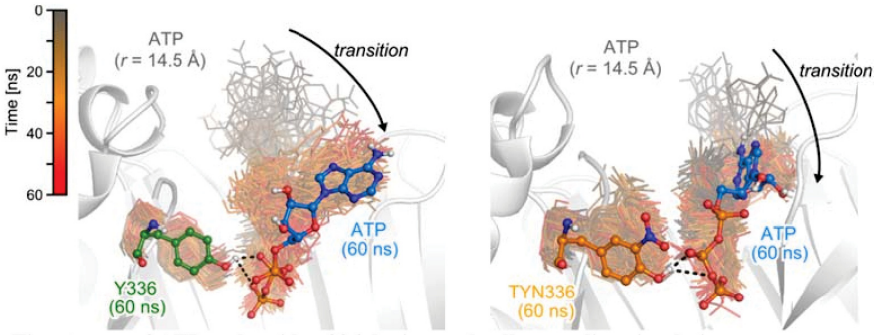

Figure S2: Time traces of ATP and residue 336 during umbrella sampling simulations.
Time traces during umbrella sampling simulations for wild type glutamine synthetase (GS) (left) and GS_{TYN} (right) that were restrained to r = 14.5 Å (colored according to the color ranges on the left). The major motion of ATP is depicted by an arrow.

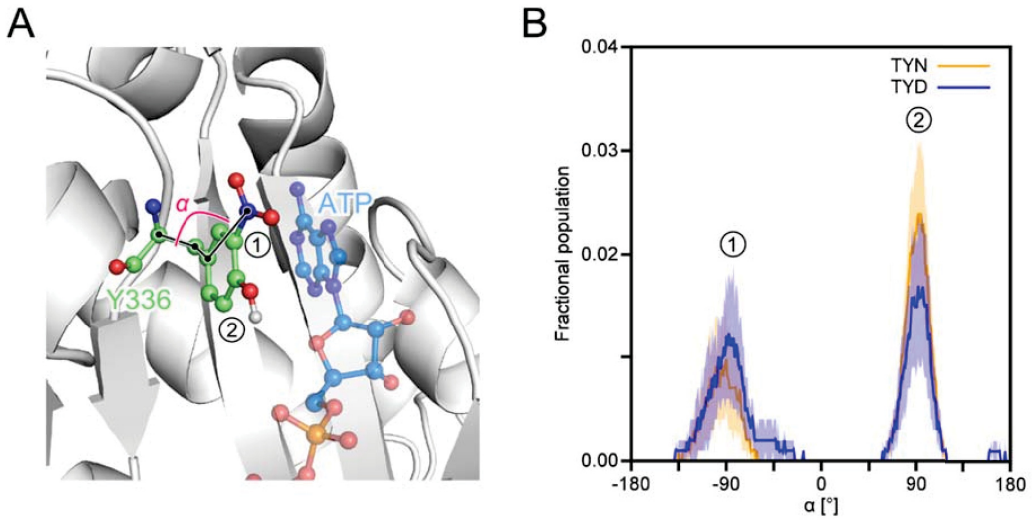

Figure S3: Conformational analyses of Y336.
A: Close-up view of nitrated Y336 (green, ball-stick model) within GS_{TYN}. ATP (blue, ball-stick model) was not present during molecular dynamics simulations in the GS_{Apo} state, but was added for visualization purposes. The dihedral α was used to measure the orientation of the nitro group within the ATP binding site; two orientations (① and ②) are primarily populated (see panel **B**). **B:** Mean fractional populations (normalized by the sum of all bins) with standard error of the mean (SEM; depicted as filled curve) of α (bin size 0.1 Å); GS_{TYN}: orange; GS_{TYD}: blue. Labels ① and ② refer to the orientations of the nitro group shown in panel A.

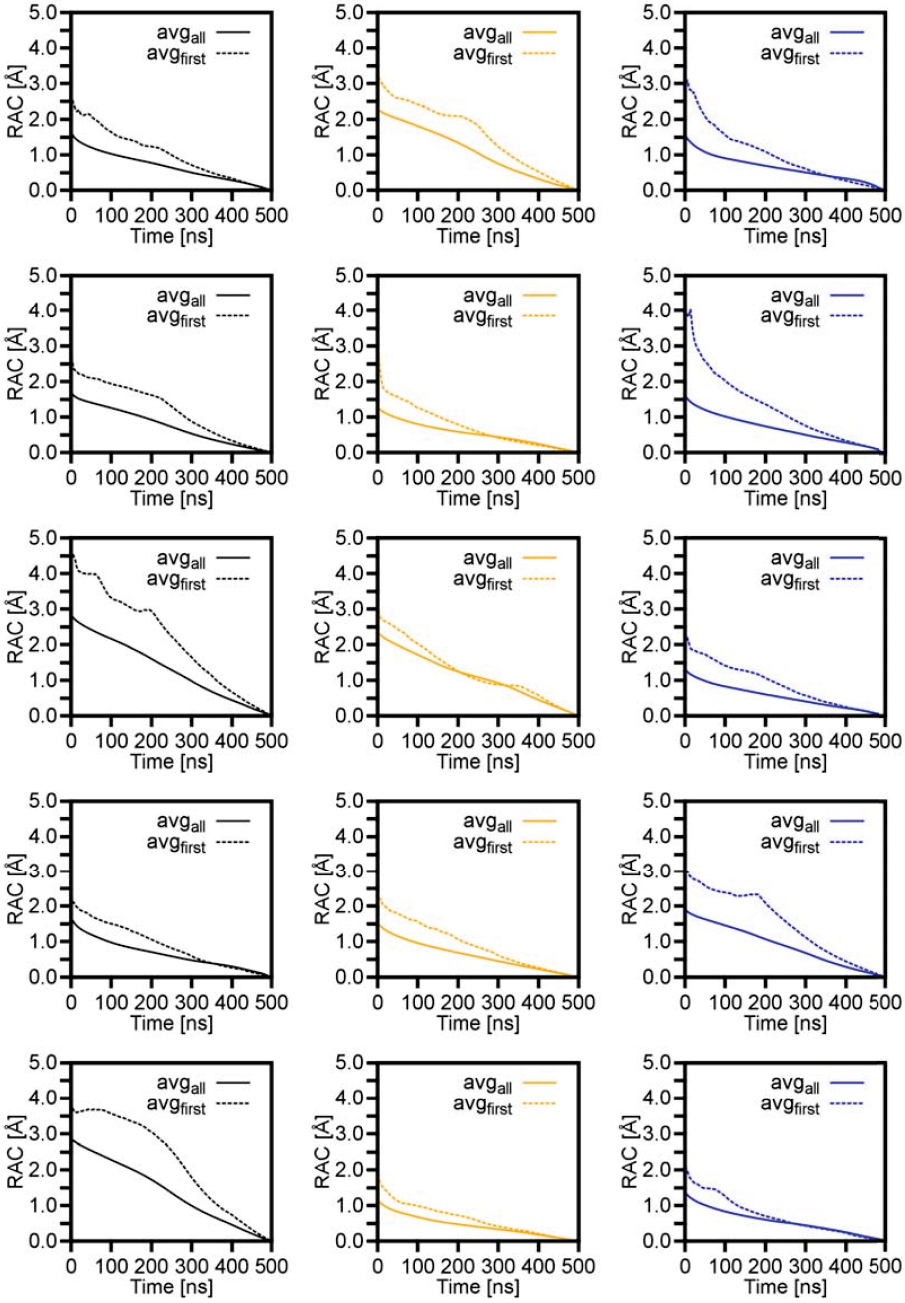

Figure S4: RMS average correlation function for all backbone atoms.
RMS average correlation (RAC) computed for all backbone atoms of the GS_{ATP} structure of wild type glutamine synthetase (GS) (black), GS_{TYN} (orange), and GS_{TYD} (blue) for five molecular dynamics trajectories each. The RMS fit was either performed to the overall average structure (solid) or the first calculated running average structure, where the averaging occurs from zero to the depicted time (dotted).

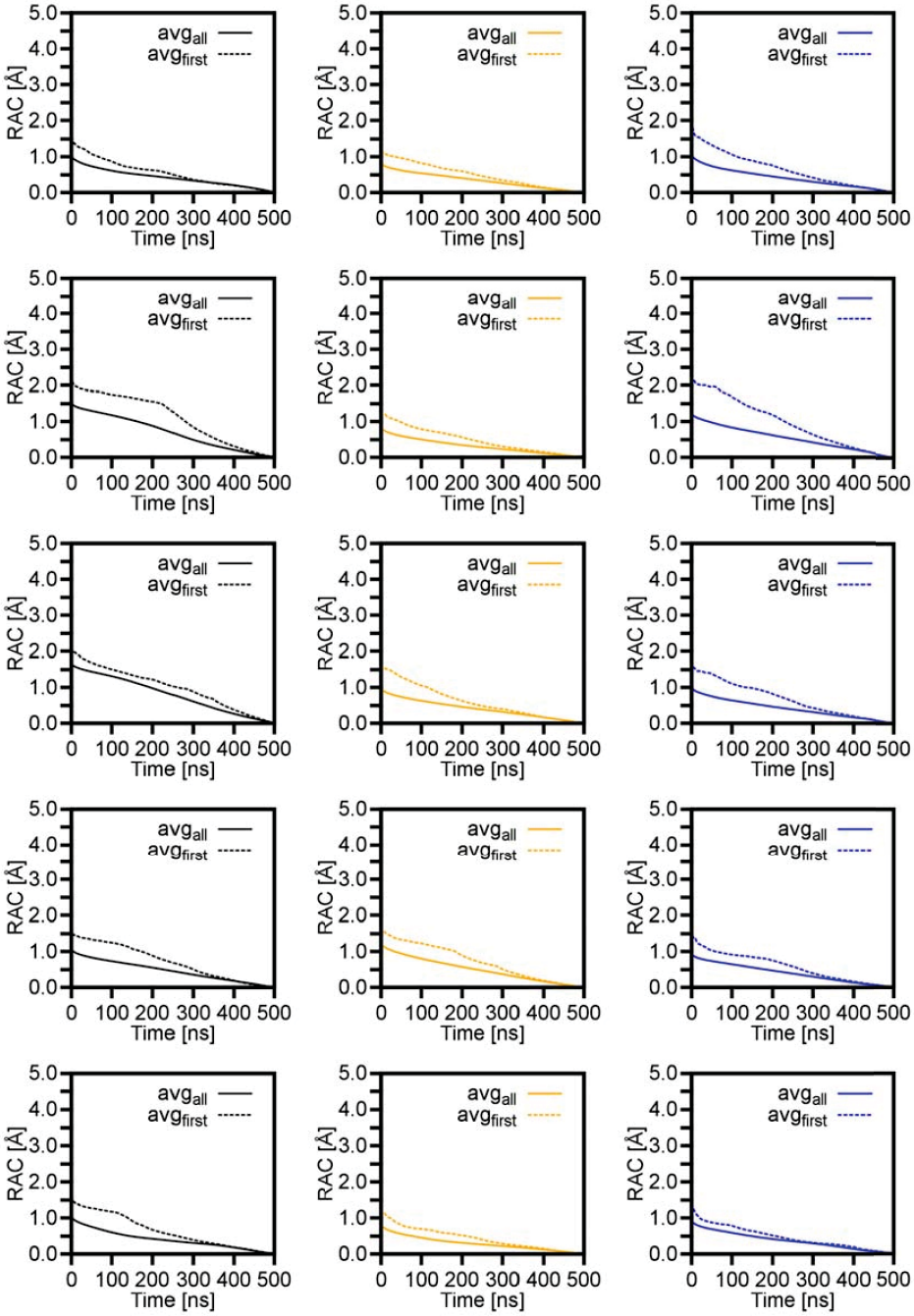

Figure S5: RMS average correlation function for GS_{core} backbone atoms.
RMS average correlation (RAC) computed for GS_{core} backbone atoms of the GS_{ATP} structure of wild type glutamine synthetase (GS) (black), GS_{TYN} (orange), and GS_{TYD} (blue) for five molecular dynamics trajectories each. The RMS fit was either performed to the overall average structure (solid) or the first calculated running average structure, where the averaging occurs from zero to the depicted time (dotted).

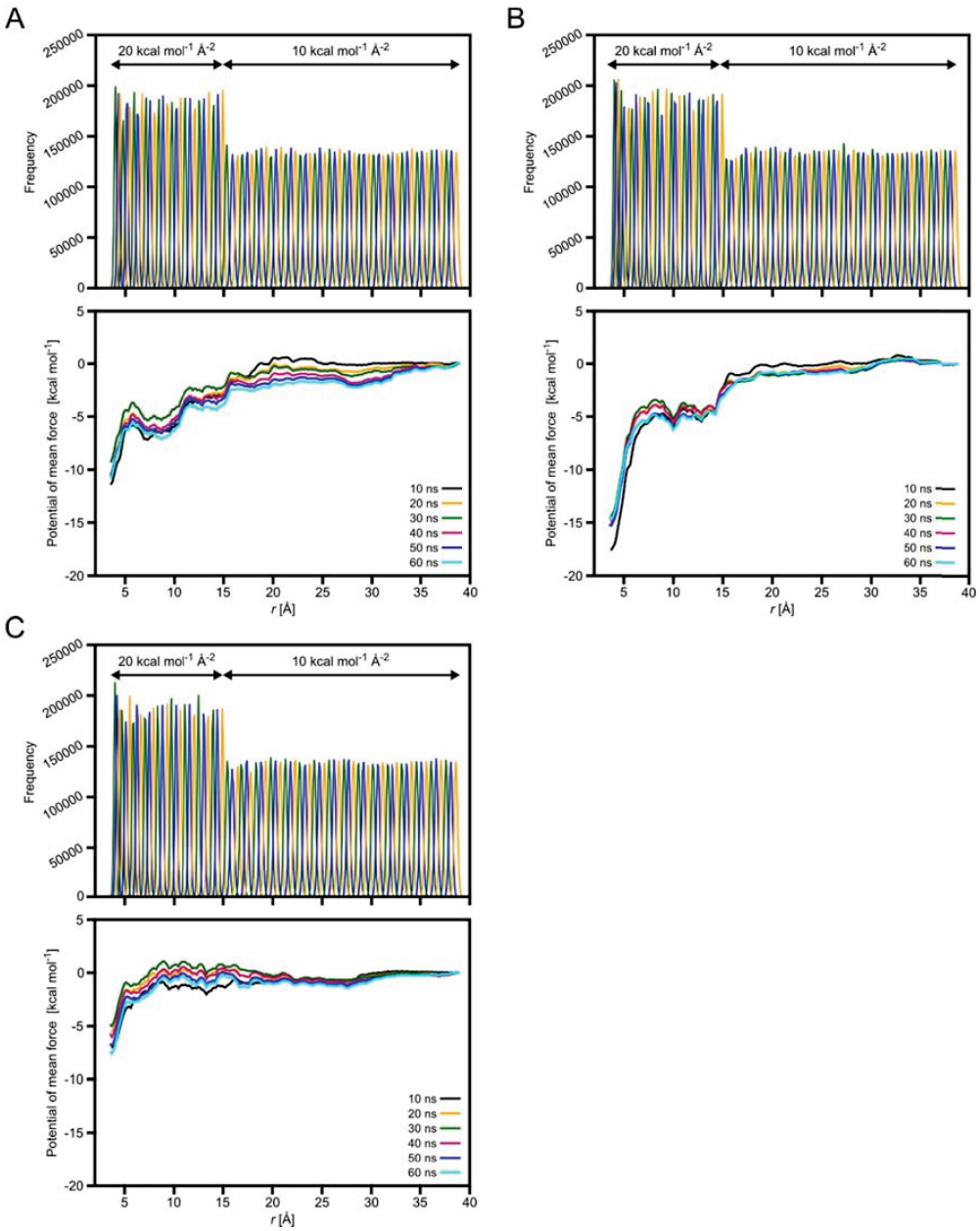

Figure S6: Umbrella sampling and potentials of mean force for ATP binding to glutamine synthetase (GS) variants.

Frequencies of sampled reaction coordinates during umbrella sampling simulations (top) and derived potentials of mean force (PMF) (bottom) for wild type glutamine synthetase (GS) (**A**), GS_{TYN} (**B**), and GS_{TYD} (**C**). The reaction coordinate is the distance between the centers of mass of the phenyl ring of Y336 (or its nitro variants) and the purine ring system of ATP and was sampled for 60 ns for each umbrella window. For the umbrella sampling, a harmonic potential with force constants of 20 kcal mol^{-1} $Å^{-2}$ for distances ≤ 15 Å and 10 kcal mol^{-1} $Å^{-2}$ for distances > 15 Å was applied (schematically depicted by arrows). The PMFs were derived for time intervals of umbrella sampling from zero to 10 ns, zero to 20 ns, and so on.

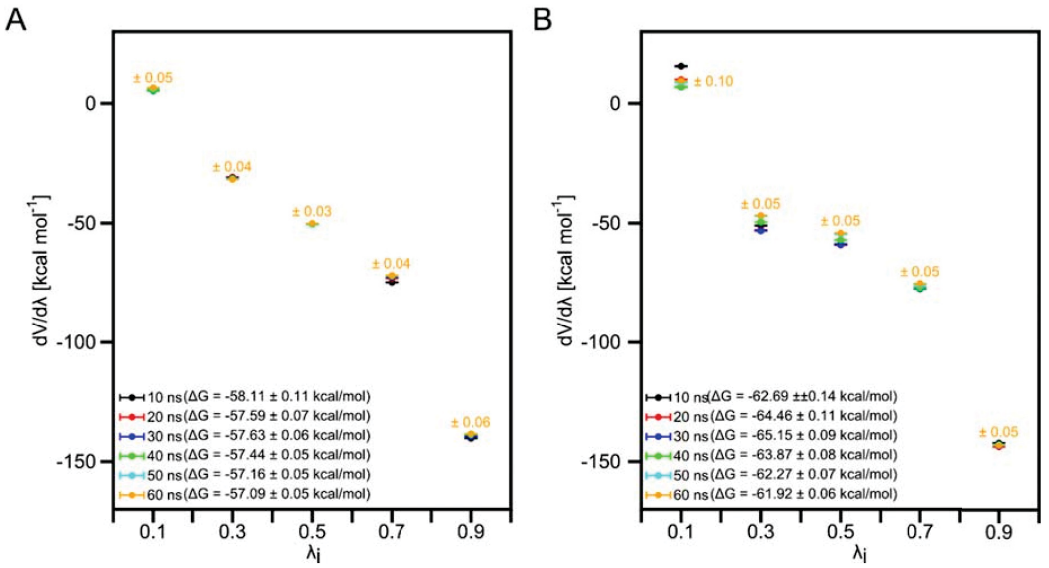

Figure S7: Results from thermodynamic integration calculations.
Average dV/dλ values after 60 ns of transformation simulations of TYN into TYD (**A**) in the model system and (**B**) embedded in glutamine synthetase (GS). Transformation simulations were performed at λ = 0.1, 0.3, …, 0.9, where λ = 0.0 corresponds to the TYN state, and λ = 1.0 to the TYD state. Error bars denote the standard error of the mean (SEM), which is always ≤ 0.1 kcal mol^{-1} after 60 ns of simulation time (orange labels). The free energies Δ*G* of the transformations were derived for time intervals of transformation simulations from zero to 10 ns, zero to 20 ns, and so on. Results are depicted in the legends and expressed as Δ*G* ± SEM.

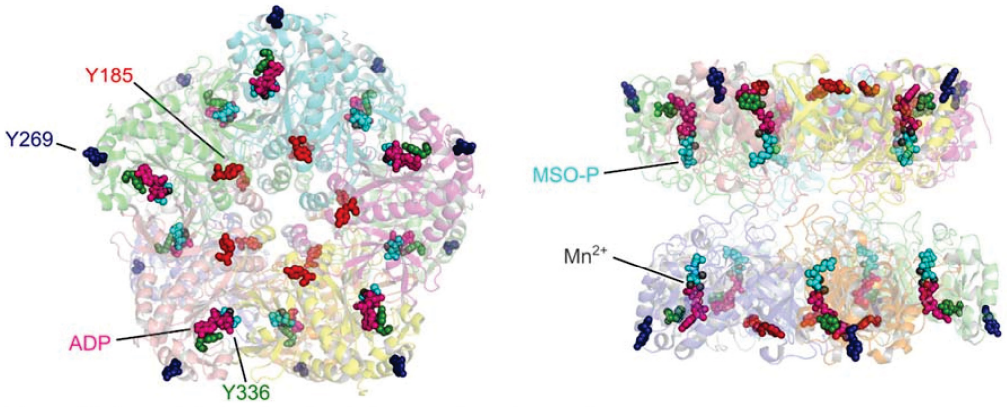

Figure S8: Potential nitration sites in human glutamine synthetase.
The X-ray structure in top view (left panel) and side view (right panel) of human glutamine synthetase (PDB-ID 2QC8[2]) shown as cartoon. The individual subunits are colored differently. The potential nitration sites Y185, Y269[3], and Y336[4,5] are shown as red, blue, and green sphere-model. Structurally bound ADP (magenta), L-methionine-*S*-sulfoximine phosphate (MSO-P, cyan), and manganese ions (Mn^{2+}, grey) are also shown as spheres and depict the location of the catalytic sites.

Supplemental Tables

Table S1. Topology and atomic partial charges for TYN

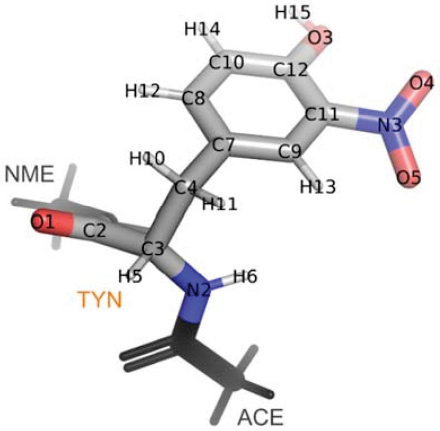

Atom name	ff99SB atom type	Atomic partial charge
C2	C	0.597300
O1	O	-0.567900
C3	CT	0.101700
N2	N	-0.415700
H6	H	0.271900
C4	CT	-0.301400
C7	CA	0.112150
C8	CA	-0.085750
C10	CA	-0.414450
C12	CA	0.402900
C11	CA	-0.113100
C9	CA	-0.247550
H13	HA	0.186350
N3	NO	0.877350
O4	O2	-0.481600
O5	O2	-0.481600
O3	OH	-0.544700
H15	HO	0.434800
H14	HA	0.198750
H12	HA	0.164050
H10	HC	0.120550
H11	HC	0.120550
H5	H1	0.065500

Table S2. Force field modifications for TYN

#Parameter file for NO2				
MASS				
NO	14.010	0.530		
BOND				
CA-NO	322.600	1.468		
NO-O2	761.200	1.219		
ANGLE				
CA-CA-NO	66.900	119.540		
CA-NO-O2	68.700	118.100		
O2-NO-O2[a]	76.400	127.550		
DIHEDRAL				
X -CA-NO-X	4.000	3.680	180.0	2
IMPROPER				
CA-O2-NO-O2		7.280	180.0	2
NONBON				
NO	1.824	0.170		

[a] As in Amber9 & 10

Table S3. Topology and atomic partial charges for TYD

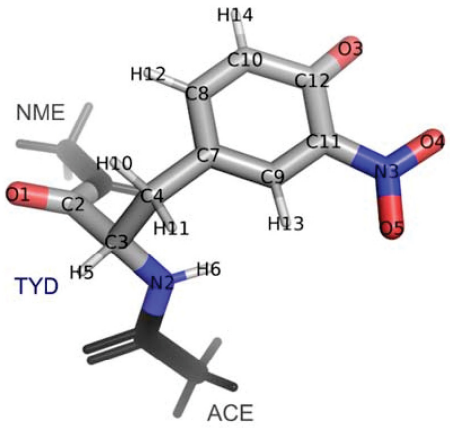

Atom name	ff99SB atom type	Atomic partial charge
C2	C	0.536600
O1	O	-0.581900
C3	CT	0.206300
N2	N	-0.516300
H6	H	0.293600
C4	CT	-0.094150
C7	CA	-0.076900
C8	CA	-0.051950
C10	CA	-0.455500
C12	CA	0.635950
C11	CA	-0.228100
C9	CA	-0.239400
H13	HA	0.118100
N3	NO	0.804400
O4	O2	-0.537600
O5	O2	-0.537600
O3	O	-0.656050
H14	HA	0.149750
H12	HA	0.150050
H10	HC	0.046150
H11	HC	0.046150
H5	H1	-0.011600

Table S4. Force field modifications for TYD

#Parameter file for NO2				
MASS				
NO	14.010	0.530		
BOND				
CA-NO	322.600	1.468		
NO-O2	761.200	1.219		
CA-O[a]	570.000	1.229		
ANGLE				
CA-CA-NO	66.900	119.540		
CA-NO-O2	68.700	118.100		
O2-NO-O2[b]	76.400	127.550		
CA-CA-O[c]	70.000	120.000		
DIHEDRAL				
X -CA-NO-X	4.000	7.50	180.0	2
IMPROPER				
CA-O2-NO-O2		7.280	180.0	2
CA-CA-CA-O[d]		1.100	180.0	2
NONBON				
NO	1.824	0.170		

[a] As C-O in parm99.
[b] As in Amber 9 & 10.
[c] As CA-C-OH in parm99.
[d] As CA-CA-C -O in parm99.

Materials & Methods

Computational procedures

Unbiased molecular dynamics simulations

We performed unbiased molecular dynamics (MD) simulations of the human glutamine synthetase (GS) bound to ATP and magnesium ions (Mg^{2+}) with water represented explicitly, using the Amber 14 and 16 software suits[6,7]. The ATP-bound state (further referred to as GS_{ATP}) was previously used by us to determine the molecular consequences of mutations on structural and energetic features of GS[8], and a detailed preparation protocol is reported therein. In short, as to GS, all simulations were started from a dimeric model of human GS extracted from PDB-ID 2QC8[2]. ATP and Mg^{2+} replaced cocrystallized and structurally bound ADP and manganese ions, such that the additional γ-phosphate group of ATP is oriented towards the center of the binding site.

We also prepared an *apo* state, in which ATP is missing (further referred to as GS_{Apo}). Hydrogen atoms not present in the crystal structure were added according to the ff99SB library[9,10]. Afterwards, to introduce residue TYN336 (referred to as GS_{TYN}) and TYD336 (referred to as GS_{TYD}), we adapted the coordinates of the wild type residue Y336. As there is no information available as to which rotamer state of the phenyl ring of TYN336 or TYD336 is preferred in the GS, we performed 3 × 100 ns MD simulations in the GS_{Apo} state for GS_{TYN} and GS_{TYD}, in which we initially placed the nitro group in positions ① or ② (**Figure S3A**). We used the dihedral α (**Figure S3A**) as a measure to investigate the relative orientation of the nitro group over the MD trajectory. The shape of the density curves is similar over both GS variants and reveals two peaks, one at $\alpha \approx -90°$ and one at $\alpha \approx 90°$, corresponding to orientations ① and ②, respectively (**Figure S3B**). Considering the uncertainty in the calculations, the occurrence frequencies of the two orientations ① and ② do not differ significantly. Taking into consideration that the nitro group in position ① is pointing towards the top of the ATP binding site and in position ② towards the center of the binding site, we used orientation ① as a starting orientation for further MD simulations. Note that except for the nitro group in GS_{TYN} and GS_{TYD} and the missing hydrogen atom in GS_{TYD}, the initial coordinates for the GS_{ATP} structure were otherwise identical throughout all GS variants. Finally, the complex structures were solvated by TIP3P water[11] using a truncated octahedron and leaving at least 11 Å between the solute and the edge of the box and neutralized by sodium counter ions.

Atomic partial charges for protein residues were taken from the ff99SB force field[9,10]. As to residues TYN and TYD, the atomic partial charges were derived according to the *RESP* procedure[12,13] (**Table S1 and 3**). Torsion parameters for the nitro group were taken from the library from Myung *et al.*[14] (**Table S2 and 4**). All other force field parameters were taken from the ff99SB force field[9,10] (**Table S2 and 4**). As to ATP and Mg^{2+}, atomic partial charges and force field paratemeters were taken form the libraries of Meagher *et al.*[15] and Allner *et al.*[16], respectively. All simulations were performed using GPU acceleration with the *pmemd.cuda* module implemented in Amber[17].

The general simulation protocol was adapted from ref.[8]. After energy minimization, thermalization, and density adaptation, the GS_{ATP} structures for wild type GS, GS_{TYN}, and GS_{TYD} were subjected to 5 × 500 ns of unbiased MD simulations. We varied the target temperature during equilibration from 299.8 K – 300.2 K in 0.1 K intervals. This procedure results in slightly different starting structures for subsequent productions simulations, such that the resulting trajectories can be considered independent.

Structural integrity of the dimeric model of human GS and convergence test

We computed the root mean square deviation (RMSD) average correlation (RAC)[18] for all protein backbone atoms using *cpptraj*[19] in order to determine the timescale of structural changes observed during MD simulations[18]. The RAC curves decrease smoothly during 500 ns of MD simulations, although we observe small bumps in one trajectory for each GS variant (**Figure S4**), indicating small structural changes. RAC curves computed for GS_{core}[8] residues (disregarding the 10% of the most mobile amino acids[8]) also decrease smoothly but without showing any bumps (**Figure S5**). Thus, the bumps apparently arose from structural changes in those regions where the adjacent subunit of the full-length GS is missing, as pointed out previously[8]. However, as these changes do not influence the binding site, which is part of GS_{core}, we conclude that our structural models are appropriate to study the influence of tyrosine nitration on ATP binding.

Geometric parameters to monitor the influence of tyrosine nitration on ATP binding

To monitor the influence of tyrosine nitration on ATP binding directly, the MD trajectories were analyzed towards structural features that characterize stacking interactions between ATP and residue 336. We measured, first, the distance between the geometric centers of the benzene ring in residue 336 and the purine ring in ATP, and, second, the angle between both ring planes. The results

are expressed as mean relative frequencies ± standard error of the mean (SEM) over five trajectories, normalized to the sum of all bins. Additionally, we computed the root mean square fluctuation (RMSF), relative to the average structure, as a measure for ATP mobility in the binding site, after superimposing all GS_{core} backbone atoms to the average structure.

Computation of effective binding energies

Subsequent to the MD simulations, we computed effective binding energies[20,21] for ATP by the molecular mechanics Poisson-Boltzmann surface area (MM-PBSA) approach[22,23]. The general settings were adapted from our previous study[8].

The computations were performed with Amber 16[24] considering configurations sampled at an interval of 100 ps (i.e., 5 × 5000 each) along the MD trajectories. Calculations were performed considering ATP as the ligand, and the protein structure and structurally bound ions as the receptor. We applied the 1-trajectory MM-PBSA approach, in which the snapshots of complex, receptor, and ligand are extracted from a single MD simulation of the complex[22]. To avoid any additional uncertainty in our calculation, we neglected contributions due to changes in the configurational entropy upon complex formation[20,25]. The effective binding energies ($\Delta G_{effective}$) were averaged over five trajectories ($\overline{\Delta G}_{effective}$). Relative effective binding energies ($\Delta\Delta G_{effective}$) were calculated by subtracting the mean $\Delta G_{effective}$ of the wild type ($\overline{\Delta G}_{wild\ type}$) from the effective binding energy of the nitro variant ($\overline{\Delta G}_{nitro}$) (eq. 1).

$$\Delta\Delta G_{effective} = \overline{\Delta G}_{nitro} - \overline{\Delta G}_{wild\ type} \quad (1)$$

The SEM over the five independent MD simulations for a system ($SEM_{1\text{-}5}$) was calculated by error propagation according to eq. 2.

$$SEM_{1\text{-}5} = \frac{1}{5}\sqrt{\sum_{i=1}^{5} SEM_i^2} \quad (2)$$

where SEM_i is the SEM for trajectory i. The total SEM (SEM_{total}) was then calculated by error propagation according to eq. 3

$$SEM_{\text{total}} = \frac{1}{2}\sqrt{(SEM_{1\text{-}5}^{\text{nitro}})^2+(SEM_{1\text{-}5}^{\text{wild type}})^2} \quad (3)$$

where $SEM_{1\text{-}5}^{\text{nitro}}$ is the SEM over five trajectories for a 3-nitro variant and $SEM_{1\text{-}5}^{\text{wild type}}$ the SEM over five trajectories for wild type GS. The results are expressed as $\Delta\Delta G_{\text{effective}} \pm SEM_{\text{total}}$. Additionally, the $\Delta G_{\text{effective}}$ values are expressed as mean distribution $\pm$ $SEM_{1\text{-}5}$, normalized to the sum of all bins.

Potential of mean force calculations

To investigate a potential influence of Y336 nitration on the binding kinetics of ATP, we performed potential of mean force (PMF) calculations of ATP unbinding from its binding site within wild type GS, GS_{TYN}, and GS_{TYD}. We computed the PMF (configurational free energy) of ATP unbinding employing umbrella sampling[26] and the Weighted Histogram Analysis Method (WHAM)[27].

To do so, we, initially, simulated the ATP unbinding path starting from the ATP-bound, minimized wild type GS structure by determining a vector for the unbinding path by random acceleration (expulsion) MD[1]. ATP was then translated along this vector in 0.5 Å steps (**Figure S1A**). The complete unbinding path covers a distance of ~37 Å, divided into 75 windows/umbrellas. In the unbound state, there is at least a distance of 12 Å between ATP and the protein structure (**Figure S1A**). Note that, similarly to our unbiased MD simulations, the starting structures for wild type GS, GS_{TYN}, and GS_{TYD} differ only in position 336.

As a reaction coordinate r, we used the distance between the centers of mass of Y/TYN/TYD336's benzene ring and ATP's purine ring (**Figure S1B**). Umbrella sampling MD simulations were performed applying harmonic potentials with a force constant of 20 kcal mol^{-1} Å^{-2} for $r \leq 15$ Å and 10 kcal mol^{-1} Å^{-2} for $r > 15$ Å. During umbrella sampling simulations, we applied positional restraints on backbone atoms of residues 211 – 231 of both subunits (**Figure S1A**) to ensure a constant relative orientation of the protein structure. Of primary importance in the selection of these residues was that they are located in the center of each subunit, but do not interfere with the binding site or binding pathway. This setup led to Gaussian-shaped frequency distributions for each reference point along the reaction coordinate, with all such distributions well overlapping (**Figure S6**). WHAM was used to derive the PMF from these distributions[27]. The uncertainty was determined by bootstrapping and is always < 0.05 kcal mol^{-1}, if not reported differently. The PMFs are qualitatively indistinguishable after 60 ns of umbrella sampling simulations (**Figure S6**). In

addition, when extending the simulation time from 50 ns to 60 ns, the changes in the PMFs are ≤ 0.76 kcal mol^{-1}. Thus, both results suggest converged PMFs. Transitions in terms of changes in configurational free energy along r are reported as $\Delta G_{r\,Å \rightarrow r+x\,Å}$ (in kcal mol^{-1}), where x represents the change of r in Å.

Calculating pK_a shifts from free energies

To calculate the pK_a shift of TYN336 due to the protein environment, we applied the method reported by Simonson *et al.*[28]. The calculation is based on the relation of the equilibrium constant K_a and the standard free energy ΔG (eq. 4)

$$\Delta G = -RT \ln K_a \tag{4}$$

where R is the gas constant of 0.001987 kcal mol^{-1} K^{-1} and T = 300 K. Eq. 4 can be alternatively expressed as eq. 5

$$pK_a = -\log K_a = \frac{1}{2.303\,RT}\Delta G \tag{5}$$

and eq. 6

$$pK_{a,prot.} = pK_{a,\,model} + \frac{1}{2.303\,RT}\Delta\Delta G \tag{6}$$

where p$K_{a,prot}$ and p$K_{a,model}$ are the pK_a's of TYN336 in the protein and free TYN in solution, respectively. $\Delta\Delta G$, the difference in free energy between two states, is calculated according to eq. 7

$$\Delta\Delta G = \Delta G_{prot.} - \Delta G_{model} \tag{7}$$

The individual error for ΔG_{prot} and ΔG_{model} was estimated by simple additive error propagation, and the total error for ΔΔG was then calculated analogously to eq. 3.

We used thermodynamic integration[21,29] (TI) to calculate ΔG for the transformation of TYN into TYD in our model structure and TYN336 into TYD336 in the protein structure (**Figure 5**). The TI transformation is performed at distinct λ-steps, where λ couples the two potential functions V_0 and V_1 of the two end states TYN and TYD, respectively. Subsequently, ΔG can be derived by

integrating over the average dV/dλ values for each λ-step. The transformation simulations were performed at λ = 0.1, 0.3, …, 0.9 for 60 ns per λ-step. After 60 ns, the SEM for average dV/dλ values for each λ-step was ≤ 0.1 kcal mol^{-1} and changes of ΔG in 10 ns intervals < 0.5 kcal mol^{-1} (**Figure S7**), indicating converged results. As the absolute charge of the system changed during transformation, we applied a uniform neutralizing plasma to reach electroneutrality[30]. We used soft-core potentials that enabled a one-step transformation[31,32]. For the transformation of the protein structures, we used the GS_{Apo} structures that carry TYN336 or TYD336 as used for unbiased MD simulations. As model structures we used ACE- and NME-capped TYN and TYD residues, respectively. The transformations were simulated in explicit TIP3P solvent[11].

Analysis of results

If not reported differently, results are expressed as mean values ± SEM and compared using a two-sided Student´s *t*-test (using the R software[33]). *P* values < 0.05 were considered statistically significant.

Experimental procedures

Materials

The monoclonal antibody directed against human GS, clone 6) was from Beckton-Dickinson (Heidelberg, Germany). The monoclonal antibody against 3´-nitrotyrosine was from Upstate Biotechnologies (Thermo Fisher, Heidelberg, Germany). Horseradish peroxidase-coupled goat anti-mouse IgG antibodies were from Biorad International (Munich, Germany). Peroxynitrite ($ONOO^-$), KOH, and KH_2PO_4 were from Merck Millipore (Darmstadt, Germany). Imidazole, sodium glutamate, adenosine 5´-triphosphate, phosphoenolpyruvate, magnesium chloride, potassium chloride, ammonium chloride, ß-nicotinamide adenine, pyruvate kinase and L-lactic dehydrogenase were from Sigma (Deisenhofen, Germany). Bovine serum albumine was from Roche (Mannheim, Germany).

Expression and purification of human glutamine synthetase

A plasmid expressing human GS was donated to us by Dr. Norma Allewell and used to transform *E. coli* and to express the enzyme in these cells, as described by Listrom *et al*.[34]. The subsequent of human GS was adapted from the methods published by Listrom *et al*.[34]. In brief, the clarified sonicates of *E. coli* suspensions expressing human GS underwent successive purification on HA

Ultrogel®, DEAE-Sepharose, and MonoQ resins, using linear: 100 to 500 mM potassium phosphate buffer (pH 7.2), step: imidazole-NaOH at pH 7.9, and linear: 0 to 250 mM NaCl in 20 mM Tris-HCl, respectively. The potassium phosphate buffer also contained 5 mM 2-mercaptoethanol. Similarly, the imidazole-NaOH buffers also contained 1 mM EDTA and 5 mM 2-mercaptoethanol. The first two separations were performed at room temperature, while the final chromatography was carried out at 4°C and yielded a protein that was > 99% pure as judged by SDS-PAGE. The purified human GS was combined with glycerol at a final concentration of 10% and stored at 4°C. GS activity during the purification was assessed using hydroxamate assay, as described by Jeitner and Cooper[35]. The reaction mixture for this assay consists of enzyme and 100 mM Tris-HCl (pH 7.4), 100 mM hydroxylamine, 10 mM ATP, 10 mM $MgCl_2$, 10 mM glutamate, and 2 mM dithiothreitol in a volume of 55 µl. Incubations were carried out at 37°C for periods up to 45 min and terminated with the addition of 165 µl of 0.37M $FeCl_3$, 0.67 M HCl, and 0.2 m trichloroacetic acid per 55 µl reaction. These mixtures were then centrifuged at 10,000 x g for ten minutes at 4°C and the absorbance of 200 µl of the supernatant fraction at 535 nm recorded. γ-Glutamylhydroxamate formation was calculated using an extinction coefficient of 850 M^{-1} cm^{-1}.

Peroxynitrite treatment of human glutamine synthetase

Purified human GS was incubated in 0.1 M KH_2PO_4 (pH 7.0) and nitrated by addition of peroxynitrite ($ONOO^-$, in 0.1 M KOH) under constant stirring as described before[36]. Samples were stirred for 5 s and incubated on ice for another 30 min. Final $ONOO^-$ concentrations were 5, 50, 100 and 200 µM. For $ONOO^-$-free control, GS was exposed to vehicle only (0.1 M KOH). Aliquots from the reaction mixture were taken for Western blot analysis of 3′-nitrotyrosine or GS and determination of enzyme activity as described below.

Western blot analysis

Western blot analysis was performed as described before[36]. Briefly, equal amounts of isolated human GS were subjected to sodium dodecyl sulfate polyacrylamid gel electrophoresis (SDS-PAGE) using 10% gels. Proteins were transferred onto nitrocellulose membranes by semi-dry blotting (BioRad, Munich, Germany). Membranes were washed in Tris-buffered saline containing 0.1% Tween20 (TBS-T) and incubated in TBS-T containing 10% bovine serum albumin (BSA) for 30 min. At the end of the incubation time, blots were probed for 2 h at room temperature with antibodies against 3′-nitrotyrosine (mAb, Upstate) or GS (mAb, Becton Dickinson, 1:5,000)

diluted in TBS-T + 5% BSA. Blots were washed three times and incubated in TBS-T + 5% BSA containing horseradish peroxidase-coupled antibodies directed against mouse immunoglobulins (1:10,000, 2 h, RT). Peroxidase activity on the membranes was detected using Western-Lightning chemiluminescence reagent plus (Perkin Elmer, Waltham, USA). Digital images were captured using the ChemiDoc MP and Image Lab software (Biorad, München, Germany).

Glutamine synthetase activity assay

Human GS activity was measured according to ref. [37] by using a commercial kit (SPGLUT11, Sigma, Deisenhofen, Germany). In this assay, the conversion of ATP to ADP by GS is coupled to the oxidation of NADH to NAD^+ by L-lactic dehydrogenase. The final reaction mixture contained 34.1 mM imidazole, 102 mM sodium glutamate, 8.5 mM adenosine 5´-triphosphate, 1.1 mM phosphoenolpyruvate, 60 mM magnesium chloride, 18.9 mM potassium chloride, 45 mM ammonium chloride, 0.25 mM ß-nicotinamide adenine, 28 units pyruvate kinase and 40 units L-lactic dehydrogenase. The pH of the reaction mixture was adjusted to pH 7.0, 6.0 or 4.0 before the reaction was initiated by addition of purified GS. The reaction mixture was incubated for ten min at 37°C, and the absorbance was measured at 340 nm using a spectrophotomer (UV-2600, Shimadzu, Duisburg, Germany). GS activity in $ONOO^-$-exposed samples is expressed relative to vehicle-treated control at pH 7.0.

Analysis of results

Experiments were repeated three times, and results are expressed as arithmetic means ± SEM. Statistical analysis was performed using one way analysis of variance (ANOVA) followed by Tukey´s multiple comparison *post hoc* test (Graph Pad Prism, Prism, USA). *P* values < 0.05 were considered statistically significant.

Supplemental Notes

Assessment of computational procedures

In this study, we have shown by molecular dynamics (MD) simulations and end-point, pathway, and alchemical transformation free energy calculations that Y336 nitration in human glutamine synthetase (GS) hampers substrate (ATP) binding if residue 336 is in the deprotonated, negatively charged TYD336 state. Here, we argue that our computations allow drawing this conclusion.

Human GS is composed by ten identical subunits that form two pentameric rings in which the C-terminus of one monomer interacts with the N-terminus of the adjacent monomer[2] (**Figure 1A**). The catalytic active site is located in the interface of two adjacent subunits and, thus, full-length GS contains ten identical catalytic sites[2]. In this study, to keep computational costs manageable, we used a dimeric GS model that contains a single catalytic site in its dimerization interface. Previously, we showed that our dimeric GS model allows to perform MD simulations in a computationally efficient way, relative to the decameric GS structure, without loss in quality[8]: Over the course of the MD simulations, the recorded structural deviations (measured as root mean square deviation (RMSD)) in the binding site region of the dimeric system were always < 1 Å and similar to the structural deviations found for the decameric structure[8]. As Y366 is part of the nucleotide binding site, Y336 thus does not undergo large structural deviations either. Furthermore, Y336 does not contribute to interface protein-protein interactions in human GS[38]. In contrast, Y366 is directly interacting with ADP in the crystal structure[2] (**Figure 1A**). We thus feel it safe to assume that the inhibitory effect of Y336 nitration originates from hampered substrate binding rather than changes in the GS oligomer stability. Overall, our dimeric GS model should be appropriate to study the influence of Y336 nitration on substrate binding in a computationally efficient way.

We used well-established force field parameters to describe the dynamics of proteins[9,10], ions[15], nucleotides[16], and solvent[11], but we note that more recent protein force fields have become available[39,40]. The force fields follow a classical mechanical representation of stacking interactions with a fixed-charge force field[41]. We note that stacking interactions described by the Amber type force field[42], as used here, have been shown to be in good agreement with stacking interactions described by sophisticated and physically complete quantum mechanical calculations[43-46]. The impact of force field deficiencies on our results is expected to be negligible due to cancellation of errors when comparatively assessing the structural and energetic features of nitrated GS (TYN or TYD variant) relative to wild type GS. We paid particular attention to the parameters describing

TYN and TYD. Parameters for the protonated, neutral TYN variant have been reported by Myung and Han[14], but structural parameters and atomic partial charges for the deprotonated, negatively charged TYD variant were not available at the beginning of this study. Initial molecular mechanics (MM) minimizations of different ACE-TYD-NME structures showed a significant rotation of the NO_2 group relative to the ring plane, whereas the NO_2 group was almost in plane with the ring in QM-optimized structures. Therefore, parameters for the torsion angle C-C-N-O in the TYD state were newly derived. In addition, to ensure consistency of the charge determination procedure, charges for both TYN and TYD were (re-)determined. To do so, we used model peptides of TYN and TYD that were capped by acetyl (ACE) and *N*-methyl (NME) groups. In consistency with the proceedings for charge determination of amino acids in the Cornell *et al.* force field[9], two conformers representing an α-helical and β-strand conformation were prepared. We also considered that the nitro group can be either oriented towards the ACE or NME group. Atomic partial charges were derived by a multi conformer least-squares-fitting procedure. In the end, for MD simulations of the TYN variant, we used the force field parameters of Myung and Han[14] with atomic partial charges computed here, and for MD simulations of the TYD variant, we used ff99SB atom types with optimized C-C-N-O torsion angle parameters and atomic partial charges calculated here. All relevant force field parameters applicable with the Amber ff99SB force field[9,10] are provided in **Table S1-S4.**

That Y336 nitration in human GS hampers substrate (ATP) binding, but only in its deprotonated and negatively charged TYD336 state, has been demonstrated by three independent ways. First, we studied the structural features upon tyrosine nitration by unbiased MD simulations, which allows to study the structural dynamics at high temporal and spatial resolution in full atomic detail[47]. For investigating the effects Y336 nitration, we followed an "ensemble average approach"[48-51] in that five independent MD simulations were performed for dimeric wild type GS and nitrated GS in its protonated, neutral GS_{TYN} state and deprotonated, negatively charged GS_{TYD} state, respectively. This procedure allows, first, to test for the influence of different starting conditions and, second, to determine the statistical uncertainties of the computed results[18,52]. We, initially, computed the RMS average correlation (RAC)[18] for all protein backbone atoms in order to determine the timescale of structural changes observed during MD simulations[18] (**Figure S4**). These RAC curves generally decrease smoothly during 500 ns of MD simulations, although we observe small bumps in one trajectory for each GS variant, indicating small structural changes

there. RAC curves computed for GS_{core}[8] residues (disregarding the 10% of the most mobile amino acids[8]) also decrease smoothly but without showing any bumps (**Figure S5**). Thus, the bumps apparently arose from structural changes in those regions where the adjacent subunit of the full-length GS is missing, as pointed out previously[8]. However, as these changes do not influence the binding site, which is part of GS_{core}, we again conclude that our structural models should be appropriate to study the influence of tyrosine nitration on the interaction with ATP.

Second, we analyzed the energetic consequences upon tyrosine nitration on substrate binding by the molecular mechanics Poisson-Boltzmann surface area (MM-PBSA) approach[22,23] (**Figure 3**). The MM-PBSA approach is an end-point free energy calculation method and allows to estimate the absolute free energy of binding a ligand, here ATP, to a receptor, here human GS [22,53]. We followed the 1-trajectory approach, such that all coordinates were extracted from MD ensembles of the complex structure[22,53]. In contrast to the 3-trajectory approach[22], the 1-trajectory approach requires fewer simulations, but neglects any changes of the ligand and receptor structure upon binding[53]. However, there is evidence that suggests that the 1-trajectory approach, in practice, often gives more accurate results compared to the 3-trajectory approach, probably due to the cancellation of errors and the limited sampling in the 3-trajectory approach[53-56]. Previous studies showed that inclusion of configurational entropy is crucial for calculating absolute binding free energies[25,53]. In this study, however, we are rather interested in relative changes upon tyrosine nitration with respect to wild type GS (expressed as $\Delta\Delta G$; see eq. 1 in Methods section) and, thus, we decided to neglect contributions due to changes in the configurational entropy of the ligand or the receptor upon complex formation, in order to avoid introducing additional uncertainty in the computations[20,25,57]. We considered five trajectories for each GS system for free energy calculations, as previous studies suggest that multiple "short" trajectories efficiently produce converged free energy estimates and meaningful error estimates[48,58-60]. As recommended for MM-PBSA calculations, we used Parse radii[61] to calculate the polar part of solvation free energies[21]. In MM-PBSA calculations, the electrostatic contribution depends on the solute dielectric constant ε[53], and for a highly charged binding interface, a higher solute dielectric constant is preferred[25]. Often best results are observed for $\varepsilon = 2 - 4$[25,53,62,63]. In human GS[2], we are facing a highly polar and charged binding site, including six negatively charged residues (E134, E136, E196, E203, E305, and E338), five positively charged residues (K43, R45, R319, R324, and R340), at least two structurally bound Mg^{2+} ions, and the negatively charged phosphate groups of ATP, such that we set $\varepsilon = 4$.

Third, we determined the influence of Y336 nitration on the actual binding process of ATP. Applying MD simulations of free ATP diffusion in the presence of the GS to reconstruct the binding pathway that way[51,64] did not seem suitable to us in this case given the high binding affinity of ATP to GS (K_M = 1.8 mM[34]) and, hence, the expected low off-rate. We, thus, decided to perform potential of mean force (PMF) calculations of ATP (un-)binding from its binding site within the GS variants. We computed the PMF for ATP (un-)binding employing umbrella sampling[26] and the Weighted Histogram Analysis Method (WHAM)[27], as this combination was successfully applied by us previously[65-67] and is expected to suffer less from relaxation problems in complex systems such as protein-ligand systems[68]. Technically, we simulated the ATP unbinding path, starting from the ATP-bound GS model that was used for prior MD simulations. That way, we avoid introducing any uncertainties that arose from arbitrarily placed ATP outside of the binding site. Instead, we determined a vector that describes a linear unbinding path by random acceleration (expulsion) MD[1], and ATP was then translated along this vector in 0.5 Å steps (**Figure S1**). The complete unbinding path covers a distance of ~37 Å, divided into 75 windows (**Figure S1**). In the completely unbound state, the minimal distance between any atom in ATP and any atom in Y336 is 23.6 Å, such that ATP can move without any bias from Y336 in the completely unbound state. Note that the starting structures for wild type GS, GS_{TYN}, and GS_{TYD} differ only in position 336, such that any relative change of the PMF between the variants are highly likely the consequence of nitrated Y336 and not biased by the initial coordinates. During umbrella sampling simulations, we restrained the distance between the centers of mass of Y/TYN/TYD336's benzene ring and ATP's purine ring as an intuitive reaction coordinate. For all GS variants, we obtained Gaussian-shaped frequency distributions for each umbrella sampling simulation along the reaction coordinate, with all such distributions well overlapping, which is a prerequisite for the subsequent derivation of the PMF[69].

Considering that the specified reaction coordinate is the same in all three cases of ATP (un-) binding from wild type GS, GS_{TYN}, or GS_{TYD} and that the sampled unbound state is very similar in all three cases (as qualitatively shown in **Figure 4B**), differences in the PMFs relative to the unbound state indicate differences in the binding energetics among the three systems. In that respect, it is encouraging that differences in the PMF values of the bound state between wild type GS and both nitrated GS variants (**Figure 4A**) are in very good agreement with results from MM-PBSA calculations (**Figure 3A**), both qualitatively and quantitatively. Thus, the results from the

PMF computations also provide an internal validation of our MM-PBSA calculations and *vice versa*.

Finally, we computed the pK_a shift of nitrated Y336 relative to (free) 3-nitro tyrosine according to eq. 6. For this, $\Delta\Delta G$ was computed by evaluating the thermodynamic cycle (**Figure 5**) by means of thermodynamic integration (TI)[21,70], simulating the (alchemical) transformation of TYN into TYD. Because of the high computational costs of these computations, we intended to keep the simulation time per λ-step as short as possible. For TI calculations, however, sufficient sampling is critical for the accuracy of the results[71]. We thus increased the sampling time, for which we recorded the dV/dλ potentials, in intervals of 10 ns. For both transformations, TYN/TYD free in solution or incorporated into the protein structure, ΔG changed only marginally when increasing the sampling time from 50 – 60 ns (**Figure S7**), such that the computation can be considered converged. This coincides with that, after 60 ns, smooth dV/dλ curves were derived, which facilitates numerical integration[21].

Supplemental References

1. Ludemann, S.K., Lounnas, V. & Wade, R.C. How do substrates enter and products exit the buried active site of cytochrome P450cam? 1. Random expulsion molecular dynamics investigation of ligand access channels and mechanisms. *Journal of Molecular Biology* **303**, 797-811 (2000).
2. Krajewski, W.W. et al. Crystal structures of mammalian glutamine synthetases illustrate substrate-induced conformational changes and provide opportunities for drug and herbicide design. *Journal of Molecular Biology* **375**, 217-28 (2008).
3. Bartesaghi, S. et al. Oxidative inactivation of human glutamine synthetase: biochemical and computational studies. *Free Radical Biology and Medicine* **100**, S19 (2016).
4. Görg, B., Wettstein, M., Metzger, S., Schliess, F. & Häussinger, D. Lipopolysaccharide-induced tyrosine nitration and inactivation of hepatic glutamine synthetase in the rat. *Hepatology* **41**, 1065-1073 (2005).
5. Görg, B., Wettstein, M., Metzger, S., Schliess, F. & Häussinger, D. LPS-induced tyrosine nitration of hepatic glutamine synthetase. *Hepatology* **42**, 499-499 (2005).
6. Case, D.A. et al. AMBER 14. *University of California, San Francisco.* (2014).
7. Case, D.A. et al. AMBER 16. *University of California, San Francisco.* (2016).
8. Frieg, B. et al. Molecular mechanisms of glutamine synthetase mutations that lead to clinically relevant pathologies. *PLoS Computational Biology* **12**, e1004693 (2016).
9. Cornell, W.D. et al. A second generation force field for the simulation of proteins, nucleic acids, and organic molecules. *Journal of the American Chemical Society* **117**, 5179–5197 (1995).
10. Hornak, V. et al. Comparison of multiple Amber force fields and development of improved protein backbone parameters. *Proteins: Structure, Function, and Bioinformatics* **65**, 712-725 (2006).
11. Jorgensen, W.L., Chandrasekhar, J., Madura, J.D., Impey, R.W. & Klein, M.L. Comparison of simple potential functions for simulating liquid water. *Journal of Chemical Physics* **79**, 926-935 (1983).
12. Bayly, C.I., Cieplak, P., Cornell, W.D. & Kollman, P.A. A well-behaved electrostatic potential based method using charge restraints for deriving atomic charges - the RESP Model. *Journal of Physical Chemistry* **97**, 10269-10280 (1993).
13. Cornell, W.D., Cieplak, P., Bayly, C.I. & Kollman, P.A. Application of RESP charges to calculate conformational energies, hydrogen bond energies, and free-energies of solvation. *Journal of the American Chemical Society* **115**, 9620-9631 (1993).
14. Myung, Y. & Han, S. Force field parameters for 3-nitrotyrosine and 6-nitrotryptophan. *Bulletin of the Korean Chemical Society* **31**, 2581-2587 (2010).
15. Meagher, K.L., Redman, L.T. & Carlson, H.A. Development of polyphosphate parameters for use with the AMBER force field. *Journal of Computational Chemistry* **24**, 1016-1025 (2003).
16. Allner, O., Nilsson, L. & Villa, A. Magnesium ion-water coordination and exchange in biomolecular simulations. *Journal of Chemical Theory and Computation* **8**, 1493-1502 (2012).
17. Salomon-Ferrer, R., Götz, A.W., Poole, D., Le Grand, S. & Walker, R.C. Routine microsecond molecular dynamics simulations with Amber on GPUs. 2. Explicit solvent particle mesh Ewald. *Journal of Chemical Theory and Computation* **9**, 3878-3888 (2013).
18. Galindo-Murillo, R., Roe, D.R. & Cheatham, T.E., 3rd. Convergence and reproducibility in molecular dynamics simulations of the DNA duplex d(GCACGAACGAACGAACGC). *Biochimica et Biophysica Acta* **1850**, 1041-58 (2015).
19. Roe, D.R. & Cheatham III, T.E. PTRAJ and CPPTRAJ: software for processing and analysis of molecular dynamics trajectory data. *Journal of Chemical Theory and Computation* **9**, 3084-3095 (2013).
20. Gohlke, H. & Case, D.A. Converging free energy estimates: MM-PB(GB)SA studies on the protein-protein complex Ras-Raf. *Journal of computational chemistry* **25**, 238-50 (2004).
21. Homeyer, N., Stoll, F., Hillisch, A. & Gohlke, H. Binding free energy calculations for lead optimization: Assessment of their accuracy in an industrial drug design context. *Journal of Chemical Theory and Computation* **10**, 3331–3344 (2014).
22. Homeyer, N. & Gohlke, H. Free energy calculations by the molecular mechanics Poisson-Boltzmann surface area method. *Molecular Informatics* **31**, 114-122 (2012).
23. Srinivasan, J., Cheatham, I., T. E., Cieplak, P., Kollman, P.A. & Case, D.A. Continuum solvent studies of the stability of DNA, RNA, and phosphoramidate - DNA helices. *Journal of the American Chemical Society* **120**, 9401-9409 (1998).
24. Case, D.A. et al. AMBER 12. *University of California, San Francisco.* (2012).

25. Hou, T., Wang, J., Li, Y. & Wang, W. Assessing the performance of the MM/PBSA and MM/GBSA methods. 1. The accuracy of binding free energy calculations based on molecular dynamics simulations. *Journal of Chemical Information and Modeling* **51**, 69-82 (2011).
26. Kottalam, J. & Case, D.A. Dynamics of ligand escape from the heme pocket of myoglobin. *Journal of the American Chemical Society* **110**, 7690-7697 (1988).
27. Kumar, S., Bouzida, D., Swendsen, R.H., Kollman, P.A. & Rosenberg, J.M. The weighted histogram analysis method for free-energy calculations on biomolecules. 1. The method. *Journal of Computational Chemistry* **13**, 1011-1021 (1992).
28. Simonson, T., Carlsson, J. & Case, D.A. Proton binding to proteins: pK(a) calculations with explicit and implicit solvent models. *Journal of the American Chemical Society* **126**, 4167-4180 (2004).
29. Kaus, J.W., Pierce, L.T., Walker, R.C. & McCammon, J.A. Improving the efficiency of free energy calculations in the Amber molecular dynamics package. *Journal of Chemical Theory and Computation* **9**, 4131-4139 (2013).
30. Darden, T., Pearlman, D. & Pedersen, L.G. Ionic charging free energies: spherical versus periodic boundary conditions. *Journal of Chemical Physics* **109**, 10921-10935 (1998).
31. Beutler, T.C., Mark, A.E., Vanschaik, R.C., Gerber, P.R. & Vangunsteren, W.F. Avoiding singularities and numerical instabilities in free-energy calculations based on molecular simulations. *Chemical Physics Letters* **222**, 529-539 (1994).
32. Steinbrecher, T., Joung, I. & Case, D.A. Soft-core potentials in thermodynamic integration: comparing one- and two-step transformations. *Journal of Computational Chemistry* **32**, 3253-63 (2011).
33. Team, R.C. TEAM: R: a language and environment for statistical computing. *R Foundation for Statistical Computing, Vienna, Austria* (2008).
34. Listrom, C.D. et al. Expression, purification, and characterization of recombinant human glutamine synthetase. *Biochemical Journal* **328**, 159-163 (1997).
35. Jeitner, T.M. & Cooper, A.J.L. Inhibition of human glutamine synthetase by L-methionine-S, R-sulfoximine-relevance to the treatment of neurological diseases. *Metabolic Brain Disease* **29**, 983-989 (2014).
36. Görg, B. et al. Reversible inhibition of mammalian glutamine synthetase by tyrosine nitration. *Febs Letters* **581**, 84-90 (2007).
37. Kingdon, H.S., Hubbard, J.S. & Stadtman, E.R. Regulation of glutamine synthetase. XI. The nature and implications of a lag phase in the Escherichia coli glutamine synthetase reaction. *Biochemistry* **7**, 2136-2142 (1968).
38. Moreira, C., Ramos, M.J. & Fernandes, P.A. Glutamine synthetase drugability beyond its active site: exploring oligomerization interfaces and pockets. *Molecules* **21**(2016).
39. Lindorff-Larsen, K. et al. Improved side-chain torsion potentials for the Amber ff99SB protein force field. *Proteins: Structure, Function, and Bioinformatics* **78**, 1950-1958 (2010).
40. Maier, J.A. et al. ff14SB: Improving the accuracy of protein side chain and backbone parameters from ff99SB. *Journal of Chemical Theory and Computation* **11**, 3696-3713 (2015).
41. Riniker, S. Fixed-charge atomistic force fields for molecular dynamics simulations in the condensed phase: An overview. *Journal of Chemical Information and Modeling* **58**, 565-578 (2018).
42. Galindo-Murillo, R. et al. Assessing the current state of Amber force field modifications for DNA. *Journal of Chemical Theory and Computation* **12**, 4114-4127 (2016).
43. Hobza, P. & Sponer, J. Structure, energetics, and dynamics of the nucleic acid base pairs: Nonempirical ab initio calculations. *Chemical Reviews* **99**, 3247-3276 (1999).
44. Sponer, J., Riley, K.E. & Hobza, P. Nature and magnitude of aromatic stacking of nucleic acid bases. *Physical Chemistry Chemical Physics* **10**, 2595-2610 (2008).
45. Sponer, J. et al. Nature and magnitude of aromatic base stacking in DNA and RNA: Quantum chemistry, molecular Mechanics, and experiment. *Biopolymers* **99**, 978-988 (2013).
46. Parker, T.M. & Sherrill, C.D. Assessment of empirical models versus high-accuracy ab initio methods for nucleobase stacking: evaluating the importance of charge penetration. *Journal of Chemical Theory and Computation* **11**, 4197-204 (2015).
47. Dror, R.O., Dirks, R.M., Grossman, J.P., Xu, H.F. & Shaw, D.E. Biomolecular simulation: a computational microscope for molecular biology. *Annual Review of Biophysics* **41**, 429-452 (2012).
48. Lee, T.S., Hu, Y., Sherborne, B., Guo, Z. & York, D.M. Toward fast and accurate binding affinity prediction with pmemdGTI: an efficient implementation of GPU-accelerated thermodynamic integration. *Journal of Chemical Theory and Computation* **13**, 3077-3084 (2017).
49. Loccisano, A.E., Acevedo, O., DeChancie, J., Schulze, B.G. & Evanseck, J.D. Enhanced sampling by multiple molecular dynamics trajectories: carbonmonoxy myoglobin 10 mu s A0 -> A(1-3) transition from ten 400 picosecond simulations. *Journal of Molecular Graphics & Modelling* **22**, 369-376 (2004).

50. Caves, L.S.D., Evanseck, J.D. & Karplus, M. Locally accessible conformations of proteins: Multiple molecular dynamics simulations of crambin. *Protein Science* **7**, 649-666 (1998).
51. Buch, I., Giorgino, T. & De Fabritiis, G. Complete reconstruction of an enzyme-inhibitor binding process by molecular dynamics simulations. *Proceedings of the National Academy of Sciences of the United States of America* **108**, 10184-10189 (2011).
52. Ryckaert, J.P., Ciccotti, G. & Berendsen, H.J.C. Numerical integration of cartesian equations of motion of a system with constraints molecular dynamics of n-alkanes. *Journal of Computational Physics* **23**, 327-341 (1977).
53. Genheden, S. & Ryde, U. The MM/PBSA and MM/GBSA methods to estimate ligand-binding affinities. *Expert Opinion on Drug Discovery* **10**, 449-461 (2015).
54. Lepsik, M., Kriz, Z. & Havlas, Z. Efficiency of a second-generation HIV-1 protease inhibitor studied by molecular dynamics and absolute binding free energy calculations. *Proteins: Structure, Function, and Genetics* **57**, 279-293 (2004).
55. Spackova, N. et al. Molecular dynamics simulations and thermodynamics analysis of DNA-drug complexes. Minor groove binding between 4 ',6-diamidino-2-phenylindole and DNA duplexes in solution. *Journal of the American Chemical Society* **125**, 1759-1769 (2003).
56. Gilson, M.K. & Zhou, H.X. Calculation of protein-ligand binding affinities. *Annual Review of Biophysics and Biomolecular Structure* **36**, 21-42 (2007).
57. Weis, A., Katebzadeh, K., Soderhjelm, P., Nilsson, I. & Ryde, U. Ligand affinities predicted with the MM/PBSA method: dependence on the simulation method and the force field. *Journal of medicinal chemistry* **49**, 6596-606 (2006).
58. Wan, S.Z., Knapp, B., Wright, D.W., Deane, C.M. & Coveney, P.V. Rapid, precise, and reproducible prediction of peptide-MHC binding affinities from molecular dynamics that correlate well with experiment. *Journal of Chemical Theory and Computation* **11**, 3346-3356 (2015).
59. Wright, D.W., Hall, B.A., Kenway, O.A., Jha, S. & Coveney, P.V. Computing clinically relevant binding free energies of HIV-1 protease inhibitors. *Journal of Chemical Theory and Computation* **10**, 1228-1241 (2014).
60. Genheden, S. & Ryde, U. How to obtain statistically converged MM/GBSA results. *Journal of Computational Chemistry* **31**, 837-846 (2010).
61. Sitkoff, D., Sharp, K.A. & Honig, B. Accurate Calculation of Hydration Free-Energies Using Macroscopic Solvent Models. *Journal of Physical Chemistry* **98**, 1978-1988 (1994).
62. Hou, T.J., Wang, J.M., Li, Y.Y. & Wang, W. Assessing the performance of the molecular mechanics/Poisson Boltzmann surface area and molecular mechanics/generalized Born surface area methods. II. The accuracy of ranking poses generated from docking. *Journal of Computational Chemistry* **32**, 866-877 (2011).
63. Sun, H.Y. et al. Assessing the performance of MM/PBSA and MM/GBSA methods. 5. Improved docking performance using high solute dielectric constant MM/GBSA and MM/PBSA rescoring. *Physical Chemistry Chemical Physics* **16**, 22035-22045 (2014).
64. Plattner, N. & Noé, F. Protein conformational plasticity and complex ligand-binding kinetics explored by atomistic simulations and Markov models. *Nature Communications* **6**(2015).
65. Koller, A.N., Bozilovic, J., Engels, J.W. & Gohlke, H. Aromatic N versus aromatic F: bioisosterism discovered in RNA base pairing interactions leads to a novel class of universal base analogs. *Nucleic Acids Research* **38**, 3133-3146 (2010).
66. Ciupka, D. & Gohlke, H. On the potential alternate binding change mechanism in a dimeric structure of Pyruvate Phosphate Dikinase. *Scientific Reports* **7**(2017).
67. Minges, A. et al. Structural intermediates and directionality of the swiveling motion of Pyruvate Phosphate Dikinase. *Scientific Reports* **7**(2017).
68. Bastug, T., Chen, P.C., Patra, S.M. & Kuyucak, S. Potential of mean force calculations of ligand binding to ion channels from Jarzynski's equality and umbrella sampling. *Journal of Chemical Physics* **128**(2008).
69. Kästner, J. Umbrella sampling. *Wiley Interdisciplinary Reviews-Computational Molecular Science* **1**, 932-942 (2011).
70. Steinbrecher, T., Case, D.A. & Labahn, A. A multistep approach to structure-based drug design: studying ligand binding at the human neutrophil elastase. *Journal of Medicinal Chemistry* **49**, 1837-1844 (2006).
71. Chodera, J.D. et al. Alchemical free energy methods for drug discovery: progress and challenges. *Current Opinion in Structural Biology* **21**, 150-160 (2011).

11.3 PUBLICATION III

Structural basis of lantibiotic recognition by the nisin resistance protein from *Streptococcus agalactiae*.

Khosa, S.[§], **Frieg, B.**[§], Mulnaes, D., Kleinschrodt, D., Hoeppner, A., Gohlke, H., Smits, S.H.J.

Sci. Rep. (2016), 6, 18679

[§] Both authors contributed equally to this work.

www.nature.com/scientificreports

OPEN

Received: 18 August 2015
Accepted: 23 November 2015
Published: 04 January 2016

Structural basis of lantibiotic recognition by the nisin resistance protein from *Streptococcus agalactiae*

Sakshi Khosa[1,*], Benedikt Frieg[2,*], Daniel Mulnaes[2], Diana Kleinschrodt[3], Astrid Hoeppner[4], Holger Gohlke[2] & Sander H. J. Smits[1]

Lantibiotics are potent antimicrobial peptides. Nisin is the most prominent member and contains five crucial lanthionine rings. Some clinically relevant bacteria express membrane-associated resistance proteins that proteolytically inactivate nisin. However, substrate recognition and specificity of these proteins is unknown. Here, we report the first three-dimensional structure of a nisin resistance protein from *Streptococcus agalactiae* (*Sa*NSR) at 2.2 Å resolution. It contains an N-terminal helical bundle, and protease cap and core domains. The latter harbors the highly conserved TASSAEM region, which lies in a hydrophobic tunnel formed by all domains. By integrative modeling, mutagenesis studies, and genetic engineering of nisin variants, a model of the *Sa*NSR/nisin complex is generated, revealing that *Sa*NSR recognizes the last C-terminally located lanthionine ring of nisin. This determines the substrate specificity of *Sa*NSR and ensures the exact coordination of the nisin cleavage site at the TASSAEM region.

Antibiotics provide a great advantage in the treatment of infections caused by bacteria such as *Streptococcus pneumoniae* and *Streptococcus agalactiae*. However, due to their widespread use, the number of resistant bacterial strains is increasing[1], leading to an urgent need for the development of new antibiotics. Several approaches have been taken to identify new antibiotics where naturally occurring compounds are found to be the most promising ones[2]. Here, small antimicrobial peptides such as lantibiotics are excellent candidates because they exhibit high effectivity against various Gram-positive human pathogenic bacteria including *Streptococcus pneumoniae* and several methicillin-resistant *Staphylococcus aureus* (MRSA) strains[3].

Lantibiotics display antimicrobial activities in the very low nanomolar range[4,5]. The anti-infective potency of lantibiotics such as nisin, mutacin, mersacidin and others has been recognized, and several are in the preclinical stages of medical application[6,7]. After translation, lantibiotics are modified and contain unusual amino acids such as dehydroalanine (Dha) and dehydrobutyrine (Dhb), which are covalently linked to the side chain of cysteine residues forming the so-called lanthionine rings[8,9]. The number as well as the exact location of the lanthionine rings vary within lantibiotics[10]. Lantibiotics have multiple modes of action, of which binding to lipid II, thereby inhibiting cell wall synthesis, and pore formation are the most predominant ones[8,11]. Nisin produced by *Lactococcus lactis* (*L. lactis*) is one of more than 50 lantibiotics discovered so far[12] and is considered to be the role model. Active nisin consists of 34 amino acids and contains five lanthionine-based rings (Supplementary Fig. 1). The first three rings (A-C) are separated from the other two intertwined rings (D-E) by a flexible hinge region. The first two rings are able to bind lipid II[13]; the hinge region and the last two intertwined rings are able to flip into the membrane and create a pore[14–16].

Due to their multiple modes of action, hardly any resistance against lantibiotics has developed over the past decades. However, some bacterial strains have been reported to be congenitally resistant against nisin[17] via various

[1]Institute of Biochemistry, Heinrich Heine University, Universitätsstr. 1, 40225 Düsseldorf, Germany. [2]Institute of Pharmaceutical and Medicinal Chemistry, Heinrich Heine University, Universitätsstr. 1, 40225 Düsseldorf, Germany. [3]Protein Production Facility, Heinrich Heine University, Universitätsstr. 1, 40225 Düsseldorf, Germany. [4]Crystal and X-ray Facility, Heinrich Heine University, Universitätsstr. 1, 40225 Düsseldorf, Germany. *These authors contributed equally to this work. Correspondence and requests for materials should be addressed to S.H.J.S. (email: sander.smits@hhu.de)

mechanisms such as cell wall modifications, biofilm formation or the expression of resistance proteins[18]. For the latter case, a *nsr* gene was identified in the *Streptococcus lactis* subspecies *diacetylactis* (DRC3) that encodes the nisin resistance protein, NSR[17,19]. Similar genes were identified in other species[17,20,21], including several human pathogenic strains[22,23]. NSR is a member of the S41 protease family, specifically the C-terminal processing peptidases (CTPs). NSR from *L. lactis* TS1640 has been shown to degrade nisin by cleaving the peptide bond between $MeLan_{28}$ in ring E and Ser_{29}. The resulting $nisin_{1\text{-}28}$ fragment displays a significantly lower bactericidal efficacy and reduced affinity towards cellular membranes[24]. Furthermore, the NSR protein from *S. agalactiae* ATCC 13813 induced a 20-fold increased resistance towards nisin when expressed in *L. lactis*[22].

NSR is localized within an operon comprising five genes, which encode for NSR, a two-component signaling system (NsrRK), and an ABC transporter (NsrFP). When expressed together, these proteins deliver full nisin resistance[22]. Interestingly, similar operon structures were also found to be associated with resistance against other lantibiotics[18,23]. These operons resemble (auto)-immunity systems found in lantibiotic producer[10] strains. Structures of SpaI from *B. subtilis*[25] conferring resistance against subtilin and MlbQ from the actinomycete *Microbispora* ATCC PTA-5024 conferring resistance against NAI-107[26] were resolved by NMR. However, no significant sequence identity is found between NSR and SpaI or MlbQ, suggesting a different mechanism for the defense against lantibiotics. Furthermore, most (auto)-immunity proteins do not cleave or manipulate the lantibiotic but rather shield the host's membrane from being harmed by its lantibiotic[10,27].

The ability of NSR to cleave nisin is impressive because it has been shown for several lantibiotics that they are not easily accessible for protease cleavage[14]. Here, the lanthionine rings are likely causing steric hindrance within the active site of proteases, thereby inhibiting proteolysis. Thus, notwithstanding the recent advances in this field, we still structurally know relatively little about lantibiotic resistance. In particular, the lantibiotic binding site in NSR and the mechanism how substrate specificity is conferred remains elusive. In this study, we report the first structure of a nisin resistance protein, NSR from *S. agalactiae* COH1 (*Sa*NSR). Mutagenesis studies guided by molecular dynamics (MD) simulations reveal that *Sa*NSR recognizes the lanthionine ring closest to the C- terminus of nisin and that this ring binds at one end of the catalytic tunnel, thereby determining the substrate specificity and ensuring the exact coordination of the nisin cleavage site at the catalytic site region.

Results

Crystal structure of *Sa*NSR. Nisin has been shown to be quite resistant against proteolytic digestion in general[14], supposedly due to the presence of lanthionine rings. Therefore, it is intriguing to understand the proteolytic resistance mechanism mediated by NSRs. To obtain a molecular view on this mechanism, we solved the structure of *Sa*NSR by X-ray crystallography.

Through sequence analyses, it was predicted that the first 30 amino acids encode for a transmembrane helix[28]. We deleted this N-terminal transmembrane helix and included a His_8-tag for purification purposes, resulting in soluble expression of *Sa*NSR. After over-expression, two-step purification yielded 5 mg of pure *Sa*NSR protein per liter of cell culture (Supplementary Fig. 2a). *Sa*NSR is a monomer in solution as determined by multiple angle light scattering (MALS) (Supplementary Fig. 2b). *Sa*NSR protein was crystallized and cubic crystals were obtained that diffracted up to 2.2 Å resolution[29]. We solved the structure by Single Anomalous Dispersion (SAD) phasing, using crystals of selenomethionine-substituted protein (data and refinement statistics are shown in Table 1).

The asymmetric unit (Supplementary Fig. 2c) contained four copies of *Sa*NSR that were virtually identical (root mean square deviation (RMSD) between the monomers = 0.15–0.5 Å over 300 amino acids). Therefore, the overall structure is described only for monomer A. The entire sequence of *Sa*NSR could be fitted into the electron density, with the exception of the N-terminal His_8-tag that was disordered. The R_{work} and R_{free} values after refinement were 0.19 and 0.24, respectively.

A *Sa*NSR monomer (Fig. 1) consists of eleven helices (α_1-α_{11}) and eleven β-strands (β_a-β_k), which form three domains: an N-terminal helical bundle and two protease subdomains. Altogether, these domains form a hydrophobic tunnel of ~10 Å width (Fig. 1b), which could very well harbor the nisin molecule. The N-terminal helical bundle (Fig. 1b, represented in green) comprises 65 amino acid residues (Lys_{31}-Gly_{96}), which form helices α_1-α_3. This domain ends in a triple glycine motif ($_{94}GGG_{96}$) before entering the protease cap domain (Fig. 1b, represented in red). The protease cap domain consists of helix α_4 and a β-hairpin structure formed by strands $\beta_{i\text{-}j}$. The protease cap forms a lid-like structure above the tunnel. The third domain is the so-called protease core domain (Fig. 1b, represented in grey), which adopts a 'protease fold' domain as observed in other S41 peptidases[30–32]. The protease core domain is formed by six strands β_b-β_g and five helices α_5-α_9. It contains the highly conserved TASSAEM region that harbors the previously identified catalytically active serine at position 236[22] (Fig. 1, represented in blue; Supplementary Fig. 3). The TASSAEM region lies in the tunnel between the two protease subdomains (Fig. 2a).

N-terminal helical bundle. A comparison of the N-terminal helical bundle with all available entries in the Protein Data Bank was performed using the Dali server[33]. The Dali server identifies similarities in 3D structures irrespective of sequence similarities. A structurally similar helical bundle has been identified in the human Factor H (Z-score of 5.2), which is responsible for tight binding of the pneumococcal protein virulence factor CbpA (choline-binding protein A)[34]. Furthermore, a similar helical bundle is present at the C-terminus of the 70 kDa human heat shock protein (HSP70) (Z-score of 5.0). This region is responsible for causing a structural switch during HSP70 allosteric activation, which is important for maintaining a proper conformation of the protein for binding to the J-domain and ATPase activity purposes[35]. Finally, a dynamic helical region is present at the N-termini of staphylococcal complement inhibitors (SCINs) (Z-score of 4.7), which is responsible for binding to the substrate C3b and is also necessary for the formation of higher order complexes of C3b, which blocks phagocytosis[36]. While these findings suggest that a certain degree of mobility of the found helical bundles is required for function, in three replicates of molecular dynamics (MD) simulations of a monomer of *Sa*NSR

	Native *Sa*NSR	SeMet *Sa*NSR
Data collection		
Space group	$P2_12_12_1$	$P4_32$
Cell dimensions		
a, b, c (Å)	58.8, 137.2, 164.0	186.1, 186.1, 186.1
α, β, γ (°)	90, 90, 90	90, 90, 90
Wavelength	0.87260	0.97625
Resolution (Å)	100.0–2.21 (2.29–2.21)	100.0–2.80 (2.9-2.8)
R_{merge}	11.5 (63.8)	29.3 (110.5)
$<I / \sigma (I)>$	8.67 (1.79)	20.33 (1.72)
Completeness (%)	99.6 (99.3)	99.8 (98.7)
Redundancy	4.5 (4.2)	75.6 (70.5)
Refinement		
Resolution (Å)	55.36-2.21 (2.28-2.21)	
No. reflections	303208 (27954)	
R_{work}/R_{free}	0.19 (0.27)/ 0.24 (0.31)	
No. of atoms	9588	
Protein	9017	
Ligand/ion	48	
Water	523	
B-factors (Å^3)	40.5	
Protein	40.3	
Ligand/ion	68.1	
Water	41.2	
R.m.s deviations		
Bond lengths (Å)	0.008	
Bond angles (°)	1.09	

Table 1. Data collection, phasing and refinement statistics for *Sa*NSR. *Values in parentheses are for highest-resolution shell.

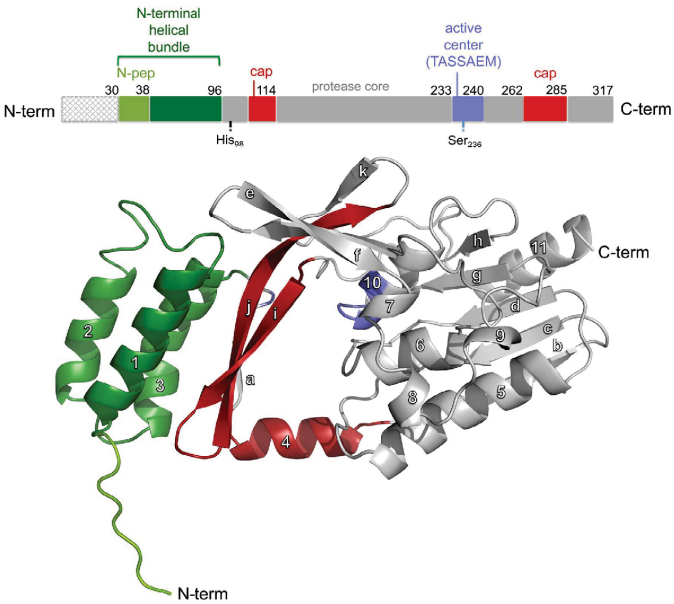

Figure 1. Structural architecture of the *Sa*NSR monomer. (**a**) Schematic illustration of the domain organization of *Sa*NSR indicating the domain borders and catalytically important residues (His_{98} and Ser_{236}). (**b**) The overall structure of a *Sa*NSR monomer in a cartoon representation. The N-terminal helical bundle is depicted in green where the light green region represents the N-pep. The protease cap and core domains are highlighted in red and grey, respectively. The catalytically important residues and the highly conserved "TASSAEM" region are depicted in blue.

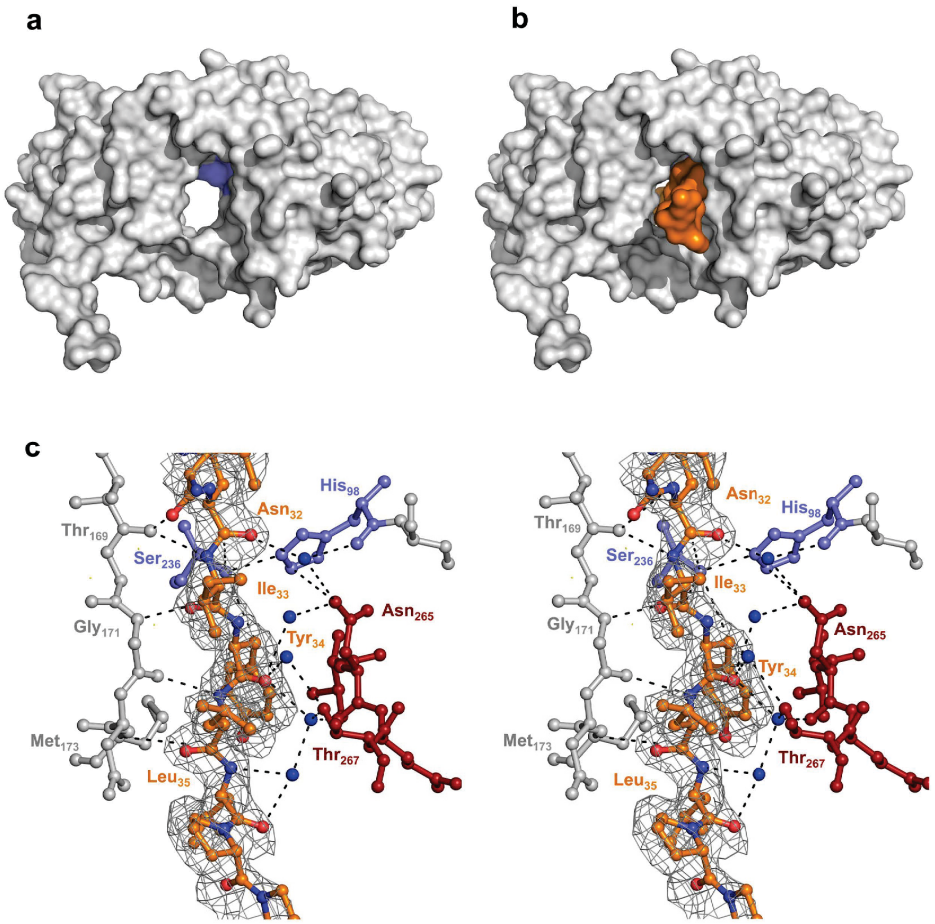

Figure 2. Surface representation of *Sa*NSR. (**a**) The surface representation of *Sa*NSR in white, highlighting the tunnel localized in between the protease cap and the core domain. The TASSAEM motif is colored in blue. (**b**) Surface representation of *Sa*NSR with bound N-pep (colored in orange). (**c**) Stereo view on the active site architecture of *Sa*NSR highlighting the N-pep that is bound within the tunnel as ball and stick representation. The corresponding $2F_oF_c$ omit electron density map is calculated at 2.2 Å and contoured at 1.0 σ. The water mediated interactions of N-pep (colored in orange) with residues of the protease cap (depicted in red) and the direct interactions with the residues of the protease core (grey color) are shown.

(termed NSR_{Apo}; see online methods for details), each of 500 ns length, the N-terminal helical bundle is rather immobile with respect to the protease core and cap domain (backbone root mean square fluctuations (RMSF) <2.5 Å; Supplementary Fig. 4a).

N-pep bound to *Sa*NSR. In the crystal structure, the hydrophobic tunnel is filled with the N-terminal residues $_{31}$KNIYLLPP$_{38}$ of a neighboring *Sa*NSR molecule (termed N-pep; Fig. 2b; shown in light green in Fig. 1). N-pep is predominantly bound to *Sa*NSR via direct backbone interactions to amino acids $_{167}$NNTGGN$_{172}$ of β-strand β_d, which is part of the protease core domain and is structurally located on the opposite site of the TASSAEM sequence motif (Fig. 2c). In addition, N-pep is stabilized via water-mediated hydrogen bonds between backbone atoms of Asn_{32}, Tyr_{34}, Leu_{35} and residues Asn_{265} and Thr_{267} of the protease cap domain (Fig. 2c). The presence of N-pep within the tunnel is clearly an induced artifact of the crystallization procedure, since in the full-length *Sa*NSR protein, another 30 amino acids are attached at the N-terminus of the N-pep sequence that form a transmembrane helix. Yet, during MD simulations of 500 ns length of a *Sa*NSR monomer complexed with N-pep (termed NSR_{Tail}; see online methods for details), N-pep remains stably bound within the hydrophobic tunnel (mean backbone RMSD < 1.6 Å; Supplementary Fig. 4b). The predominance of backbone interactions of N-pep with the protease core and cap domains could explain why N-pep binds into the putative binding region of nisin despite its sequence being very dissimilar to the one of nisin.

Substructures of nisin determining its molecular recognition. To investigate the substrate specificity of *Sa*NSR and determine substructures of nisin important for its recognition by the protein, we used different

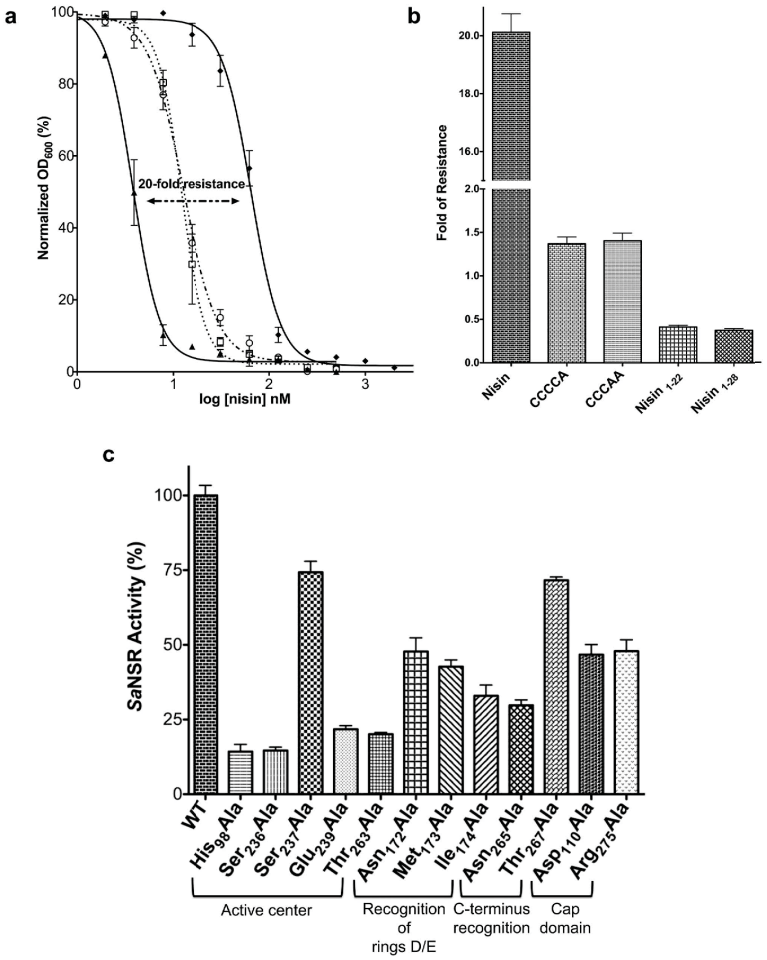

Figure 3. Influence of wild type *Sa*NSR and its mutations against nisin and its variants. (**a**) Growth inhibition experiment of *Sa*NSR with nisin. The activity of *Sa*NSR is determined using the *L. lactis* NZ9000 strain, where the plasmid encoding the *Sa*NSR wildtype and the mutations were transformed, and the IC_{50} against nisin was determined. As a control, the empty vector was transformed and used in the IC_{50} study (termed NZ9000Erm). Black lines represent the NZ9000Erm (filled Δ) and NZ9000-*Sa*NSR (◆) strains, respectively. The black dotted lines represent the NZ9000-*Sa*NSR-His_{98}Ala (□) and NZ9000-*Sa*NSR-Ser_{236}Ala (O) strains. The data were fitted and evaluated as described in ref. 51. The difference in the growth exhibited by the strains was used to calculate the percentage of activity. Each experiment was performed at least in triplicates. (**b**) Graphical representation of the fold of resistance exhibited by *Sa*NSR with nisin and different nisin variants (CCCCA, CCCAA, $nisin_{1\text{-}22}$ and $nisin_{1\text{-}28}$). The NZ9000Erm and NZ9000*Sa*NSR strains were used to determine the activity of all the nisin variants. The error bars indicate the standard error of at least three independent experiments. (**c**) The activity of *Sa*NSR and its mutations is determined using the *L. lactis* NZ9000 strain. A normalization of the IC_{50} values were done by setting the values exhibited by the empty vector (NZ9000Erm) and NZ9000*Sa*NSR to 0% and 100%, respectively. The error bars indicate the standard error of at least three independent experiments.

nisin variants. In order to test the influence of rings D and E located next to the cleavage site of nisin, we genetically replaced the last or the last two cysteine(s) in nisin by alanine, resulting in the expression of active nisin containing only rings A-D (termed CCCCA) or A-C (termed CCCAA), respectively[27]. Similarly, we removed the last six amino acids of nisin (termed $nisin_{1\text{-}28}$), resulting in the product of the proteolysis reaction mediated by *Sa*NSR. Furthermore, a truncated variant ($nisin_{1\text{-}22}$) was expressed, which contained the rings A-C but lacked the rest of the C-terminus of nisin[27]. Since all variants show a different activity against the nisin sensitive *L. lactis* NZ9000Erm strain (Supplementary Table 1a), we analyzed them with respect to the fold of resistance mediated by the expression of the *Sa*NSR protein in the NZ9000*Sa*NSR strain. From current and previous work, it is known that *Sa*NSR confers a 20-fold increased resistance against wildtype nisin (Fig. 3a)[22].

For CCCCA as well as CCCAA, the resistance mediated by *Sa*NSR decreased to roughly 1.4–1.7 fold when comparing the IC_{50} values of the different strains (Fig. 3b; Supplementary Table 1a). For the truncated variants, $nisin_{1\text{-}22}$ and $nisin_{1\text{-}28}$, no resistance was observed anymore as the IC_{50} values dropped to the levels observed for the NZ9000Erm strain. Thus, the lanthionine ring E is clearly important for the recognition by *Sa*NSR.

Structural model of nisin binding to *Sa*NSR. Despite intensive trials, we were not successful in obtaining a crystal structure of a *Sa*NSR/nisin complex. Thus, we resorted to generating a structural model by integrative modeling and validating it by mutagenesis studies. Initially, we structurally aligned the backbone of residues 31–36 of nisin to the backbone of N-pep such that the nisin cleavage site between ring E and Ser_{29} was oriented towards the catalytically active Ser_{236} in *Sa*NSR. Rings D and E were then manually placed in three orientations at the tunnel entrances such that they showed good complementarity with the *Sa*NSR surface. This resulted in three structural models of *Sa*NSR/nisin complexes, two (termed $NSR_{Nisin,1}$, $NSR_{Nisin,2}$) where rings D and E are located close to Asn_{172}, Met_{173}, and Ile_{174}, and one (termed $NSR_{Nisin,3}$) where nisin is oriented oppositely with respect to the tunnel axis such that Tyr_{261} stacks onto rings D and E (Supplementary Fig. 5a). The three models were subjected to MD simulations[37] of 500 ns length, with three replicate simulations each.

The average distances between the side chain oxygen of Ser_{236}, previously identified as the catalytically active serine[22], and the carbonyl carbon of Ser_{29} at the nisin cleavage site[24] are 3.71 Å, 4.13 Å, and 7.74 Å for $NSR_{Nisin,1}$, $NSR_{Nisin,2}$ and $NSR_{Nisin,3}$, respectively (Fig. 4a). This strongly indicates that a nucleophilic attack of the side chain of Ser_{236} at the nisin cleavage site as a first step in the catalytic mechanism[24] is possible for the first two models but not for the third, suggesting that $NSR_{Nisin,1}$ and $NSR_{Nisin,2}$ represent the most likely orientation of nisin within the *Sa*NSR tunnel. Thus, we focused further analyses on the $NSR_{Nisin,1}$ and $NSR_{Nisin,2}$ models.

Visual inspection of the MD trajectories and computations of the backbone RMSF identified residues Lys_{22}, His_{31}, Val_{32}, Dha_{33}, and Lys_{34} of nisin as highly mobile (RMSF values up to $6.39\,Å \pm 0.49\,Å$) (Fig. 4b). In contrast, the core region ($Nisin_{Core}$) composed of the rings D and E, and residues Ser_{29} and Ile_{30} revealed RMSF values $< 1.85\,Å \pm 0.24\,Å$ (Fig. 4b) suggesting a tightly bound $Nisin_{Core}$ region. This was corroborated by a per-residue decomposition of effective binding energies computed by the MM-PBSA approach[38]. Here, rings D and E (treated as one residue in the energy decomposition) and Ile_{30} are identified as essential for nisin binding (residue-wise effective binding energies in the range from $-4.26\,kcal\,mol^{-1}$ to $-8.63\,kcal\,mol^{-1}$) (Fig. 4c). In contrast, for Ser_{29}, a smaller contribution to the effective binding energy of $-1.64\,kcal\,mol^{-1}$ ($-0.70\,kcal\,mol^{-1}$) for $SaNSR_{Nisin,1}$ ($SaNSR_{Nisin,2}$) was found (Fig. 4c). Overall, this suggests that the rings D and E as well as Ile_{30} form a binding motive, that way ensuring that also Ser_{29} at the nisin cleavage site is correctly positioned within the catalytic site.

In Figure 4d, a representative set of six nisin structures within the *Sa*NSR tunnel is shown. For this, the structure with the smallest backbone RMSD to the average structure was extracted from each of the $NSR_{Nisin,1}$ and $NSR_{Nisin,2}$ MD trajectories. The set shows that the location and orientation of rings D and E, Ser_{29}, and Ile_{30} agree well in all cases, with RMSD values with respect to the average structure for the $Nisin_{Core}$ ranging from 0.80 Å to 2.27 Å (Supplementary Fig. 5b). Thus, both $NSR_{Nisin,1}$ and $NSR_{Nisin,2}$ models were considered equivalent and used to identify residues in *Sa*NSR important for catalysis and nisin binding for mutagenesis studies. The remaining residues of nisin show large structural deviations, in agreement with the above analyses (Supplementary Fig. 5b, Fig. 4b,c).

The TASSAEM region and His_{98} form the active site. The NSR superfamily contains a highly conserved sequence motif "TASSAEM" (Supplementary Fig. 3) located at the rear end of the protease core domain. Within this TASSAEM region, Ser_{236} has been previously identified as the catalytically active serine[22]. This serine is in close proximity to the strictly conserved His_{98} residue, which is localized at the end of the N-terminal helical bundle directly next to the $_{94}GGG_{96}$ motif (Fig. 1) and is in hydrogen bonds distance with the side chain of Ser_{236}. In the $NSR_{Nisin,1}$ and $NSR_{Nisin,2}$ MD simulations, hydrogen bonds were found in up to ~23% of all conformations (Supplementary Fig. 6a), which indicates that both residues likely interact also in the nisin-bound state. Based on the interactions of Ser_{236} and His_{98} and the absence of any other lysine or aspartate residue localized nearby, we presume that *Sa*NSR acts via a catalytic dyad mechanism as observed for some other serine proteases[39,40]. The NZ9000*Sa*NSR-Ser_{236}Ala strain displayed a low background activity as observed by an IC_{50} value of 12.6 ± 0.7 nM (Supplementary Table 1b), which relates to a *Sa*NSR residual activity of 14% (Fig. 3c). The His_{98}Ala mutation displayed a similar IC_{50} value of 12.3 ± 1.5 nM and a residual activity of 14% (Fig. 3c, Supplementary Table 1a). The residual activity displayed by both variants is likely due to the binding of nisin to that particular *Sa*NSR variant such that a higher concentration of nisin is required to kill the corresponding nisin sensitive NZ9000Erm *L. lactis* strain.

Within the TASSAEM sequence, a second serine residue, Ser_{237}, is present. In the $NSR_{Nisin,1}$ and $NSR_{Nisin,2}$ MD simulations, the mean distance between the side chain oxygen and the carbonyl carbon of ring E is < 5.7 Å (Supplementary Fig. 6b). However, the distance to the δ-nitrogen of His_{98} is > 9 Å (Supplementary Fig. 6c), and no hydrogen bonds were detected between both residues, making a proton shift between Ser_{237} and His_{98} unlikely. Instead, we observed hydrogen bond formation between the side chain of Ser_{237} and the backbone of Gly_{171} of the protease core in at least 46% of the conformations that may be relevant for nisin recognition (see section "Residues involved in nisin recognition and *Sa*NSR specificity") but not for catalytic activity. Thus, Ser_{237} is not expected to be involved in the catalytic mechanism. In accordance, a Ser_{237}Ala mutation does not have a pronounced effect on the activity of *Sa*NSR (residual activity 74%; see Fig. 3c, Supplementary Table 1b).

The next residue in the TASSAEM motif is Glu_{239}, which is pointing away from the active site. In the crystal structure, the Glu_{239} side chain interacts with backbone atoms of Gly_{260} and Tyr_{261} via hydrogen bonds, and during the $NSR_{Nisin,1}$ and $NSR_{Nisin,2}$ MD simulations this interaction is present in at least 82% of all conformations (Supplementary Fig. 6a). Additionally, we found hydrogen bond interactions between Glu_{239} and Ser_{236} in at least 25% of the cases (Supplementary Fig. 6a). These interactions are likely important for the correct positioning of the TASSAEM region. This is in line with the drastically lowered activity of the Glu_{239}Ala mutant (IC_{50} value

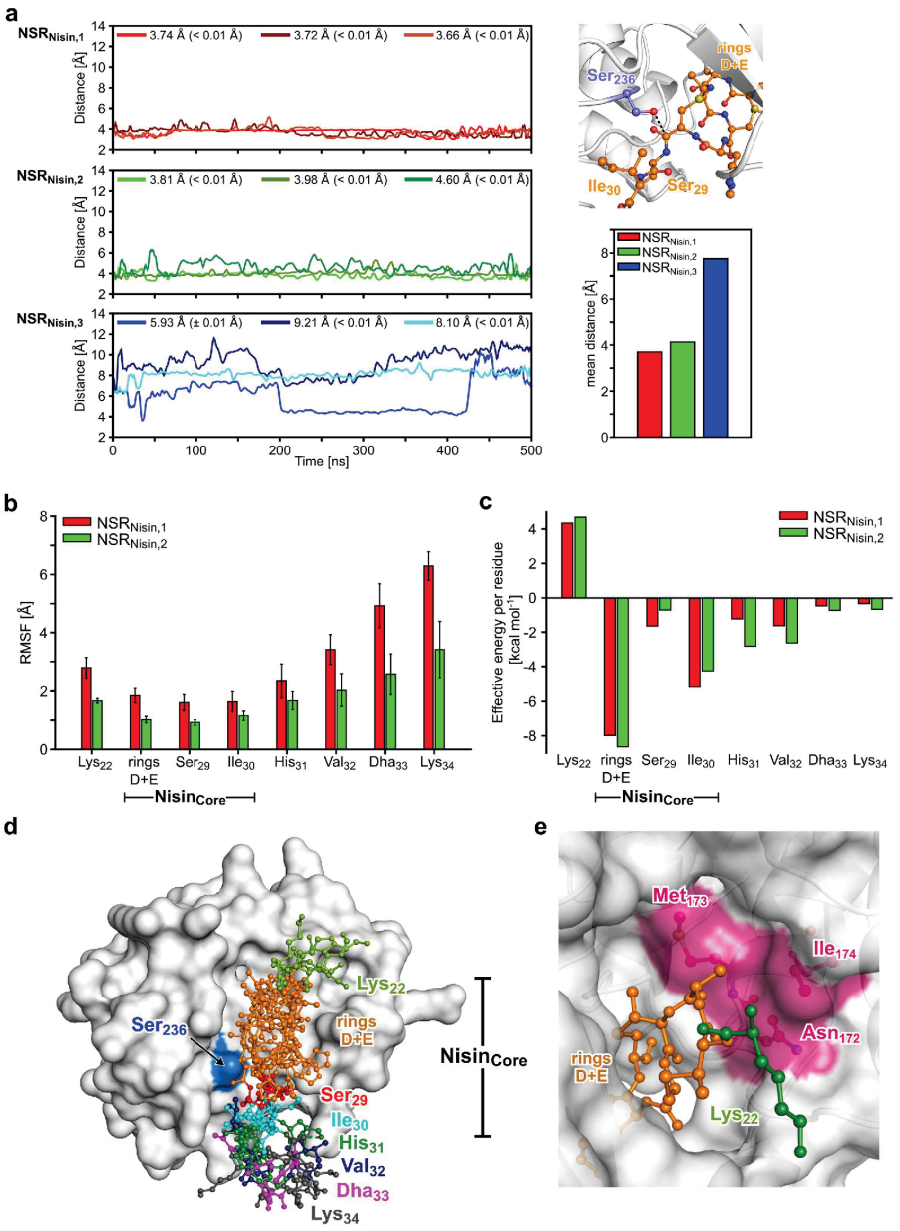

Figure 4. Structural and energetic analysis of MD simulations of *Sa*NSR/nisin model complexes. (**a**) Distance between the side chain oxygen of Ser_{236} and the carbonyl carbon of ring E at the nisin cleavage site (black dotted line in the upper right panel) in $NSR_{Nisin,\{1,2,3\}}$ during 500 ns of MD simulations; lines were smoothed by cubic splines. Mean values and standard error of the mean (SEM; in parentheses) are shown in the legend. The mean distance over all three MD simulations is shown in the lower right panel (SEM < 0.1 Å and not shown). (**b**) Mean backbone RMSF (SEM indicated as error bars) for $NSR_{Nisin,\{1,2\}}$ models over three trajectories each of 500 ns length. Rings D and E, Ser_{29}, and Ile_{30} compose the $Nisin_{Core}$. (**c**) Mean effective binding energy per residue for $NSR_{Nisin,\{1,2\}}$ models. Error bars indicate SEM over three trajectories. (**d**) Superimposition of six close-to-average structures (based on the backbone RMSD) of nisin (ball-and-stick models each colored differently), extracted from three independent MD simulations each of $NSR_{Nisin,1}$ and $NSR_{Nisin,2}$, within the tunnel of *Sa*NSR (white surface representation). Ser_{236} of the catalytic dyad is colored in blue. For clarity, the N-terminal helical bundle and part of the cap region of *Sa*NSR have been omitted. (**e**) Representative nisin model (orange and green ball-and-stick model) within the tunnel of *Sa*NSR (white cartoon representation with transparent surface). Residues Asn_{172}, Met_{173}, and Ile_{174} that bind to rings D and E are colored in magenta.

of 17.1 ± 0.7 nM; residual activity of 22%; Fig. 3c, Supplementary Table 1b). Furthermore, we found stabilizing hydrogen bonds between Thr_{263} and His_{98} in up to ~28%, and between Asn_{265} and His_{98} in up to ~20% of all cases (Supplementary Fig. 6a). These interactions likely ensure a correct orientation of His_{98} as the mutations Thr_{263}Ala and Asn_{265}Ala decreased the residual activities of *Sa*NSR to 20% and 30%, respectively, (Fig. 3c) with associated IC_{50} values of 16.0 ± 0.3 and 22.1 ± 1.1 nM (Supplementary Table 1b). Taken together, the TASSAEM sequence is crucial for the activity of *Sa*NSR and contains the catalytically active serine as well as a glutamic acid residue, which is likely responsible for a correct positioning of the TASSAEM helix.

Residues involved in nisin recognition and *Sa*NSR specificity. Next, we investigated nisin recognition by *Sa*NSR. Residue-wise effective binding energies were computed for both the $NSR_{Nisin,1}$ and $NSR_{Nisin,2}$ MD trajectories to identify *Sa*NSR residues likely to be important for nisin binding (Supplementary Fig. 7a). Considering energies < -0.8 kcal mol^{-1} resulted in seven candidates (Leu_{102}, Leu_{137}, Asn_{172}, Met_{173}, Ile_{174}, Glu_{266}, Ala_{277}). Our model (Fig. 4d) suggests that the hydrophobic residues Leu_{102}, Leu_{137}, Met_{173}, Ile_{174}, Ala_{277} and the polar/charged ones Asn_{172} and Glu_{266} bind to rings D and E in nisin. Asn_{172}, Met_{173}, and Ile_{174} form a pocket that harbors rings D and E in our model (Fig. 4e). The Asn_{172}Ala mutant displayed an activity of 47% (IC_{50} value of 33.5 ± 2.9 nM) (Fig. 3c, Supplementary Table 1b). Furthermore, when mutating the strictly conserved Met_{173} residue (Supplementary Fig. 3), a reduced activity of 42% compared to the wild type value was observed (IC_{50} value of 30.3 ± 1.4 nM). Additionally, the Ile_{174}Ala mutant exhibited an activity of 33% (IC_{50} value of 24.1 ± 2.2 nM) (Fig. 3c, Supplementary Table 1b).

Moreover, we found hydrogen bonds between backbone atoms of Thr_{169} and Gly_{171} with the $Nisin_{Core}$ residues (Supplementary Fig. 7b). These interactions are reminiscent to those found for N-pep (Fig. 2c) and likely ensure a proper placement of the $Nisin_{Core}$ within the binding site. Additional stabilizing hydrogen bonds were observed between Asn_{168} and Gly_{170} (Supplementary Fig. 7b), which could contribute to nisin binding indirectly. A similar indirect effect was found for Glu_{266}, for which we observed salt-bridge formation with Arg_{54} from the N-terminal helical bundle (Supplementary Fig. 7c; mean distance <3.4 Å). We also found water-mediated hydrogen bonds between backbone atoms of rings D and E, and Asn_{265} and Thr_{267}, respectively (Supplementary Fig. 7d), again mimicking what was observed for the bound N-pep (Fig. 2c). Accordingly, the mutations Asn_{265}Ala (see above) and Thr_{267}Ala decreased the residual activity of *Sa*NSR to 30% and 71%, respectively, (Fig. 3c) with associated IC_{50} values of 22.1 ± 1.1 and 48.5 ± 0.6 nM (Supplementary Table 1b).

Role of the protease cap domain in *Sa*NSR. Other S41 peptidases also contain a protease cap domain comprising a helix and a β-hairpin structure, where the helix appears to open and close depending on the presence of the peptide substrate: once a peptide is bound, the cap closes and seals the active site. As such, the protease CtpB from *Bacillus subtilis* has been crystallized in an open and closed state with the helix of the protease cap moving by 10–15 Å towards the active site once the peptide was bound[30]. In *Sa*NSR, helix α_4 ($_{103}$SKETVRRDTLDS$_{114}$) was identified as the protease cap helix, localized directly after the N-terminal helical bundle. Out of all residues of this helix, only the side chain of Asp_{110} is intruding into the tunnel, which neither forms an interaction to N-pep in the crystal structure nor in the NSR_{Tail} MD simulations. This suggests that the protease cap is not adopting a fully closed state, rather an intermediate state. MD simulations show a salt-bridge formation between Asp_{110} and Arg_{275} of the protease cap domain for both $NSR_{Nisin1,2}$ models (Supplementary Fig. 8a). In those cases where the salt-bridge formation is weak (mean distance is > 10 Å), a loss of the secondary structures of helix α_4 is observed (Supplementary Fig. 8b). The Asp_{110}Ala mutant of *Sa*NSR is still active although with a lower IC_{50} value of 32.8 ± 2.1 nM (residual activity of 46%; Fig. 3c, Supplementary Table 1b). The Arg_{275}Ala mutant revealed an identical IC_{50} value of 33.6 ± 2.3 nM (residual activity of 48%). Taken together, this suggests that a proper secondary structure of helix α_4 is required for *Sa*NSR function, and that Asp_{110} contributes to the stability of the secondary structure.

Discussion

The present study reveals that the lanthionine ring E of nisin determines substrate specificity of the nisin resistance protein (NSR) and contributes to the coordination of the nisin cleavage site at the catalytic center. These results are based on the first structure of a nisin resistance protein from *S. agalactiae* COH1 (*Sa*NSR) at 2.2 Å resolution and subsequent integrative modeling and mutagenesis studies. The *Sa*NSR structure consists of an N-terminal helical bundle, a protease cap domain, and a protease core domain (Fig. 1). The core domain harbors the highly conserved TASSAEM motif, which contains the catalytically important Ser_{236} residue, in a hydrophobic tunnel formed by all three domains. In this tunnel, an N-terminal peptide from another *Sa*NSR protomer (N-pep) in the asymmetric unit is bound predominantly by direct and water-mediated backbone hydrogen bonds (Fig. 2). A very similar binding pattern is found for the C-terminal lanthionine rings D and E, and residues Ser_{29}, and Ile_{30} of nisin in our model of the *Sa*NSR/nisin complex (Fig. 5a,b; Supplementary Fig. 7d). According to this model, lanthionine ring E binds at one end of the hydrophobic tunnel (Fig. 5a,b) and ensures the exact coordination of the nisin cleavage site at the highly conserved TASSAEM region (Fig. 5a,b).

In contrast to some other C-terminal processing proteases[30,32], the active center of *Sa*NSR consists of a catalytic dyad formed by residues Ser_{236}[22], which is part of the TASSAEM motif, and His_{98} as determined by mutational analysis and also described for some other proteases[41] (Fig. 5a–c). Mutational analysis and geometric parameters in the crystal structure and during MD simulations exclude that the neighboring Ser_{237} participates in the catalytic step. Residues Glu_{239}, Gly_{260}, Tyr_{261} and Thr_{263}, form hydrogen bonds with either Ser_{236} or His_{98} during all-atom MD simulations of the *Sa*NSR/nisin complexes (Supplementary Fig. 6a, Figure 5a–c) and, thus, likely stabilize the catalytic residues, as also indicated by alanine mutations of these residues that lead to a decrease in *Sa*NSR activity (Fig. 3c).

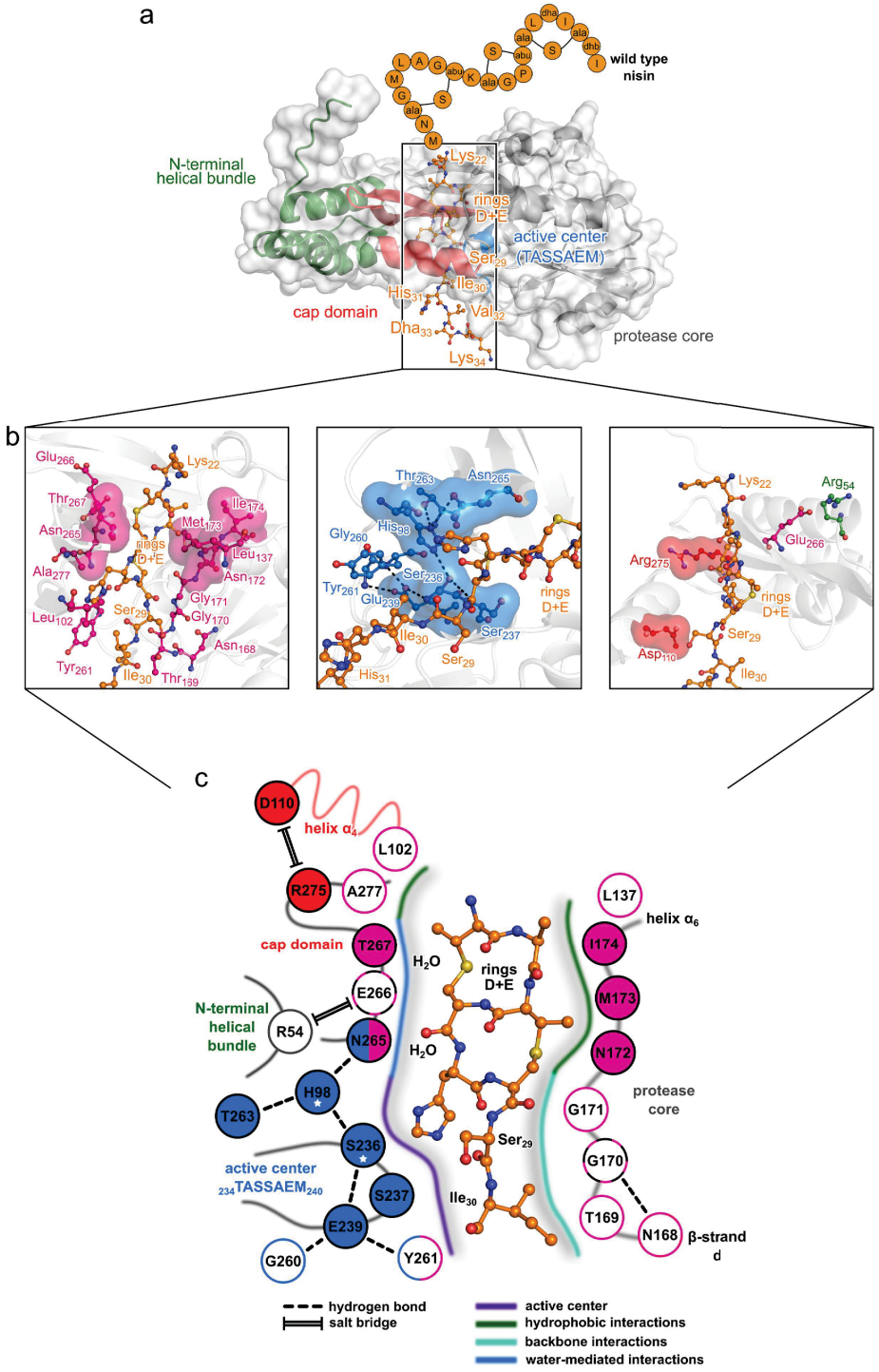

Figure 5. Nisin/*Sa*NSR binding model. (**a**) Representative structure of nisin (residues 22-34; extracted from the $NSR_{Nisin,1}$ model) bound to the crystal structure of *Sa*NSR (cartoon representation with transparent surface; each domain is colored differently). Orange spheres with one-letter/three letter amino acid code indicate nisin residues 1–21 not considered for modeling studies (abbreviations: abu = aminobutyric acid; dha = dehydroalanine; dhb = dehydrobutyrine; ala-S-X = lanthionine derivatives). (**b**) Close up view of nisin binding to *Sa*NSR residues important for nisin recognition (left), residues with catalytic function (middle),

and residues with a regulatory function (right). Amino acids of interest are depicted as ball-and-stick model; residues for which experimental data is reported in this study are, additionally, shown in transparent surface representation. (**c**) Schematic representation of the $Nisin_{core}$ bound to *Sa*NSR residues (residue numbers according to the crystal structure described here). Residues that compose the catalytic site are colored in blue, residues that contribute to nisin binding in magenta, residues that have an indirect effect on binding in black-magenta, and residues with a supposedly regulatory function in *Sa*NSR in red. For residues with colored background, *Sa*NSR activity information for alanine mutants is available (see Fig. 3c). Residues marked with a star form the catalytic dyad. In panels a, b, and c, the nisin structure is depicted as orange ball-and-stick model.

Since all our efforts to obtain crystals of *Sa*NSR with bound nisin were unsuccessful, we generated a model (Fig. 5a–c) of the *Sa*NSR/nisin complex by integrative modeling and subsequent site-directed mutagenesis studies and activity measurements for validation. The modeling step was guided by exploiting the knowledge on the location of N-pep in the *Sa*NSR crystal structure as well as on the substructures of nisin determining its molecular recognition. As to the latter, we focused on the C-terminus of nisin ($nisin_{22-34}$) where NSR from *L. lactis* TS1640 has been shown to cleave[24]. As a result, nisin variants in which the bulky lanthionine rings D and E, or only E, were replaced by a linear sequence (CCCCA, CCCAA) showed a large drop in the fold of resistance comparable to those exhibited when the last 12 or 6 residues of nisin ($nisin_{1-22}$, $nisin_{1-28}$) were missing (Fig. 3b). These results demonstrated that ring E is essential for nisin recognition by *Sa*NSR.

Initial models of *Sa*NSR/nisin complexes were generated in which the linear, C-terminal sequence (sequence Lys_{22} - Lys_{34}) were placed at the location of the backbone trace of N-pep and where rings D and E showed a good complementarity with the *Sa*NSR surface at the tunnel entrance. We considered that no *a priori* knowledge on the direction of nisin with respect to the tunnel axis was available by generating models with both possible directions. By subsequent all-atom MD simulations, we could exclude one of the possibilities ($NSR_{Nisin,3}$) as in this case the distance between Ser_{236} and the nisin cleavage site was too large as to allow for a nucleophilic attack of the serine side chain (Fig. 4a). In contrast, for the other direction ($NSR_{Nisin,1}$, $NSR_{Nisin,2}$), such an attack is very likely according to distances that are only slightly larger than the sum of van der Waals radii of oxygen and carbon. This model of a *Sa*NSR/nisin complex is further supported by rather immobile residues of the core region of nisin (rings D and E, Ser_{29} and Ile_{30}), which is considered to facilitate a nucleophilic attack, in contrast to the more mobile C-terminal residues 31-34 (Fig. 4b), and by a residue-wise decomposition of the effective binding energy, which identified rings D and E as well as Ile_{30} as major contributors to the binding affinity (Fig. 4c).

The model (Fig. 5a–c) reveals that *Sa*NSR binding to rings D and E of nisin is dominated by hydrophobic interactions (Fig. 5b,c). Within the protease core Asn_{172}, Met_{173}, and Ile_{174} form a pocket that harbors both rings D and E (Figs 4e,5b). In agreement with this model, mutation of these residues reduces the activity of *Sa*NSR. Furthermore, water-mediated hydrogen bonds between backbone atoms of rings D and E and side chains of Asn_{265} and Thr_{267}, respectively, were identified, mimicking interactions with N-pep. Asn_{265}Ala and Thr_{267}Ala mutations decreased the residual activity of *Sa*NSR (Fig. 3c). Finally, along the tunnel, hydrogen bonds between backbone atoms of Thr_{169} and Gly_{171} of *Sa*NSR with Ser_{29} and Ile_{30} of nisin were found (Fig. 5b,c; Supplementary Fig. 7b), which likely contribute towards the correct orientation of the nisin cleavage site at the catalytic center and are again reminiscent of interactions observed for N-pep in the crystal structure.

N-pep and the C-terminus of nisin are not similar on the amino acid level. Together with the above findings of similar interactions along the tunnel between backbone atoms of *Sa*NSR and the two peptides, respectively, this suggests that the tunnel's role in peptide binding is not to confer substrate specificity but rather to "rope in" the peptide while establishing these interactions. In the case of nisin, this "roping in" is stopped when the lanthionine ring E starts interacting with *Sa*NSR, thereby acting as a plug on the tunnel (Fig. 5c). These interactions are highly relevant for the molecular recognition of nisin and the substrate specificity of *Sa*NSR, as shown by a decrease in the fold of resistance for the nisin variants CCCCA and CCCAA (Fig. 3b) and a decrease in the activity of *Sa*NSR mutants Asn_{172}Ala, Met_{173}Ala, and Ile_{174}Ala (Fig. 3c). In addition, rings D and E are highly likely relevant for a proper placement of the nisin cleavage site with respect to the catalytic Ser_{236}, as only with nisin a distance to this residue compatible with a nucleophilic attack and, simultaneously, hydrogen bonds with His_{98} are found in the MD simulations. In contrast, during MD simulations of NSR_{Tail}, no hydrogen bond formation between Ser_{236} and His_{98} was detected. This may explain why N-pep binds to *Sa*NSR but is not cleaved.

Previously, an "inhibiting role" of lanthionine rings has been recognized in that they protect lantibiotics from degradation by standard proteases[42], likely because of their bulky 3D structure which prevents a proper placement in the substrate binding regions of proteases evolved to cleave linear peptides. In turn, the findings in this study for the first time reveal a significant "fostering role" of the lanthionine rings D and E in nisin for the highly specific cleavage of this lantibiotic by *Sa*NSR. These findings and our structural model of the *Sa*NSR/nisin complex open up a new avenue in the understanding of lantibiotic resistance by human pathogens. They may also facilitate the development of therapeutics to overcome nisin resistance.

Methods

Cloning, expression and purification of *Sa*NSR. The *nsr* gene from *Streptococcus agalactiae* COH1 was cloned into pET28b and purified as previously described. For details see Supplementary Information.

Multiple angle light scattering. For HPLC-MALS analysis, a Bio SEC-5 HPLC column (Agilent Technologies Deutschland GmbH, Böblingen, Germany) with a pore size of 300 Å was equilibrated with 25 mM MES pH 6.0, 150 mM NaCl for HPLC using a system from Agilent Technologies connected to a triple-angle light-scattering detector (miniDAWN TREOS, Wyatt Technology Europe GmbH, Dernbach, Germany) followed

by a differential refractive index detector (OPTILab T-rEX, Wyatt Technology). Typically, 100 µl of purified *Sa*NSR (2.0 mg/ml) was loaded onto the Bio SEC-5 HPLC column, and the obtained data were analyzed with the ASTRA software package (Wyatt Technology).

Crystallization, data collection and structure determination of *Sa*NSR. Crystals were obtained and optimized as described in the Supplementary Information. X-ray diffraction data were collected at the ID23eh2 or ID29 beamlines of the European Synchrotron Radiation Facility (ESRF), Grenoble. All the data sets were processed and scaled using XDS and XSCALE software package[43]. Data sets from native crystals were collected at a wavelength of 0.872 Å at 100 K. For selenomethionine-substituted crystals, the ID29 beamline (ESRF Synchrotron, Grenoble)[44] was used for anomalous diffraction data collection, done at 100 K. The structure was solved by single-wavelength anomalous dispersion (SAD) from a single selenomethionine derivative crystal measured at 0.976 Å, which diffracted up to 2.7 Å. The Auto-Rickshaw program[45] was then used to phase the protein and build an initial model, which was further manually build and refined using COOT[46] and phenix.refine from the Phenix package[47]. This model was then used to phase the native data set at a resolution of 2.2 Å. After molecular replacement, automatic model building was performed with the program ARP/wARP[48], followed by manual iterative cycles of model refinement using the program phenix.refine[47]. Manual adjustments between the refinement cycles were done with the program Coot[46] and Ramachandran validation was done using MolProbity[49]. Almost all residues (96.3%) were in the preferred regions of the Ramachandran plot, and the remaining 3.7% were in the additionally allowed regions. The data collection and refinement statistics are listed in Table 1. The images of the models were prepared using MacPyMOL[50].

IC_{50} determination of nisin and its variants. Cells from the different expressing strains were grown overnight in GM17 media supplemented with 5 $\mu g ml^{-1}$ erythromycin in the presence of 1 $ng ml^{-1}$ nisin. The diluted cells (final OD_{600} of 0.1) were incubated with a serial dilution of nisin or its variants in a 96-well plate. The total volume in each well was 200 µl, consisting of 50 µl nisin or its variants and 150 µl GM17 containing the corresponding *L. lactis* strain. The plate was then incubated at 30 °C and after 5 hours, the optical density was measured at 600 nm *via* 96-well plate reader BMG. The IC_{50} value was determined as previously described[51].

Molecular dynamics simulations. In order to investigate nisin recognition by *Sa*NSR we performed molecular dynamics (MD) simulations of an unbound *Sa*NSR monomer (NSR_{Apo}), a *Sa*NSR monomer bound to the N-terminal part of *Sa*NSR (residues 31–36; in the following named "Tail") from an adjacent subunit (NSR_{Tail}) in the crystal structure (see Fig. 1), and a *Sa*NSR monomer bound to the C-terminal part (residues 22–34; Supplementary Fig. 2c) of nisin (NSR_{Nisin}). Initial coordinates for NSR_{Apo} and NSR_{Tail} were taken from the crystal structure described here. Since no structural information is available for nisin bound to *Sa*NSR, we generated models as starting structures for MD simulations by structurally aligning the nisin part to the Tail using the program Moloc. The nisin cleavage site between ring E and Ser_{29} was oriented towards the catalytically active Ser_{236} in *Sa*NSR[22]. Rings D and E were manually placed in three orientations within the binding site such that they showed good complementarity with the *Sa*NSR surface, resulting in three different models of *Sa*NSR/nisin complexes ($NSR_{Nisin,1}$, $NSR_{Nisin,2}$, and $NSR_{Nisin,3}$, Supplementary Fig. 4a).

For the MD simulations, structures of NSR_{Apo}, NSR_{Tail}, and $NSR_{Nisin,1\text{-}3}$ were prepared, relaxed, and thermalized as described in detail in the Supporting Information. Three independent production runs of MD simulations of 500 ns length in the canonical (NVT) ensemble at 300 K were then conducted for each of the five systems, leading to a total simulation time of $5 \times 3 \times 500\,ns = 7.5\,\mu s$; see Supporting Information for details.

The trajectories were analyzed with respect to distances, root mean square fluctuations (RMSF) and deviations (RMSD) as a measure for mobility and structural similarity, respectively, and hydrogen bonds defined by a distance between the two donor and acceptor atoms <3.2 Å and an angle (donor atom, H, acceptor atom) between 120° and 180° using *cpptraj*[52]. Salt-bridge interactions are defined by a distance <4.0 Å between the center of mass of both charged groups. The set of structural models binding to *Sa*NSR (see section "Structural model of nisin binding to *Sa*NSR) was generated by structurally aligning *Sa*NSR and subsequent RMSD calculations for the nisin peptide.

Calculation of the effective binding energy. In order to identify amino acids in *Sa*NSR that contribute most to nisin binding, we computed the residue-wise contribution to binding effective energies by the "single trajectory" molecular mechanics Poisson-Boltzman area (MM-PBSA) approach[53–55]. To determine the per-residue contribution, the decomposition scheme[56] as implemented in the mm_pbsa.pl script in Amber 14[37] was applied. The calculations were performed with the ff99SB force field[57,58]. The polar part of the solvation free energy was determined by applying the PBSA solver using a dielectric constant of 1 (solute) and 80 (solvent) together with Parse radii[59]. The conformational ensemble consists of 10,000 snapshots and was extracted from the 1–200 ns interval of each of the $NSR_{Nisin,1\text{-}2}$ trajectories. Prior to the MM-PBSA computations, counter ions and water molecules were stripped from the snapshots. For the computations, we considered the *Sa*NSR protein the receptor, whereas the nisin C-terminus was considered the ligand. All residues in *Sa*NSR and nisin were considered for per-residue decomposition. Rings D and E in nisin were treated as one residue.

PDB Deposition

The final model has been deposited in the PDB database under the accession code: 4Y68.

References

1. Levy, S. B. Antibiotic Resistance: Consequences of Inaction. *Clin. Infect. Dis.* **33,** S124–S129 (2001).
2. Ling, L. L. *et al.* A new antibiotic kills pathogens without detectable resistance. *Nature* **517,** 455–459 (2015).

3. Sahl, H.-G. & Bierbaum, G. Lantibiotics: biosynthesis and biological activities of uniquely modified peptides from gram-positive bacteria. *Annu. Rev. Microbiol.* **52,** 41–79 (1998).
4. Willey, J. M. & van der Donk, W. A. Lantibiotics: peptides of diverse structure and function. *Annu. Rev. Microbiol.* **61,** 477–501 (2007).
5. Breukink, E. *et al.* Use of the cell wall precursor lipid II by a pore-forming peptide antibiotic. *Sci* **286,** 2361–2364 (1999).
6. Breukink, E. & de Kruijff, B. Lipid II as a target for antibiotics. *Nat. Rev. Drug Discov.* **5,** 321–323 (2006).
7. Hancock, R. E. & Sahl, H.-G. Antimicrobial and host-defense peptides as new anti-infective therapeutic strategies. *Nat. Biotechnol.* **24,** 1551–1557 (2006).
8. Bierbaum, G. & Sahl, H. G. Lantibiotics: Mode of Action, Biosynthesis and Bioengineering. *Curr. Pharm. Biotechnol.* **10,** 2–18 (2009).
9. Xie, L. & Van Der Donk, W. A. Post-translational modifications during lantibiotic biosynthesis. *Curr. Opin. Chem. Biol.* **8,** 498–507 (2004).
10. Chatterjee, C., Paul, M., Xie, L. L. & van der Donk, W. A. Biosynthesis and mode of action of lantibiotics. *Chem. Rev.* **105,** 633–683 (2005).
11. Héchard, Y. & Sahl, H.-G. Mode of action of modified and unmodified bacteriocins from Gram-positive bacteria. *Biochimie* **84,** 545–557 (2002).
12. Dischinger, J., Basi Chipalu, S. & Bierbaum, G. Lantibiotics: promising candidates for future applications in health care. *Int. J. Med. Microbiol.* **304,** 51–62 (2014).
13. Hsu, S. T. *et al.* The nisin-lipid II complex reveals a pyrophosphate cage that provides a blueprint for novel antibiotics. *Nat. Struct. Mol. Biol.* **11,** 963–7 (2004).
14. Wiedemann, I. *et al.* Specific Binding of Nisin to the Peptidoglycan Precursor Lipid II Combines Pore Formation and Inhibition of Cell Wall Biosynthesis for Potent Antibiotic Activity. *J. Biol. Chem.* **276,** 1772–1779 (2001).
15. van Heusden, H. E., de Kruijff, B. & Breukink, E. Lipid II induces a transmembrane orientation of the pore-forming peptide lantibiotic nisin. *Biochemistry* **41,** 12171–12178 (2002).
16. Hasper, H. E., de Kruijff, B. & Breukink, E. Assembly and stability of nisin-lipid II pores. *Biochemistry* **43,** 11567–75 (2004).
17. Froseth, B. R. & Mckay, L. L. Molecular characterization of the nisin resistance region of *Lactococcus lactis* subsp. *lactis* biovar diacetylactis DRC3. *Appl. Environ. Microbiol.* **57,** 804–811 (1991).
18. Draper, L. A., Cotter, P. D., Hill, C. & Ross, R. P. Lantibiotic Resistance. *Microbiol. Mol. Biol. Rev.* **79,** 171–191 (2015).
19. McKay, L. L. & Baldwin, K. A. Conjugative 40-megadalton plasmid in *Streptococcus lactis* subsp. *diacetylactis* DRC3 is associated with resistance to nisin and bacteriophage. *Appl. .Environ. Microbiol.* **47,** 68–74 (1984).
20. Duan, K., Harvey, M., Liu, C. Q. & Dunn, N. Identification and characterization of a mobilizing plasmid, pND300, in *Lactococcus lactis* M189 and its encoded nisin resistance determinant. *J. Appl. Bacteriol.* **81,** 493–500 (1996).
21. Klaenhammer, T. R. & Sanozky, R. B. Conjugal transfer from *Streptococcus lactis* ME2 of plasmids encoding phage resistance, nisin resistance and lactose-fermenting ability: evidence for a high-frequency conjugative plasmid responsible for abortive infection of virulent bacteriophage. *J. Gen. Microbiol.* **131,** 1531–1541 (1985).
22. Khosa, S., Alkhatib, Z. & Smits, S. H. NSR from *Streptococcus agalactiae* confers resistance against nisin and is encoded by a conserved nsr operon. *Biol. Chem.* **394,** 1543–1549 (2013).
23. Kawada-Matsuo, M. *et al.* Three distinct two-component systems are involved in resistance to the class I bacteriocins, nukacin ISK-1 and nisin A, in *Staphylococcus aureus*. *PLoS One* **8,** e69455 (2013).
24. Sun, Z. *et al.* Novel mechanism for nisin resistance via proteolytic degradation of nisin by the nisin resistance protein NSR. *Antimicrob. Agents Chemother.* **53,** 1964–1973 (2009).
25. Christ, N. A. *et al.* The First structure of a lantibiotic immunity protein, SpaI from *Bacillus subtilis*, reveals a novel fold. *J. Biol. Chem.* **287,** 35286–98 (2012).
26. Pozzi, R. *et al.* Distinct mechanisms contribute to immunity in the lantibiotic NAI-107 producer strain *Microbispora* ATCC PTA-5024. *Environ. Microbiol.* (2015).
27. Alkhatib, Z. *et al.* The C-terminus of nisin is important for the ABC transporter NisFEG to confer immunity in *Lactococcus lactis*. *MicrobiologyOpen* **3,** 752–763 (2014).
28. Bernsel, A., Viklund, H., Hennerdal, A. & Elofsson, A. TOPCONS: consensus prediction of membrane protein topology. *Nucleic Acids Res.* gkp363 (2009).
29. Khosa, S., Hoeppner, A., Kleinschrodt, D. & Smits, S. Overexpression, purification, crystallization and preliminary X-ray diffraction of the nisin resistance protein from *Streptococcus agalactiae*. *Acta Crystallogr. F Biol. Crystallogr.* **71,** 671–675 (2015).
30. Mastny, M. *et al.* CtpB assembles a gated protease tunnel regulating cell-cell signaling during spore formation in *Bacillus subtilis*. *Cell* **155,** 647–658 (2013).
31. Kim, J.-S. *et al.* Navigation inside a protease: substrate selection and product exit in the tricorn protease from *Thermoplasma acidophilum*. *J. Mol. Biol.* **324,** 1041–1050 (2002).
32. Liao, D.-I., Qian, J., Chisholm, D. A., Jordan, D. B. & Diner, B. A. Crystal structures of the photosystem II D1 C-terminal processing protease. *Nat. Struct. Mol. Biol.* **7,** 749–753 (2000).
33. Holm, L. & Rosenström, P. Dali server: conservation mapping in 3D. *Nucleic Acids Res.* **38,** W545–W549 (2010).
34. David, A. *et al.* Structural determinants of host specificity of complement Factor H recruitment by *Streptococcus pneumoniae*. *Biochem. J* **465,** 325–335 (2015).
35. Gao, X.-C. *et al.* The C-terminal Helices of Heat Shock Protein 70 Are Essential for J-domain Binding and ATPase Activation. *J. Biol. Chem.* **287,** 6044–6052 (2012).
36. Garcia, B. L. *et al.* A structurally dynamic N-terminal helix is a key functional determinant in staphylococcal complement inhibitor (SCIN) proteins. *J. Biol. Chem.* **288,** 2870–2881 (2013).
37. Case, D. A. *et al. AMBER 14.* University of California, San Francisco. (2014).
38. Metz, A. *et al.* Hotspots and transient pockets: predicting the determinants of small-molecule binding to a protein-protein interface. *J Chem. Inf. Model* **52,** 120–133 (2012).
39. Wang, Y., Zhang, Y. & Ha, Y. Crystal structure of a rhomboid family intramembrane protease. *Nature* **444,** 179–180 (2006).
40. Hodel, A. E. *et al.* The Three-Dimensional Structure of the Autoproteolytic, Nuclear Pore-Targeting Domain of the Human Nucleoporin Nup98. *Mol. Cell* **10,** 347–358 (2002).
41. Page, M. & Di Cera, E. Serine peptidases: classification, structure and function. *Cell. Mol. Life Sci.* **65,** 1220–1236 (2008).
42. Bierbaum, G. *et al.* Engineering of a novel thioether bridge and role of modified residues in the lantibiotic Pep5. *Appl. Environ. Microbiol.* **62,** 385–392 (1996).
43. Kabsch, W. Xds. *Acta Crystallogr. D Biol. Crystallogr.* **66,** 125–132 (2010).
44. de Sanctis, D. *et al.* ID29: a high-intensity highly automated ESRF beamline for macromolecular crystallography experiments exploiting anomalous scattering. *J. Synchrotron Radiat.* **19,** 455–461 (2012).
45. Panjikar, S., Parthasarathy, V., Lamzin, V. S., Weiss, M. S. & Tucker, P. A. On the combination of molecular replacement and single-wavelength anomalous diffraction phasing for automated structure determination. *Acta Crystallogr. D Biol. Crystallogr.* **65,** 1089–97 (2009).
46. Emsley, P., Lohkamp, B., Scott, W. G. & Cowtan, K. Features and development of Coot. *Acta Crystallogr. D Biol. Crystallogr.* **66,** 486–501 (2010).
47. Adams, P. D. *et al.* PHENIX: a comprehensive Python-based system for macromolecular structure solution. *Acta Crystallogr. D Biol. Crystallogr.* **66,** 213–221 (2010).

48. Langer, G., Cohen, S. X., Lamzin, V. S. & Perrakis, A. Automated macromolecular model building for X-ray crystallography using ARP/wARP version 7. *Nat. Protoc.* **3,** 1171–1179 (2008).
49. Chen, V. B. *et al.* MolProbity: all-atom structure validation for macromolecular crystallography. *Acta Crystallogr. D Biol. Crystallogr.* **66,** 12–21 (2010).
50. Delano, W. L. The PyMOL molecular graphics system. (2002).
51. Abts, A. *et al.* Easy and Rapid Purification of Highly Active Nisin. *International Journal of Peptides* **2011,** 9 (2011).
52. Roe, D. R. & Cheatham, T. E. PTRAJ and CPPTRAJ: software for processing and analysis of molecular dynamics trajectory data. *J. Chem. Theory Comput.* **9,** 3084–3095 (2013).
53. Srinivasan, J., Cheatham, I., T. E., Cieplak, P., Kollman, P. A. & Case, D. A. Continuum solvent studies of the stability of DNA, RNA, and phosphoramidate - DNA helices. *J. Am. Chem. Soc.* **120,** 9401–9409 (1998).
54. Gohlke, H. & Case, D. A. Converging free energy estimates: MM-PB(GB)SA studies on the protein-protein complex Ras-Raf. *J. Comput. Chem.* **25,** 238–50 (2004).
55. Homeyer, N. & Gohlke, H. Free energy calculations by the molecular mechanics Poisson-Boltzmann surface area method. *Molecular Informatics* **31,** 114–122 (2012).
56. Gohlke, H., Kiel, C. & Case, D. A. Insights into protein–protein binding by binding free energy calculation and free energy decomposition for the Ras–Raf and Ras–RalGDS complexes. *J. Mol. Biol.* **330,** 891–913 (2003).
57. Cornell, W. D. *et al.* A second generation force field for the simulation of proteins, nucleic acids, and organic molecules. *J. Am. Chem. Soc.* **118,** 2309–2309 (1996).
58. Hornak, V. *et al.* Comparison of multiple Amber force fields and development of improved protein backbone parameters. *Proteins: Struct., Funct., Bioinf.* **65,** 712–725 (2006).
59. Sitkoff, D., Sharp, K. A. & Honig, B. Accurate Calculation of Hydration Free-Energies Using Macroscopic Solvent Models. *J. Phys. Chem.* **98,** 1978–1988 (1994).

Acknowledgements

We thank Lutz Schmitt for fruitful discussions, encouragement, support and invaluable advice. We are grateful to Philipp Ellinger for initiating the project, André Abts for stimulating discussions, Michael Lenders and Iris Fey for technical assistance. We acknowledge the European Synchrotron Radiation Facility for provision of synchrotron radiation facilities and are grateful to the staff of ESRF ID23-2 and ID29 for support during crystal screening and data collection, especially Christoph Mueller-Dieckmann for his enormous patience, assistance and support. We are thankful to Heinrich Heine International Graduate School of Protein Science and Technology (iGRASPseed) for providing a scholarship to S.K and to the International NRW Research School BioStruct, granted by the Ministry of Innovation, Science and Research of the State North Rhine-Westphalia, the Heinrich Heine University Düsseldorf, and the Entrepreneur Foundation at the Heinrich Heine University Düsseldorf for a scholarship to B.F. We are also grateful to the "Zentrum für Informations- und Medientechnologie" (ZIM) at the Heinrich-Heine-University Düsseldorf for providing computational support.

Author Contributions

S.K., A.H., D.K. performed the biochemical and structural experiments. B.F., D.M. performed molecular modeling and M.D. simulations. S.K., B.F., H.G., S.S. designed the experiments, evaluated the data, and wrote the manuscript. All authors reviewed the manuscript.

Additional Information

Supplementary information accompanies this paper at http://www.nature.com/srep

Competing financial interests: The authors declare no competing financial interests.

How to cite this article: Khosa, S. *et al.* Structural basis of lantibiotic recognition by the nisin resistance protein from *Streptococcus agalactiae*. *Sci. Rep.* **6**, 18679; doi: 10.1038/srep18679 (2016).

Supplementary information

Structural basis of lantibiotic recognition by the nisin resistance protein from *Streptococcus agalactiae*

Sakshi Khosa[a#], Benedikt Frieg[b#], Daniel Mulnaes[b] Diana Kleinschrodt[c], Astrid Hoeppner[d], Holger Gohlke[b] and Sander H.J. Smits[a]*

[a]Institute of Biochemistry, Heinrich Heine University, Universitätsstr. 1, 40225 Düsseldorf, Germany
[b]Institute of Pharmaceutical and Medicinal Chemistry, Heinrich Heine University, Universitätsstr. 1, 40225 Düsseldorf, Germany
[c]Protein Production Facility, Heinrich Heine University, Universitätsstr. 1, 40225 Düsseldorf, Germany
[d]Crystal and X-ray Facility, Heinrich Heine University, Universitätsstr. 1, 40225 Düsseldorf, Germany

[#]Both authors contributed equally.
*Corresponding author: Phone: +49-211-81-12647; Fax: +49-211-81-15310; E-Mail: sander.smits@hhu.de

Material and Methods

Cloning, expression and purification of *Sa*NSR

The primers were designed in such a way that the first 30 amino acids encoding for the transmembrane helix were not present in the construct. This allowed soluble expression and included an 8xhis-tag at the N-terminus for purification purposes. *Sa*NSR was expressed and purified via two-step purification protocol. A single transformed colony was inoculated into 20 ml LB media containing 30 μg ml^{-1} kanamycin. The culture was grown for 14 h at 310 K with shaking at 200 rev min^{-1}. 2 L LB media with 30 μg ml^{-1} kanamycin was inoculated with the overnight culture at an OD600 of 0.05 and grown at 310 K with shaking at 170 rev min^{-1} till OD_{600} of 0.3 was reached. The temperature was lowered to 291 K and the cells were further grown till OD_{600} of 0.8 before induction with 1 mM IPTG. The cells were further grown for 15 h.

The cells were harvested by centrifugation at 8000 rev min^{-1} for 20 min at 277 K. The harvested cell pellet was stored at 253 K till further use. The stored cell pellet was thawed and resuspended in 10 ml of buffer A (50 mM Tris pH 8.0, 50 mM NaCl and 10% glycerol) and 10 mg of DNase (Deoxyribonuclease I from bovine pancreas, Sigma Aldrich) was added. The cells were lysed five times using a cell disruptor (Constant Cell Disruption Systems, United Kingdom) at 37709 psi (1kbar = 14.50 psi). The lysate was centrifuged at 42000 rev min^{-1} for 60 min using a Ti60 rotor to remove unlysed cells and debris.

Histidine was added to the cleared lysate at a final concentration of 1 mM. The lysate was then applied to a Ni^{2+} loaded HiTrap HP Chelating column (GE Healthcare) pre-equilibrated with buffer B (20 mM Tris pH 8.0, 250 mM NaCl and 1 mM Histidine) at a flow rate of 1 ml min^{-1}. The column was washed with six column volumes of buffer B. The protein was then eluted with increasing concentrations of Histidine from 1 mM to 120 mM, in form of a linear gradient spanning 60 min with a flow rate of 2 ml min^{-1}. The fractions containing the protein of interest were pooled and concentrated up to 12 mg ml^{-1} in an Amicon centrifugal filter concentrator with a 10 kDa cut-off membrane (Millipore). The concentrated protein was then further purified by size exclusion chromatography using Superose 12 GL 10/300 column (GE Healthcare), equilibrated with buffer C (25 mM MES pH 6.0, 150 mM NaCl). The protein eluted as a single homogeneous peak and the concerned fractions were pooled and concentrated to 8.6 mg ml^{-1} as mentioned before. The purity of the protein was analyzed with SDS-PAGE and colloidal coomassie stain.

To determine the oligomeric state of *Sa*NSR protein in solution, we used conventional size-exclusion chromatography (SEC) and high performance liquid chromatography coupled to multi angle light scattering detection (HPLC-MALS). SEC was performed as described previously[1] and the size-exclusion column was standardized with a gel filtration markers kit (Sigma).

Crystallization

Crystallization screening was performed at 285 K using NT8 robot (Formulatrix) and sitting-drop vapour diffusion method in Corning 3553 sitting drop plates. For initial screening different commercial crystallization screens were used {Nextal JCSG Core Suites I, Classics Suite, PEGs Suite, MPD Suite (Qiagen, Germany) and MIDAS (Molecular Dimensions, England)}. Nanodrops consisting of 0.1 µl each of protein and reservoir solution were mixed and equilibrated over 50 µl reservoir solution. The screening yielded some initial rod shaped crystals after three days in the condition 0.5 M lithium sulfate and 15% (w/v) PEG 8000 (Classic I suite, condition F5). The initial crystals were optimized by varying the concentration of PEG (5, 10, 15, 20, 25 and 30% (w/v)) and salt (0.4, 0.5, 0.6 and 0.7 M), using hanging and sitting-drop vapour diffusion methods at 297 K and 285 K, respectively. Each drop consisted of 1 µl of protein solution (concentration of 9 mg ml^{-1}) mixed with 1 µl of reservoir solution, equilibrated over a reservoir volume of 500 µl. Crystals were obtained after one day and grew to their maximum dimensions within 5 days. For preliminary analysis of the crystals see [1].

Expression, purification and crystallization of selenomethionine-substituted SaNSR

For selenomethionine substitution, *E. coli* BL834 (DE3) cells were grown according to manufacturer's protocol in M9 minimal media (Molecular Dimensions) supplemented with 50 µg ml^{-1} of L-seleno-methionine. Expression and purification were identical to the native SaNSR [1]. Selenomethionine derivatized *Sa*NSR was crystallized in a similar manner as the native protein, using the hanging drop vapor diffusion method with a protein concentration of 10 mg ml^{-1}.

Cloning of pNZ-SV-*Sa*NSR and variants

The plasmid pNZ-SV-*Sa*NSR (N-His) was cloned with the In-Fusion HD PCR Cloning Kit (Clontech) as previously published [2]. Different mutations were introduced into the pNZ-SV-

*Sa*NSR (N-His) using standard site-directed mutagenesis protocol. The used primers are listed in Supplementary Table 1a.

Expression of *Sa*NSR and its variants in *L. lactis* NZ9000

The plasmid encoding pNZ-SV-*Sa*NSR and its variants were transformed into the nisin sensitive *L. lactis* strain NZ9000. As a control the empty vector was also transformed, termed NZ9000Erm. The strains expressing NZ9000SaNSR and its mutations were grown in GM17 media supplemented with 5 μg ml^{-1} erythromycin to an OD_{600} of 0.8. The expression was induced by the addition of nisin (at a final concentration of 1 $ngml^{-1}$) and the cultures were further grown overnight. The cells were then diluted to an OD_{600} of 0.1 in fresh GM17 media supplemented with 5μg ml^{-1} erythromycin. These cells were then used for the assays described below.

Cloning, Overexpression and purification of nisin and its variants

Nisin was purified from commercially available powder as described [3]. The cloning, overexpression and purification of precursor nisin variants were performed as described previously [3,4], excepting that the elution buffer of the cationic exchange chromatography of the various precursor nisin variants were changed to 50 mM HEPES-NaOH, pH 7.0, 1 M NaCl, and 10% glycerol. The concentrations of nisin and its variants were determined by using RP-HPLC and in order to activate the nisin variants, the leader peptide was cleaved off using the protease NisP as previously described, thereby [5].

Molecular dynamics simulations

Structures of NSR_{Apo}, NSR_{Tail}, and $NSR_{Nisin,1-3}$ were prepared using LEaP[6] of the Amber 14 suite of programs [7]. First, missing hydrogen atoms were added by LEaP [6], and histidine residues were assigned the HIE state. Second, counter ions were added to neutralize each system. Finally, systems were solvated using the TIP3P water model [8]. The obtained systems comprised ~ 60.000 atoms. Atomic partial charges for Dha33 (dehydroalanine) and rings D and E in nisin, which are treated as one "residue" in the Amber scheme, were obtained following the RESP procedure[9] using Gaussian09 [10]. For the non-standard amino acid Dha33, force field parameters were adapted from ref. [11]. All other parameters were taken from the Amber ff99SB force field [12,13]. Structural relaxation, thermalization, and

production runs of MD simulations were conducted with pmemd.cuda [14] of Amber 14 [7]. Two steps of energy minimization were performed to relax the systems. First, harmonic restraints with a force constant of 25 kcalmol^{-1}Å^{-2} were applied to all protein atoms while all other atoms were free to move during 50 cycles of steepest descent (SD) and 200 cycles of conjugate gradient (CG) minimization. Second, the force constant of the harmonic restraints was reduced to 5 kcalmol^{-1}Å^{-2}, and 50 cycles of SD and 200 cycles of CG minimization were performed. Subsequently, the systems were heated from 100 K to 299.9 K, 300 K, or 300.1 K during canonical (NVT) MD simulations of 50 ps length to setup three independent MD production simulations for NSR_{Apo}, NSR_{Tail}, and $NSR_{Nisin,1-3}$, respectively. Afterwards, the density was adjusted to 1 g·cm-3 during 30 ps of isobaric-isothermal (NPT) MD simulations. During heating and density adaptation, positional restraints of 5 kcal·mol^{-1}·Å^{-2} were applied to all protein atoms. Finally, these positional restraints were removed by gradually decreasing the force constant from 5 to 0 kcal·mol^{-1}·Å^{-2} in six NVT-MD runs of 10 ps length each. For MD simulations, the particle mesh Ewald (PME) method [15-17] was employed to treat long-range electrostatic interactions. For short-range non-bonded interactions, we set a distance cutoff of 8 Å. The SHAKE algorithm [18] was applied to all bonds involving hydrogens, allowing a 2 fs time step for integrating Newton's equations of motion. Production MD simulations were performed in the NVT ensemble at 300 K for 500 ns. Coordinates were saved every 20 ps and used for analyses. This led to a total simulation time of 5 x 3 x 500 ns = 7.5 μs.

Supplementary Table 1

(a) IC_{50} values of nisin and its variants against the NZ9000Erm and NZ9000-*Sa*NSR strains as well as the calculated "Fold of resistance".

	NZ9000Erm (nM)	**NZ9000-*Sa*NSR (nM)**	***Fold of resistance***
Nisin	3.3±0.1	66.4±2.1	20.1
CCCCA	42.2±0.7	57.8±3.3	1.7
CCCAA	184.9±9.7	259.5±16.6	1.4
$Nisin_{1-22}$	294.7±9.7	121.1±6.1	0.4
$Nisin_{1-28}$	277.1±14.0	103.5±5.5	0.4

The values reported are the average over minimum triplicates ± SEM.

(b) IC_{50} values of nisin against the NZ9000Erm, NZ9000-*Sa*NSR, and NZ9000-*Sa*NSR variant strains.

	IC_{50} value (nM)	*Activity (%)*
NZ9000Erm	3.3±0.1	0
NZ9000-*Sa*NSR (wildtype)	66.4±2.1	100
NZ9000-*Sa*NSR-His_{98}Ala	12.3±1.5	14.2
NZ9000-*Sa*NSR-Ser_{236}Ala	12.6±0.7	14.6
NZ9000-*Sa*NSR-Ser_{237}Ala	50.2±2.3	74.3
NZ9000-*Sa*NSR-Glu_{239}Ala	17.1±0.7	21.7
NZ9000-*Sa*NSR-Asn_{172}Ala	33.5±2.9	47.7
NZ9000-*Sa*NSR-Met_{173}Ala	30.3±1.4	42.7
NZ9000-*Sa*NSR-Ile_{174}Ala	24.1±2.2	32.9
NZ9000-*Sa*NSR-Thr_{263}Ala	16.0±0.3	20.1
NZ9000-*Sa*NSR-Asn_{265}Ala	22.1±1.1	29.7
NZ9000-*Sa*NSR-Thr_{267}Ala	48.5±0.6	71.6
NZ9000-*Sa*NSR-Asp_{110}Ala	32.8±2.1	46.7
NZ9000-*Sa*NSR-Arg_{275}Ala	33.6±2.3	47.9

The values reported are the average over minimum triplicates ± SEM.

Supplementary Table 2: Primers used in this study.

Shown below are the primers used to create the point mutations within the expression plasmid pNZ-SV-*Sa*NSR-NHis [1] .

Primer Name	***Sequence (5'-3')***
His_{98}Ala-for	CGGTATGGAGGAGGTAAAGCAAGTCAAATATTATCC
His_{98}Ala-rev	GGATAATATTTGACTTGCTTTACCTCCTCCATACCG
Ser_{236}Ala-for	CTAATCATAAAACTGCTGCGTCGGCAGAAATGAC
Ser_{236}Ala-rev	GTCATTTCTGCCGACGCAGCAGTTTTATGATTAG
Ser_{237}Ala-for	CTAATCATAAAACTGCTAGTGCAGCAGAAATGACTTTTTTATC
Ser_{237}Ala-rev	GATAAAAAAGTCATTTCTGCTGCACTAGCAGTTTTATGATTAG
Glu_{239}Ala-for	CTGCTAGTTCGGCAGCAATGACTTTTTTATC
Glu_{239}Ala-rev	GATAAAAAAGTCATTGCTGCCGAACTAGCAG
Asn_{172}Ala-for	CGAATAATACTGGCGGCGCAATGATCCCTATGATTG
Asn_{172}Ala-rev	CAATCATAGGGATCATTGCGCCGCCAGTATTATTCG
Met_{173}Ala-for	GAATAATACTGGCGGCAATGCAATCCCTATGATTGGG
Met_{173}Ala-rev	CCCAATCATAGGGATTGCATTGCCGCCAGTATTATTC
Ile_{174}Ala-for	CTGGCGGCAATATGGCACCTATGATTGGGGG
Ile_{174}Ala-rev	CCCCCAATCATAGGTGCCATATTGCCGCCAG
Thr_{263}Ala-for	CAGCAGGATATACGGCAGTTAATGAAACTTTC
Thr_{263}Ala-rev	GAAAGTTTCATTAACTGCCGTATATCCTGCTG
Asn_{265}Ala-for	GCAGGATATACGACTGTTGCAGAAACTTTCATGCTTTAC
Asn_{265}Ala-rev	GTAAAGCATGAAAGTTTCTGCAACAGTCGTATATCCTGC
Thr_{267}Ala-for	GATATACGACTGTTAATGAAGCATTCATGCTTTACGACG
Thr_{267}Ala-rev	CGTCGTAAAGCATGAATGCTTCATTAACAGTCGTATATC
Asp_{110}Ala-for	GAGACTGTACGAAGAGCAACCCTAGATAGTCG
Asp_{110}Ala-rev	CGACTATCTAGGGTTGCTCTTCGTACAGTCTC
Arg_{275}Ala-for	GCTTTACGACGGTGCTGCATTAGCTTTAACTACAG
Arg_{275}Ala-rev	CTGTAGTTAAAGCTAATGCAGCACCGTCGTAAAGC

Supplementary Figure 1: Schematic representation of the structure of nisin and the different variants used in this study.

Shown are structural representations of wildtype nisin and the variants CCCCA, CCCAA, nisin$_{1-22}$ and nisin$_{1-28}$. Highlighted in yellow are the dehydrated amino acids while the amino acids which are dehydrated as well as cyclized are shown in orange. The lanthionine rings are also shown in orange and are numbered A-E.

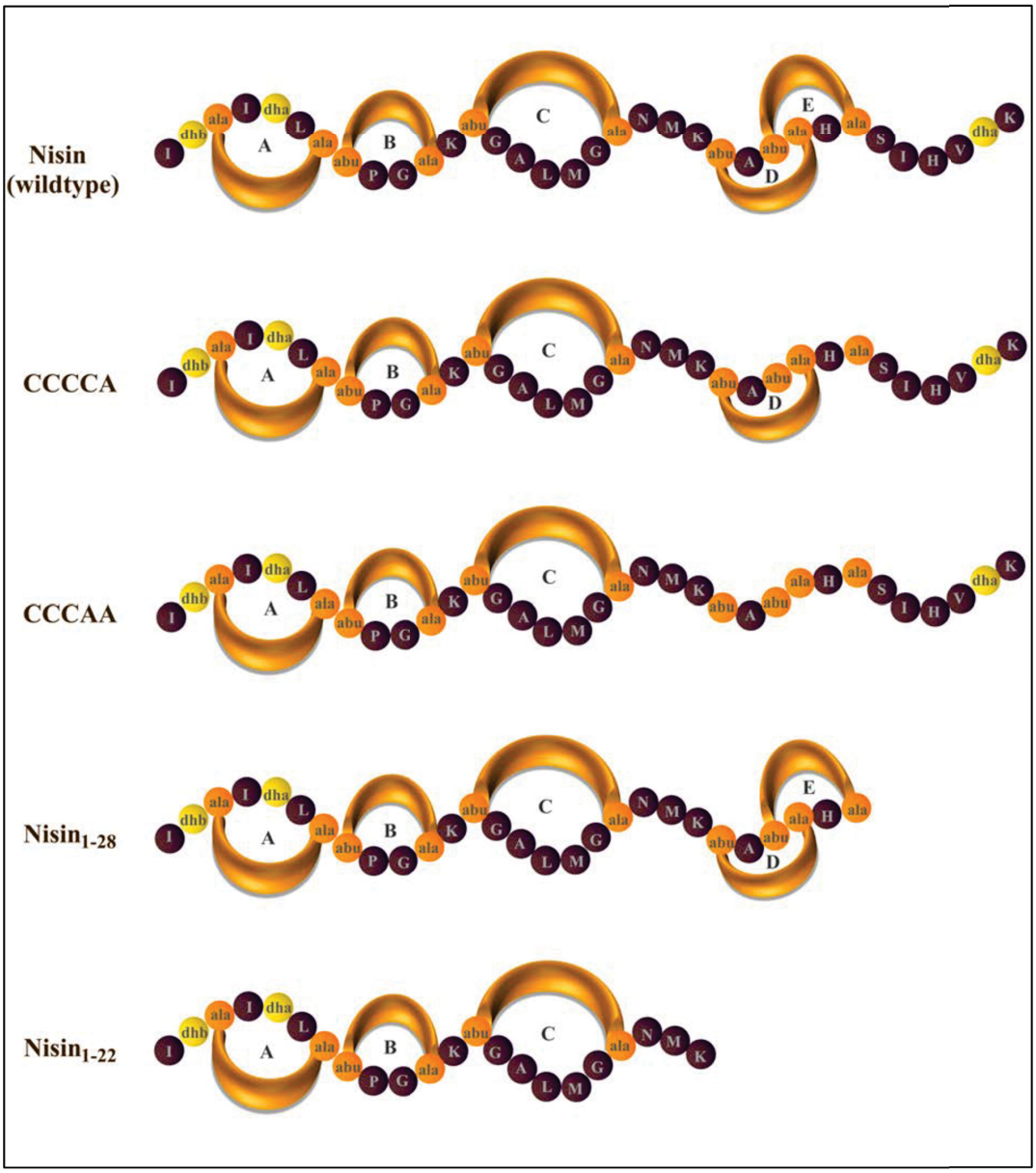

Supplementary Figure 2: Purification, oligomeric state and structure of *Sa*NSR.

(a) 15% SDS gel showing purified *Sa*NSR after the two-step purification involving IMAC and SEC. Lane M represents PageRuler Unstained Protein Ladder; the remaining lanes are the purified *Sa*NSR fractions at 35 kDa. The lower 30 kDa band also arises from *Sa*NSR, as verified by mass spectrometry, and could likely be a degradation product. (b) Determination of the oligomeric state of the purified *Sa*NSR protein using HPLC-MALS. The x-axis represents the time in minutes; the left and right y-axes depict the relative intensity and molecular mass, respectively. The blue line is the differential refractive index signal; the blue dotted line indicates the calculated molar mass. (c) The structure of *Sa*NSR in the asymmetric unit. The four copies of the monomer are colored in green, cyan, pink and yellow for chains A, B, C and D, respectively.

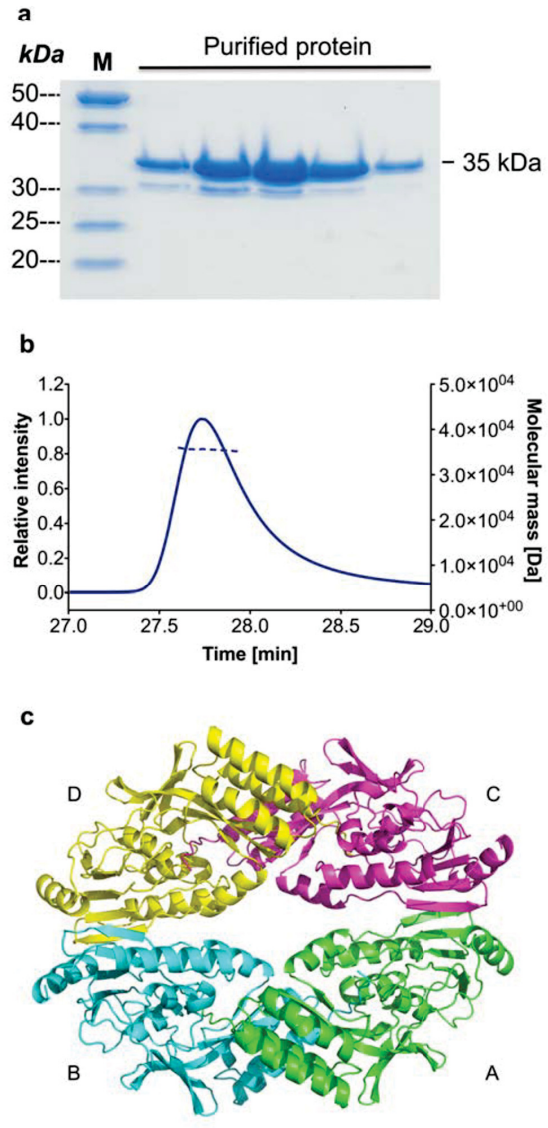

Supplementary Figure 3: Alignment of the nisin resistance proteins.

Homolog sequences of nisin resistance protein were aligned using ClustalW2 [2]. Visualization of the sequence alignment was performed by ESPript [3]. Secondary structure elements were calculated based on the *Sa*NSR structure. The TASSAEM motif is marked by a dotted blue line.

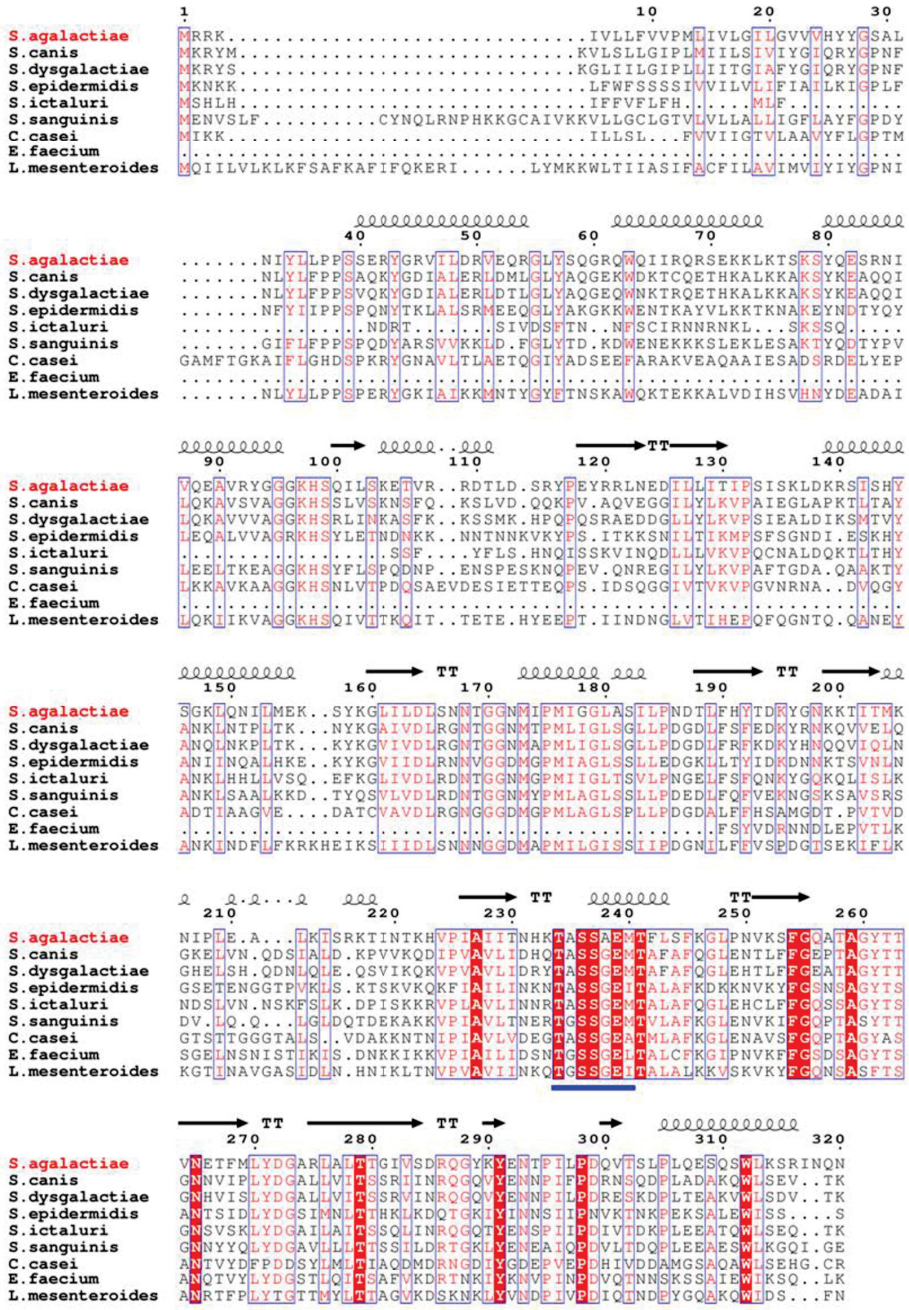

Supplementary Figure 4: Mobility and structural deviations in MD simulations of NSR_{Apo} and NSR_{Tail}.
(a) Mean backbone RMSF of residues of the N-terminal helical bundle in NSR_{Apo} models after superimposition of the cap domain and the protease core for three trajectories (colored differently) of 500 ns length each. (b) Backbone RMSD for N-pep in the NSR_{Tail} model for three independent MD simulations. Mean values are shown in the legend. Mean standard error < 0.1 Å and not shown.

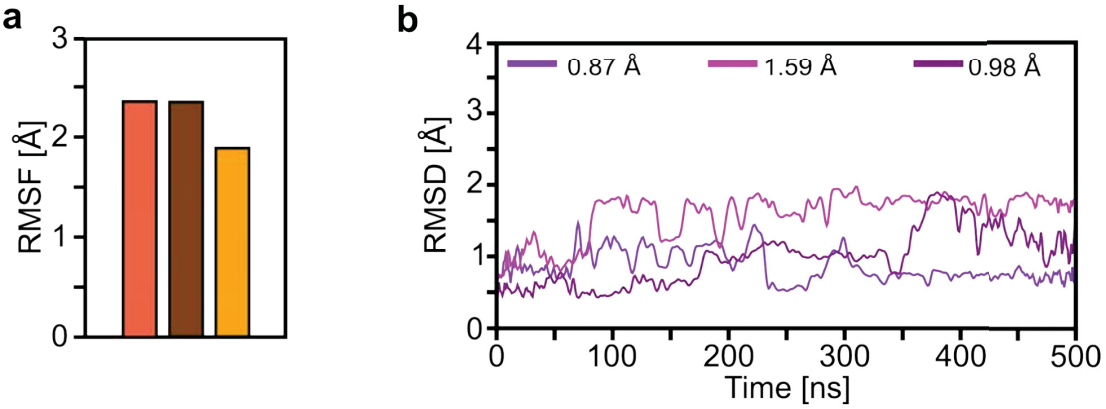

Supplementary Figure 5: Models of *Sa*NSR/nisin complexes used as starting structures for and RMSD analysis of MD simulations.

(a) View into the binding site of *Sa*NSR with Asn_{172}, Met_{173}, and Ile_{174} colored in magenta, Ser_{236} in blue, and Tyr_{261} in orange; for clarity, the N-terminal bundle and protease core domains of *Sa*NSR were omitted. The C-terminus of nisin (residues 22 - 34) is shown in ball and stick representation. The right panels show a close-up view of all initial NSR/nisin complexes used as starting structures for the MD simulations (red: $NSR_{Nisin,1}$; green: $NSR_{Nisin,2}$; blue: $NSR_{Nisin,3}$).

(b) All atom RMSD values, relative to the respective average structures, over 500 ns of MD simulations for the C-terminus of nisin and for the $Nisin_{core}$ (composed of rings D and E, Ser_{29}, and Ile_{30}; see Figure 4b-d). RMSD values are shown for each of the three independent MD trajectories.

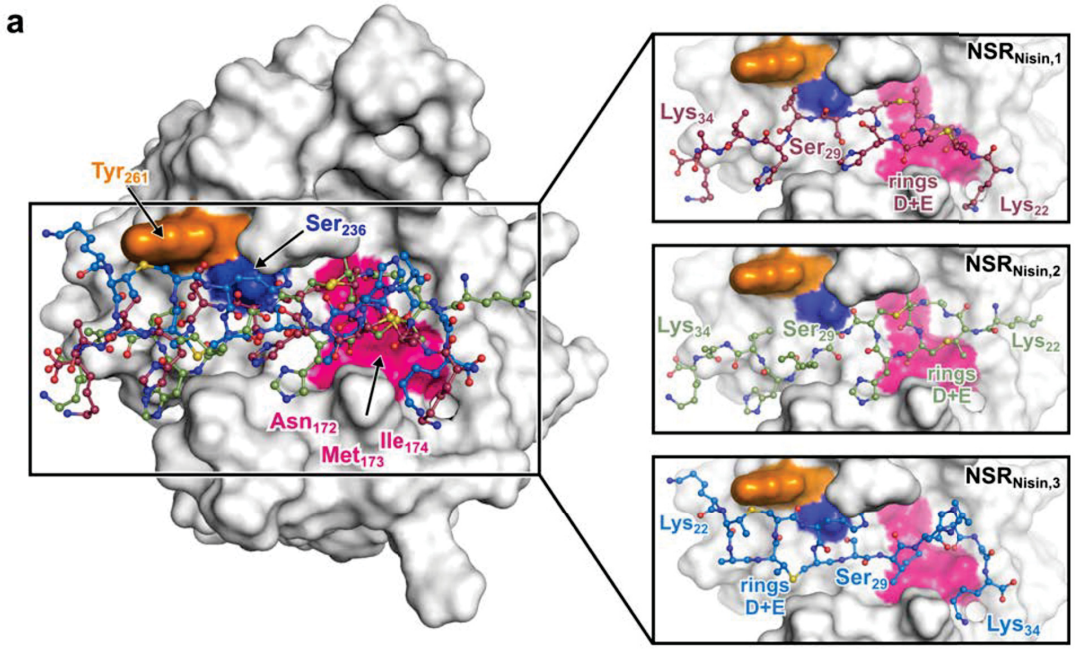

b

Model \ RMSD [Å][a]	mean $Nisin_{C\text{-}terminus}$ [b]	mean $Nisin_{core}$ [b]
$NSR_{Nisin,1}$ (1)	2.75	1.38
$NSR_{Nisin,1}$ (2)	2.60	1.34
$NSR_{Nisin,1}$ (3)	3.19	2.27
$NSR_{Nisin,2}$ (1)	1.44	0.80
$NSR_{Nisin,2}$ (2)	1.80	1.34
$NSR_{Nisin,2}$ (3)	2.16	1.28

[a] relative to average structure
[b] MSE < 0.01 Å

Supplementary Figure 6: Structural analyses of the TASSAEM region over the MD trajectories.

(a) Close-up view of the catalytic site residues in blue and Gly_{171} from the protease core in magenta ball-and-stick representation. Identified hydrogen bonds (1 – 7) are depicted as orange dotted lines. The table shows minimum (min.) and maximum (max.) occupancies of hydrogen bonds 1 to 7 across the six MD trajectories. Distance between the side chain oxygen in Ser_{237} and the carbonyl carbon of ring E from the nisin cleavage site (b), and the side chain oxygen in Ser_{237} and the δ-nitrogen in His_{98} (c) for both $Nsr_{Nisin,1}$ (top panel) and $Nsr_{Nisin,2}$ (bottom panel) models during the three independent MD simulations. Mean values over each trajectory are shown in the legend.

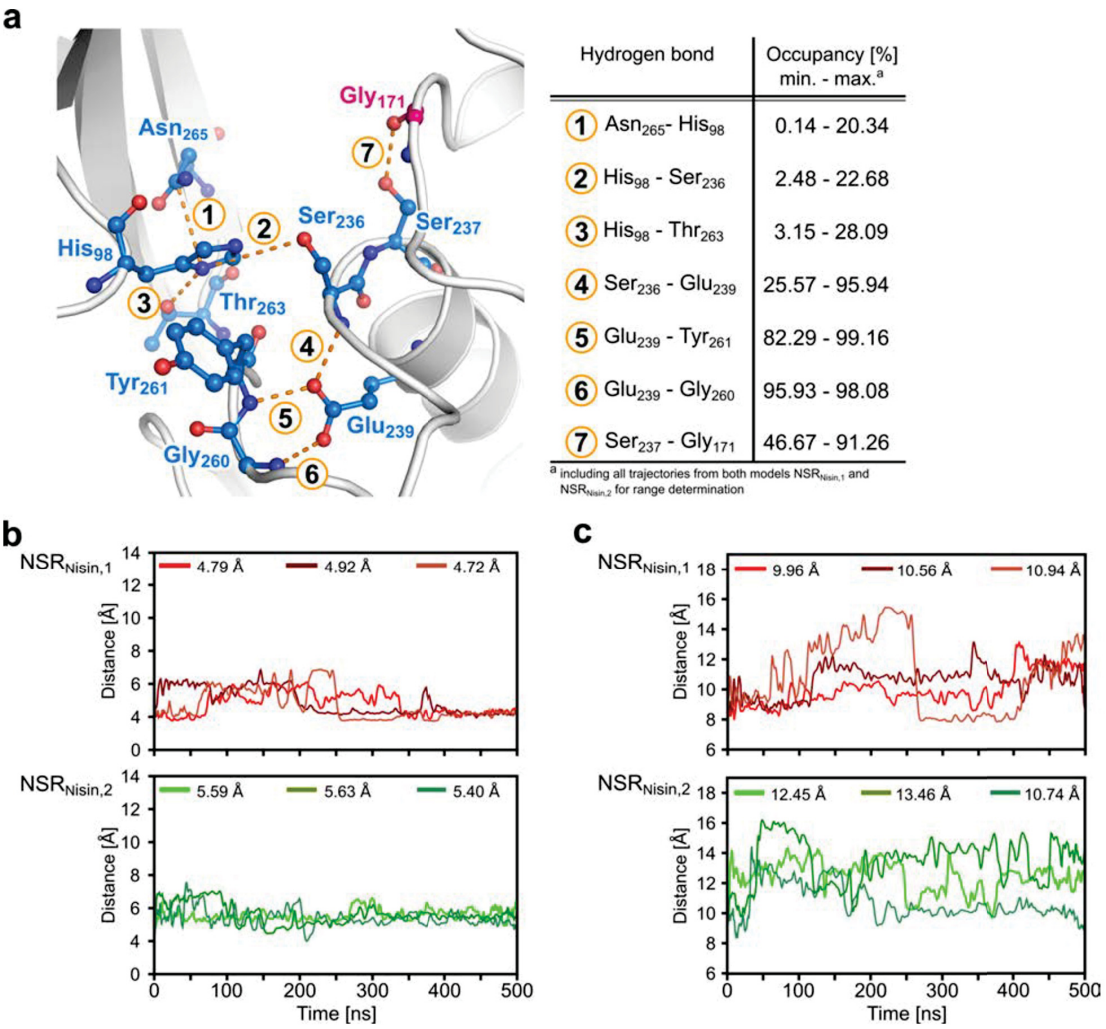

Hydrogen bond	Occupancy [%] min. - max.[a]
1 Asn_{265} - His_{98}	0.14 - 20.34
2 His_{98} - Ser_{236}	2.48 - 22.68
3 His_{98} - Thr_{263}	3.15 - 28.09
4 Ser_{236} - Glu_{239}	25.57 - 95.94
5 Glu_{239} - Tyr_{261}	82.29 - 99.16
6 Glu_{239} - Gly_{260}	95.93 - 98.08
7 Ser_{237} - Gly_{171}	46.67 - 91.26

[a] including all trajectories from both models $NSR_{Nisin,1}$ and $NSR_{Nisin,2}$ for range determination

Supplementary Figure 7: Energetic and structural analyses of nisin binding over the MD trajectories.

(a) Per-residue effective binding energies computed by the MM-PBSA approach for residues within 5 Å of the C-terminus of nisin occupying the catalytic site of *Sa*NSR for model $NSR_{Nisin,1}$ (red) and $NSR_{Nisin,2}$ (green). The gray lines indicate a threshold of ± 0.8 kcal mol^{-1}. (b) Close-up view of the binding site residues (magenta) in the crystal structure bound to nisin (orange). Identified hydrogen bonds (1 – 3) are depicted as orange dotted lines. (c) Distance between the side chain carboxylate of residue Glu_{266} and the guanidino group of Arg_{54} from the N-terminal helical bundle for both $NSR_{Nisin,1}$ (top panel) and $NSR_{Nisin,2}$ (bottom panel) over the course of 500 ns MD simulations. Mean values for each MD trajectory are shown in the legend. (d) Close-up view of the binding site residues (magenta) and nisin (orange). Water-mediated interactions (1 – 2) are indicated by dark blue dotted lines. In (b) and (d), the tables show minimum and maximum occupancies of hydrogen bonds or water-mediated interactions. Hydrogen bonds and water-mediated interactions were determined for each of the $NSR_{Nisin,1}$ and $NSR_{Nisin,2}$ trajectories.

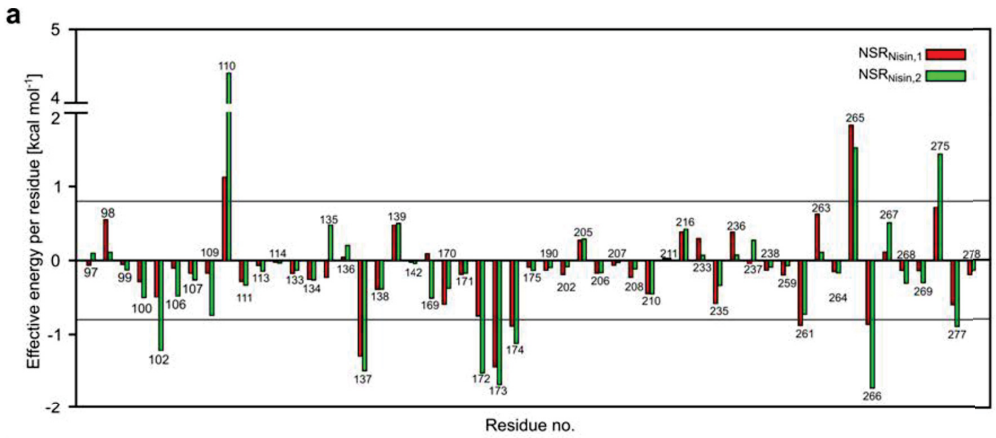

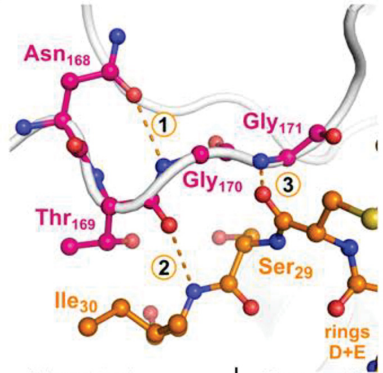

Hydrogen bond	Occupancy [%] min. - max.[a]
(1) Asn_{168} - Gly_{170}	44.46 - 83.00
(2) Thr_{169} - Nisin Ile_{30}	0.00 - 68.87
(3) Gly_{171} - Nisin rings D+E	0.00 - 75.67

[a] including all trajectories from both models $NSR_{Nisin,1}$ and $NSR_{Nisin,2}$ for range determination

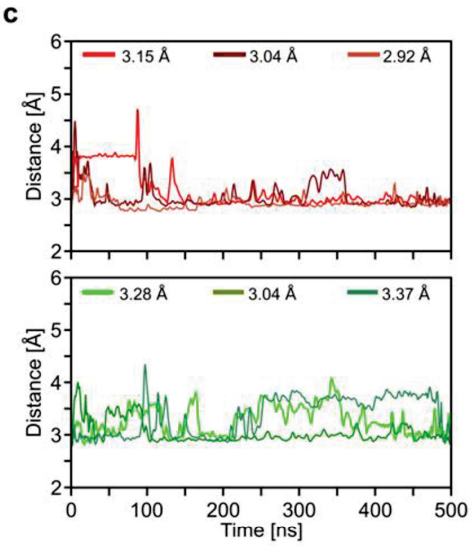

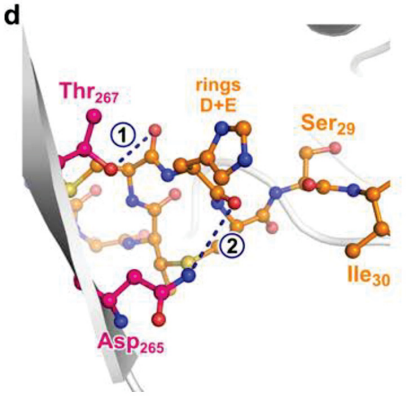

Water-mediated interaction	Occupancy [%] min. - max.[a]
(1) Thr_{267} - Nisin rings D+E	0.18 - 28.26
(2) Asn_{265} - Nisin rings D+E	9.92 - 20.46

[a] including all trajectories from both models $NSR_{Nisin,1}$ and $NSR_{Nisin,2}$ for range determination

Supplementary Figure 8: Structural analysis of helix α4 over the MD trajectories.
(a) For models $NSR_{Nisin,1}$, and $NSR_{Nisin,2}$ distances were measured between the side chain carboxylate of Asp_{110} and the guanidino group of Arg_{275}. (b) Residue-wise α-helix probability for residues that compose helix α4. Mean distances and mean α-helix probabilities over the independent MD trajectories are shown in the legend.

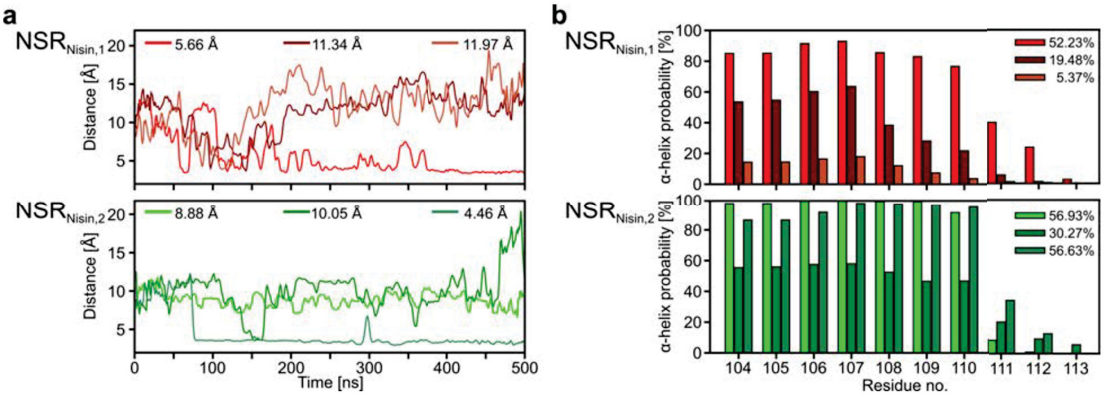

Supplementary References

1. Khosa, S., Hoeppner, A., Kleinschrodt, D. & Smits, S. Overexpression, purification, crystallization and preliminary X-ray diffraction of the nisin resistance protein from *Streptococcus agalactiae*. *Acta Crystallogr. F Biol. Crystallogr.* **71**, 671-675 (2015).

2. Khosa, S., Alkhatib, Z. & Smits, S.H. NSR from *Streptococcus agalactiae* confers resistance against nisin and is encoded by a conserved nsr operon. *Biol. Chem.* **394**, 1543-1549 (2013).

3. Abts, A. et al. Easy and Rapid Purification of Highly Active Nisin. *International Journal of Peptides* **2011**, 9 (2011).

4. Mavaro, A. et al. Substrate recognition and specificity of the NisB protein, the lantibiotic dehydratase involved in nisin biosynthesis. *J. Biol. Chem.* **286**, 30552-30560 (2011).

5. Abts, A., Montalban-Lopez, M., Kuipers, O.P., Smits, S.H. & Schmitt, L. NisC binds the FxLx motif of the nisin leader peptide. *Biochemistry* **52**, 5387-5395 (2013).

6. Zhang, W., Hou, T., Schafmeister, C., Ross, W.S. & Case, D.A. LEaP. *University of California, San Francisco* (1995).

7. Case, D.A. et al. AMBER 14. *University of California, San Francisco.* (2014).

8. Jorgensen, W.L., Chandrasekhar, J., Madura, J.D., Impey, R.W. & Klein, M.L. Comparison of simple potential functions for simulating liquid water. *J. Chem. Phys.* **79**, 926-935 (1983).

9. Bayly, C.I., Cieplak, P., Cornell, W.D. & Kollman, P.A. A well-behaved electrostatic potential based method using charge restraints for deriving atomic charges - the RESP Model. *J. Phys. Chem.* **97**, 10269-10280 (1993).

10. Frisch, M.J. et al. Gaussian 09. (Gaussian, Inc., Wallingford, CT, USA, 2009).

11. Alagona, G. & Ghio, C. Force field parameters for molecular mechanical simulation of dehydroamino acid residues. *J. Comput. Chem.* **12**, 934-942 (1991).

12. Cornell, W.D. et al. A second generation force field for the simulation of proteins, nucleic acids, and organic molecules. *J. Am. Chem. Soc.* **118**, 2309-2309 (1996).

13. Hornak, V. et al. Comparison of multiple Amber force fields and development of improved protein backbone parameters. *Proteins: Struct., Funct., Bioinf.* **65**, 712-725 (2006).

14. Salomon-Ferrer, R., Gotz, A.W., Poole, D., Le Grand, S. & Walker, R.C. Routine microsecond molecular dynamics simulations with Amber on GPUs. 2. Explicit solvent particle mesh ewald. *J. Chem. Theory Comput.* **9**, 3878-3888 (2013).

15. York, D.M., Darden, T.A. & Pedersen, L.G. The effect of long-range electrostatic interactions in simulations of macromolecular crystals - a comparison of the ewald and truncated list methods. *J. Chem. Phys.* **99**, 8345-8348 (1993).

16. Darden, T., York, D. & Pedersen, L. Particle mesh Ewald: An N· log (N) method for Ewald sums in large systems. *J. Chem. Phys.* **98**, 10089-10092 (1993).

17. Srinivasan, J., Cheatham, I., T. E., Cieplak, P., Kollman, P.A. & Case, D.A. Continuum solvent studies of the stability of DNA, RNA, and phosphoramidate - DNA helices. *J. Am. Chem. Soc.* **120**, 9401-9409 (1998).

18. Ryckaert, J.P., Ciccotti, G. & Berendsen, H.J.C. Numerical integration of cartesian equations of motion of a system with constraints molecular dynamics of n-alkanes. *J. Comput. Phys.* **23**, 327-341 (1977).

19. Larkin, M.A. et al. Clustal W and Clustal X version 2.0. *Bioinformatics* **23**, 2947-2948 (2007).

20. Robert, X. & Gouet, P. Deciphering key features in protein structures with the new ENDscript server. *Nucleic Acids Res.* **42**, W320-W324 (2014).

11.4 PUBLICATION IV

Targeting HSP90's C-terminus is effective in Imatinib resistant CML and lacks heat shock response induction.

Bhatia, S., Diedrich, D., **Frieg, B.**, Ahlert, H., Stein, S., Bopp, B., Lang, F., Zang, T., Kröger, T., Ernst, T., Kögler, G., Krieg, A., Lüdeke, S., Kunkel, H., Rodrigues Moita, A. J., Kassack, M. U., Marquardt, V., Opitz, F. V., Oldenburg, M., Remke, M., Babor, F., Grez, M., Hochhaus, A., Borkhardt, A., Groth, G., Nagel-Steger, L., Jose, J., Kurz, T., Gohlke, H., Hansen, F. K., Hauer, J.

Blood (2018), 132, 307 – 320.

blood® Regular Article

MYELOID NEOPLASIA

Targeting HSP90 dimerization via the C terminus is effective in imatinib-resistant CML and lacks the heat shock response

Sanil Bhatia,[1] Daniela Diedrich,[2] Benedikt Frieg,[2,3] Heinz Ahlert,[1] Stefan Stein,[4] Bertan Bopp,[5] Franziska Lang,[1] Tao Zang,[6,7] Tobias Kröger,[2] Thomas Ernst,[8] Gesine Kögler,[9] Andreas Krieg,[10] Steffen Lüdeke,[11] Hana Kunkel,[4] Ana J. Rodrigues Moita,[2] Matthias U. Kassack,[2] Viktoria Marquardt,[1,2,12,13] Friederike V. Opitz,[1] Marina Oldenburg,[1] Marc Remke,[1,12,13] Florian Babor,[1] Manuel Grez,[4] Andreas Hochhaus,[8] Arndt Borkhardt,[1] Georg Groth,[14] Luitgard Nagel-Steger,[6,7] Joachim Jose,[5] Thomas Kurz,[2] Holger Gohlke,[2,3] Finn K. Hansen,[2,15,*] and Julia Hauer[1,*]

[1]Department of Pediatric Oncology, Hematology and Clinical Immunology, Medical Faculty, and [2]Institute for Pharmaceutical and Medicinal Chemistry, Heinrich Heine University Düsseldorf, Düsseldorf, Germany; [3]John von Neumann Institute for Computing, Jülich Supercomputing Centre, Institute for Complex Systems–Structural Biochemistry (ICS-6), Forschungszentrum Jülich GmbH, Jülich, Germany; [4]Institute for Tumor Biology and Experimental Therapy, Georg-Speyer-Haus, Frankfurt, Germany; [5]Institute for Pharmaceutical and Medicinal Chemistry, PharmaCampus, Westphalian Wilhelms University, Münster, Germany; [6]Institute for Physical Biology, Heinrich Heine University Düsseldorf, Düsseldorf, Germany; [7]Institute of Complex Systems, Structural Biochemistry (ICS-6), Forschungszentrum Jülich GmbH, Jülich, Germany; [8]Hematology/Oncology, Internal Medicine II, Jena University Hospital, Jena, Germany; [9]Institute for Transplantation Diagnostics and Cell Therapeutics and [10]Department of Surgery (A), Heinrich Heine University Düsseldorf, Düsseldorf, Germany; [11]Institute of Pharmaceutical Sciences, University of Freiburg, Freiburg, Germany; [12]Institute of Neuropathology, Medical Faculty, Heinrich Heine University Düsseldorf, Düsseldorf, Germany; [13]Division of Pediatric Neuro-Oncogenomics, German Cancer Consortium, partner site University Hospital Düsseldorf, Düsseldorf, Germany; [14]Institute for Biochemical Plant Physiology, Heinrich Heine University Düsseldorf, Düsseldorf, Germany; and [15]Pharmaceutical/Medicinal Chemistry, Institute of Pharmacy, Leipzig University, Leipzig, Germany

KEY POINTS

- **We have developed a first-in-class C-terminal HSP90 inhibitor (AX) that is effective against TKI-resistant CML and leukemic stem cells.**
- **Unlike the majority of HSP90 inhibitors, AX does not induce the HSR as a resistance mechanism.**

Heat shock protein 90 (HSP90) stabilizes many client proteins, including the BCR-ABL1 oncoprotein. BCR-ABL1 is the hallmark of chronic myeloid leukemia (CML) in which treatment-free remission (TFR) is limited, with clinical and economic consequences. Thus, there is an urgent need for novel therapeutics that synergize with current treatment approaches. Several inhibitors targeting the N-terminal domain of HSP90 are under investigation, but side effects such as induction of the heat shock response (HSR) and toxicity have so far precluded their US Food and Drug Administration approval. We have developed a novel inhibitor (aminoxyrone [AX]) of HSP90 function by targeting HSP90 dimerization via the C-terminal domain. This was achieved by structure-based molecular design, chemical synthesis, and functional preclinical in vitro and in vivo validation using CML cell lines and patient-derived CML cells. AX is a promising potential candidate that induces apoptosis in the leukemic stem cell fraction ($CD34^+CD38^-$) as well as the leukemic bulk ($CD34^+CD38^+$) of primary CML and in tyrosine kinase inhibitor (TKI)–resistant cells. Furthermore, BCR-ABL1 oncoprotein and related pro-oncogenic cellular responses are downregulated, and targeting the HSP90 C terminus by AX does not induce the HSR in vitro and in vivo. We also probed the potential of AX in other therapy-refractory leukemias. Therefore, AX is the first peptidomimetic C-terminal HSP90 inhibitor with the potential to increase TFR in TKI-sensitive and refractory CML patients and also offers a novel therapeutic option for patients with other types of therapy-refractory leukemia because of its low toxicity profile and lack of HSR. (*Blood*. 2018;132(3):307-320)

Introduction

Heat shock protein 90 (HSP90) acts as a molecular chaperone, thereby ensuring correct protein folding of several oncogenic proteins involved in leukemia such as BCR-ABL1 and its downstream signaling partners.[1-5] HSP90 expression is also enriched in several leukemia subtypes, making HSP90 a promising therapeutic approach in the treatment of therapy-refractory leukemia, such as BCR-ABL1+ leukemia,[1,6-8] FLT3-ITD+ acute myeloid leukemia (AML)[9-11] and Philadelphia chromosome (Ph)-like B-cell precursor acute lymphoblastic leukemia (BCP-ALL).[12,13] Several HSP90 inhibitors have been developed, but none have been clinically approved by the US Food and Drug Association (supplemental Table 1, available on the *Blood* Web site).[8,14] The majority of the HSP90 inhibitors target the adenosine triphosphate binding pocket

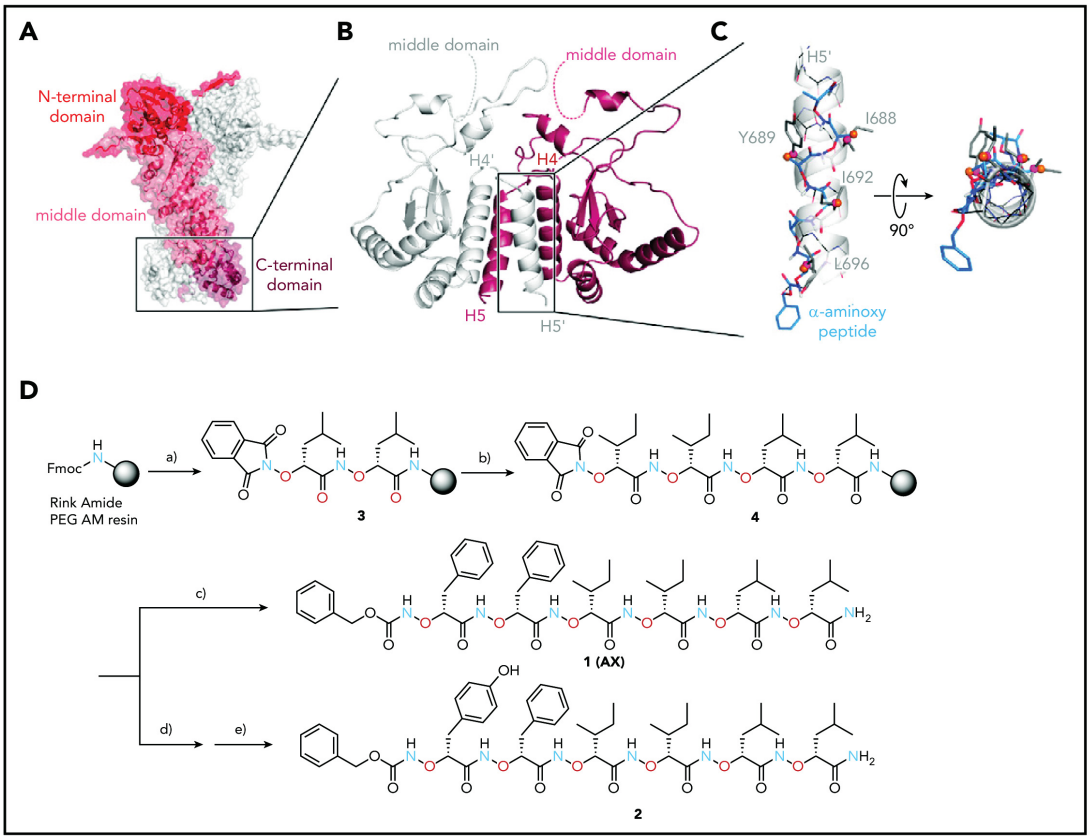

Figure 1. Design and synthesis of HSP90 CTD dimerization inhibitors. (A) Crystal structure of the HSP90 dimer from *Saccharomyces cerevisiae* (Protein Data Bank [PDB] accession number 2CG9[56]), shown as a transparent surface with cartoon representation. One monomer is colored in white and one in red, with 3 domains (N terminal, middle, and C terminal) colored in different shades of red. (B) Dimeric CTD from human HSP90 (PDB accession number 3Q6M[57]). Both subunits are colored differently. Helices H4, H4′, and H5, H5′ form the CTD dimerization interface. Dashed lines show where the middle domains would be located. (C) Overlay of a hexameric α-aminoxy peptide with all-methyl side chains (blue sticks) onto C_β atoms of hot spot amino acids I688, Y689, I692, and L696[34] (gray sticks) on helix H5′ (sequence P681 to D699) shown in transparent cartoon representation, with backbone atoms shown as black lines. The right panel shows the structures rotated by 90° such that the helix C terminus is oriented toward the viewer. C_β reference atoms of hot spot amino acids are depicted as magenta spheres and C_β atoms of the α-aminoxy peptide as orange spheres. (D) Solid-phase synthesis of α-aminoxy hexapeptides 1 (AX) and 2. Reagents and conditions: a), (i) 20% piperidine in *N,N*-dimethylformamide (DMF), room temperature, 2 × 15 min; (ii) Phth-^{NO}Leu-^{NO}Leu-OH, BOP, HOBt, *N*-ethylmorpholine (NEM) in DMF, room temperature, 24 hours; b) 5% hydrazine hydrate in MeOH, 2 × 15 min; (ii) Phth-^{NO}Ile-^{NO}Ile-OH, BOP, HOBt, NEM in DMF, room temperature, 24 hours; c) (i) 5% hydrazine hydrate in MeOH, 2 × 15 min; (ii) Cbz-^{NO}Phe-^{NO}Phe-OH, BOP, HOBt, NEM in DMF, room temperature, 24 hours; (iii) trifluoroacetic acid/triethylsilane (98:2, v:v), room temperature, 1.5 hours; d) (i) 5% hydrazine hydrate in MeOH, 2 × 15 min; (ii) Phth-^{NO}Phe-OH, BOP, HOBt, NEM in DMF, room temperature, 24 hours; e) 5% hydrazine hydrate in MeOH, 2 × 15 min; (ii) Cbz-^{NO}Tyr (*t*-Bu)-OH, BOP, HOBt, NEM in DMF, room temperature, 24 hours; (iii) trifluoroacetic acid/triethylsilane (98:2, v:v), room temperature, 1.5 hours. PEG AM resin, polyethylene glycol aminomethyl-polystyrene resin.

in the HSP90 N terminus,[14,15] leading to dissociation of heat shock factor-1 (HSF-1), which gets subsequently phosphorylated, trimerized, and translocated to the nucleus.[16] Here, HSF-1 induces the transcription of other HSPs, such as HSP70, HSP40, or HSP27, that act as antiapoptotic chaperones and protect proteins from degradation, thereby inducing a resistance mechanism called the heat shock response (HSR),[17] which potentially weakens the cytotoxic effect of HSP90 inhibitors.[14,15,18-22] C-terminal inhibitors of HSP90, such as novobiocin and its analogs, do not trigger an HSR.[23,24] The reason for the induction of the HSR by classical HSP90 inhibitors is not well understood. It has been hypothesized that inhibition of HSP90 might trigger cellular effects through mechanisms that involve targets other than HSP90 (off-target effects).[23,25] The off-target effects hypothesis is further supported by the significant difference (100-fold) between the efficiency of N-terminal inhibitors in killing cancer cells and their binding affinity to HSP90 in biochemical assays.[23] For instance, the well-known N-terminal HSP90 inhibitor AUY922 induces cell death at low nanomolar concentrations but binds to HSP90 with micromolar affinity.[23] In contrast, C-terminal HSP90 inhibitors are likely selective for HSP90 given that their cytotoxicity against cancer cells correlates with their binding affinity for HSP90.[23,24] Thus, targeting the HSP90 C-terminal domain may ultimately be the most promising route to discover safe and efficacious HSP90 inhibitors.

In the present study, we evaluated a novel HSP90 inhibitor aminoxyrone (AX) in chronic myeloid leukemia (CML), a stem cell disease that can in most cases be controlled by tyrosine kinase inhibitor (TKI) treatment, but treatment-free remission (TFR) is still not satisfactory. Approximately 40% to 60% of patients who discontinue TKI treatment develop molecular relapse and need to restart them.[26] TKIs target proliferating leukemic clones but are unable to eradicate persisting leukemia stem cells (LSCs).[27,28] This implicates long-term dependence on them with consequences for patients' quality-of-life

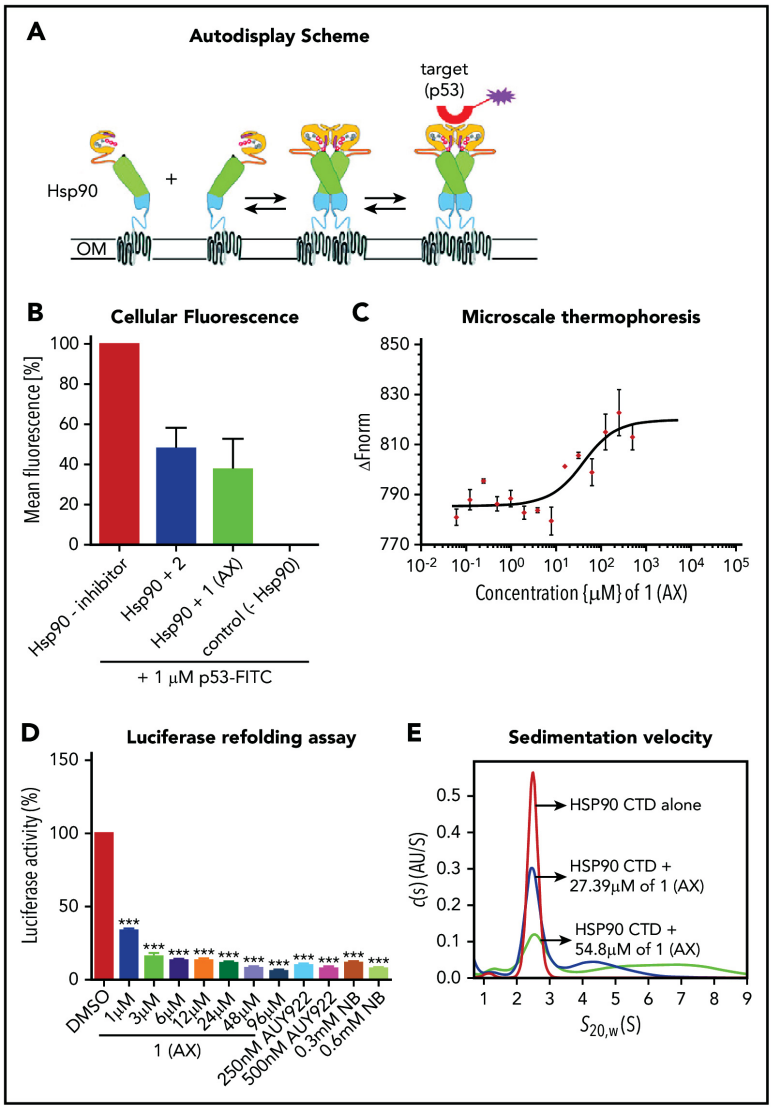

Figure 2. Selective binding of compound 1 (AX) and 2 to the HSP90 C terminus. (A) Scheme of the HSP90 dimerization assay using Autodisplay. HSP90 is displayed on the surface of *E coli* cells via the Autodisplay technique. The motility of the anchoring domain within the outer membrane of *E coli* facilitates the dimerization of Hsp90. Dimerized HSP90 on the surface of *E coli* is capable of binding to fluorescein isothiocyanate (FITC)–labeled p53. This leads to an increase of cellular fluorescence, which can then be detected via flow cytometry. Blocking the dimerization of surface displayed Hsp90 inhibits the binding of FITC-labeled p53 to HSP90 and thus leads to a decrease of cellular fluorescence.[33] (B) Inhibition of dimerization of on *E coli* cells displayed HSP90 measured via flow cytometry. Experiments were performed 3 times independently (n = 3), and error bars denote the standard deviation. Incubation of *E coli* BL21 (DE3) cells displaying HSP90 with 1 μM FITC-labeled p53 leads to a high cellular fluorescence, indicating dimerization of HSP90, whereas no cellular fluorescence was detectable in *E coli* cells without displaying HSP90 (control cells). Preincubation of cells with surface displayed HSP90 with 50 μM of 1 (AX) and 2, respectively, leads to a loss in cellular fluorescence, indicating a lowered binding affinity of FITC-labeled p53 to surface-displayed HSP90. (C) Determination of the apparent K_d value of the NT-647–labeled C-terminal domain of HSP90 and 1 (AX) via MST. A constant amount of the 50 nM–labeled C-terminal domain of HSP90 was used (n = 3). The resulting mean values were determined and used in the K_d fit formula. This yielded an apparent K_d of 27.39 μM for 1 (AX). (D) A cell-based HSP90-dependent luciferase assay was performed on stably expressing K562-luciferase cells. The extent of thermally denatured luciferase refolding (3 minutes at 50°C) in the presence of 1 (AX), NB, and AUY922 was monitored after 180 minutes. (E) Influence of 1 (AX) on the size distribution of HSP90 CTD revealed by sedimentation velocity analysis. 20 μM HSP90 CTD alone (purple), 20 μM HSP90 CTD plus 27.4 μM 1 (AX) (blue), and 20 μM HSP90 CTD plus 54.8 μM 1 (AX) (cyan) were analyzed at 50 000 rpm at 20°C, and the continuous c(s) model was applied to evaluate the data. The *s*-values were standardized to $s_{20,w}$-values. Columns depict the mean of 3 independent experiments (n = 3). Significance analyses of normally distributed data with variance similar between groups used paired, 2-tailed Student *t* test. $^*P < .05$, $^{**}P < .005$, $^{***}P < .001$.

and economic resources. Patients feel chronically ill, which is not related to their CML but due to the moderate to severe TKI side effects, which ~30% of patients experience.[29] For instance, acute side effects of imatinib (IM) are impaired physical and mental health status in patients <60 years of age,[30] whereas dasatinib can cause pleural effusion and arterial hypertension,[31] and nilotinib causes vascular events.[32] The use of TKIs is especially controversially discussed in young adults and children, because none of the TKIs are recommended during pregnancy and/or lactation, and their effects on fertility and skeletal growth have not been systematically analyzed. Hence, the development and characterization of novel therapeutic agents that specifically target CML LSCs and are capable of inducing sustained TFR are of enormous clinical and economic value.

We show that AX targets LSCs in CML patients and is effective in TKI-resistant CML subtypes and therefore promising in adding value to sustained TFR. In addition, inhibition of the HSP90 C terminus is effective in high-risk BCR-ABL1+ BCP-ALL, FLT3-ITD+ AML, and Ph-like BCP-ALL, comprising a relevant proportion of therapy-resistant leukemia in adults and children.

Methods

Chemical synthesis and 2-dimensional nuclear magnetic resonance spectroscopy

See supplemental Note 1 for general methods, synthetic protocols, compound characterization, and spectral data.

Circular dichroism (CD) spectroscopy

CD spectra in trifluoroethanol (50 μM, 1 mm path length) and sodium phosphate buffer (10 μM, 5 mm path length) were recorded on a J-810 Spectropolarimeter (Jasco) at 20°C and background corrected by solvent subtraction.

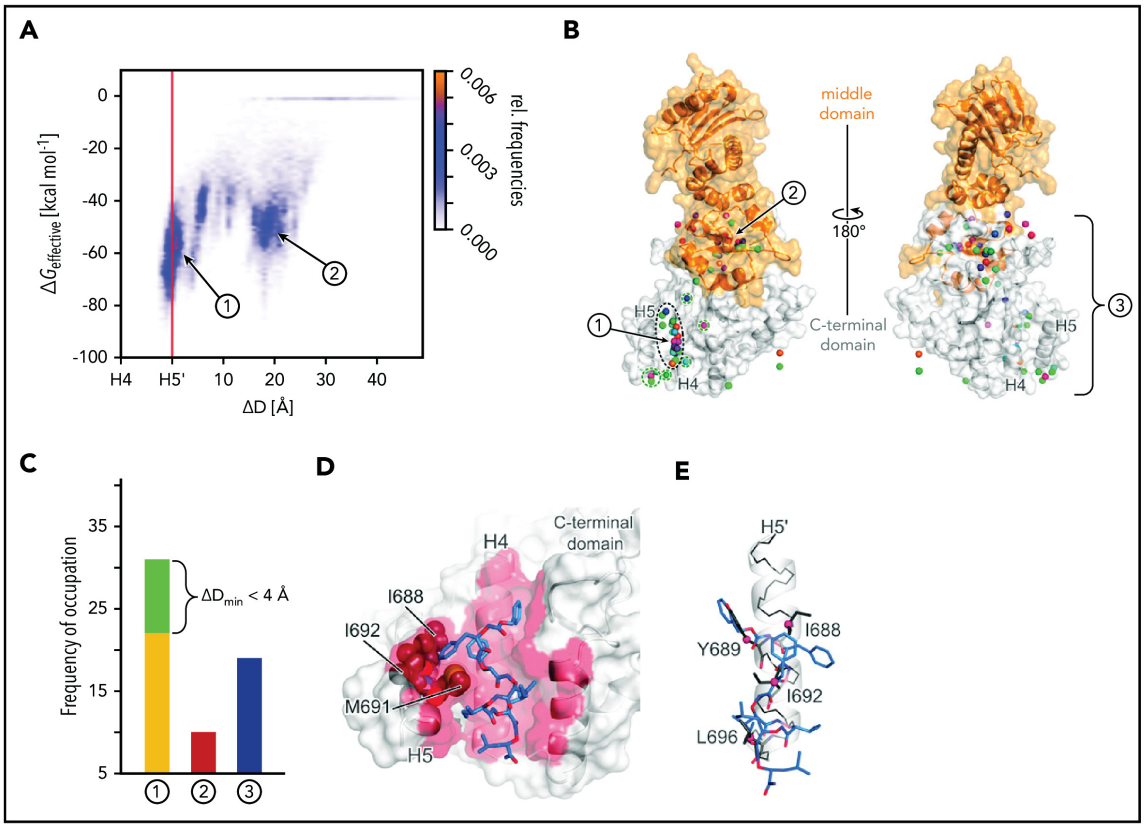

Figure 3. Results of MD simulations of free diffusion of AX. (A) Relative frequencies of ligand pose (see color scale) as a function of the relative distance between the center of mass of AX and helix H4 (ΔD) and computed effective energies of binding ($\Delta G_{effective}$). (B) Locations of the center of mass of AX (spheres) after 60 MD simulations of 400 nanosecond length each, with each simulation result colored differently. The black dashed line highlights all conformations that are bound to dimerization interface 1 with $\Delta D_{min} \leq 0$ Å, and the green dashed line highlights those with $\Delta D_{min} < 4$ Å. The protein structure is shown as surface representation with the middle domain (not present during MD simulations) in orange and the CTD in white. In the panel, the structure is rotated by 180° around the y-axis. (C) Frequency of occupation of binding sites 1 (yellow), close to 1 (green; see definition in the main text), 2 (red), or 3 (blue) by AX across 60 MD simulations. (D) Binding mode model of AX. A representative conformation of AX bound to the CTD, extracted from the MD trajectory. Residues I688, I692, and M691 (gray spheres) bind to the side chain that distinguishes AX from 2. (E) An overlay of AX onto helix H5′ (Figure 1B-C) extracted from the crystal structure (PDB accession number 3Q6M[57]). In panels D and E, AX is depicted as blue sticks; hot spot amino acids I688, Y689, I692, and L696[34] as gray sticks with C_β atoms as magenta spheres; helix H5′ as a white cartoon with black backbone atoms; and the CTD in the left panel as surface representation, with all residues within 3 Å of AX colored in red. In panels A-C, 1, 2, and 3 denote the binding sites of AX, where 3 represents all binding sites besides 1 and 2.

Autodisplay dimerization assay

Surface display of HSP90 on *Escherichia coli* BL21 (DE3) cells was performed as described before.[33] See supplemental Note 2 for further details.

Microscale thermophoresis (MST)

The HSP90 CTD was purified as described before[34] and labeled with the Monolith NT Protein Labeling Kit RED-NHS (Amine-reactive; NanoTemper Technologies GmbH, Munich, Germany) according to the manufacturer's protocol. See supplemental note 2 for further details.

Analytical ultracentrifugation

Sedimentation velocity experiments were carried out using a Beckman Proteome Laboratory XL-A ultracentrifuge (Beckman Coulter, Indianapolis, IN) equipped with an absorbance detection system and an 8-hole rotor. See supplemental Note 2 for further details.

Luciferase refolding assay

The luciferase assay was performed with K562 cells stably expressing luciferase transgene, as described previously,[24] with some modifications. See supplemental Note 2 for further details.

Drug-affinity responsive target stability (DARTS)

The DARTS assay was carried to evaluate the protease protection of AX from thermolysin, as described previously.[24] See supplemental Note 2 for further details.

Western blot (WB) and Blue-native gel

Cell lysates were generated after 48-hour treatment of leukemic cells with AX, IM, novobiocin (NB), or AUY922. Blue-native gels were performed following the manufacturer's instructions (Invitrogen) and as described previously.[24] See supplemental Note 2 for further details.

Table 1. IC_{50} values after treament with AX

Cell line	Origin	Growth inhibition (IC_{50}), μM
K562 and K562 IMr	CML (BCR-ABL1+)	5.72 ± 0.31 and 6.24 ± 0.52
KCL22 and KCL22 IMr	CML (BCR-ABL1+)	2.74 ± 0.52 and 2.86 ± 0.63
BA/F3	Murine pro B cell line	3.12 ± 0.09
BA/F3 (T315I)	Murine pro–B-cell line (BCR-ABL1+)	3.02 ± 0.22
BA/F3 (T315I) PNr	Murine pro–B-cell line (BCR-ABL1+)	4.02 ± 0.22
BA/F3 (M351T)	Murine pro–B-cell line (BCR-ABL1+)	3.11 ± 0.12
BA/F3 (E255K)	Murine pro–B-cell line (BCR-ABL1+)	3.02 ± 0.41
SUP-B15 and SUP-B15 IMr	BCP-ALL (BCR-ABL1+)	2.9 ± 0.67 and 3.97 ± 0.47
HL60	AML	7.17 ± 1.7
Mutz-2	AML	10.10 ± 0.46
Kasumi	AML	6.0 ± 0.03
SEM	BCP-ALL	5.9 ± 0.07
697	BCP-ALL	3.9 ± 0.10

IM-sensitive/resistant human- and murine-derived pro–B-cell lines expressing clinically relevant BCR-ABL1 mutant isoforms (T315I, T315I (PNr), M351T, and E255K) were treated with AX at different concentrations for 72 hours, and the average IC_{50} was then determined by CellTiter-Glo assay (n = 3).

IMr, IM resistant; PNr, ponatinib resistant.

Molecular dynamics (MD) simulations and computation of effective binding energies

To provide a structural model of the binding mode of AX at the HSP90 CTD, we performed 60 MD simulations of at least 400 nanosecond length of free diffusion[35] of AX in the presence of the CTD. During the MD simulations, AX was not biased by any guiding force. Resulting MD trajectories were analyzed with respect to potential binding sites of AX and its binding mode. Furthermore, effective binding energy calculations of AX binding to the CTD were performed.[36] See supplemental Note 3 for further details.

Cell culture

K562, KCL22, HL60, Kasumi, 697, SEM, and Mutz-2 leukemic cell lines were cultured in RPMI 1640 supplemented with 10% fetal calf serum (FCS) and maintained at 37°C with 5% CO_2, except for the Mutz-2[37] and SUP-B15 (BCR-ABL1) BCP-ALL cell lines, which were cultured in McCoy 5A supplemented with 20% FCS (DSMZ, Braunschweig, Germany). Normal Ba/F3 (murine pro-B cell line) or expressing BCR-ABL1$^{T315I,\ M351T,\ and\ E255K}$ mutants[38] were cultured in RPMI 1640 (10% FCS) supplemented with or without interleukin-3 (IL-3) (10 ng/mL), respectively. The BA/F3^{T315I} ponatinib-resistant cell line was generated as described previously[39] and is referred to as BA/F3$^{T315I\ (PNr)}$. In addition, the IM-resistant K562 (1 μM), KCL22 (2.5 μM), and SUP-B15 (2 μM) lines were generated as described previously[40] and are referred to as K562 IMr, KCL22 IMr, and SUP-B15 IMr, respectively. In IM-resistant cell line models, ABL1 kinase domain was sequenced for BCR-ABL1 point mutation using Sanger sequencing, including K562 and K562 IMr, KCL22 (T315I, F317L) and KCL22 IMr (T315I and F317L), SUP-B15 (T315I) and SUP-B15 IMr (T315I), BA/F3^{T315I} (T315I and Y272H), and BA/F3$^{T315I\ (PNr)}$ (T315I and Y272H).

Primary cell culture

Fresh cord blood (CB) samples were obtained from the Institute for Transplantation Diagnostics and Cell Therapeutics (Heinrich Heine University, Duesseldorf) after informed consent approval of the local ethical committee. Mononuclear cells (MNCs) were isolated by Ficoll density gradient centrifugation using standard procedures and later cultured in Mononuclear Cell Medium (PromoCell, Heidelberg, Germany). $CD34^+$ cells were later sorted from these MNCs using magnetic-activated cell sorting (MACS; Miltenyi Biotec, Bergisch Gladbach, Germany).[37] Primary T ($CD3^+$), natural killer (NK) ($CD56^+$), and B ($CD19^+$) cells were isolated from PB MNCs from healthy individuals after using MACS (Miltenyi Biotec). Cytokine profiling was performed on supernatant recovered from primary T, NK, and B cells after 48-hour treatment with respective compounds using Cytokine 25-Plex Human ProcartaPlex Panel 1B (Thermo Fisher Scientific) following the supplier's guidelines.

Primary patient samples were obtained from newly diagnosed or relapsed patients (supplemental Table 2) after informed consent approval of the local ethics committee and were cultured either in Stemline II Hematopoietic Stem Cell Expansion Medium (Sigma-Aldrich) or in Mononuclear Cell Medium (PromoCell). CML and BCR-ABL1+ BCP-ALL samples were sorted for $CD34^+CD38^{+/-}$ using the $CD34^+CD38^-$ Cell Isolation Kit, human (Miltenyi Biotec).

Viability assay

Inhibitors were printed on white 96-well or 384-well plates (Thermo Fisher Scientific) with their increasing concentration (50 nM to 25 μM) along with respective controls by using a digital dispenser (D300e; Tecan, Männedorf, Switzerland). Cell viability

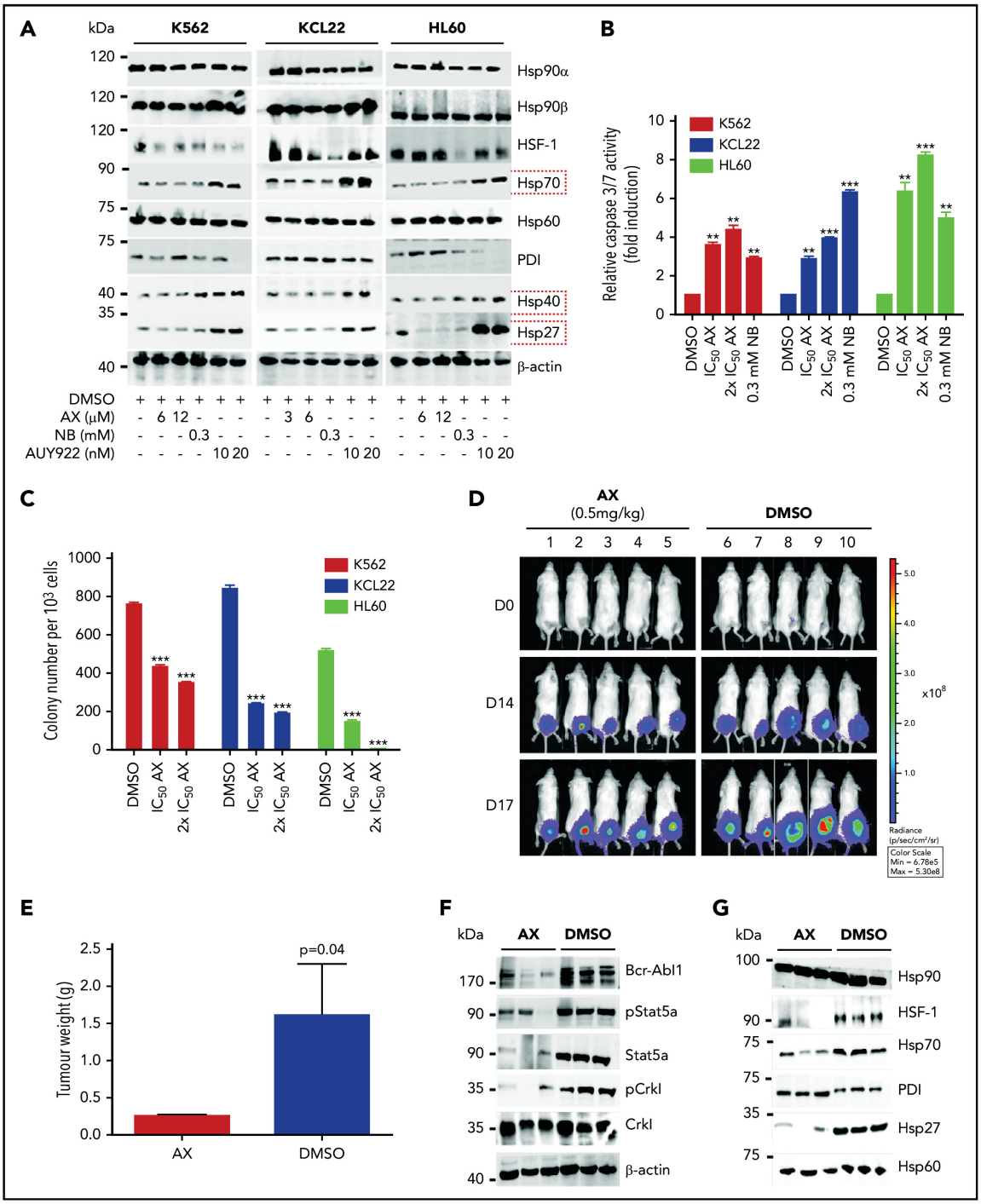

Figure 4. AX is a potent inhibitor in leukemic cell lines without inducing any HSR. (A) K562, KCL22, and HL60 were treated with the indicated (cytotoxic) concentration of AX, NB and AUY922 for 48 hours, and protein lysates were later subjected to immunoblot analysis. AX and NB (C-terminal HSP90 inhibitors) do not induce expression of HSP70, HSP40, and HSP27, whereas AUY922 (an N-terminal HSP90 inhibitor) demonstrates HSR induction by triggering their expression. HSP60 (primarily present in mitochondria) and PDI (primarily present in endoplasmic reticulum) served as controls for the HSR in the cytoplasm, in response to inhibition of HSP90 dimerization via the CTD. (B) K562, KCL22, and HL60 (Mutz-2; data not shown) were treated with AX for 48 hours, and enzymatic activity of caspase-3/7 was later examined by caspase-3/7–dependent Glo assay (absorbance at 405 nm). (C) K562, HL60, KCL22 cells were seeded in methylcellulose medium containing respective compounds at indicated concentration after treatment in liquid medium for 24 hours. Colonies were counted after 14 days. (D) 5 × 10^5 luciferase-expressing K562 cells were subcutaneously transplanted into NSG mice. Starting the day after

was monitored after 72 hours using CellTitre-Glo luminescent assay (Promega, Madison, WI) using a microplate reader (Spark, Tecan). The 50% inhibitory concentration (IC_{50}) for compounds (all inhibitors were bought from MedChemExpress) were determined by plotting raw data (normalized to controls) using sigmoid dose curve and nonlinear regression (GraphPad Prism, San Diego, CA).

Proliferation assay

Cell proliferation was examined after treatment with respective compounds using an automated cell counter, which uses trypan exclusion method (Vi-CELL XR, Beckman Coulter). Proliferation was measured after every 24-hour interval.

Cell cycle assay

AX- or NB-treated cells (48 hours) were fixed with chilled (70%) ethanol for 24 hours to allow the access of propidium iodide (PI) to the DNA. Fixed cells were treated with ribonuclease to digest RNA and later incubated with 200 μL PI (50 μg/mL stock) for 10 minutes at 37°C and immediately subjected to fluorescence-activated cell sorter (FACS) analysis.

Annexin V staining

To evaluate apoptosis, cells treated with respective compounds or control for 48 hours were stained with Annexin V and PI and later subjected to FACS following the supplier's guidelines (Invitrogen, Carlsbad, CA).

Caspase-3/7-Glo assay

Cells were treated with respective compounds or control in white 96-well or 384-well plates. Enzymatic activity of caspase-3/7 was then examined by caspase-3/7–dependent Glo assay (absorbance at 405 nm) following the manufacturer's instructions (Promega) using a microplate reader (Spark, Tecan).

FACS

FACS was performed on FACSCalibur (Becton Dickinson, Heidelberg, Germany) using fluorochrome-coupled monoclonal antibodies along with the following matched isotype controls: anti-CD34 (8G12; BD Biosciences), anti-CD11b (Bear1), anti-CD14 (RMO52), anti-CD13 (Beckman Coulter), and anti-CD33 (Miltenyi Biotec)

Colony-forming unit assay

Colony-forming unit assays were performed initially by treating cells in the liquid medium for 24 hour. Later, treated cells were seeded in a semisolid methylcellulose-based medium containing respective compounds or control.[37] Colonies were counted after 14 days.

In vivo xenograft tumor model

A total of 5×10^5 K-562-luciferase–expressing (stably transduced) cells mixed with Matrigel matrix (Corning) were injected subcutaneously in the dorsal flank of NSG (B6 NOD.Cg-Prkdc^{scid} Il2rg^{tm1Wjl}/SzJ) mice (005557; The Jackson Laboratory, Bar Harbor, ME). Engraftment was monitored by measuring luminescence 3 or 4 days after intraperitoneal injection of 150 μg/100 μL D-Luciferin Firefly sodium salt monohydrate (Biosynth, Staad, Switzerland) using the Caliper IVIS Lumina II Multispectral Imaging System (Perkin Elmer, Rodgau, Germany) and Living Image Software. AX (0.5 mg/kg dose) or vehicle (dimethyl sulfoxide [DMSO]) was administered starting from the day after the transplantation by peritumoral injection for 17 days (n = 5 per group). Mice were sacrificed on day 17, and excised tumors were weighed and subjected to WB analysis. No blinding experiment was performed. Animal husbandry and experiments were conducted in accordance with the German Animal Welfare Act at the Institute for Tumor Biology and Experimental Therapy, Georg-Speyer-Haus, Frankfurt, Germany.

Results

Design and synthesis of HSP90 CTD dimerization inhibitors

HSP90 is a homodimer, with each monomer consisting of three major functional domains, of which the C-terminal domain (CTD) mediates HSP90 dimerization (Figure 1A). The CTD dimerization interface is formed by a characteristic 4-helix bundle (Figure 1B).[41] We recently resolved hot spots in the HSP90 CTD dimerization interface (I688, Y689, I692, and L696; Figure 1C) and identified the first peptidic inhibitors shown to bind to the CTD.[33,34] Subsequently, we demonstrated that α-aminoxy peptides, a novel class of peptidomimetic foldamers, can fold into a unique 2_8-helical conformation.[42] Molecular modeling studies revealed that this 2_8-helix can mimic the spatial arrangement of peptide side chains in α-helices.[42] Herein, we found that side chains of an α-aminoxy hexapeptide can accurately mimic the HSP90 dimerization hot spots (Figure 1C). Based on this knowledge, we designed 2 tailor-made potential HSP90 CTD dimerization inhibitors (α-aminoxy hexapeptides 1 (later referred to as AX) and 2, Figure 1D). A combination of solution- and solid-phase supported methods was used to synthesize 1 (AX) and 2 (Figure 1D; supplemental Note 1). Our investigation of the conformational properties by 2-dimensional nuclear magnetic resonance spectroscopy (supplemental Figures 1 and 2) and CD spectroscopy (supplemental Figure 3) confirmed that 1 (AX) and 2 are able to fold into the desired 2_8-helical conformation indicating that they can adopt the required secondary structure to mimic the HSP90 CTD dimerization hot spots.

AX inhibits HSP90 dimer formation and specifically binds to the CTD of HSP90

To elucidate the biological properties of 1 (AX) and 2, we first showed by means of a dimerization assay based on the autodisplay technology[33] that 1 (AX) and 2 inhibit HSP90 dimer formation (Figure 2A-B). Furthermore, binding of 1 (AX) and 2 to the CTD of HSP90 was revealed by MST measurements with the

Figure 4 (continued) transplantation, animals were treated by peritumoral injection (15 μg) of compound AX (0.5 mg/kg dose) or solvent only (DMSO). One control DMSO-treated mouse was sacrificed earlier (on day 16) because of large tumor size. Luminescence was monitored every 3 or 4 days after intraperitoneal injection of 100 μL luciferin, and the final analysis was performed on day 17 (n = 5 mice per group). (E) AX reduced tumor burden with respect to tumor weight 0.24 ± 0.01 g vs vehicle 1.6 ± 0.6 g ($P = .04$; 1-tailed *t* test). (F) Immunoblot analysis of tumor samples derived from mice treated with AX revealed downregulation of BCR-ABL1 kinase activity and its associated downstream signaling pathways involving Stat5a and Crkl. (G) Immunoblot analysis of tumor samples derived from mice after treatment with AX. Samples displayed no HSR, as evaluated by expression of HSF-1, HSP70, and HSP27; PDI and HSP60 were used as controls. Columns depict the mean of 3 independent experiments (n = 3). Significance analyses of normally distributed data with variance similar between groups used paired, 2-tailed Student *t* test. *$P < .05$, **$P < .005$, ***$P < .001$.

purified, recombinant, NT-647 labeled CTD of HSP90 (1 (AX): K_d = 27.4 μM; 2: K_d = 44.2 μM; Figure 2C; supplemental Figure 4A).

A cell-based luciferase refolding assay[24] using K562 cells revealed a dose-dependent reduction in the luciferase activity after application of 1 (AX) or 2 comparable to NB (CTD HSP90 inhibitor) and AUY922 (NTD HSP90 inhibitor) (Figure 2D; supplemental Figure 4B). Hence, 1 (AX) (IC_{50}: 5.72 ± 0.31 μM [K562]; 7.1 ± 1.7 μM [HL60]) was selected for further experiments due to the higher efficacy in autodisplay, MST, the luciferase refolding assay, and the viability assay compared with 2 (IC_{50}: 16.8 ± 0.11 μM [K562]; 17.4 ± 0.4 μM [HL60]) (supplemental Figure 4C). We proved specific binding of AX to HSP90 complexes by native gel analysis, resulting in a more potent disruption of HSP90α and HSP90β (also HSP40 and HSP27) complexes (including their monomers/dimers) at cytotoxic concentrations (supplemental Figure 5A) than NB and AUY922. In contrast, treatment with AUY922 resulted in an elevated expression of HSR-associated protein complexes (including their monomers/dimers) of HSP40 and HSP27 (supplemental Figure 5A). AX protected recombinant HSP90α protein from degradation against thermolysin digestion, an assay commonly used to quantify DARTS[24] (supplemental Figure 5B). Immunoblotting was performed under reducing (+dithiothreitol) and nonreducing (−dithiothreitol) conditions, which revealed that AX acts on HSP90 oligomers, in contrast to NB but in concordance with AUY922 (supplemental Figure 5C). Sedimentation velocity analysis revealed that AX influences the size distribution of HSP90 CTD, in that AX is able to either dissociate oligomeric species of or suppress HSP90 CTD oligomerization (Figure 2E; supplemental Note 2).

In summary, these results reveal that AX specifically binds to the CTD of HSP90 and inhibits its dimerization.

AX is predicted to bind to the HSP90 CTD dimerization interface and mimic hot spot residues on helix H5′

To provide a binding mode model of AX at the HSP90 CTD, we performed 60 MD simulations of at least 400 nanosecond length of free diffusion of AX in the presence of the CTD (supplemental Figure 7 and supplemental Note 3). In 22 simulations, AX binds between helices H4 and H5 in the dimerization interface (site 1 in Figure 3A; supplemental Figure 7). In the remaining cases, AX either binds to a hydrophobic site occupied by the middle domain in full-length HSP90 (site 2 in Figure 3A-B; supplemental Figures 7 and 8) or gets trapped in locations scattered across the CTD (site 3 in Figure 3B-C; supplemental Figures 7 and 9). Effective binding energy calculations corroborate these results in that the most favorable energies are found for AX at site 1 (Figure 3A; supplemental Figures 10 and 11). The conformations of AX at site 1 revealed side chains partially aligned with side chains of hot spot residues of helix H5′ (Figure 3D-E). The side chain that distinguishes AX from 2 (Figure 1D) binds to a hydrophobic groove formed by I688, I692, and M691 (Figure 3D), where the additional polar hydroxyl group in 2 would be disfavorable, which may explain the lower apparent K_d of 2. Taken together, the computational results suggest that AX binds to the HSP90 CTD dimerization interface and mimics hot spot residues on helix H5′.[34]

AX destabilizes BCR-ABL1 without inducing HSR in vitro and in vivo

HSP90 expression is high in BCR-ABL1$^{+/-}$ leukemia cell lines such as HL60, K562, and Mutz-2 (supplemental Figure 12A). Later, we determined the average IC_{50} for AX in selected leukemic cell lines (Table 1). Upon 48-hour exposure to AX, K562 and KCL22 cells downregulated BCR-ABL1 levels as well as downstream signaling pathways such as STAT5a and CRKL, as evaluated by WB analysis (supplemental Figure 12B). AX additionally reduced pAKT-S473, pS6 expression, and expression of client proteins associated with HSP90 chaperone activity, involving *t*-AKT, *t*-STAT5a, *t*-CRKL, cMYC, and BCL2 (supplemental Figure 12B).

Furthermore, AX triggered the degradation of HSP90 client proteins without elevating the expression of HSPs (HSP70, HSP40, and HSP27) involved in the HSR, in contrast to AUY922 (Figure 4A; supplemental Figure 5A). We observed inhibition of cell proliferation (supplemental Figure 12C) and induction of both late apoptotic (Annexin$^+$PI$^+$) and necrotic (Annexin$^-$PI$^+$) cells after the exposure to AX at its IC_{50} concentration (Table 1) in K562, HL60, and KCL22 cell lines (supplemental Figure 12D). Caspase-3/7 enzyme–dependent apoptosis assays with an induction of approximately three- to fivefold of apoptotic cells in K562, HL60, Mutz-2 (data not shown), and KCL22 corroborated the observations from cell proliferation studies, similarly to exposure with NB (Figure 4B). K562 cells were dose-dependently arrested in G1 phase, and we observed a reduction in G2/M phase after exposure to AX (supplemental Figure 12E). Furthermore, AX facilitated early differentiation in a liquid medium, as measured by expression of myelomonocytic antigens markers involving CD13 and CD38 in K562 cells and CD11b in HL60 cells (supplemental Figure 12F). Moreover, 48-hour exposure of AX to K562, HL60, Mutz-2 (data not shown), and KCL22 significantly reduced their colony-forming capacity (Figure 4C) in accordance to NB, whereas AX was effective at micromolar concentrations ~100-fold below those of NB in the millimolar range. We additionally transplanted K562-Luc (stably expressing the luciferase reporter gene) in an in vivo xenograft model and treated the tumor locally with AX (0.5 mg/kg dose) for 17 days. We obtained a significant reduction in tumor weight (Figure 4D-E), indicating that AX has an antioncogenic potential in vivo. BCR-ABL1 protein and its downstream signaling pathways (STAT5a and CRKL) (Figure 4F) were downregulated, and HSR was not initiated in the excised tumors (Figure 4G).

In summary, these data confirm a potent anti–BCR-ABL1 effect of AX in the absence of HSR induction and at low cytotoxic concentrations in vitro and in vivo.

AX is effective in TKI-resistant leukemic cell line models

BCR-ABL1$^{T315I,\ E255K,\ and\ M351T}$ are the clinically relevant mutations leading to constitutive ABL1 kinase activity and a severe TKI-resistance profile. The effect of AX is superior to that of IM and other second- and third-generation TKIs (including PN) in murine BA/F3 cell line models encompassing BCR-ABL1$^{T315I,\ T315I\ (PNr),\ E255K,\ and\ M351T}$ mutants (supplemental Figure 13A; Figure 5A). In these cell line models, AX reduced cell viability (IC_{50} ~3-4 μM) (Table 1) and proliferation (supplemental Figure 13B) and induced apoptosis (Figure 5B) in a manner similar to NB (0.3 mM). Additionally, after

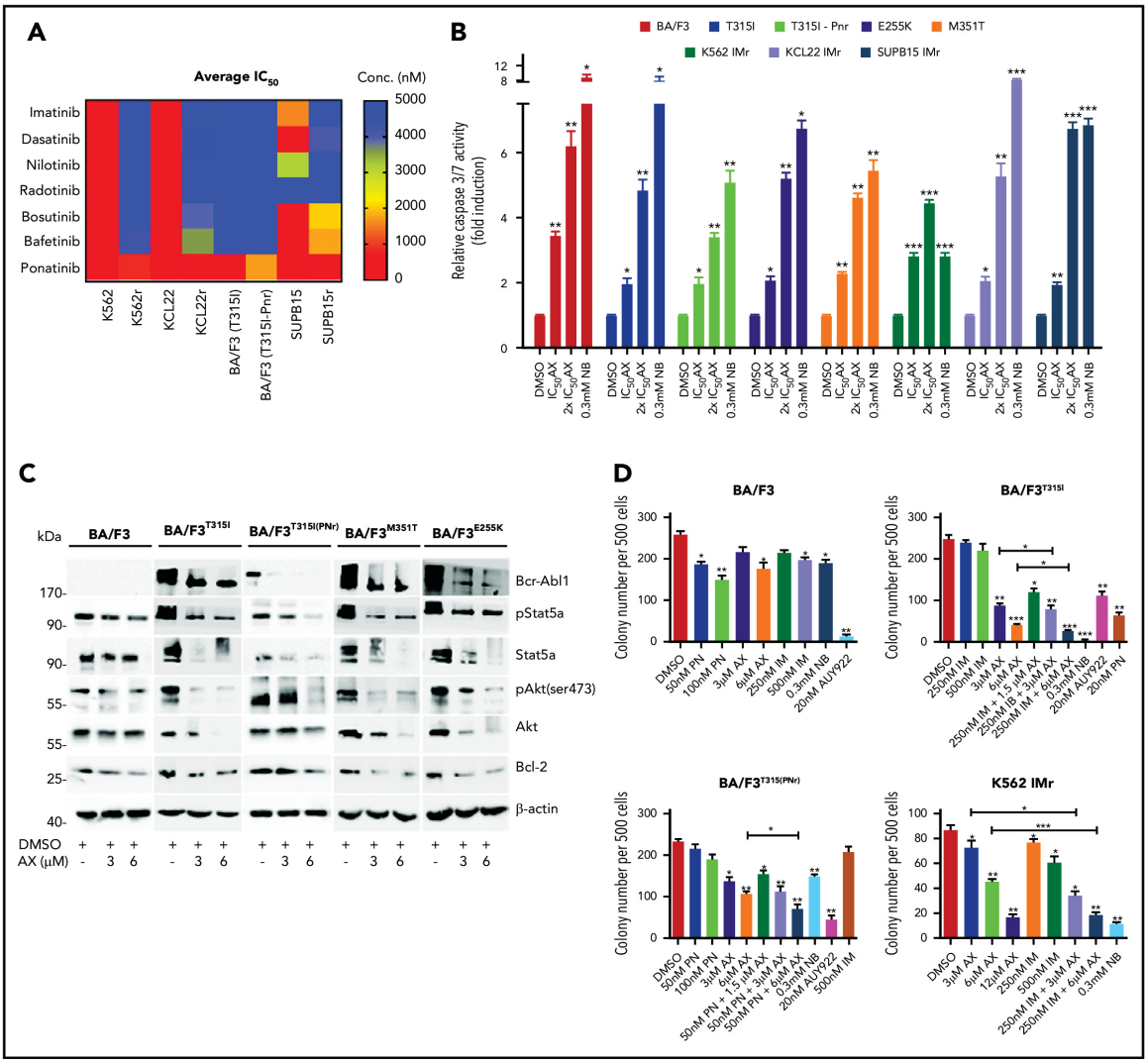

Figure 5. Efficacy of AX in TKI-resistant leukemic cell line models. (A) IM-resistant K562, KCL22, SUP-B15, and BA/F3-expressing BCR-ABL1$^{T315I,\ T315I\ (PNr)}$ along with their respective normal cell lines were treated with second- and third-generation TKIs (dasatinib, nilotinib, radotinib, bosutinib, befetinib, and ponatinib) at 7 different concentrations (ranging from 50 nM to 25 μM) for 72 hours. Later, the average IC_{50} was determined and plotted on a heat map. (B) BA/F3 cells expressing BCR-ABL1$^{T315I,\ T315I\ (PNr),\ M351T,\ and\ E255K}$ mutants, K562 IMr, KCL22 IMr, and SUP-B15 IMr cells were treated with the indicated concentration of AX (48 hours) and later enzymatic activity of caspase-3/7 were examined by caspase-3/7 dependent-Glo assay (absorbance at 405 nm). (C) Likewise, in human leukemia cell lines, AX causes downregulation of BCR-ABL1 and subsequently its associated downstream signaling pathways, including Stat5a, Akt, and Bcl-2 in BA/F3 cells expressing BCR-ABL1$^{T315I,\ T315I\ (PNr),\ M351T,\ and\ E255K}$ mutants. (D) Normal BA/F3 cells, BA/F3-expressing BCR-ABL1$^{T315I\ and\ T315I\ (PNr)}$ mutants, and K562 IMr cells were seeded in methylcellulose medium containing respective compounds at indicated concentration after treatment in liquid medium for 24 hours. Colonies were counted after 14 days. Significance analysis of normally distributed data with variance similar between groups used paired, 2-tailed Student *t* test. $^*P < .05$, $^{**}P < .005$, $^{***}P < .001$.

application of AX, BCR-ABL1 oncoprotein was destabilized, and downstream signaling pathways (AKT, STAT5a, and BCL-2) were blocked with increasing concentrations of AX, which is comparable to the results from TKI-sensitive leukemic cell lines and in vivo xenograft model (Figure 5C). To evaluate the effect of AX in combination with IM, colony-forming assays were performed in which AX was administered alone or coadministered (at lower doses) with IM. Coadministration of AX with IM further reduced the colony-forming capacity of BCR-ABL1$^{T315I\ and\ T315I\ (PNr)}$ cells when compared with treatment with AX alone, NB, AUY922, and PN, which were taken as controls (Figure 5D). Furthermore, we have generated human BCR-ABL1+ IM resistant cell lines, including K562 IMr, KCL22 IMr, and SUP-B15 IMr.[40] These cell lines were also found to be resistant to second- and third-generation TKIs when compared with their normal counterparts (Figure 5A). In analogy to murine BA/F3 cell line models and respective sensitive cell lines, AX reduced the viability of human IM-resistant cell lines at nearly similar IC_{50} concentrations (Table 1) and in addition inhibited proliferation, induced apoptosis, destabilized BCR-ABL1 oncoproteins,

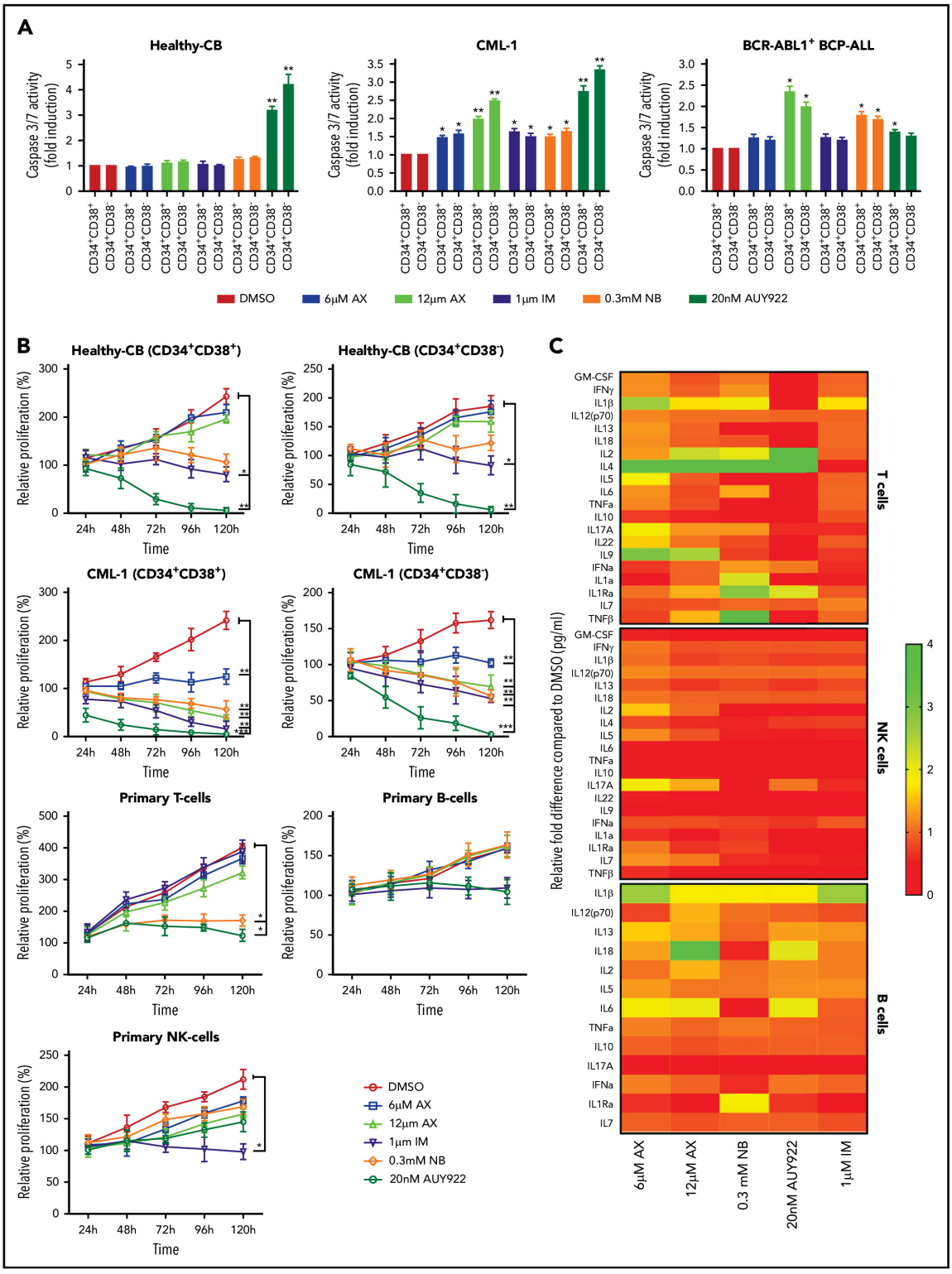

Figure 6.

Figure 6. (Continued).

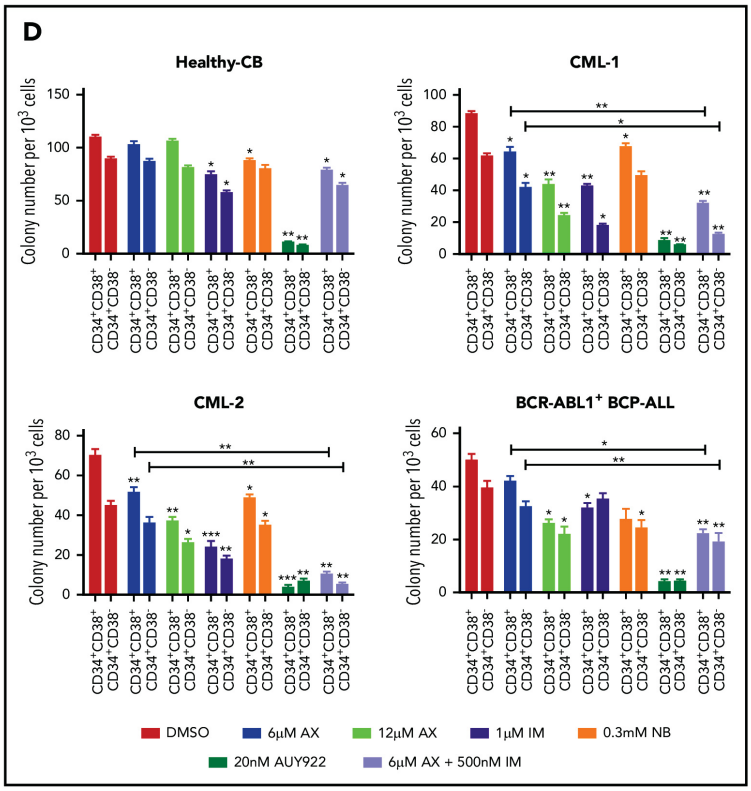

blocked downstream signaling, and further reduced colony-forming ability when used in combination with IM as compared with AX treatment alone (Figure 5D; supplemental Figures 14-16).

AX suppresses human LSCs and acts in a reasonable therapeutic window

The major challenge in treating CML and other stem cell diseases is the elimination of LSCs to establish sustained TFR.[43,44] We therefore have cell sorted 2 patient-derived CML samples taken from diagnosis without prior treatment (clinical data provided in supplemental Table 2) and 1 relapse BCR-ABL1+ BCP-ALL sample for $CD34^+CD38^-$ as markers for CML/BCP-ALL LSCs. AX did not differentiate between $CD34^+CD38^+$ and $CD34^+CD38^-$ subpopulations and significantly inhibited cell growth and induced apoptosis in these leukemic fractions as compared with healthy-CB-derived $CD34^+CD38^+$ or $CD34^+CD38^-$ counterparts, where IM, NB, and AUY922 were used as a control (Figure 6A-B; supplemental Figure 17A-B). The clinical value of AX depends on its therapeutic window. In this regard, we have evaluated the average IC_{50} (20.94 ± 3.07 μM) (supplemental Figure 18A) similar to leukemic cell lines and assessed the cell viability using trypan exclusion method in healthy-CB MNCs (supplemental Figure 18B) after exposure to AX. The cytotoxic effect of AX was significantly less pronounced on healthy fraction than on leukemia cell line models (Table 1). Unlike in leukemic cell lines, AX did not induce early differentiation of CB-$CD34^+$ cells in liquid medium (supplemental Figure 18C) and did not affect the cell proliferation of different healthy blood fractions, including, T, NK, and B cells (Figure 6b). Cytokine profiling (25 cytokines) was performed from the supernatants obtained from these healthy blood cell fractions after treatment with AX (Figure 6C; supplemental

Figure 6. AX suppresses human LSCs and acts in a reasonable therapeutic window. (A) One BCR-ABL1+ CML patient sample and a relapse BCP-ALL patient sample, along with a healthy human-CB-derived $CD34^+CD38^{+/-}$ (sorted by MACS) sample, were treated with increasing concentrations of AX or controls (NB, AUY922, or IM). Later, the enzymatic activity of caspase-3/7 was examined using a caspase-3/7–dependent Glo assay after 5 days of treatment. (B) Primary patient samples along with healthy control cells (including primary B, T, and NK cells) were treated with the indicated concentration of AX or controls (NB, AUY922, or IM), and viable cells were counted after every 24-hour interval for 5 days. AX specifically targets leukemic samples (both the leukemic bulk and leukemic stem cell fractions) contrary to healthy control cells. (C) Supernatants were collected from primary T, NK, and B cells after 48-hour treatment with respective compound and then evaluated for the detection of 25 different human cytokines. Heat maps depict the fold difference relative to the control (DMSO) in picograms per milliliter. Some cytokines were omitted from the analysis because their concentration was below the detection limit. (D) $CD34^+CD38^{+/-}$ cells from 2 BCR-ABL1+ CML (CML-1 and CML-2) patient samples and 1 TKI-resistant BCR-ABL1+ BCR-ALL patient sample, along with healthy CB controls, were seeded in methylcellulose medium containing respective compounds at the indicated concentration after treatment in liquid medium for 24 hours. Colonies were counted after 14 days (n = 5). Significance analysis of normally distributed data with variance similar between groups used a paired, 2-tailed Student *t* test. $^*P < .05$, $^{**}P < .005$, $^{***}P < .001$. IFNa, interferon α; GM-CSF, granulocyte-macrophage colony-stimulating factor; TNFa, tumor necrosis factor α.

Table 3). As compared with AUY922, there was a modest change in the cytokine profile with AX, especially in T cells, with the exception for IL-17a in NK cells and IL-6 in B cells (Figure 6C; supplemental Table 3). Moreover, AX specifically inhibited the colony-forming capacity of the CML (n = 3) and BCP-ALL (n = 1) patient-derived $CD34^+CD38^+$ and $CD34^+CD38^-$ fraction as compared with their healthy-CB-derived counterparts (Figure 6D; supplemental Figure 17C). The co-administration of AX along with IM further blocked the colony formation of both $CD34^+CD38^+$ and $CD34^+CD38^-$ leukemic fractions (Figure 6D). Like in leukemic cell lines, AX did not inflict any HSR (supplemental Figure 19A) and induced early differentiation in CML^{CD34+} in liquid medium (supplemental Figure 19B).

As HSP90 is involved in chaperoning several other oncoproteins besides BCR-ABL1,[4,45] which is involved in several other leukemia subtypes, we evaluated the effect of AX on BCR-ABL1− leukemia involving, FLT3 ITD+ AML (n = 2), Ph-like ALL (n = 1), and CLL (n = 1) clinical samples. Likewise, in BCR-ABL1+ CML samples, AX inhibited growth and induced apoptosis in FLT3-ITD+ AML and reduced colony formation in all 4 patient samples (Figure 6D; supplemental Figures 20 and 21).

Discussion

The involvement in a plethora of oncogenic pathways has positioned HSP90 as a prominent therapeutic target. Malignant cells are particularly sensitive to HSP90 inhibition.[14,46] Over the last decade, ~15 different inhibitors targeting the adenosine triphosphate binding pocket in HSP90's N terminus have been assessed in >40 different clinical trials; however, the entire class of these inhibitors instigates an HSR.[8,14,15,18-22,24,47-49] Ocular toxicity is a major concern with HSP90 inhibitors; for instance, in a phase 1 clinical trial, the maximum tolerated dose of AUY922 induced night blindness in 20% of patients, and ~7% of the patients developed grade ≥3 eye disorders (supplemental Table 1).[45,50] These reports suggest that the nonselectivity of N-terminal HSP90 inhibitors leads to toxicity and to induction of the HSR, which could be why N-terminal HSP90 inhibitors fail in advanced clinical trials.[8,14,45] Functional assays have shown that the silencing of HSF-1, HSP70, and HSP27 in addition to HSP90 considerably enhances the cytotoxic effect of HSP90 inhibitors against malignant cells.[18,20,21] Accordingly, some HSP90 C-terminal inhibitors have been developed that appear not to induce any HSR; however, they have not yet entered clinical trials.[15,23,24,51,52] None of these inhibitors have been reported to act as protein–protein interaction inhibitors that interfere with CTD dimerization.[23,51,53,54] Here, we developed the α-aminoxy hexapeptide AX, which blocks HSP90 function by specifically binding to the CTD of HSP90 and then either dissociating oligomeric species or suppressing HSP90 CTD oligomerization, which ultimately leads to inhibition of HSP90 dimer formation.

The CTD is essential for the dimerization of HSP90 and therefore crucial for HSP90 function.[41] Targeting protein–protein interactions is generally considered challenging due to the size, hydrophobicity, and lack of deep binding pockets at the protein–protein interfaces.[55] Based on our MD simulation, AX binds to the HSP90 CTD dimerization interface and mimics hot spot residues on helix H5′. Thus, the mode of action of AX differs from all other known HSP90 inhibitors, which makes AX the first-in-class HSP90 C-terminal dimerization inhibitor. The absence of HSR upon administration of AX is in agreement with previous reports that the modulation of HSP90 function via the C terminus does not trigger an HSR response.[15,23,24,51,52]

We evaluated AX in CML and showed that it targets BCR-ABL1–expressing precursor cells, which are dependent on BCR-ABL1 expression, and CML LSCs, which are independent of BCR-ABL1 expression and therefore not targetable by TKIs. We showed that this mechanism also applies to highly resistant BCP-ALL, including BCR-ABL1+ BCP-ALL, in which AX is equally effective. Especially in Ph-like BCP-ALL, inhibition of HSP90 by AX is of major importance because of its poor response to TKI treatment and its 3-times-higher frequency compared with BCR-ABL1+ BCP-ALL, especially in young adults. Thus, in the future, AX or its analogs might also be applied to other leukemia entities that still have an intolerably poor prognosis, such as BCR-ABL1+ BCP-ALL, Ph-like BCP-ALL, and FLT3-ITD+ AML. Moreover, AX constitutes a promising compound in many solid tumor entities, which are characterized by expression of HSP90 client proteins (eg, AKT, HER2, BRAF, and EGFR) with key functions in multiple myelomas and solid carcinomas (supplemental Table 4).

Acknowledgments

The authors thank all members of their groups for useful discussions and critical reading of the manuscript. Kathleen Mohs is acknowledged for her technical assistance during animal experiments.

J.H. is supported by the German Cancer Aid (Project 110997 and Translational Oncology Program 70112951), the German Jose Carreras Leukemia Foundation (DJCLS 02R/2016), the Kinderkrebsstiftung (2016/17), the Deutsches Konsortium für Translationale Krebsforschung (DKTK) Joint funding (Targeting MYC L*10), and the Elterninitiative Kinderkrebsklinik. F.K.H. acknowledges financial support from the Fonds der Chemischen Industrie and the Strategischer Forschungsfonds of Heinrich Heine University (HHU) (SFF - F 2012/79-17). T. Kurz, H.G., G.G., and M.U.K. are supported by funds from the Strategischer Forschungsfonds of HHU. Computational support and infrastructure were provided by the Centre for Information and Media Technology at HHU Düsseldorf (Germany). We are grateful to the John von Neumann Institute for Computing (NIC) and the Jülich Supercomputing Centre for computing time on the supercomputer JURECA (NIC project HKF 7 (H.G., B.F.). Financial support by Deutsche Forschungsgemeinschaft through funds to purchase the hybrid computer cluster used in this study (INST 208/704-1 FUGG) (H.G.) is gratefully acknowledged. The Deutsche Forschungsgemeinschaft is acknowledged for funds used to purchase the UHR-TOF maXis 4G, Bruker Daltonics, Bremen HRMS instrument used in this research. V.M. is supported by the Düsseldorf School of Oncology (funded by the Comprehensive Cancer Centre Düsseldorf/Deutsche Krebshilfe and the Medical Faculty of the Heinrich Heine University Düsseldorf). The Georg-Speyer-Haus is funded jointly by the German Federal Ministry of Health and the Ministry of Higher Education, Research and the Arts of the State of Hessen. A.B. is supported by the German Children's Cancer Foundation and the Federal Ministry of Education and Research (Bonn, Germany).

Authorship

Contribution: H.G., T. Kurz, F.K.H., and J.H. contributed to conception and design of the project and supervision of the study; D.D., B.B., S.B., H.A., B.F., T.Z., T. Kröger, S.L., A.J.R.M., H.K., S.S., F.V.O., M.O., F.L., and V.M. acquired data; S.B., T.E., G.K., A.K., D.D., B.F., A.B., A.H., F.B., M.G., G.G., M.R., M.U.K., T. Kurz, H.G., F.K.H., and J.H. developed methodology; S.B., D.D., B.F., B.B., S.L., A.J.R.M., M.U.K., S.S., A.B., A.H., G.G., L.N.-S., J.J., T. Kurz, H.G., F.K.H., and J.H. were responsible for analysis and interpretation of data; and S.B., D.D., B.F., S.L., M.U.K., G.G.,

L.N.-S., J.J., T. Kurz, H.G., F.K.H., and J.H. wrote, reviewed, and/or revised the manuscript.

Conflict-of-interest disclosure: The authors declare no competing financial interests.

ORCID profiles: S.B., 0000-0001-6494-7744; B.F., 0000-0002-7877-0262; T. Kurz, 0000-0002-9474-4224; H.G., 0000-0001-8613-1447; F.K.H., 0000-0001-9765-5975; J.H., 0000-0002-4058-3058.

Correspondence: Julia Hauer, Department of Pediatric Oncology, Hematology and Clinical Immunology, Medical Faculty, Heinrich Heine University Düsseldorf, Düsseldorf, Germany; e-mail: julia.hauer@med.uni-duesseldorf.de; and Finn K. Hansen, Pharmaceutical/Medicinal Chemistry, Institute of Pharmacy, Leipzig University, Leipzig, Germany; e-mail: finn.hansen@uni-leipzig.de.

Footnotes

Submitted 12 October 2017; accepted 19 April 2018. Prepublished online as *Blood* First Edition paper, 3 May 2018; DOI 10.1182/blood-2017-10-810986.

*F.K.H. and J.H. contributed equally to this study.

The online version of this article contains a data supplement.

There is a *Blood* Commentary on this article in this issue.

The publication costs of this article were defrayed in part by page charge payment. Therefore, and solely to indicate this fact, this article is hereby marked "advertisement" in accordance with 18 USC section 1734.

REFERENCES

1. Mahalingam D, Swords R, Carew JS, Nawrocki ST, Bhalla K, Giles FJ. Targeting HSP90 for cancer therapy. *Br J Cancer*. 2009;100(10):1523-1529.
2. Khajapeer KV, Baskaran R. Hsp90 inhibitors for the treatment of chronic myeloid leukemia. *Leuk Res Treatment*. 2015;2015:757694.
3. Lazenby M, Hills R, Burnett AK, Zabkiewicz J. The HSP90 inhibitor ganetespib: A potential effective agent for Acute Myeloid Leukemia in combination with cytarabine. *Leuk Res*. 2015;39(6):617-624.
4. Miyata Y, Nakamoto H, Neckers L. The therapeutic target Hsp90 and cancer hallmarks. *Curr Pharm Des*. 2013;19(3):347-365.
5. Yamaki H, Nakajima M, Shimotohno KW, Tanaka N. Molecular basis for the actions of Hsp90 inhibitors and cancer therapy. *J Antibiot (Tokyo)*. 2011;64(9):635-644.
6. Wu LX, Xu JH, Zhang KZ, et al. Disruption of the Bcr-Abl/Hsp90 protein complex: a possible mechanism to inhibit Bcr-Abl-positive human leukemic blasts by novobiocin. *Leukemia*. 2008;22(7):1402-1409.
7. Blagosklonny MV, Toretsky J, Neckers L. Geldanamycin selectively destabilizes and conformationally alters mutated p53. *Oncogene*. 1995;11(5):933-939.
8. Wang M, Shen A, Zhang C, et al. Development of heat shock protein (Hsp90) inhibitors to combat resistance to tyrosine kinase inhibitors through Hsp90-kinase Interactions. *J Med Chem*. 2016;59(12):5563-5586.
9. Reikvam H, Hatfield KJ, Ersvaer E, et al. Expression profile of heat shock proteins in acute myeloid leukaemia patients reveals a distinct signature strongly associated with FLT3 mutation status–consequences and potentials for pharmacological intervention. *Br J Haematol*. 2012;156(4):468-480.
10. Flandrin P, Guyotat D, Duval A, et al. Significance of heat-shock protein (HSP) 90 expression in acute myeloid leukemia cells. *Cell Stress Chaperones*. 2008;13(3):357-364.
11. Zong H, Gozman A, Caldas-Lopes E, et al. A hyperactive signalosome in acute myeloid leukemia drives addiction to a tumor-specific Hsp90 species. *Cell Reports*. 2015;13(10):2159-2173.
12. Kucine N, Marubayashi S, Bhagwat N, et al. Tumor-specific HSP90 inhibition as a therapeutic approach in JAK-mutant acute lymphoblastic leukemias. *Blood*. 2015;126(22):2479-2483.
13. Wells J, Jain N, Konopleva M. Philadelphia chromosome-like acute lymphoblastic leukemia: progress in a new cancer subtype. *Clin Adv Hematol Oncol*. 2017;15(7):554-561.
14. Butler LM, Ferraldeschi R, Armstrong HK, Centenera MM, Workman P. Maximizing the therapeutic potential of HSP90 inhibitors. *Mol Cancer Res*. 2015;13(11):1445-1451.
15. Wang Y, McAlpine SR. Heat-shock protein 90 inhibitors: will they ever succeed as chemotherapeutics? *Future Med Chem*. 2015;7(2):87-90.
16. Whitesell L, Santagata S, Lin NU. Inhibiting HSP90 to treat cancer: a strategy in evolution. *Curr Mol Med*. 2012;12(9):1108-1124.
17. Duerfeldt AS, Blagg BS. Hsp90 inhibition: elimination of shock and stress. *Bioorg Med Chem Lett*. 2010;20(17):4983-4987.
18. Maloney A, Clarke PA, Naaby-Hansen S, et al. Gene and protein expression profiling of human ovarian cancer cells treated with the heat shock protein 90 inhibitor 17-allylamino-17-demethoxygeldanamycin. *Cancer Res*. 2007;67(7):3239-3253.
19. Bagatell R, Paine-Murrieta GD, Taylor CW, et al. Induction of a heat shock factor 1-dependent stress response alters the cytotoxic activity of hsp90-binding agents. *Clin Cancer Res*. 2000;6(8):3312-3318.
20. McCollum AK, Teneyck CJ, Sauer BM, Toft DO, Erlichman C. Up-regulation of heat shock protein 27 induces resistance to 17-allylamino-demethoxygeldanamycin through a glutathione-mediated mechanism. *Cancer Res*. 2006;66(22):10967-10975.
21. Guo F, Rocha K, Bali P, et al. Abrogation of heat shock protein 70 induction as a strategy to increase antileukemia activity of heat shock protein 90 inhibitor 17-allylamino-demethoxy geldanamycin. *Cancer Res*. 2005;65(22):10536-10544.
22. Hall JA, Forsberg LK, Blagg BS. Alternative approaches to Hsp90 modulation for the treatment of cancer. *Future Med Chem*. 2014;6(14):1587-1605.
23. Wang Y, McAlpine SR. N-terminal and C-terminal modulation of Hsp90 produce dissimilar phenotypes. *Chem Commun (Camb)*. 2015;51(8):1410-1413.
24. Eskew JD, Sadikot T, Morales P, et al. Development and characterization of a novel C-terminal inhibitor of Hsp90 in androgen dependent and independent prostate cancer cells. *BMC Cancer*. 2011;11(1):468.
25. Wang Y, Koay YC, McAlpine SR. How selective are Hsp90 inhibitors for cancer cells over normal cells? *ChemMedChem*. 2017;12(5):353-357.
26. Hughes TP, Ross DM. Moving treatment-free remission into mainstream clinical practice in CML. *Blood*. 2016;128(1):17-23.
27. Wieczorek A, Uharek L. Management of chronic myeloid leukemia patients resistant to tyrosine kinase inhibitors treatment. *Biomark Insights*. 2016;10(Suppl 3):49-54.
28. Ursan ID, Jiang R, Pickard EM, Lee TA, Ng D, Pickard AS. Emergence of BCR-ABL kinase domain mutations associated with newly diagnosed chronic myeloid leukemia: a meta-analysis of clinical trials of tyrosine kinase inhibitors. *J Manag Care Spec Pharm*. 2015;21(2):114-122.
29. Williams LA, Garcia Gonzalez AG, Ault P, et al. Measuring the symptom burden associated with the treatment of chronic myeloid leukemia. *Blood*. 2013;122(5):641-647.
30. Efficace F, Baccarani M, Breccia M, et al; GIMEMA. Health-related quality of life in chronic myeloid leukemia patients receiving long-term therapy with imatinib compared with the general population. *Blood*. 2011;118(17):4554-4560.
31. Kantarjian HM, Shah NP, Cortes JE, et al. Dasatinib or imatinib in newly diagnosed chronic-phase chronic myeloid leukemia: 2-year follow-up from a randomized phase 3 trial (DASISION). *Blood*. 2012;119(5):1123-1129.
32. Chai-Adisaksopha C, Lam W, Hillis C. Major arterial events in patients with chronic myeloid leukemia treated with tyrosine kinase inhibitors: a meta-analysis. *Leuk Lymphoma*. 2016;57(6):1300-1310.
33. Bopp B, Ciglia E, Ouald-Chaib A, Groth G, Gohlke H, Jose J. Design and biological testing of peptidic dimerization inhibitors of human Hsp90 that target the C-terminal domain. *Biochim Biophys Acta*. 2016;1860(6):1043-1055.
34. Ciglia E, Vergin J, Reimann S, et al. Resolving hot spots in the C-terminal dimerization domain that determine the stability of the

molecular chaperone Hsp90. *PLoS One*. 2014;9(4):e96031.

35. Gohlke H, Hergert U, Meyer T, et al. Binding region of alanopine dehydrogenase predicted by unbiased molecular dynamics simulations of ligand diffusion. *J Chem Inf Model*. 2013; 53(10):2493-2498.

36. Miller BR III, McGee TD Jr, Swails JM, Homeyer N, Gohlke H, Roitberg AE. MMPBSA.py: an efficient program for end-state free energy calculations. *J Chem Theory Comput*. 2012;8(9):3314-3321.

37. Bhatia S, Reister S, Mahotka C, Meisel R, Borkhardt A, Grinstein E. Control of AC133/CD133 and impact on human hematopoietic progenitor cells through nucleolin. *Leukemia*. 2015;29(11):2208-2220.

38. Ernst T, Gruber FX, Pelz-Ackermann O, et al. A co-operative evaluation of different methods of detecting BCR-ABL kinase domain mutations in patients with chronic myeloid leukemia on second-line dasatinib or nilotinib therapy after failure of imatinib. *Haematologica*. 2009;94(9):1227-1235.

39. Okabe S, Tauchi T, Tanaka Y, Katagiri S, Kitahara T, Ohyashiki K. Activity of omacetaxine mepesuccinate against ponatinib-resistant BCR-ABL-positive cells. *Blood*. 2013;122(17): 3086-3088.

40. Mahon FX, Deininger MW, Schultheis B, et al. Selection and characterization of BCR-ABL positive cell lines with differential sensitivity to the tyrosine kinase inhibitor STI571: diverse mechanisms of resistance. *Blood*. 2000;96(3): 1070-1079.

41. Pearl LH, Prodromou C. Structure and mechanism of the Hsp90 molecular chaperone machinery. *Annu Rev Biochem*. 2006;75(1): 271-294.

42. Diedrich D, Moita AJ, Rüther A, et al. α-Aminoxy oligopeptides: synthesis, secondary structure, and cytotoxicity of a new class of anticancer foldamers. *Chem Eur J*. 2016; 22(49):17600-17611.

43. Shah NP, Nicoll JM, Nagar B, et al. Multiple BCR-ABL kinase domain mutations confer polyclonal resistance to the tyrosine kinase inhibitor imatinib (STI571) in chronic phase and blast crisis chronic myeloid leukemia. *Cancer Cell*. 2002;2(2):117-125.

44. Gorre ME, Mohammed M, Ellwood K, et al. Clinical resistance to STI-571 cancer therapy caused by BCR-ABL gene mutation or amplification. *Science*. 2001;293(5531):876-880.

45. Jhaveri K, Ochiana SO, Dunphy MP, et al. Heat shock protein 90 inhibitors in the treatment of cancer: current status and future directions. *Expert Opin Investig Drugs*. 2014; 23(5):611-628.

46. Trepel J, Mollapour M, Giaccone G, Neckers L. Targeting the dynamic HSP90 complex in cancer. *Nat Rev Cancer*. 2010;10(8):537-549.

47. Hsu HS, Lin JH, Huang WC, et al. Chemoresistance of lung cancer stemlike cells depends on activation of Hsp27. *Cancer*. 2011;117(7):1516-1528.

48. Gandhi N, Wild AT, Chettiar ST, et al. Novel Hsp90 inhibitor NVP-AUY922 radiosensitizes prostate cancer cells. *Cancer Biol Ther*. 2013;14(4):347-356.

49. Modi S, Saura C, Henderson C, et al. A multicenter trial evaluating retaspimycin HCL (IPI-504) plus trastuzumab in patients with advanced or metastatic HER2-positive breast cancer. *Breast Cancer Res Treat*. 2013;139(1): 107-113.

50. Zhou D, Liu Y, Ye J, et al. A rat retinal damage model predicts for potential clinical visual disturbances induced by Hsp90 inhibitors. *Toxicol Appl Pharmacol*. 2013;273(2): 401-409.

51. Koay YC, McConnell JR, Wang Y, et al. Chemically accessible hsp90 inhibitor that does not induce a heat shock response. *ACS Med Chem Lett*. 2014;5(7):771-776.

52. Sellers RP, Alexander LD, Johnson VA, et al. Design and synthesis of Hsp90 inhibitors: exploring the SAR of Sansalvamide A derivatives. *Bioorg Med Chem*. 2010;18(18): 6822-6856.

53. Marcu MG, Chadli A, Bouhouche I, Catelli M, Neckers LM. The heat shock protein 90 antagonist novobiocin interacts with a previously unrecognized ATP-binding domain in the carboxyl terminus of the chaperone. *J Biol Chem*. 2000;275(47):37181-37186.

54. Yun BG, Huang W, Leach N, Hartson SD, Matts RL. Novobiocin induces a distinct conformation of Hsp90 and alters Hsp90-cochaperone-client interactions. *Biochemistry*. 2004;43(25):8217-8229.

55. Metz A, Ciglia E, Gohlke H. Modulating protein-protein interactions: from structural determinants of binding to druggability prediction to application. *Curr Pharm Des*. 2012; 18(30):4630-4647.

56. Ali MMU, Roe SM, Vaughan CK, et al. Crystal structure of an Hsp90-nucleotide-p23/Sba1 closed chaperone complex. *Nature*. 2006; 440(7087):1013-1017.

57. Lee CC, Lin TW, Ko TP, Wang AH. The hexameric structures of human heat shock protein 90. *PLoS One*. 2011;6(5):e19961.

Supplemental Information

Table of Content:

Table S1: List of selected HSP90i inhibitors either in preclinical or clinical stage.

	Target domain	HSR	Clinical Trials or in vitro/vivo	Side effects/Toxicity	References
GM	N-terminal	Yes	Never evaluated in the clinic due to poor drug like properties		[1]
17-AAG (Tanespimycin)	N-terminal	Yes	Solid and hematological malignancies in more than 30 clinical trials phase I/II	Early Phase I trials were disappointing due to modest activity, dose limiting toxicity	[2,3]
17-DMAG (Alvespimycin)	N-terminal	Yes	Applied in prostate cancer, melanoma, AML and HER2+ breast cancer	Clinical development was stopped due to commercial consideration	[4-6]
IPI-504 (Retaspimycin)	N-terminal	Yes	Phase III GIST tumours and Phase Ib for prostate cancer	Terminated due to high mortality and unexpected toxicity	[7,8]
AUY922 (Luminespib)	N-terminal	Yes	In phase II applied to EGFR mutated lung cancer and several other phase I and II clinical trials	Duration of treatment was limited due to toxicity especially night blindness for EGFR mutated lung cancer trial	[9,10]
AT13387 (Onalespib)	N-terminal	Yes	Currently in phase III applied for gastrointestinal tumors, ALK+ NSCLC	Visual disturbance noticed at higher doses	[7,9,11]
STA-9090 (Ganetespib)	N-terminal	Yes	Various phase I and phase II in solid tumours and haematological malignancies. Also in Phase III study for NSCLC, however the study was terminated due to futility	Most promising single agent in NSCLC patients but in phase I/ II metastatic pancreatic cancer grade 3 treatment related toxicity was noticed	[7,9,12] NCT01798485
PU-H71	N-terminal	Yes	Phase I, Non Hodgkin lymphoma, Solid tumour, AML	Ongoing or trial for Non Hodgkin lymphoma was terminated due to unviability of the compound, some trials are still ongoing	NCT01581541,[7,13]
BIIB021	N-terminal	Yes	Phase I for B-CLL, Phase II GIST	Terminated or no result posted	NCT00344786, NCT00618319
PF-04929113 (SNX-5422)	N-terminal	Yes	Phase I, advanced malignancies	Discontinue due to ocular toxicity and irreversible retinal damage	[14]
Novobiocin	C-terminal	No	In vitro/in vivo		[15]
Coumermycin analogues	C-terminal	No	In vitro/in vivo		[16]
SM145	C-terminal	No	In vitro/in vivo		[17]
SM-122	C-terminal	No	In vitro/in vivo		[18]
SM-253	C-terminal	No	In vitro/in vivo		[18]
SM258	C-terminal	No	In vitro/in vivo		[18,19]
KU-174	C-terminal	No	In vitro/in vivo		[20]
Aminoxyrone	C-terminal	No	In vitro/in vivo		

Table S2: List of primary patient samples related to figure 6, supplemental figure 20 and 21.

Sample ID	Age at diagnosis (years)	Disease	Cytogenetics	BCR-ABL transcript/ other mutations
CML-1	42	CML	46,XX,t(9;22)(q34;q11)[16]; 46,XX[1]	b3a2
CML-2	75	CML	45,X,-Y,t(9;22)(q34;q11)	e1a2
CML-3	37	CML	46,XY,t(9;22)(q34;q11)	b3a2
CML-4	44	CML	46,XX,t(9;22)(q34;q11)	b2a2
BCP-ALL-1	5	BCP-ALL	46, XY, t(9;22)(q34;q11) [8], 46, XY [4]	IKZF1 Deletion
AML-1	14	AML	46, XY	FLT3-ITD+
AML-2	15	AML	46, XY	FLT3-ITD+
Ph like – BCP-ALL	4	Ph-like BCP-ALL	45, XY, dic(9;20)(p12;q11) [2]; 46, XY [19]	CDKN2A-Deletion, Proof of a 20qter- and 20q12-Deletion, Deletion Exon 4 -7 in IKZF1-Gene
CLL-1	-	CLL	-	no information available

Table S3: Raw data which was plotted as heat map in figure 6c for cytokine profiling assay. Table is showing average fold difference relative to control (DMSO) in pg/ml, which was calculated from the supernatant obtained from primary T, NK and B cells after 48h treatment with the respective compounds.

	GM-CSF	IGNg	IL1ß	IL12(p70)	IL13	IL18	IL2	IL4	IL5	IL6	TNFa	IL10	IL17A	IL22	IL9	IFNa	IL1a	IL1Ra	IL7	TNFß
DMSO (T cells)	1,0	1,0	1,0	1,0	1,0	1,0	1,0	1,0	1,0	1,0	1,0	1,0	1,0	1,0	1,0	1,0	1,0	1,0	1,0	1,0
6uM (AX)	1,2	1,2	2,7	1,2	1,3	1,2	1,3	3,8	1,8	1,3	1,2	0,7	1,9	1,6	3,0	0,7	0,5	1,0	0,8	0,8
12uM (AX)	0,9	0,9	1,7	1,0	0,9	0,9	2,3	5,6	0,9	0,8	0,8	0,6	1,3	1,1	2,5	1,0	1,0	1,4	0,9	1,5
0.3mM NB	1,1	1,3	1,9	1,0	0,2	0,9	2,0	8,4	0,3	1,4	0,3	0,4	1,3	0,8	0,7	1,3	2,2	2,9	1,0	4,2
20nM AUY922	0,1	0,1	0,1	1,0	0,0	0,1	4,6	4,8	0,1	0,4	0,1	0,4	0,6	0,0	0,1	1,1	0,5	2,2	0,9	0,0
1uM IM	1,0	1,0	1,7	1,0	1,0	1,0	1,0	0,4	1,0	1,0	1,0	0,8	0,6	0,9	0,7	0,6	0,5	0,9	1,2	1,0

	GM-CSF	IGNg	IL1ß	IL12(p70)	IL13	IL18	IL2	IL4	IL5	IL6	TNFa	IL10	IL17A	IL22	IL9	IFNa	IL1a	IL1Ra	IL7	TNFß
DMSO (NK cells)	1,0	1,0	1,0	1,0	1,0	1,0	1,0	1,0	1,0	1,0	1,0	1,0	1,0	1,0	1,0	1,0	1,0	1,0	1,0	1,0
6uM (AX)	0,5	1,1	1,0	1,2	0,9	1,1	1,5	0,8	1,2	0,5	0,5	0,5	1,9	0,5	0,1	0,8	0,6	1,1	1,2	0,6
12uM (AX)	0,3	0,8	0,7	1,0	0,7	1,0	1,0	0,6	0,9	0,2	0,2	0,2	1,4	0,4	0,5	0,8	0,3	0,7	1,1	0,3
0.3mM NB	0,2	0,9	0,8	1,0	0,8	0,9	0,4	0,6	0,5	0,1	0,1	0,1	0,1	0,4	0,3	0,8	0,7	0,8	0,6	0,2
20nM AUY922	0,1	0,9	0,7	1,0	0,7	0,9	0,3	0,7	0,5	0,0	0,1	0,1	1,1	0,1	0,4	0,7	0,3	0,4	0,6	0,1
1uM IM	0,2	0,9	0,7	1,1	0,8	0,9	0,4	0,7	0,5	0,2	0,1	0,3	0,6	0,3	0,3	0,9	0,2	0,3	0,5	0,2

	GM-CSF	IGNg	IL1ß	IL12(p70)	IL13	IL18	IL2	IL4	IL5	IL6	TNFa	IL10	IL17A	IL22	IL9	IFNa	IL1a	IL1Ra	IL7	TNFß
DMSO (B cells)	0,0	0,0	1,0	1,0	1,0	1,0	1,0	0,0	1,0	1,0	1,0	1,0	1,0	0,0	0,0	1,0	0,0	1,0	1,0	0,0
6uM (AX)	0,0	0,0	2,7	0,8	1,6	1,3	1,1	0,0	1,3	1,9	1,1	0,9	0,5	0,0	0,0	1,1	0,0	0,6	0,9	0,0
12uM (AX)	0,0	0,0	1,8	1,4	1,4	4,9	1,5	0,0	1,1	2,1	1,0	0,8	0,5	0,0	0,0	1,0	0,0	0,4	0,8	0,0
0.3mM NB	0,0	0,0	1,8	1,1	1,0	0,6	1,1	0,0	1,1	0,5	1,1	0,9	0,5	0,0	0,0	0,6	0,0	1,9	0,9	0,0
20nM AUY922	0,0	0,0	1,8	0,9	1,3	2,1	1,2	0,0	1,2	2,1	1,0	0,9	0,1	0,0	0,0	1,1	0,0	0,7	0,9	0,0
1uM IM	0,0	0,0	2,7	0,8	1,3	1,1	1,1	0,0	1,2	0,9	0,9	0,9	0,1	0,0	0,0	1,0	0,0	0,2	0,8	0,0

Table S4: In addition to leukemic cell line models' the cytotoxicity (IC_{50}) of **AX** against solid carcinoma cell line models such as cisplatin sensitive/resistant ovarian and esophageal carcinoma, and a brain tumor cell line was also evaluated after treatment with **AX** for 72h and later the average IC_{50} was determined by Celltitre-Glo assay (n=3). CisR (Cisplatin resistant)

Cell lines	Origin	Growth inhibition (IC_{50}) µM
A2780 sens	Ovarian carcinoma (cisplatin sensitive)	7.1 ± 1.1
A2780 CisR	Ovarian carcinoma (cisplatin resistant)	5.8 ± 0.8
Kyse sens	Esophageal carcinoma (cisplatin sensitive)	2.9 ± 0.6
Kyse CisR	Esophageal carcinoma (cisplatin resistant)	6.9 ± 1.1
D425	Medulloblastoma	6.3 ± 0.2
HEK293	Human Embryonic Kidney 293 cells	10.7 ± 2.0

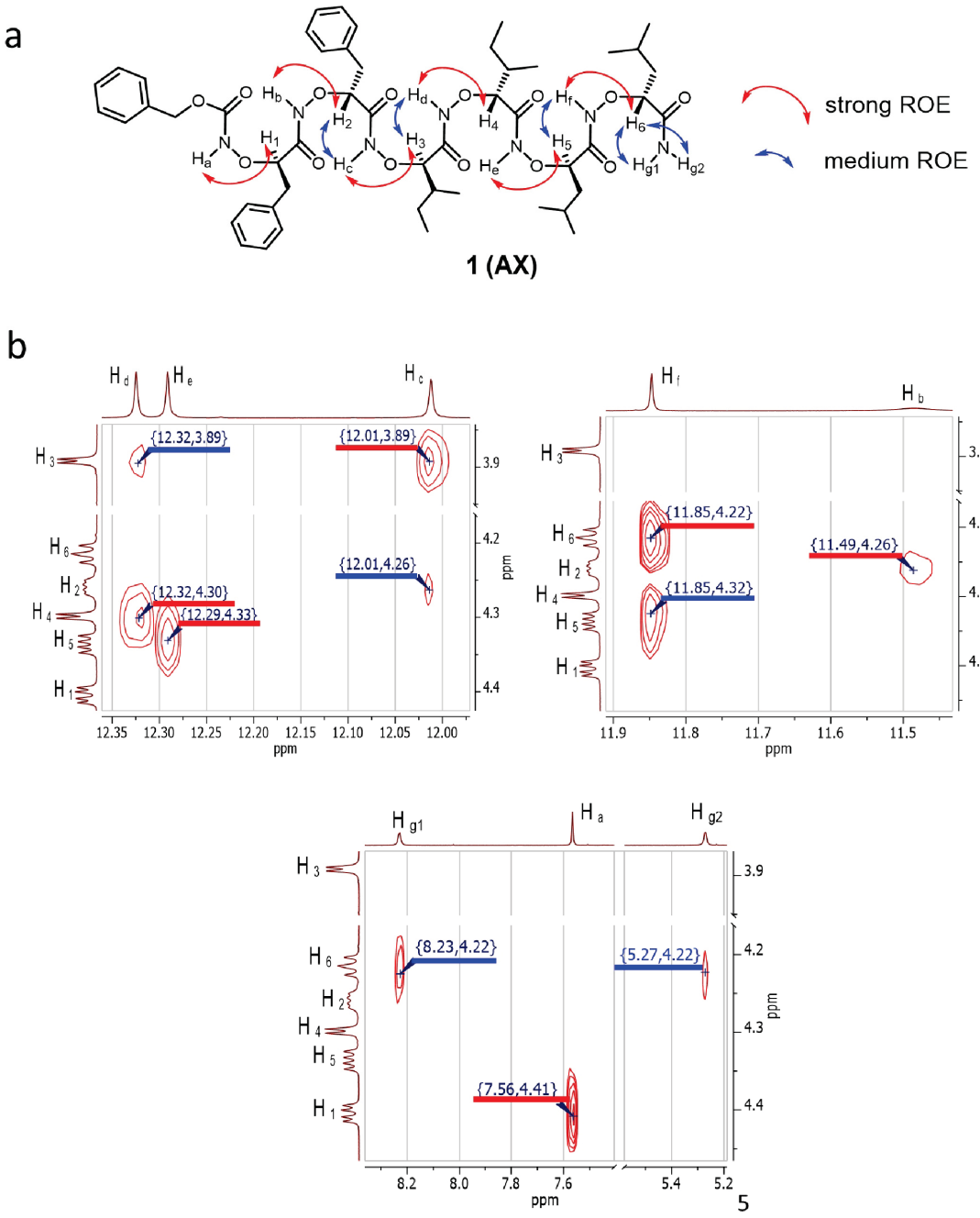

Figure S1: (**a**) **α-Aminoxy peptide 1 (AX) folds into a 2_8-helical conformation consisting of repetitive α N-O turns.** A typical α N-O turn is characterized by a ROE pattern in which the aminoxy proton shows a strong ROE to its own α-methine proton and a weaker ROE cross-peak to the neighboring backbone methine proton. (**a**) Key ROEs observed in the 2D-ROESY spectrum of **1** (**AX**). (**b**) Expansions of important ROE cross peaks (see Supplementary Note 1 for full 2D ROESY spectrum of **1** (**AX**) in $CDCl_3$).

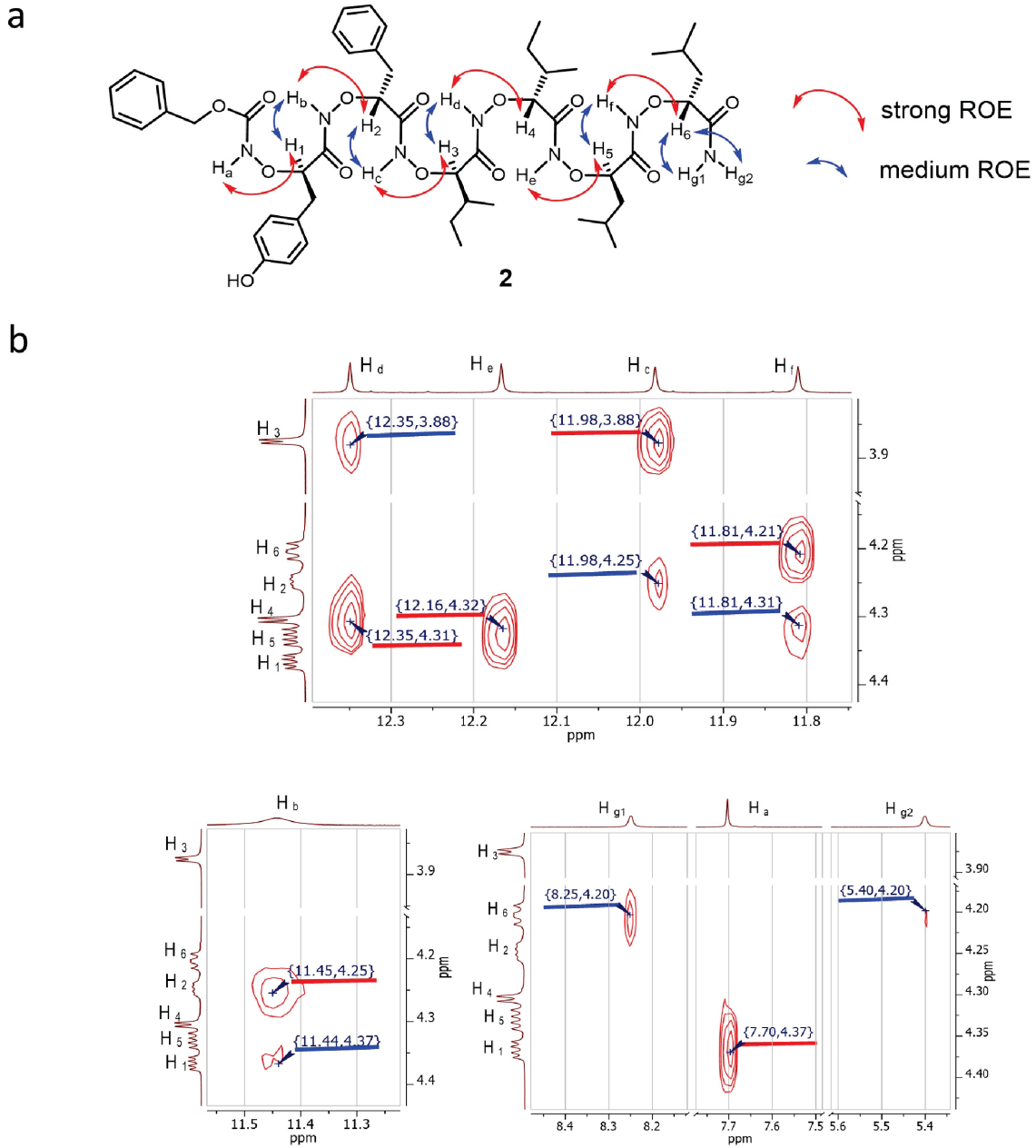

Figure S2: (a) α-Aminoxy peptide 2 folds into a 2_8-helical conformation consisting of repetitive α N-O turns. A typical α N-O turn is characterized by a ROE pattern in which the aminoxy proton shows a strong ROE to its own α-methine proton and a weaker ROE cross-peak to the neighboring backbone methine proton. (**a**) Key ROEs observed in the 2D-ROESY spectrum of **2**. (**b**) Expansions of important ROE cross peaks (see Supplementary Note 1 for full 2D ROESY spectrum of **2** in $CDCl_3$).

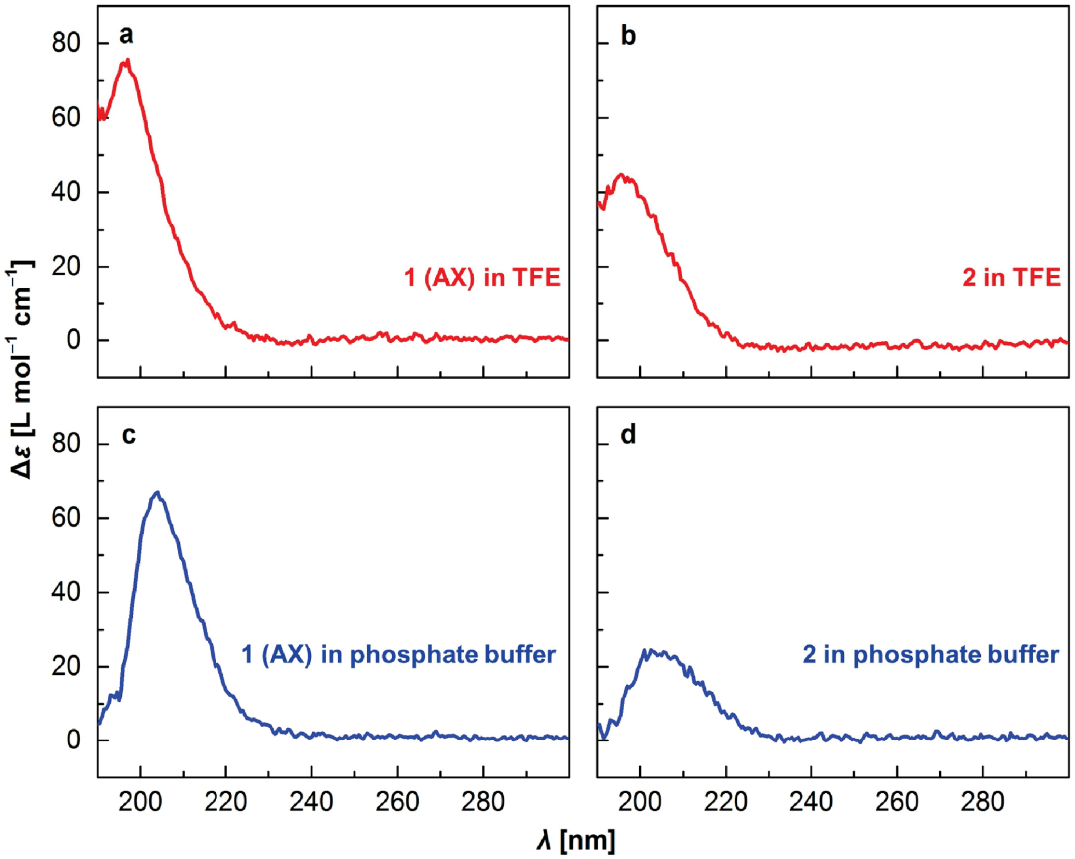

Figure S3: CD spectra of **1** (**AX**) (left panel) and **2** (right panel). In the organic solvent trifluoroethanol (TFE) a characteristic CD band at 196 nm is present both for **1** (**AX**) (**a**) and **2** (**b**) indicating 2_8 helix conformation. In sodium phosphate buffer (1 mM, pH 7) the maximum is slightly red shifted (**c** and **d**) being in accordance with previous observations for CD spectra of α-aminoxy peptides with similar conformation (Yang et. al, 2010, PMID: 20408163) CD spectra in TFE (50 μM, 1 mm path length) and buffer (10 μM, 5 mm path length) were recorded on a J-810 Spectropolarimeter (Jasco) at 20 ° C and background corrected by solvent subtraction.

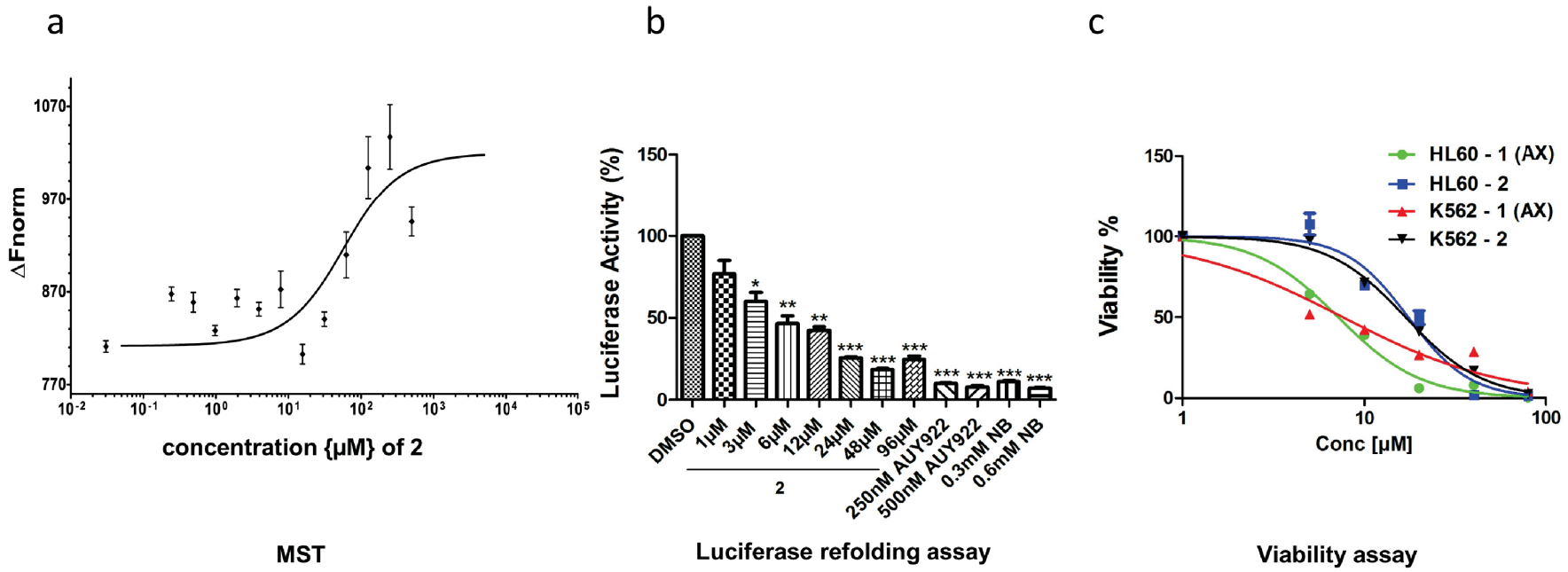

Figure S4: Selective binding of 1 (or AX) and 2 to HSP90. (a) Determination of the apparent KD value of NT-647 labeled C-terminal domain of HSP90 and 2 via Microscale Thermophoresis (MST). A constant amount of 50 nM labeled C terminal domain of HSP90 was used (n=3). The resulting mean values were determined and used in the KD Fit formula. This yielded an apparent KD of 44.2 μM for **2**. (**b**) Cell based HSP90 dependent luciferase assay was performed K562-Luciferase (stably) expressing cells. The extent of thermally denatured luciferase refolding (3 min at 50 ° C) in the presence of **2**, NB and AUY922 was monitored after 180 min. Columns depicts the mean of 3 independent experiments (n=3). (**c**) Viability assay of the leukemic cell lines K562 and HL60 were carried out using Celltitre Glo assay (promega) and later **1** (**AX**) (IC_{50} - 5.72 ± 0.31 μM - K562; 7.1 ± 1.7 μM - HL60) was selected on the basis of its enhanced potency as compared to **2** (IC_{50} - 16.8 ± 0.11 μM - K562; 17.4 ± 0.4 μM – HL60). Significance analyses of normally distributed data with variance similar between groups used paired, two-tailed Student's t-test. * < P 0.05, ** < P 0.005, *** < P 0.001.

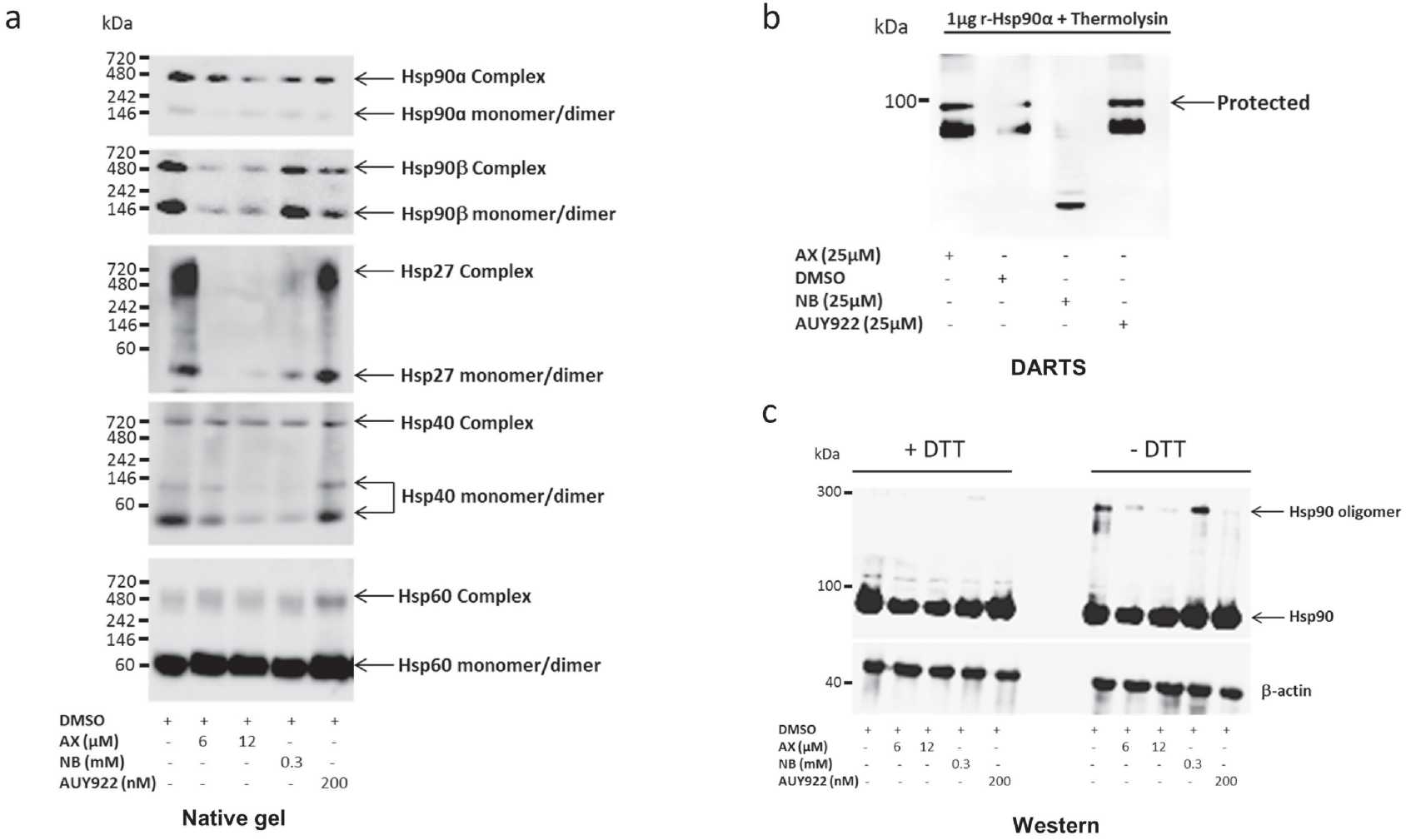

Figure S5: Functional specificity of AX to HSP90. (**a**) Native HSP90 complexes in K562 were identified by running Blue-Native gels followed by immunoblotting. Application of cytotoxic concentration of **AX** to K562 cells resulted in the potent disruption of HSP90α, HSP90β, HSP40 and HSP27 complexes and monomers/dimers. Addition of AUY922 resulted in the elevated expression of HSR associated protein complexes as well as monomers/dimers (HSP40 & HSP27), whereas HSP60 served as loading controls showing relative equal loading. (**b**) DARTS was used to evaluate the specificity of **AX** to HSP90. Recombinant HSP90α (1 μg) was incubated with 25 μM **AX**, NB and AUY922, respectively, followed by digestion with thermolysin. Treated samples were electrophoresed (SDS-PAGE) and immunoblotted with anti-HSP90α for detecting protection of HSP90 protein by **AX** (upper band is protected from proteolysis). Digestion of recombinant HSP90α was not protected by NB. This could have been due to low affinity of NB to HSP90 at this concentration (25 μM). (**c**) After treating K562 cells with **AX**, NB or AUY922 for 48 h, lysates were generated with or without DTT and subjected to immunoblotting using anti-HSP90 antibody. An additional HSP90 oligomer band appeared in lysates without DTT.

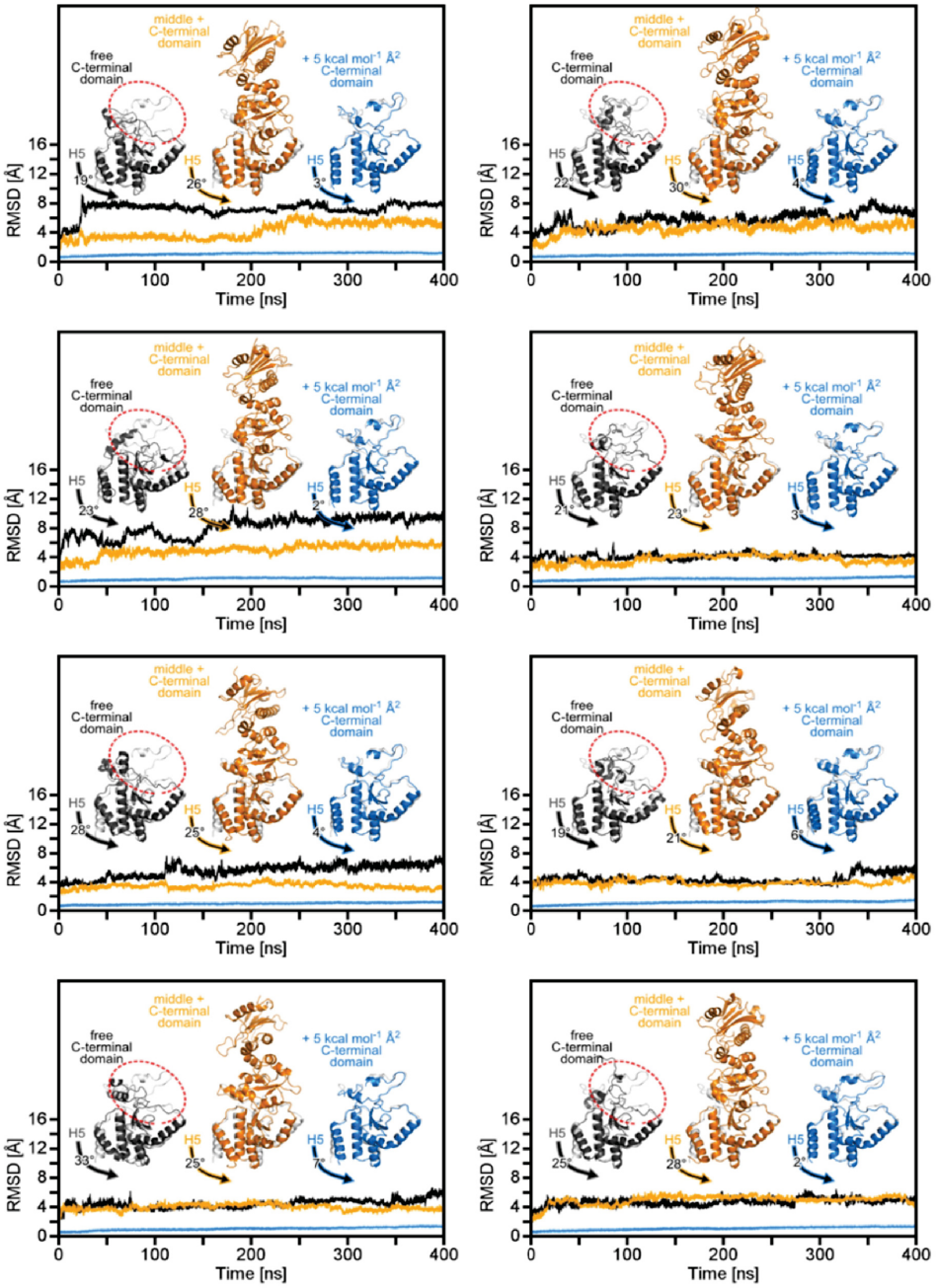

Figure S6: Validation of the model of the monomeric C-terminal domain. Backbone RMSD of the C-terminal domain (CTD) relative to the crystal structure (extracted from PDB code 3Q6M[13]) during eight MD simulations of 400 ns length. The black lines show results for unbiased MD simulations, the blue lines for MD simulations with positional restraints of 5 kcal mol^{-1} Å^2 applied to all backbone atoms, and the orange lines for a MD/CTD structure (here only CTD residues were considered for RMSD calculations). The structures in the respective panels, shown in cartoon representation, were extracted from the trajectories after 400 ns and superimposed onto the CTD of the crystal structure[13]. The arrows depict the helix H5 movement, the labels on these arrows the average angle η (see Methods section for definition), and the red circles those areas, where distinct structural deviations, relative to the crystal structure[13], were observed during the MD simulations.

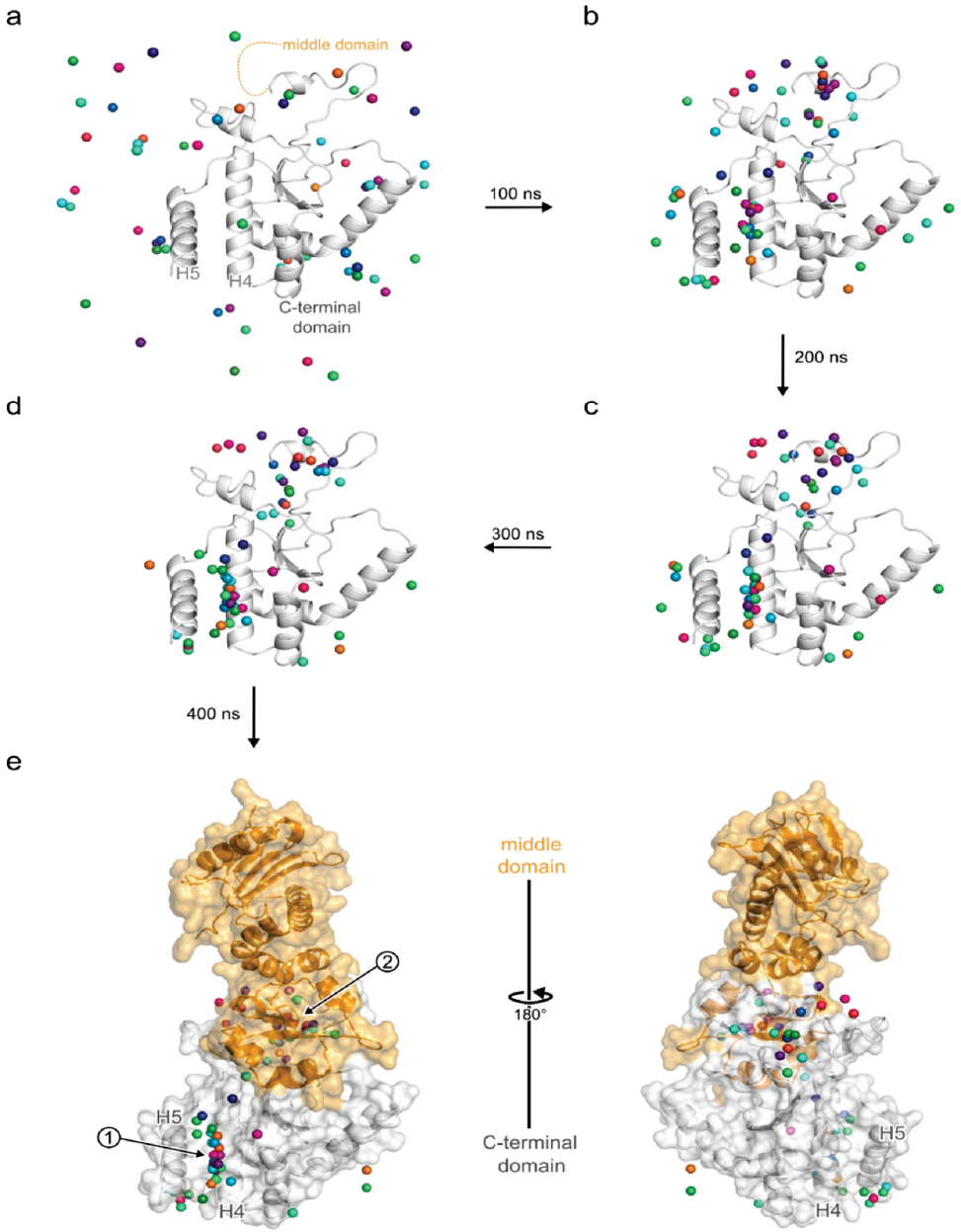

Figure S7: Results of MD simulations of free ligand diffusion. (**a**) The 60 starting configurations of **AX** used for 60 individual MD simulations of free ligand diffusion after superimposition of the C-terminal domain (CTD). The dashed line indicates where the middle domain would be located. (**b – e**): Locations of **AX** after 100 ns (**b**), 200 ns (**c**), 300 ns (**d**), and 400 ns (**e**) each of 60 MD simulations of free **AX** diffusion. ① and ② depict the most frequently populated binding sites of **AX**. In (**a – e**), for clarity reasons, only the center of mass of **AX** is shown as spheres, colored differently for each MD simulation. The protein structure is shown in white cartoon representation. In (**e**), a middle domain-CTD part of HSP90 is additionally shown in orange (middle domain) and white (CTD) surface representation (in the right panel the structure is rotated by 180° around the y-axis; extracted from PDB code 3Q6M[13]).

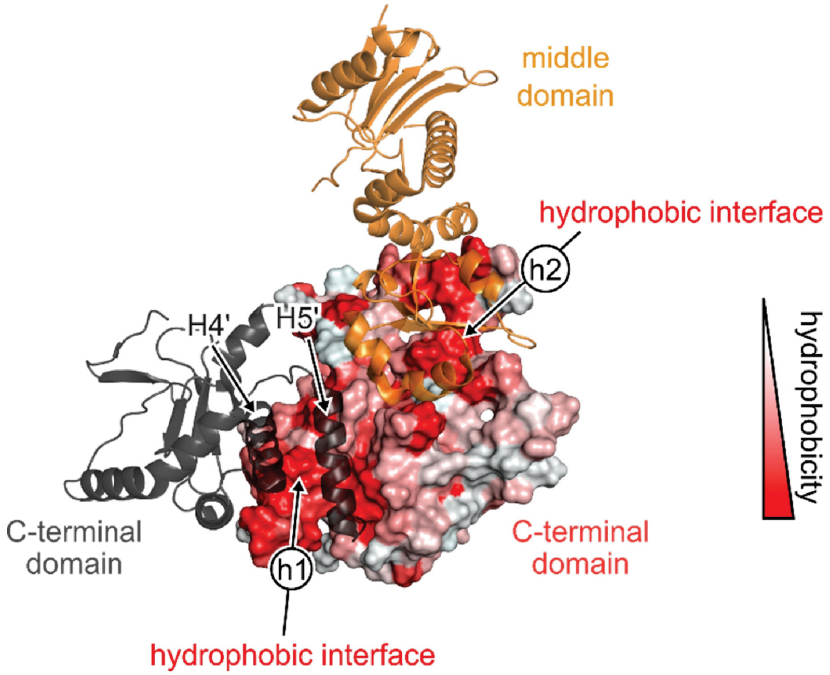

Figure S8: Hydrophobic interfaces in HSP90. Dimeric C-terminal domain (CTD) and one middle domain of HSP90 (extracted from PDB code 3Q6M[13]). The CTD used for MD simulations is shown in surface representation colored according to the hydrophobicity spectrum. The adjacent CTD in the crystal structure is shown in black cartoon, with helices H4' and H5' as part of the dimerization interface, and the middle domain in orange cartoon representation. (h1) and (h2) show the identified hydrophobic interfaces on the protein surface.

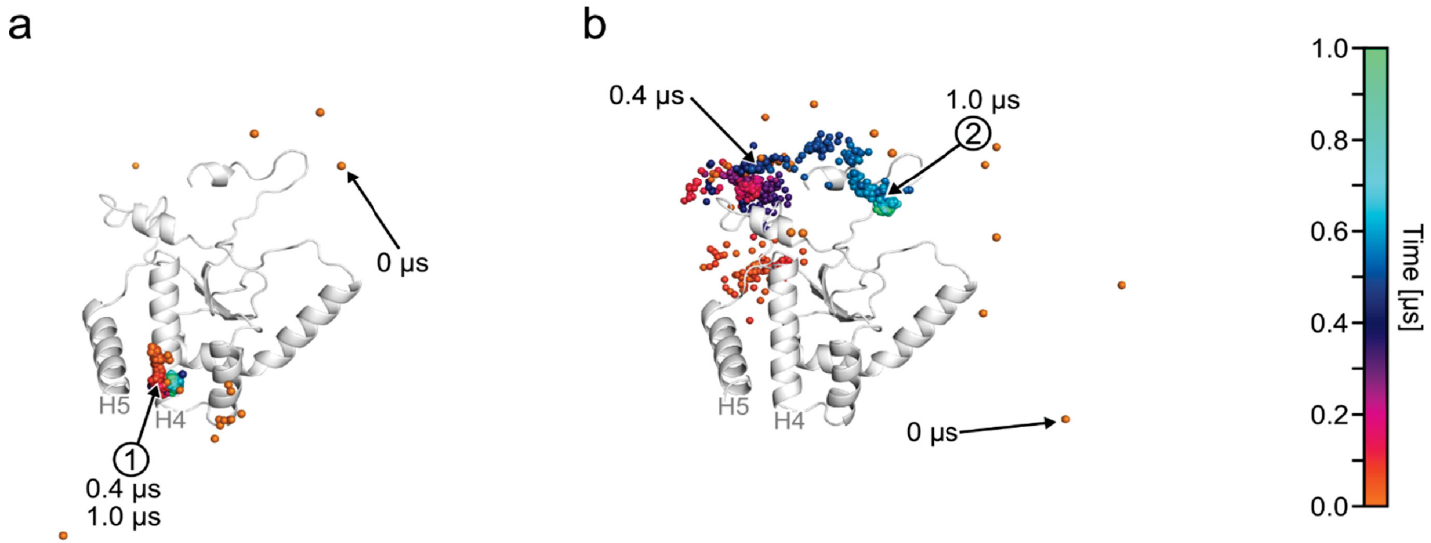

Figure S9: Traces of compound 1 movement during MD simulations. Traces of **AX** in two MD simulations of 1 µs length in which **AX** binds to the dimerization interface of the C-terminal domain (CTD) (binding site ①, (**a**)) or to the interface between the middle domain and the CTD (binding site ②, (**b**)). The centers of mass of **AX** are depicted as spheres colored according to the elapsed time (see scale on the right). For clarity reasons only the initial structures of the CTD and conformations of **AX** extracted in 1 ns intervals from the MD trajectories are shown. Arrows depict positions of **AX** after 0 µs, 0.4 µs, and 1.0 µs.

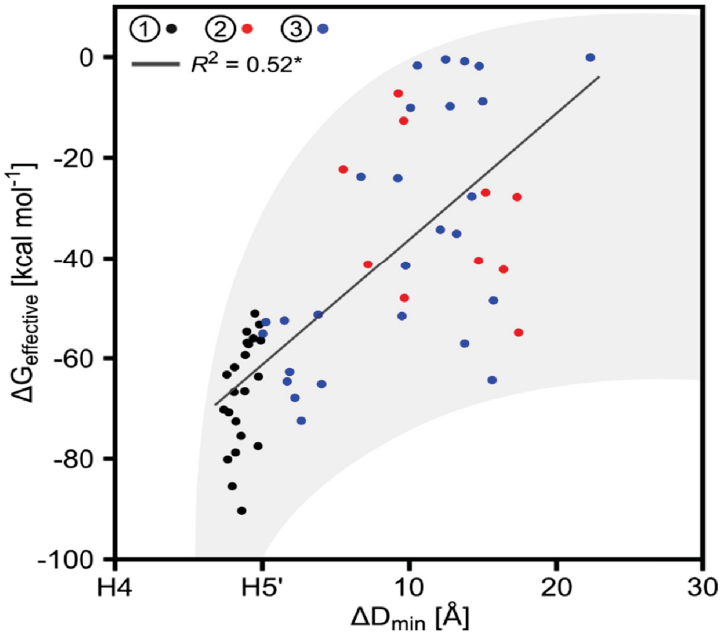

Figure S10: Correlation between effective binding energy and minimal distance. Effective energies ($\Delta G_{effective}$) were calculated for **AX** binding to the HSP90 C-terminal domain, for configurations at the minimal relative distance (ΔD_{min}) between **AX** and helix H4 during 60 MD simulations of 400 ns length. Black points show results for **AX** binding to interface ①, red for interface ②, and blue for ③ (see main text and **Figure 2a – c** for definition). The gray background represents the binding funnel that gets narrow close to binding site ①. In the legend, R^2 depicts the coefficient of determination including all data points (dark gray line), with $p < 0.01$ (*).

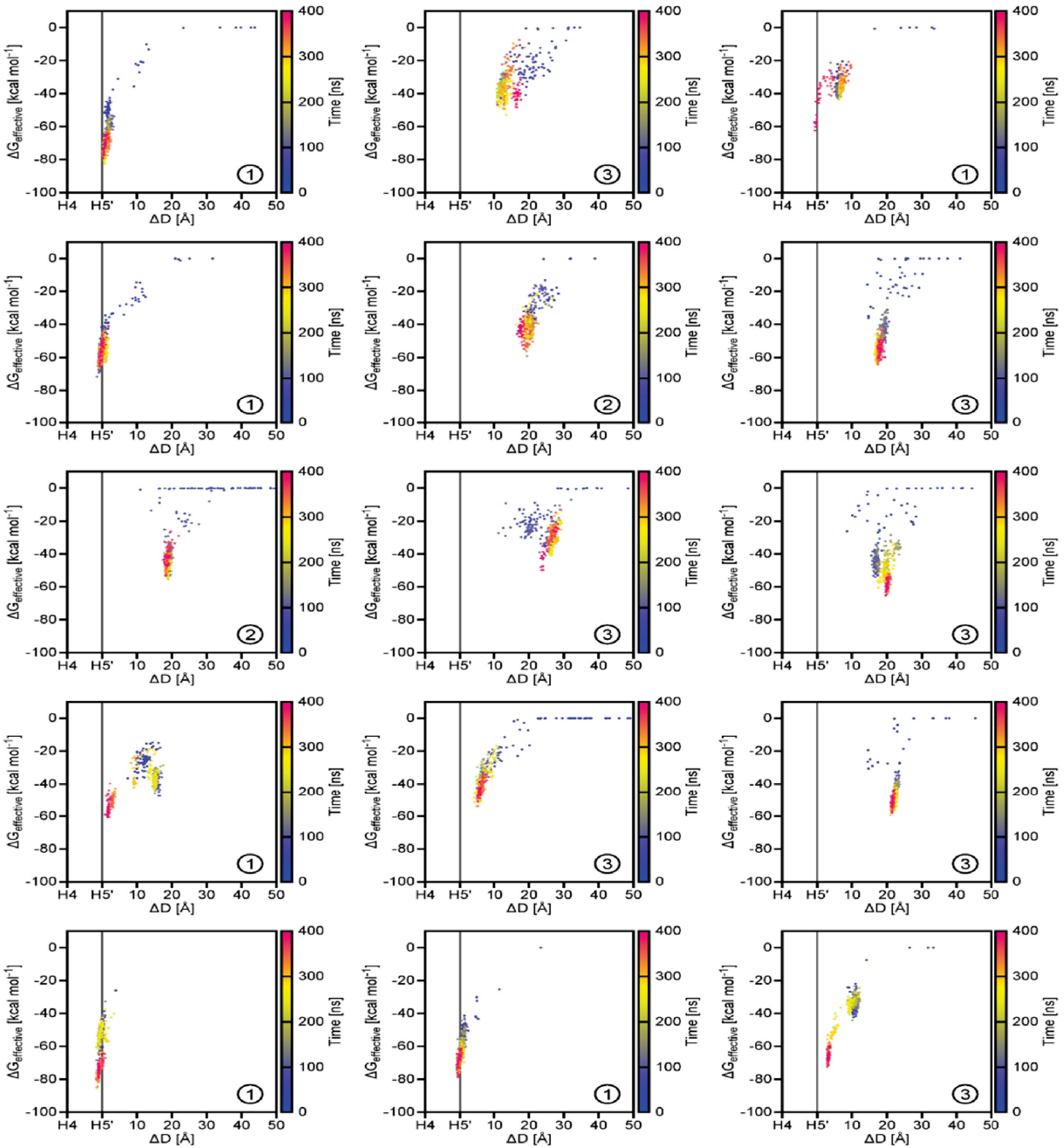

Figure S11 (ext.): Relative distances and effective energies of AX binding to HSP90.

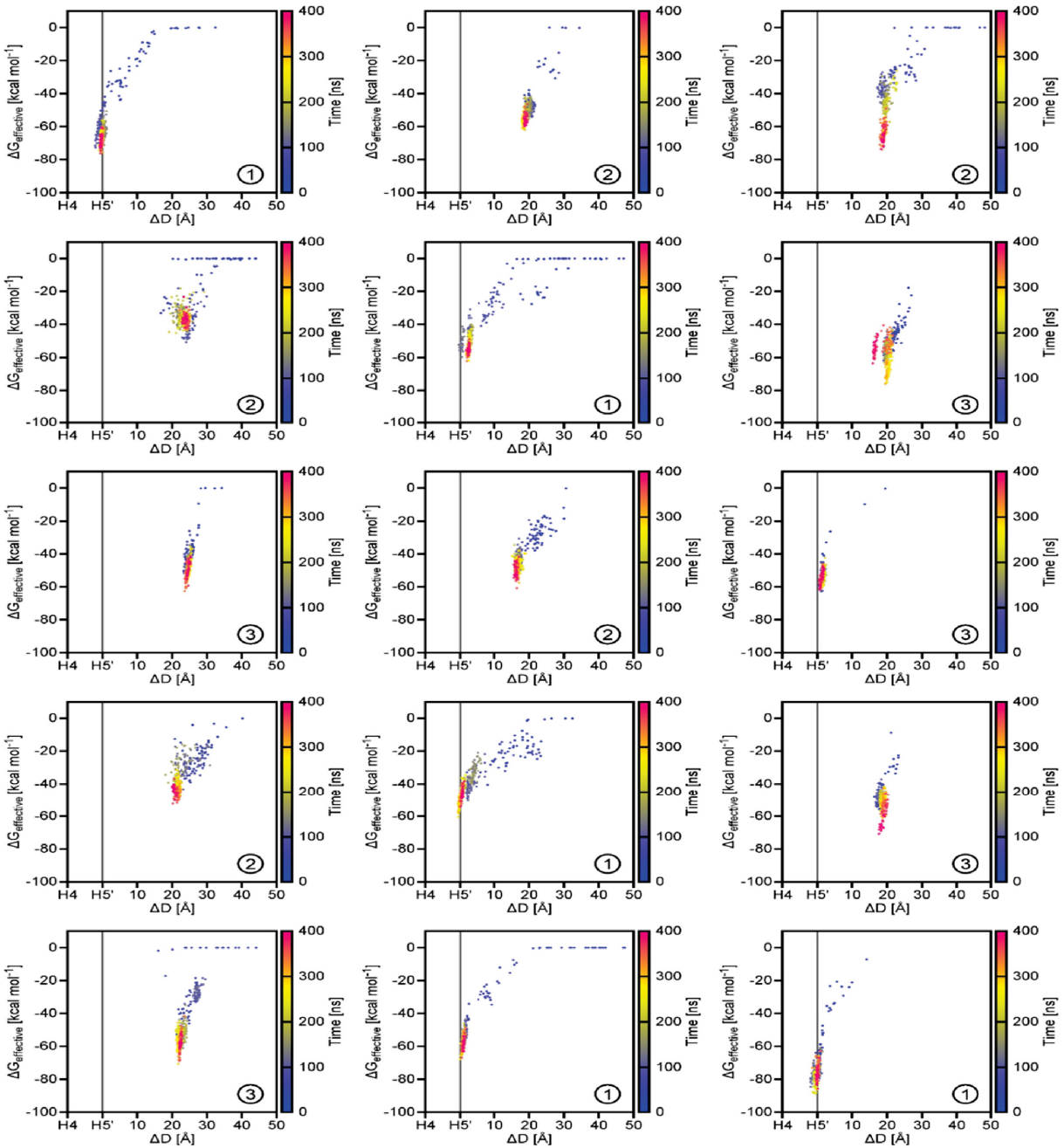

Figure S11 (ext.): Relative distances and effective energies of AX binding to HSP90.

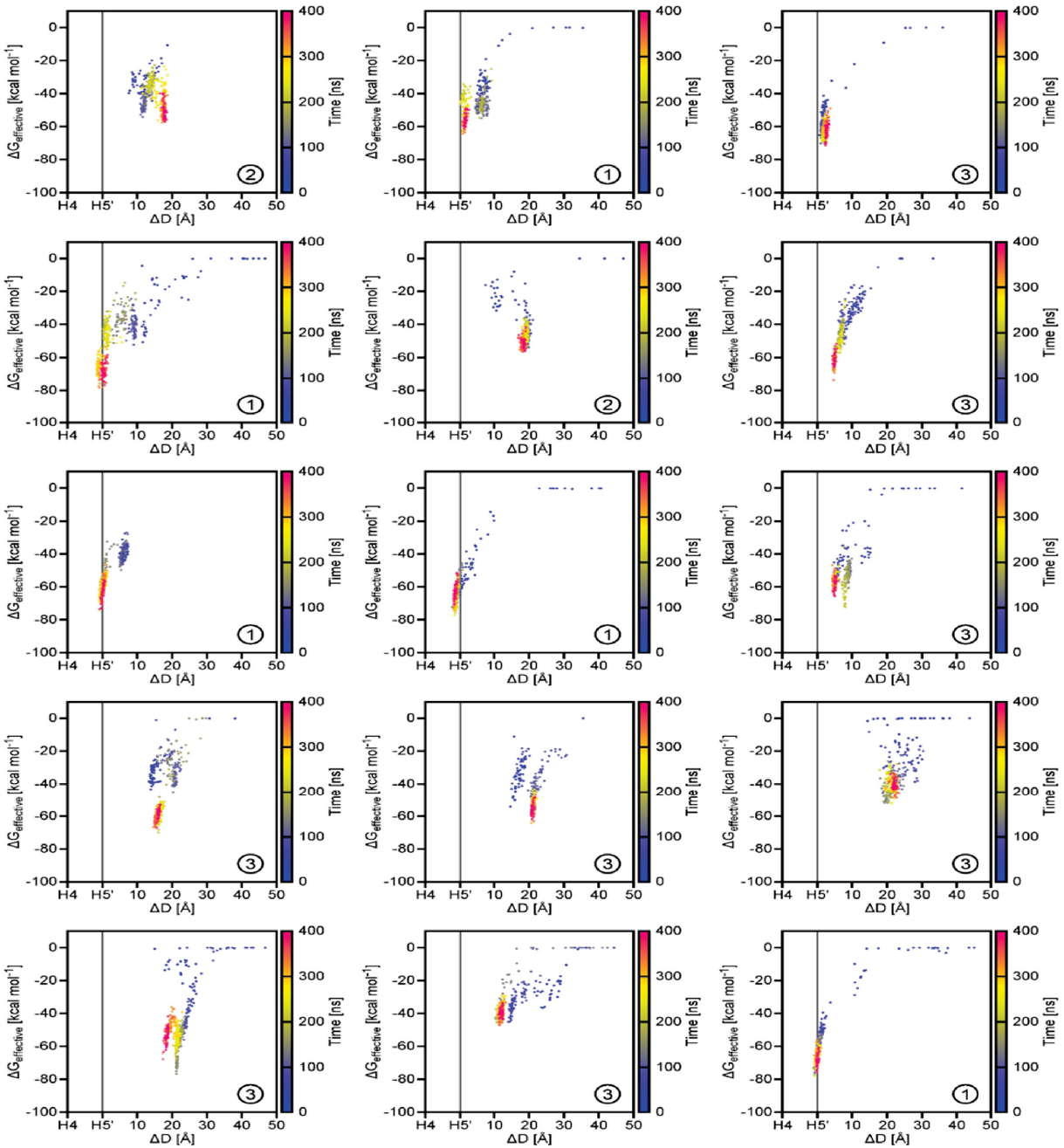

Figure S11 (ext.): Relative distances and effective energies of AX binding to HSP90.

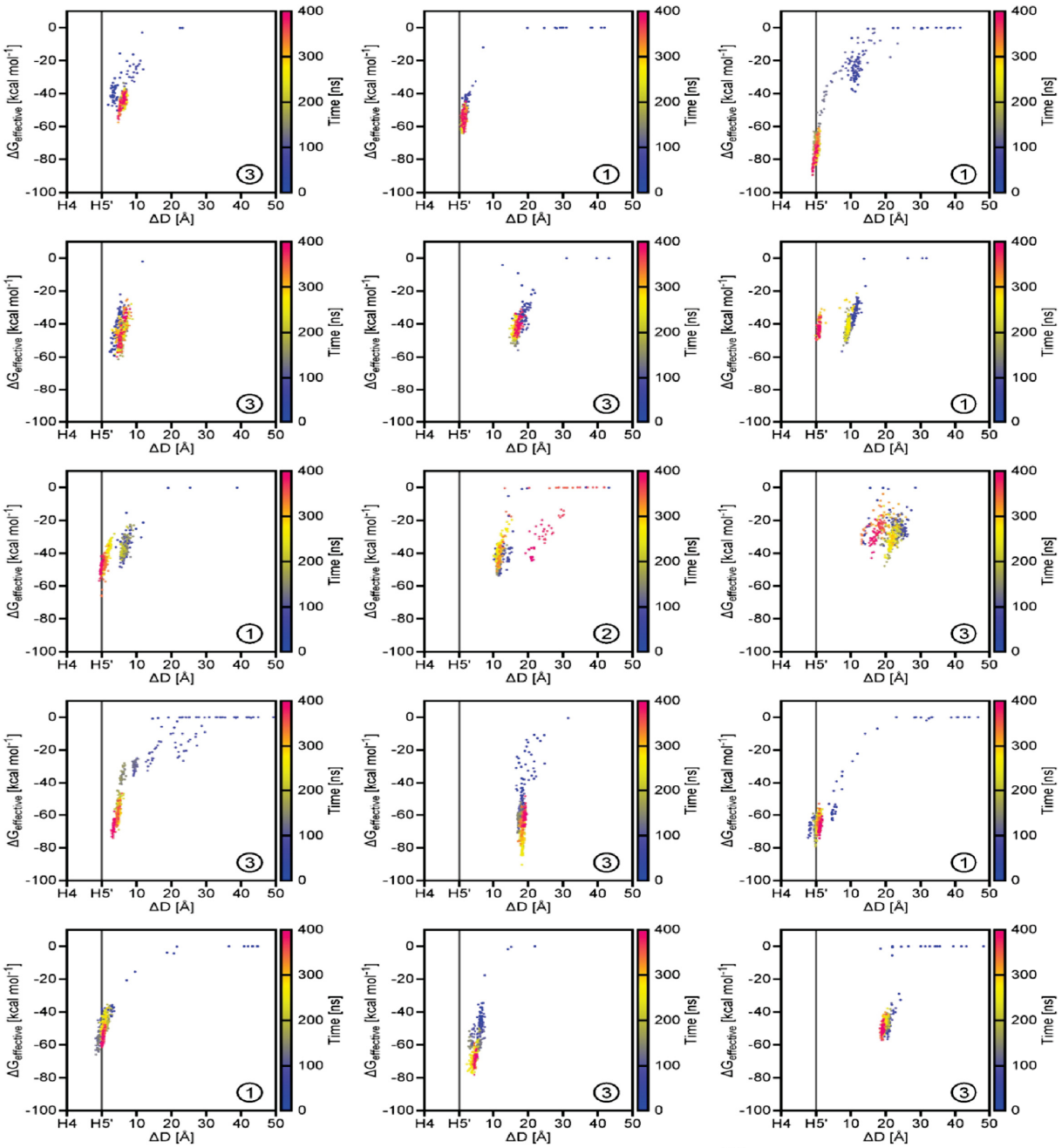

Figure S11: Relative distances and effective energies of AX binding to HSP90. Calculated effective binding energies ($\Delta G_{effective}$) for 60 MD trajectories, plotted against the relative distance (ΔD; see Methods section for definition) between **AX** and helix H4. The plots are colored according to the elapsed time (see scale on the right of each panel). The gray line at ΔD = H5' (= 0 Å) shows the location of helix H5' relative to helix H4 in the crystal structure[13]. The labels ①, ②, and ③ in the lower right corner depict the interfaces to which **AX** is bound after 400 ns of MD simulations.

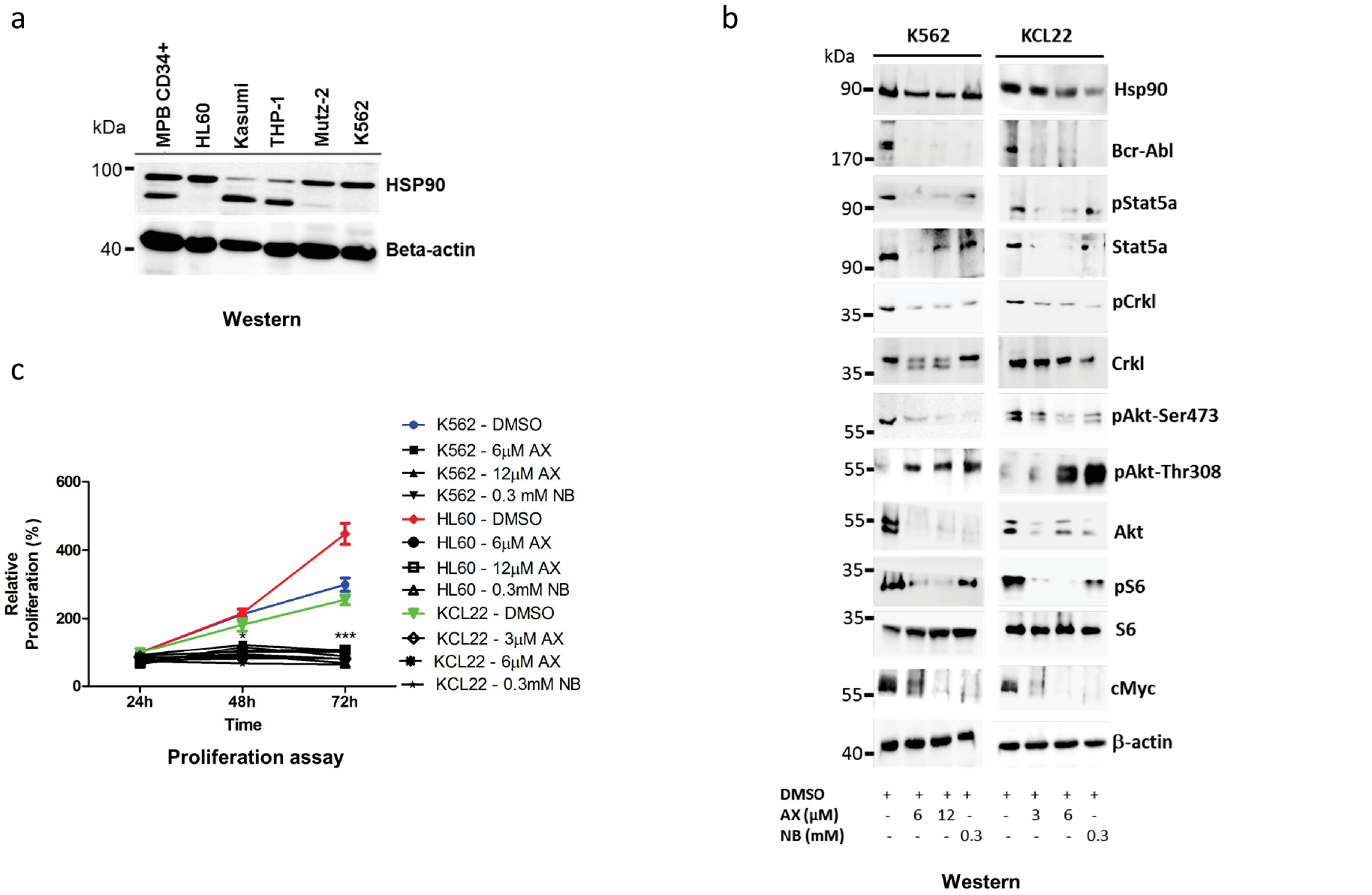

Figure S12 (ext.): AX as a potent inhibitor in leukemic cell line models without inducing any HSR.

d

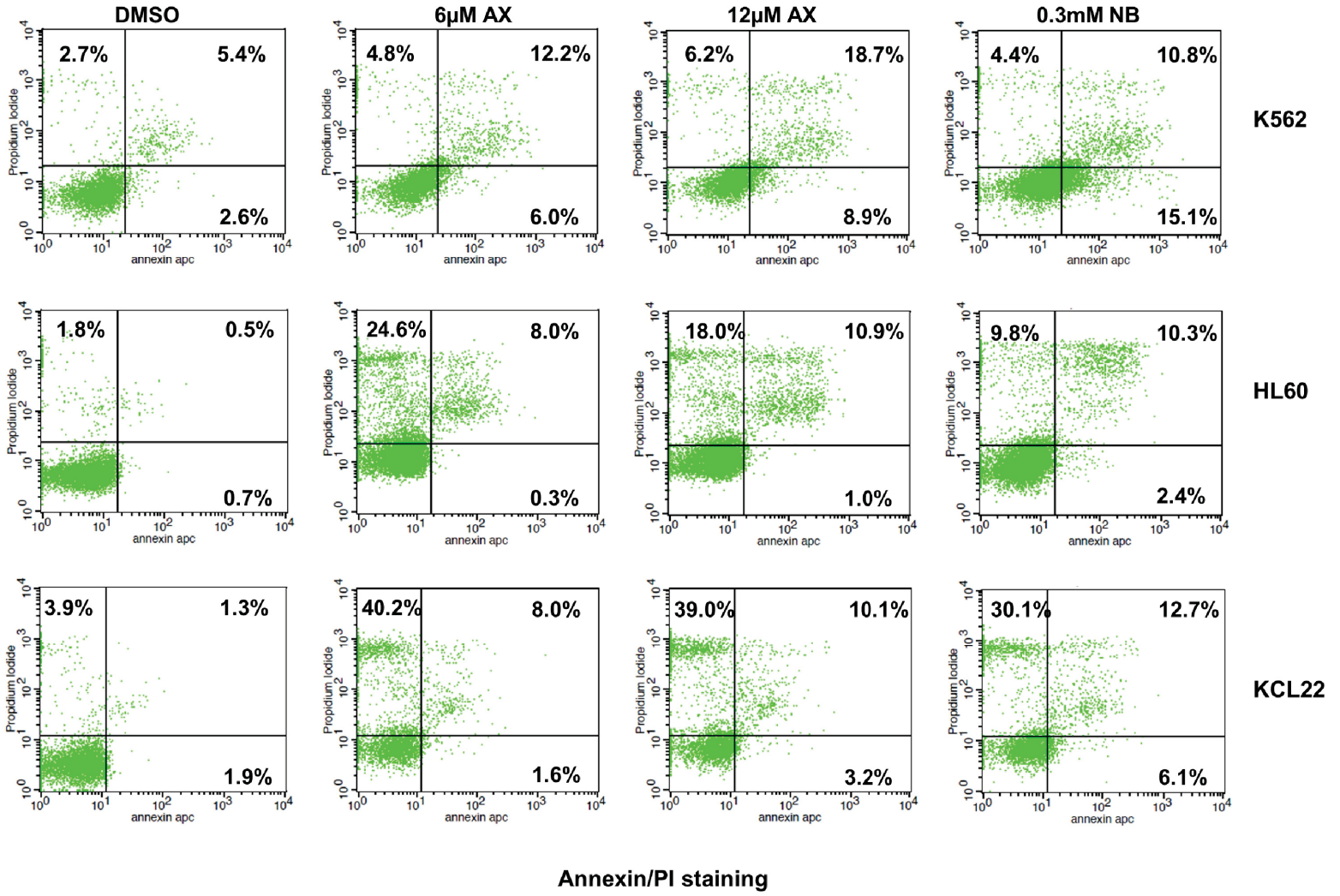

Figure S12 (ext.): AX as a potent inhibitor in leukemic cell line models without inducing any HSR.

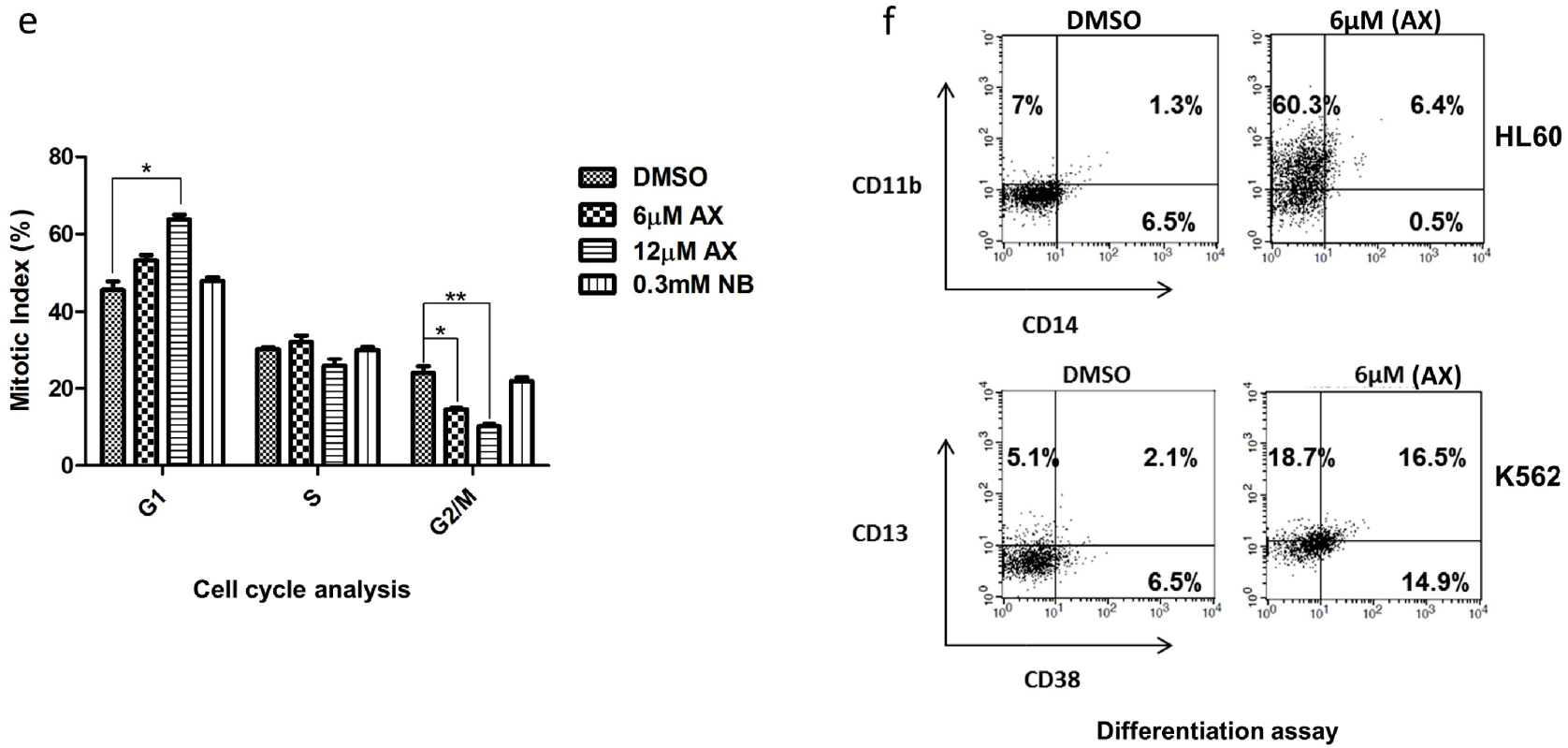

Figure S12: AX as a potent inhibitor in leukemic cell line models without inducing any HSR. (**a**) Expression of HSP90 in leukemic cell line models (HL60, Kasumi, THP-1, Mutz-2 and K562) and in mobilized peripheral blood (MPB) derived CD34+ cells. (**b**) Treatment of K562 & KCL22 with **AX**, NB & respective controls (DMSO) for 48 h, resulted in the downregulation of BCR-ABL1 and subsequently downstream signaling pathways including pStat5a, pCrkl, pAkt (Ser473), pS6 (mTOR) and cMyc. (**c**) K562, KCL22 and HL60 (Mutz-2 - data not shown) were treated with the indicated concentration of **AX** and viable cells were counted at 24 h, 48 h and 72 h (n=3). (**d**) K562, HL60 and KCL22 cells (Mutz-2 - data not shown) were treated with the indicated concentration of **AX** for 48 h and later dually stained with annexin V/PI and consequently measured by FACS where viable cells (-ve for annexin V/PI) were compared to necrotic (+ve for PI) and early (+ve for annexin V) or late (+ve for both annexin/PI) apoptotic stage. (**e**) K562 cells were treated with **AX** for 48 h and were subjected to cell cycle analysis using FACS (PI staining). **(f)** HL60 & K562 cells were treated with **AX** for 72 h and were subjected to FACS after staining with CD11b, CD14 & CD38 CD13 antibodies respectively. Diagrams show bivariate FACS analysis of CD11b vs. CD14 for HL60 cells & CD38 vs. CD13 for K562. Columns depicts the mean of 3 independent experiments (n=3). Significance analyses of normally distributed data with variance similar between groups used paired, two-tailed Student's t-test. * $p < 0.05$, ** $p < 0.005$, *** $p < 0.001$.

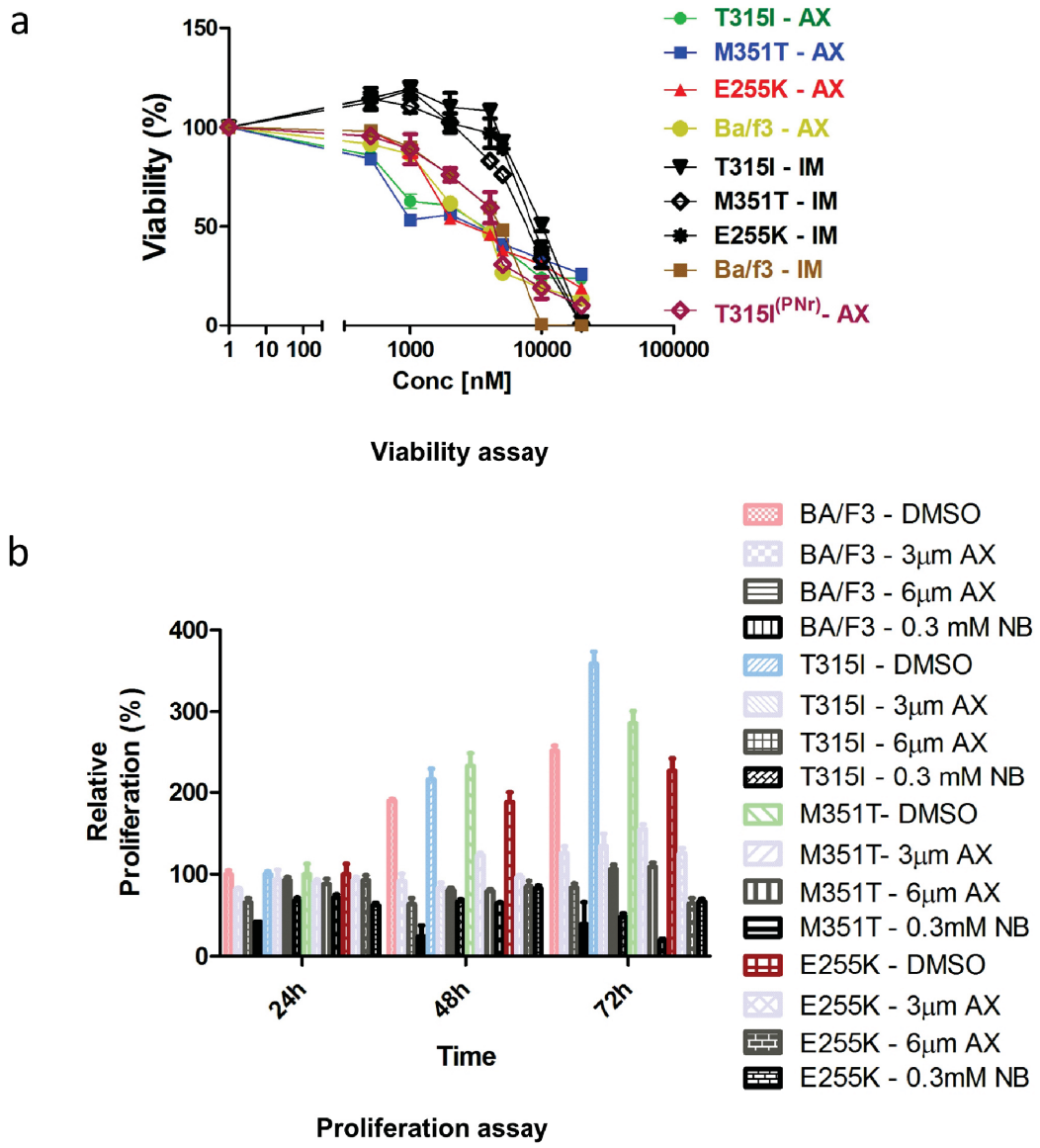

Figure S13: Efficacy of AX in imatinib resistant clinically relevant BCR-ABL1 mutants. (**a**) BA/F3 cells expressing BCR-ABL1$^{T315I,\ T315I\ (PNr),\ M351T\ \&\ E255K}$ mutants were subjected to different concentrations (4nM-25µM) of either **AX** or IB (48 h), found to be resistant to IB (till ~ 10 µM), whereas sensitive against **AX** (at ~3 µM). (**b**) BA/F3 cells expressing BCR-ABL1$^{T315I,\ T315I\ (PNr),\ M351T\ \&\ E255K}$ mutants were grown at indicated concentration of **AX** and NB, later the proliferation was measured after ever 24 h interval for 72 h.

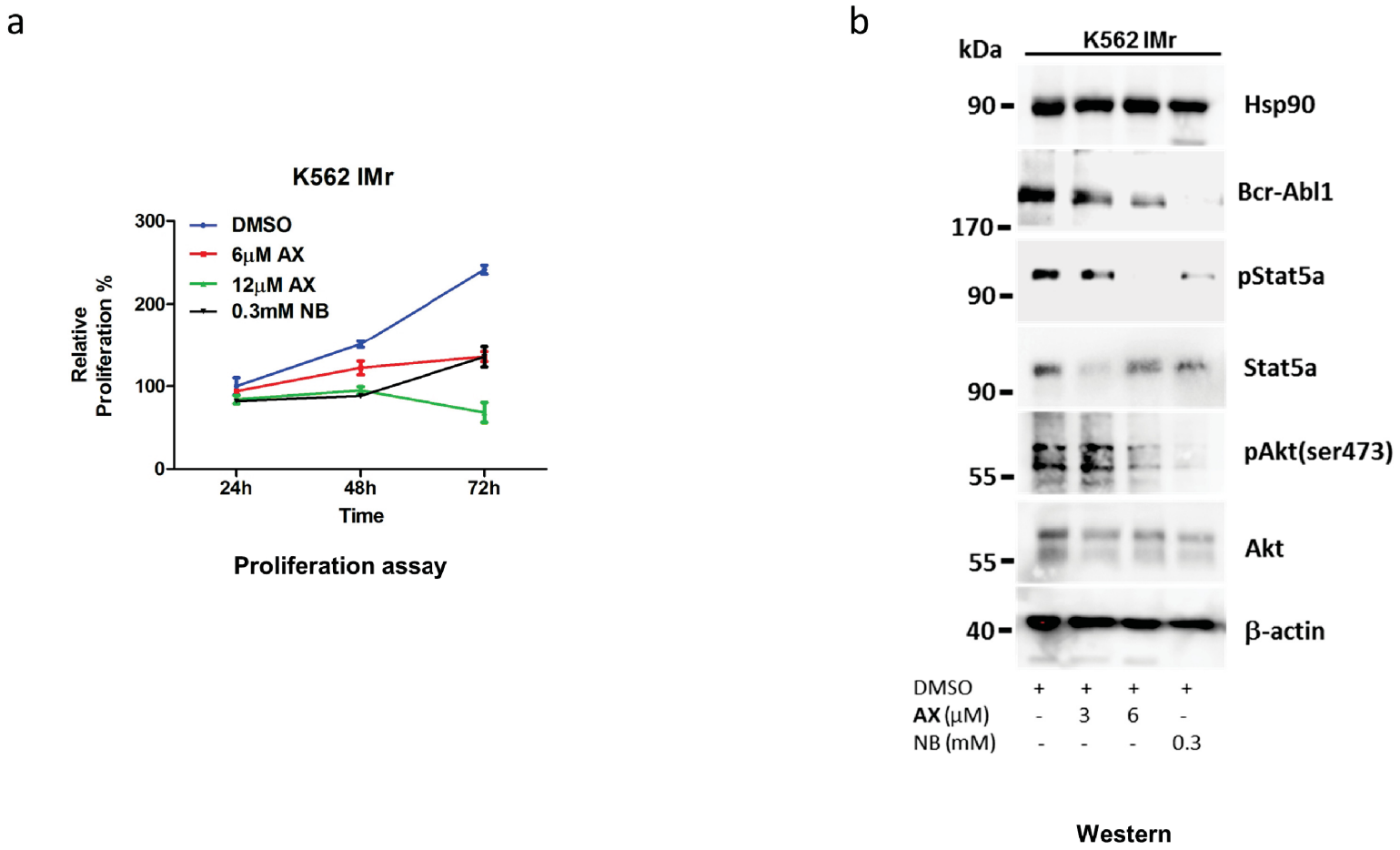

Figure S14: AX as potent inhibitor in BCR-ABL1⁺ K562 IMr. (**a**) K562 IMr cells were treated with indicated concentration of **AX** along with NB and later the proliferation was evaluated by counting the cells at every 24 h interval for 72 h (n=3). (**b**) Like in normal K562 cells, **AX** causes downregulation of BCR-ABL1 and subsequently its associated downstream signaling pathways including Stat5a, Akt, which was evaluated by WB. Lysates were generated after 48 h treatment with either **AX**, NB or solvent alone.

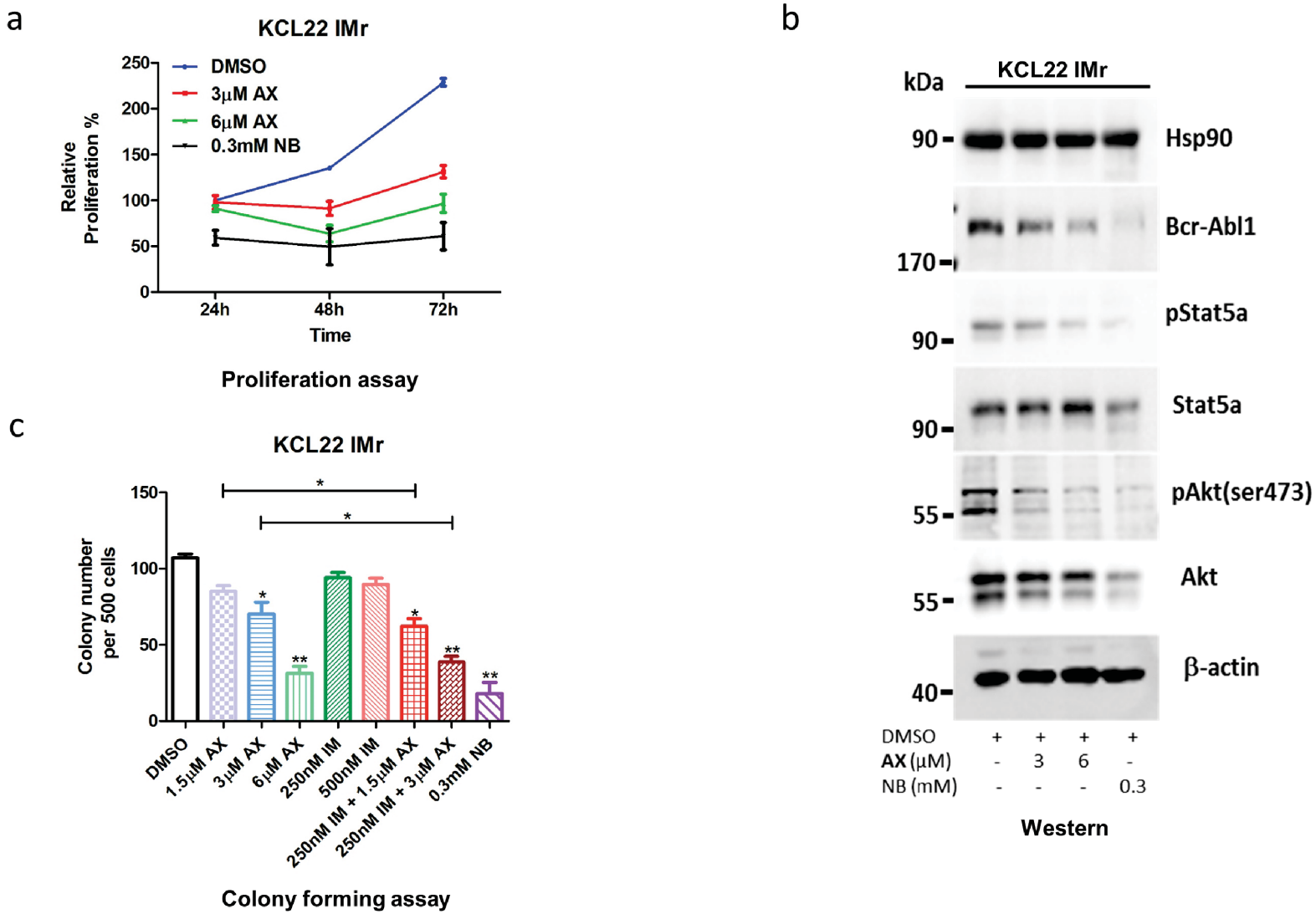

Figure S15: AX as potent inhibitor in BCR-ABL1⁺ KCL22 IMr. (**a**) KCL22 IMr cells were treated with indicated concentration of **AX** along with NB and later the proliferation was evaluated by counting the cells at every 24 h interval for 72 h. (**b**) Like in normal KCL22 cells, **AX** causes downregulation of BCR-ABL1 and subsequently its associated downstream signaling pathways including Stat5a, Akt, which was evaluated by WB. Lysates were generated after 48 h treatment with either **AX**, NB or solvent alone. (**c**) KCL22 IMr cells were seeded in methylcellulose medium after treatment with **AX**, IM, IM+**AX** and NB for 48 h. Colonies were counted after 14 days. Columns depicts the mean of 3 independent experiments (n=3). Significance analyses of normally distributed data with variance similar between groups used paired, two-tailed Student's t-test. * $p < 0.05$, ** $p < 0.005$, *** $p < 0.001$.

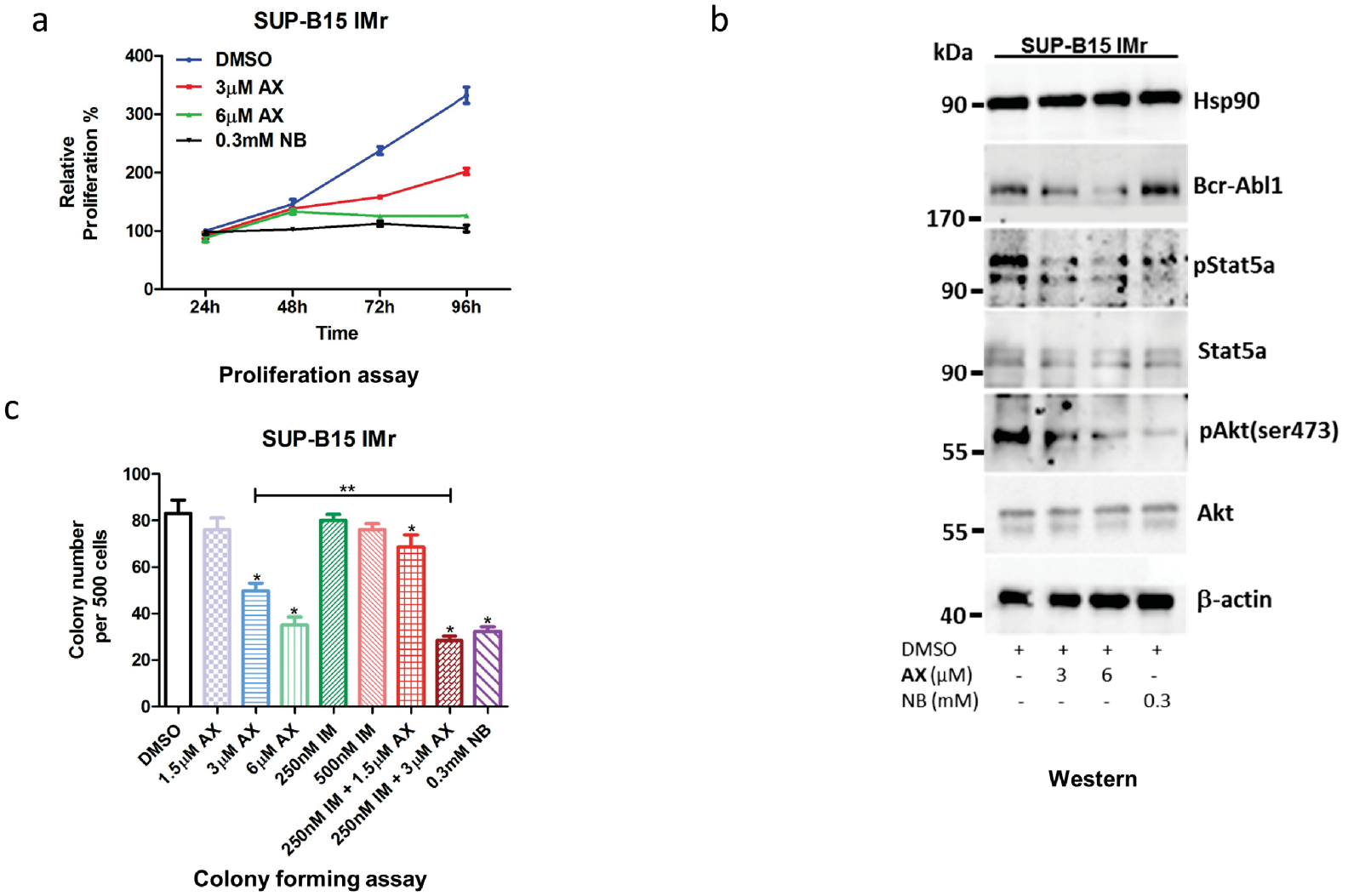

Figure S16: AX as potent inhibitor in BCR-ABL1⁺ (BCP-ALL) SUP-B15 IMr. (**a**) SUP-B15 IMr cells were treated with indicated concentration of **AX** along with NB and later the proliferation was evaluated by counting the cells at every 24 h interval for 72 h. (**b**) **AX** causes downregulation of BCR-ABL1 in SUP-B15 IMr and subsequently its associated downstream signaling pathways including Stat5a, Akt, which was evaluated by WB. Lysates were generated after 48 h treatment with either **1**, NB or solvent alone. (**c**) SUP-B15 IMr cells were seeded in methylcellulose medium after treatment with **AX**, IM, IM+**AX** and NB for 48 h. Colonies were counted after 14 days. Columns depicts the mean of 3 independent experiments (n=3). Significance analyses of normally distributed data with variance similar between groups used paired, two-tailed Student's t-test. * $p < 0.05$, ** $p < 0.005$, *** $p < 0.001$.

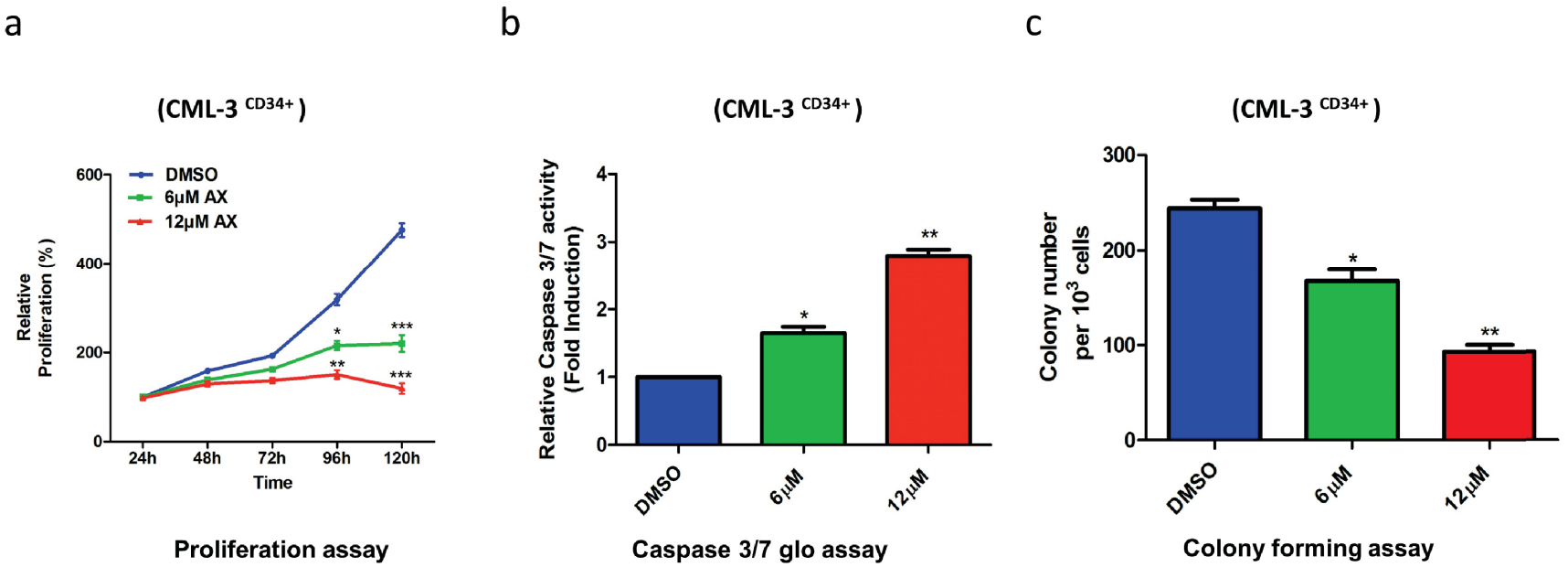

Figure S17: AX as a potent inhibitor in primary CML^{CD34+} blast cells. (**a**) Primary CML^{CD34+} cells from patient were treated with the indicated concentration of **AX** and viable cells were counted after every 24 h interval for 5 days (n=3). (**b**) Primary CML^{CD34+} cells were treated with the indicated concentration of **AX** (48 h) and later enzymatic activity of caspase 3/7 was examined by caspase 3/7 dependent glo assay (absorbance at 405 nm). (**d**) Primary CML-patient derived CD34+ were seeded in methylcellulose medium after treatment with **AX** for 48 h. Colonies were counted after 14 days (n=3). Significance analyses of normally distributed data with variance similar between groups used paired, two-tailed Student's t-test. * $p < 0.05$, ** $p < 0.005$, *** $p < 0.001$.

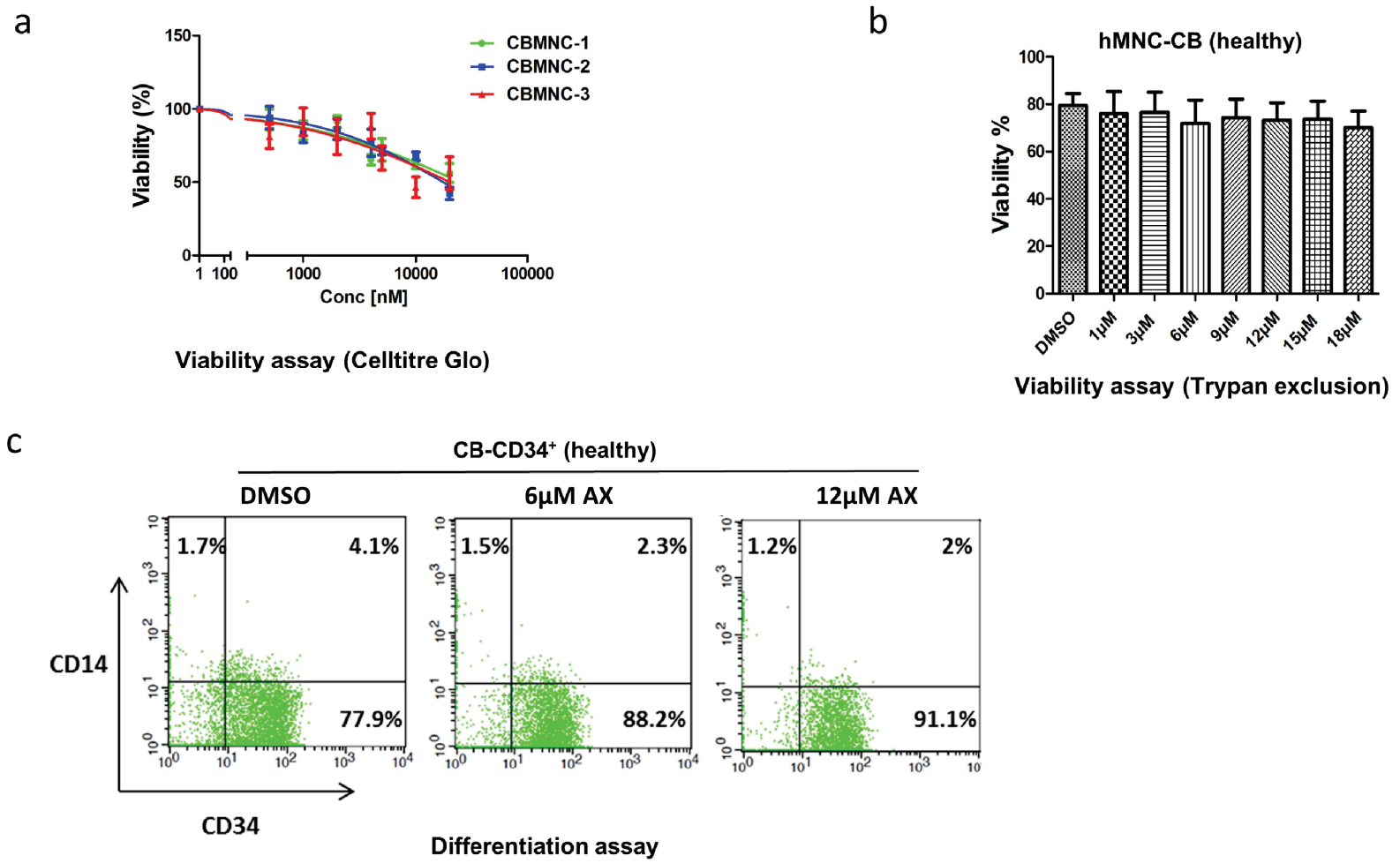

Figure S18: Effect of AX on healthy CB derived MNC and CB derived CD34⁺ cells. (**a**) Healthy cord blood derived mononuclear cells (CBMNCs) form three healthy controls were treated with **AX** for 48 h to determine the sensitivity as compared to leukemic cell lines using Celltitre glo assay and later found out that the IC_{50} was significantly higher than leukemic cells (20.94±3.07 µM). (**b**) Healthy human cord blood (CB) derived MNC were treated for 48 h with increasing concentrations of **AX** and later viability was monitored by trypan exclusion method. **AX** did not show any reduction in the viability even at approx. 3 times (18 µM) more concentration than the IC_{50} (3-6µM) for leukemic cells (n=3). (**c**) Effect of **AX** on differentiation of CB derived CD34⁺ cells were determined by FACS after staining with CD34 & CD11b antibodies. Diagrams show bivariate FACS analysis of CD34 versus CD14 for CD34+ cells.

a

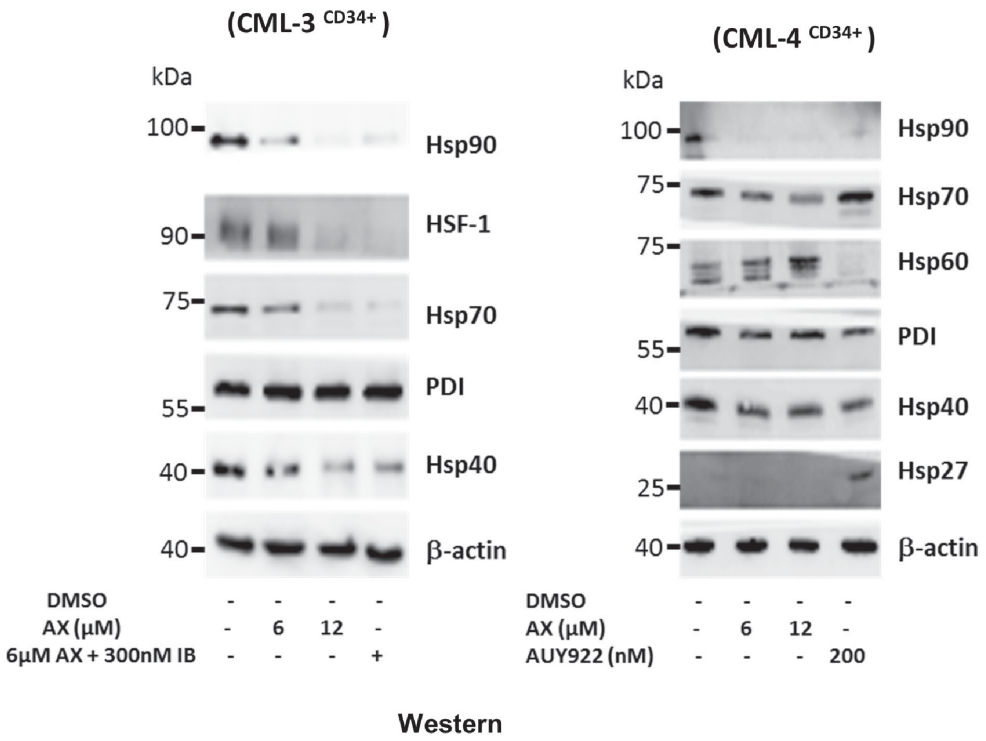

b

(CML-3 CD34+)

	CD19 +	CD14 +
DMSO	1.30%	14.26%
6μM (**AX**)	12.02%	31.22%
12μM (**AX**)	43.14%	52.41%

(CML-4 CD34+)

	CD19 +	CD14 +
DMSO	11.36%	36.09%
6μM (**AX**)	18.97%	45.64%
12μM (**AX**)	53.22%	65.55%

Differentiation assay

Figure S19: AX did not induce HSR and cause early differentiation in CML^{CD34+} blast cells. (**a**) Primary CML^{CD34+} cells from two patients were either treated with the indicated (cytotoxic) concentration of **AX** alone or in combination with IB or with **AX** and AUY922 for 48 h. Later the protein lysates were subjected to immunoblot analysis. As opposed to AUY922 treatment, administration of **AX** alone or in combination with IB does not induce HSR which was evaluated by the expression of HSF-1, HSP70, HSP40 and HSP27, whereas PDI and HSP60 served as a control for HSR in the cytoplasm. (**b**) Effect of **AX** on early differentiation of CML^{CD34+} cells in the liquid medium was determined by FACS after staining with CD34 & CD11b antibodies. Diagrams show bivariate FACS analysis of CD34 versus CD14 for CD34+ cells.

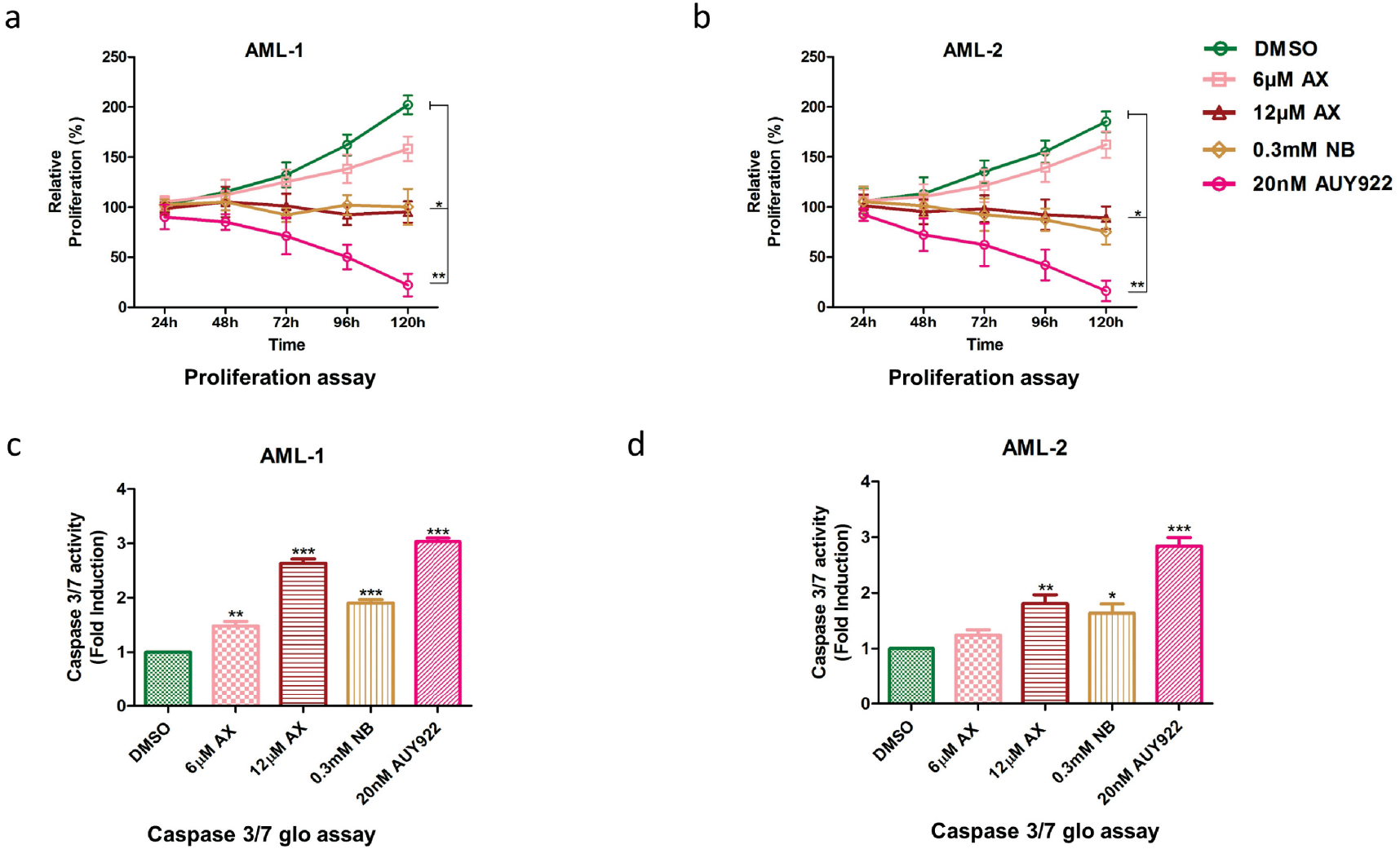

Figure S20: AX blocked proliferation and induce apoptosis in primary AML blast cells. (**a**) Primary AML cells (>80% blast cells) from two different FLT3-ITD+ patient samples (AML-1 and AML-2) were treated with the indicated concentration of **AX** along with mentioned controls (NB, AUY922 or IM) and the viable cells were counted after every 24 h interval for 5 days. (**b**) These primary AML cells were treated for 48 h with increasing concentrations of **AX** or with mentioned controls (NB, AUY922 or IM) and later the enzymatic activity of caspase 3/7 were examined by caspase 3/7 dependent Glo assay after 5 days of treatment.

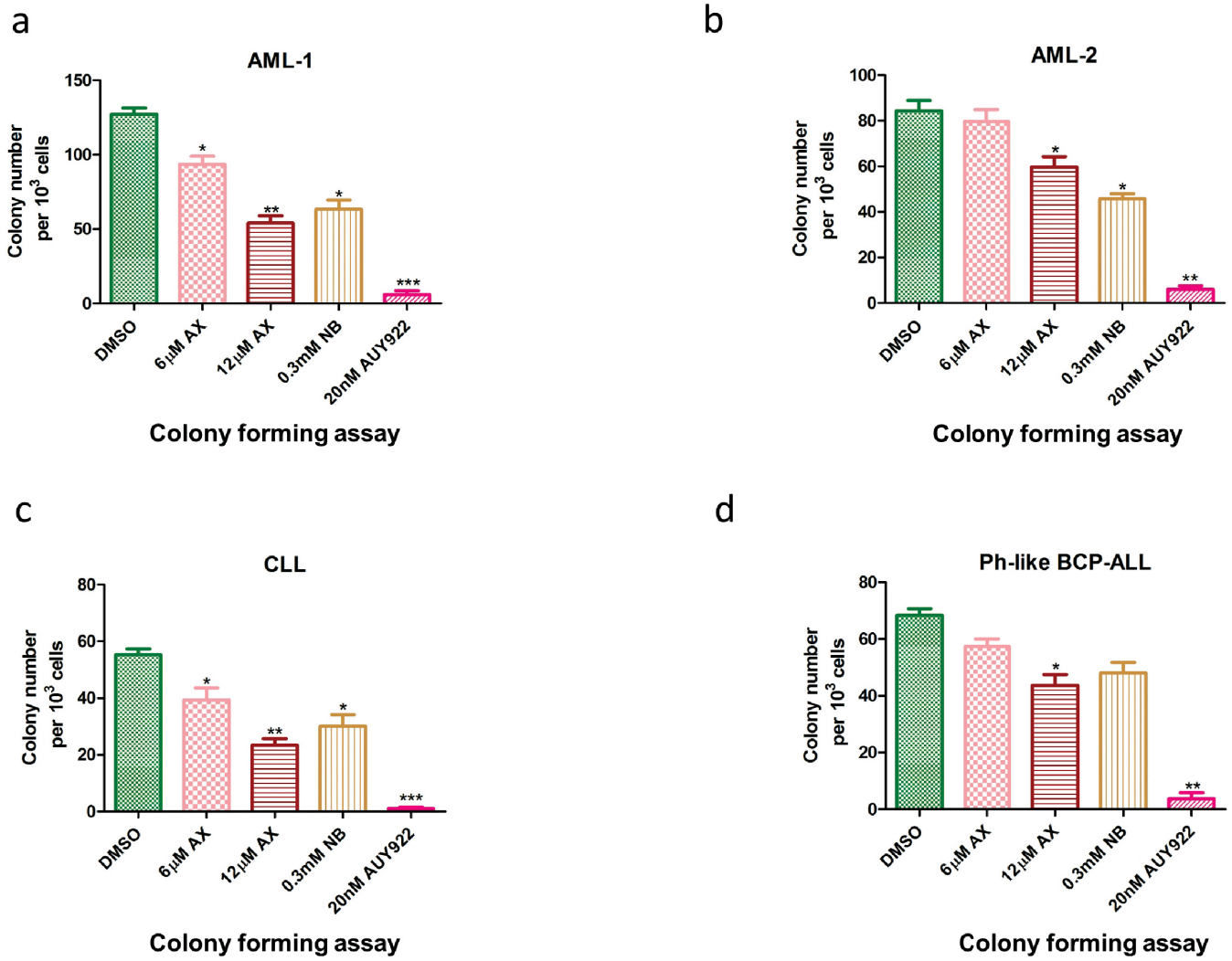

Figure S21: AX block colony formation in primary AML, CLL and Ph-like BCP-ALL patient samples. (**a, b, c and d**) Primary AML cells (>80% blast cells) from two different FLT3-ITD$^+$ patient samples (AML-1 and AML-2), one CLL and one relapse Ph-like BCP-ALL) patient samples, respectively; were seeded in methylcellulose medium after treatment with the indicated concentration of **AX** or with respective controls (NB, IM or AUY922) for 48h. Colonies were counted after 14 days (n=5). Significance analysis of normally distributed data with variance similar between groups used paired, two-tailed Student's t-test. * $p < 0.05$, ** $p < 0.005$, *** $p < 0.001$.

Supplemental Note 1

1. Chemistry

Materials and Methods

All chemicals and solvents were obtained from commercial suppliers (Sigma-Aldrich, Acros Organics, Carbolution Chemicals) and used as purchased without further purification. Fmoc-Rink-Amide PEG AM Resin (200-400 mesh, 0.56 mmol/g) was purchased from Iris Biotech, Germany. Solution-phase reactions were monitored by thin layer chromatography (TLC) using MN silica gel plates, precoated with fluorescence indicator UV_{254}, using ethyl acetate/*n*-hexane as the mobile phase. Components were visualized by irradiation with ultraviolet light (254 nm) or staining in potassium permanganate solution followed by heating. Flash column chromatography was performed with prepacked silica cartridge or Fluka silica gel 60 (230-400 mesh ASTM) with the solvent mixtures specified in the corresponding experiment. Proton (^1H) and carbon (^{13}C) NMR spectra were recorded on a Bruker Avance 600 using $CDCl_3$ as solvent. Chemical shifts are given in parts per million (ppm), relative to residual solvent peak for ^1H and ^{13}C. 2D NMR data were collected on a Bruker Avance 600 instrument operating at 600 MHz. ROESY acquisitions were performed at 298 K with the following parameters: spectralwindow = 8474.58 Hz in both dimensions; mixing time = 0.05 ms; number of transients = 16; number of increaments = 256; number of points = 1024. Square cosine window functions were applied in both dimensions. HRMS analysis was performed on a UHR-TOF maXis 4G, Bruker Daltonics, Bremen. All HPLC analyses and purifications were carried out on a Varian Prostar system equipped with a Prostar 410 (autosampler), 210 (pumps) and 330 (UV-detector). HPLC-grade water +0.1% TFA (solvent A) and HPLC-grade acetonitril +0.1% TFA (solvent B) were used as solvents. Analytical HPLC analyses were performed on a *Macherey-Nagel Nucleosil* C8 RP-HPLC column (EC 250/4 Nucleosil 100-5 C8) using a linear gradient from 50% B to 100% B in 40 min at a flow rate of 1 ml/min. For semipreparative purification a *MN Nucleosil* C8 RP-HPLC column (VP 250/10 Nucleosil 100-5 C8ec) was used at a flow rate of 4 mL/min. The Phthaloyl-protected monomers[1] and dimers[2] and the carboxybenzyl-protected monomers[3,4] were synthesized according to literature procedures.

Synthesis of Cbz-^{NO}Leu-^{NO}Leu-O*t*Bu (8)

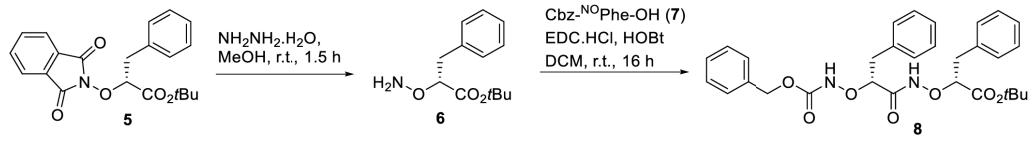

Hydrazine monohydrate (0.44 mL, 9.0 mmol, 3.0 eq.) was added to a solution of **5** (3.0 mmol, 1.0 eq.) in methanol (15 mL). The reaction was stirred for 1.5 h and the solvent was subsequently removed under reduced pressure. The residue was dissolved in 5% aqueous sodium carbonate solution (15 mL) and extracted with diethyl ether (3 x 20 mL) The organic layer was dried over anhydrous sodium sulfate and concentrated under reduced pressure to provide the phthaloyl-deprotected monomer **6** as colorless oil which was immediately used in the next step without further purification. The phthaloyl-deprotected monomer **6** was dissolved in DCM (5 mL) and added to a stirred solution of Cbz-^{NO}Phe-OH **7** (3.0 mmol, 1.0 eq.), HOBt (486.4 mg, 3.6 mmol, 1.2 eq.) and EDC·HCl (690.1 mg, 3.6 mmol, 1.2 eq.). in dry DCM (20 mL) and the reaction was stirred overnight at room temperature. The solvent was removed under reduced pressure and the crude product was purified by flash column chromatography using hexane-ethyl acetate as eluent (gradient: 90:10 → 60:40 in 20 min) to afford the *α*-aminoxy dipeptide **8**.

Experimental data for compound 8

Colorless oil; yield: 1.43 g (2.68 mmol, 89%). ^{1}H NMR (600 MHz, $CDCl_3$) δ 10.51 (s, 1H), 7.43 (s, 1H), 7.39-7.19 (m, 15H), 5.20-5.06 (m, 2H), 4.66-4.57 (m, 1H), 4.50-4.42 (m, 1H), 3.36-3.26 (m, 1H), 3.21-3.09 (m, 2H), 3.02-2.91 (m, 1H), 1.35 (s, 9H). ^{13}C NMR (75 MHz, $CDCl_3$) δ 169.7, 167.3, 158.2, 136.6, 135.9, 135.0, 129.7, 129.5, 128.8, 128.8, 128.7, 128.6, 128.4, 127.1, 126.9, 87.5, 84.1, 82.5, 68.4, 37.6, 37.2, 28.0. Anal. Calcd. for $C_{30}H_{35}N_2O_7$ 535.2439 $[M+H]^+$; found 535.2438.

Synthesis of Cbz-^{NO}Tyr(*t*Bu)-OH (11)

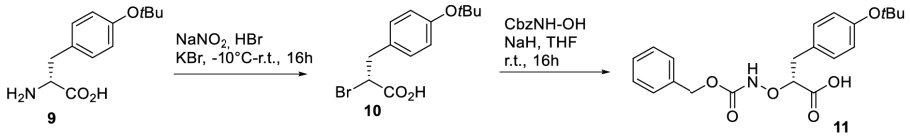

Compound **10** and **11** were synthesized according to literature protocols[3,4] as followed: KBr (9.28 g, 78.0 mmol, 3.7 equiv.) was diluted in 0.75 M aq. HBr[†] (125 mL, 92.7 mmol, 4.4 equiv.) and cooled to -7 °C. $NaNO_2$ (2.76 g, 40.0 mmol, 1.9 equiv.) was then added in one portion, followed by the portionwise addition of L-tyrosin *tert*-butyl ether (5.0 g, 21.1 mmol, 1.0 equiv.) while maintaining the temperature of the reaction mixture between -7 and -4 °C. The reaction was stirred for 1.5 h and then extracted with EtOAc that had been precooled to 0 °C (3 x 200 mL). The organic layers were dried over $NaSO_4$ and the solvent was removed under reduced pressure to afford **10** in 78% yield as a solid compound which was used without further purification.

NaH (60% in mineral oil, 320.0 mg, 8.0 mmol, 2.0 equiv.) was added in small portions to a stirred solution of benzyl hydroxycarbamate (668.6 mg, 4.0 mmol, 1.0 equiv.) in THF (20 mL) at -5 °C. The resulting reaction mixture was stirred for 10 min. A solution of **10** (1.20 g, 4.0 mmol, 1.0 equiv.) in THF (3 mL) was added dropwise and the resulting reaction mixture was stirred for 15 h at room temperature. The solvent was removed under reduced pressure. The resulting precipitate was dissolved in water and acidified with 4 M HCl to pH = 2 and extracted with diethyl ether (3 x 30 mL). The organic layer was dried over $NaSO_4$ and the solvent was removed under reduced pressure. Next, 30 mL of diethyl ether and *N*,*N*-dicyclohexylamine (725.3 mg, 4.0 mmol, 1.0 equiv.) were added and the resulting precipitate was collected and washed with diethyl ether (3 x 20 mL). The precipitate was suspended in water (60 mL), the mixture was acidified with 4 M HCl to pH = 2 and extracted with ether (3 x 30 mL). The organic layer was dried over $NaSO_4$ and the solvent was removed under reduced pressure to give **11**.

Experimental data for compound 11

Colorless oil; yield: 0.91 g (2.36 mmol, 59%). ^{1}H NMR (600 MHz, $CDCl_3$) δ 9.24 (s, 1H), 8.08 (s, 1H), 7.47-7.29 (m, 5H), 7.21-7.00 (m, 2H), 7.01-6.79 (m, 2H), 5.16 (s, 2H), 4.56 (dd, *J* = 9.3, 3.7 Hz, 1H), 3.22 (dd, *J* = 15.0, 3.7 Hz, 1H), 3.00 (dd, *J* = 15.0, 9.3 Hz, 1H), 1.33 (s, 9H). ^{13}C NMR (151 MHz, $CDCl_3$) δ 173.0, 159.1, 154.4, 134.8, 131.0, 129.9, 128.9, 128.8, 128.6, 124.3, 86.5, 78.7, 77.2, 68.75, 36.7, 29.0. Anal. Calcd. for $C_{21}H_{26}NO_6$ 388.1755 $[M+H]^+$; found 388.1755.

[†] Prior to the preparation of the acidic media, the concentrated HBr (48% aq.) was washed with 5% tributyl phosphate in chloroform (3 x 20 mL) to remove Br_2. Disappearance of the brown color indicates the complete removal of Br_2.

Solid-phase synthesis of α-aminoxy hexapeptides 1 and 2

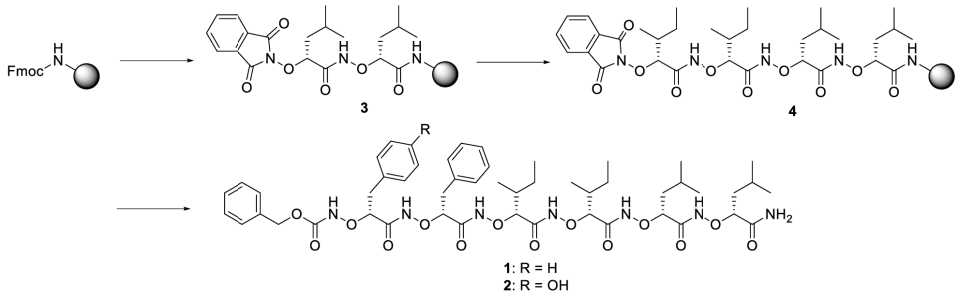

Peptide synthesis was conducted in fritted PE-syringes on a 0.2 mmol scale. After resin swelling for 60 min in DMF, the Fmoc group of the Fmoc-Rink-Amide PEG resin (loading 0.56 mmol/g) was removed by treatment with 20% piperidine in DMF (2 x 15 min, 2 ml/100 mg of resin) before the resin was sequentially washed with DMF, CH_2Cl_2, DMF (3 x 2 ml/100 mg resin, agitating for 15 sec and then drained). Then a solution of Phth-^{NO}Leu-^{NO}Leu-OH‡ (243.7 mg, 0.6 mmol, 3.0 equiv.), BOP (265.4 mg, 0.6 mmol, 3.0 equiv.) and HOBt (81.1 mg, 0.6 mmol, 3.0 equiv.) in DMF (5 mL) was agiated for 1 min, NEM (101 µL, 0.8 mmol, 4.0 equiv.) was added and this solution was added to the resin. The amide coupling was performed for 24 h at room temperature. Afterwards, the resin was sequentially washed with DMF, CH_2Cl_2 and DMF. Then, the phthaloyl group was removed by treatment with 5% hydrazine monohydrate in methanol for 15 min (2x) and the resin was sequentially washed with DMF, MeOH, CH_2Cl_2 and DMF. A subsequent amide coupling reaction with Phth-^{NO}Ile-^{NO}Ile-OH‡ (243.7 mg, 0.6 mmol, 3.0 equiv.) in the presence of the BOP/HOBt/NEM coupling system provided the resin-bound *α*-aminoxy tetrapeptide **4**. The resin-bound target compound **1** was prepared starting from compound **4** by an additional cycle of phthaloyl-deprotection and amide coupling reaction with the *α*-aminoxy dipeptide acid Cbz-^{NO}Phe-^{NO}Phe-OH‡ (284.7 mg, 0.6 mmol, 3 equiv.). In the case of compound **2** the final two *α*-aminoxy acids Phth-^{NO}Phe-OH (186.8 mg, 0.6 mmol, 3 equiv.) and Cbz-^{NO}Tyr(*t*Bu)-OH (232.4 mg, 0.6 mmol, 3 equiv.) were coupled as monomeric building blocks to the resin-bound tetrapeptide **4** by two iterative cycles of phthaloyl deprotection, amide coupling reaction and washing cycles. In both cases the final washing was achieved with CH_2Cl_2 before the crude products were cleaved from the resin by treatment with TFA/TES (98:2, v/v, 2 ml/100 mg of resin) for 1.5 h. The filtrates were concentrated in a stream of nitrogen to a volume <1 ml, and the crude products were precipitated with cold diethyl ether, centrifugated and the diethyl ether was discarded. This procedure was repeated twice to obtain the crude peptides **1** and **2**. For semipreparative purification the crude peptides were re-dissolved in acetonitrile and purified on a *MN Nucleosil* C8 RP-HPLC column (VP 250/10 Nucleosil 100-5 C8ec) at a flow rate of 4 mL/min. Fractions containing only the desired peptide were collected and lyophilized from HPLC solvents yielding the purified peptides in >95% purity in both cases.

‡ Free carboxylic acids were prepared immediately before use from their respective *t*Bu protected aminoxy acids or dipeptides by treatment with TFA/DCM (1:1, v/v, 10 mL / 0.5 mmol) for 1 h at room temperature. The solvent was removed under reduced pressure and the residue was azeotroped with toluene twice to give the free acid in quantitative yields.

Characterization data for compound 1 and 2

Cbz-^{NO}Phe-^{NO}Phe-^{NO}Ile-^{NO}Ile-^{NO}Leu-^{NO}Leu-NH$_2$ (1)

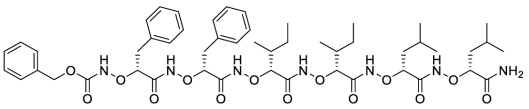

Colorless solid; 39% yield; 96.2% purity as determined by HPLC (50% B → 100% B in 40 min, 1mL/min) t_R = 18.44 min; HRMS (ESI): *m/z* calcd. for $C_{50}H_{71}N_7O_{14}$ $[M+H]^+$ 994.5132, found 994.5140.

Cbz-^{NO}Tyr-^{NO}Phe-^{NO}Ile-^{NO}Ile-^{NO}Leu-^{NO}Leu-NH$_2$ (2)

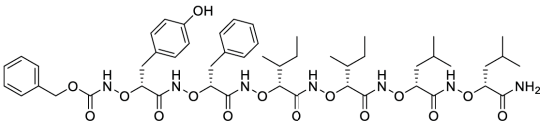

Colorless solid; 30% yield; 97.8% purity as determined by HPLC (50% B → 100% B in 40 min, 1mL/min) t_R = 15.75 min; HRMS (ESI): *m/z* calcd. for $C_{50}H_{72}N_7O_{15}$ $[M+H]^+$ 1010.5081, found 1010.5090.

2. References only for supplemental note 1

[1] D. Yang, B. Li, F.-F. Ng, Y.-L. Yan, J. Qu and Y.-D. Wu, *J. Org. Chem*., 2001, **66**, 7303.

[2] D. Diedrich, A. J. R Moita, A. Rüther, B. Frieg, G. J. Reiss, A. Hoeppner, T. Kurz, H. Gohlke, S. Lüdeke, M. U. Kassack and F. K. Hansen, *Chem. Eur. J.*, 2016, doi:10.1002/chem.201602521

[3] (a) B. Draghici, F. K. Hansen, A.-M. Buciumas, B. E.-D. M. El-Gendy, E. Todadze and A. R. Katritzky, *RSC Adv*., 2011, **1**, 602. (b) A. Katritzky, A. Ilker and S. R. Tala, *J. Org. Chem*., 2009, **74**, 8690.

[4] A. J. Souers, S. Schürer, H. Kwack, A. A. Virgilio, J. A. Ellman, *Synthesis*, 1999, **4**, 583-585.

3. Spectral data and HPLC chromatograms

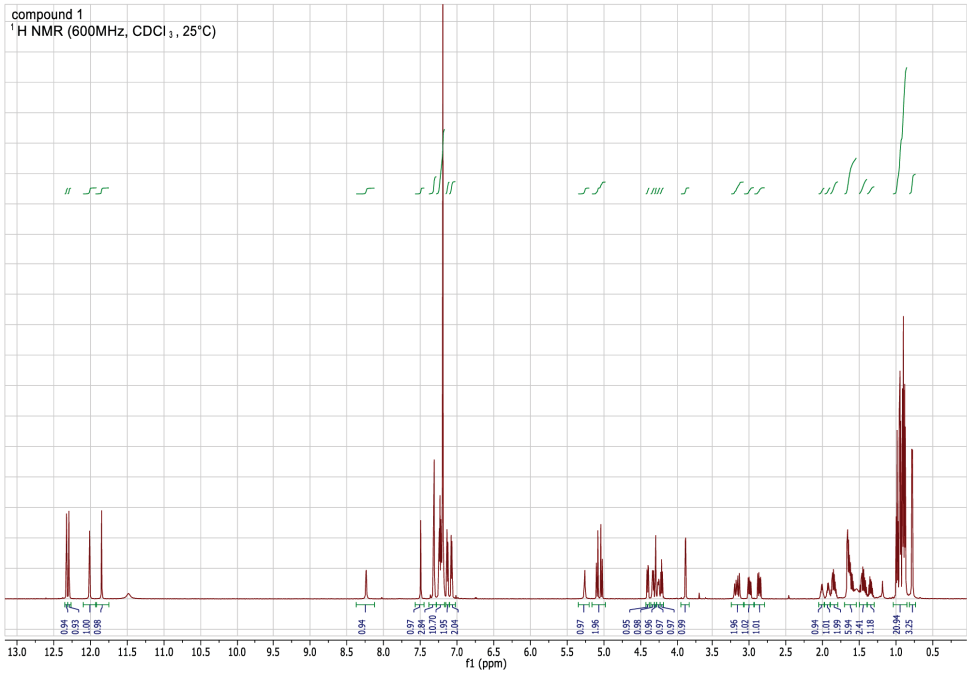

^{1}H NMR of compound **1** in $CDCl_3$ (25 °C).

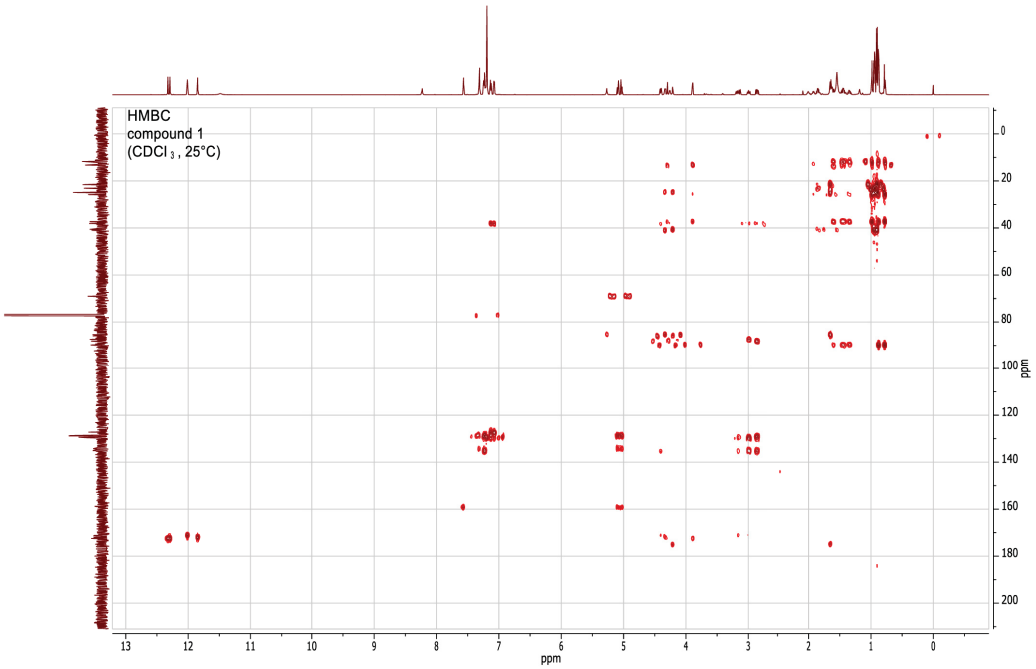

HMBC spectrum of compound **1** in $CDCl_3$ (25 °C).

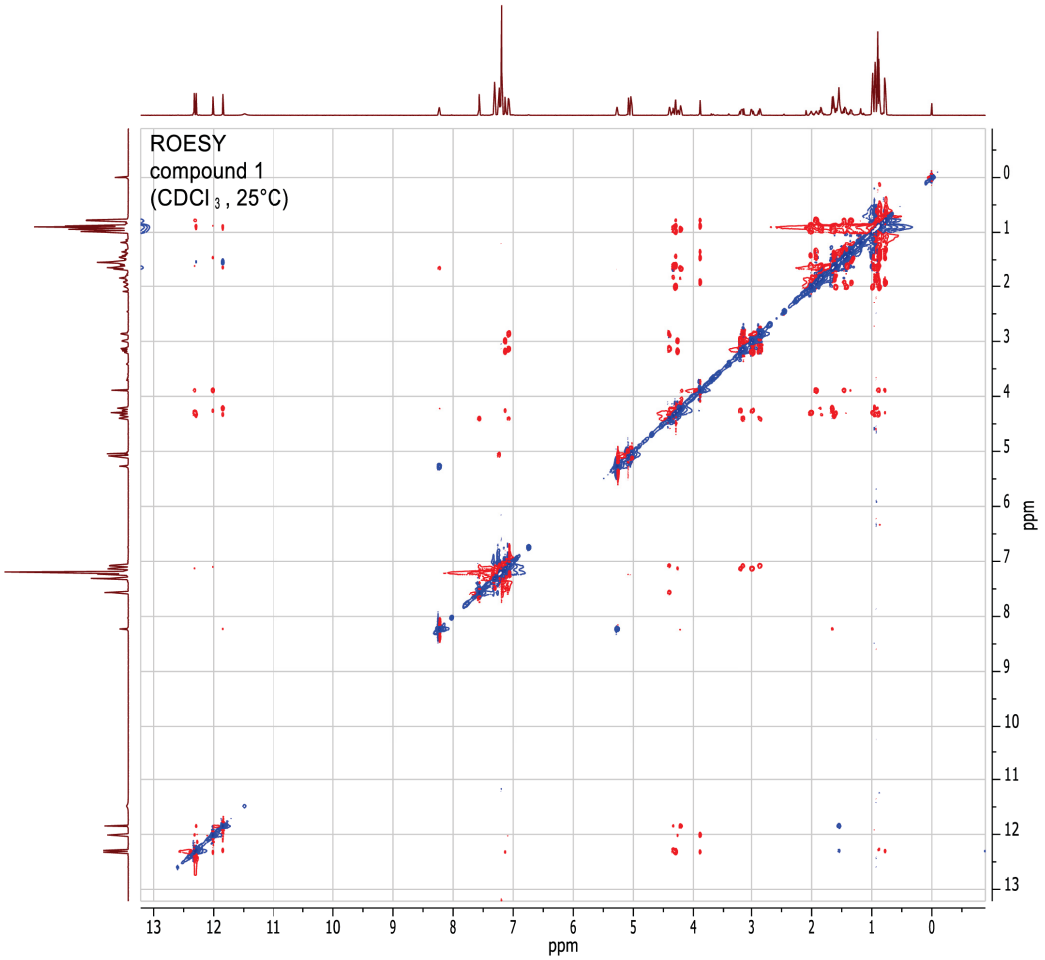

2D ROESY spectrum of compound **1** in $CDCl_3$ (25 °C).

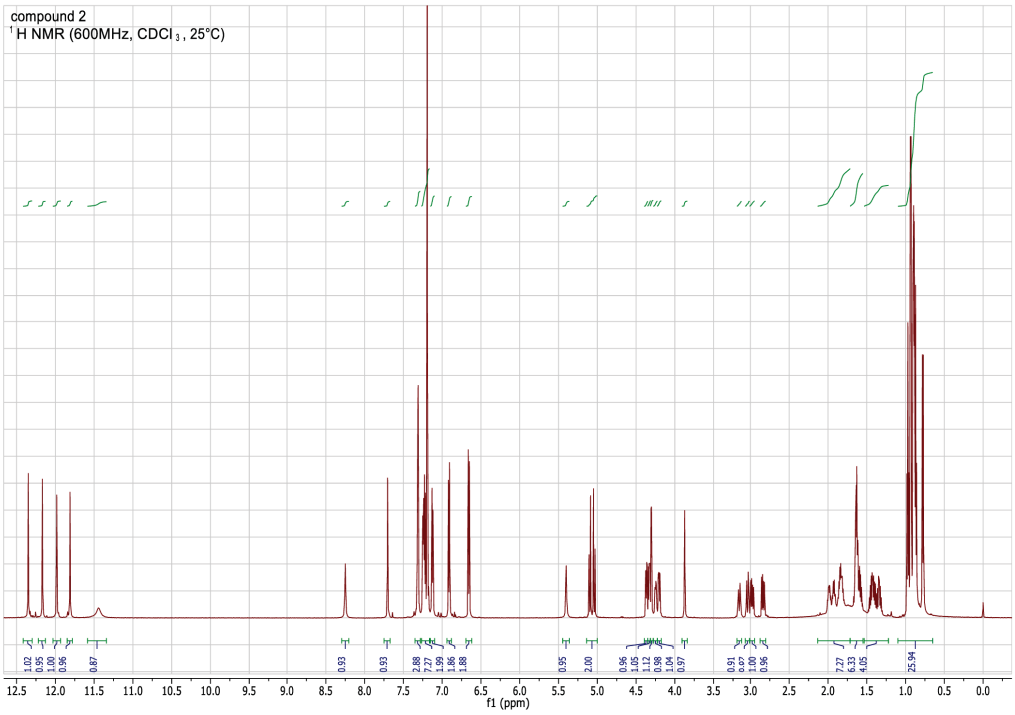

^{1}H NMR (600 MHz) of compound **2** in $CDCl_3$ (25 °C).

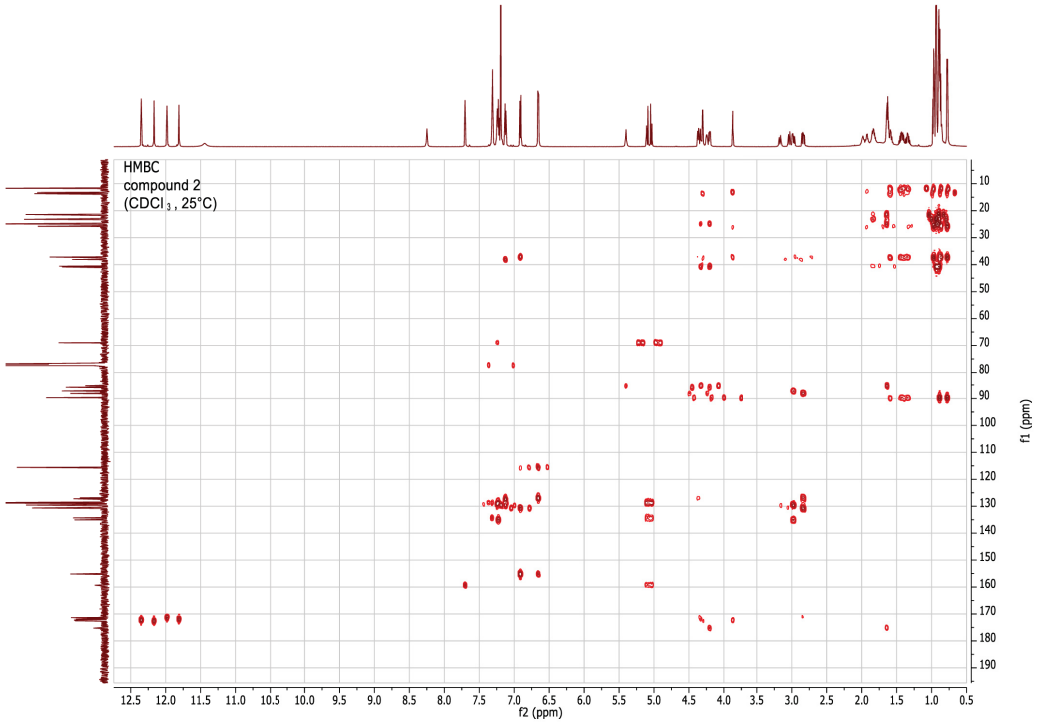

HMBC spectrum of compound **2** in $CDCl_3$ (25 °C).

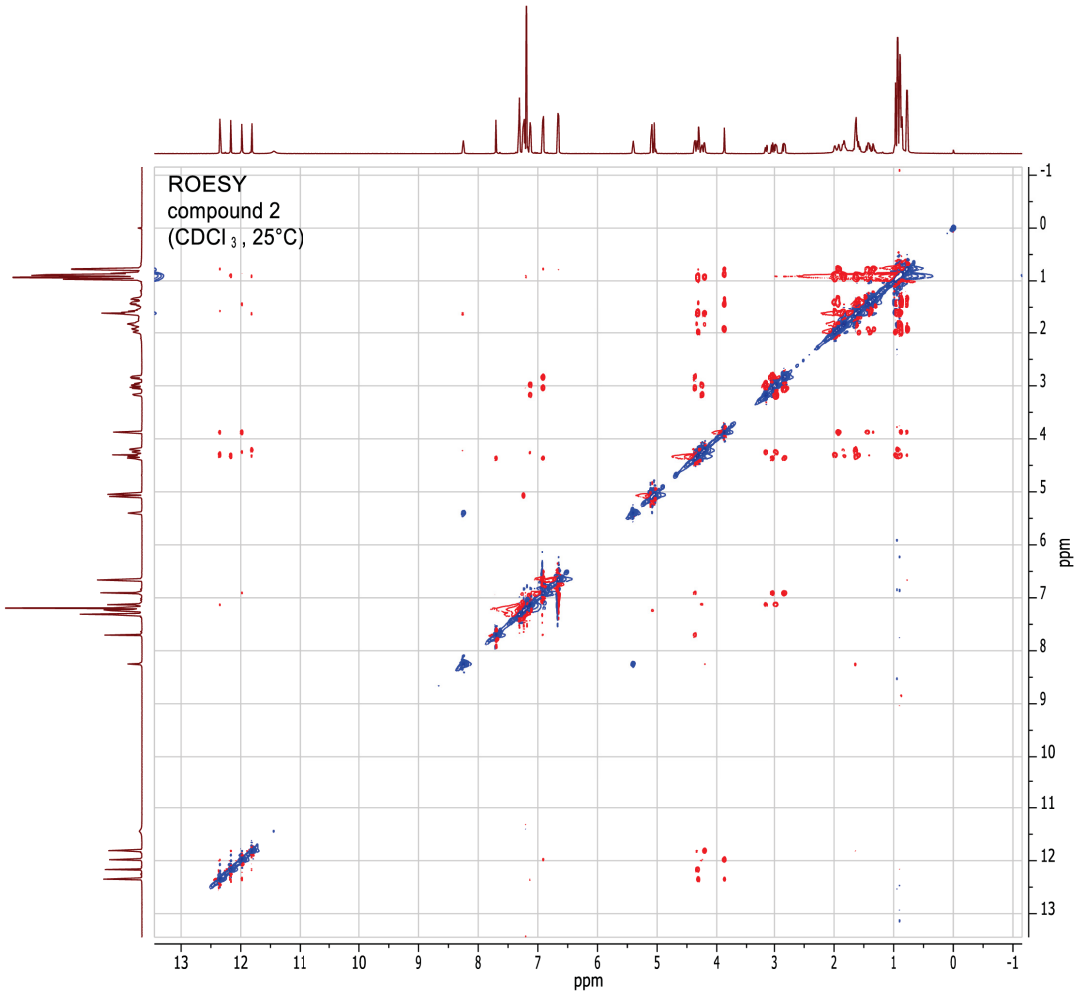

2D ROESY spectrum of compound **2** in $CDCl_3$ (25 °C).

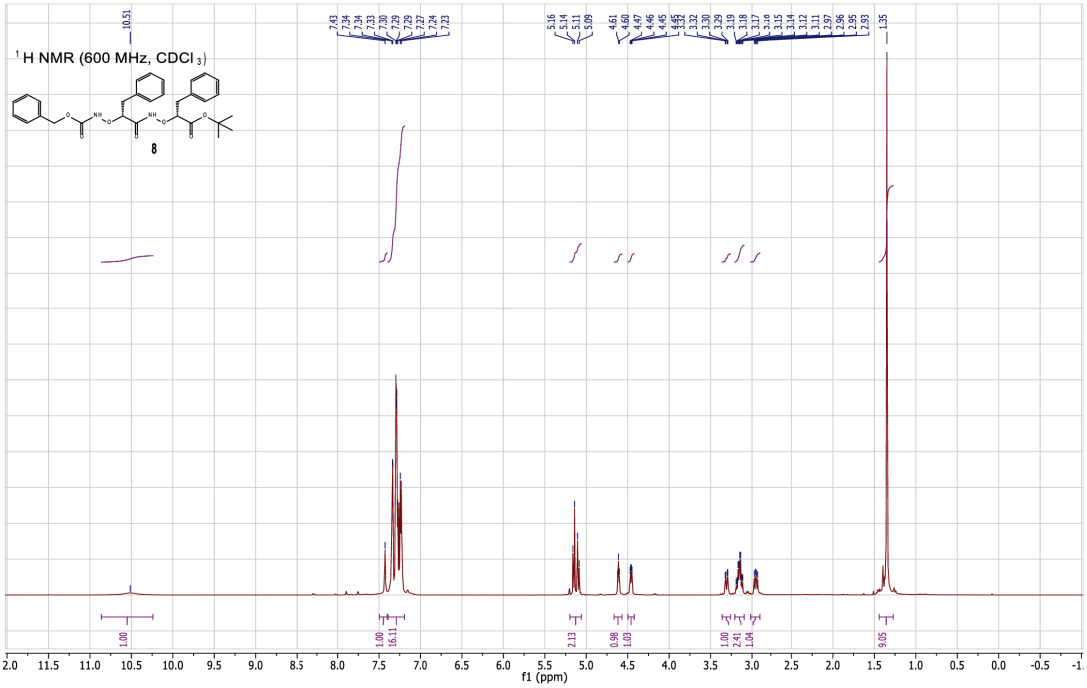

^{1}H NMR (600 MHz) of compound **8** in $CDCl_3$ (25 °C).

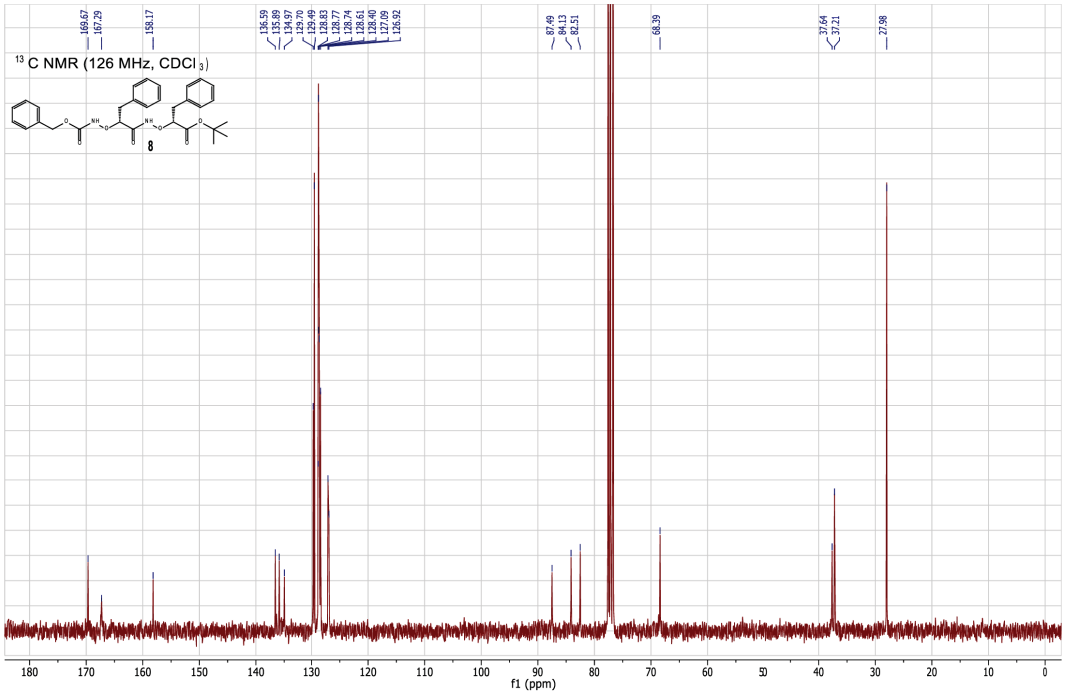

^{13}C NMR (126 MHz) of compound **8** in $CDCl_3$ (25 °C).

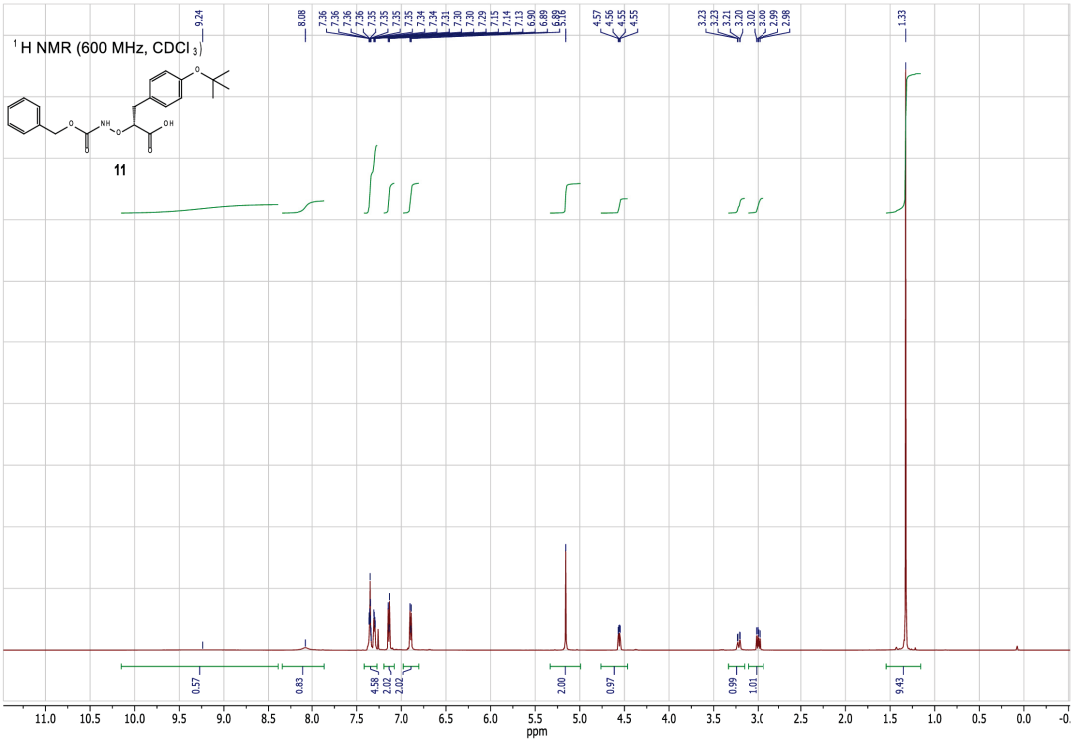

^{1}H NMR (600 MHz) of compound **11** in $CDCl_3$ (25 °C).

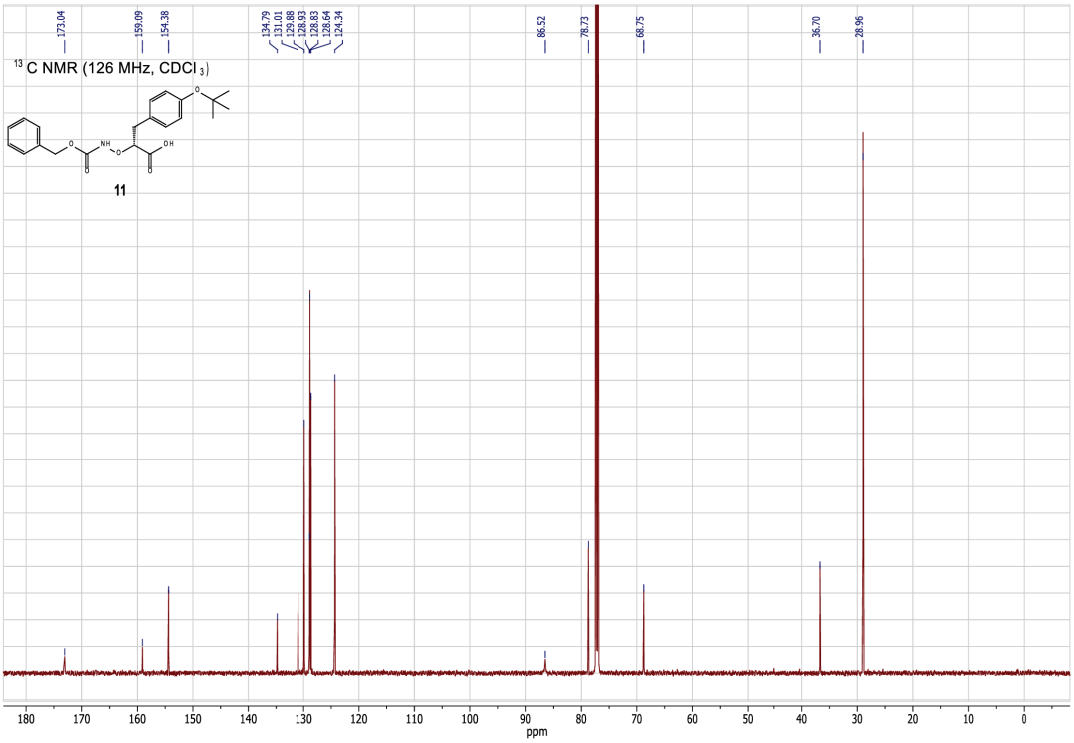

^{13}C NMR (126 MHz) of compound **11** in $CDCl_3$ (25 °C).

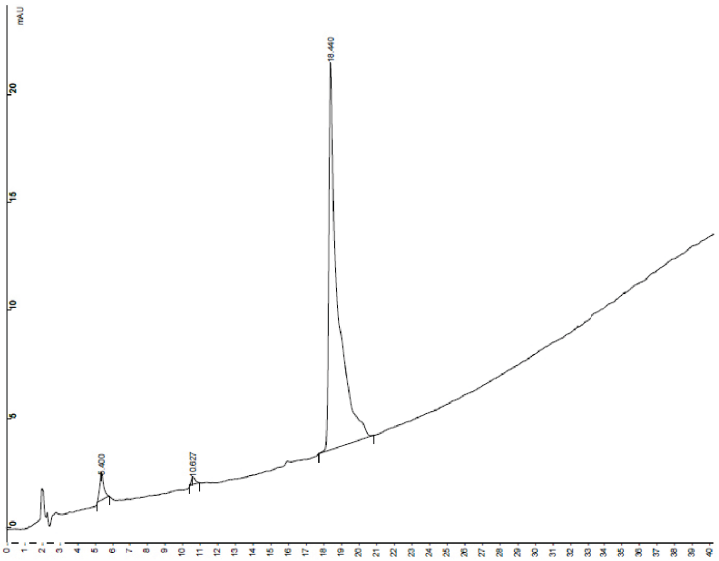

Peak No.	Peak Name	Result ()	Ret. Time (min)	Time Offset (min)	Area (counts)	Sep. Code	Width 1/2 (sec)
1		2.9845	5.400	0.000	98515	BB	14.5
2		0.8055	10.627	0.000	26587	BB	15.3
3		96.2100	18.440	0.000	3175746	BB	21.3
	Totals:	100.0000		0.000	3300848		

HPLC chromatogram of compound **1** (purity 96.2%)

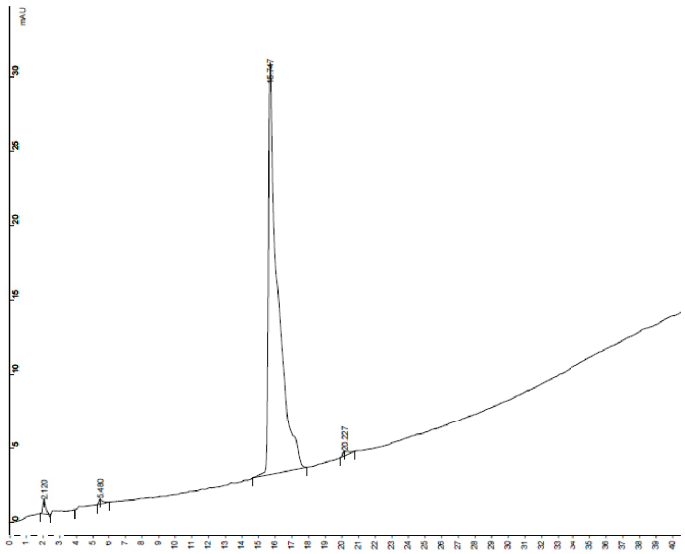

Peak No.	Peak Name	Result ()	Ret. Time (min)	Time Offset (min)	Area (counts)	Sep. Code	Width 1/2 (sec)
1		0.9986	2.120	0.000	55854	BB	10.6
2		0.5111	5.480	0.000	28585	BB	27.3
3		97.8194	15.747	0.000	5471353	BB	27.3
4		0.6710	20.227	0.000	37531	BB	9.0
	Totals:	100.0001		0.000	5593323		

HPLC chromatogram of compound **2** (purity 97.8%)

Supplemental note 2

Autodisplay dimerization assay

Surface display of HSP90 on *E. coli* BL21 (DE3) cells was performed as described before[21]. Cells were washed three times and suspended in PBS to a final OD_{600} = 0.35 in a final volume of 50 µl. Cells were incubated for 15 min either with or without addition of the respective compounds. Cells were then again washed three times with PBS containing 0.1 % Tween-20 to avoid unspecific binding. Subsequently, FITC labeled p53 was added to the cells in a final concentration of 1 µM. Cells were incubated for 1 h in the dark at RT, and again were washed three times with filter sterilized PBS containing 0.1 % Tween-20. *E. coli* cells without displaying a passenger were used as control and were treated the same. Cellular mean fluorescence was measured with a FACS Aria III (BD, Heidelberg, Germany), using 488 nm as excitation wavelength, 530 nm for detection, and filter sterilized PBS as sheath fluid as described before.[21] For each sample, at least 50,000 events were counted using a flow rate of 1000 events per second.

Microscale Thermophoresis (MST)

The HSP90 CTD was purified as described before[22] and labeled with the Monolith NT™ Protein Labeling Kit RED-NHS (Amine reactive) of NanoTemper (NanoTemper Technologies GmbH, München, Germany) according to the manufacturer's protocol. The determination of the apparent K_D values of HSP90 CTD and **1** (**AX**) and **2** were performed by using a constant amount of 50 nM of labeled HSP90 CTD in PBS including 0.5 % BSA and 0.1 %Tween-20 and addition of 10 µl **1** (**AX**) or **2** in different concentrations ranging from 30 nM to 500 µM. These mixtures were incubated for 15 min at RT in the dark. Subsequently, thermophoresis of each concentration was measured using the Monolith NT.115 (NanoTemper Technologies GmbH, München, Germany) [23]. Each measurement was performed at 25 °C for 25 s at 90 % LED power and 40 % infrared laser power. The measurement was repeated three times independently for each sample. The fluorescence of each measurement was normalized and

plotted against the different concentrations of the titrant. The K_D Fit formula Y = E + (A - E) / 2 * (T + x + K_D - sqrt((T + x + K_D)^2 – 4 * T * x)) was used to calculate the apparent K_D value using the GraphPad Prism software (GraphPad Software, Inc. La Jolla, CA, USA). The concentration value for the labelled CTD protein was set to 50 nM for determining the apparent K_D of HSP90 CTD with respect to **1** (**AX**) and **2**.

Analytical ultracentrifugation

Sedimentation velocity experiments were carried out using a Beckman ProteomeLab XL-A ultracentrifuge (Beckman Coulter, Inc., Indianapolis, INUS) equipped with an absorbance detection system and an eight-hole rotor. HSP90 CTD and ligand were dissolved in 20 mM NaPi, 50 mM KCl with 8 % DMSO (pH 8.0) as vehicle. Solutions of 20 µM HSP90 CTD treated with (27.4 µM or 54.8 µM) **1** (**AX**) and the control sample (20 µM HSP90 CTD alone) were loaded into 12-mm double-sector aluminum cells with quartz glass windows, respectively. All samples were analyzed at 50,000 rpm at 20°C. Protein samples were monitored by UV absorbance at 280 nm in continuous mode with a time interval of 360 s and a step size of 0.002 cm. Recorded data were evaluated with Sedfit (version 15.01b) using the continuous c(*s*) distribution model[24]. A minimization of the rmsd value was achieved by alternated and repeated fitting based on either a Simplex algorithm or Marquardt Levenberg. The resolution in *s*-value was set to 0.05 S. The chosen F-ratio was 0.95. As a final step meniscus as well as bottom positions had been floated. The partial specific volume of HSP90 CTD was calculated using Sednterp (version 20130813BETA)[25]. The influence of DMSO on the density and viscosity of the buffer had been experimentally determined in a densitometer and a viscometer, respectively. The following parameters were used for the fitting procedures: density ρ =1.03945 g/cm³; viscosity η =1.278 cP; partial specific volume $\bar{\nu}$ =0.7302 cm³/g[26]. Graphical outputs were generated by GUSSI (version 1.2.1)[27]. The final sedimentation coefficient values (*s*-values) were corrected to the *s*-values in water at 20 °C ($s_{20,w}$-values).

The major peak of HSP90 CTD samples in the absence of **1** (**AX**) as well as in the presence of 27.4 µM and 54.8 µM **1** (**AX**) has an *s*-value of 3.27 S. This *s*-value species most probably represents the HSP90 CTD dimer. A monomer cannot sediment with 3.27 S even if it has a near spherical shape and can therefore be excluded. Applying the molecular scaling law

$$\left(\frac{M}{N_A}\right)^{2/3} = \frac{s \cdot f/f_0}{1-\bar{\nu}\rho} 6\pi\eta \left(\frac{3\bar{\nu}}{4\pi}\right)^{1/3}$$

(M molecular mass, N_A Avogadro's number, s sedimentation coefficient, $\bar{\nu}$ partial specific volume, ρ density, η viscosity) in order to calculate the mass of the sedimenting species based on an $s_{20,w}$-value of 3.27 S and a weight-average frictional ratio f/f_0 of 1.30 leads to a mass of 42.196 g/mol, which is in perfect agreement with the expected mass of a dimer (42.660 g/mol). Aside from this dimer with 3.27 S, about 60 % of oligomers with *s*-values between 4 and 9 S were detected in samples without **1** (**AX**). Analytical techniques such as PAGE, size exclusion chromatography, and analytical ultracentrifugation previously indicated that both HSP90[28,29] and isolated CTD[29,30] can exist as higher oligomers than dimers. Furthermore, recombinant CTD carrying a C-terminal His-tag, as in our case, was shown to form tetramers[31]. However, while the dimerization interface of human HSP90 was mapped to amino acids 660-696[22,28], no study has yet resolved the interaction site for higher oligomer formation in the CTD. Upon addition of **1** (**AX**), these larger oligomers disappear in a concentration-dependent manner, while the amount of the 3.27 S species increases. This demonstrates that the ligand is able to either dissociate oligomeric species of or suppress HSP90 CTD oligomerization.

Luciferase refolding assay

Luciferase assay was performed with K562 cells, stably expressing (transduced) luciferase-transgene, as described in[20] with some modifications. Briefly, cells were resuspended in pre-warmed (50°C) media. After optimization, 3 min of heat shock was sufficient to denature the endogenous luciferase activity, however insufficient to affect the viability of the cells. Later 50000 cells / well were seeded in white plates at 37°C in the presence of **1** (**AX**), **2,** NB (Sigma-Aldrich, St. Louis, MO, USA) or AUY922 (Selleckchem.com, Houston, TX, USA) to allow refolding of denatured luciferase. After 180 min, luciferase activity was measured by addition of luciferin (Promega) and read out was performed using a luminometer (integration 0.1 sec/well). Inhibition with the compounds was calculated using GraphPad Prism software (GraphPad Software).

DARTS

Ligand binding to a target protein can result in conformational changes that lead to a stabilization against proteolytic lysis by dropping the sensitivity to proteases. Drug Affinity Responsive Target Stability (DARTS) assay was carried to evaluate the protease protection of **1** (**AX**) from thermolysin, described in[20]. Briefly, 1 µg of recombinant HSP90α was incubated on ice for 15 min with 25 µM of **1** (**AX**), NB, AUY922 and DMSO. After incubation, the samples were treated with thermolysin (1:50 of protein) for 5 min. The reaction was stopped by addition of 50 mM EDTA and later examined by immunoblot analysis using anti-HSP90α antibody.

Western blotting (WB)

Cell lysates were generated after 48 h treatment of leukemic cells with **1** (**AX**), IB, NB or AUY922. Immunoblot analysis was performed by following standard protocol using antibodies: anti-Hsp90, anti-Hsp70, anti-Hsp40, anti-Hsp27, anti-HSF-1, anti-Hsp60, anti-PDI, anti-Hsp90α, anti-Hsp90β, anti-c-Abl, anti-phospho-c-Abl (T245), anti-Stat5a, anti-pStat5a (T694), anti-pCrkl (T207), anti-Crkl, anti-Akt, anti-pAkt (S473), anti-pS6, anti-S6, anti-cMyc (Cell Signaling Technology, Danvers, MA), anti-pAkt (T308), anti-Bcl-2 (Santa Cruz Biotechnology, TX, USA) & β-actin (Sigma-Aldrich).

Blue-native gels

Blue-native gels were performed following manufacturer's instructions (Invitrogen) and as described in[20]. Briefly, lysates were generated after 48 h treatment with **1** (**AX**) using NativePAGE Sample Prep kit (Invitrogen) by 2-3 freezing thawing cycles followed by centrifugation at 20,000 x g for 25-30 min 4 ˚C. Protein concentration was determined by Dye reagent (BioRad Laboratories, Hercules, CA, USA) and subsequently equal amount of protein (25 - 30 µg) was loaded on Native PAGE 3 - 12% Bis - tris gel (Invitrogen) and electrophoresed using NativePAGE running buffer (Invitrogen) following supplier's guidelines.

Supplemental note 3

Molecular dynamics simulations and computation of effective binding energies

We used molecular dynamics (MD) simulations of free diffusion of **AX** in the presence of the C-terminal domain (CTD) of HSP90 to provide structural insights how **AX** binds to this domain. **AX** was designed to mimic hotspot residues[22] within the dimerization interface of the CTD. We used a monomeric CTD model (sequence E527 – G697; extracted from the crystal structure[32]) rather than a full-length HSP90 structure in our MD simulations in order to focus the computational time available on sampling of **AX** configurations around the CTD. We evaluated the structural stability of this model by, first, calculating the protein backbone root mean square-deviation (RMSD) with respect to the crystal structure[32]. Second, we calculated the angle η as a measure of helix H5 orientation; H5 is part of the dimerization interface[32]. η is the average angle between the vector along H5 during 0.4 µs of MD simulations and the vector along H5 in the crystal structure[32]. See next chapter for details. All results are summarized in **Supplementary Fig. 1**.

Initially, we performed 8 × 400 ns of unbiased MD simulations of **AX** diffusion in the presence of the HSP90 CTD. The backbone RMSD increases up to ~11 Å with mean RMSD values > 4 Å, indicating distinct structural deviations relative to the crystal structure, in particular in regions where the adjacent middle domain is missing. Additionally, η increases up to 33°, indicating a reorientation of H5 towards helix H4 in the dimerization interface, that way narrowing the space between the two helices. A plausible explanation is that the CTD in the crystal structure[32] is stabilized by the middle domain and/or the CTD of the adjacent subunit. This explanation is supported by backbone RMSD values of the CTD dimer being generally smaller[22] than the backbone RMSD values found here for the CTD monomer.

Next, we performed 8 × 400 ns of unbiased MD simulations of **AX** diffusion in the presence of the HSP90 MD/CTD structure (sequence K294 – G697; extracted from the crystal structure[32]). Here, the backbone RMSD of the CTD is < 6 Å, indicating a partial stabilization of the CTD. This is in line with our suggestion that the middle domain likely stabilizes the CTD. However, similar to the CTD alone, η increases up to 30°.

Finally, we performed 8 × 400 ns MD simulations of **AX** diffusion in the presence of the HSP90 CTD restraining all backbone atoms by harmonic potentials, that way mimicking the stabilizing influence of the presence of the MD and another CTD. During 400 ns of MD simulations, the backbone RMSD of the CTD is < 2 Å, revealing only small structural changes. Furthermore, η remains < 7°, indicating that H5 barely moves to H4. This setup was thus used to investigate binding of **AX** to the CTD by free ligand diffusion.

Molecular dynamics simulations

This method was successfully applied to investigate ligand binding by us[33,34] and others[35-37]. As to HSP90, coordinates are available from the Protein Data Bank[38] (PDB entry 3Q6M[32]). We extracted a structure that contains the middle domain and CTD (sequence K294 – D699; using the numbering of HSP90 in the crystal structure[32]), which we further refer to as the middle domain – CTD structure (MD/CTD structure). Additionally, we extracted only a CTD from the crystal structure[32] (sequence Glu527 – Gly697), which we further refer to as the CTD structure. Both protein structures were subsequently prepared using the *protein preparation wizard*[39] available in the *Maestro* suite of programs[40]. First, we added amino acids that were not resolved in the crystal structure (sequence A615 – A628). Second, we assigned H633, H684 to the HID state and H640 to the HIE state. Third, we attached acetyl and *N*-methyl cap groups to the N- and C-terminal ends of the protein structures. Finally, hydrogen atoms were added to the protein structure. As to **AX**, the molecule was generated according to the structural formula in **Fig. 1d**. The 3D structure was subjected to a quantum mechanical geometry optimization at the HF/6-31G* level. The calculations were conducted with Gaussian 09[41]. The HF/6-31G* optimized structure was later used as initial structure for MD simulations.

To provide a structural model of the binding mode of **AX** at the HSP90 CTD, we performed 60 MD simulations of at least 0.4 µs length of free diffusion of **AX** in the presence of the CTD. We randomly placed **AX** and the CTD structure, leaving at least 10 Å between any atoms in **AX** and the protein structure, by using *PACKMOL*[42]. These structures were solvated by TIP3P water[43], leaving at least 11 Å between the solute and the edge of the box, using the *LEaP* program in Amber 14[44], resulting in concentrations of **AX** in the mM range. We added sodium counter ions (Na^+) to enforce neutrality of the systems. Following this procedure, we generated 60 different starting structures in total

(**Supplementary Fig. 9a**). Analogously, we prepared eight different starting structures that contain one **AX** molecule and one HSP90 MD/CTD structure.

Atomic partial charges for **AX** were derived according to the restraint electrostatic potential fit (RESP) procedure[45] using Gaussian 09[41]. Force field parameters for **AX** were taken from the general amber force field (gaff)[46], as used previously[47]. As to Na^+, we used ion parameters described by Joung and Cheatham[48]. All other partial charges and force field parameters were taken from the ff14SB force field[49]. Both gaff[46] and ff14SB[49] force fields are available in Amber 14[44].

For subsequent MD simulations, we used a slightly modified simulation protocol as described in ref.[47,50]. The overall minimization, thermalization, and density adaptation scheme is adapted from ref.[47,50]. Here, we kept the protein backbone fixed during the whole equilibration procedure (force constant of 5 $kcal \cdot mol^{-1} \cdot Å^{-2}$). As a control, we also performed a free equilibration by gradually removing all positional restraints. These simulations are explicitly mentioned in the text (see further detail in Supplementary Notes "Model validation"). Note that during all MD simulations **AX** was not biased by any guiding force.

All production NVT MD simulations were conducted at 300 K for at least 0.4 µs with positional restraints (force constant of 5 $kcal \cdot mol^{-1} \cdot Å^{-2}$) applied to all protein backbone atoms, if not reported differently. Coordinates were saved in a trajectory file every 20 ps. The particle mesh Ewald (PME) method[51,52] was applied to treat long-range electrostatic interactions. We used the SHAKE algorithm[53] for all bonds involving hydrogen atoms. This allows one using a 2 fs time step for integrating Newton's equations of motion. All minimization, thermalization, and production calculations were performed with the *pmemd.cuda* module[54] in Amber 14[44].

We analyzed the MD trajectories using *cpptraj*[55] of AmberTools 14. During the model validation procedure, the trajectories were analyzed with respect to the protein root mean square-deviation (RMSD) relative to the crystal structure, as a measure of the structural similarity. Further, we calculated the angle η as a measure of helix H5 orientation; H5 is part of the dimerization interface[32]. η is the average angle between the vector along H5 during 0.4 µs of MD simulations and the vector along H5 in the crystal structure[32] after superimposing conformations of the CTD extracted from the MD simulations onto the crystal structure. The vector along H5 is defined by the backbone centers of mass (COM) of the amino acids (Pro681 – His684) and (Ile692 – Gly695) located at the termini of H5.

To investigate **AX** binding to the CTD, we calculated the distance between the COM of **AX** and COM of the helix H4 backbone, which is part of the CTD dimerization interface[32]. As **AX** was designed to mimic hotspots[32] on helix H5' of the adjacent subunit, distances are expressed as relative distances (ΔD) with respect to the distance between the backbone COMs of helices H4 and H5' in the crystal structure[32]. We considered **AX** bound to the CTD interface if it is at least as close as or closer to helix H4 than helix H5' ($\Delta D < 0$). To elucidate how **AX** binds to the CTD, we extracted a representative conformation from the MD trajectories after superimposing the CTD onto the crystal structure.

Computation of effective binding energies

Effective binding energies ($\Delta G_{effective}$), i.e., the sum of gas-phase energies plus solvation free energies, for **1** binding to the CTD structure were calculated by the molecular mechanics generalized Born surface area (MM-GBSA) approach[56]. MM-GBSA calculations were performed employing the "single trajectory approach", in which snapshots of complex (CTD/ **AX**), receptor (CTD), and ligand (**AX**) are obtained from 60 MD trajectories of free ligand diffusion. 400 snapshots were extracted in 1 ns intervals from each trajectory. Additionally, we extracted the conformations that showed the smallest relative distance (ΔD_{min}) between **1** and helix H4 during MD simulations. Prior to the MM-GBSA computations, counter ions and water molecules were stripped from the snapshots.

The computations were performed with the *mm_pbsa.pl* module available in Amber 14[44]. Gas phase energies were computed based on the gaff[46] (**AX**) and ff14SB[49] (CTD) force fields. Polar contributions to solvation free energy were computed at 100 mM ionic strength using Onuvfriev's GB model[57] for a dielectric constant of 1 (solute) and 80 (solvent), together with Parse radii[58]. To avoid introducing additional uncertainty in the calculations, changes in the configurational entropy upon **AX** binding to the CTD were not considered[56,59].

References for supplemental information

1. Supko JG, Hickman RL, Grever MR, Malspeis L. Preclinical pharmacologic evaluation of geldanamycin as an antitumor agent. *Cancer Chemother Pharmacol*. 1995;36(4):305-315.
2. Neckers L, Workman P. Hsp90 molecular chaperone inhibitors: are we there yet? *Clin Cancer Res*. 2012;18(1):64-76.
3. Banerji U, O'Donnell A, Scurr M, et al. Phase I pharmacokinetic and pharmacodynamic study of 17-allylamino, 17-demethoxygeldanamycin in patients with advanced malignancies. *J Clin Oncol*. 2005;23(18):4152-4161.
4. Jhaveri K, Miller K, Rosen L, et al. A phase I dose-escalation trial of trastuzumab and alvespimycin hydrochloride (KOS-1022; 17 DMAG) in the treatment of advanced solid tumors. *Clin Cancer Res*. 2012;18(18):5090-5098.
5. Pacey S, Wilson RH, Walton M, et al. A phase I study of the heat shock protein 90 inhibitor alvespimycin (17-DMAG) given intravenously to patients with advanced solid tumors. *Clin Cancer Res*. 2011;17(6):1561-1570.
6. Arteaga CL. Why is this effective HSP90 inhibitor not being developed in HER2+ breast cancer? *Clin Cancer Res*. 2011;17(15):4919-4921.
7. Wang M, Shen A, Zhang C, et al. Development of Heat Shock Protein (Hsp90) Inhibitors To Combat Resistance to Tyrosine Kinase Inhibitors through Hsp90-Kinase Interactions. *J Med Chem*. 2016;59(12):5563-5586.
8. Oh WK, Galsky MD, Stadler WM, et al. Multicenter phase II trial of the heat shock protein 90 inhibitor, retaspimycin hydrochloride (IPI-504), in patients with castration-resistant prostate cancer. *Urology*. 2011;78(3):626-630.
9. Butler LM, Ferraldeschi R, Armstrong HK, Centenera MM, Workman P. Maximizing the Therapeutic Potential of HSP90 Inhibitors. *Mol Cancer Res*. 2015;13(11):1445-1451.
10. Johnson ML, Yu HA, Hart EM, et al. Phase I/II Study of HSP90 Inhibitor AUY922 and Erlotinib for EGFR-Mutant Lung Cancer With Acquired Resistance to Epidermal Growth Factor Receptor Tyrosine Kinase Inhibitors. *J Clin Oncol*. 2015;33(15):1666-1673.
11. Shapiro GI, Kwak E, Dezube BJ, et al. First-in-human phase I dose escalation study of a second-generation non-ansamycin HSP90 inhibitor, AT13387, in patients with advanced solid tumors. *Clin Cancer Res*. 2015;21(1):87-97.
12. Cardin DB, Thota R, Goff LW, et al. A Phase II Study of Ganetespib as Second-line or Third-line Therapy for Metastatic Pancreatic Cancer. *Am J Clin Oncol*. 2017.
13. Zong H, Gozman A, Caldas-Lopes E, et al. A Hyperactive Signalosome in Acute Myeloid Leukemia Drives Addiction to a Tumor-Specific Hsp90 Species. *Cell Rep*. 2015;13(10):2159-2173.
14. Rajan A, Kelly RJ, Trepel JB, et al. A phase I study of PF-04929113 (SNX-5422), an orally bioavailable heat shock protein 90 inhibitor, in patients with refractory solid tumor malignancies and lymphomas. *Clin Cancer Res*. 2011;17(21):6831-6839.
15. Marcu MG, Schulte TW, Neckers L. Novobiocin and related coumarins and depletion of heat shock protein 90-dependent signaling proteins. *J Natl Cancer Inst*. 2000;92(3):242-248.
16. Kusuma BR, Peterson LB, Zhao H, Vielhauer G, Holzbeierlein J, Blagg BS. Targeting the heat shock protein 90 dimer with dimeric inhibitors. *J Med Chem*. 2011;54(18):6234-6253.

17. Koay YC, Wahyudi H, McAlpine SR. Reinventing Hsp90 Inhibitors: Blocking C-Terminal Binding Events to Hsp90 by Using Dimerized Inhibitors. *Chemistry*. 2016;22(51):18572-18582.
18. Wang Y, McAlpine SR. N-terminal and C-terminal modulation of Hsp90 produce dissimilar phenotypes. *Chem Commun (Camb)*. 2015;51(8):1410-1413.
19. Wang Y, Koay YC, McAlpine SR. How Selective are Hsp90 Inhibitors for Cancer Cells over Normal Cells? *ChemMedChem*. 2017;12(5):353-357.
20. Eskew JD, Sadikot T, Morales P, et al. Development and characterization of a novel C-terminal inhibitor of Hsp90 in androgen dependent and independent prostate cancer cells. *BMC Cancer*. 2011;11:468.
21. Bopp B, Ciglia E, Ouald-Chaib A, Groth G, Gohlke H, Jose J. Design and biological testing of peptidic dimerization inhibitors of human Hsp90 that target the C-terminal domain. *Biochim Biophys Acta*. 2016;1860(6):1043-1055.
22. Ciglia E, Vergin J, Reimann S, et al. Resolving hot spots in the C-terminal dimerization domain that determine the stability of the molecular chaperone Hsp90. *PLoS One*. 2014;9(4):e96031.
23. Seidel SA, Dijkman PM, Lea WA, et al. Microscale thermophoresis quantifies biomolecular interactions under previously challenging conditions. *Methods*. 2013;59(3):301-315.
24. Schuck P. Size-distribution analysis of macromolecules by sedimentation velocity ultracentrifugation and lamm equation modeling. *Biophys J*. 2000;78(3):1606-1619.
25. Hurton T WA, Deubler G, Bashir B, Hayes DB, Laue TM, et al. SEDNTERP http://bitcwiki.sr.unh.edu/index.php/Main_Page 2016.
26. R. G. LeBel DAIG. Density, Viscosity, Refractive Index, and Hygroscopicity of Mixtures of Water and Dimethyl Sulfoxide. *J Chem Eng Data*. 1962;7(1):100–101.
27. Brautigam CA. Calculations and Publication-Quality Illustrations for Analytical Ultracentrifugation Data. *Methods Enzymol*. 2015;562:109-133.
28. Lee CC, Lin TW, Ko TP, Wang AH. The hexameric structures of human heat shock protein 90. *PLoS One*. 2011;6(5):e19961.
29. Nemoto T, Sato N. Oligomeric forms of the 90-kDa heat shock protein. *Biochem J*. 1998;330 (Pt 2):989-995.
30. Minami Y, Kawasaki H, Miyata Y, Suzuki K, Yahara I. Analysis of native forms and isoform compositions of the mouse 90-kDa heat shock protein, HSP90. *J Biol Chem*. 1991;266(16):10099-10103.
31. Krishna P, Reddy RK, Sacco M, Frappier JR, Felsheim RF. Analysis of the native forms of the 90 kDa heat shock protein (hsp90) in plant cytosolic extracts. *Plant Mol Biol*. 1997;33(3):457-466.
32. Lee CC, Lin TW, Ko TP, Wang AHJ. The hexameric structures of human heat shock protein 90. *Plos One*. 2011;6(5).
33. Gohlke H, Hergert U, Meyer T, et al. Binding region of alanopine dehydrogenase predicted by unbiased molecular dynamics simulations of ligand diffusion. *J Chem Inf Model*. 2013;53(10):2493-2498.
34. Frieg B, Häussinger D, Gohlke H. Towards restoring catalytic activity of glutamine synthetase with a clinically relevant mutation. In: Binder K, Müller M, Kremer M, Schnurpfeil A, eds. Proceedings of the NIC Symposium 2016. Jülich; 2016:97-104.
35. Buch I, Giorgino T, De Fabritiis G. Complete reconstruction of an enzyme-inhibitor binding process by molecular dynamics simulations. *Proc Natl Acad Sci U S A*. 2011;108(25):10184-10189.

36. Dror RO, Pan AC, Arlow DH, et al. Pathway and mechanism of drug binding to G-protein-coupled receptors. *Proc Natl Acad Sci U S A*. 2011;108(32):13118-13123.
37. Shan YB, Kim ET, Eastwood MP, Dror RO, Seeliger MA, Shaw DE. How Does a Drug Molecule Find Its Target Binding Site? *J Am Chem Soc*. 2011;133(24):9181-9183.
38. Bernstein FC, Koetzle TF, Williams GJ, et al. The Protein Data Bank. A computer-based archival file for macromolecular structures. *Eur J Biochem*. 1977;80(2):319-324.
39. Schrodinger L. Schrödinger Release 2015-2: Schrödinger Suite 2015-2; Protein Preparation Wizard; Epik version 3.2, Impact version 6.7, Prime version 4.0 *Schrödinger, LLC, New York, NY*. 2015.
40. Schrodinger L. Schrödinger Release 2015-2: Maestro, version 10.2. *Schrödinger, LLC, New York, NY*. 2015.
41. Frisch MJ, Trucks GW, Schlegel HB, et al. Gaussian 09. *Wallingford, CT, USA*. 2009.
42. Martinez L, Andrade R, Birgin EG, Martinez JM. PACKMOL: a package for building initial configurations for molecular dynamics simulations. *J Comput Chem*. 2009;30(13):2157-2164.
43. Jorgensen WL, Chandrasekhar J, Madura JD, Impey RW, Klein ML. Comparison of simple potential functions for simulating liquid water. *J Chem Phys*. 1983;79(2):926-935.
44. Case DA, Babin V, Berryman JT, et al. AMBER 14. *University of California, San Francisco*. 2014.
45. Bayly CI, Cieplak P, Cornell WD, Kollman PA. A well-behaved electrostatic potential based method using charge restraints for deriving atomic charges - the RESP Model. *J Phys Chem*. 1993;97(40):10269-10280.
46. Wang JM, Wolf RM, Caldwell JW, Kollman PA, Case DA. Development and testing of a general amber force field. *J Comput Chem*. 2004;25(9):1157-1174.
47. Diedrich D, Moita AJ, Ruther A, et al. alpha-Aminoxy oligopeptides: synthesis, secondary structure, and cytotoxicity of a new class of anticancer foldamers. *Chem - Eur J*. 2016.
48. Joung IS, Cheatham TE. Determination of alkali and halide monovalent ion parameters for use in explicitly solvated biomolecular simulations. *J Phys Chem B*. 2008;112(30):9020-9041.
49. Maier JA, Martinez C, Kasavajhala K, Wickstrom L, Hauser KE, Simmerling C. ff14SB: Improving the accuracy of protein side chain and backbone parameters from ff99SB. *J Chem Theory Comput*. 2015;11(8):3696-3713.
50. Frieg B, Görg B, Homeyer N, Keitel V, Häussinger D, Gohlke H. Molecular mechanisms of glutamine synthetase mutations that lead to clinically relevant pathologies. *PLoS Comput Biol*. 2016;12(2):e1004693.
51. Darden T, York DM, Pedersen LG. Particle mesh Ewald: An N· log (N) method for Ewald sums in large systems. *J Chem Phys*. 1993;98(12):10089-10092.
52. York DM, Darden TA, Pedersen LG. The effect of long-range electrostatic interactions in simulations of macromolecular crystals - a comparison of the ewald and truncated list methods. *J Chem Phys*. 1993;99(10):8345-8348.
53. Ryckaert JP, Ciccotti G, Berendsen HJC. Numerical integration of cartesian equations of motion of a system with constraints molecular dynamics of n-alkanes. *J Comput Phys*. 1977;23(3):327-341.
54. Salomon-Ferrer R, Gotz AW, Poole D, Le Grand S, Walker RC. Routine microsecond molecular dynamics simulations with Amber on GPUs. 2. Explicit solvent particle mesh ewald. *J Chem Theory Comput*. 2013;9(9):3878-3888.

55. Roe DR, Cheatham TE. PTRAJ and CPPTRAJ: software for processing and analysis of molecular dynamics trajectory data. *J Chem Theory Comput*. 2013;9(7):3084-3095.
56. Gohlke H, Case DA. Converging free energy estimates: MM-PB(GB)SA studies on the protein-protein complex Ras-Raf. *J Comput Chem*. 2004;25(2):238-250.
57. Onufriev A, Bashford D, Case DA. Exploring protein native states and large-scale conformational changes with a modified generalized born model. *Proteins: Struct, Funct, Bioinf*. 2004;55(2):383-394.
58. Sitkoff D, Sharp KA, Honig B. Accurate Calculation of Hydration Free-Energies Using Macroscopic Solvent Models. *J Phys Chem*. 1994;98(7):1978-1988.
59. Hou T, Wang J, Li Y, Wang W. Assessing the performance of the MM/PBSA and MM/GBSA methods. 1. The accuracy of binding free energy calculations based on molecular dynamics simulations. *J Chem Inf Model*. 2011;51(1):69-82.

12. CURRICULUM VITAE

Professional and scientific career

07.17 – present

Scientist at the Forschungszentrum Jülich GmbH at the Jülich Supercomputing Centre (JSC), Institute for Complex Systems - Structural Biochemistry (ICS-6), and John von Neumann, Institute for Computing (NIC).

- Investigation of protein-ligand, protein-peptide, protein-protein, and protein-DNA interactions,
- Identification and design of protein-ligand and protein-protein interaction modulators,
- Determination of the molecular mechanisms of enzyme regulation and deactivation for soluble and transmembrane systems,
- Fragment-based lead discovery,
- Proposal writing,
- Mentoring of junior Ph.D. students, master students, and technical assistants,
- System admin for group-internal computing resources (incl. HPC environment) for Linux and Windows systems.

11.13 – 06.17

Ph.D. student at the Institute for Pharmaceutical und Medicinal Chemistry, Heinrich Heine University Düsseldorf in the research group of Prof. Dr. Holger Gohlke.

- Determining the molecular mechanisms of enzyme regulation and deactivation,
- Investigate the determinants of protein-ligand, protein-peptide, and protein-protein interactions,
- Teaching of pharmaceutical chemistry including lectures and practical laboratory work,
- Assistance in proposal writing,
- Supervision of master students and technical assistants,
- System admin substitute for group-internal computing resources for Linux and Windows systems.

11.14 – 03.17

Professional experience as pharmacist at the Neue Apotheke in der Kö
Galerie, Düsseldorf.

- Advice and care for patients, customers, and physicians.

04.14

License to practice pharmacy (Approbation).

05.13 – 10.13

Trainee pharmacist in the research group of Prof. Dr. Holger Gohlke at the Institute for Pharmaceutical und Medicinal Chemistry, Heinrich Heine University Düsseldorf.

11.12 – 04.13

Trainee pharmacist at the Sebastianus Apotheke, Neuss.

10.08 – 10.12	Pharmacy studies at Heinrich Heine University Düsseldorf, Düsseldorf.

Skills

Scientific computing	Computational chemistry/biology software packages AMBER, Schrödinger Maestro®, OpenEye Scientific, MOE, VMD, Glide, AutoDock (**very good**) ▪ Molecular dynamics simulations/enhanced sampling methods ▪ Free energy calculations ▪ Molecular docking, and virtual screening in drug discovery ▪ Fragment-based drug discovery Experience in usage of high-performance computing resources (**very good**) ▪ JUROPA, JURECA, and JUWELS at the Forschungszentrum Jülich GmbH ▪ HILBERT, and CPCSRV at the Heinrich Heine University Düsseldorf Linux system admin (incl. HPC environment) (**good**) Scientific programming using Python, Bash, and R (**good**) Machine learning and data science toolkits, e.g. RDKit, scikit-learn, and tensorflow (**basic knowledge**) GPU programming using C++ and openACC (**basic knowledge**) General computing MS office (**very good**) Inkscape (**very good**) Gimp (**good**)
Languages	German, written and spoken (**native language**) English, written and spoken (**fluent**)
Additional soft skills	Leadership qualifications (iGRAD Workshop) Writing a research paper (iGRAD Workshop)

Scientific successes

Recent publications

Porta, Schumacher, Frieg, *et al.*: Small-molecule inhibitors of nisin resistance protein NSR from the human pathogen *Streptococcus agalactiae*.
submitted (2019)

Krater, Frieg, *et al.*: Partially inserted nascent chain unzips the lateral gate of the translocon.
submitted (2019)

Frieg, *et al.*: Mechanism of fully-reversible, pH-sensitive inhibition of human glutamine synthetase by tyrosine nitration.
submitted (2019)

Kondapuram, […], Frieg, *et al.*: Opposing subunits interact to stabilize the closed state in HCN2 channels.
Biophys. J., 2019, 116(3), 108a

Bhatia, Diedrich, Frieg, *et al.*: Targeting HSP90's C-terminus is effective in Imatinib resistant CML and lacks heat shock response induction.
Blood, 2018, 132, 307-320.

Kroeger, Frieg, *et al.*: EDTA aggregates induce SYPRO Orange-based fluorescence in thermal shift assay.
PLoS ONE, 2017, 12, e0177024

Krieger, […], Frieg, *et al.*: α-Aminoxy peptoids: a unique peptoid backbone with a preference for cis-amide bonds.
Chem. Eur. J., 2017, 23, 3699-3707

(Please, find a full list of all publications here.)

Oral presentations

Mechanism of fully-reversible, pH-sensitive inhibition of human glutamine synthetase by tyrosine nitration.
33rd Molecular Modelling Workshop, Erlangen, 2019.

- **1st Lecture award**
  (Speaker slot at the Young Modellers Forum in London, organized by the MGMS-UK.)

Molecular mechanisms of human glutamine synthetase deactivation.
SFB 974 Retreat, Trier, 2017.

Determining the molecular consequences of clinically relevant glutamine synthetase mutations.
Annual meeting of GASL, Düsseldorf, 2016.

Poster presentations

Molecular determinants of glutamine synthetase deactivation by tyrosine nitration
NIC Symposium, Jülich, 2018.

Molecular determinants of glutamine synthetase deactivation by tyrosine nitration
DeLIVER Symposium, Düsseldorf, 2017.

Consequences of clinically relevant glutamine synthetase mutations at the atomic level.
NIC Symposium, Jülich, 2016.

Determining the molecular consequences of clinically relevant glutamine synthetase mutations.
Annual meeting of GASL, Düsseldorf, 2016.

Grants and funding

05.17 – present
Computing time grant on JURECA and JUWELS, Jülich Supercomputing Centre. (Project ID: HDD17)
"*Disinhibition and inhibition of HCN2 channel function by ligand binding to the cyclic nucleotide binding domain*".

05.14 – 04.17
Computing time grant on JURECA/JUROPA, Jülich Supercomputing Centre (Project ID: HDD13)
"*Molecular mechanisms of human glutamine synthetase regulation and deactivation*".

05.13 – 10.13
Research fellowship funded by the NRW Researchschool "*BioStruct - Biological structures in molecular medicine and biotechnology*".

Associated research communities

04.17. – present
Research associate of the Research Unit 2518
"*Functional dynamics of ion channels and transporters - DynIon*".

11.13 – present
Research associate of the Collaborative Research Center SFB 974
"*Liver damage and regeneration*".

05.13 – 10.13
Research fellow of the NRW Researchschool
"*BioStruct - Biological structures in molecular medicine and biotechnology*".

13. REFERENCES

1. Du, X. et al. Insights into protein-ligand interactions: mechanisms, models, and methods. *International Journal of Molecular Sciences* **17**(2016).
2. Fischer, E. Einfluss der Configuration auf die Wirkung der Enzyme. *Berichte der Deutschen Chemischen Gesellschaft* **27**, 2985-2993 (1894).
3. Koshland, D.E. Application of a theory of enzyme specificity to protein synthesis. *Proceedings of the National Academy of Sciences of the United States of America* **44**, 98-104 (1958).
4. Ma, B.Y., Kumar, S., Tsai, C.J. & Nussinov, R. Folding funnels and binding mechanisms. *Protein Engineering* **12**, 713-720 (1999).
5. Tobi, D. & Bahar, I. Structural changes involved in protein binding correlate with intrinsic motions of proteins in the unbound state. *Proceedings of the National Academy of Sciences of the United States of America* **102**, 18908-18913 (2005).
6. Tsai, C.J., Kumar, S., Ma, B.Y. & Nussinov, R. Folding funnels, binding funnels, and protein function. *Protein Science* **8**, 1181-1190 (1999).
7. Csermely, P., Palotai, R. & Nussinov, R. Induced fit, conformational selection and independent dynamic segments: an extended view of binding events. *Trends in Biochemical Sciences* **35**, 539-546 (2010).
8. Grünberg, R., Leckner, J. & Nilges, M. Complementarity of structure ensembles in protein-protein binding. *Structure* **12**, 2125-2136 (2004).
9. Wlodarski, T. & Zagrovic, B. Conformational selection and induced fit mechanism underlie specificity in noncovalent interactions with ubiquitin. *Proceedings of the National Academy of Sciences of the United States of America* **106**, 19346-19351 (2009).
10. Klebe, G. Applying thermodynamic profiling in lead finding and optimization. *Nature Reviews Drug Discovery* **14**, 95-110 (2015).
11. Baker, B.M. & Murphy, K.P. Evaluation of linked protonation effects in protein binding reactions using isothermal titration calorimetry. *Biophysical Journal* **71**, 2049-2055 (1996).
12. Perozzo, R., Folkers, G. & Scapozza, L. Thermodynamics of protein-ligand interactions: History, presence, and future aspects. *Journal of Receptor and Signal Transduction Research* **24**, 1-52 (2004).
13. Dror, R.O., Dirks, R.M., Grossman, J.P., Xu, H.F. & Shaw, D.E. Biomolecular simulation: a computational microscope for molecular biology. *Annual Review of Biophysics* **41**, 429-452 (2012).
14. Bottaro, S. & Lindorff-Larsen, K. Biophysical experiments and biomolecular simulations: A perfect match? *Science* **361**, 355-360 (2018).
15. De Vivo, M., Masetti, M., Bottegoni, G. & Cavalli, A. Role of molecular dynamics and related methods in drug discovery. *Journal of Medicinal Chemistry* **59**, 4035-4061 (2016).
16. Häberle, J. et al. Brief report - Congenital glutamine deficiency with glutamine synthetase mutations. *New England Journal of Medicine* **353**, 1926-1933 (2005).
17. Häberle, J. et al. Inborn error of amino acid synthesis: human glutamine synthetase deficiency. *Journal of Inherited Metabolic Disease* **29**, 352-358 (2006).
18. Häberle, J. et al. Glutamine supplementation in a child with inherited GS deficiency improves the clinical status and partially corrects the peripheral and central amino acid imbalance. *Orphanet Journal of Rare Diseases* **7**, 1-10 (2012).
19. Spodenkiewicz, M., Diez-Fernandez, C., Rufenacht, V., Gemperle-Britschgi, C. & Häberle, J. Minireview on glutamine synthetase deficiency, an ultra-rare inborn error of amino acid biosynthesis. *Biology (Basel)* **5**(2016).
20. Görg, B., Wettstein, M., Metzger, S., Schliess, F. & Häussinger, D. Lipopolysaccharide-induced tyrosine nitration and inactivation of hepatic glutamine synthetase in the rat. *Hepatology* **41**, 1065-1073 (2005).
21. Görg, B. et al. Benzodiazepine-induced protein tyrosine nitration in rat astrocytes. *Hepatology* **37**, 334-342 (2003).
22. Görg, B. et al. Inflammatory cytokines induce protein tyrosine nitration in rat astrocytes. *Archives of Biochemistry and Biophysics* **449**, 104-114 (2006).
23. Khosa, S., AlKhatib, Z. & Smits, S.H.J. NSR from Streptococcus agalactiae confers resistance against nisin and is encoded by a conserved nsr operon. *Biological Chemistry* **394**, 1543-1549 (2013).
24. Khosa, S., Lagedroste, M. & Smits, S.H.J. Protein defense systems against the lantibiotic nisin: function of the immunity protein NisI and the resistance protein NSR. *Frontiers in Microbiology* **7**, 504 (2016).
25. Krajewski, W.W. et al. Crystal structures of mammalian glutamine synthetases illustrate substrate-induced conformational changes and provide opportunities for drug and herbicide design. *Journal of Molecular Biology* **375**, 217-28 (2008).

26. Shapiro, B.M. & Ginsburg, A. Effects of specific divalent cations on some physical and chemical properties of glutamine synthetase from Escherichia coli. Taut and relaxed enzyme forms. *Biochemistry* **7**, 2153-67 (1968).
27. Hsu, S.T. et al. The nisin-lipid II complex reveals a pyrophosphate cage that provides a blueprint for novel antibiotics. *Nature Structural & Molecular Biology* **11**, 963-7 (2004).
28. Khosa, S. et al. Structural basis of lantibiotic recognition by the nisin resistance protein from Streptococcus agalactiae. *Scientific Reports* **6**, 18679 (2016).
29. Ali, M.M.U. et al. Crystal structure of an Hsp90-nucleotide-p23/Sba1 closed chaperone complex. *Nature* **440**, 1013-1017 (2006).
30. Goodsell, D.S. *The machinery of life*, (Springer Science & Business Media, 2009).
31. Pan, A.C., Borhani, D.W., Dror, R.O. & Shaw, D.E. Molecular determinants of drug-receptor binding kinetics. *Drug Discovery Today* **18**, 667-673 (2013).
32. Sharp, K.A. Statistical thermodynamics of binding and molecular recognition models. in *Protein-Ligand Interactions*, Vol. 3 (ed. Gohlke, H.) (Wiley-VCH Verlag GmbH & Co. KGaA, Weinheim, 2012).
33. General, I.J. A note on the standard state's binding free energy. *Journal of Chemical Theory and Computation* **6**, 2520-2524 (2010).
34. Baron, R. & McCammon, J.A. Molecular recognition and ligand association. *Annual Review of Physical Chemistry* **64**, 151-175 (2013).
35. Amaro, R.E. & Mulholland, A.J. Multiscale methods in drug design bridge chemical and biological complexity in the search for cures. *Nature Reviews Chemistry* **2**(2018).
36. Kmiecik, S. et al. Coarse-grained protein models and their applications. *Chemical Reviews* **116**, 7898-7936 (2016).
37. Huggins, D.J. et al. Biomolecular simulations: From dynamics and mechanisms to computational assays of biological activity. *Wiley Interdisciplinary Reviews: Computational Molecular Science*, e1393 (2018).
38. Fanning, S.W. et al. Estrogen receptor alpha somatic mutations Y537S and D538G confer breast cancer endocrine resistance by stabilizing the activating function-2 binding conformation. *Elife* **5**(2016).
39. Toy, W. et al. ESR1 ligand-binding domain mutations in hormone-resistant breast cancer. *Nature Genetics* **45**, 1439-U189 (2013).
40. Feig, M. et al. Complete atomistic model of a bacterial cytoplasm for integrating physics, biochemistry, and systems biology. *Journal of Molecular Graphics & Modelling* **58**, 1-9 (2015).
41. Yu, I. et al. Biomolecular interactions modulate macromolecular structure and dynamics in atomistic model of a bacterial cytoplasm. *Elife* **5**(2016).
42. Leach, A.R. *Molecular modelling: principles and applications*, (Pearson education, 2001).
43. Hopkins, C.W., Le Grand, S., Walker, R.C. & Roitberg, A.E. Long-time-step molecular dynamics through hydrogen mass repartitioning. *Journal of Chemical Theory and Computation* **11**, 1864-1874 (2015).
44. Friedman, R., Boye, K. & Flatmark, K. Molecular modelling and simulations in cancer research. *Biochimica et Biophysica Acta, Reviews on Cancer* **1836**, 1-14 (2013).
45. Cornell, W.D. et al. A second generation force field for the simulation of proteins, nucleic acids, and organic molecules. *Journal of the American Chemical Society* **117**, 5179–5197 (1995).
46. Wang, J.M., Cieplak, P. & Kollman, P.A. How well does a restrained electrostatic potential (RESP) model perform in calculating conformational energies of organic and biological molecules? *Journal of Computational Chemistry* **21**, 1049-1074 (2000).
47. Hornak, V. et al. Comparison of multiple Amber force fields and development of improved protein backbone parameters. *Proteins: Structure, Function, and Bioinformatics* **65**, 712-725 (2006).
48. Maier, J.A. et al. ff14SB: Improving the accuracy of protein side chain and backbone parameters from ff99SB. *Journal of Chemical Theory and Computation* **11**, 3696-3713 (2015).
49. Zgarbova, M. et al. Refinement of the Cornell et al. nucleic acids force field based on reference quantum chemical calculations of glycosidic torsion profiles. *Journal of Chemical Theory and Computation* **7**, 2886-2902 (2011).
50. Ivani, I. et al. Parmbsc1: a refined force field for DNA simulations. *Nature Methods* **13**, 55-+ (2016).
51. Dickson, C.J. et al. Lipid14: The Amber lipid force field. *Journal of Chemical Theory and Computation* **10**, 865-879 (2014).
52. Pastor, R.W. & MacKerell, A.D. Development of the CHARMM force field for lipids. *Journal of Physical Chemistry Letters* **2**, 1526-1532 (2011).
53. Kirschner, K.N. et al. GLYCAM06: a generalizable biomolecular force field. Carbohydrates. *Journal of Computational Chemistry* **29**, 622-655 (2008).

54. Wang, J.M., Wolf, R.M., Caldwell, J.W., Kollman, P.A. & Case, D.A. Development and testing of a general amber force field. *Journal of Computational Chemistry* **25**, 1157-1174 (2004).
55. Rosenbaum, D.M. et al. Structure and function of an irreversible agonist-beta(2) adrenoceptor complex. *Nature* **469**, 236-240 (2011).
56. Nygaard, R. et al. The dynamic process of beta(2)-adrenergic receptor activation. *Cell* **152**, 532-542 (2013).
57. Piana, S., Lindorff-Larsen, K. & Shaw, D.E. Atomic-level description of ubiquitin folding. *Proceedings of the National Academy of Sciences of the United States of America* **110**, 5915-20 (2013).
58. Shaw, D.E. et al. Atomic-Level characterization of the structural dynamics of proteins. *Science* **330**, 341-346 (2010).
59. Snow, C.D., Nguyen, N., Pande, V.S. & Gruebele, M. Absolute comparison of simulated and experimental protein-folding dynamics. *Nature* **420**, 102-106 (2002).
60. Shan, Y.B. et al. How does a drug molecule find its target binding site? *Journal of the American Chemical Society* **133**, 9181-9183 (2011).
61. Buch, I., Giorgino, T. & De Fabritiis, G. Complete reconstruction of an enzyme-inhibitor binding process by molecular dynamics simulations. *Proceedings of the National Academy of Sciences of the United States of America* **108**, 10184-10189 (2011).
62. Shaw, D.E. et al. Anton, a special-purpose machine for molecular dynamics simulation. *Communications of the Acm* **51**, 91-97 (2008).
63. Shaw, D.E. et al. Millisecond-scale molecular dynamics simulations on Anton. *Proceedings of the Conference on High Performance Computing Networking, Storage and Analysis* (2009).
64. Shaw, D.E. et al. Atomic-level characterization of the structural dynamics of proteins. *Science* **330**, 341-6 (2010).
65. Shan, Y.B. et al. Oncogenic mutations counteract intrinsic disorder in the EGFR kinase and promote receptor dimerization. *Cell* **149**, 860-870 (2012).
66. Dror, R.O. et al. Pathway and mechanism of drug binding to G-protein-coupled receptors. *Proceedings of the National Academy of Sciences of the United States of America* **108**, 13118-13123 (2011).
67. Bowman, G.R., Pande, V.S. & Noé, F. *An introduction to Markov state models and their application to long timescale molecular simulation*, (Springer Science & Business Media, 2013).
68. Chodera, J.D. & Noé, F. Markov state models of biomolecular conformational dynamics. *Current Opinion in Structural Biology* **25**, 135-144 (2014).
69. Pang, X. & Zhou, H.X. Rate constants and mechanisms of protein-ligand binding. *Annual Review of Biophysics* **46**, 105-130 (2017).
70. Plattner, N. & Noé, F. Protein conformational plasticity and complex ligand-binding kinetics explored by atomistic simulations and Markov models. *Nature Communications* **6**(2015).
71. Plattner, N., Doerr, S., De Fabritiis, G. & Noé, F. Complete protein–protein association kinetics in atomic detail revealed by molecular dynamics simulations and Markov modelling. *Nature Chemistry* **9**, 1005–1011 (2017).
72. Decherchi, S., Berteotti, A., Bottegoni, G., Rocchia, W. & Cavalli, A. The ligand binding mechanism to purine nucleoside phosphorylase elucidated via molecular dynamics and machine learning. *Nature Communications* **6**(2015).
73. Dror, R.O. et al. Structural basis for modulation of a G protein-coupled receptor by allosteric drugs. *Nature* **503**, 295-+ (2013).
74. Kruse, A.C. et al. Activation and allosteric modulation of a muscarinic acetylcholine receptor. *Nature* **504**, 101-+ (2013).
75. Bowman, G.R., Bolin, E.R., Hart, K.M., Maguire, B.C. & Marqusee, S. Discovery of multiple hidden allosteric sites by combining Markov state models and experiments. *Proceedings of the National Academy of Sciences of the United States of America* **112**, 2734-2739 (2015).
76. Schames, J.R. et al. Discovery of a novel binding trench in HIV integrase. *Journal of Medicinal Chemistry* **47**, 1879-1881 (2004).
77. Summa, V. et al. Discovery of Raltegravir, a potent, selective orally bioavailable HIV-integrase inhibitor for the treatment of HIV-AIDS infection. *Journal of Medicinal Chemistry* **51**, 5843-5855 (2008).
78. Latorraca, N.R., Venkatakrishnan, A.J. & Dror, R.O. GPCR dynamics: structures in motion. *Chemical Reviews* **117**, 139-155 (2017).
79. Rasmussen, S.G.F. et al. Crystal structure of the human beta(2) adrenergic G-protein-coupled receptor. *Nature* **450**, 383-U4 (2007).
80. Rasmussen, S.G.F. et al. Crystal structure of the beta(2) adrenergic receptor-Gs protein complex. *Nature* **477**, 549-U311 (2011).

81. Rasmussen, S.G.F. et al. Structure of a nanobody-stabilized active state of the beta(2) adrenoceptor. *Nature* **469**, 175-180 (2011).
82. Cherezov, V. et al. High-resolution crystal structure of an engineered human beta(2)-adrenergic G protein-coupled receptor. *Science* **318**, 1258-1265 (2007).
83. Rosenbaum, D.M. et al. GPCR engineering yields high-resolution structural insights into beta(2)-adrenergic receptor function. *Science* **318**, 1266-1273 (2007).
84. Dror, R.O. et al. Activation mechanism of the beta(2)-adrenergic receptor. *Proceedings of the National Academy of Sciences of the United States of America* **108**, 18684-18689 (2011).
85. Dawaliby, R. et al. Allosteric regulation of G protein-coupled receptor activity by phospholipids. *Nature Chemical Biology* **12**, 35-+ (2016).
86. Neale, C., Herce, H.D., Pomes, R. & Garcia, A.E. Can specific protein-lipid interactions stabilize an active state of the beta 2 adrenergic receptor? *Biophysical Journal* **109**, 1652-1662 (2015).
87. Dror, R.O. et al. Structural basis for nucleotide exchange in heterotrimeric G proteins. *Science* **348**, 1361-1365 (2015).
88. Ihle, N.T. et al. Effect of KRAS oncogene substitutions on protein behavior: implications for signaling and clinical Outcome. *Journal of the National Cancer Institute* **104**, 228-239 (2012).
89. Pan, A.C., Xu, H.F., Palpant, T. & Shaw, D.E. Quantitative characterization of the binding and unbinding of millimolar drug fragments with molecular dynamics simulations. *Journal of Chemical Theory and Computation* **13**, 3372-3377 (2017).
90. Mobley, D.L. & Gilson, M.K. Predicting binding free energies: frontiers and benchmarks. *Annual Review of Biophysics* **46**, 531-558 (2017).
91. Aleksandrov, A., Thompson, D. & Simonson, T. Alchemical free energy simulations for biological complexes: powerful but temperamental... *Journal of Molecular Recognition* **23**, 117-127 (2010).
92. Chodera, J.D. et al. Alchemical free energy methods for drug discovery: progress and challenges. *Current Opinion in Structural Biology* **21**, 150-160 (2011).
93. Chipot, C. & Pohorille, A. Calculating free energy differences using perturbation theory. in *Free energy calculations* (eds. Chipot, C. & Pohorille, A.) 33-75 (2007).
94. Cournia, Z., Allen, B. & Sherman, W. Relative binding free energy calculations in drug discovery: recent advances and practical considerations. *Journal of Chemical Information and Modeling* **57**, 2911-2937 (2017).
95. Persch, E., Dumele, O. & Diederich, F. Molecular recognition in chemical and biological systems. *Angewandte Chemie-International Edition* **54**, 3290-3327 (2015).
96. Steinbrecher, T. & Labahn, A. Towards accurate free energy calculations in ligand protein-binding studies. *Current Medicinal Chemistry* **17**, 767-785 (2010).
97. Pohorille, A., Jarzynski, C. & Chipot, C. Good practices in free-energy calculations. *Journal of Physical Chemistry B* **114**, 10235-10253 (2010).
98. Shirts, M.R. Best practices in free energy calculations for drug design. *Computational Drug Discovery and Design* **819**, 425-467 (2012).
99. Jorgensen, W.L. & Thomas, L.L. Perspective on free-energy perturbation calculations for chemical equilibria. *Journal of Chemical Theory and Computation* **4**, 869-876 (2008).
100. Zwanzig, R.W. High temperature equation of state by a perturbation method. 1. Nonpolar gases. *Journal of Chemical Physics* **22**, 1420-1426 (1954).
101. Kirkwood, J.G. Statistical mechanics of fluid mixtures. *Journal of Chemical Physics* **3**, 300-313 (1935).
102. Michel, J. & Essex, J.W. Prediction of protein-ligand binding affinity by free energy simulations: assumptions, pitfalls and expectations. *Journal of Computer-Aided Molecular Design* **24**, 639-658 (2010).
103. Gutierrez-de-Teran, H. & Aqvist, J. Linear interaction energy: method and applications in drug design. *Methods in Molecular Biology* **819**, 305-23 (2012).
104. Jorgensen, W.L. & Ravimohan, C. Monte-carlo simulation of differences in free-energies of hydration. *Journal of Chemical Physics* **83**, 3050-3054 (1985).
105. Abel, R., Wang, L.L., Mobley, D.L. & Friesner, R.A. A critical review of validation, blind testing, and real-world use of alchemical protein-ligand binding free energy calculations. *Current Topics in Medicinal Chemistry* **17**, 2577-2585 (2017).
106. Wong, C.F. & McCammon, J.A. Dynamics and design of enzymes and inhibitors. *Journal of the American Chemical Society* **108**, 3830-3832 (1986).
107. Mobley, D.L. et al. Predicting absolute ligand binding free energies to a simple model site. *Journal of Molecular Biology* **371**, 1118-1134 (2007).
108. Boyce, S.E. et al. Predicting ligand binding affinity with alchemical free energy methods in a polar model ninding site. *Journal of Molecular Biology* **394**, 747-763 (2009).

109. Abel, R. et al. Accelerating drug discovery through tight integration of expert molecular design and predictive scoring. *Current Opinion in Structural Biology* **43**, 38-44 (2017).
110. Mey, A.S.J.S., Juarez-Jimenez, J., Hennessy, A. & Michel, J. Blinded predictions of binding modes and energies of HSP90-alpha ligands for the 2015 D3R grand challenge. *Bioorganic & Medicinal Chemistry* **24**, 4890-4899 (2016).
111. Rombouts, F.J.R. et al. Pyrido[4,3-e][1,2,4]triazolo[4,3-a]pyrazines as selective, brain penetrant phosphodiesterase 2 (PDE2) inhibitors. *ACS Medicinal Chemistry Letters* **6**, 282-286 (2015).
112. Ciordia, M., Perez-Benito, L., Delgado, F., Trabanco, A.A. & Tresadern, G. Application of free energy perturbation for the design of BACE1 inhibitors. *Journal of Chemical Information and Modeling* **56**, 1856-1871 (2016).
113. Keränen, H. et al. Acylguanidine beta secretase 1 inhibitors: a combined experimental and free energy perturbation study. *Journal of Chemical Theory and Computation* **13**, 1439-1453 (2017).
114. Kuhn, B. et al. Prospective evaluation of free energy calculations for the prioritization of cathepsin L inhibitors. *Journal of Medicinal Chemistry* **60**, 2485-2497 (2017).
115. Wang, L. et al. Accurate and reliable prediction of relative ligand binding potency in prospective drug discovery by way of a modern free-energy calculation protocol and force field. *Journal of the American Chemical Society* **137**, 2695-2703 (2015).
116. Homeyer, N. & Gohlke, H. Extension of the free energy workflow FEW towards implicit solvent/implicit membrane MM-PBSA calculations. *Biochimica et Biophysica Acta, General Subjects* **1850**, 972-982 (2015).
117. Homeyer, N. & Gohlke, H. FEW: A workflow tool for free energy calculations of ligand binding. *Journal of Computational Chemistry* **34**, 965-973 (2013).
118. Deupi, X. & Kobilka, B.K. Energy landscapes as a tool to integrate GPCR structure, dynamics, and function. *Physiology* **25**, 293-303 (2010).
119. Doudou, S., Burton, N.A. & Henchman, R.H. Standard free energy of binding from a one-dimensional potential of mean force. *Journal of Chemical Theory and Computation* **5**, 909-918 (2009).
120. Woo, H.J. & Roux, B. Calculation of absolute protein-ligand binding free energy from computer simulations. *Proceedings of the National Academy of Sciences of the United States of America* **102**, 6825-6830 (2005).
121. Torrie, G.M. & Valleau, J.P. Non-physical sampling distributions in Monte-Carlo free energy estimation - umbrella sampling. *Journal of Computational Physics* **23**, 187-199 (1977).
122. Jarzynski, C. Nonequilibrium equality for free energy differences. *Physical Review Letters* **78**, 2690-2693 (1997).
123. Park, S. & Schulten, K. Calculating potentials of mean force from steered molecular dynamics simulations. *Journal of Chemical Physics* **120**, 5946-5961 (2004).
124. Kästner, J. Umbrella sampling. *Wiley Interdisciplinary Reviews-Computational Molecular Science* **1**, 932-942 (2011).
125. Kumar, S., Bouzida, D., Swendsen, R.H., Kollman, P.A. & Rosenberg, J.M. The weighted histogram analysis method for free-energy calculations on biomolecules. 1. The method. *Journal of Computational Chemistry* **13**, 1011-1021 (1992).
126. Kästner, J. & Thiel, W. Bridging the gap between thermodynamic integration and umbrella sampling provides a novel analysis method: "Umbrella integration". *Journal of Chemical Physics* **123**, 144104 (2005).
127. Isralewitz, B., Gao, M. & Schulten, K. Steered molecular dynamics and mechanical functions of proteins. *Current Opinion in Structural Biology* **11**, 224-230 (2001).
128. Park, S., Khalili-Araghi, F., Tajkhorshid, E. & Schulten, K. Free energy calculation from steered molecular dynamics simulations using Jarzynski's equality. *Journal of Chemical Physics* **119**, 3559-3566 (2003).
129. Bastug, T., Chen, P.C., Patra, S.M. & Kuyucak, S. Potential of mean force calculations of ligand binding to ion channels from Jarzynski's equality and umbrella sampling. *Journal of Chemical Physics* **128**(2008).
130. Allen, T.W., Andersen, O.S. & Roux, B. Energetics of ion conduction through the gramicidin channel. *Proceedings of the National Academy of Sciences of the United States of America* **101**, 117-122 (2004).
131. Allen, T.W., Andersen, O.S. & Roux, B. Molecular dynamics - potential of mean force calculations as a tool for understanding ion permeation and selectivity in narrow channels. *Biophysical Chemistry* **124**, 251-267 (2006).
132. Berneche, S. & Roux, B. Energetics of ion conduction through the K+ channel. *Nature* **414**, 73-77 (2001).
133. Berneche, S. & Roux, B. A microscopic view of ion conduction through the K+ channel. *Proceedings of the National Academy of Sciences of the United States of America* **100**, 8644-8648 (2003).

134. Corry, B. & Thomas, M. Mechanism of ion permeation and selectivity in a voltage gated sodium channel. *Journal of the American Chemical Society* **134**, 1840-1846 (2012).
135. Pongprayoon, P., Beckstein, O., Wee, C.L. & Sansom, M.S.P. Simulations of anion transport through OprP reveal the molecular basis for high affinity and selectivity for phosphate. *Proceedings of the National Academy of Sciences of the United States of America* **106**, 21614-21618 (2009).
136. Sun, H.Y. et al. Revealing the favorable dissociation pathway of type II kinase inhibitors via enhanced sampling simulations and two-end-state calculations. *Scientific Reports* **5**(2015).
137. Colizzi, F., Perozzo, R., Scapozza, L., Recanatini, M. & Cavalli, A. Single-molecule pulling simulations can discern active from inactive enzyme inhibitors. *Journal of the American Chemical Society* **132**, 7361-7371 (2010).
138. Patel, J.S., Berteotti, A., Ronsisvalle, S., Rocchia, W. & Cavalli, A. Steered molecular dynamics simulations for studying protein-ligand interaction in cyclin-dependent kinase 5. *Journal of Chemical Information and Modeling* **54**, 470-480 (2014).
139. Mai, B.K., Viet, M.H. & Li, M.S. Top leads for swine influenza A/H1N1 virus revealed by steered molecular dynamics approach. *Journal of Chemical Information and Modeling* **50**, 2236-2247 (2010).
140. Palermo, G. et al. An optimized polyamine moiety boosts the potency of human type II topoisomerase poisons as quantified by comparative analysis centered on the clinical candidate F14512. *Chemical Communications* **51**, 14310-14313 (2015).
141. Ge, X.X. & Roux, B. Absolute binding free energy calculations of sparsomycin analogs to the bacterial ribosome. *Journal of Physical Chemistry B* **114**, 9525-9539 (2010).
142. Lee, M.S. & Olson, M.A. Calculation of absolute protein-ligand binding affinity using path and endpoint approaches. *Biophysical Journal* **90**, 864-877 (2006).
143. Wojtas-Niziurski, W., Meng, Y.L., Roux, B. & Berneche, S. Self-learning adaptive umbrella sampling method for the determination of free energy landscapes in multiple dimensions. *Journal of Chemical Theory and Computation* **9**, 1885-1895 (2013).
144. Homeyer, N. & Gohlke, H. Free energy calculations by the molecular mechanics Poisson-Boltzmann surface area method. *Molecular Informatics* **31**, 114-122 (2012).
145. Aqvist, J., Medina, C. & Samuelsson, J.E. A new method for predicting binding affinity in computer-aided drug design. *Protein Engineering* **7**, 385-91 (1994).
146. Genheden, S. & Ryde, U. The MM/PBSA and MM/GBSA methods to estimate ligand-binding affinities. *Expert Opinion on Drug Discovery* **10**, 449-461 (2015).
147. Srinivasan, J., Cheatham, I., T. E., Cieplak, P., Kollman, P.A. & Case, D.A. Continuum solvent studies of the stability of DNA, RNA, and phosphoramidate - DNA helices. *Journal of the American Chemical Society* **120**, 9401-9409 (1998).
148. Hou, T., Wang, J., Li, Y. & Wang, W. Assessing the performance of the MM/PBSA and MM/GBSA methods. 1. The accuracy of binding free energy calculations based on molecular dynamics simulations. *Journal of Chemical Information and Modeling* **51**, 69-82 (2011).
149. Hou, T.J., Wang, J.M., Li, Y.Y. & Wang, W. Assessing the performance of the molecular mechanics/Poisson Boltzmann surface area and molecular mechanics/generalized Born surface area methods. II. The accuracy of ranking poses generated from docking. *Journal of Computational Chemistry* **32**, 866-877 (2011).
150. Xu, L., Sun, H., Li, Y., Wang, J. & Hou, T. Assessing the performance of MM/PBSA and MM/GBSA methods. 3. The impact of force fields and ligand charge models. *Journal of Physical Chemistry B* **117**, 8408-21 (2013).
151. Sun, H.Y., Li, Y.Y., Tian, S., Xu, L. & Hou, T.J. Assessing the performance of MM/PBSA and MM/GBSA methods. 4. Accuracies of MM/PBSA and MM/GBSA methodologies evaluated by various simulation protocols using PDBbind data set. *Physical Chemistry Chemical Physics* **16**, 16719-16729 (2014).
152. Gohlke, H., Kiel, C. & Case, D.A. Insights into protein-protein binding by binding free energy calculation and free energy decomposition for the Ras-Raf and Ras-RaIGDS complexes. *Journal of Molecular Biology* **330**, 891-913 (2003).
153. Adler, M. & Beroza, P. Improved ligand binding energies derived from molecular dynamics: replicate sampling enhances the search of conformational space. *Journal of Chemical Information and Modeling* **53**, 2065-2072 (2013).
154. Genheden, S. & Ryde, U. How to obtain statistically converged MM/GBSA results. *Journal of Computational Chemistry* **31**, 837-846 (2010).
155. Metz, A. et al. Hot spots and transient pockets: predicting the determinants of small-molecule binding to a protein-protein interface. *Journal of Chemical Information and Modeling* **52**, 120-133 (2012).
156. Yang, T.Y. et al. Virtual screening using molecular simulations. *Proteins: Structure, Function, and Bioinformatics* **79**, 1940-1951 (2011).

157. Homeyer, N., Stoll, F., Hillisch, A. & Gohlke, H. Binding free energy calculations for lead optimization: Assessment of their accuracy in an industrial drug design context. *Journal of Chemical Theory and Computation* **10**, 3331–3344 (2014).
158. Leonis, G., Steinbrecher, T. & Papadopoulos, M.G. A contribution to the drug resistance mechanism of darunavir, amprenavir, indinavir, and saquinavir complexes with HIV-1 protease due to flap mutation I50V: a systematic MM-PBSA and thermodynamic integration study. *Journal of Chemical Information and Modeling* **53**, 2141-53 (2013).
159. Chen, J., Wang, X., Zhu, T., Zhang, Q. & Zhang, J.Z. A comparative insight into Amprenavir resistance of mutations V32I, G48V, I50V, I54V, and I84V in HIV-1 protease based on thermodynamic integration and MM-PBSA methods. *Journal of Chemical Information and Modeling* **55**, 1903-13 (2015).
160. Tzoupis, H., Leonis, G., Mavromoustakos, T. & Papadopoulos, M.G. A comparative molecular dynamics, MM-PBSA and thermodynamic integration study of Saquinavir complexes with wild type HIV-1 PR and L10I, G48V, L63P, A71V, G73S, V82A and I84V single mutants. *Journal of Chemical Theory and Computation* **9**, 1754-64 (2013).
161. Dimura, M. et al. Quantitative FRET studies and integrative modeling unravel the structure and dynamics of biomolecular systems. *Current Opinion in Structural Biology* **40**, 163-185 (2016).
162. Sali, A. et al. Outcome of the First wwPDB Hybrid/Integrative Methods Task Force Workshop. *Structure* **23**, 1156-1167 (2015).
163. Schröder, G.F. Hybrid methods for macromolecular structure determination: experiment with expectations. *Current Opinion in Structural Biology* **31**, 20-27 (2015).
164. Alber, F. et al. Determining the architectures of macromolecular assemblies. *Nature* **450**, 683-694 (2007).
165. Alber, F. et al. The molecular architecture of the nuclear pore complex. *Nature* **450**, 695-701 (2007).
166. Degiacomi, M.T. & Dal Peraro, M. Macromolecular symmetric assembly prediction using swarm intelligence dynamic modeling. *Structure* **21**, 1097-1106 (2013).
167. Degiacomi, M.T. et al. Molecular assembly of the aerolysin pore reveals a swirling membrane-insertion mechanism. *Nature Chemical Biology* **9**, 623-629 (2013).
168. Kalinin, S. et al. A toolkit and benchmark study for FRET-restrained high-precision structural modeling. *Nature Methods* **9**, 1218-U129 (2012).
169. Boomsma, W., Ferkinghoff-Borg, J. & Lindorff-Larsen, K. Combining experiments and simulations using the maximum entropy principle. *PloS Computational Biology* **10**(2014).
170. Shen, Y. et al. Consistent blind protein structure generation from NMR chemical shift data. *Proceedings of the National Academy of Sciences of the United States of America* **105**, 4685-4690 (2008).
171. Boomsma, W. et al. Equilibrium simulations of proteins using molecular fragment replacement and NMR chemical shifts. *Proceedings of the National Academy of Sciences of the United States of America* **111**, 13852-13857 (2014).
172. Folmer, R.H.A., Nilges, M., Folkers, P.J.M., Konings, R.N.H. & Hilbers, C.W. A Model of the Complex between Single-Stranded-DNA and the Single-Stranded-DNA Binding-Protein Encoded by Gene-V of Filamentous Bacteriophage-M13. *Journal of Molecular Biology* **240**, 341-357 (1994).
173. Loquet, A. et al. Atomic model of the type III secretion system needle. *Nature* **486**, 276-+ (2012).
174. Russel, D. et al. Putting the pieces together: Integrative modeling platform software for structure determination of macromolecular assemblies. *PloS Biology* **10**(2012).
175. Lasker, K. et al. Molecular architecture of the 26S proteasome holocomplex determined by an integrative approach. *Proceedings of the National Academy of Sciences of the United States of America* **109**, 1380-1387 (2012).
176. Latorraca, N.R. et al. Mechanism of substrate translocation in an alternating access transporter. *Cell* **169**, 96-+ (2017).
177. Fukuda, M. et al. Structural basis for dynamic mechanism of nitrate/nitrite antiport by NarK. *Nature Communications* **6**(2015).
178. Vashisth, H., Storaska, A.J., Neubig, R.R. & Brooks, C.L. Conformational dynamics of a regulator of G-protein signaling protein reveals a mechanism of allosteric inhibition by a small molecule. *Acs Chemical Biology* **8**, 2778-2784 (2013).
179. Beuming, T. et al. The binding sites for cocaine and dopamine in the dopamine transporter overlap. *Nature Neuroscience* **11**, 780-789 (2008).
180. Pogoryelov, D. et al. Microscopic rotary mechanism of ion translocation in the F0 complex of ATP synthases. *Nature Chemical Biology* **6**, 891-899 (2010).
181. Reddy, T. et al. Nothing to Sneeze At: A Dynamic and Integrative Computational Model of an Influenza A Virion. *Structure* **23**, 584-597 (2015).
182. Meister, A. 23. Glutamine synthetase of mammals. *The Enzymes* **10**, 699-754 (1974).

183. Brown, J.R., Masuchi, Y., Robb, F.T. & Doolittle, W.F. Evolutionary relationships of bacterial and archaeal glutamine synthetase genes. *Journal of Molecular Evolution* **38**, 566-576 (1994).
184. Yamashita, M.M., Almassy, R.J., Janson, C.A., Cascio, D. & Eisenberg, D. Refined atomic model of glutamine synthetase at 3.5 A resolution. *Journal of Biological Chemistry* **264**, 17681-17690 (1989).
185. Murray, D.S. et al. Structures of the Bacillus subtilis glutamine synthetase dodecamer reveal large intersubunit catalytic conformational changes linked to a anique feedback inhibition mechanism. *Journal of Biological Chemistry* **288**, 35801-35811 (2013).
186. Darrow, R.A. & Knotts, R.R. Two forms of glutamine synthetase in free-living root-nodule bacteria. *Biochemical and Biophysical Research Communications* **78**, 554-9 (1977).
187. Edmands, J., Noridge, N.A. & Benson, D.R. The actinorhizal root-nodule symbiont Frankia sp. strain Cpi1 has two glutamine synthetases. *Proceedings of the National Academy of Sciences of the United States of America* **84**, 6126-6130 (1987).
188. Kumada, Y., Takano, E., Nagaoka, K. & Thompson, C. Streptomyces hygroscopicus has two glutamine synthetase genes. *Journal of Bacteriology* **172**, 5343-5351 (1990).
189. van Rooyen, J.M., Abratt, V.R., Belrhali, H. & Sewell, T. Crystal structure of type III glutamine synthetase: surprising reversal of the inter-ring interface. *Structure* **19**, 471-483 (2011).
190. Southern, J.A., Parker, J.R. & Woods, D.R. Expression and purification of glutamine synthetase cloned from Bacteroides fragilis. *Journal of General Microbiology* **132**, 2827-2835 (1986).
191. Kinoshita, S. et al. The occurrence of eukaryotic type III glutamine synthetase in the marine diatom Chaetoceros compressum. *Marine Genomics* **2**, 103-111 (2009).
192. Wang, Y.M. et al. Chromosomal mapping of a family of human glutamine synthetase genes: Functional gene (GLUL) on 1q25, pseudogene (GLULP) on 9p13, and three related genes (GLULL1, GLULL2, GLULL3) on 5q33, 11p15, and 11q24. *Genomics* **37**, 195-199 (1996).
193. Liaw, S.H. & Eisenberg, D. Structural model for the reaction-mechanism of glutamine synthetase, based on five crystal structures of enzyme-substrate complexes. *Biochemistry* **33**, 675-681 (1994).
194. Eisenberg, D., Gill, H.S., Pfluegl, G.M. & Rotstein, S.H. Structure-function relationships of glutamine synthetases. *Biochimica et Biophysica Acta* **1477**, 122-45 (2000).
195. Wedler, F.C. & Boyer, P.D. Substrate binding and reaction intermediates of glutamine synthetase (Escherichia coli W) as studied by isotape exchanges. *Journal of Biological Chemistry* **247**, 984-& (1972).
196. Wedler, F.C. & Horn, B.R. Catalytic mechanisms of glutamine synthetase enzymes - studies with Analogs of possible intermediates and transition states. *Journal of Biological Chemistry* **251**, 7530-7538 (1976).
197. Issoglio, F.M. et al. Exploring the catalytic mechanism of human glutamine synthetase by computer simulations. *Biochemistry* (2016).
198. Moreira, C., Ramos, M.J. & Fernandes, P.A. Clarifying the catalytic mechanism of human glutamine synthetase: a QM/MM study. *Journal of Physical Chemistry B* (2017).
199. Moreira, C., Ramos, M.J. & Fernandes, P.A. Reaction mechanism of Mycobacterium tuberculosis glutamine synthetase using quantum mechanics/molecular mechanics calculations. *Chemistry - A European Journal* **22**, 9218-9225 (2016).
200. Krajewski, W.W., Jones, T.A. & Mowbray, S.L. Structure of Mycobacterium tuberculosis glutamine synthetase in complex with a transition-state mimic provides functional insights. *Proceedings of the National Academy of Sciences of the United States of America* **102**, 10499-10504 (2005).
201. Cuff, M., Tan, K., Mack, J., Clancy, S. & Joachimiak, A. The crystal structure of glutamine synthetase from Bifidobacterium adolescentis ATCC 15703. *To Be Published*.
202. Zeth, K. Structure of glutamine synthetase from Streptomyces coelicolor. *To Be Published*.
203. Unno, H. et al. Atomic structure of plant glutamine synthetase - a key enzyme for plant productivity. *Journal of Biological Chemistry* **281**, 29287-29296 (2006).
204. He, Y.X. et al. Crystal structure of Saccharomyces cerevisiae glutamine synthetase Gln1 suggests a nanotube-like supramolecular assembly. *Proteins: Structure, Function, and Bioinformatics* **76**, 249-254 (2009).
205. Bernstein, F.C. et al. The Protein Data Bank. A computer-based archival file for macromolecular structures. *European journal of biochemistry* **80**, 319-24 (1977).
206. Berman, H.M. et al. The Protein Data Bank, 1999–. in *International Tables for Crystallography Volume F: Crystallography of Biological Macromolecules* 675-684 (Springer, 2006).
207. Martinez-Hernandez, A., Bell, K.P. & Norenberg, M.D. Glutamine synthetase: glial localization in brain. *Science* **195**, 1356-8 (1977).
208. Norenberg, M.D. & Martinez-Hernandez, A. Fine structural localization of glutamine synthetase in astrocytes of rat brain. *Brain Research* **161**, 303-310 (1979).

209. Bernstein, H.G. et al. Distribution of immunoreactive glutamine synthetase in the adult human and mouse brain. Qualitative and quantitative observations with special emphasis on extra-astroglial protein localization. *Journal of Chemical Neuroanatomy* **61-62**, 33-50 (2014).
210. Cooper, A., McDonald, J., Gelbard, A., Gledhill, R. & Duffy, T. The metabolic fate of 13N-labeled ammonia in rat brain. *Journal of Biological Chemistry* **254**, 4982-4992 (1979).
211. Okada, M. et al. In vivo monitoring of extracellular N-13-glutamine derived from blood-borne N-13-ammonia in rat striatum using microdialysis with radio-LC method. *Journal of Neuroscience Methods* **184**, 37-41 (2009).
212. Cooper, A.J.L., Mora, S.N., Cruz, N.F. & Gelbard, A.S. Cerebral ammonia metabolism in hyperammonemic rats. *Journal of Neurochemistry* **44**, 1716-1723 (1985).
213. Brusilow, S.W., Koehler, R.C., Traystman, R.J. & Cooper, A.J.L. Astrocyte glutamine synthetase: importance in hyperammonemic syndromes and potential target for therapy. *Neurotherapeutics* **7**, 452-470 (2010).
214. Raichle, M.E. & Larson, K.B. The significance of the NH3-NH4+ equilibrium on the passage of 13N-ammonia from blood to brain. A new regional residue detection model. *Circulation Research* **48**, 913-37 (1981).
215. Cooper, A.J.L. & Lai, J.C.K. Cerebral ammonia metabolism in normal and hyperammonemic rats. *Neurochemical Pathology* **6**, 67-95 (1987).
216. Cooper, A.J.L. & Jeitner, T.M. Central role of glutamate metabolism in the maintenance of nitrogen homeostasis in normal and hyperammonemic brain. *Biomolecules* **6**(2016).
217. Benjamin, A.M. & Quastel, J.H. Metabolism of amino acids and ammonia in rat brain cortex slices in vitro: a possible role of ammonia in brain function. *Journal of Neurochemistry* **25**, 197-206 (1975).
218. Petroff, O.A.C., Errante, L.D., Rothman, D.L., Kim, J.H. & Spencer, D.D. Glutamate-glutamine cycling in the epileptic human hippocampus. *Epilepsia* **43**, 703-710 (2002).
219. Eid, T., Tu, N., Lee, T.S.W. & Lai, J.C.K. Regulation of astrocyte glutamine synthetase in epilepsy. *Neurochemistry International* **63**, 670-681 (2013).
220. Häussinger, D. Nitrogen metabolism in liver: structural and functional organization and physiological relevance. *Biochemical Journal* **267**, 281-90 (1990).
221. Häussinger, D. Hepatocyte heterogeneity in glutamine and ammonia metabolism and the role of an intercellular glutamine cycle during ureogenesis in perfused-rat-liver. *European Journal of Biochemistry* **133**, 269-275 (1983).
222. Gebhardt, R. & Mecke, D. Heterogeneous distribution of glutamine synthetase among rat liver parenchymal cells in situ and in primary culture. *Embo Journal* **2**, 567-570 (1983).
223. Häussinger, D., Sies, H. & Gerok, W. Functional hepatocyte heterogeneity in ammonia metabolism - the intercellular glutamine cycle. *Journal of Hepatology* **1**, 3-14 (1985).
224. Qvartskhava, N. et al. Hyperammonemia in gene-targeted mice lacking functional hepatic glutamine synthetase. *Proceedings of the National Academy of Sciences of the United States of America* **112**, 5521-5526 (2015).
225. Häussinger, D. & Gerok, W. Hepatocyte heterogeneity in ammonia metabolism - impairment of glutamine synthesis in CCl4 induced liver-cell necrosis with no effect on urea Synthesis. *Chemico-Biological Interactions* **48**, 191-194 (1984).
226. Häussinger, D. & Stehle, T. Hepatocyte heterogeneity in response to icosanoids - the perivenous scavenger cell hypothesis. *European Journal of Biochemistry* **175**, 395-403 (1988).
227. Häussinger, D. Hepatic glutamine transport and metabolism. *Advances in Enzymology and Related Areas of Molecular Biology* **72**, 43-86 (1998).
228. Hensley, K. et al. Brain regional correspondence between Alzheimer's disease histopathology and biomarkers of protein oxidation. *Journal of Neurochemistry* **65**, 2146-2156 (1995).
229. Gunnersen, D. & Haley, B. Detection of glutamine synthetase in the cerebrospinal-fluid of Alzheimer diseased patients - a potential diagnostic biochemical marker. *Proceedings of the National Academy of Sciences of the United States of America* **89**, 11949-11953 (1992).
230. Tumani, H., Shen, G., Peter, J.B. & Bruck, W. Glutamine synthetase in cerebrospinal fluid, serum, and brain: a diagnostic marker for Alzheimer disease? *Archives of Neurology* **56**, 1241-6 (1999).
231. Häussinger, D. et al. Proton magnetic-resonance spectroscopy studies on human brain myo-Iinositol in hypo-osmolarity and hepatic-encephalopathy. *Gastroenterology* **107**, 1475-1480 (1994).
232. Häussinger, D., Kircheis, G., Fischer, R., Schliess, F. & vom Dahl, S. Hepatic encephalopathy in chronic liver disease: a clinical manifestation of astrocyte swelling and low-grade cerebral edema? *Journal of Hepatology* **32**, 1035-1038 (2000).
233. Eid, T., Behar, K., Dhaher, R., Bumanglag, A.V. & Lee, T.S.W. Roles of glutamine synthetase inhibition in epilepsy. *Neurochemical Research* **37**, 2339-2350 (2012).

234. Eid, T. et al. Loss of glutamine synthetase in the human epileptogenic hippocampus: possible mechanism for raised extracellular glutamate in mesial temporal lobe epilepsy. *Lancet* **363**, 28-37 (2004).
235. van der Hel, W.S. et al. Reduced glutamine synthetase in hippocampal areas with neuron loss in temporal lobe epilepsy. *Neurology* **64**, 326-333 (2005).
236. Smith, C.D. et al. Excess brain protein oxidation and enzyme dysfunction in normal aging and in Alzheimer disease. *Proceedings of the National Academy of Sciences of the United States of America* **88**, 10540-10543 (1991).
237. Gibbs, M.E. et al. Inhibition of glutamine synthetase activity prevents memory consolidation. *Cognitive Brain Research* **4**, 57-64 (1996).
238. Ng, K.T. et al. Complex roles of glutamate in the Gibbs-Ng model of one-trial aversive learning in the new-born chick. *Neuroscience and Biobehavioral Reviews* **21**, 45-54 (1997).
239. Häberle, J., Shahbeck, N., Ibrahim, K., Hoffmann, G.F. & Ben-Omran, T. Natural course of glutamine synthetase deficiency in a 3 year old patient. *Molecular Genetics and Metabolism* **103**, 89-91 (2011).
240. Frieg, B., Häussinger, D. & Gohlke, H. Towards restoring catalytic activity of glutamine synthetase with a clinically relevant mutation. in *Proceedings of the NIC Symposium 2016* (eds. Binder, K., Müller, M., Kremer, M. & Schnurpfeil, A.) 97-104 (Jülich, 2016).
241. Fleming, A. On the antibacterial action of cultures of a penicillium, with special reference to their use in the isolation of B. influenzae. *British Journal of Experimental Pathology* **10**, 226 (1929).
242. Kardos, N. & Demain, A.L. Penicillin: the medicine with the greatest impact on therapeutic outcomes. *Applied Microbiology and Biotechnology* **92**, 677-687 (2011).
243. Bell, B.G., Schellevis, F., Stobberingh, E., Goossens, H. & Pringle, M. A systematic review and meta-analysis of the effects of antibiotic consumption on antibiotic resistance. *Bmc Infectious Diseases* **14**(2014).
244. Levy, S.B. Antibiotic resistance: consequences of inaction. *Clinical Infectious Diseases* **33**, S124-S129 (2001).
245. Fact sheet: antibiotic resistance http://www.who.int/mediacentre/factsheets/antibiotic-resistance/en/ (2016).
246. Global priority list of antibiotic-resistant bacteria to guide research, discovery, and development of new antibiotics. http://www.who.int/medicines/publications/WHO-PPL-Short_Summary_25Feb-ET_NM_WHO.pdf?ua=1 (2017).
247. Ahmad, V. et al. Antimicrobial potential of bacteriocins: in therapy, agriculture and food preservation. *International Journal of Antimicrobial Agents* **49**, 1-11 (2017).
248. Papagianni, M. Ribosomally synthesized peptides with antimicrobial properties: biosynthesis, structure, function, and applications. *Biotechnology Advances* **21**, 465-499 (2003).
249. van Heel, A.J., Montalban-Lopez, M. & Kuipers, O.P. Evaluating the feasibility of lantibiotics as an alternative therapy against bacterial infections in humans. *Expert Opinion on Drug Metabolism & Toxicology* **7**, 675-680 (2011).
250. Chatterjee, S. et al. Mersacidin, a new antibiotic from Bacillus. In vitro and in vivo antibacterial activity. *Journal of Antibiotics* **45**, 839-45 (1992).
251. Cotter, P.D., Hill, C. & Ross, R.P. Bacteriocins: developing innate immunity for food. *Nature Reviews Microbiology* **3**, 777-88 (2005).
252. Schnell, N. et al. Prepeptide sequence of epidermin, a ribosomally synthesized antibiotic with 4 sulfide-rings. *Nature* **333**, 276-278 (1988).
253. Jung, G. Lantibiotics - ribosomally synthesized biologically-active polypeptides containing sulfide bridges and alpha-beta-didehydroamino acids. *Angewandte Chemie-International Edition* **30**, 1051-1068 (1991).
254. Willey, J.M. & van der Donk, W.A. Lantibiotics: peptides of diverse structure and function. *Annual Review of Microbiology* **61**, 477-501 (2007).
255. Breukink, E. et al. Use of the cell wall precursor lipid II by a pore-forming peptide antibiotic. *Science* **286**, 2361-2364 (1999).
256. Bierbaum, G. & Sahl, H.G. Lantibiotics: mode of action, biosynthesis and bioengineering. *Current Pharmaceutical Biotechnology* **10**, 2-18 (2009).
257. Mattick, A.T.R. & Hirsch, A. A powerful inhibitory substance produced by group N streptococci. *Nature* **154**, 551 (1944).
258. Ongey, E.L., Yassi, H., Pflugmacher, S. & Neubauer, P. Pharmacological and pharmacokinetic properties of lanthipeptides undergoing clinical studies. *Biotechnology Letters* **39**, 473-482 (2017).
259. Chatterjee, C., Paul, M., Xie, L.L. & van der Donk, W.A. Biosynthesis and mode of action of lantibiotics. *Chemical Reviews* **105**, 633-683 (2005).

260. Rogers, L.A. The inhibiting effect of Streptococcus Lactis on Lactobacillus Bulgaricus. *Journal of Bacteriology* **16**, 321-5 (1928).
261. Okuda, K. et al. Effects of bacteriocins on methicillin-resistant Staphylococcus aureus biofilm. *Antimicrobial Agents and Chemotherapy* **57**, 5572-5579 (2013).
262. Dosler, S. & Gerceker, A.A. In vitro activities of nisin Alone or in combination with vancomycin and ciprofloxacin against methicillin-resistant and methicillin-susceptible Staphylococcus aureus strains. *Chemotherapy* **57**, 511-516 (2011).
263. Piper, C., Draper, L.A., Cotter, P.D., Ross, R.P. & Hill, C. A comparison of the activities of lacticin 3147 and nisin against drug-resistant Staphylococcus aureus and Enterococcus species. *Journal of Antimicrobial Chemotherapy* **64**, 546-551 (2009).
264. Piper, C., Hill, C., Cotter, P.D. & Ross, R.P. Bioengineering of a nisin A-producing Lactococcus lactis to create isogenic strains producing the natural variants nisin F, Q and Z. *Microbial Biotechnology* **4**, 375-382 (2011).
265. Shin, J.M. et al. Biomedical applications of nisin. *Journal of Applied Microbiology* (2015).
266. Van de Ven, F., Van den Hooven, H., Konings, R. & Hilbers, C. The spatial structure of nisin in aqueous solution. in *Nisin and Novel Lantibiotics* (eds. Jung, G. & Sahl, H.-G.) 35-42 (Escom Publishers, Leiden, 1991).
267. Zhou, L., van Heel, A.J. & Kuipers, O.P. The length of a lantibiotic hinge region has profound influence on antimicrobial activity and host specificity. *Frontiers in Microbiology* **6**, 11 (2015).
268. Wiedemann, I., Benz, R. & Sahl, H.G. Lipid II-mediated pore formation by the peptide antibiotic nisin: a black lipid membrane study. *Journal of Bacteriology* **186**, 3259-3261 (2004).
269. Wiedemann, I. et al. Specific binding of nisin to the peptidoglycan precursor lipid II combines pore formation and inhibition of cell wall biosynthesis for potent antibiotic activity. *Journal of Biological Chemistry* **276**, 1772-9 (2001).
270. Dischinger, J., Chipalu, S.B. & Bierbaum, G. Lantibiotics: promising candidates for future applications in health care. *International Journal of Medical Microbiology* **304**, 51-62 (2014).
271. Breukink, E. et al. Lipid II is an intrinsic component of the pore induced by nisin in bacterial membranes. *Journal of Biological Chemistry* **278**, 19898-19903 (2003).
272. Brötz, H. et al. Role of lipid-bound peptidoglycan precursors in the formation of pores by nisin, epidermin and other lantibiotics. *Molecular Microbiology* **30**, 317-27 (1998).
273. Hasper, H.E., de Kruijff, B. & Breukink, E. Assembly and stability of nisin-lipid II pores. *Biochemistry* **43**, 11567-75 (2004).
274. Froseth, B.R. & Mckay, L.L. Molecular characterization of the nisin resistance region of Lactococcus Lactis subsp. Lactis Biovar Diacetylactis Drc3. *Applied and Environmental Microbiology* **57**, 804-811 (1991).
275. Draper, L.A., Cotter, P.D., Hill, C. & Ross, R.P. Lantibiotic resistance. *Microbiology and Molecular Biology Reviews* **79**, 171-191 (2015).
276. Reiners, J. et al. The N-terminal region of nisin is important for the BceAB-type ABC transporter NsrFP from Streptococcus agalactiae COH1. *Frontiers in Microbiology* **8**(2017).
277. Khosa, S., Hoeppner, A., Gohlke, H., Schmitt, L. & Smits, S.H. Structure of the response regulator NsrR from Streptococcus agalactiae, which is involved in lantibiotic resistance. *PLoS One* **11**, e0149903 (2016).
278. Sun, Z.Z. et al. Novel mechanism for nisin resistance via proteolytic degradation of nisin by the nisin resistance protein NSR. *Antimicrobial Agents and Chemotherapy* **53**, 1964-1973 (2009).
279. Rao, V.S., Srinivas, K., Sujini, G.N. & Kumar, G.N. Protein-protein interaction detection: methods and analysis. *International Journal of Proteomics* **2014**, 147648 (2014).
280. Berggard, T., Linse, S. & James, P. Methods for the detection and analysis of protein-protein interactions. *Proteomics* **7**, 2833-2842 (2007).
281. Arkin, M.R., Tang, Y.Y. & Wells, J.A. Small molecule inhibitors of protein-protein interactions: progressing toward the reality. *Chemistry & Biology* **21**, 1102-1114 (2014).
282. Ivanov, A.A., Khuri, F.R. & Fu, H.A. Targeting protein-protein interactions as an anticancer strategy. *Trends in Pharmacological Sciences* **34**, 393-400 (2013).
283. Schopf, F.H., Biebl, M.M. & Buchner, J. The Hsp90 chaperone machinery. *Nature Reviews Molecular Cell Biology* **18**, 345-360 (2017).
284. Balch, W.E., Morimoto, R.I., Dillin, A. & Kelly, J.W. Adapting proteostasis for disease intervention. *Science* **319**, 916-919 (2008).
285. Taipale, M., Jarosz, D.F. & Lindquist, S. Hsp90 at the hub of protein homeostasis: emerging mechanistic insights. *Nature Reviews Molecular Cell Biology* **11**, 515-528 (2010).
286. Saibil, H. Chaperone machines for protein folding, unfolding and disaggregation. *Nature Reviews Molecular Cell Biology* **14**, 630-642 (2013).

287. Dutta, R. & Inouye, M. GHKL, an emergent ATPase/kinase superfamily. *Trends in Biochemical Sciences* **25**, 24-28 (2000).
288. Minami, Y., Kimura, Y., Kawasaki, H., Suzuki, K. & Yahara, I. The carboxy-terminal region of mammalian Hsp90 is required for its dimerization and function in vivo. *Molecular and Cellular Biology* **14**, 1459-1464 (1994).
289. Wayne, N. & Bolon, D.N. Dimerization of Hsp90 is required for in vivo function: Design and analysis of monomers and dimers. *Journal of Biological Chemistry* **282**, 35386-35395 (2007).
290. Lee, C.C., Lin, T.W., Ko, T.P. & Wang, A.H.J. The hexameric structures of human heat shock protein 90. *PLoS One* **6**(2011).
291. Moullintraffort, L. et al. Biochemical and biophysical characterization of the Mg2+-induced 90-kDa heat shock protein oligomers. *Journal of Biological Chemistry* **285**, 15100-15110 (2010).
292. Meyer, P. et al. Structural and functional analysis of the middle segment of Hsp90: Implications for ATP hydrolysis and client protein and cochaperone interactions. *Molecular Cell* **11**, 647-658 (2003).
293. Verba, K.A. et al. Atomic structure of Hsp90-Cdc37-Cdk4 reveals that Hsp90 traps and stabilizes an unfolded kinase. *Science* **352**, 1542-1547 (2016).
294. Sato, S., Fujita, N. & Tsuruo, T. Modulation of Akt kinase activity by binding to Hsp90. *Proceedings of the National Academy of Sciences of the United States of America* **97**, 10832-10837 (2000).
295. Harris, S.F., Shiau, A.K. & Agard, D.A. The crystal structure of the carboxy-terminal dimerization domain of htpG, the Escherichia coli Hsp90, reveals a potential substrate binding site. *Structure* **12**, 1087-1097 (2004).
296. Ciglia, E. et al. Resolving hot spots in the C-terminal dimerization domain that determine the stability of the molecular chaperone Hsp90. *PLoS One* **9**, e96031 (2014).
297. Garnier, C. et al. Binding of ATP to heat shock protein 90 - Evidence for an ATP-binding site in the C-terminal domain. *Journal of Biological Chemistry* **277**, 12208-12214 (2002).
298. Marcu, M.G., Chadli, A., Bouhouche, I., Catelli, M. & Neckers, L.M. The heat shock protein 90 antagonist Novobiocin interacts with a previously unrecognized ATP-binding domain in the carboxyl terminus of the chaperone. *Journal of Biological Chemistry* **275**, 37181-6 (2000).
299. Young, J.C., Obermann, W.M.J. & Hartl, F.U. Specific binding of tetratricopeptide repeat proteins to the C-terminal 12-kDa domain of hsp90. *Journal of Biological Chemistry* **273**, 18007-18010 (1998).
300. Li, J., Soroka, J. & Buchner, J. The Hsp90 chaperone machinery: conformational dynamics and regulation by co-chaperones. *Biochimica et Biophysica Acta, Molecular Cell Research* **1823**, 624-635 (2012).
301. Pearl, L.H. & Prodromou, C. Structure and mechanism of the Hsp90 molecular chaperone machinery. *Annual Review of Biochemistry* **75**, 271-94 (2006).
302. Shiau, A.K., Harris, S.F., Southworth, D.R. & Agard, D.A. Structural analysis of E-coli Hsp90 reveals dramatic nucleotide-dependent conformational rearrangements. *Cell* **127**, 329-340 (2006).
303. Richter, K., Muschler, P., Hainzl, O. & Buchner, J. Coordinated ATP hydrolysis by the Hsp90 dimer. *Journal of Biological Chemistry* **276**, 33689-33696 (2001).
304. Ratzke, C., Mickler, M., Hellenkamp, B., Buchner, J. & Hugel, T. Dynamics of heat shock protein 90 C-terminal dimerization is an important part of its conformational cycle. *Proceedings of the National Academy of Sciences of the United States of America* **107**, 16101-6 (2010).
305. Weikl, T. et al. C-terminal regions of Hsp90 are important for trapping the nucleotide during the ATPase cycle. *Journal of Molecular Biology* **303**, 583-592 (2000).
306. Hessling, M., Richter, K. & Buchner, J. Dissection of the ATP-induced conformational cycle of the molecular chaperone Hsp90. *Nature Structural & Molecular Biology* **16**, 287-293 (2009).
307. Scheibel, T. et al. ATP-binding properties of human Hsp90. *Journal of Biological Chemistry* **272**, 18608-18613 (1997).
308. Prodromou, C. et al. Identification and structural characterization of the ATP/ADP-binding site in the Hsp90 molecular chaperone. *Cell* **90**, 65-75 (1997).
309. Cunningham, C.N., Krukenberg, K.A. & Agard, D.A. Intra- and intermonomer interactions are required to synergistically facilitate ATP hydrolysis in Hsp90. *Journal of Biological Chemistry* **283**, 21170-21178 (2008).
310. Rohl, A., Rohrberg, J. & Buchner, J. The chaperone Hsp90: changing partners for demanding clients. *Trends in Biochemical Sciences* **38**, 253-262 (2013).
311. Southworth, D.R. & Agard, D.A. Species-dependent ensembles of conserved conformational states define the Hsp90 chaperone ATPase cycle. *Molecular Cell* **32**, 631-640 (2008).
312. Kim, Y.E., Hipp, M.S., Bracher, A., Hayer-Hartl, M. & Hartl, F.U. Molecular chaperone functions in protein folding and proteostasis. *Annual Review of Biochemistry* **82**, 323-355 (2013).

313. Dollins, D.E., Warren, J.J., Immormino, R.M. & Gewirth, D.T. Structures of GRP94-Nucleotide complexes reveal mechanistic differences between the hsp90 chaperones. *Molecular Cell* **28**, 41-56 (2007).
314. Hagn, F. et al. Structural analysis of the interaction between Hsp90 and the tumor suppressor protein p53. *Nature Structural & Molecular Biology* **18**, 1086-U112 (2011).
315. Kirschke, E., Goswami, D., Southworth, D., Griffin, P.R. & Agard, D.A. Glucocorticoid receptor function regulated by coordinated action of the Hsp90 and Hsp70 chaperone cycles. *Cell* **157**, 1685-1697 (2014).
316. Boczek, E.E. et al. Conformational processing of oncogenic v-Src kinase by the molecular chaperone Hsp90. *Proceedings of the National Academy of Sciences of the United States of America* **112**, E3189-E3198 (2015).
317. Hanahan, D. & Weinberg, R.A. The hallmarks of cancer. *Cell* **100**, 57-70 (2000).
318. Jego, G., Hazoume, A., Seigneuric, R. & Garrido, C. Targeting heat shock proteins in cancer. *Cancer Letters* **332**, 275-285 (2013).
319. Kamal, A. et al. A high-affinity conformation of Hsp90 confers tumour selectivity on Hsp90 inhibitors. *Nature* **425**, 407-410 (2003).
320. Pick, E. et al. High HSP90 expression is associated with decreased survival in breast cancer. *Cancer Research* **67**, 2932-2937 (2007).
321. Balchin, D., Hayer-Hartl, M. & Hartl, F.U. In vivo aspects of protein folding and quality control. *Science* **353**(2016).
322. Vartholomaiou, E., Echeverria, P.C. & Picard, D. Unusual suspects in the twilight zone between the Hsp90 interactome and carcinogenesis. *Hsp90 in Cancer: Beyond the Usual Suspects* **129**, 1-30 (2016).
323. Butler, L.M., Ferraldeschi, R., Armstrong, H.K., Centenera, M.M. & Workman, P. Maximizing the therapeutic potential of Hsp90 inhibitors. *Molecular Cancer Research* **13**, 1445-1451 (2015).
324. Wang, M. et al. Development of heat shock protein (Hsp90) inhibitors to combat resistance to tyrosine kinase inhibitors through Hsp90-kinase interactions. *Journal of Medicinal Chemistry* (2016).
325. Li, J. et al. Structure insights into mechanisms of ATP hydrolysis and the activation of human heat-shock protein 90. *Acta Biochimica Et Biophysica Sinica* **44**, 300-306 (2012).
326. Stebbins, C.E. et al. Crystal structure of an Hsp90-geldanamycin complex: targeting of a protein chaperone by an antitumor agent. *Cell* **89**, 239-250 (1997).
327. Miyata, Y. Hsp90 inhibitor geldanamycin and its derivatives as novel cancer chemotherapeutic agents. *Current Pharmaceutical Design* **11**, 1131-1138 (2005).
328. Garcia-Carbonero, R., Carnero, A. & Paz-Ares, L. Inhibition of Hsp90 molecular chaperones: moving into the clinic. *Lancet Oncology* **14**, E358-E369 (2013).
329. Wu, L.X. et al. Disruption of the Bcr-Abl/Hsp90 protein complex: a possible mechanism to inhibit Bcr-Abl-positive human leukemic blasts by novobiocin. *Leukemia* **22**, 1402-9 (2008).
330. Brough, P.A. et al. 4,5-diarylisoxazole Hsp90 chaperone inhibitors: potential therapeutic agents for the treatment of cancer. *Journal of Medicinal Chemistry* **51**, 196-218 (2008).
331. Wang, Y. & McAlpine, S.R. N-terminal and C-terminal modulation of Hsp90 produce dissimilar phenotypes. *Chemical Communications* **51**, 1410-3 (2015).
332. Matthews, S.B. et al. Characterization of a novel Novobiocin analogue as a putative C-terminal inhibitor of Heat Shock Protein 90 in prostate cancer cells. *Prostate* **70**, 27-36 (2010).
333. Marcu, M.G., Schulte, T.W. & Neckers, L. Novobiocin and related coumarins and depletion of heat shock protein 90-dependent signaling proteins. *Journal of the National Cancer Institute* **92**, 242-248 (2000).
334. Daley, G.Q., Van Etten, R.A. & Baltimore, D. Induction of chronic myelogenous leukemia in mice by the P210bcr/abl gene of the Philadelphia chromosome. *Science* **247**, 824-30 (1990).
335. Garg, G., Khandelwal, A. & Blagg, B.S.J. Anticancer inhibitors of Hsp90 function: beyond the usual suspects. *Advances in Cancer Research* **129**, 51-88 (2016).
336. Bopp, B. et al. Design and biological testing of peptidic dimerization inhibitors of human Hsp90 that target the C-terminal domain. *Biochimica et Biophysica Acta* **1860**, 1043-1055 (2016).
337. Fosgerau, K. & Hoffmann, T. Peptide therapeutics: current status and future directions. *Drug Discovery Today* **20**, 122-128 (2015).
338. Otvos, L. & Wade, J.D. Current challenges in peptide-based drug discovery. *Frontiers in Chemistry* **2**(2014).
339. Vagner, J., Qu, H.C. & Hruby, V.J. Peptidomimetics, a synthetic tool of drug discovery. *Current Opinion in Chemical Biology* **12**, 292-296 (2008).
340. Diedrich, D. et al. alpha-Aminoxy oligopeptides: synthesis, secondary structure, and cytotoxicity of a new class of anticancer foldamers. *Chemistry - A European Journal* (2016).

341. Frieg, B. et al. Molecular mechanisms of glutamine synthetase mutations that lead to clinically relevant pathologies. *PLoS Computational Biology* **12**, e1004693 (2016).
342. Matsuoka, D. & Nakasako, M. Probability distributions of hydration water molecules around polar protein atoms obtained by a database analysis. *Journal of Physical Chemistry B* **113**, 11274-11292 (2009).
343. Desiraju, G.R. & Steiner, T. *Weak hydrogen Bond*, (Oxford University Press New York, 2001).
344. Rajagopal, S. & Vishveshwara, S. Short hydrogen bonds in proteins. *FEBS Journal* **272**, 1819-1832 (2005).
345. Pfleger, C., Rathi, P.C., Klein, D.L., Radestock, S. & Gohlke, H. Constraint Network Analysis (CNA): a python software package for efficiently linking biomacromolecular structure, flexibility, (thermo-)stability, and function. *Journal of Chemical Information and Modeling* **53**, 1007-1015 (2013).
346. Pfleger, C., Radestock, S., Schmidt, E. & Gohlke, H. Global and local indices for characterizing biomolecular flexibility and rigidity. *Journal of Computational Chemistry* **34**, 220-33 (2013).
347. Bidmon, H.J. et al. Glutamine synthetase becomes nitrated and its activity is reduced during repetitive seizure activity in the pentylentetrazole model of epilepsy. *Epilepsia* **49**, 1733-1748 (2008).
348. Ronzio, R.A. & Meister, A. Phosphorylation of methionine sulfoximine by glutamine synthetase. *Proceedings of the National Academy of Sciences of the United States of America* **59**, 164-170 (1968).
349. Chondrogianni, N. et al. Protein damage, repair and proteolysis. *Molecular Aspects of Medicine* **35**, 1-71 (2014).
350. Radi, R. Nitric oxide, oxidants, and protein tyrosine nitration. *Proceedings of the National Academy of Sciences of the United States of America* **101**, 4003-8 (2004).
351. Radi, R. Protein tyrosine nitration: biochemical mechanisms and structural basis of functional effects. *Accounts of Chemical Research* **46**, 550-559 (2013).
352. Souza, J.M., Peluffo, G. & Radi, R. Protein tyrosine nitration - functional alteration or just a biomarker? *Free Radical Biology and Medicine* **45**, 357-366 (2008).
353. Görg, B., Wettstein, M., Metzger, S., Schliess, F. & Häussinger, D. LPS-induced tyrosine nitration of hepatic glutamine synthetase. *Hepatology* **42**, 499-499 (2005).
354. Batthyany, C. et al. Tyrosine-nitrated proteins: proteomic and bioanalytical aspects. *Antioxidants & Redox Signaling* **26**, 313-U83 (2017).
355. Copeland, K.L., Pellock, S.J., Cox, J.R., Cafiero, M.L. & Tschumper, G.S. Examination of Tyrosine/Adenine Stacking Interactions in Protein Complexes. *Journal of Physical Chemistry B* **117**, 14001-14008 (2013).
356. Li, H., Robertson, A.D. & Jensen, J.H. Very fast empirical prediction and rationalization of protein pKa values. *Proteins: Structure, Function, and Bioinformatics* **61**, 704-21 (2005).
357. Simonson, T., Carlsson, J. & Case, D.A. Proton binding to proteins: pK(a) calculations with explicit and implicit solvent models. *Journal of the American Chemical Society* **126**, 4167-4180 (2004).
358. Görg, B. et al. Reversible inhibition of mammalian glutamine synthetase by tyrosine nitration. *Febs Letters* **581**, 84-90 (2007).
359. Ferrer-Sueta, G. et al. Biochemistry of peroxynitrite and protein tyrosine nitration. *Chemical Reviews* **118**, 462-1408 (2018).
360. Pollock, A.S. Intracellular pH of hepatocytes in primary monolayer-culture. *American Journal of Physiology* **246**, F738-F744 (1984).
361. Alvarez-Sieiro, P., Montalban-Lopez, M., Mu, D.D. & Kuipers, O.P. Bacteriocins of lactic acid bacteria: extending the family. *Applied Microbiology and Biotechnology* **100**, 2939-2951 (2016).
362. Fernandez, L., Delgado, S., Herrero, H., Maldonado, A. & Rodriguez, J.M. The bacteriocin nisin, an effective agent for the treatment of staphylococcal mastitis during lactation. *Journal of Human Lactation* **24**, 311-316 (2008).
363. Cao, L., Wu, J., Xie, F., Hu, S. & Mo, Y. Efficacy of nisin in treatment of clinical mastitis in lactating dairy cows. *Journal of Dairy Science* **90**, 3980-3985 (2007).
364. Scannell, A.G.M. et al. Development of bioactive food packaging materials using immobilised bacteriocins Lacticin 3147 and Nisaplin(R). *International Journal of Food Microbiology* **60**, 241-249 (2000).
365. Pei, J.J., Jiang, L., Dai, H.P. & Chen, P. Application of nisin - the well-known lactic acid bacteria bacteriocin - against spoilage bacteria in tangerine wine. *Czech Journal of Food Sciences* **34**, 488-494 (2016).
366. DelvesBroughton, J., Blackburn, P., Evans, R.J. & Hugenholtz, J. Applications of the bacteriocin, nisin. *Antonie Van Leeuwenhoek International Journal of General and Molecular Microbiology* **69**, 193-202 (1996).
367. van Heusden, H.E., de Kruijff, B. & Breukink, E. Lipid II induces a transmembrane orientation of the pore-forming peptide lantibiotic nisin. *Biochemistry* **41**, 12171-12178 (2002).

368. Ariad suspends ponatinib sales. *Cancer Discov* **4**, 6-7 (2014).
369. Wong, S. & Witte, O.N. The BCR-ABL story: bench to bedside and back. *Annual Review of Immunology* **22**, 247-306 (2004).
370. Kurzrock, R., Gutterman, J.U. & Talpaz, M. The molecular-genetics of Philadelphia chromosome positive leukemias. *New England Journal of Medicine* **319**, 990-998 (1988).
371. Greuber, E.K., Smith-Pearson, P., Wang, J. & Pendergast, A.M. Role of ABL family kinases in cancer: from leukaemia to solid tumours. *Nature Reviews Cancer* **13**, 559-571 (2013).
372. Wieczorek, A. & Uharek, L. Management of chronic myeloid leukemia patients resistant to tyrosine kinase inhibitors treatment. *Biomark Insights* **10**, 49-54 (2015).
373. Khajapeer, K.V. & Baskaran, R. Hsp90 inhibitors for the treatment of chronic myeloid leukemia. *Leukemia Research and Treatment* **2015**, 757694 (2015).
374. Tao, W., Chakraborty, S.N., Leng, X., Ma, H. & Arlinghaus, R.B. HSP90 inhibitor AUY922 induces cell death by disruption of the Bcr-Abl, Jak2 and HSP90 signaling network complex in leukemia cells. *Genes & Cancer* **6**, 19-29 (2015).
375. Pelay-Gimeno, M., Glas, A., Koch, O. & Grossmann, T.N. Structure-based design of inhibitors of protein-protein interactions: mimicking peptide binding epitopes. *Angewandte Chemie-International Edition* **54**, 8896-8927 (2015).
376. Metz, A., Ciglia, E. & Gohlke, H. Modulating protein-protein interactions: from structural determinants of binding to druggability prediction to application. *Current Pharmaceutical Design* **18**, 4630-4647 (2012).
377. Scott, D.E., Bayly, A.R., Abell, C. & Skidmore, J. Small molecules, big targets: drug discovery faces the protein-protein interaction challenge. *Nature Reviews Drug Discovery* **15**, 533-550 (2016).
378. Smith, M.C. & Gestwicki, J.E. Features of protein-protein interactions that translate into potent inhibitors: topology, surface area and affinity. *Expert Reviews in Molecular Medicine* **14**(2012).
379. Jones, S. & Thornton, J.M. Principles of protein-protein interactions. *Proceedings of the National Academy of Sciences of the United States of America* **93**, 13-20 (1996).
380. Cheng, A.C. et al. Structure-based maximal affinity model predicts small-molecule druggability. *Nature Biotechnology* **25**, 71-5 (2007).
381. Görg, B. et al. Oxidative stress markers in the brain of patients with cirrhosis and hepatic encephalopathy. *Hepatology* **52**, 256-265 (2010).
382. Schliess, F. et al. Ammonia induces MK-801-sensitive nitration and phosphorylation of protein tyrosine residues in rat astrocytes. *Faseb Journal* **16**, 739-741 (2002).
383. Spanier, L. et al. Design, synthesis, and conformational analysis of trispyrimidonamides as alpha-helix mimetics. *Journal of Organic Chemistry* **79**, 1582-1593 (2014).